AFRL-RZ-WP-TR-2009-2089

PROPULSION AND POWER RAPID RESPONSE RESEARCH AND DEVELOPMENT (R&D) SUPPORT

Delivery Order 0010: Propulsion and Power Student and Faculty Research and Technical Report

Donald B. Hanson

Universal Technology Corporation

JANUARY 2009
Final Report

Approved for public release; distribution unlimited.

See additional restrictions described on inside pages

AIR FORCE RESEARCH LABORATORY
PROPULSION DIRECTORATE
WRIGHT-PATTERSON AIR FORCE BASE, OH 45433-7251
AIR FORCE MATERIEL COMMAND
UNITED STATES AIR FORCE

NOTICE AND SIGNATURE PAGE

Using Government drawings, specifications, or other data included in this document for any purpose other than Government procurement does not in any way obligate the U.S. Government. The fact that the Government formulated or supplied the drawings, specifications, or other data does not license the holder or any other person or corporation; or convey any rights or permission to manufacture, use, or sell any patented invention that may relate to them.

This report was cleared for public release by the USAF 88th Air Base Wing (88 ABW) Public Affairs Office (PAO) and is available to the general public, including foreign nationals. Copies may be obtained from the Defense Technical Information Center (DTIC) (http://www.dtic.mil).

AFRL-RZ-WP-TR-2009-2089 HAS BEEN REVIEWED AND IS APPROVED FOR PUBLICATION IN ACCORDANCE WITH ASSIGNED DISTRIBUTION STATEMENT.

*//Signature//	//Signature//
JOHN HORNER	CURTIS M. REEVES
Assistant to the Chief Scientist	Chief, Plans & Programs Branch

This report is published in the interest of scientific and technical information exchange and its publication does not constitute the Government's approval or disapproval of its ideas or findings.

*Disseminated copies will show "//Signature//" stamped or typed above the signature blocks.

REPORT DOCUMENTATION PAGE

Form Approved
OMB No. 0704-0188

The public reporting burden for this collection of information is estimated to average 1 hour per response, including the time for reviewing instructions, searching existing data sources, searching existing data sources, gathering and maintaining the data needed, and completing and reviewing the collection of information. Send comments regarding this burden estimate or any other aspect of this collection of information, including suggestions for reducing this burden, to Department of Defense, Washington Headquarters Services, Directorate for Information Operations and Reports (0704-0188), 1215 Jefferson Davis Highway, Suite 1204, Arlington, VA 22202-4302. Respondents should be aware that notwithstanding any other provision of law, no person shall be subject to any penalty for failing to comply with a collection of information if it does not display a currently valid OMB control number. **PLEASE DO NOT RETURN YOUR FORM TO THE ABOVE ADDRESS**.

1. REPORT DATE *(DD-MM-YY)*	2. REPORT TYPE	3. DATES COVERED *(From - To)*
January 2009	Final	28 March 2003 – 27 March 2008

4. TITLE AND SUBTITLE
PROPULSION AND POWER RAPID RESPONSE RESEARCH AND DEVELOPMENT (R&D) SUPPORT
Delivery Order 0010: Propulsion and Power Student and Faculty Research and Technical Report

5a. CONTRACT NUMBER
F33615-02-D-2299-0010

5b. GRANT NUMBER

5c. PROGRAM ELEMENT NUMBER
62203F

6. AUTHOR(S)
Donald B. Hanson

5d. PROJECT NUMBER
06WP

5e. TASK NUMBER
T0

5f. WORK UNIT NUMBER
06WPUT01

7. PERFORMING ORGANIZATION NAME(S) AND ADDRESS(ES)

Universal Technology Corporation
1270 N. Fairfield Road
Dayton, OH 45432-2600

8. PERFORMING ORGANIZATION REPORT NUMBER

9. SPONSORING/MONITORING AGENCY NAME(S) AND ADDRESS(ES)

Air Force Research Laboratory
Propulsion Directorate
Wright-Patterson Air Force Base, OH 45433-7251
Air Force Materiel Command
United States Air Force

10. SPONSORING/MONITORING AGENCY ACRONYM(S)
AFRL/RZOP

11. SPONSORING/MONITORING AGENCY REPORT NUMBER(S)
AFRL-RZ-WP-TR-2009-2089

12. DISTRIBUTION/AVAILABILITY STATEMENT
Approved for public release; distribution unlimited.

13. SUPPLEMENTARY NOTES
PAO Case Number: 88ABW-2009-1162; Clearance Date: 23 March 2009.

14. ABSTRACT
Research was conducted for the Propulsion Directorate's research and development efforts. A variety of technical tasks and operating procedures involving assembly, installation, and operation of test articles and equipment were performed. Proper maintenance and functioning of R&D instrumentation and equipment were accomplished and experiments in a variety of technical areas including turbine engines, hypersonics, and aerospace power were observed/conducted. Basic practical engineering and scientific principles were applied and routine analyses of standard data and other information using formulas and data acquisition systems were performed. The information was transferred/reported via reports, graphs, diagrams, charts, and tables, as appropriate.

15. SUBJECT TERMS

16. SECURITY CLASSIFICATION OF:			17. LIMITATION OF ABSTRACT:	18. NUMBER OF PAGES	19a. NAME OF RESPONSIBLE PERSON (Monitor)
a. REPORT	b. ABSTRACT	c. THIS PAGE			John Horner
Unclassified	Unclassified	Unclassified	SAR	608	19b. TELEPHONE NUMBER *(Include Area Code)* (937) 255-6710

Standard Form 298 (Rev. 8-98)
Prescribed by ANSI Std. Z39-18

TABLE OF CONTENTS

Section **Page**

1.0 SUMMARY 1

2.0 INTRODUCTION 2

3.0 DISCUSSION 3

APPENDIX A
Trailing Edge Geometry Influences of Transonic IGV/Rotor Interactions 16

APPENDIX B
Use of Room-Temperature Ionic Liquids as Electrolytes for Ethanol Based Fuel Cells 34

APPENDIX C
Development of an Transient Infrared Technique for Film Cooling Measurements 38

APPENDIX D
A Frequency Response Analysis of Thermocouples in a Shock Tube Environment 55

APPENDIX E
Pinning Force and U_0 in YBCO Thin Film Conductors With and Without
Artificial 211 Inclusions 67

APPENDIX F
Characterization of the Thin Film High Temperature Superconductors 103

APPENDIX G
Test Equipment Data Package for the Microgravity Spray Cooling Experiment 109

APPENDIX H
AC Loss and Pinning in YBCO and Coated Conductors 195

APPENDIX I
A New Energy Approach for High Cycle Axial and Bending Fatigue Life Prediction 268

APPENDIX J
Electric-Field-Induced Flame Speed Modification 300

APPENDIX K
Numerical Modeling of Spray Cooling Phenomena for Thermal Management of
High Power Systems 316

APPENDIX L
H.T.V. Using an ArF Excimer Laser 342

APPENDIX M
Behavior of an RF-Pulsed, Inductively Coupled Argon Plasma....351

APPENDIX N
Fuel Cell Study....352

APPENDIX O
Simulation Software Technology for Turbine Engine Research in Engine Controls and Health Management....356

APPENDIX P
Electric-Pressure-Initiated Instabilities in Premixed Propane-Air Flames....376

APPENDIX Q
Measurements (B* and J-B Characteristics) for Various YBCO Samples – Pinning Strength Results....384

APPENDIX R
Scalar Filtered Density Function for Improving Large Eddy Simulation....426

APPENDIX S
Design and Development of a High Temperature DC-DC Power Converter Utilizing SiC Power Devices....427

APPENDIX T
Pinning Properties of YBCO Samples Pinned With Various Methods of Addition....446

APPENDIX U
Electrical Control of the Thermodiffusive Instability in Pre-Mixed Propane-Air Flames....468

APPENDIX V
Increasing the Performance and Reliability of Ceramic Fuel Cells....486

APPENDIX W
Dynamic Plastic Modeling of Fatigue Failure in Bearings....488

APPENDIX X
An Energy-Based Fatigue Life Prediction Methods for Objects Under Multi-Axial Loading....497

APPENDIX Y
Initial Resistance Measurements – Sample TJ1959 – $SrRuO_3$ Doped....523

APPENDIX Z
Microwave Enhanced Combustion....538

APPENDIX AA
Three-Dimensional Quench Simulation and Protection in HTS Devices....543

1.0 SUMMARY

This Task Order was initiated to provide technical support to AFRL/RZTS from 7 May 2003 through 27 November 2008 to conduct research for the Propulsion Directorate's Research and Development efforts. The requirements were as follows:

1.1 REQUIREMENTS

The Statement of Work specified that the contractor shall conduct research for the Propulsion Directorate's research and development efforts. The contractor shall perform a variety of technical tasks and operating procedures involving assembly, installation, and operation of test articles and equipment. The contractor shall ensure proper maintenance and functioning of R&D instrumentation and equipment and observe/conduct experiments in a variety of technical areas including turbine engines, hypersonics, and aerospace power. The contractor shall apply basic practical engineering and scientific principles, and perform routine analyses of standard data and other information using formulas and data acquisition systems. The contractor shall transfer/report the information via reports, graphs, diagrams, charts, and tables, as appropriate.

2.0 INTRODUCTION

Under Prime Contract F33615-02-D-2299, Task Order 0010 was initiated to provide technical support to AFRL/RZ to conduct research for the Propulsion Directorate's Research and Development efforts from 7 May 2003 through 27 November 2008.

3.0 DISCUSSION

The overall objective of this task was to conduct research for the Propulsion Directorate's research and development efforts. A variety of technical tasks and operating procedures involving assembly, installation, and operation of test articles and equipment were performed. Proper maintenance and functioning of R&D instrumentation and equipment were accomplished and experiments in a variety of technical areas including turbine engines, hypersonics, and aerospace power were observed/conducted. Basic practical engineering and scientific principles were applied and routine analyses of standard data and other information using formulas and data acquisition systems were performed. The information was transferred/reported via reports, graphs, diagrams, charts, and tables, as appropriate.

The effort was accomplished by subcontracts with various individuals and institutions.

Subcontracted Efforts

0010-01-C1

Trailing Edge Geometry Influences on Transonic IGV/Rotor Interactions

From 14 May 03 – 14 Aug 03, technical support was provided to AFRL/RZTF with research efforts involving trailing edge geometry influences on transonic IGV/rotor interactions.

This Task is complete and a Final Report was submitted to AFRL/RZTF for review and comment. (See Appendix A)

0010-01-C2

Use of Room-Temperature Ionic Liquids as Electrolytes for Ethanol-Based Fuel Cells

From 15 May03 – 18 Jul 03, technical support was provided to AFRL/RZPS with research efforts involving the use of various room-temperature ionic liquids as electrolytes for electro-oxidation of ethanol to be used for direct fuel cells.

This Task is complete and a Final Report was submitted to AFRL/RZPS for review and comment. (See Appendix B)

0010-01-C3

Performance Evaluation of an IGBT-Based Inverter for Potential Space Application

From 27 May 03 – 29 Aug 03, technical support was provided to AFRL/RZPE with research efforts involving radiation testing and performance evaluation of IGBT-based inverters for potential space application.

0010-01-C4

Turbine Cooling and Heat Transfer

From 2 Jun 03 – 22 Aug 03, technical support was provided to AFRL/RZT with research efforts involving the use of film cooling as a cooling technique for hot components in gas turbine engines.

This Task is complete and a Final Report was submitted to AFRL/RZT for review and comment. (See Appendix C)

0010-01-C5

Turbine Cooling and Heat Transfer

From 2 Jun 03 – 15 Aug 03, technical support was provided to AFRL/RZT with research efforts involving the use of film cooling as a cooling technique for hot components in gas turbine engines.

This Task is complete and a Final Report was submitted to AFRL/RZT for review and comment. (See Appendix D)

0010-01-C6

Physics and Materials Science of Superconducting Materials

From 2 Jun 03 – 5 Sep 03, technical support was provided to AFRL/RZPG with research efforts involving pinning and AC loss in superconducting YBCO.

This Task is complete and a Final Report was submitted to AFRL/RZPG for review and comment. (See Appendix E)

0010-01-C7

High Cycle Fatigue

From 16 Jun 03 – 19 Sep 03. technical support was provided to AFRL/RZTS with research efforts involving High Cycle Fatigue (HCF) as it relates to gas turbine engines.

0010-01-C8

Characterization of Thin Films and Interfaces

From 16 Jun 03 – 19 Sep 03, technical support was provided to AFRL/RZPG with investigative research efforts involving correlations between interfacial chemistry, microstructure and electrical properties of high temperature superconducting films.

This Task is complete and a Final Report was submitted to AFRL/RZPG for review and comment. (See Appendix F)

0010-01-C9

Microgravity Thermophysics Research for High Power Systems

From 15 May 04 – 07 Aug 04, technical support was provided to AFRL/RZPS with research efforts involving microgravity thermophysics for high power systems.

This Task is complete and a Final Report was submitted to AFRL/RZPS for review and comment. (See Appendix G)

0010-01-C10

Microgravity Thermophysics Research for High Power Systems

From 31 May 04 – 25 Aug 04, technical support was provided to AFRL/RZPS with research efforts involving microgravity thermophysics for high power systems.

This Task is complete and a Final Report was submitted to AFRL/RZPS for review and comment. (See Appendix G)

0010-01-C11

Fundamental Steps of Ethanol Electrocatalytic Oxidation on Pt Electrodes in $HClO_4/H_2O$ and Ionic Liquids of Importance in Ethanol-Based Fuel Cells

From 10 May 04 – 5 Aug 04, technical support was provided to AFRL/RZPS with research efforts involving the fundamental steps of ethanol electrocatalytic oxidation on Pt electrodes in $HClO_4/H_2O$ and ionic liquids of importance in ethanol-based fuel Cells.

0010-01-C12

Magnetic J_c & Associated Pinning in YBCO Coated Conductors w/ 211 Enhanced Pinning

From 1 Jun 04 – 15 Sep 04, technical support was provided to AFRLRZPG with research efforts involving magnetic J_c and associated pinning in YBCO coated conductors with 211 enhanced pinning.

This Task is complete and a Final Report was submitted to AFRL/RZPG for review and comment. (See Appendix H)

0010-01-C13

Developing an Improved Multi-Axial High Cycle Fatigue Criterion

From 17 May 04 – 13 Aug 04, technical support was provided to AFRL/RZTS with research efforts involving the development of an improved multi-axial high cycle fatigue criterion.

This Task is complete and a Final Report was submitted to AFRL/RZTS for review and comment. (See Appendix I)

0010-01-C14

Experimental Study of Electric-Field-Induced Modifications of Pre-Mixed Hydrocarbon-Air Flame Reaction Zones

From 17 May 04 – 9 Aug 04, technical support was provided to AFRL/RZPE with an experimental study involving electric-field-induced modifications of pre-mixed hydrocarbon-air flame reaction zones.

This Task is complete and a Final Report was submitted to AFRL/RZPE for review and comment. (See Appendix J)

0010-01-C15

Numerical Modeling of Spray Cooling Phenomena for Thermal Management of High Power Systems

From 24 May 04 – 16 Aug 04, technical support was provided to RZPS with research efforts involving the numerical modeling of spray cooling phenomena for thermal management of high power systems.

This Task is complete and a Final Report was submitted to AFRL/RZPS for review and comment. (See Appendix K)

0010-01-C16

Application of Hydroxyl Flow Tagging Velocimetry and Linewise Raman to Scramjet Flows

From 17 May 04 – 20 Aug 04, technical support was provided to AFRL/RZAS with research efforts involving the application of hydroxyl flow tagging velocimetry and linewise raman to scramjet flows.

This Task is complete and a Final Report was submitted to AFRL/RZAS for review and comment. (See Appendix L)

0010-01-C17

Application of Hydroxyl Flow Tagging and Line Raman to Hypersonic Propulsion Flows

From 24 May 04 – 16 Sep 04, technical support was provided to AFRL/RZAS with research efforts involving the application of hydroxyl flow tagging and line raman to hypersonic propulsion flows.

0010-01-C18

Technical Support to AFRL/RZPG with Research Efforts Involving Power Generation

From 10 May 04 – 20 Aug 04, technical support was provided to AFRL/RZPG with research efforts involving power generation.

This Task is complete and a Final Report was submitted to AFRL/RZAS for review and comment. (See Appendix M)

0010-01-C19

Technical Support to AFRL/RZPS with Research Efforts Involving Energy Storage & Thermal Science

From 19 May 04 – 6 Aug 04, technical support was provided to AFRL/RZPS with research efforts involving energy storage and thermal science.

This Task is complete and a Final Report was submitted to AFRL/RZPS for review and comment. (See Appendix N)

0010-01-C20

Technical Support to AFRL/RZTM with Research Efforts Involving Mechanical Systems

From 19 May 04 – 11 Aug 04, technical support was provided to AFRL/RZTM with research efforts involving mechanical systems.

0010-01-C21

Research in Gas Turbine Engine Health Monitoring and Management

From 1 Jun 04 – 22 Aug 04, technical support was provided to AFRL/RZTS with research efforts involving gas turbine engine health monitoring and management. This research included simulation studies and engine modeling at the Intelligent Controls Facility (ICF). The following objectives were accomplished:

1. Surveyed current techniques for engine health monitoring for gas turbine engines and compared and contrasted these techniques with those used for monitoring performance in the civilian aviation industry.
2. Compared engine performance data collected during flight operations in civil aircraft with data collected from tests in the ICF and resolved any differences observed.
3. Developed engine operating lifetime performance models based on test data and explored ways to automate the trend analysis used for health monitoring.
4. Used the ICF to develop, simulate, and test models for engine operational events that reduced the expected lifetime of gas turbine engines.
5. Explored the feasibility of the use of traditional and novel methods for gas turbine engine health monitoring techniques to engines of interest to the Air Force; and explored possible improvements for and tested these techniques in the ICF.

Developed novel techniques in engine health management that included the use of intelligent control and modeling in Matlab/Simulink/Stateflow/Real-Time workshop.

This Task is complete and a Final Report was submitted to AFRL/RZTS for review and comment. (See Appendix O)

0010-01-C22

Technical and Programmatic Support to AFRL/RZTS

From 21 Jun 04 – 30 Jun 04, technical support was provided to AFRL/RZTS with research efforts involving the structures and controls areas of turbine engines. This support involved the following three tasks:

1. Provided technical and programmatic support to project engineers working the application of advanced materials to turbine engine components. Specifically, design, analysis, and manufacturing of composite components for high strength and weight reduction.
    a. Provided assistance in conducting literature searches and documenting the findings of efforts in composite components over the last 10 years, in the areas of Polymeric Matrix Composites, Ceramic Matrix Composites, and Metal Matrix Composites.

b. Performed job shadowing to several technical meetings.

2. Provided technical and administrative support in the preparation of a training document for engineering new hires in the Structures Group.
    a. Reviewed the document, asked questions, provided comments, and helped to consolidate and finalize the training document into its final form.
    b. Provided beneficial input to its structure and content.
3. Provided technical and administrative support to the Structures Group.
    a. Provided programming support to the Structural Analysis Group, testing set-up support in the Turbine Engine Fatigue Facility, obtaining data and/or programmatic information, and helping to generate PowerPoint slides for an important briefing, as needed.

0010-01-C23

Experimental Investigation of the Electric Pressure Effect on Pre-mixed Hydrocarbon-Air Flames

From 27 Jun 05 – 21 Aug 05, technical support was provided to AFRL/RZPE with an experimental investigation of the effects of continuous and pulsed DC electric fields on pre-mixed hydrocarbon/air flames.

This Task is complete and a Final Report was submitted to AFRL/RZPE for review and comment. (See Appendix P)

0010-01-C24

Flux pinning and AC loss in YBCO

From 1 Jun 05 – 30 Sep 05, technical support was provided to AFRL/RZPG with on-going research efforts associated with YBCO coated conductor development. More specifically, this support shall involve studies in flux pinning enhancement and also AC loss reduction.

This Task is complete and a Final Report was submitted to AFRL/RZPG for review and comment. (See Appendix Q)

0010-01-C25

Reactions of Metal Carbides with Lubricant Esters and Additives--Investigation of Changes in the Structure of the Metal Carbide

From 16 May 05 – 29 Jul 05, technical support was provided to AFRL/RZTM with a study involving the reactions of ester-based lubricants and phosphate esters, alone and in combinations in the presence of metal carbides. Particular attention was paid to changes in the metal carbide that occurred on contact with the lubricant and additive.

0010-01-C26 - Canceled

0010-01-C27

Experimental Study of Subgrid-Scale Filtered Density Function in Three-Stream Mixing To Improve Large Eddy Simulation of Turbulent Flames

From 1 Jun 05 – 21 Aug 05, technical support was provided to AFRL/ RZAS with an experimental study involving subgrid-scale filtered density function in three-stream mixing to improve Large Eddy Simulation of turbulent flames.

This Task is complete and a Final Report was submitted to AFRL/RZAS for review and comment. (See Appendix R)

0010-01-C28 - Canceled

0010-01-C29

Development of a Direct-Writing Process for Functional Grading of Solid Oxide Fuel Cell Layers

From 5 Jun 06 – 27 Aug 06, technical support was provided to AFRL/ RZPS with the development of a direct-writing process for functional grading of Solid Oxide Fuel Cell (SOFC) layers.

0010-01-C30

Design and Development of a High Temperature DC-DC Power Converter Utilizing SiC Power Devices

From 12 Jun 06 – 20 Aug 06, technical support was provided to AFRL/RZPE with research efforts involving the design and development of a high temperature DC-DC power converter utilizing SiC power devices. This support involved the following tasks—

- Finalized the converter electrical specifications.
- Completed the power stage design, including the selection of capacitors and power semi-conductor switches.
- Implemented the JFET driver circuit.
- Implemented and tested the open-loop version of the power converter integrating JFET driver and PWM control circuits.
- Studied the voltage regulation capability against load and input voltage variations.
- Implemented and tested the closed-loop control of the converter.
- Recorded the converter performance characteristics.
- Implemented the design changes to improve the steady-state and transient performance of the power converter.

Prepared technical documentation and a final report for the overall project.

This Task is complete and a Final Report was submitted to AFRL/RZPE for review and comment. (See Appendix S)

0010-01-C31

Experimental Study of Scalar Filtered Joint Density Function in Three-Stream mixing for Improving Large Eddy Simulation of Turbulent Combustion

From 1 Jun 06 – 28 Jul 06, technical support was provided to AFRL/RZAS with an experimental study involving the scalar filtered joint density function in three-stream mixing for improving large eddy simulation of turbulent combustion.

0010-01-C32

YBCO Coated Conductor Developmental Research

From 30 May 06 – 25 Aug 06, technical support was provided to AFRL/RZPG with research efforts involving YBCO coated conductor development; specifically, flux pinning enhancement and AC loss reduction.

This Task is complete and a Final Report was submitted to AFRL/RZPG for review and comment. (See Appendix T)

0010-01-C33

Experimental Investigation of the Role of CH Radicals in the Electric Pressure Effect on Pre-Mixed Hydrocarbon-Air Flames

From 26 Jun 06 – 20 Aug 06, technical support was provided to AFRL/RZPE with an experimental study involving the effects of continuous and pulsed DC electric fields on pre-mixed hydrocarbon/air flames.

This Task is complete and a Final Report was submitted to AFRL/RZPE for review and comment. (See Appendix U)

0010-01-C34

The Interaction of Chromium in Stainless Steel with Phosphate Esters and the Effects of Heat Treatment on the Surface Properties of Stainless Steels

From 22 May 06 – 31 Jul 06, technical support was provided to AFRL/RZTM with a study involving the interaction of Chromium in Stainless Steel with Phosphate Esters and the effect that heat treatment has on the surface properties of Stainless Steels. Specifically, this study addressed the following two objectives—

1. To understand the changes in lubricant-additive combinations that are needed when high chromium alloys are used for turbine engine bearing materials by gaining a better understanding of the surface interactions present in stainless steels and carburized stainless steels.
2. To determine the changes introduced when steels are heat treated and carburized.

To accomplish these objectives, the overall effort was divided into the following tasks—

- Conduct sealed tube tests and flowing gas tests on 440C stainless steel Pyrowear 675 samples with lubricant esters and phosphate ester model compounds at temperatures in the range of 300-350°C.
- Analyze volatiles by GC/MS to determine conditions where reaction occurs.

- Conduct analysis of reacted stainless steel and Pyrowear samples using FT-IR microscopy, scanning electron microscopy, XPS and Auger.
- Conduct Raman analysis of samples.
- Submit presentation abstracts for national and regional meetings.
- Complete any remaining experiments necessary to prepare manuscript and final reports.
- Prepare written reports and manuscript for publication.

0010-01-C35

Increasing the Performance and Reliability of Ceramic Fuel Cells

From 30 Apr 08 – 1 Sep 08, technical support was provided to AFRL/RZPS to examine methods for significantly increasing the performance and reliability of ceramic fuel cells through modification and gradation of thin interfacial layers. The technical plan was well established and appeared to extend an existing effort toward more fundamental objectives. A clear technical plan was presented which appeared to be achievable during the proposed duration of study (12 months). All equipment was in place and was used for related studies in this area. This effort also leveraged a strong and established teaming arrangement between two small businesses (Optomec and Xradia) and Wright State University. The objectives of the study were realistic and provided considerable insight into pertinent topics in interfacial electrochemistry. Additionally, given that the approach impacted a ubiquitous issue in thin film electronics, balancing dissimilar material properties, it appeared as though successes in this project could be more widespread. The research was innovative in the approach and was based upon well established concepts in colloidal chemistry, direct write, and thin film deposition.

This Task is complete and a Final Report was submitted to AFRL/RZPS for review and comment. (See Appendix V)

0010-01-C36

Radio Frequency Inductively Coupled Plasma

From 1 May 08 – 10 Aug 08, technical support was provided to AFRL/RZPE with research in Radio Frequency Inductively Coupled Plasma (RF-ICP). In the previous year, research was done on the effects of ICP discharges with Oxygen gas. From these results, a method was derived to affect the ICP Discharge through altering the initial conditions of the plasma thus affecting its plasma density.

0010-01-C37

Ball Bearing Raceway Fatigue Spall Propagation

From 9 May 08 – 5 Aug 08, technical support was provided to AFRL/RZTM with research efforts involving ball bearing raceway fatigue spall propagation.

This Task is complete and a Final Report was submitted to AFRL/RZTM for review and comment. (See Appendix W)

0010-01-C38

Applied Superconductivity

From 29 May 08 – 26 Aug 08, technical support was provided to AFRL/RZPG with research efforts involving superconductivity and propogation models for conductors.

0010-01-C39

Analysis ofHigh Performance Combustors for Military Gas Turbine Engines

From 16 May 08 – 25 Aug 08, technical support was provided to AFRL/RZTC with prediction of the performance, pattern factor, heat loads and optimization in high pressure combustion systems and augmentors, leading to improved design.

Specific Objectives: Simulations of high-pressure spray combustion were carried out to determine the behavior of fuel sprays in advanced military engine combustors. High pressure spray combustion was not well understood and experiments suggested that high-pressure spray performance is very complex and can also create unacceptable dynamical changes in the flow leading to instability. An accurate predictive capability currently did not exist to address this phenomenon but was critically needed to optimize new military engine designs.

Technical Approach: A design methodology, using Reynolds Averaged Navier-Stokes Solver (RANS) was applied to simulate high fuel-air ratio combustion with sprays under high-pressure conditions. The specific configuration includeed Inter Turbine Burner (ITB) configuration, for which the base line grid was available. It was desirable to include variations in the baseline geometry of this burner, to improve the performance of this combustion system. This included Grid Generation of the design variations in geometry of these combustor Systems and simulating the mixing characteristics of fuel-air in these complex systems. Post processing the obtained mixing flows was carried out to extract pertinent information, in predicting the performance aspects of the incorporated design variations in the ITB. GRIDGEN, FLUENT , Field view and TECPLOT softwares was used during the course of this study.

Technical and Computational Challenges: The project attempted to simulate and study liquid spray combustion in a realistic high-pressure military gas turbine engine using Reynolds Averaged Navier-Stokes Simulations (RANS)and large Eddy Simulation (LES). The grids generated for this configuration were of the order of 1-9 million nodes and thus required ASC/MSRC resources.

0010-01-C40

Energy Based Fatigue Prediction

From 23 May 08 – 27 Aug 08, technical support was provided to AFRL/RZTT with energy based fatigue prediction, previously demonstrated for the room temperature case, into the high temperature turbine environment.

The research involved experimental testing and therefore was subject to technical delays but the proposed work generated an initial data set and analytical prediction in the proposed timeframe.

Accurate lifing and understanding of the physical process of thermo mechanical fatigue was essential for correctly designing and operating modern highly cooled turbine blades. The work aided AFRL's understanding of these issues. The proposed experimental work was conducted utilizing existing equipment at The Ohio State University. The existing equipment was sufficient

to generate a suitable data set, albeit at lower thermal heating rates than would be typical in a gas turbine blade. The heating rate and temperature was sufficient to evaluate the analytical model however. A research activity was established in TMF to creat an experimental capability in RZTS for TMF experimentation with heating and cooling rates that effectively simulate those generated in a gas turbine engine.

This Task is complete and a Final Report was submitted to AFRL/RZTT for review and comment. (See Appendix X)

0010-01-C41

Nanoscale Pinning Centers in the High Temperature Superconductor YBCO

From 31 May 08 – 3 Oct 08, technical support was provided to AFRL/RZPG with research to better understand the pinning mechanism developed by AFRL to improve the current capacity of the YBCO coated conductor. A better understanding of how the pinning center works helped to determine the difference in the character of different pinning center dopants and guide AFRL in making even better educated choices of which pinning material will be best to evaluate.

Since the realization of nanoparticulate pinning, there have been a variety of material used as the nanoparticles with different results. This study was aimed as shedding insight to the different behaviors of the various inclusions. For some pinning types (e.g. 211), the dominant effect is an increase in Fp stemming from the addition of pinning centers. In other samples (e.g., BZO) the main effect was an increase in Birr. For still other pinning additions, in particular BSO, both attributes were present. In the proposal, Birr and Fp enhancements were compared to determine the level of correlation, and also to investigate the influence of pinning addition type on the power law exponent for the field dependence of Jc.

This Task is complete and a Final Report was submitted to AFRL/RZPG for review and comment. (See Appendix Y)

0010-01-C42

Microwave Enhanced Combustion

From 13 Jun 08 – 27 Aug 08, technical support was provided to AFRL/RZAS with research to collaborate with Wright-Patterson Air Force Base to provide several key resources for the advancement of Princeton University's microwave enhanced combustion project. By propagating microwave energy through a resonant cavity, strong electric fields were generated in the combustion region of a flat, premixed methane/air stagnation flame. The interaction with 1.3 kilowatts of 2.45 GHz, continuous wave (CW) microwave power was quantitatively measured to produce a 20% enhancement of the laminar flame speed. Laser diagnostics for flame speed, temperature, and OH concentration provided support to the hypothesis that the microwave energy accelerated chemical processes to create the observed enhancements in the CW system. The strong coupling effect was applicable to the engine configurations of scramjets, turbines, and even pulse detonation systems. Any move toward a practical, integrated microwave-enhanced combustion device required an efficient and compact system that generated performance boosts that outweigh the cost of added the power requirements.

Preliminary work at Princeton with a 30 watt average power, 0.1% duty cycle pulsed magnetron showed an enhancement of the premixed, laminar methane-air flame on par with that generated by the CW magnetron. Operating at roughly 40 times less power than the CW system, the pulsed

microwave flame speed concept has the added potential to operate in conjunction with the pulsed microwave ignition and flow control devices being pursued throughout hypersonic research. This more efficient pulsed microwave configuration required the same exhaustive experimental analysis performed on the CW magnetron system.

The measurements wereconducted in the order listed and a new set of experiments with an evanescent microwave system were considered. The pulsed microwave research has several variables that were parametrically studied throughout all diagnostics. The effects of pulse power, duty cycle, and repetition rate on the flame enhancement were measured over the course of the summer program toward the end goal of designing an optimal configuration for the potential deployment of an advanced microwave enhanced combustion system into a scramjet engine.

The results from work at Wright-Patterson provided the final, conclusive experimental dataset for pulsed and CW microwave experiments. These measurements were essential for the simulation under development. The data collected under this summer fellowship provided insight into the interesting phenomenon for the researchers and the plasma assisted combustion community. More importantly, the scientific collaboration provided this very fundamentals-based experiment with the stimulus needed to be incorporated into a practical combusting environment.

This Task is complete and a Final Report was submitted to AFRL/RZAS for review and comment. (See Appendix Z)

0010-03-C1

TRF Support to AFRL/RZT

From 1 Aug 05 – 31 Oct 05, technical support was provided to AFRL/RZT in the following areas.

Task 1:

Review of the exiting temperature and pressure measurement instrumentation at the TRF and recommend improvements where needed to increase the accuracy of the aerodynamic performance and low Re wake loss measurements. Provide a) detailed construction drawings for the instruments, b) technical advice and assistance in their construction, c) technical recommendations on the accuracy/stability of the requisite signal conditioning and data acquisition components, d) technical advice and assistance on the calibration system for the temperature instrumentation.

Task 2:

Address issues and recommend techniques to alleviate the adverse start-up transients for film cooled experiments in the TRF.

0010-06-C1

Three-Dimensional Quench Simulation and Protection in HTS Devices

From 1 Jan 07 – 30 Apr 08, technical support was provided to AFRL/RZP with the development of a quench analysis code capable of addressing quench performance and protection of HTS coils. Specifically, this effort will encompassed the first three tasks of a proposed multi-task effort. These tasks are defined as follows—

Task 1:

Evaluate alternatives to proceed with model development, and reach a decision on what platform is best suited for a 3D model of HTS devices. In particular, assess alternatives for FEM codes that could be employed. At least the following platforms will be evaluated: Ansoft/Maxwell, Flux3D, Ansys, Vector Fields/Opera, and CERN's modified SABER. Establish the requirements and criteria to be used in the selection. Determine, in consultation with Air Force personnel, which one represents the best option to proceed with quench model development or if in-house simulation tool needs to be developed (Completed by Month 3)

Task 2:

Electrical, thermal and mechanical characterization of HTS conductors and other coil materials, including insulation and dielectrics as well as their interactions due to their different properties (thermal expansion, etc.) through collaboration with Prof. Schwartz group, interaction with conductor manufacturers or/and literature search. (Completed by Month 5)

Task 3:

Develop a combined thermal/electrodynamic 3D model of a quenching HTS tape including all pertinent material property models. Simulations will be validated using experimental data. This task will include collaboration with Dr. Breschi. (Completed by Month 12)

This Task is complete and a Final Report was submitted to AFRL/RZP for review and comment. (See Appendix AA)

APPENDIX A

Air Force Contract #: F33615-02-D-2299
Propulsion Directorate Rapid Response R&D Final Report
Summer 2003

Trailing Edge Geometry Influences of Transonic IGV/Rotor Interactions

by

Robert Darbe
School of Mechanical and Aerospace Engineering
Oklahoma State University
Stillwater, OK 74078
Tel: (405) 744-4638
E-Mail: darbe@okstate.edu

Host Advisor:
Steven Gorrell
Air Force Research Laboratory
Wright Patterson AFB, OH

Tenure: 14 May 2003 to 14 August 2003

Submitted 14 August 2003 to:
Universal Technology Corporation
and Host Advisor

ABSTRACT

Work accomplished under the Air Force contract number F33615-02-D-2299, funded by the Air Force Research Laboratory Propulsion Directorate (AFRL/PRTF), is covered in this report. The goal was to investigate vane trailing edge geometry on unsteady vane/blade interactions that would be found in an embedded compressor stage. These interactions were investigated using the computational algorithm, Fluent. This report details developments occurring prior to this contract as well as the accomplishments made during the summer of 2003 work. Prior developments included building computational grids with Gambit. All progress made under this contract is reported in a descriptive manor. The current progress includes the construction of computational grids, representing the Stage Matching Investigation experiments, with Gridgen. The process of exporting these grids and running Fluent steady and unsteady simulations is detailed. Any obstacles that had to be overcome in running Fluent to observe vane/blade interactions are well documented. Steady state results for the blunt far and near case are presented. Unfortunately, time ran out before the accompanying unsteady simulations were fully converged. Nonetheless, the setup is detailed.

TABLE OF CONTENTS

Abstract i
Table of contents ii
List of Tables ii
List of Figures ii
1.0 Introduction 1
2.0 Prior Developments with Gambit and Fluent 2
2.1. Gambit Grid Generation Process 2
2.2. Fluent Simulation Process 3
2.3. Summary of Prior Developments 3
3.0 Current Developments with Gridgen 4
3.1. Gridgen Development Process 4
4.0 Current Developments with Fluent 8
4.1. Grid Manipulation 8
4.2. Using Fluent for a Steady State Simulation 9
4.3. Steady State Results 10
4.4. Using Fluent for an Unsteady Simulation 12
5.0 Current Developments with APG and MSU-Turbo 14
6.0 Summary 14
7.0 Future Work 14
8.0 References 14
Acknowledgements 15

LIST OF TABLES

Table 1 - Dimensions and Distributions for the Rotor 6
Table 2 - Dimensions and Distributions for the Vane at Near Axial Spacing 6
Table 3 - Dimensions and Distributions for the Vane at Far Axial Spacing 6
Table 4 - Elliptical Smoother Attributes for Edges Away from Blade 7
Table 5 - Elliptical Smoother Attributes for the Edges Close to the Blade 7
Table 6 - Fluent Parameters used for the Steady Simulation 9
Table 7 - Boundary Conditions used for the Steady State Simulation 10
Table 8 - Fluent Parameters used for the Unsteady Simulation 13
Table 9 - Boundary Conditions used for the Unsteady Simulation 13

LIST OF FIGURES

Figure 1 - Static Pressure (lb/ft2) Results for the Blunt Far Steady State Simulation at 75% Span 11
Figure 2 - Static Pressure (lb/ft2) Results for the Blunt Near Steady State Simulation at 75% Span 11

1.0 INTRODUCTION

The current trends in aircraft engine design are to increase the thrust to weight ratio and reduce the amount of fuel consumption. These trends are applied to the compressor by increasing airfoil loading, minimizing the space between blade rows, reducing the number of stages, and increasing stage efficiencies. As a result, advanced compressors designs generally feature thin low-aspect ratio airfoils that are highly susceptible to flow induced vibrations thus leading to high cycle fatigue (HCF) [10]. One source for such HCF is the unsteady interactions that occur between a stationary vane and rotating blade.

Vane/blade unsteady aerodynamic interactions are typically attributed to two primary sources: vortical wakes, developed by viscous fluid-structure interactions, and inviscid potential disturbances, such as rotor bow shocks [2]. It is known that the potential disturbances propagate upstream at acoustic speeds directly affecting the trailing edge of an upstream vane.

In an attempt to understand the rearward forcing of a compressor vane row; several experiments have been conducted were surface pressure data is taken on an upstream vane, references [2] through [10]. Koch et all [7], Probasco et al. [9], and Gorrell et al. [3] presented static pressure measurements made on a wake generating IGV row with no camber. The wake generator is part of the Stage Matching Investigation (SMI) rig located at Wright Patterson Air Force Base (WPAFB) Compressor Aero Research Laboratory (CARL). The wake generator is characterized by a small leading edge and blunt trailing edge geometry. The blunt trailing edge was designed with the intent of creating a wake typically found in a modern embedded compressor stage. However, the wake is produced by a large base drag that is turbulent with no swirl. It is theorized that the thick trailing edge may not represent actual embedded blade row interactions in total.

In response, there is an effort to determine if similar changes in vane trailing edge loading, as documented in Reference [7], will occur with a wake generator that is characterized by a thinner trailing edge. To accomplish this, a new wake generator was designed with a thinner trailing edge and a high camber that will produce a wake from diffusion instead of base drag.

For the remainder of this paper the thick trailing edge vane will be referred to as the blunt vane, the highly cambered sharp trailing edge vane as the sharp vane.

The present investigation attempts to address the question of trailing edge geometry effects on unsteady vane/blade interactions through computational analysis. Computational fluid dynamics (CFD) is preformed on the SMI rig with both the blunt vane and the sharp vane at two axial spacings, denoted as near and far.

This paper consists of three main sections. The first details prior developments in building a computational mesh with Gambit and trying to run a simulation in Fluent. This work was completed before starting the present research. The second section details the process of developing the grids with Gridgen. It is written in a manor such that the reader can understand the process in developing a grid representing a vane/blade configuration. There is enough detail that the grids can be reproduced exactly. The third section discusses the Fluent setup process, as well as gives some steady state results for the blunt vane case. Although unsteady simulations were not completed at this time, this paper makes as a good guide to understanding the process being used to obtain these simulations. A future work section is included describing the work that will be done following this summers achievements. Included, is the continuation of the unsteady simulations.

2.0 PRIOR DEVELOPMENTS WITH GAMBIT AND FLUENT

Some relevant work had been completed prior to starting the current summer efforts. Most significantly, 3D models where developed in Gambit, a CAD and grid generating preprocessor from Fluent, Inc. The first attempt was to model the SMI configuration with the vane/blade ratio of 24:33. This would allow CFD simulations to be performed at the same vane/blade periodicity as previous experiments conducted by reference [3] and [7]. In order for an accurate model to be developed for importing into Fluent, the grid had to consist of 8 vanes and 11 blades. This large grid is attributed to the fact that Fluent does not support phase-lag boundary conditions. As such, the vane/blade count of 8:11 was developed by modifying 3D grids previously developed by reference [1]. These grids were proven to be too large and therefore, never used in a simulation. However, a description of the grid development process is provided below to assist future users of Gambit trying to develop similar models.

2.1. Gambit Grid Generation Process

For the case described here, Gambit 2.0 was executed on svw10.asc.hpc.mil and x emulated to any computer terminal with the command:

Gambit –id *filename.dbs* –dev x11

This section attempts to give a brief overview on how Gambit was used to create a grid for the fore mentioned simulations. In doing so, the process for developing a mesh to represent a stage of compression will be presented as well as any shortcomings involved. The rotor geometry developed by Falk (summer 02) was used. Therefore, the process of developing the vane and adding it to the preexisting rotor file is covered. All commands as found in the application are denoted by italics.

The Process of developing the physical geometry for the SMI in Gambit was extensive. Gambit essentially builds the geometry as any CAD program then the grid is constructed on top of the preexisting geometry. Therefore, any geometrical changes made will result in deleting the previous grid and starting at the CAD level of development. This was found to be very frustrating. The ability to smooth the grid to eliminate mesh skewness was never explored. As such, all mesh changes were made through geometric changes leading to the extremely long time for grid development in Gambit.

The original geometry describing the SMI rig comes in the form of (X,Y,Z) points in Cartesian coordinates. In Gambit's terminology, these are called vortices, which are easily imported into Gambit using the *import/ vortex data* command. Using the appropriate defining points, the hub line was defined with the *geometry/ edge/ nurbs* command and the vane surface is defined with the *geometry/ face/ vertex rows* command. Note however, that it was found to work best when two faces were developed to define the vane, one for the upper and one for the lower surface. The two faces shared vortices on the leading and trailing edge.

The only constraining data gambit utilizes are the hub and case profile developed from the imported vortices plus the vortices that make up the vane and blade faces. Beyond this, all geometrical properties rely on Gambits ability to manipulate geometry in a comparable manor as a CAD program would. In this case, the hub and case profiles were revolved into faces. Faces were then constructed from scratch at the inlet to the vane and at the axisymmetric periodic plane locations. The inlet to the rotor was copied for use as the outlet to the vane. All these faces were combined into a volume using the *geometry/ volume/ stitch faces* command. The faces defining

the surface of the vane were also made into a volume that was subtracted from the vane fluid volume. Note that the interface between the vane volume and the blade volume had to be duplicated in order to have separated volumes with no linked geometry. Fluent requires two separate volumes with identical faces for an interface, which will eventually be applied at this location.

A problem arose when trying to match the vane outlet with the blade inlet. Somehow, Gambit defines the curved lines as a series of straight lines. It was observed that the straight lines did not match for the two faces, possibly do to tolerances Gambit imposes on CAD manipulation. This mismatch in Geometry led to concern that Fluent would not accept the two faces as an interface.

Despite many obstacles, grids were developed with Gambit. These grids were large (~1 GB) due to the large number of vanes and blades. The files consisted of a number of nodes around 4.5 million. The size was proven to add to the problems in prior development as will be explained below.

2.2. Fluent Simulation Process

Having developed large vane/blade grid files, the next step was to import them into Fluent and begin an iterative simulation. This imposed a problem. The grids were too large to be read on a single processor, but the grid information needed to manually partitioned form a serial solver in order to function properly when running a simulation involving a grid interface. All this resulted in Fluent never completing a single iteration. Fluent's limitations thus attributed to the development of grids with the vane/blade ratio of 24:32 (discussed in the Gridgen sections) in order to minimize the size of the grid files that were to be read by Fluent.

An issue of importance should be discussed here. A possible solution could be to read the initial grid into a serial 64-bit processor for partitioning. This was never attempted. Therefore, it may or may not work. The command to execute Fluent for the mentioned case was:

fluent 3d

A 64-bit processor could have easily been utilized by entering the command:

fluent 3d -64

This was not well understood at the time and never tried.

2.3. Summary of Prior Developments

This section is a summary of the accomplishments completed before the beginning of the work attempted this summer. It explains some of the problems that resulted in some of the actions performed this summer. Thus, it is included to give an understanding as to where progress actually began.

Gambit was utilized in the grid generation for the SMI simulations. It was found that developing a grid with Gambit was very time intensive and often resulted in unsatisfactory grid quality. The biggest issues included Gambits CAD abilities and grid smoothing process. The geometry was seen to have discrepancies, but it was never determined how this would effect the final simulation. The grid smoothing was never looked into. Mainly because in was not covered in detail in the tutorials and the functionality of grid smoothing was not known at this time. Despite the problems, extremely large grids where produced.

These large grids imposed more problems on the Fluent process. It was impossible to read the large grid into a serial fluent solver, but it had to be partitioned in the serial solver. Therefore, no simulations where ran with grids representing the vane/blade ratio of 24:33.

3.0 CURRENT DEVELOPMENTS WITH GRIDGEN

The decision was made to use a vane/blade count of 24:32. This was done to reduce the amount of geometry to grid, as the least common ratio of 3:4 can be modeled. Having to start from scratch, it was suggested by David Carr of AFRL/PRTF to use Gridgen for the development of the grids for use in Fluent. Since Gridgen was specifically not designed to output a Fluent case file, a couple of tests were performed to make sure that an exported could be run in Fluent and give valid results. Both the periodic boundary conditions and the grid interface were of concern. After a few simple tests, it was determined that Gridgen could export in the appropriate format and Fluent could read this grid and use it to run an unsteady vane/blade simulation. Consequently, Gridgen was utilized in the development of grids representing the vane/blade ratio of 24:32.

Gridgen is similar to Gambit in the fact that it has a graphical user interface where the user constructs geometry and builds the grid around that geometry. It is dissimilar because it allows the use of databases to constrain the geometry. With this added constraint, the geometry more accurately represents the physical characteristics of the compressor stage being modeled. For the present grid generation being covered by this report, the databases were supplied by David Car of AFRL/PRTF. However, the databases are nothing more than 3D vortex data and could be created by manipulating the same files as those inputted into Gambit. With the databases supplied, a semi detailed description of the grid generation process with the use of Gridgen is given. A detailed description is not necessary; Gridgen has excellent tutorials. However, there are specifics given to the grid dimensions for the current case being investigated.

3.1. Gridgen Development Process

For the grid generation described here, Gridgen 14.05 was executed on svw10.asc.hpc.mil and svw11.asc.hpc.mil from the Science Visualization (SciVis) Lab located in the Aeronautical System Center (ASC) Major Shared Resource Center (MSRC). The command to execute Gridgen is:

gridgen

Gridgen cannot be x emulated to any computer terminal. Therefore, another SGI machine must be used to access Gridgen.

Once the interface was up and running, the databases were imported. Since the databases given for this case where in Plot 3D format, the command *input/ database/ import* was used. Once the appropriate name was selected, the file attribute of *network, Plot 3D, binary, and single precision* were applied. It is important not to rename the database entities at this point, because any file attributes will look for a database with that particular name. It was never determined that specific database entity names could be saved with a database file. Therefore, every time the database is imported, the entities would have to be renamed before a previously saved file could be opened and constrained to that particular database. The databases used for the grid development consisted of a rotor and a vane passage. Since there was only one of each, the geometry was made then copied and rotated until the desired vane/blade count of 3:4 was reached.

With the database files read in, connectors (equivalent to Gambit's line) were made by executing the *connectors/ create/ add segment/ on DB entities* command. This added a connector at the edges of the enabled databases. This was the first step in creating the geometry that the grid was built on.

At this point in the grid development, any redundant or unnecessary connectors were deleted. There were redundant connectors at the edge of a database where another database had an edge. These connectors were removed with the *connectors/ merge cons/ -2 (con tol)/ all/ done* command. The unnecessary connectors are those that the periodic boundary condition will replace. It will be shown that the two domains (labeled faces in Gambit) that are periodically linked will be defined by a periodic rotate command described later.

It was predetermined that a rotor passage would consist of three blocks (labeled volumes in Gambit) and a vane passage would consist of two blocks. The databases were developed to create a blade and vane centered grid. Therefore, the rotor passage was made with a block above and below the blade and a third block in the tip clearance region. Likewise, the vane passage was made with a block above and below the vane. In order to make the multi blocks, connectors had to be placed from the leading edge of the vane and blade to the inlet of the given volume. Similar connectors had to be placed from the trailing edge to the outlet of the given volume. This addition of connectors was a three-step process. First, the location of the of the blade and vane endpoints was determined with the *connectors/ modify/ (select connector) – done/ split* command. No split was actually performed. The connectors selected were the ones defining the edge of the blade or vane. The above command aloud the splitting point to be moved by the mouse. Therefore, the splitting point was moved to the end of the connector and the location of that point was taken. The command was then aborted before an actual split was performed. This step was redone until all the endpoints were determined. The second step was to split the connectors at the volume inlet and exit at the appropriate location. For the grids described here, this location was the y-coordinate of the endpoint that corresponded with the connector. The command for this operation is *connectors/ modify/ (select connector) – done/ split/ move via keyboard/ y/ (enter y location) – enter/ split at cursor/ abort/ done replace*. The final step was to make a new connector from the endpoint to the node where the corresponding connector was split. This was done with the command *connectors/ create/ 2 point/ (select two node points) – done*.

These new connectors were only constrained to the two points that made them. Since the databases represents the physical geometry being modeled, these connectors were projected on the nearest database to insure that they where constrained to the physical geometry along their entire length. To do this, only the database of interest was enabled with the *database/ enable/ (select database) – done* command. Then the connector was projected with the *connector/ modify/ (select connector) – done/ project/ cylindrical/ use x-principal axis/ project out, inter points/ done – project/ done replace/ maintain links* command. This step was repeated until all the connectors were constrained with the appropriate database.

At this point, all the connectors were in place. The next step was to redimension the connectors with the desired amount of grid points. The command to redimension is *connectors/ modify/ (select connector) – done/ redimension.* Once a connecter was re-dimensioned, a distribution was applied to group the grid points in the manor to catch boundary layers, shocks, and other phenomena of interest. The command to redistribute is *connectors/ modify/ (select connector) – done/ redistribute.* Table 1 lists all the dimensions and distributions for the rotor. Table 2 and Table 3 do the same for the vane at near and far axial spacings, respectfully. Note that all distributions use the geometric progression distribution function.

Connector Description	# of Nodes	ΔS Begin	ΔS End
Blade (in axial direction)	70	0.004	0.004
Blade (around leading and Trailing Edge)	6	1	1
Periodic (corresponding to blade in axial direction)	75	0.004	0.004
Forward of Blade (in axial direction)	16	1	1
Rearward of Blade (in axial direction)	31	0.01	1
Spanwise (all that are not in clearance)	41	0.003	0.003
Spanwise (in the clearance region)	6	1	1
Circumferentially (all)	21	0.001	1

Table 1 - Dimensions and Distributions for the Rotor

Connector Description	# of Nodes	ΔS Begin	ΔS End
Vane (in axial direction)	75	0.004	0.004
Periodic (corresponding to vane in axial direction)	75	0.004	0.004
Forward of Vane (in axial direction)	35	0.01	1
Rearward of Vane (in axial direction)	35	0.004	1
Spanwise (all)	45	0.005	0.005
Circumferentially (all)	31	0.001	1

Table 2 - Dimensions and Distributions for the Vane at Near Axial Spacing

Connector Description	# of Nodes	ΔS Begin	ΔS End
Vane (in axial direction)	75	0.004	0.004
Periodic (corresponding to vane in axial direction)	75	0.004	0.004
Forward of Vane (in axial direction)	25	0.01	1
Rearward of Vane (in axial direction)	45	0.004	0.01
Spanwise (all)	45	0.005	0.005
Circumferentially (all)	31	0.001	1

Table 3 - Dimensions and Distributions for the Vane at Far Axial Spacing

The connectors that made up the tip of the blade were the first to be made into a domain. This was done with the command *domain/ create/ assemble edges/ (select four connectors) – done*. The tip domain was created first so it could be projected to the casing, thus leading to the tip-flow region of the grid. The projection of the domain was done in the same manor as the connectors. With the additional domain, new connectors were developed. The leading and

trailing edges of these connectors where used to add connectors in the axial direction as described before.

The tip region was completed by creating the four domains that follow the blade surface. The six domains where then constructed to make the first using the command *block/ create/ assemble faces.*

The domains below the blade at the hub and casing databases were constructed next. These domains are significant because a structured solver was run to elliptically smooth for better mesh quality. This was done by selecting the domain and using the *domain/ run solver – structured/ (select domain) – done.* The solver attributes where set to the values shown in Table 4 for all edges except that touching the blade. These edges had the attributes shown in Table 5 applied to it.

ΔS		Angle			
Type	**Decay**	**Type**	**Decay**	**Base**	**Boundary Cond**
Inter	6	Current	6	Hilg	Fixed

Table 4 - Elliptical Smoother Attributes for Edges Away from Blade

ΔS		Angle			
Type	**Decay**	**Type**	**Decay**	**Base**	**Boundary Cond**
0.001	6	Orthogonal	6	Hilg	Fixed

Table 5 - Elliptical Smoother Attributes for the Edges Close to the Blade

All the domains needed to construct the block below the blade where then created and the block was assembled.

The creation of the periodic boundary condition for the rotor will be described here as if only one blade was being meshed. The periodic boundary was created using the *domain/ periodic – rotate/ (select domain) – done/ use X-principal axis/ enter rotation angle/ (enter angle) – enter/ done – rotate*. Although this is described as here, it was actually applied after the third block was created and all blocks were copied and rotated with the result of four blades. Once the periodic domain was rotated, the last block was created.

The vane domains and blocks are not described here. The specific data for the vane grid development is given in the tables above. The vane can be made in the same fashion as the blade.

Once the entire grid was developed, it needed to be given boundary conditions and exported to Fluent. To set the boundary conditions the CFD software was specified by *Analysis S/W/ select analysis S/W/ 3D, Fluent v5/ done*. The boundary conditions were the set with the *Analysis S/W/ set BCs* command. The periodic and interior conditions were specified by default. Pressure inlet, pressure outlet, and wall boundary conditions were applied appropriately. The file was then exported with the *Analysis S/W/ export analysis data* command. This file was ready to be read into fluent, but some manipulations had to be made because of exporting more than one block grid. These manipulations will be discussed below in the grid manipulation section.

4.0 CURRENT DEVELOPMENTS WITH FLUENT

After the completion of the grids, computational fluid dynamics (CFD) setup was begun. It was decided to use Fluent as the CFD algorithm. Fluent solves the Reynolds Averaged Navier-Stokes (RANS) equations. The setup was executed on svw11.asc.hpc.mil where the fluent command used was:

fluent 3d -64

The simulations were actually run on the Compaq computers at the MSRC using scripts. To produce an unsteady simulation with the grids created with Gridgen, three major steps were completed. First, the grids had to be manipulated with Fluent commands to insure that the boundaries were in the desired setup. Second, a steady simulation had to be performed. This gave a good starting point for the third step, which was to setup and run the unsteady simulation. All three of these steps are described in detail in the following subsections.

4.1. Grid Manipulation

When a grid created in Gridgen is read, Fluent observes each block separately. In doing so, fluent will group everything from a single block with the same boundary condition together. For example, the tip region would have a boundary condition of wall that encompassed both the casing and blade tip. This imposed a problem. The tip wall needs to rotate while the case wall is held stationary, thus requiring two separate boundary conditions. Another area of concern was the inlet to the rotor and the outlet of the vane (the location where the interface was to be imposed). Fluent read the boundary condition for each blade and vane block separately, so that there were actually six vane outlets and eight blade inlets. For the interface to work properly, the vane outlet needed to be one boundary just as the rotor inlet needed to be one boundary. The solution to this problem was found by using a series of *merge* and *separate* commands within the fluent interface. The following paragraphs give an explanation to how the commands were applied to the current grids.

The grid file was initially read into Fluent with the *file/ read/ case* command. Once the grid was imported, a merge of all the zones representing the rotor fluid volume were merged into one. The command to do this was *grid/ merge/ fluid/ (select zones) – merge*. The same was done for the vane fluid volume. With the all the blocks representing the fluid merged into two main zone volumes, the zones were renamed through the *define/ boundary conditions/ (select boundary)* dialog box.

Next, the inlets to the rotor and vane were merged as pressure inlets. The outlets to the rotor and vane were merged to pressure outlets. The command utilized here was *grid/ merge/ pressure outlet (or inlet)/ (select zones)/* merge. These four newly merged zones were then renamed appropriately.

The last boundary condition of concern was the walls. All the walls that were contained in the rotor volume were separated using the command *grids/ separate/ faces/ by regions/ (select zones)/ separate*. This separated the walls that made the casing from the walls that made the blade and hub. It was desired to go ahead and separate the hub from the blade. This was done by *grids/ separate/ face/ by angle =45°/ (select zones)/ separate*. All the walls that made up the case where merged as well as the entire group of walls that made up the hub. None of the walls that made up the blades was merged. All walls in the rotor volume were renamed appropriately.

A similar process was done for the vane walls. All the walls were separated by an angle of 45°, and then the hub and casing were merged to make two boundary conditions. The vane surfaces were just renamed.

This was all that was done as far as grid manipulation. The rest of the Fluent setup process is detailed in the following section. All cases were saved at this point to simplify the setup process. As of now, the case file only represents the grid.

4.2. Using Fluent for a Steady State Simulation

To aid in obtaining an unsteady simulation, a steady state simulation was ran. The steady solution was used as an initial starting condition for the unsteady solution. The steady simulation setup was begun by scaling the grid. The grid created in Gambit was created in inches, but Fluent defaults to meters. To change this the *grid/ scale/ grid was created in in./ scale* command was executed. Since SI units are default, this was changed to British units with the command *define/ units/ british/ close*.

The solver was specified to coupled implicit through the *define/ models/ solver* dialog box. Similarly, the energy equation was activated from the *define/ models/ energy* dialog box. Moreover, the viscous model was set to the standard k-ε model from the *define/ models/ viscous* dialog box. The fluid was made an ideal gas by selecting ideal-gas from the density drop-down menu in the *define/ material* dialog box. Finally, the operating condition was set at 0 lb/ft^2 utilizing the *define/ operating conditions* window. These parameters are reiterated in Table 6 below.

FLUENT Parameter	**Value**
FLUENT Solver	Coupled-Implicit
Discretization Scheme	Second-Order (Momentum and Viscosity)
Material Properties (Air, Standard Day)	Ideal-Gas
Operating Pressure	0 lb_f/ft^2
Viscosity Model	Standard *k-ε* Turbulence Model
Units	British

Table 6 - Fluent Parameters used for the Steady Simulation

The boundary conditions was specified through the *define/ boundary conditions* dialog box. A list of the boundary conditions is given in Table 7 below. The interface location was treated as separate boundary condition in contrast to a mixing plane. This was primary done to save time. The mixing plane takes more time per iteration. The conditions at this location were known well enough to provide an approximate boundary condition at this point for both the vane outlet and the rotor inlet. The mixing plane would have been necessary to produce accurate steady state results. However, the steady state results for these simulations are only an initial starting point for the unsteady. Therefore, the values for the vane pressure outlet and rotor pressure-inlet boundary conditions are inserted in Table 7 below.

Fluid	Rot. Axis Dir.	Motion Type	Rotation Vel.		
- Rotor	X,Y,Z=1,0,0	Moving Reference Frame	-1414.76 rad/s		
- Vane	X,Y,Z=1,0,0	Stationary	-		

Wall	Wall Motion	Motion	Speed	Rot. Axis Dir.	
- Blade	Moving Wall	Relative	0	X,Y,Z=1,0,0	
- Rotor Hub	Moving Wall	Relative	0	X,Y,Z=1,0,0	
- Rotor Case	Stationary Wall	Absolute	0	X,Y,Z=1,0,0	
- Vane	Stationary Wall	-	-	-	
- Vane Hub	Stationary Wall	-	-	-	
- Vane Case	Stationary Wall	-	-	-	

Pressure Inlet	Total Press	Total Temp	Direction Spec	Turb Intensity	Viscosity Ratio
- Rotor	1979 lb/ft2	505 R	Axial Vector	1	10
- Vane	2116.23 lb/ft2	518.7 R	Axial Vector	1	10

Pressure Out	Gauge Press	Total Temp	Direction Spec	Turb Intensity	Viscosity Ratio
- Rotor	2494 lb/ft2	630.85 R	Normal	1	10
- Vane	1318.87 lb/ft2	514.12 R	Normal	1	10

Periodic	Periodic Type
- Rotor	Rotational
- Vane	Rotational

Table 7 - Boundary Conditions used for the Steady State Simulation

After all boundary conditions were entered, the steady state simulations were initialized to the vane inlet condition with the command *solve/ initialize/ initialize/ compute from (select)/ init*. The simulations were run with the command *solve/ iterate*. In the cases ran here, the actual rotational speed had to be started lower and gradually increased until the desired speed was reached. This also required dropping the backpressure to account for the loss in work done by the rotor. It was found that stepping into full speed would cause divergence problems. It is recommended that any rotor simulations be stepped in speed.

After the steady state simulations were run to a desired convergence, the solutions were exported with *file/ interpolate/ write data/ (select and zones and fields)* command. This interpolation can be read over the grid that is setup for the unsteady simulation.

4.3. Steady State Results

This section shows the results of the steady state simulation conducted with Fluent. The results are not fully converged. They did not need to be fully converged for the use as an initial solution to the unsteady simulations. At the time of this report, only the two blunt trailing edge cases were run. Therefore, only the blunt near case and the blunt far case can be presented. Figure 1 and Figure 2 show the static pressure contours at 75% span for the blunt trailing edge geometry for the far and near axial spacing, respectively.

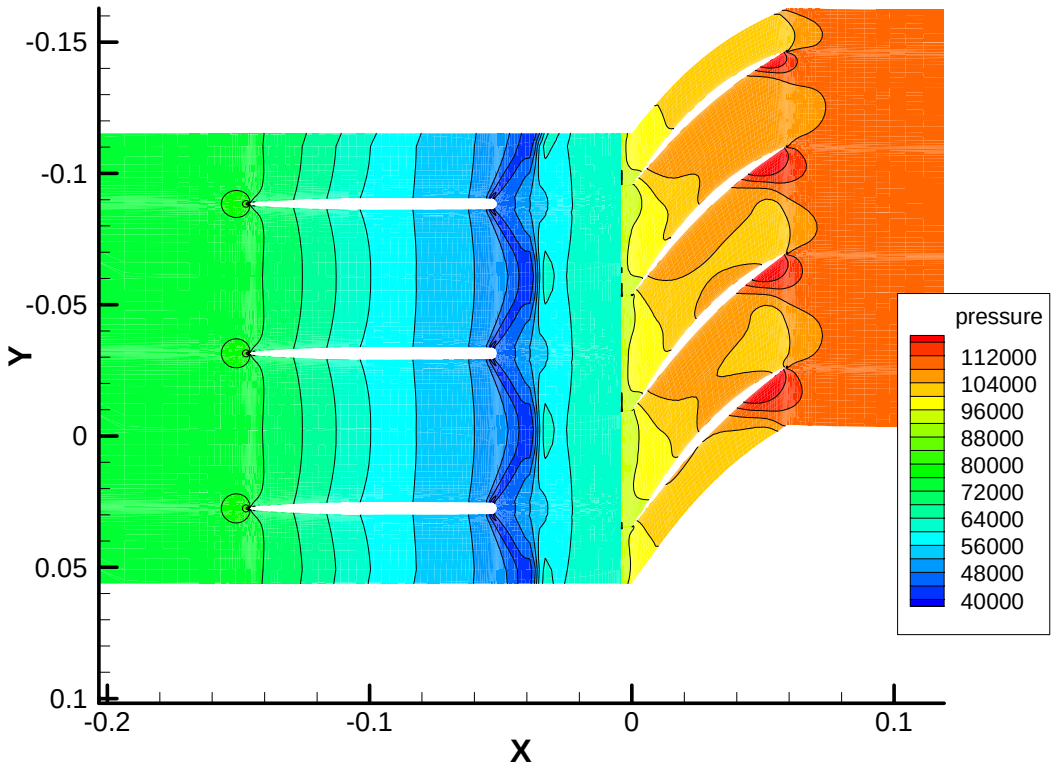

Figure 1 - Static Pressure (lb/ft2) Results for the Blunt Far Steady State Simulation at 75% Span

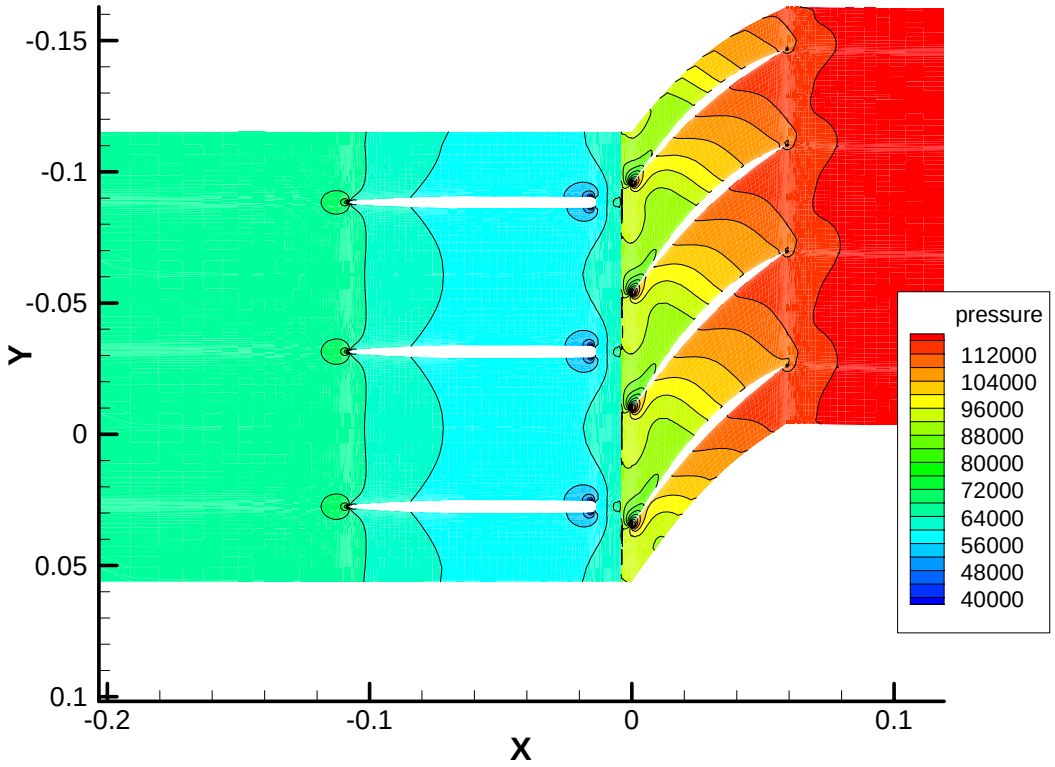

Figure 2 - Static Pressure (lb/ft2) Results for the Blunt Near Steady State Simulation at 75% Span

It is important to note again that these results are not fully converged. However, they made an excellent starting condition for the unsteady simulation. From the above results, the effect of not using a mixing plane is seen as the contours abruptly change across the interface location located between the vane and blade.

4.4. Using Fluent for an Unsteady Simulation

The unsteady simulation can be started in one of two ways. The first way is to open up the steady simulation and make the changes discussed below. The second, is to open the grid file, supply all the Fluent parameters and boundary condition information (included changes discussed below), and read the interpolation file written after the steady simulation was complete. The first method is faster and thus applied to the cases discussed in this report.

Several changes needed to be made to the steady case before it could produce an unsteady simulation. The first change occurred with the solver specification. A 2^{nd}- order coupled implicit unsteady solver was specified for the current investigation.

The next change was to create the interface between the vane and rotor. The boundary conditions for the vane pressure outlet and rotor pressure inlet needed to be changed to interfaces. After the boundary conditions were changed for the current cases, it was found that a fix needed to be manually made. The first part of the fix was to correct the rotational axis of the periodic conditions. This was done by typing the following commands into the fluent interface window.

/ grid/ modify-zones > r-p
periodic zone [()] *(enter number for one of the two periodic zones)*
New rotation angle (deg) [] *("45" degrees was entered)*
Repair rotational periodic zone? *(entered "yes")*

This command was repeated for the second of the two periodic zones. The next step was to enter two text commands into the fluent interface window. These commands were entered exactly as shown.

(rpsetvar 'nonconformal/allow-interface-at-periodic-boundary 0)
(rpsetvar 'nonconformal/cell-faces 0)

The effect of the above commands was not fully understood, but the grid interface could not be made without them. The final step to making the grid interface was to open the *define/ grid interface* dialog box. In the box, the vane outlet was selected as interface zone 1 and the rotor inlet was selected as interface zone 2; plus the interface type of periodic was also chosen before selecting the create button.

It should be noted here that for an interface to work in a parallel Fluent solver, the grid must be manually partitioned. This is done with *parallel/ partition/ (select encapsulate for adaption)/ (enter number of partitions)/ partition.*

The last change made to the steady case to solve an unsteady simulation was to enter a time step. This is done in the iterate command box. For the current investigation, it was determined to use 180 time steps per blade passing period. This calculated to be 7.7104e-7 seconds.

The values for the Fluent parameters and boundary conditions for the unsteady simulation are repeated in Table 8 and Table 9 below, respectively.

FLUENT Parameter	Value
FLUENT Solver	Second-Order Coupled-Implicit
Discretization Scheme	Second-Order (Momentum and Viscosity)
Material Properties (Air, Standard Day)	Ideal-Gas
Operating Pressure	0 lb_f/ft^2
Viscosity Model	Standard k-ε Turbulence Model
Units	British
Time step (seconds)	7.7104 x 10^{-7}

Table 8 - Fluent Parameters used for the Unsteady Simulation

Fluid	Rot. Axis Dir.	Motion Type	Rotation Vel.		
- Rotor	X,Y,Z=1,0,0	Moving Reference Frame	-1414.76 rad/s		
- Vane	X,Y,Z=1,0,0	Stationary	-		
Wall	**Wall Motion**	**Motion**	**Speed**	**Rot. Axis Dir.**	
- Blade	Moving Wall	Relative	0	X,Y,Z=1,0,0	
- Rotor Hub	Moving Wall	Relative	0	X,Y,Z=1,0,0	
- Rotor Case	Stationary Wall	Absolute	0	X,Y,Z=1,0,0	
- Vane	Stationary Wall	-	-	-	
- Vane Hub	Stationary Wall	-	-	-	
- Vane Case	Stationary Wall	-	-	-	
Pressure Inlet	**Total Press**	**Total Temp**	**Direction Spec**	**Turb Intensity**	**Viscosity Ratio**
- Rotor	Use as Interface				
- Vane	2116.23 lb/ft2	518.7 R	Axial Vector	1	10
Pressure Out	**Gauge Press**	**Total Temp**	**Direction Spec**	**Turb Intensity**	**Viscosity Ratio**
- Rotor	2494 lb/ft2	630.85 R	Normal	1	10
- Vane	Use as Interface				
Periodic	**Periodic Type**				
- Rotor	Rotational				
- Vane	Rotational				

Table 9 - Boundary Conditions used for the Unsteady Simulation

Unfortunately, the simulations had not converged at the time this report was written. Therefore, unsteady results are not reported.

5.0 CURRENT DEVELOPMENTS WITH APG AND MSU-TURBO

The last part of this summers work was devoted to learning Average Passage Grid (APG) in order to develop grids for the use in MSU-Turbo. The goal shifted from running all four Fluent simulations to running all four simulations in MSU-Turbo. As such, APG has been applied to the rotor, blunt IGV, and sharp IGV geometries. As of now, the rotor mesh is complete. The blunt IGV needs to be shifted around to the near and far axial spacings. In addition, the sharp IGV surface vortex data needs to be modified slightly. As of now, these are there are no further details to this work.

6.0 SUMMARY

The process to developing the computational grids, representing the SMI experiments, in Gambit in Gridgen was detailed. The procedure for importing these grids in Fluent was described. Two simulations were run in Fluent and steady simulation results were reported. These steady solutions were used as initial conditions for running unsteady simulations in Fluent. The unsteady simulations had not converged at the time of this report. However, all commands and methods were included, which completely describe all setup procedures.

7.0 FUTURE WORK

Work that has not been completed now, but will be attempted is included in this section.

1) Continue the blunt far and blunt near unsteady simulations in Fluent until convergence.
2) Start steady simulations for the sharp far and sharp near cases in Fluent. This will be attempted only if Fluent proves to accurately simulate vane/blade interactions.
3) Use APG to develop all four grids
4) Run all four APG grids in MSU-Turbo to get unsteady solution in a quicker time.

8.0 REFERENCES

[1] Falk, E. A., 2002, “Three-Dimensional Computational Simulations of Compressible Flow Through a Transonic Compressor,” Air Force Summer 2002 Faculty Fellowship Program Final Report, WPAFB, Dayton, Ohio

[2] Falk, E. A., Kirk, J. F., Jumper, E. J., Haven, B. A., and Stermer, J., 2001, “Unsteady Forcing of an IGV Forward of a Fan in Subsonic Flow: Amplitude Results,” AIAA Paper No. 2001-3475, 37th AIAA/ASME/SAE/ ASEE Joint Propulsion Conference and Exhibit, Salt Lake City, Utah.

[3] Gorrell, S. E., Okiishi, T. H., and Copenhaver, W. W., 2002a, “Stator-Rotor Interactions in a Transonic Compressor: Part 1 - Effect of Blade-Row Spacing on Performance,” *Proceedings of the ASME Turbo Expo 2002*, GT-2002-30494, June 3-6, Amsterdam, The Netherlands.

[4] Gorrell, S. E., Okiishi, T. H., and Copenhaver, W. W., 2002b, “Stator-Rotor Interactions in a Transonic Compressor: Part 2 - Description of a Loss Producing Mechanism,” *Proceedings of the ASME Turbo Expo 2002*, GT-2002-30495, June 3-6, Amsterdam, The Netherlands.

[5] Kirk, J. F., Jumper, E. J., Falk, E. A., Haven, B. A., and Stermer, J., 2001, “Unsteady Forcing of an IGV Forward of a Fan in Subsonic Flow: Phase Results,” AIAA Paper No.

2001-3474, 37th AIAA/ASME/SAE/ ASEE Joint Propulsion Conference and Exhibit, Salt Lake City, Utah.

[6] Koch, P. J., Moran, J., and Wolff, J. M., 1999, "3-D Inlet Guide Vane Generated Vortical Forcing Functions," AIAA Paper No. 99-2677, 35th AIAA/ASME/SAE/ASEE Joint Propulsion Conference and Exhibit, Los Angeles, CA.

[7] Koch, P. J., Probasco, D. P., Wolff, J. M., Copenhaver, W. W., and Chriss, R. M., 2000, "Transonic Compressor Influences on Upstream Surface Pressures with Axial Spacing," *Journal of Propulsion*, 17(2), pp. 474 – 477.

[8] Probasco, D. P., Wolff, J. M., Copenhaver, W. W., and Chriss, R. M., 1997, "Unsteady Blade Row Potential Interaction in a Compression Stage," AIAA Paper No. 97-3285, 33rd AIAA/ ASME/SAE/ASEE Joint Propulsion Conference and Exhibit, Seattle, WA.

[9] Probasco, D. P., Wolff, J. M., Copenhaver, W. W., and Chriss, R. M., 1998, "Axial Spacing Effects in a Transonic Compressor on the Upstream Vane Loading," AIAA Paper No. 98-3431, 34th AIAA/ASME/SAE/ASEE Joint Propulsion Conference and Exhibit, Cleveland, OH.

[10] Sanders, A. and Fleeter, J., 2000, "Experimental Investigation of Rotor-Inlet Guide Vane Interactions in Transonic Axial-Flow Compressor," *Journal of Propulsion and Power*, 16(3), pp. 421 – 430.

ACKNOWLEDGEMENTS

The author would like to thank the members of the CARL group at WPAFB for all there guidance in this work. Specifically, the efforts and advice of Dr. Steven Gorrell, Mr. Dave Car, Dr. Greg Block, Mr. Pete Koch, and Dr. Steven Puterbaugh are gratefully acknowledged. The author would also like to thank Dr. Mark Turner of the University of Cincinnati for assistance with APG and Dr. Eric Falk of Oklahoma State University for overall advisement. The staff at the Aeronautical Systems Center (ASC) Major Shared Resource Center (MSRC), particularly Mr. Jason Blair and Mr. Hugh Thornburg, are also recognized. Finally, the author recognizes Roger Rucker and Michele Puterbaugh of the Universal Technology Corporation (UTC). Support for this endeavor was provided by the AFRL Propulsion Directorate through the UTC.

Vladimir Katovic
Department of Chemistry
Wright State University

Summer Research Fellowship Program Report

Prime Contract Number F 33615-02-D-2299
Period of Performance : May 15, 2003 – July 12, 2003

Title: Use of Room-Temperature Ionic Liquids as Electrolytes for Ethanol Based Fuel Cells

1. Syntheses of Room-temperature Ionic Liquids

   The following room-temperature ionic liquids were synthesized and purified: $MEImBF_4$ (1-methyl-3-ethylimidazolium tetrafluoroborate) and $MBImBF_4$ (1-methyl-2-bultylimidazolium tetrafluoroborate). The first step in the syntheses involved the conversion of N-metyl imidazole to alkyl N-methyl imidazxolium chlorides. Replacement of the chloride anions was done by potentiometric titration with $AgBF_4$. The purity of the ionic liquids was checked by cyclic voltammetry. In the absence of Cl^- and/or Ag^+ ions a wide potentioal window of ~ 4.2 V was obtained.

2. Oxidation of ethanol in 0.1 M $HClO_4$

   A cyclic voltammogram of 0.1 M solution of Ethanol in 0.10 M $HClO_4$ obtained on a clean Pt electrode is shown in Figure 2. On the positive forward sweep the voltammogram displays two oxidation peaks at $E_{p,a} = 0.6$ V and $E_{p,a} = 1.1$ V vs. Ag/AgCl electrode. On the reverse sweep the peaks do not display cathodic currents. However, a new oxidation peak at $E_{p,a} = 0.4$ V was obtained (peak 3). Based on previous voltammetric data those peaks were assigned as follows:

   Peak 1.

   The first oxidation peak at $E_{p,a} = 0.6$ V corresponds to a chemisorption and a fast one electron oxidation of EtOH .

$$CH_3CH_2OH \text{ --------> } CH_3CH^*OH + H^+ + e \qquad (1)$$

   This process is followed by a slower step of oxidation of adsorbed species to aldehyde:

$$CH_3CH^*OH \text{ --------> } CH_3CHO + H^+ + e \qquad (2)$$

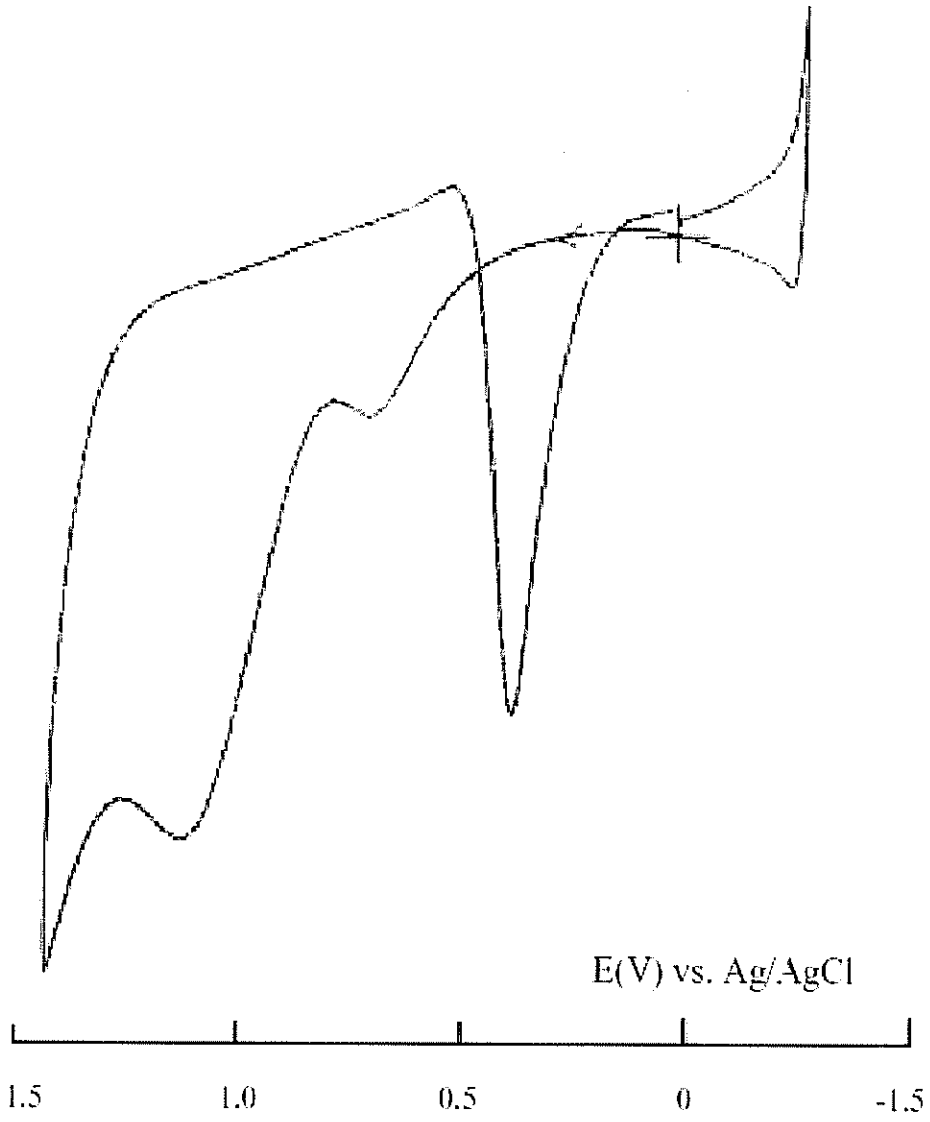

Figure 1. Cyclic voltammogram of EtOH on a Pt electrode in 0.1 M $HclO_4$

At the same potential a surface oxidation of the Pt and formation of PtO film takes place (3) and (4):

$$Pt + H_2O \text{ --------> } Pt(OH) + H^+ + e \quad (3)$$

$$Pt(OH) \text{ --------> } PtO + H^+ + e \quad (4)$$

Peak 2.

The second oxidation peak at $E_{p,a} = 1.1$ V involves a slow one e oxidation of Pt and a formation of PtOEt;

$$Pt + CH_3CH_2OH \text{ --------> } Pt(O\,CH_2CH_3) + H^+ + e \quad (5)$$

This is followed by both a one electron oxidation of $Pt(O\,CH_2CH_3)$ to PtO (6a) and the oxidation of $Pt(O\,CH_2CH_3)$ to aldehyde (6b):

$$Pt(O\,CH_2CH_3) + H_2O \text{ --------> } PtO + CH_3CH_2OH + H^+ + e \quad (6a)$$

$$Pt(O\,CH_2CH_3) \text{ --------> } Pt + CH_2CHO + H^+ + e \quad (6b)$$

When the the reaction 6a is faster then 6b, poisoning of the electrode will occur (i.e. formation of PtO). If reaction 6b is faster then 6a, poisoning of the electrode will not occur.

Peak 3.

The oxidation peak 3 at $E_{p,a} = 0.4$ V is observed only on the reverse scan and has been attributed to the activation of the Pt surface:

$$CH_3CH_2OH + PtO \text{ --------> } CH_2CHO + PtOH \quad (7)$$

$$PtOH \text{ --------> } PtO + e + H^+ \quad (8)$$

The peak is observed because above 0.8 V the reaction (7) will not occur and below 0.6 V the reaction 8 does not proceed.

3. Design and construction of an IR spectroelectrochemical cell

A special IR reflectance spectroelectrochemical cell was designed and constructed that will allow simultaneous measurements of cyclic voltammograms, constant potential electrolysis as well as IR reflectance spectra from the Pt working electrode.

This will allow us to identify the identity of oxidized species adsorbed on the surface of the Pt electrode by FTIR spectroscopy as a function of the applied potential. In addition, the analysis of the solution after electrolysis will allow the identification of the oxidation products in the solution obtained by bulk electrolysis at a controlled potential. The schematic and the picture of the cell are shown in Figure 2.
The cell consists of a Pt disk working electrode ($1cm^2$) , an Ag/AgCl reference electrode and a Pt auxiliary electrode. The bottom part of the cell is made of a CaF_2 window so that reflectance FTIR spectra of the Pt electrode could be obtained. After electrolysis at the desired potential the Pt disk electrode was positioned close to the CaF_2 window to minimize the absorption of IR light by sample solution.
The performance of the cell was tested by obtaining a background reflectance spectrum of the Pt electrode in a solution before electrolysis, and a spectrum of a plastic film as a test sample.

Figure2. Spectroelectrochemical cell used for obtaining IR reflectance spectra of species adsorbed on the Pt electrode

APPENDIX C

FINAL REPORT

Development of an Transient Infrared Technique for Film Cooling Measurements

SUMMER FACULTY FELLOWSHIP
PROPULSION DIRECTORATE
SUMMER 2003

Submitted by

Srinath V. Ekkad, Ph.D., PE
Louisiana State University
Baton Rouge, LA

To

Universal Technology Corporation
Dayton, OH

and

Dr. Richard B. Rivir
Propulsion Directorate
WPAFB, Dayton, OH

August 14, 2003

ABSTRACT

In film cooling situations, there is a need to determine both local adiabatic wall temperature and heat transfer coefficient to fully assess the local heat flux into the surface. Typical film cooling situations are termed three temperature problems where the complex interaction between the jets and mainstream dictates the surface temperature. The coolant temperature is much cooler than the mainstream resulting in a mixed temperature in the film region downstream of injection. An infrared thermography technique in relation with a transient test is described to determine both the heat transfer coefficient and film effectiveness (non-dimensional adiabatic wall temperature) from a single test. Hot mainstream and cooler air injected through discrete holes are imposed suddenly on an ambient temperature surface and the wall temperature response is captured using an infrared thermography system. The wall temperature and the known mainstream and coolant temperatures are used to determine the two unknowns (heat transfer coefficient and film effectiveness) at every point on the test surface. The main advantage of this technique over existing techniques is the ability to obtain the information with only one single transient test without a need for a thermochromic coating as in liquid crystal techniques. This technique is also more robust and requires less intensive calibration than liquid crystal techniques. Results are presented for film cooling downstream of a single hole on a turbine blade leading edge model.

Additional focus was on the effect of jet pulsation on film effectiveness and heat transfer. Two different jet pulsing frequencies have been studied at 5 Hz and 10 Hz. The duty cycle effect created by the valve opening and closing was also set at different levels of 25%, 50%, and 75% of the designated 100% flow rate. The combination of pulsing

frequency and duty cycle was investigated for different blowing ratios on the same leading edge hole. However, the results seem to indicate that higher effectiveness and lower heat transfer coefficients are obtained at reduced blowing ratios. The effect of pulsing frequency is not discernable beyond the level of experimental uncertainty. The effective blowing ratio seems to play a more important role for this type of hole geometry than the pulsing effect. Experiments are underway to test the pulsing effect on a streamwise inclined hole on a flat surface.

PART I – INFRARED TECHNIQUE

The purpose of this section of the report is to demonstrate a new Infrared thermography technique for simultaneous heat transfer coefficient and film cooling effectiveness measurements from a single experiment. More particularly, a method and apparatus for evaluating cooling geometries more effectively and quickly.

Background

Film cooling is used extensively in modern gas turbines to cool hot gas path components by injecting cooler fluid on to the surface through discrete holes or slots. Due to complex flow mixing and boundary layer behavior, film cooling enhances heat transfer coefficients downstream of the hole and produces lower near surface gas temperatures. A combination of the known heat transfer coefficient and adiabatic wall temperature is necessary to ascertain the benefits and the level of heat flux reduction due to film cooling. To do this, both heat transfer coefficient and film effectiveness measurements are required for each geometry and this information is compared to the no

film cooling surface. In three temperature situations, such as film cooling, there are two unknowns in the experiment. Typically, all heat transfer measurement techniques have used two different related experiments to obtain heat transfer coefficient and film effectiveness separately. Some of the techniques used low resolution methods such as thermocouples and heater foils, mass transfer analogy methods, etc. In the past decade, the most popular technique to obtain high resolution measurements has been the liquid crystal technique. The liquid crystal technique has the foundation similar to the present IR technique. Vedula and Metzger [1] proposed that they could make simultaneous measurements of heat transfer coefficient and film effectiveness from a single test using liquid crystal coatings. However, there were some logistical difficulties associated with obtaining both measurements from a single test due to the nature of the color change phenomena associated to liquid crystals. To solve this problem, Vedula and Metzger [1], Ekkad et al. [2, 3], and other studies have used two similar related tests to resolve the heat transfer coefficient and film effectiveness values at every point on the test surface. Since then, several investigators have attempted various techniques to obtain both heat transfer coefficient and film effectiveness values from a single test unsuccessfully. Some studies have just focused on obtaining detailed film effectiveness measurements using IR thermography [3]. However, without heat transfer coefficient measurements, film effectiveness results present only half the story in film cooling assessment.

To solve this problem, an IR thermography system which will not face the inherent difficulties associated with liquid crystals was proposed and tested successfully. A full description is presented below.

Description

Figure 1 shows the experimental set up associated with a film cooling experiment. A high-resolution commercially available IR thermography system was used. The film cooling hole is on a leading edge model simulating the turbine blade leading edge. The preparation for the actual tests requires pre-processing steps that are basically to calibrate the entire thermogrpahy system and the IR signal.

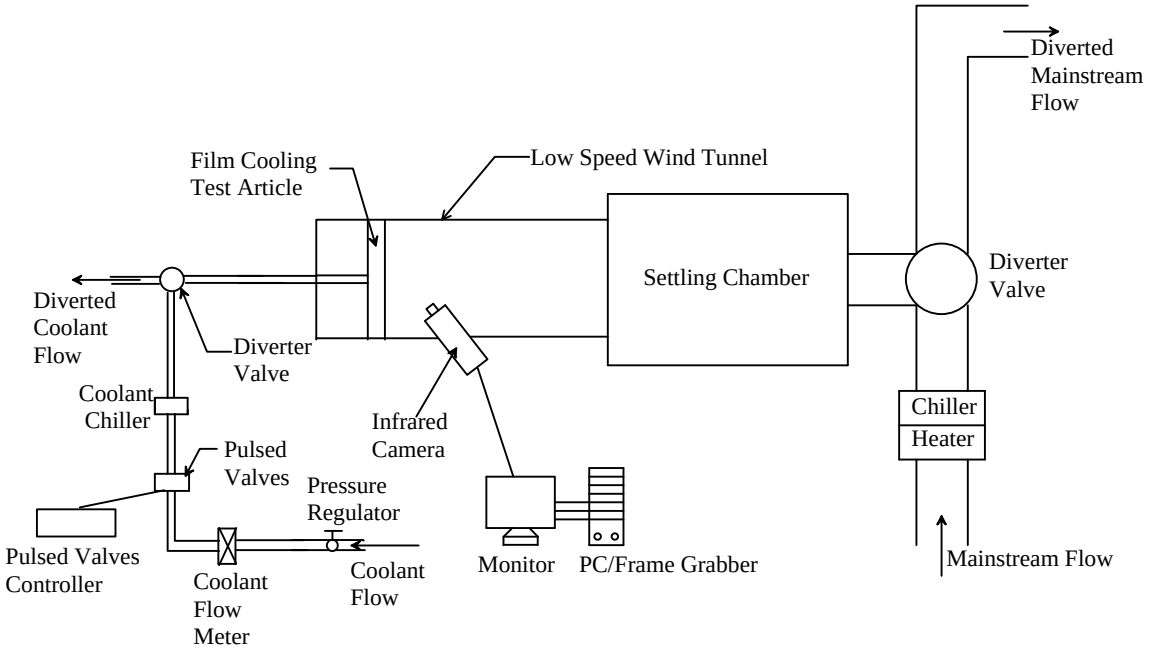

Figure 1. Schematic of Test Facility

1. The camera was focused on the hole and the surface was painted using flat black paint.
2. Thermocouples were attached to the surface using aluminum tape. The surface was then heated using hot air from the blower.
3. The thermocouples are monitored during the heat up and subsequent achievement of steady state.

4. The IR camera is focused on the test surface. The IR system can directly indicate temperature values on the thermocouple point using the software available with the system. The IR temperature and the thermocouple temperature are compared and the emissivity of the surface is adjusted on the software setting to match the two temperature readings. Care must be taken to indicate the distance between the camera and the test surface and the ambient room temperature and relative humidity settings for the software. All these affect the IR temperature reading.
5. The emissivity with flat black coating on the surface is typically in the range of 0.93-0.97.

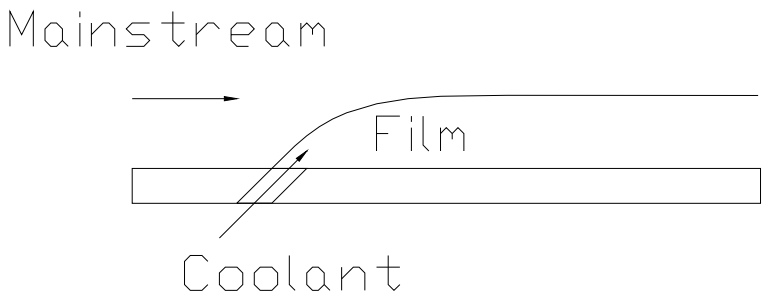

Figure 2. Film Cooling Representation

Figure 2 shows a typical film cooling hole situation. The mainstream is the air coming over the wall and the temperature of the flow is indicated as mainstream temperature (T_m). The coolant temperature (T_c) is the temperature before injection through the hole. The mainstream and coolant mix after injection and produce the local film temperature (T_f). The film temperature is closer to coolant temperature immediately after the injection hole and then degrades as the coolant coverage decreases downstream

and ultimately is closer in value to the mainstream temperature. Film effectiveness is the non-dimensional temperature associated to the film temperature as $\eta = \frac{T_m - T_f}{T_m - T_c}$. The heat transfer coefficient is the convective heat transfer coefficient defined from the heat flux equation $q'' = h(T_m - T_w)$. Heat transfer coefficient is independent of the heat flux and temperature gradient and is a function of flow, fluid, and geometry. The knowledge of film temperature in film cooling situations defines the local heat flux as $q''_f = h_f(T_f - T_w)$. If the heat flux with film cooling is lower than the heat flux without film cooling, then the film cooling is accepted as helping in reducing the heat transfer. It is very possible for a film cooling hole at a particular coolant flow rate to produce reasonable film effectiveness but much more significant rise in local heat transfer coefficient resulting in increase in heat flux.

The procedure for a typical test requires the following steps:

1. The test surface is painted black and the IR camera is focused on the test surface region (typically downstream of the hole).
2. The mainstream air flow is routed away from the test section and heated to a required temperature.
3. The coolant flow is maintained at ambient temperature and also routed away from the test section.
4. Once the mainstream reaches the required temperature, the camera is initiated to take images at the same instant as the mainstream and the coolant flows are routed into the test section.

5. Thermocouples are placed in the mainstream and upstream of the coolant hole to measure the transient responses of the air temperature during the transient heating test.
6. The images are stored into the computer hardware and the air temperatures are digitized through an A/D system.
7. The image files from the IR camera are converted to actual temperature files at different instants of time. A typical IR image is shown In Figure 3.
8. The mainstream temperature increases from the initial temperature to the set temperature during the first 10-15 seconds and then steadies. Figure 4 shows the typical mainstream temperature rise during the transient test.

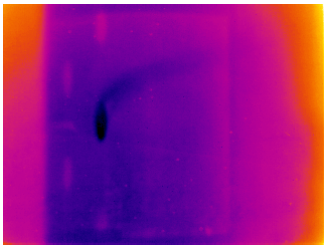

(a) Initial Image (Time = 0 seconds)

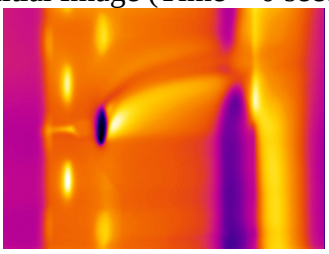

(b) Intermediate time (Time =25 seconds)

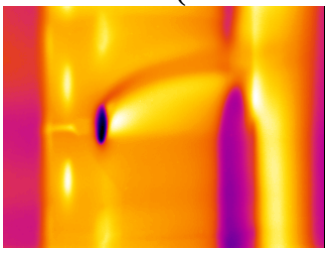

(c) Final Time (Time =70 seconds)

Figure 3: IR images from camera

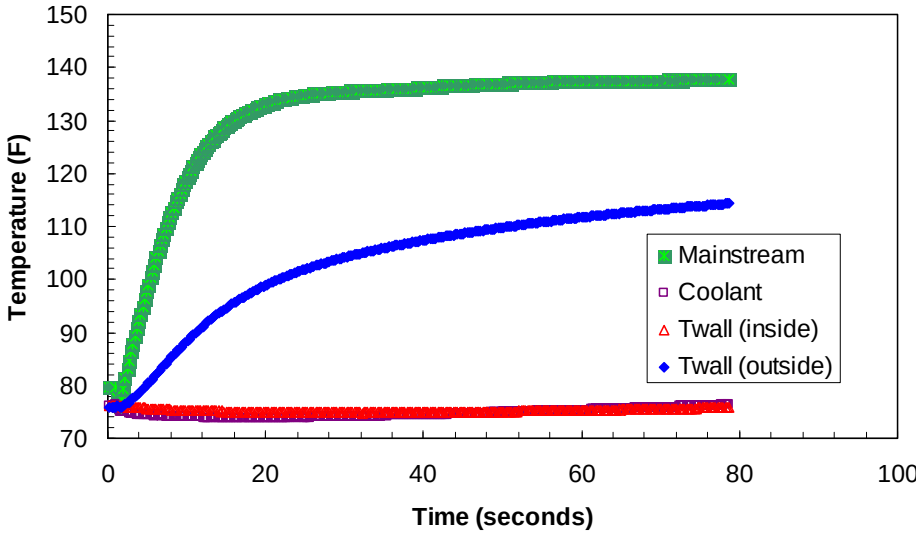

Figure 4: Temperature response of different thermocouples

The mainstream temperature, the coolant temperature and the surface temperature distributions from the IR images are input into a program to calculate the local heat transfer coefficient and film effectiveness at every pixel point on the IR image. To calculate heat transfer coefficient and film effectiveness distributions, two images are required. The first image is typically around 15-20 seconds after the initiation of the test and the second image is around 60-70 seconds after the test initiation. Both the surface temperature distributions are different as seen in Figure 3. These two surface temperatures and the mainstream response are used to calculate heat transfer coefficient simultaneously from the two equations below

$$\frac{T_{w1}-T_i}{T_f-T_i}=1-\exp\left(\frac{h^2\alpha t_1}{k^2}\right)erfc\left(\frac{h\sqrt{\alpha t_1}}{k}\right)$$ and

$$\frac{T_{w2}-T_i}{T_f-T_i}=1-\exp\left(\frac{h^2\alpha t_2}{k^2}\right)erfc\left(\frac{h\sqrt{\alpha t_2}}{k}\right)$$ where T_{w1} and T_{w2} are surface temperatures at times t_1 and t_2 and the two unknowns are heat transfer coefficient (h) and film

temperature (T_f). The initial temperature for any point is obtained from the first frame which is at the start of the test.

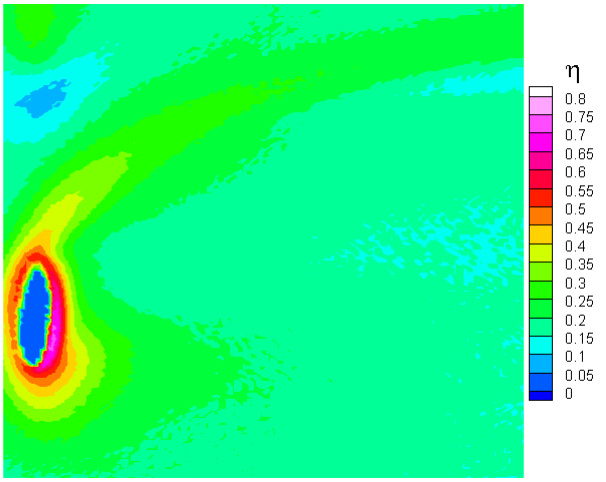

(a) Effectiveness contours

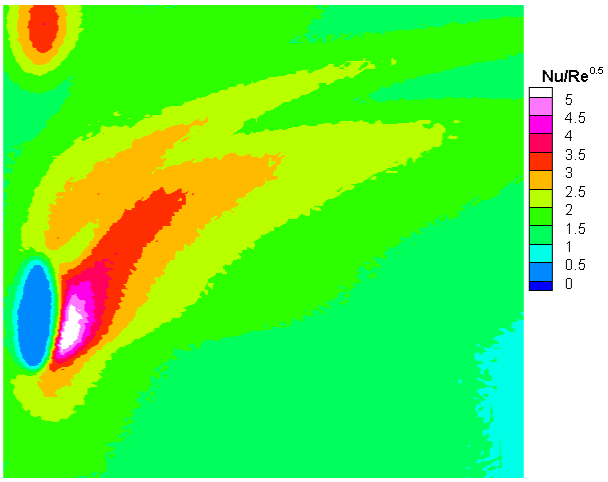

(b) Nusselt number (heat transfer) contours

Figure 5: Results from a typical transient IR test

The Duhamel's superposition integral theorem is used to incorporate the transient response of the mainstream using the definition of film effectiveness $\eta = \frac{T_m - T_f}{T_m - T_c}$. Figure 5 shows a typical result from the IR thermography system for both heat transfer coefficients and film effectiveness.

Advantages

There are many advantages of this new technique.

1. There is no need for spraying expensive liquid crystals on the surface. Typical surface preparation requires only black paint.
2. The experiment does not require two experiments thus reducing run time and also uncertainties relating to running two different tests at two different times.
3. The test is not limited by the operating point of the liquid crystals. Liquid crystals cannot operate beyond 50 C whereas the present technique has no such limits as long as the surface is non-conductive.
4. The IR camera also provides initial temperature distribution on the surface which is very difficult to obtain from liquid crystals.
5. The coolant does not require to be heated as in the case of two test techniques resulting in reduced capital costs and time savings.

Alternatives

There are alternative methods to the procedure presented. It is possible to obtain the same measurements by heating the test surface to a high initial temperature and cooling it suddenly with a cold mainstream and cold coolant flows. The subsequent transient test removes the need for Duhamels' integral representation of the mainstream flow.

PART II – PULSED JET FILM COOLING

The effect of jet pulsing is studied for the first time. The frequency and duty cycle of the jet pulsation are controlled by a high speed solenoid valve located upstream of the coolant flow meter. The solenoid is controlled by a General Valve Inc. Iota One pulse driver which has a frequency range from 0.1 Hz to 250 Hz with a minimum “open” pulse duration of 1 less than 1 ms. The maximum open condition was set at 99.95% open for the valve as there is no fully open flow condition setting. Frequencies of 5, 10 and 20 Hz were studied. Different duty cycle conditions were simulated by varying the open and shut settings to obtain 100% (almost), 75%, 50%, and 25%. The duty cycle setting produces lower average flow compared to the fully open setting (or continuous flow). It is expected that the reduced flow with pulsing will produce the same or better effect than the continuous maximum flow condition.

Firstly, the effect of increasing blowing ratio on both the heat transfer coefficient and film effectiveness has been explored. This provides the baseline for continuous flow to which pulsing jet results will be compared. As expected, higher blowing ratio provides higher heat transfer coefficients due to increase jet mixing and turbulence. Figure 6a shows the effect of blowing ratio on normalized heat transfer coefficient distributions. At low blowing ratios, there is no enhancement downstream of injection due to low mixing and attached jets. Figure 6b shows the effect of blowing ratio on film effectiveness distributions. Lower blowing ratios produced attached jets downstream of the hole creating very high effectiveness and subsequently reducing downstream. Higher blowing

ratios produce stronger jets that tend to lift off along the hole direction. The higher effectiveness region is along the hole direction and decreases downstream.

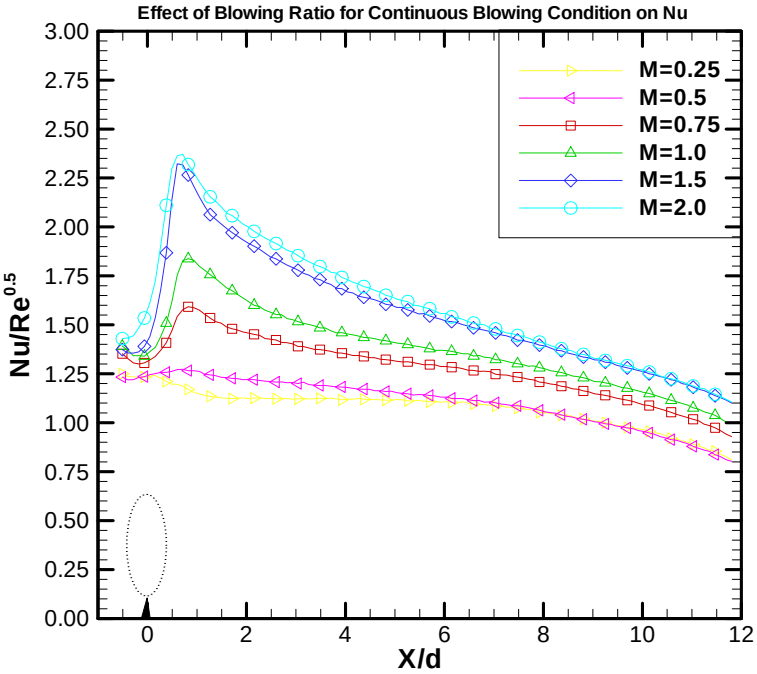

Figure 6a

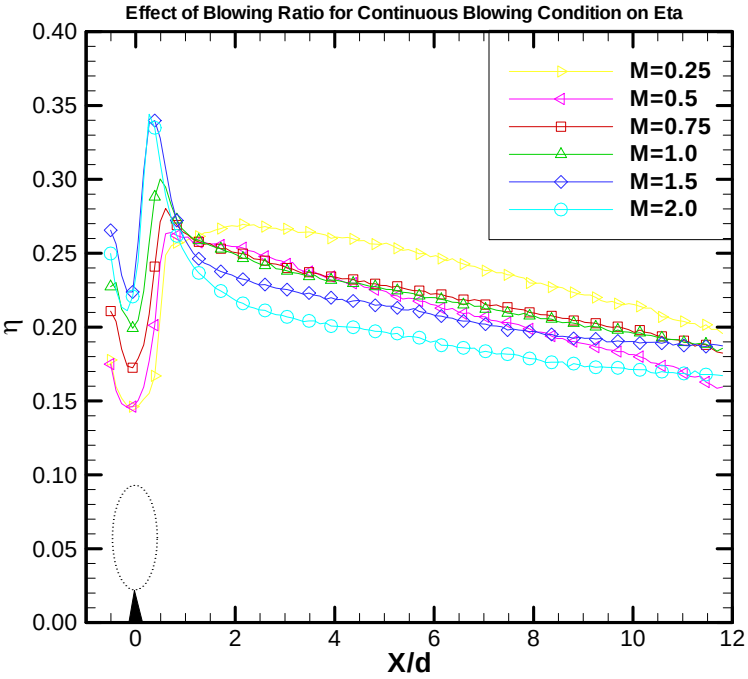

Figure 6b

Figure 6 Effect of blowing ratio on heat transfer coefficient and film effectiveness

Effect of Pulsing and Duty Cycle

Primarily results showed that pulsing frequency does not cause significant effect as duty cycle does. Varying frequency between 5 and 10 Hz did not provide significant differences in both heat transfer coefficient and film effectiveness. The duty cycle effect is compared only for a pulsing frequency of 10 Hz. Typically duty cycle effect is to reduce total mass flow and thus reduce the average blowing ratio compared to the continuous flow. To avoid confusion, the average simulated flow rate due to pulsing and duty cycle is compared to a similar continuous blowing rate. This will clearly indicate if pulsing has any significant effect on the film cooling performance.

Figure 7 compares the Nusselt number distributions for different effective blowing ratios. Four different blowing ratios are studied, M=0.25, 0.5, 1.0, and 1.5. Results show that the heat transfer coefficients are unaffected as long as the effective blowing ratios are equal. At M=0.5, there are some differences between pulsed and unpulsed jets but the differences are within the uncertainty levels. Overall, it appears that the pulsing jets do not provide any significant difference compared to the continuous jets.

Figure 8 compares the film effectiveness distributions for different effective blowing ratios. Again, at high and low blowing ratios, there is negligible effect of pulsing. At M=0.5, it does appear that pulsing enhances film effectiveness. It is a very small window in the large parametric changes studied. However, pulsing overall may cause the jet to spread more on the surface and provide similar or slightly higher effectiveness. It may not be beneficial to pulse the jets as the gains are relatively small compared to the capital costs associated with pulsing the jets.

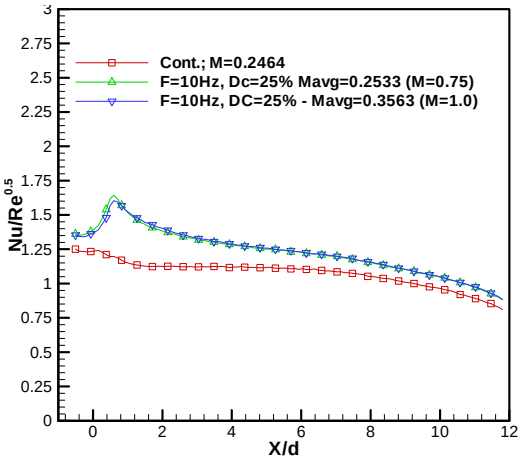

Figure 7a M=0.25

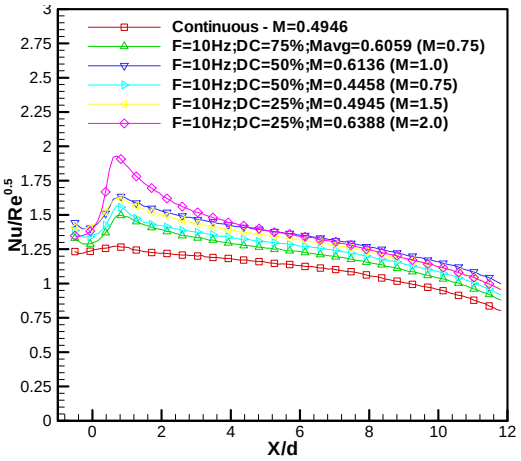

Figure 7b M=0.5

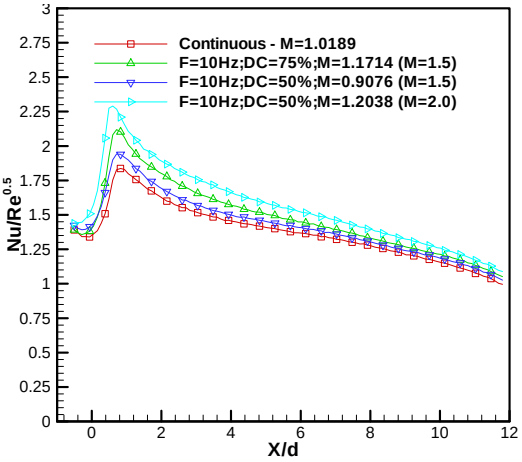

Figure 7c M=1.0

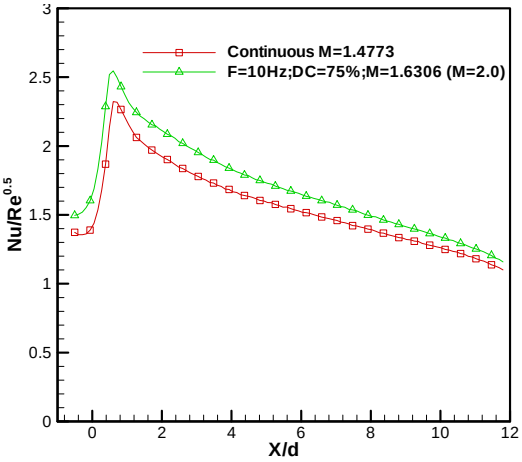

Figure 7d M=1.5

Figure 7 Effect of pulsing frequency on Nusselt number for a Particular Effective Blowing Ratio

CONCLUSIONS

The entire summer was divided into two main tasks. The first task was to develop the transient Infrared technique to obtain film effectiveness and heat transfer coefficient from a single test. This task was achieved and the technique has been demonstrated with success. The technique is more robust and simpler than comparable existing techniques used for film cooling measurements. The other task was to evaluate the beneficial effects of jet pulsing on film cooling performance. Although the results do not indicate any significant benefit for pulsing, there is a clear need for further research on this topic. Efforts are underway to study the same effects on a simple streamwise injection hole on a flat surface.

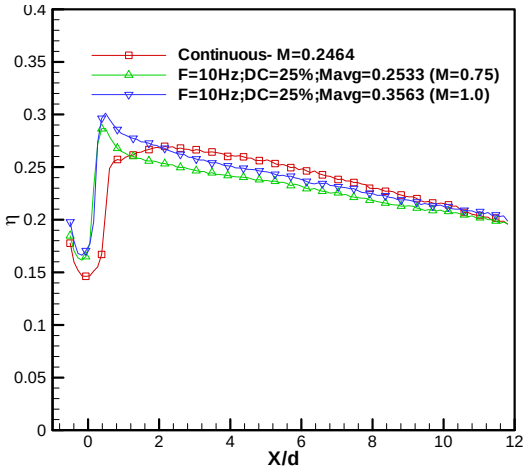

Figure 8a M=0.25

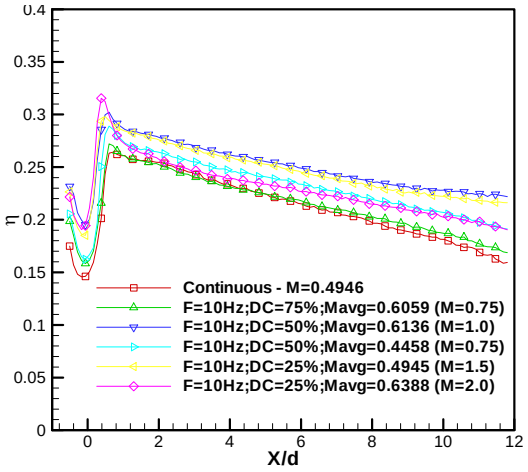

Figure 8b M=0.5

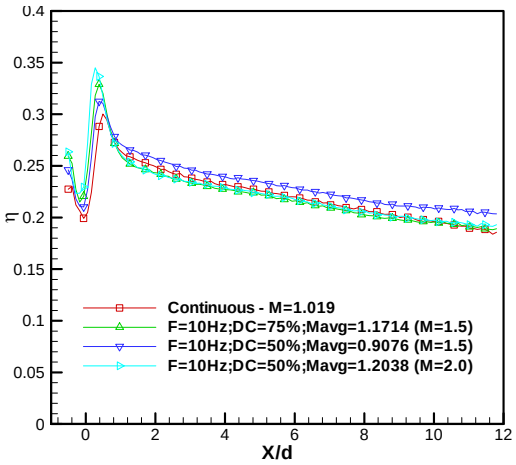

Figure 8c M=1.0

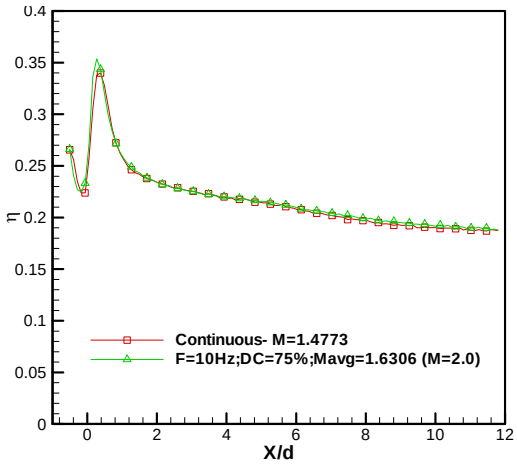

Figure 8d M=1.5

Figure 8 Effect of pulsing frequency on film effectiveness for a particular effective blowing ratio.

A Frequency Response Analysis of Thermocouples in a Shock Tube Environment

Submitted by: Ryan Thomas Hebert

For: AFRL-PRTT and UTC

Date: August, 15, 2003

Abstract

When conducting any type of transient experiment, it is important to know the rate at which a thermocouple (TC) can sense an instantaneous temperature change, also known as the frequency response or time constant. Without such information, the accuracy of TC measurements is always in question. However, it can be difficult to produce the necessary conditions to measure frequency response of a TC.

The sudden increase in temperature associated with the passing of a normal shock is one of the best ways to produce the type of temperature change needed to measure response time. With the transient response of a TC during a shock tube experiment, data extrapolation can be carried out to measure frequency response. This analysis will show that because of the high speed at which normal shock waves travel TCs must have extremely fast response times to sense the temperature change associated with this type of shock tube experiment.

In this study, J type TCs are examined, and the two major TC properties that were found to affect frequency response are wire diameter and junction type. Through a lumped capacitance analysis of TCs, smaller wire diameters were found to produce faster responses, and bare wire junctions are shown to have better reaction times than beaded junctions. Because most TCs available will show no response to passing shock waves, it is suggested that as soon as a 1 mil (.001”) TC becomes available it should be further tested in the shock tube available in Building 19. Further suggestions are also given at the end of this report.

General Shock Tube Analysis

Shock tube environments have been studied by countless researchers over the years; therefore their behavior is well understood and extremely predictable. The shock tube in Building 19 consists of two rectangular ducts separated by a kapton diaphragm. The left duct, which is the driver section, is three times larger than the right side, as seen in Figure 1. A vacuum pump is used to evacuate this side to a minimum value of 2 psia. The right duct has a pneumatically controlled plunger that is charged up to 60 psia and triggered by a foot pedal.

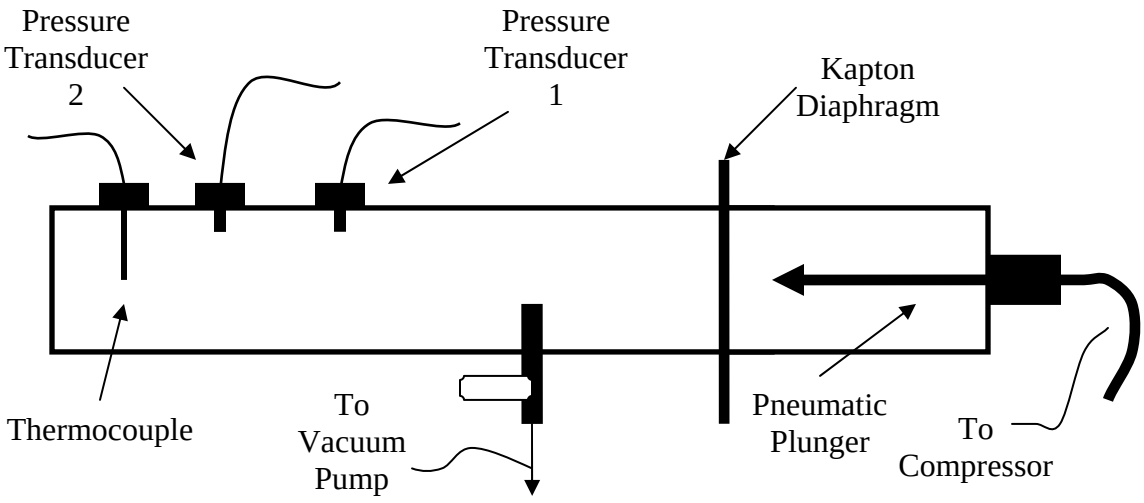

Figure 1: Shock Tube Schematic

The instrumentation of this shock tube is made up of two Model 8530-15 Endevco pressure transducers placed near the end of the driver section and a TC placed between the end wall and the second pressure transducer. Both transducers are charged

with 10Vdc, with one producing 10.68 mV/psi and the other 13.93 mV/psi. Two Model 8255 Pacific bridge conditioners are used to process the pressure transducer signals.

As one can see in Figure 2, the pressure readings obtained in this study completely coincide with expected results. First a sharp increase in pressure from the passing of the incident shock is seen in the pressure transducer closest to the diaphragm, P_1. Next, a double rise in pressure is seen at the second pressure transducer, P_2, which represents the passing of the incident shock and moments later the reflected shock. All pressure signals observed in the test were of exponential form, and each reading trailed off as time passed.

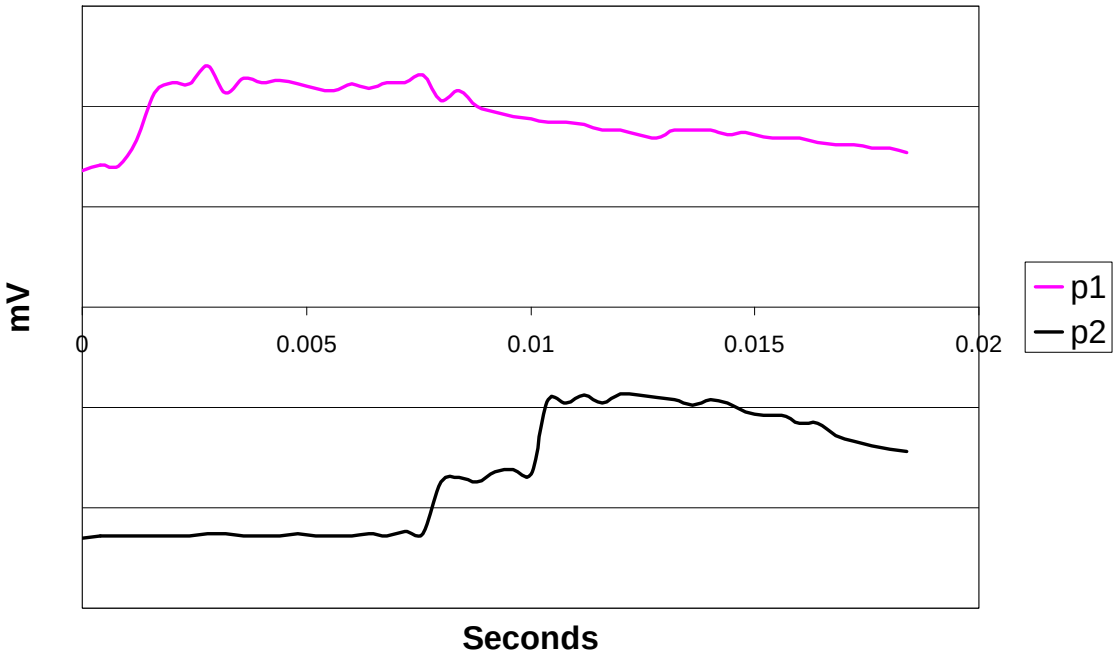

Figure 2: Pressure Readings for Shock Tube Test

The TC used in this test, as it will be shown in later analysis, was too large to sense the passing of the incident or reflected shock. However, if a smaller TC could be obtained, perhaps 1mil diameter, or more powerful shocks could be produced, a double

rise in temperature, similar to the second pressure transducer signal, would be seen. This response would be observed between the first and second pressure rises at P_2 because the TC is located between the transducer and the wall. The first temperature rise would occur from heat transferred to the TC from the incident shock, which would be in the form of forced convection to a cylinder in crossflow for the bare junction and a sphere for the beaded. The second temperature rise would result from the high temperature still air environment created after the passing of a reflected shock. In this situation heat is transferred by free convection and is minimal, if not negligible.

Lumped Capacitance Analysis of a Thermocouple in Crossflow

To approximate the frequency response of a TC in a shock tube environment, a simple lumped capacitance analysis was performed. A general energy balance was performed on both TC types: bare wire and beaded. Diagrams of both types can be seen in Figure 3 and 4.

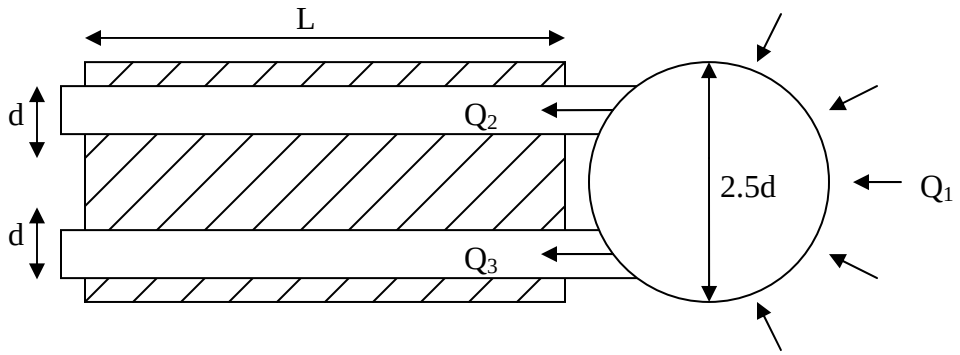

Figure 3: Beaded Thermocouple

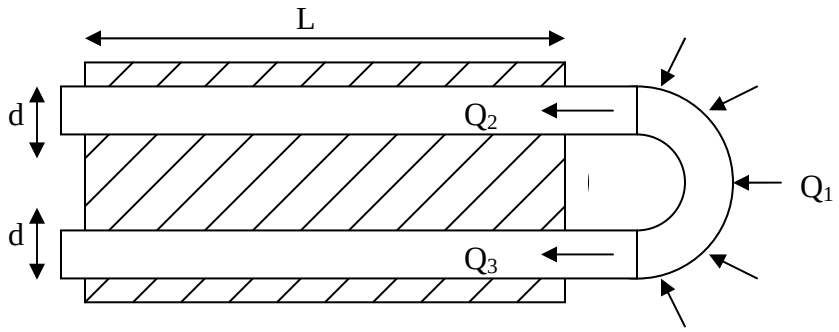

Figure 4: Bare Wire Thermocouple

For this analysis, certain assumptions were made:

- J type TCs made up iron and constantan are considered to have the following material properties:

- Iron: $\rho = 7870\frac{kg}{m^3}$, $k = 80.2\frac{W}{m \cdot K}$, $C_v = 447\frac{J}{kg \cdot K}$
- Constantan: $\rho = 8920\frac{kg}{m^3}$, $k = 23\frac{W}{m \cdot K}$, $C_v = 384\frac{J}{kg \cdot K}$

- Air properties remain constant.
- No internal temperature gradients in the TC
- The material properties of the TC junction are approximated as the average of both materials: iron and constantan.

After these assumptions the energy balance for a beaded TC can be simplified to:

$$-2.5h(T - T_\infty) - k_I \frac{T - T_0}{4L} - k_C \frac{T - T_0}{4L} = \frac{1}{6}\overline{\rho} d \overline{C}_v \frac{dT}{dt} \qquad (1)$$

Where T is the is the instantaneous TC temperature, T_∞ is the mainstream temperature, T_0 is the initial temperature, h is heat transfer coefficient, k_I and k_C are the thermal conductivity of iron and constantan, $\overline{\rho}$ is the average density of iron and constantan and $\overline{C}_v$ is the average specific heat. The conduction terms in Eq. 1 can be neglected through an order of magnitude analysis to produce:

$$-2.5h(T - T_\infty) = \frac{1}{6}\overline{\rho} d \overline{C}_v \frac{dT}{dt} \qquad (2)$$

A similar result is obtained for the bare wire TC, which was approximated as a single cylinder in crossflow.

$$-4h(T - T_\infty) = \overline{\rho} d \overline{C}_v \frac{dT}{dt} \qquad (3)$$

These equations can then be integrated over time to obtain a relationship for time and temperature.

$$T(t) = T_\infty + (T_0 - T_\infty)\exp\left(\frac{-2.4ht}{\overline{\rho} d \overline{C}_v}\right) \quad \text{Beaded (4)}$$

$$T(t) = T_\infty + (T_0 - T_\infty)\exp\left(\frac{-4ht}{\overline{\rho} d \overline{C}_v}\right) \quad \text{Bare (5)}$$

With this relationship the heat transfer coefficient is the only remaining piece of information needed to approximate the response times of any size onr type of TC.

The heat transfer coefficient (htc) for bare wire and beaded TCs are obtained from known correlations for the average Nusselt number, $\overline{Nu}$ of a sphere and cylinder in crossflow, respectively. These correlations are:

$$\overline{Nu}_d = 2 + \left(.4\,\mathrm{Re}_d^{\,1/2} + .06\,\mathrm{Re}_d^{\,2/3}\right)\mathrm{Pr}^{.4}\left(\frac{\mu_\infty}{\mu_s}\right) \quad \text{Beaded (6)}$$

$$\overline{Nu}_d = C\,\mathrm{Re}_d^{\,m}\,\mathrm{Pr}^{1/3} \quad \text{Bare (7)}$$

where μ_∞ and μ_s are the dynamic viscosity of air at the T_∞ and T_s (surface temperature). The constants *C* and *m* are found in Table 1, for different Reynolds numbers.

$\mathrm{Re_d}$	***C***	***m***
.4 - 4	0.989	0.330
4 – 40	0.911	0.385
40 – 4,000	0.683	0.466
4,000 – 40,000	0.193	0.618
40,000 -400,000	0.027	0.805

Table 1: Constants for Cylinder in Crossflow Correlations

Time Constant Calculations

With the average Nusselt number correlations, the temperature of TCs of all sizes can be found as a function of time. This temperature vs. time relationship can then be used to find the time constant for any TC diameter or junction type. The time constants shown in Table 2 represent the time required for a TC to reach 63.2% of the total temperature change.

Wire Dia.	τ - beaded	τ - bare
0.001”	2.3 ms	1.76 ms
0.005”	25.1 ms	20.8 ms
0.015”	123.7 ms	104.0 ms
0.032”	367.5 ms	296.3 ms

Table 2: Time Constants for Beaded and Bare Thermocouples

Table 3 shows the temperature the TC will reach in 1 ms, which is the time it would be exposed to the temperature change in the shock tube’s current configuration. The initial temperature of the TC is 77.4˚F and the mainstream, or final, temperature is 146.1˚F. Table 3 also shows the mV change for a J type TC associated with each ΔT.

Wire Dia.	T - beaded	Δ mV	T - bare	Δ mV
0.001”	93.3˚F	.4577	107.5˚F	.8705
0.005”	79.3˚F	.054	80.9˚F	.362
0.015”	78.0˚F	.0174	78.3˚F	.0247
0.032”	77.8˚F	.0116	77.9˚F	.0145

Table 3: Temperature Reached After 1ms

As one can see, the temperature increases associated with this shock tube experiment are extremely small, and the only size that would have a chance of adequately sensing a ΔT would be the .001" diameter.

For the reflected shock situation, the same lumped capacitance method is also used resulting in eqns 4 and 5. The only difference is that the maximum htc for free convection of gases was used. Maximum htc for free convection is 25 W/m^2K compared to 10,000 W/m^2K for forced convection at approximately 1300ft/s. Much higher temperatures are seen after the reflected shock (usually about twice the incident shock temperature, around 300ºF), but because the htc and thermal conductivity of air is so small, very little temperature rise is measured. Table 4 shows the change in temperature sensed in 1 ms after the reflected shock passes for both beaded and bare TCs, with T_0 equal to those temperatures found in Table 3 and $T_\infty \approx 300^\circ F$.

Wire Dia.	ΔT - beaded	ΔT - bare
0.001"	0.065˚F	0.080˚F
0.005"	0.017˚F	0.027˚F
0.015"	0.006˚F	0.009˚F
0.032"	0.003˚F	0.004˚F

Table 4: Temperature Change Due to Free Convection after the Reflected Shock

Suggestions

As one can see through this analysis, a 1 mil (.001”) TC produces a small response, .4577 mV, during the current shock tube configuration in Building 19. With enough amplification and filtering, there may be enough data to extrapolate a curve which could measure the time constant; however, a certain modification in the shock tube could be made that would improve its ability to measure a 1mil TC’s frequency response. This modification would produce more powerful shocks and higher temperatures after the incident shock. It would however decrease the amount of time the TC would be exposed to these higher temperatures.

Right now the shock tubes left side is evacuated with a vacuum pump to produce a pressure ratio and a shock wave when the diaphragm is ruptured. However, because evacuation is being used as the driving force, a limit is reached where no more air can be removed from the chamber. If the right side was also pressurized while the left side was evacuated, much stronger shock waves could be formed, which in turn would produce a larger TC temperature change. This would give the researcher more data to extrapolate, and thus improve the overall accuracy of the measurement.

There are some concerns with this modification that would have to be addressed before these stronger tests should be run. First, would the extremely delicate 1 mil thermocouple be able to withstand the force associated with much stronger shock waves. The fragility of these instruments has already been one major drawback to completing this study, so it must be determined whether or not the TC would survive such a large force. The second major consideration or limit with this type of modification is the

pressure limit of the transducers. The current transducers in the shock tube have a range of 0-45 psia, so an upper limit of 45 psia or 30 psig would be a limiting factor on this shock strengthening configuration. Finally, the kapton material currently being used may not be strong enough to support such large pressure differences. This concern could easily be addressed by using thicker mylar diaphragms that are currently available in Building 19.

Lastly, it should be noted that this modification would not drastically increase the percentage of ΔT that could be sensed. That percentage could only reach about 30%, but it could increase the size of the ΔT or ΔmV relative to the amount of noise associated with this type of measurement. Increasing the change in signal without increasing noise would definitely improve the accuracy of this study.

Conclusion

It is been shown that the current configuration of the shock tube in Building 19 could be used to sense a $\Delta T=15.9^{\circ}F$ or 22.2% of the total ΔT for a 1 mil thermocouple. This amount of temperature change could be adequate to approximate the time response. However, small modifications could be made to produce much larger changes in temperature and output voltage, while also increasing the percentage of total ΔT reached from 22% to 30%.

APPENDIX E

PINNING FORCE AND U_0 IN YBCO THIN FILM CONDUCTORS WITH AND WITHOUT ARTIFICIAL 211 INCLUSIONS

A DRAFT FINAL REPORT

M.D. SUMPTION

Sept 13, 2003

EXECUTIVE SUMMARY

First Segment of the Work

There were two main areas investigated during this time: a comparison of effective ramp rates for magnetization loops taken on YBCO conductors, and a comparison of important AC loss components and an estimation of a weak-link arrangement for the improvement of current sharing in striped YBCO conductors.

In the first topic, effective ramp rates of *M-H* loops measured using a stepping mode were calculated. All superconducting materials have critical current and magnetization decay with time, thus all measurements of *M-H* are to some extend dependent upon the time required for measurement. Since magnetization and J_c are the items of interest for YBCO coated conductors, this variation in measured value is important to quantify. In order to do so the standard expressions for decay were used, and combined with the standard expressions for ramp-rate variation to model the apparent (effective) ramp rate for the somewhat more complicated step-and-hold type loop measurements.

The second topic was the investigation of the use of weak-links to improve current sharing in filamentarized YBCO coated conductors. The conductors themselves are filamentarized in order to reduce losses, however, the individual filaments which are then generated are susceptible to defects. These defects are potentially very damaging to the current flow through the conductor, so a scheme to bypass them using weak links has been proposed. This scheme is already present (accidentally) in some other HTSC conductors, however it also increases the AC loss, thus possibly removing the original motivation for filamentarization. The present efforts focussed on determining whether a controlled level of weak leak values could in theory be chosen to allow current sharing but prevent AC loss degradation, and to compare this to the more standard scheme of normal metal current sharing paths. These two efforts are detailed in Section 1.

Second Segment of the Work

There were two main areas investigated during this time: an extraction of pinning potential values from the ramp rate dependence of the magnetization, and the construction of computer programs for interpreting the data coming from the magnetometer measurements.

In the first topic, *M-H* loops were measured for a sample TJ127C which exhibited strong pinning due to the implantation of 211 inclusions. These samples had been fabricated by T. Haugan (WPAFB). The *M-H* loops of these samples were measured at 10, 20, 30, 40, 50, 60, 70, and 77 K. At all of these temperatures, the *M-H* loops were taken at various ramp rates, associated with 2, 2.5, 3, 4, 5, 6, 8, 10, 20, and 60 minutes. The ramp rate response of the magnetization was then plotted (as $M = M_0 + S \times \mathrm{Ln}(dH/dt)$). The linearity of the resulting response was noted, and further work is planned to extract the U_0 values in order to fully characterize the pinning in this sample. Measurements on control samples are underway.

The second topic was the construction of two computer programs to aid the interpretation of WPAFB data. They were both written with quickbasic, and the final form was an executable file. The first of these took the *M-H* loops being generated by the MPMS machine and

converted then from *M-H* loops to curves of ΔM vs *H* (using a simple interpolative scheme to report magnetization widths between corresponding fields on the shielding and trapping branches of the *M-H*). The second was a program to correct the semi-Bean extracted J_c vs field curves for the self field effect. This program started with the initial data and iteratively improved it, such that it more closely approached the true J_c vs *H* curve. It was constructed assuming a semi-infinite slab with zero demagnetization correction. This may be added later. These two efforts are detailed in Section 2.

Third Portion of the Work

There were two main areas investigated during this time: an extraction of pinning potential values from the ramp rate dependence of the magnetization, and the extraction of pinning force densities from *M-H* loops directly. In the first topic, *M-H* loops were measured for a sample TJ127C which exhibited strong pinning due to the implantation of 211 inclusions. These samples had been fabricated by T. Haugan (WPAFB). The *M-H* loops of these samples were measured at 10, 20, 30, 40, 50, 60, 70, and 77 K. At all of these temperatures, the *M-H* loops were taken at various ramp rates, associated with 2, 2.5, 3, 4, 5, 6, 8, 10, 20, and 60 minutes. The ramp rate response of the magnetization was then plotted (as $M = M_0 + S$ x Ln(dH/dt)). The linearity of the resulting response was noted, and U_0 values were extracted in order to fully characterize the pinning in this sample. Measurements on control sample TJ360 were also performed and the results compared.
The second topic was the direct extraction of F_p curves from *M-H* loops. The results for TJ127C and TJ360 were compared, and the clear effect of the 211 inclusions present in TJ127C were observed. These two efforts are detailed below in section 3.

Section 1

Ramp Time Comparisons Between Continuous And Stepping Sweeps For Materials With Various Logarithmic And Exponential Components

We would like to make some comparisons of ramp times between samples with continuous loops and stepping loops. The samples can be imagined to have either logarithmic type decays or exponential type decays. Now

$$M_{tot} = M_s + M_{dynamic}$$

But

$$M_{dynamic} = M_{EO}\exp(-t/t_e) + M_{L0}[1 - RLn(t/t_L))]$$

Now a field stepping profile can be described as follows (in Figure 1).

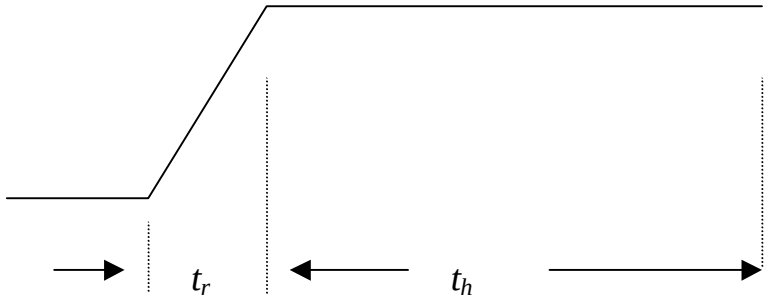

Figure 1. A schematic of a stepping field profile.

We can define p such that $t_r = t_{tot}p$, and $t_h = t_{tot}(1-p)$. We can also set H_m to be the field sweep amplitude, and n be the number of points in the loop, such that the field jump during t_r is $4H_m/n$.

Exponential Decay Component

The component of magnetization of a material which decays exponentially will have a linear dependence upon dB/dt, thus

$$M_E = C\frac{dB}{dt}$$

We can define an effective ramp rate for a stepping mode loop as that associated with the same prefactor but the magnetization exhibited (read, measured) at the end of time t_h, thus

$$M_E(t_h) \equiv C\left(\frac{dB}{dt}\right)_{eff}$$

But the magnetization at time t_h is just the magnetization at the time t_r, reduced by the exponential decay during t_h, leading to

$$M_E(t_h) = M_E(t_r)\exp(-t_h / t_E) = C\left(\frac{dB}{dt}\right)_{eff}$$

But then

$$M_E(t_r) = C\left(\frac{dB}{dt}\right)_{ramp} \Rightarrow \left(\frac{dB}{dt}\right)_{ramp} \exp(-t_h / t_E) = \left(\frac{dB}{dt}\right)_{eff}$$

which is the same as

$$\left(\frac{dB}{dt}\right)_{eff} = \left(\frac{dB}{dt}\right)_{ramp} \exp(-t_h / t_E)$$

Now

$$\left(\frac{dB}{dt}\right)_{ramp} = \frac{4H_m}{t_{tot}\,pn} \Rightarrow \left(\frac{dB}{dt}\right)_{eff} = \frac{4H_m}{t_{tot}\,pn}\exp(-t_h / t_E)$$

and since for a continuous loop,

$$\left(\frac{dB}{dt}\right)_{cont} = \frac{4H_m}{t_{tot}\,n}$$

we get

$$\left(\frac{dB}{dt}\right)_{eff} = \frac{1}{p}\left(\frac{dB}{dt}\right)_{cont} \exp\left(\frac{-t_{tot}(1-p)}{t_E}\right)$$

Logarithmic Decay Component

The component of magnetization of a material which decays logarithmically will have a logarithmic dependence upon *dB/dt*, thus

$$M_L = G\ln\left(\frac{dB}{dt}\right)$$

We can define an effective ramp rate for a stepping mode loop as that associated with the same prefactor but the magnetization exhibited (read, measured) at the end of time t_h, thus

$$M_L(t_h) \equiv G\ln\left(\frac{dB}{dt}\right)_{eff}$$

But then

$$M_L(t_h) = M_{LR}(1 - R\ln t_h) = G\ln\left(\frac{dB}{dt}\right)_{eff}$$

But then

$$M_{LR} = G\ln\left(\frac{dB}{dt}\right)_{ramp} \Rightarrow \ln\left(\frac{dB}{dt}\right)_{ramp}[1 - R\ln t_h] = \ln\left(\frac{dB}{dt}\right)_{eff}$$

which gives

$$\left(\frac{dB}{dt}\right)_{eff} = \exp\left[\ln\frac{dB}{dt} \otimes (1 - R\ln t_h)\right] = \left[\exp\left(\ln\frac{dB}{dt}\right)\right]^{[1-R\ln t_h]}$$

$$\left(\frac{dB}{dt}\right)_{eff} = \left[\frac{1}{p}\left(\frac{dB}{dt}\right)_{cont}\right]^{[1-R\ln\{t_{tot}(1-p)\}]}$$

Calculations

Figure 2 shows the ratio of *dB/dt* for a stepping type loop relative to the *dB/dt* of a comparable continuous loop (same loop time) as a function of the fraction of time devoted to the ramp, *p*, and the ratio of the hold time to the time constant of the exponential function (a materials property). We note that for almost all combinations of *t/t* and *p*, the stepping loop has a lower effective ramp rate than the continuous loop. This is to be expected, since the increase in M for the stepping loop is occurring as a 1/*p*,while the decrease in *M* is occurring as exponential in 1-*p*, and thus for all cases except very near *p* = 0, we would expect the exponential to dominate.

The situation is different for the logarithmic component, where 1/*p* is competing with a logarithmic decay. In this case we have plotted $(dB/dt)_{eff}$ as a function of *p* and *t/t*, assuming a continuous ramp rate of unity and an *R* = 0.2. This would be a reasonable value of *R*, with U_0 values ranging from 50-100 meV, depending upon the temperature. Nevertheless, in order to make specific predictions in this case, values of *dB/dt*, *t*, and U_0 Should be inserted directly.

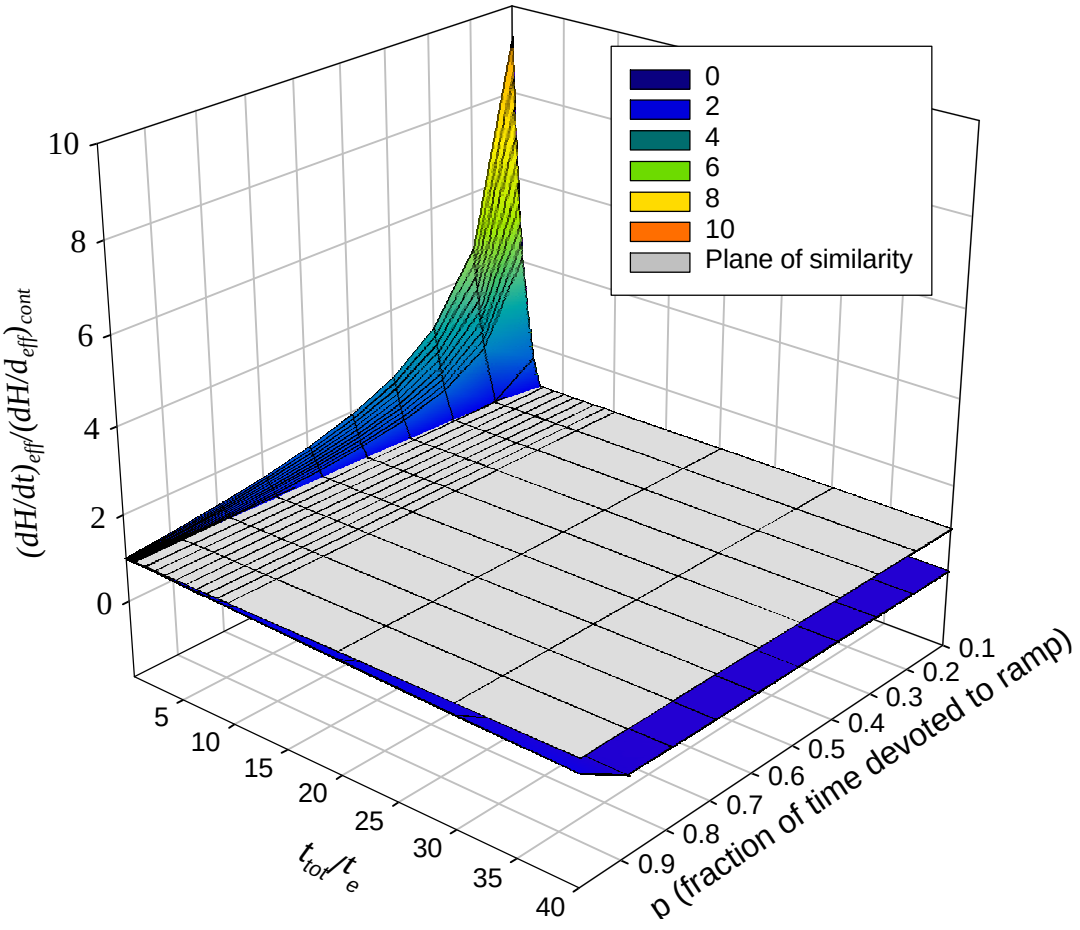

Figure 2. Ramp rate of stepping loop compared to continuous loop for exponential decay-related materials plotted as a function of time constants and ramp-pulse fraction.

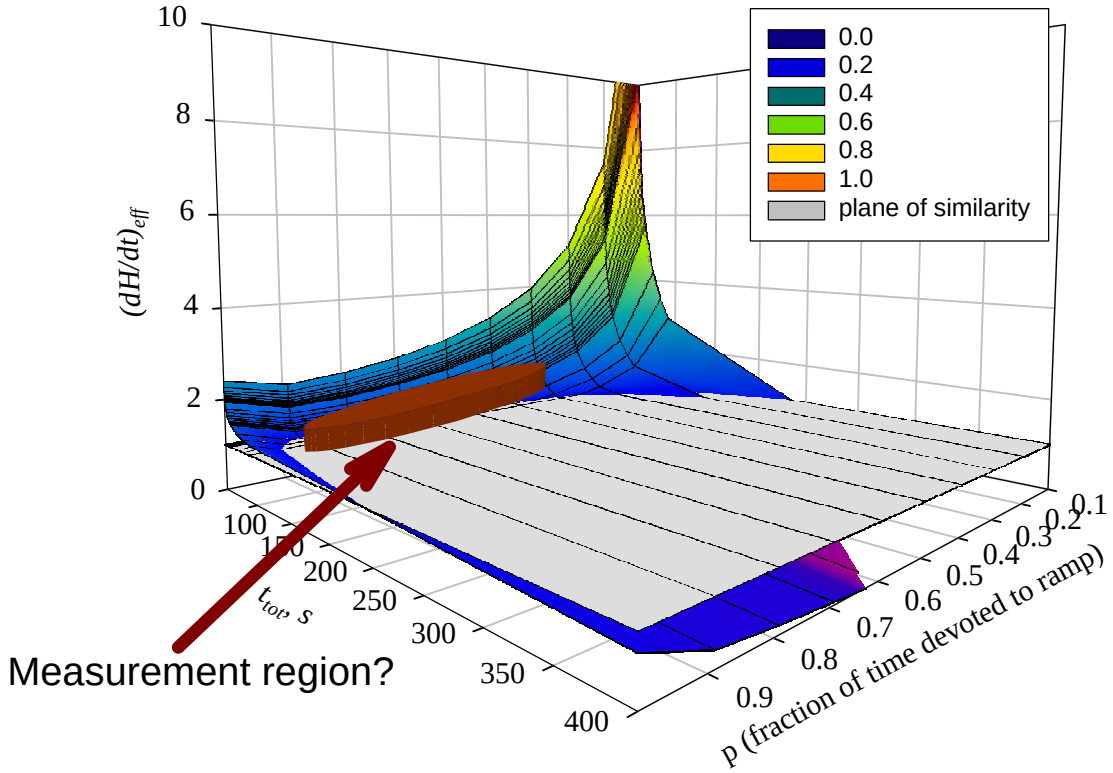

Figure 3. Ramp rate of stepping loop compared to continuous loop for exponential decay-related materials plotted as a function of time constants and ramp-pulse fraction.

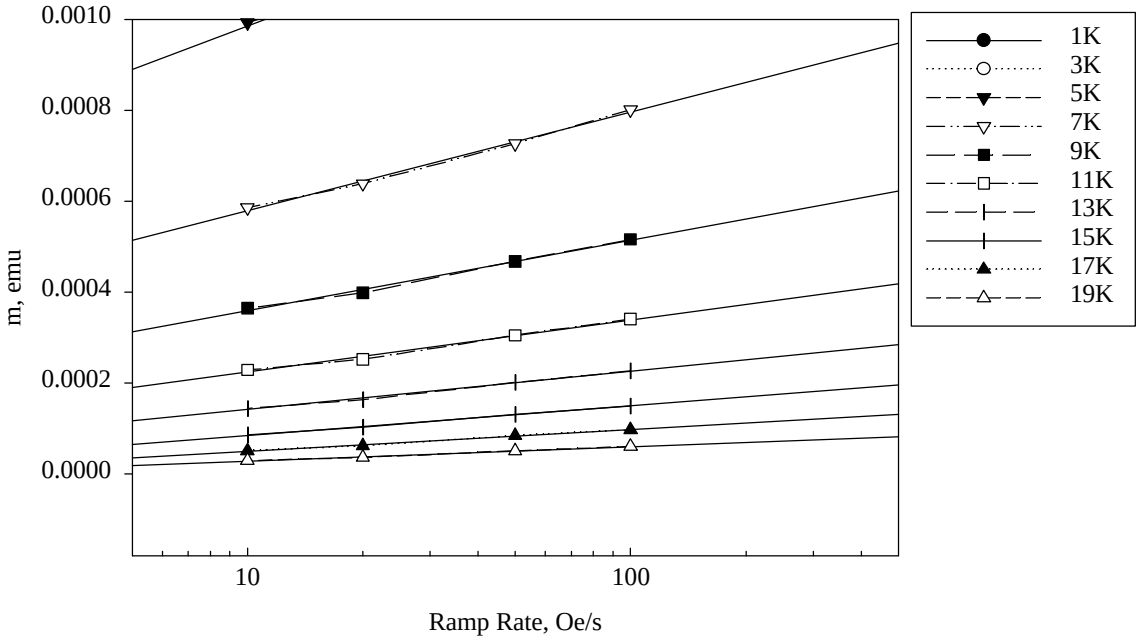

Figure 4. Ramp rate analysis for 381.

Various Conductor Options For YBCO Loss Suppression

In what follows the idea of partial filament coupling of YBCO striped conductors using weakly superconducting filamentary links is addressed. The idea is to allow for some current sharing between the filaments of a conductor, while not significantly degrading the loss benefit of filamentarization. Such current sharing possibilities are typically present for low Tc conductors by the nature of their fabrication. If it makes sense to retain current sharing for YBCO coated conductor filaments, then it could be done using either normal metals paths (as for LTSC) or weak superconducting paths (a practical reality for Bi/Ag strands). However, we note that the coupling induced by normal metal connections will be quite frequency dependent, and it may be of interest to look at the frequency independent SC alternative.

The losses in YBCO coated conductors come from; (1) normal metal effects, (2) ferromagnetic contributions, (3) hysteretic components, (4) coupling eddy currents, and (5) transport current related effects. We will concentrate on the applied field generated losses (i.e., ignore the transport current effects). In addition, ferromagnetic losses are usually small, and will be ignored. For an unfilamentarized conductor, hysteretic losses dominate at low frequencies, while at very high frequencies normal metal eddy currents may be quite important. Frequently, conductors (other than YBCO) are filamentarized in part to reduce hysteretic AC losses. While hysteretic losses are reduced, a coupling eddy current effect is generated which strives to "re-couple" the filaments and the associated large hysteretic losses.

In general, there are three ways to reduce applied-field induced losses (hysteretic and eddy current) in superconductors in general, and YBCO coated conductors in particular.

1. Reduce the field applied perpendicular to the wide side of the sample – apply fields EO, or reduce fields.

2. Make the conductor smaller or thinner to reduce the effective width, *d*, perpendicular to the field. The penalty of this is an increase inductance and decreased wire handle-ability.

3. Filamentarize the sample. In this case, however, it will always be necessary to introduce a twist or an effective twist, if only because of the connections at the ends. So, striped conductors will always need to be twisted or have some effective twist – thus, some connectivity will always be allowable – the question is how much. The filamentarization acts to reduce loss – but does allowing current sharing between filaments fulfill a useful goal? The only reasons to do so are two-fold: (1) some portion of the strand (some filament) is either defective in a small region (i.e, an analog to sausaged material) or it locally has a heating and a flux jump which does not propagate to neighboring filaments. In either case, it may be useful to have both a stabilizer and a bit of interfilamentary current sharing. It will be necessary to limit this to an amount which does not recouple the filaments, but is still useful for limiting the effects of limited filament degradation or localized instabilities.

It might not be too unlikely for there to be localized degradations – either stemming from variations in J_c, or small levels of degradation associated with the twisting procedure. This is pictured in Figure 1 (where the dotted lines indicate local degradation). The red arrows indicate current paths.

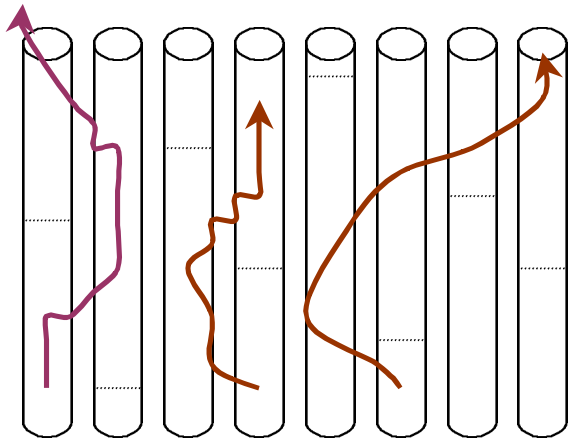

Figure 1. Current sharing between filaments with degraded regions.

In order to have a usefulness current sharing scheme, we need to make several assumptions. First, we must assume that the degraded regions we wish to compenstate are not too frequent, and are not localized. For instance, if all of the filaments are broken in a particular region of the strand (severe damage) no filamentry current sharing scheme will be effective. We must in general assume a picture where all of the filaments may have degraded regions, but these regions will occur only ocassionaly, and randomly, and we will describe their separation (of any one from another) by a length L_b. In addition, we must assume that when the current is being re-routed around a given filament, the current is able to reistribute to all filaments in the cross section (not just a nearest neighbor). The need for this requirement can be seen if we imagine a system where we imagine a conductor long enough that all filaments have at least one degraded region, but the degraded regions are separated by a minimum distance L_b, which is greater than the distance required to transfer the current to the other strand or strands, L_c. If we allow only nearest neighbor strands to share, then I_c will only be $I_c/2$ because all of the current from two strands is being chanelled into one. On the other hand if we allow current sharing between all strands, then I_c is only degraded by J_c/n.

Of course it is neccesary to make sure that the linkages that allow current sharing do not substantially degrade the loss improvements. If we denote the magnetization of the unfilamentarized material as DM_{unfil}, and that of the filamentarized as DM_{fil}, then $DM_{fil} = DM_{unfil}/n$, where n is the number of filaments. If we require that the coupling currents add a magnetization no more than that of one of the filaments, then

$$J_{cw}L_c = J_{cf}d_f \qquad thus \qquad J_{cw} = \frac{J_{cw}d_f}{L_c}$$

If we assumed that even 100% of the filaments were degraded somewhere along their length, but that the degraded regions were well distributed (such that we had on average less than one per L_c, say), the J_c would be only slightly degraded. For example, if we take a length of 100 m, and assume that each of the filaments has one break and that there are 20 filaments, relatively evenly distributed, then the breaks will be every 5 m. If J_{cw} is chosen such that L_c is 0.2 m, from the above expression, then L_c « L_b, and the current sharing will be sufficient to transfer all the current from the filament in question to the other filaments (the length required to make current transfer is L_c, under the above prescription). The strand must of course should be twisted, at a twist pitch of say L_p, but this is not a directly related consideration. We can see that it is possible to define a frequency independent value of J_{cw} which can be helpful in current sharing.

This scheme must be compared to the standard one of using normal metal to allow current sharing between filaments. The calculation has a different character here. First we must ask what resistivity and cross section of normal metal is needed to allow for acceptable current sharing. In order to estimate this we will use the fact that the transfer current will generate a voltage

$$V = IR = \frac{I_c}{n}\frac{rw}{L_c t}$$

Here I_c/n is the current in an individual strand, w is the whole conductor width, t is the normal metal thickness, r is the normal metal resistivity and L_c is again the transfer length. If we associate this voltage with the electric field criterion for superconducting transition, viz. 1 μV/cm for HTSC, then we must use the fact that $V_{tot} = N_b V$, where V_{tot} is the total voltage along the conductor of length L_{tot}, N_b is the number of degraded regions, and V is the voltage from the individual degraded zone. Since then 1 μV/cm = V_{tot}/L_{tot}, we get

$$1mV/cm = \frac{L_B I_c w}{L_c n t} r$$

This now needs to be coupled with expressions for loss and reconfigured to lead to a limitation on L_p, L_c, and ρ.

Section 2

U_0 in YBCO Thin Films with 211 inclusions

Introduction

There were two main areas investigated during this time: an extraction of pinning potential values from the ramp rate dependence of the magnetization, and the construction of computer programs for interpreting the data coming from the magnetometer measurements.

In the first topic, *M-H* loops were measured for a sample TJ127C which exhibited strong pinning due to the implantation of 211 inclusions. These samples had been fabricated by T. Haugan (WPAFB). The *M-H* loops of these samples were measured at 10, 20, 30, 40, 50, 60, 70, and 77 K. At all of these temperatures, the *M-H* loops were taken at various ramp rates, associated with 2, 2.5, 3, 4, 5, 6, 8, 10, 20, and 60 minutes. The ramp rate response of the magnetization was then plotted (as $M = M_0 + S$ x Ln(dH/dt)). The linearity of the resulting response was noted, and further work is planned to extract the U_0 values in order to fully characterize the pinning in this sample. Measurements on control samples are underway.

The second topic was the construction of two computer programs to aid the interpretation of WPAFB data. They were both written with quickbasic, and the final form was an executable file. The first of these took the *M-H* loops being generated by the MPMS machine and converted then from *M-H* loops to curves of ΔM vs H (using a simple interpolative scheme to report magnetization widths between corresponding fields on the shielding and trapping branches of the *M-H*). The second was a program to correct the semi-Bean extracted J_c vs field curves for the self field effect. This program started with the initial data and iteratively improved it, such that it more closely approached the true J_c vs H curve. It was constructed assuming a semi-infinite slab with zero demagnetization correction. This may be added later. These two efforts are detailed below. Much of this work is ongoing, with full U_0 analysis awaiting measurement of the control samples.

Ramp Rate Results and Pinning Strength in YBCO Coated Conductors

The M-H response of sample TJ127C was measured at various fields and temperatures, as described below. The response was plotted as a function of ln(dH/dt), since we expect that

$$M = M_0 + SLn\left(\frac{dH}{dt}\right) \tag{1}$$

This can be connected to the more standard expression for magnetization decay

$$M = M'[1 - R\ln(t)] \tag{2}$$

by $R = S/M_0$. We note then that $R = k_BT/U_0$, where U_0 is the uncorrected apparent pinning potential. This of course must be corrected by the slope factor – this work is ongoing. Below we plot, however, the response of the samples, note the functional dependence on ln(*dH/dt)*, and begin to extract normalized U_0 values (these in Fig 9 are in arbitrary units).

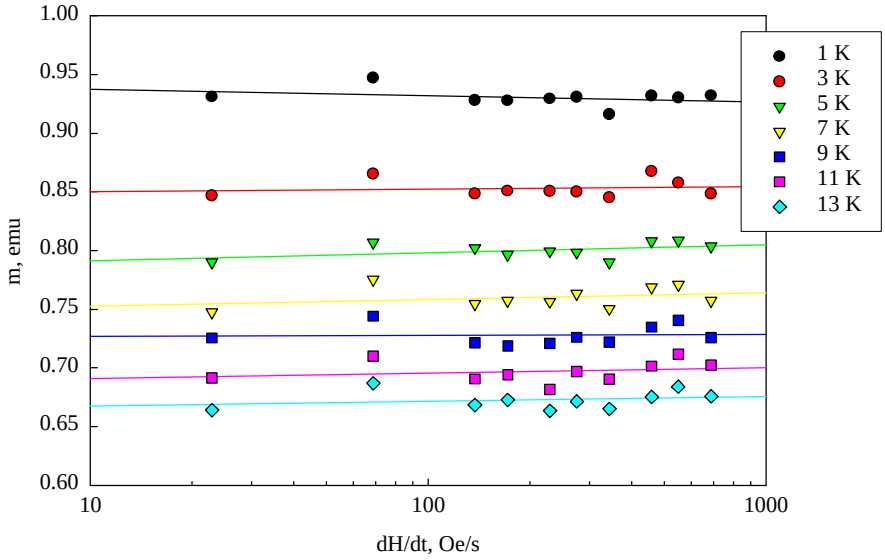

Figure. 1. Ramp rate response of M-H curve at T = 10 K.

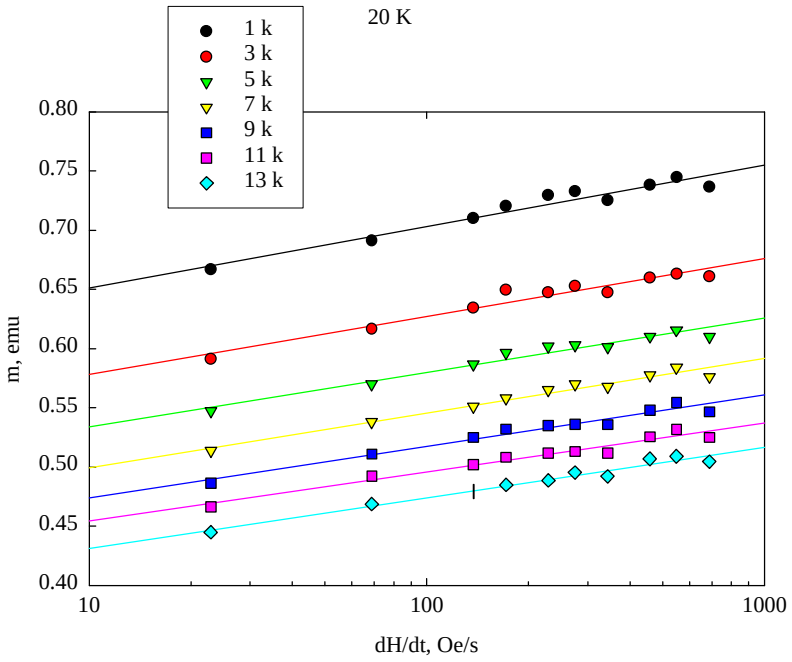

Figure 2. Ramp rate response of M-H curve at T = 20 K.

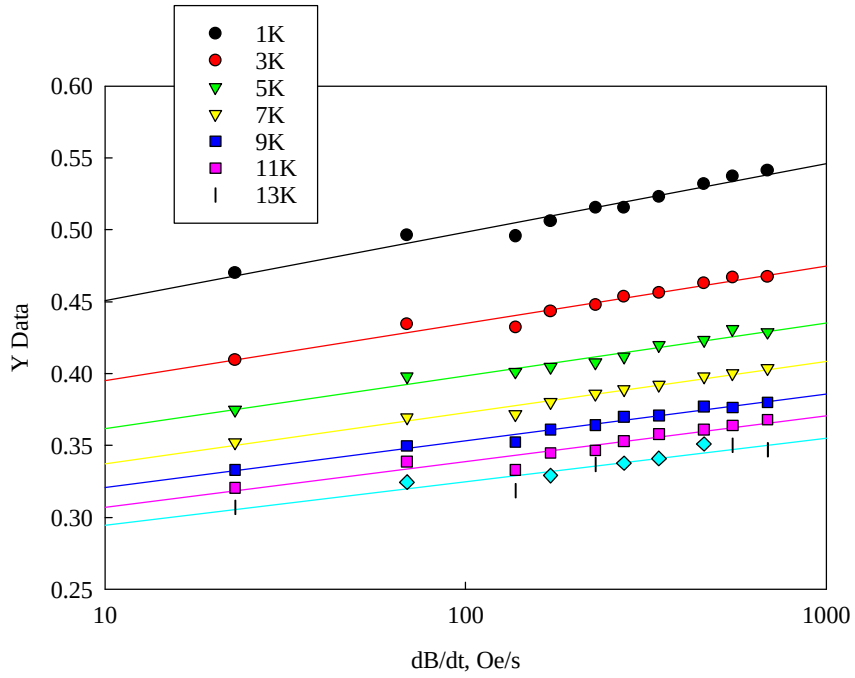

Figure 3. Ramp rate response of M-H curve at T = 30 K.

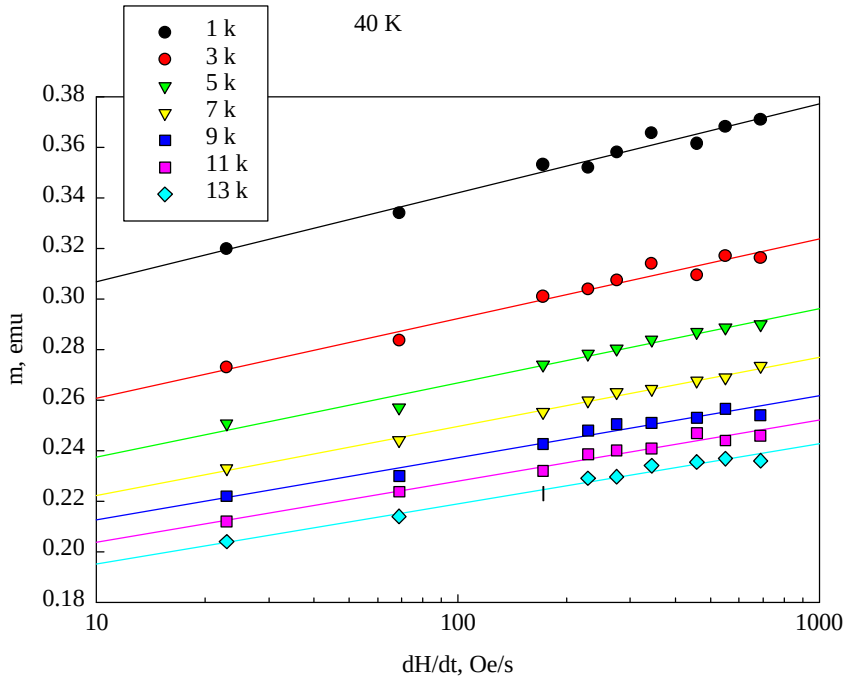

Figure 4. Ramp rate response of M-H curve at T = 40 K.

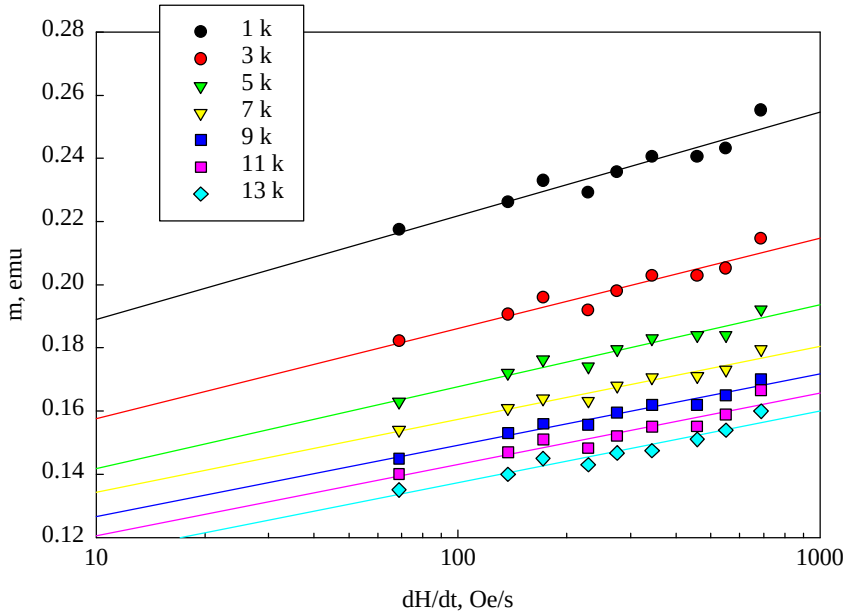

Figure 5. Ramp rate response of M-H curve at T = 50 K.

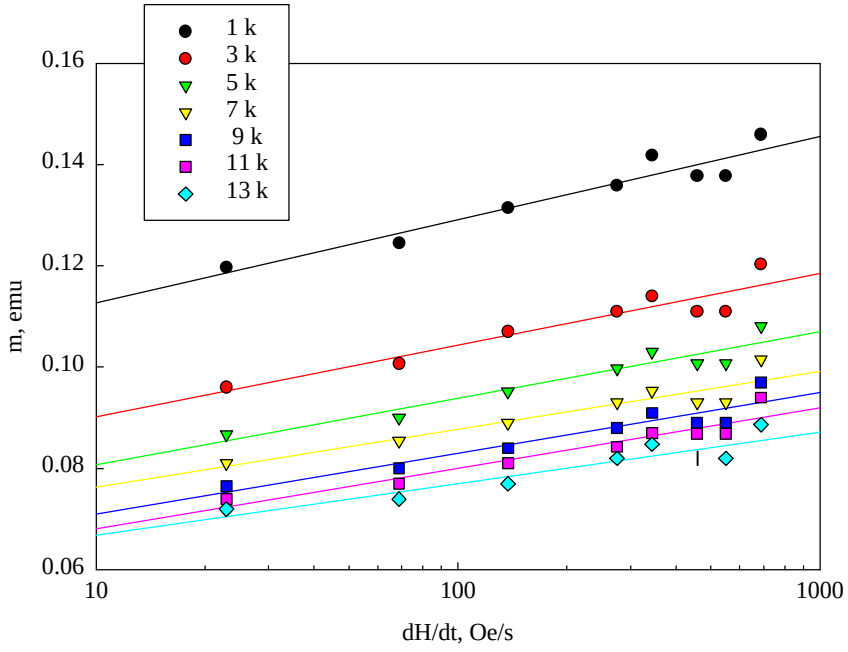

Figure 6. Ramp rate response of M-H curve at T = 60 K.

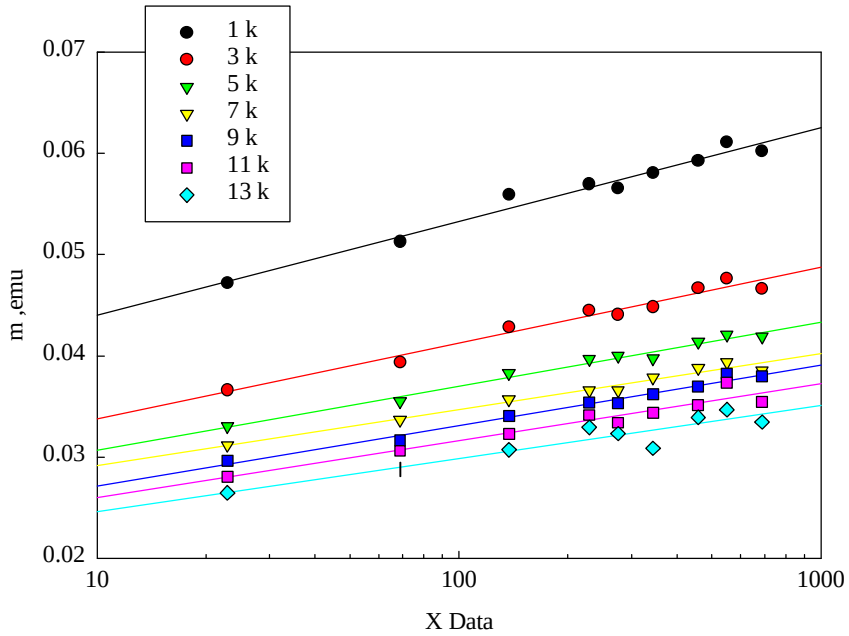

Figure 7. Ramp rate response of M-H curve at T = 70 K.

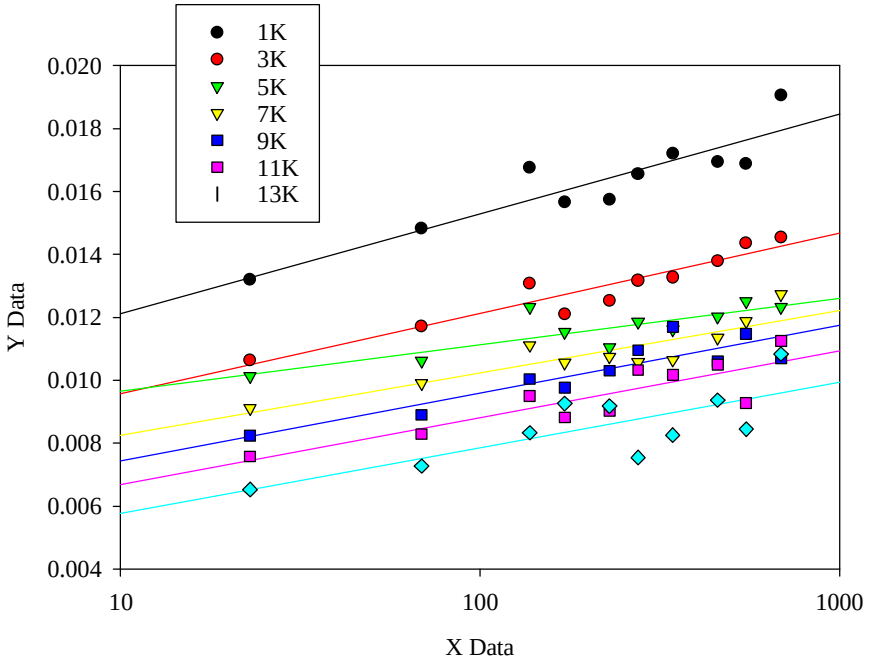

Figure 8. Ramp rate response of M-H curve at T = 77 K.

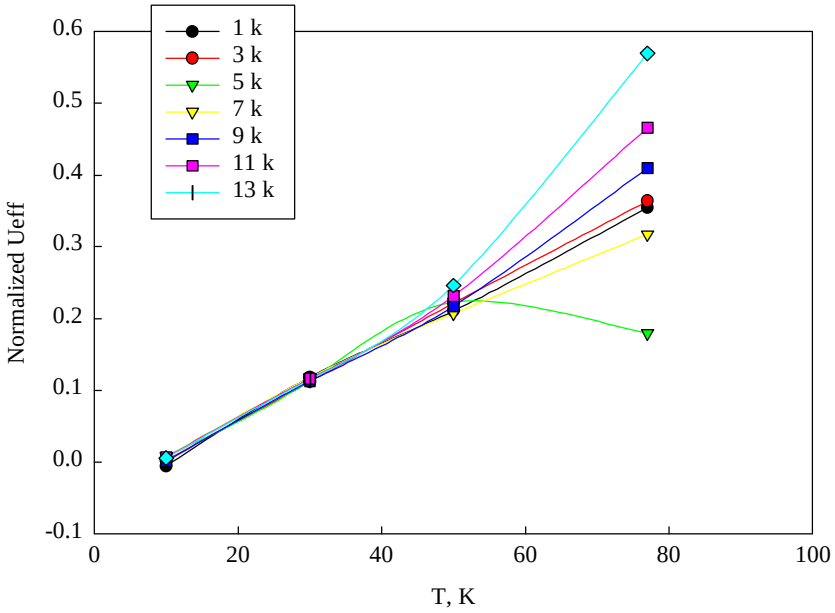

Figure 9. Apparent pinning energy, without Jc slope correction (i.e., kT/R)..

Programs for data analysis

Two programs were constructed. The first took the *M-H* loops coming form the MPMS, which were typically 5000 points, and broke them into five parts. Only one trapping and one shielding branch were retained, the other were discarded. After this the field values on the trapping branch were stepped through, and the data on the bottom branch (which were taken at slightly different field values) were interpolated to the values on the trapping branch. These are then outputted, along with the reversible magnetization. This program is listed in Appendix A.

The second program took the J_c vs H curve that had been extracted using a semi-Bean assumption and then used this to construct the field profiles within the samples. From these, which incorporated the local field dependence, the apparent Jc vs H curve was constructed, and compared with the original one. Interative variations were used to obtain a true J_c vs H curve, and to then project the apparent J_c vs H curve closest to the measured one. This program is listed in Appendix B.

Section 3. J_c and F_p in Thin Film YBCO with and Without 211 Inclusions

Introduction

The main focus of the latest segment of the work has been on the magnetic J_c and the pinning force density of two YBCO samples. The object was to both directly measure the magnetic J_c to show the influence of 211 inclusions, and also to look at the pinning force curves, to see if a different pinning force character is evident. The two samples were TJ127C, one of the best of the samples with 211 inclusions, and sample TJ360, a typical control sample. Previous experiments had shown TJ360 and TJ127C to be a useful comparison, and also showed significant enhancement at 77 K for TJ127C, as compared to TJ360.

The samples were mounted in a vibrating sample magnetometer, and measured at temperatures from 10 K to 77 K, with varying ramp rates. The 10 minute loops are displayed below. The temperature was measured by a Si-diode placed near the sample. The field was applied perpendicular to the wide face of the sample, and thus the currents measured were *a-b* type. The resulting *M-H* loops were volume normalized, and then the magnetic J_c was extracted via

$$J_c = \frac{30\Delta M}{d}$$

The results are shown in Fig. 1 and 2.

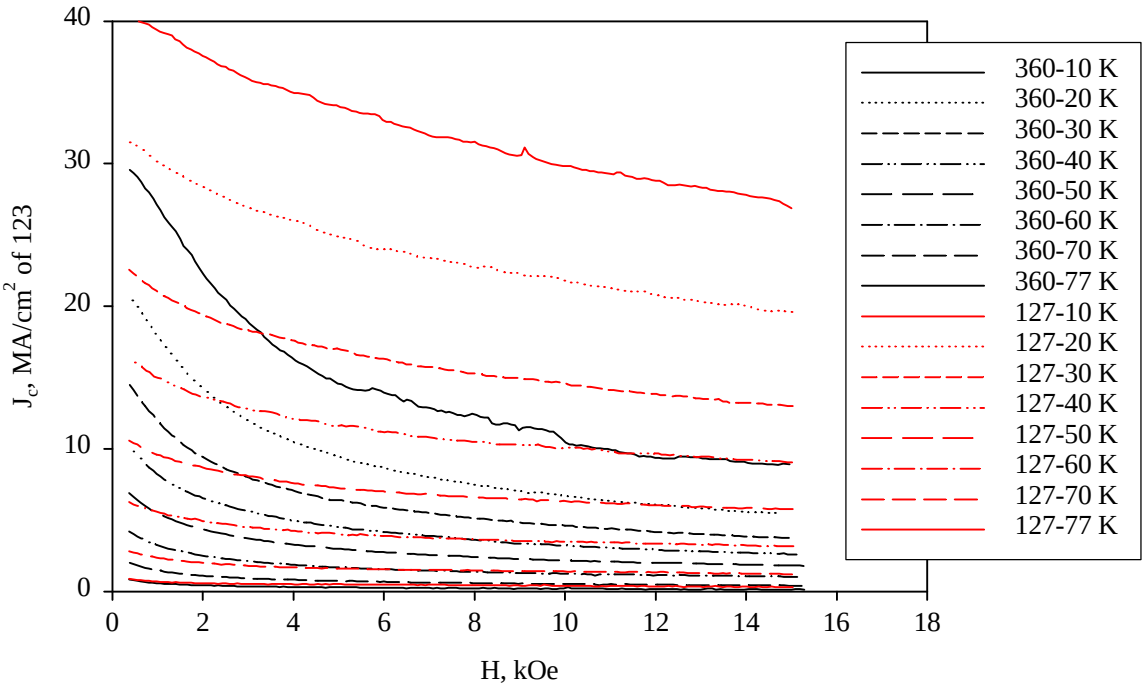

Fig. 1. Magnetic J_c for samples TJ360 and TJ127C at temperatures 10 to 77 K.

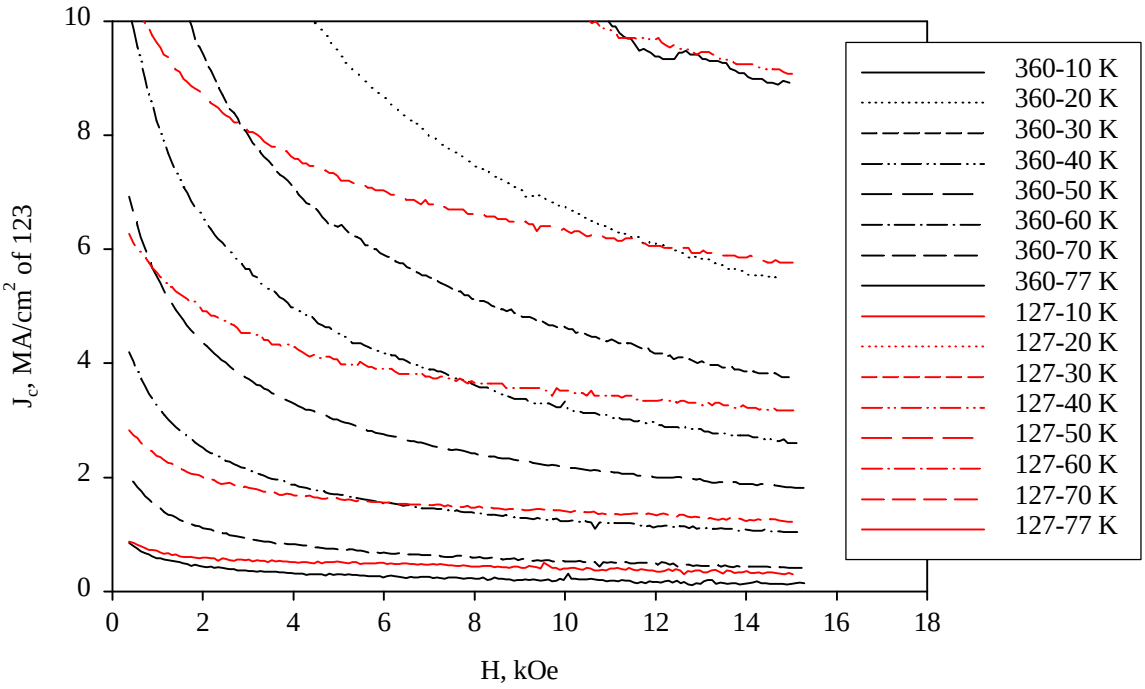

Fig. 2. Magnetic J_c for samples TJ360 and TJ27C at temperatures from 10 K to 77 K – high temperature values.

Clearly, the values at low temperatures are very much greater for TJ127C – a much larger improvement than is evident at 77 K. This confirms the flux pinning advantages conferred by the 211 inclusions. Figures 3-5 show this in terms of the pinning force curves. Here $F_p = J_cB$ was used, and the force is in GN/m^2. The results are comparable to those of Foltyn et al [1].

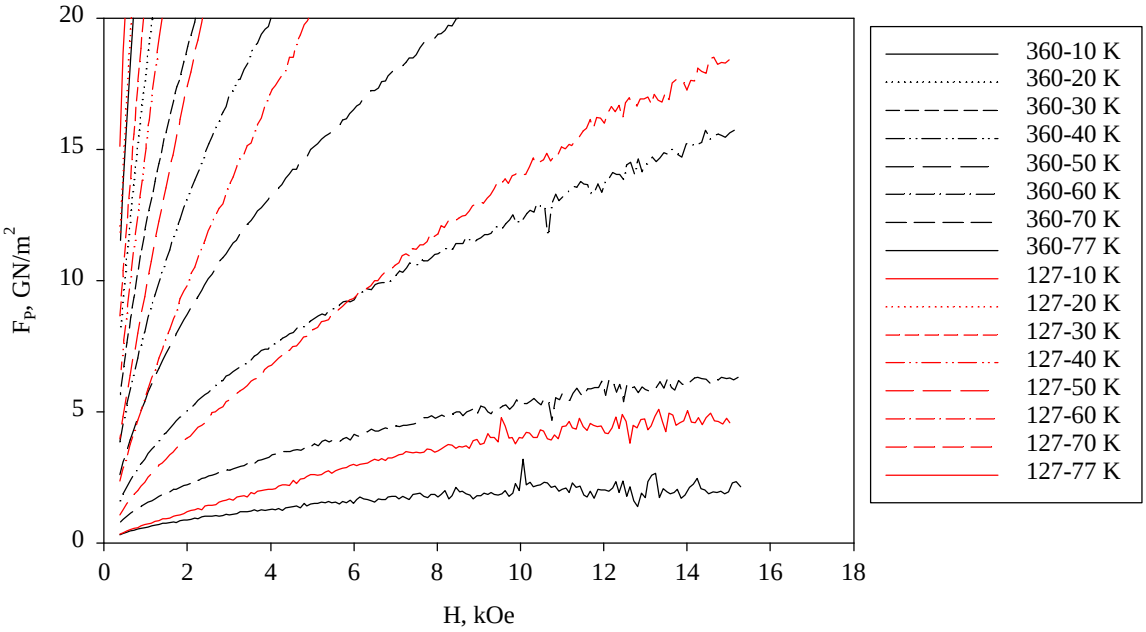

Fig. 3. F_p vs H for samples TJ127C and TJ360 at high temperatures.

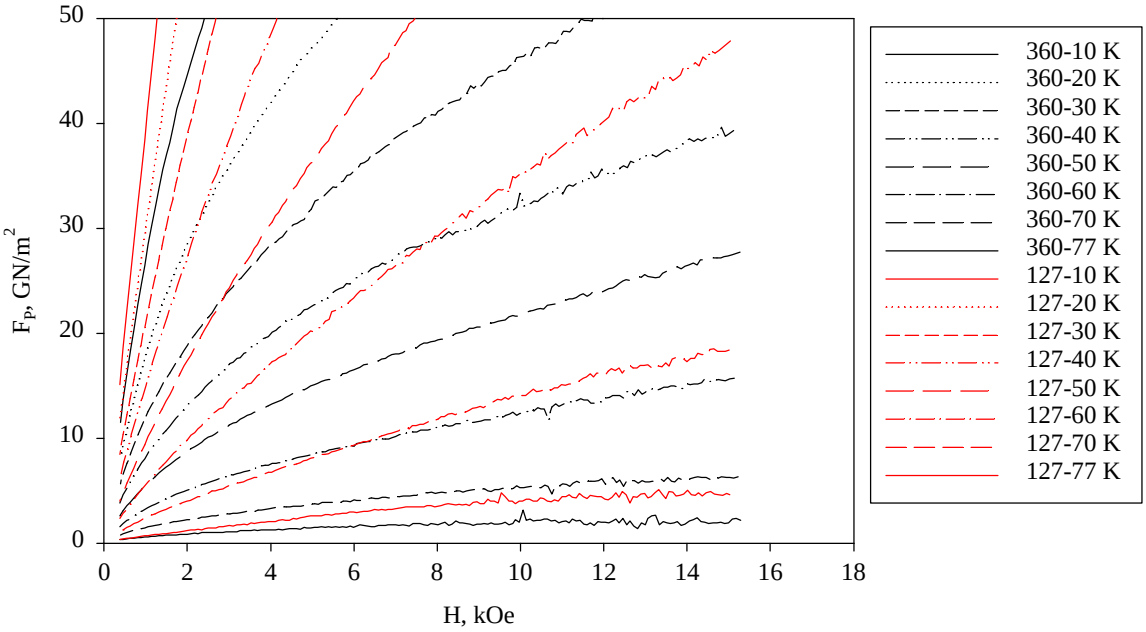

Fig. 4. F_p vs H for samples TJ127C and TJ360 at intermediate temperatures.

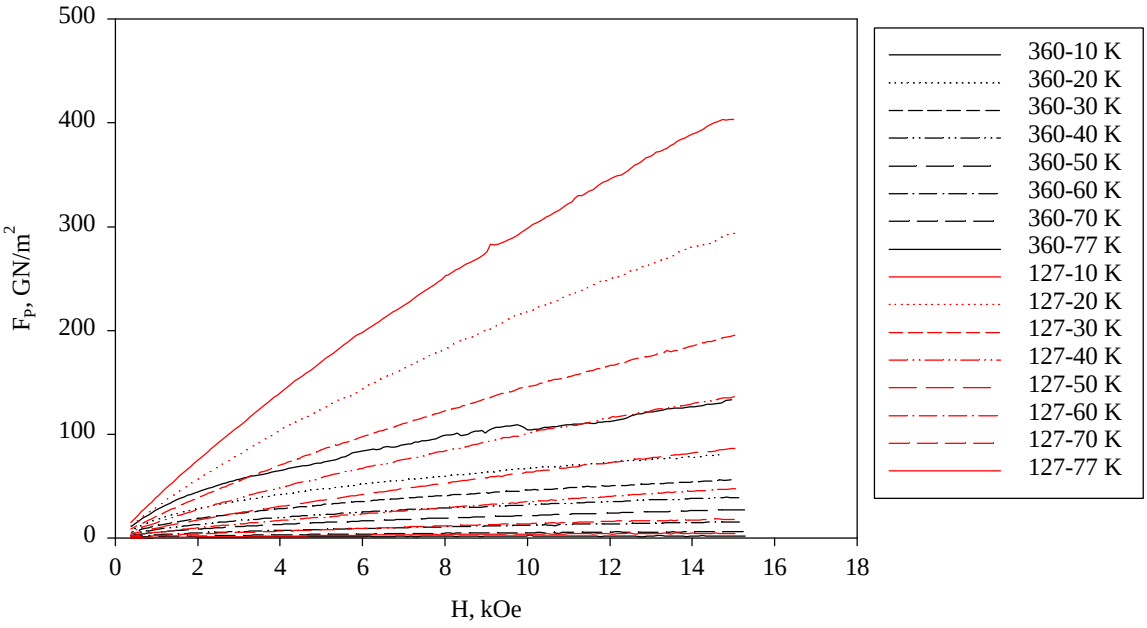

Fig. 5. F_p vs H for samples TJ127C and TJ360 at temperatures from 10-77 K.

Conclusions

The addition of 211 inclusions significantly enhances YBCO thin film performance. The direct extraction of F_p conclusively demonstrates that this is so, and underscores the large increases in low temperature J_cs which are seen.

References

[1] Folytn et al., LANL (1996) YBCO/Ni/YSZ 1 micron microbridge.

APPENDIX A: LOOP ANALYSIS PROGRAM

Downloadable At http://www.mse.eng.ohio-state.edu/~sumption/

```
REM --------------------PROGRAM LOOP ANALYSIS-----------------------------------

REM      JUST USES POSITIVE BRANCH OF CURVE
REM
REM
REM                 VARIABLES:
REM
REM
REM       DA1, DA2: ARRAYS WHICH HOLD M AND H DATA (H,M) OF THE
UPPER AND
REM               LOWER BRANCHES, RESPECTIVELY, OF THE POSITIVE BRANCH
REM               OF THE LOOP.

REM-----------------------------------------------------------------------

REM ---DECLARATION-----------------------------------------------------
DEFSNG A-H, J-Z
DIM DA1(2000, 2), DA2(2000, 2)

REM-----------------------------------------------------------------
COLOR 15, 9

REM--------------SETTING UP-----------------------------------------

CLS : LOCATE 8, 28: PRINT "LOOP ANALYSIS PROGRAM"

LOCATE 12, 5: PRINT "DERMINES DELTA M IRR AND M REV AS A FUNCTION
OF H"
LOCATE 12, 5: PRINT "INTENDED FOR USE ON LOOPS WITH FIVE BRANCHES
AND EVENLY DISTRIBUTED POINTS"
LOCATE 16, 5: INPUT "ENTER THE NAME OF THE FILE TO BE ANALYZED"; D1$
LOCATE 18, 5: INPUT "ENTER THE NAME OF THE FILE WHICH IS TO CONTAIN
THE OUPUT DATA"; D2$
LOCATE 20, 5: INPUT "ENTER THE NUMBER OF LINES TO BE STRIPPED FROM
THE TOP OF THE FILE"; GLIM
LOCATE 22, 5: INPUT "ENTER THE TOTAL NUMBER OF POINTS IN THE M-H
LOOP"; NPL
LOCATE 24, 5: INPUT "ENTER THE INITIAL TIME STAMP"; Ts

REM -----OPENING FILES

OPEN D1$ FOR INPUT AS #1
OPEN D2$ FOR OUTPUT AS #2

REM-----------------------------------------------------------------
```

```
REM --- GET RID OF FIRST "GLIM" LINES, AND THEN FIRST M-H LOOP
BRANCH-------------------------

FOR i1 = 1 TO GLIM: INPUT #1, garb$
PRINT garb$

NEXT i1

nplb = INT(NPL / 5)
i33 = 0
10 FOR I2 = 1 TO 1000
  INPUT #1, garb1
  IF i33 = nplb - 1 GOTO 20
  IF garb1 > Ts - 1 THEN
  i33 = i33 + 1
  PRINT garb1
  END IF
  GOTO 10

  NEXT I2
20

CLS
REM----------------------------------------------------------------

REM ---CALL ALL DATA IN FROM THE UPPER PORTION OF CURVE-----
I112 = 1
25 INPUT #1, garb
      IF I112 = nplb THEN GOTO 35
      IF garb > Ts - 1 THEN GOTO 30
      GOTO 25

30 INPUT #1, garb2, DA1(I112, 1), DA1(I112, 2)
PRINT garb, DA1(I112, 1), DA1(I112, 2)

I112 = I112 + 1
GOTO 25
35

NPLB2 = 2 * nplb
REM get rid of two branches
i34 = 0
40 FOR I2a = 1 TO 1000
```

```
  INPUT #1, garb1
  IF i34 = 2 * nplb - 1 GOTO 50
  IF garb1 > Ts - 1 THEN
  i34 = i34 + 1
  PRINT garb1
  END IF
  GOTO 40

  NEXT I2a
50

REM ---CALL ALL DATA IN FROM THE LOWER PORTION OF THE CURVE------
I113 = 1
55 INPUT #1, garb4
      IF I113 = nplb THEN GOTO 85
      IF garb4 > Ts - 1 THEN GOTO 60
      GOTO 55

60 INPUT #1, garb5, DA2(nplb + 1 - I113, 1), DA2(nplb + 1 - I113, 2)
PRINT garb5, DA2(nplb + 1 - I113, 1), DA2(nplb + 1 - I113, 2)

I113 = I113 + 1
GOTO 55
85

REM-----NOTE NOTE THAT DA2 IS FILLED BACKWARDS----------

FOR I = 3 TO nplb - 3
      HT = DA1(I, 1)
      MT = DA1(I, 2)
      FOR I2 = 2 TO nplb
REM             PRINT HT, DA2(I2, 1)

           IF DA2(I2, 1) = HT THEN
                MS = DA2(I2, 2)
                GOTO 1024
                              ELSEIF DA2(I2, 1) < HT THEN
                IF DA2(I2 - 1, 1) > HT THEN
                     HSH = DA2(I2 - 1, 1): MSH = DA2(I2, 2)
                     HSL = DA2(I2, 1): MSL = DA2(I2, 2)
                     MS = MSH + ((MSL - MSH) / (ABS(HSH - HSL))) * (ABS(HT -
HSH))
                     GOTO 1024
                ELSE
                     IF I2 = nplb THEN
                          PRINT "ERROR"
```

```
                        GOTO 1055
                    END IF
                END IF
            ELSE
                IF I2 = nplb THEN
                    PRINT "ERROR"
                    GOTO 1055
                END IF
            END IF
        NEXT I2
1024    REM SINCE DELM=M TRAPPING-MSHIELDING, AND MREV=(MT+MS)/2
        DELM = MT - MS
        MREV = (MT + MS) / 2
        H = HT
        PRINT "   H   ", "   DELM   ", "    MREV    "
        PRINT H, DELM, MREV
        WRITE #2, H, DELM, MREV

1055    REM PROGRAM GOES HERE IF THERE IS NO H MATCH

NEXT I

CLOSE ALL
CLS
LOCATE 20, 5: PRINT "COMPLETED"

END
```

APPENDIX B: J_c vs FIELD SELF-FIELD CORRECTION PROGRAM

Downloadable At http://www.mse.eng.ohio-state.edu/~sumption/

```
REM ----------PROGRAM Jc-FIELD ANALYSIS----------

REM
REM
REM
REM                VARIABLES:
REM
REM
REM       DA1, DA2: ARRAYS WHICH HOLD "initial" AND "modified" DATA (J,H)
OF JC VS FIELD
REM             DA1 IS INITIALLY THE SEMI-BEAN VALUE, WHILE DA2 IS THE
VALUE WHICH IS EXPECTED BASED ON THAT FIELD
REM               DEPENDENCE ASSUMING VARIATION WITHIN THE SAMPLE.
THESE THEN INTERATE
REM       DA0, DAPP; ARRAYS PARALLELING DA1 AND DA2. DA0 IS THE
"ORIGINAL DATA"
REM             AND DAPP IS THE APPARENT JC VS EXTERNAL FIELD CURVE
REM       NOTE THAT DA1, AND DA2 ARE MEANT TO EVENTUALLY
CONVERGE TO A TRUE
REM             JC VS H CURVE, WHILE DA0 AND DAPP ARE APPARENT JC
(DERIVED FROM
REM             MAGNETIZATION) VS EXTERNAL FIELD
REM       DFT,DFS: ARRAYS WHICH GIVE THE FIELD AS A FUNCTION OF
POSITION WITH THE SAMPLE
REM       D1$, D2$, D3$: THE FILENAMES OF THE STARTING DELm DATA, THE
ENDING Jc VS H DATA, AND THE ORIGINAL
REM             CONVERTED DATA (Jc VS H)
REM
REM----------



REM ---DECLARATION----------
DEFSNG A-H, J-Z
DIM DA0(250, 2), DA1(250, 2), DA2(250, 2), DFT(100), DFS(100), DAPP(250, 2)


REM----------


REM----------SETTING UP----------
REM CLEAR AND COLOR THE SCREEN, PROMPT THE USER
SCREEN 0
COLOR 15, 9, 4
CLS : LOCATE 8, 28: PRINT "JC-FIELD ANALYSIS PROGRAM"
```

```
LOCATE 10, 5: PRINT "DETERMINES THE REAL Jc VS H GIVEN A SEMI-BEAN
STARTING POINT"
LOCATE 12, 5: PRINT "INTENDED FOR SEMI-INFINITE SLABS WITH NO DEMAG
AND WIDTH 2*R, AND Jc IN A/CM2"
LOCATE 14, 5: INPUT "ENTER THE NAME OF THE FILE TO BE ANALYZED"; D1$
LOCATE 16, 5: INPUT "ENTER THE NAME OF THE FILE FOR THE Jc
CONVERSION OF THE INITIAL DATA"; D3$
LOCATE 18, 5: INPUT "ENTER THE NAME OF THE FILE WHICH IS TO CONTAIN
THE OUPUT DATA"; D2$
LOCATE 20, 5: INPUT "ENTER THE WIDTH OF THE SAMPLE IN CM"; D
LOCATE 22, 5: INPUT "ENTER THE TOTAL VOLUME IN CM3"; V
LOCATE 24, 5: INPUT "ENTER THE TOTAL NUMBER OF POINTS IN DATA FILE";
NP


REM -----OPENING FILES

OPEN D1$ FOR INPUT AS #1
OPEN D2$ FOR OUTPUT AS #2
OPEN D3$ FOR OUTPUT AS #3

REM----------------------------------------------------------------

REM GET R FROM D
R = D / 2

REM----------------------------------------------------------------

REM ---CALL ALL DATA (IN THE FORM OF DELTA m) -----

FOR I = 1 TO NP: INPUT #1, DA1(I, 1), DA1(I, 2), GARB

REM CONVERT THE ARRAY DA1 FROM DELm TO JC
DA1(I, 2) = (10 * DA1(I, 2)) / (R * V)

REM STORE DA1 DATA (AS Jc VS H) INTO A STORAGE ARRAY DA0

DA0(I, 1) = DA1(I, 1)
DA0(I, 2) = DA1(I, 2)
PRINT I, DA1(I, 1), DA1(I, 2)
NEXT I

CLS
REM THIS STATEMENT IS ASSOCIATED WITH THE "KEY" KEYTRAPPING
STATEMENT
```

```
LOCATE 8, 5: PRINT "WHEN YOU ARE READY TO STOP AND RETAIN DATA
PRESS F1"

REM ----  THIS IS THE FIRST SECTION OF THE PROGRAM, IT CALCULATES
REM ----  THE FIELD PROFILE WITH THE SAMPLE AT A GIVEN FIELD (I) BY
ASSUMING THAT THE
REM ----  ARRAY DA1 IS THE REAL Jc VS H DATA, USING A SEMI-INIFINTE
SLAB OF WIDTH D
REM ----  AND ASSUMING NO DEMAGNETIZATION

IPP = 0
REM ----  Bs = He + 4PiMs, Bt = He + 4PiMt, Bt-Bs = 4pIDELM
REM ----  THUS DELM = (Bt-Bs)/4Pi, AND Jc = (10/4)*(Bt-Bs)/(4Pi)
REM ----  LEADING TO THE PREFACTOR WHICH CONVERTS TRAPPING AND
SHIELDING
REM ----  FIELD DIFFERCES TO JcS

PREFAC = (10 / 4) * (1 / 3.14) * (1 / R)


1078 REM ANOTHER ITERATION

LR = R / 100

REM I STEPS THROUGH THE FIELD

FOR I = 1 TO NP
REM     J STEPS US THROUGH THE SAMPLE CROSS SECTION
      FOR J = 1 TO 100
           IF J = 1 THEN

REM ----  4Pi/10 CONVERTS Jc*X INTO FIELD
REM ----  THIS PART DOES THE FIRST STEP IN FROM THE RIM

                DFS(J) = DA1(I, 1) - DA1(I, 2) * LR * (4 * 3.14 / 10)
                DFT(J) = DA1(I, 1) + DA1(I, 2) * LR * (4 * 3.14 / 10)

           ELSE
REM ----  THIS PART DOES MOST OF THE SAMPLE. LOCAL FIELD IS TAKEN
REM ----  TO BE THE FIELD OUT STEP OUT, WHICH IS THEN MODIFIED BELOW
REM ----  LOCAL JC IS "SET DEFAULT" TO BE THAT OF THE JC AT THE
EXTERNAL FIELD
REM ----  BUT THAT IS LOWERED OR RAISED BELOW TO CORRESPOND TO
THE FIELD OF LOCAL REGION

                LOCALHS = DFS(J - 1)
```

```
                LOCALHT = DFT(J - 1)
                LOCALJS = DA1(I, 2)
                LOCALJT = DA1(I, 2)

REM ----  THIS PART FINDS THE SECTION ON THE Jc VS H FILE WHERE THE
FIELD CORRESPONDS
REM ----  TO THE LOCAL FIELD, Jc LOCAL IS THEN SET TO THAT ASSOCIATED
FIELD
REM ----  THIS IS DONE BY RUNNING THROUGH THE ARRAY FIRST FOR THE
SHEILDING, THEN
REM ----  FOR THE TRAPPING SEGMENTS

                FOR J2 = 1 TO NP
                    IF LOCALHS < DA1(J2, 1) THEN
                        OLJS = DA1(J2, 2)
                    ELSEIF LOCALHS > DA1(J2, 1) THEN
                        LOCALJS = (OLJS + DA1(J2, 2)) / 2
                        GOTO 100
                    ELSEIF LOCALHS = DA1(J2, 1) THEN
                        OLJS = DA1(J2, 2)
                        GOTO 100
                    END IF
                NEXT J2
100               FOR J6 = 1 TO NP
                    IF LOCALHT < DA1(J6, 1) THEN
                        OLJT = DA1(J6, 2)
                    ELSEIF LOCALHT > DA1(J6, 1) THEN
                        LOCALJT = (OLJT + DA1(J6, 2)) / 2
                        GOTO 200
                    ELSEIF LOCALHT = DA1(J6, 1) THEN
                        OLJT = DA1(J6, 2)
                        GOTO 200
                    END IF
                NEXT J6

REM ----  THIS PART CALCULATES THE LOCAL FIELD AT EXTERNAL FIELD "I"
AND POSITION "J"
REM ----  USING THE LOCAL FIELD AND LOCAL Jc

200                 DFS(J) = DFS(J - 1) - LOCALJS * LR * (4 * 3.14 / 10)
                DFT(J) = DFT(J - 1) + LOCALJT * LR * (4 * 3.14 / 10)
            END IF
        NEXT J

REM ----  CALCULATION OF APPARENT MAGNETIZATION AND JC FOR DA1
(FOR A GIVEN FIELD -- ASSOCIATED WITH THE I-STEP)
```

```
REM ----  AT THIS POINT, FOR THE PRESENT I, THE ARRAY DTF AND DFS ARE
THE FIELD PROFILES WITHIN THE SAMPLE CROSS-SCETION
REM ----  AS J3 IS INCREMENTED FROM 1 TO 100 (THE RADIUS R HAS BEEN
DIVIDED INTO 100 SEGMENTS)
REM ----  THE FIELD DIFFERENCE BETWEEN THE TRAPPING AND SHIELDING
FIELD PROFILES IS SUMMED
REM ----  IDH IS THE DIFFERENCE AT A GIVEN POSITION IN THE SAMPLE, AND
TDH IS THE TOTAL MAGNETIZATION DIFFERENCE
REM ----  OVER THE WHOLE SAMPLE. RTDH IS THE AVERAGE FIELD
DIFFERENCE (NORMALIZED TO THE 100 POSITIONS)
REM ----  DAPP IS THEN (FOR A GIVEN I) SET TO BE RDTH CONVERTED (BY
THE PREFACTOR) TO JC APPARENT

      TDH = 0
      FOR J3 = 1 TO 100
            IDH = DFT(J3) - DFS(J3)
            TDH = TDH + IDH
      NEXT J3
      RTDH = (TDH * 2) / 100
      DAPP(I, 2) = RTDH * PREFAC

REM ---  END OF APPARENT JC CALCULATION FROM DA1 AT I

NEXT I

REM ----  THIS IS THE END OF THE FIRST LOOP. AT THIS POINT THE ARRAY
DAPP
REM ----  HAS BEEN FILLED WITH THE "APPARENT JC" STEMMING FROM
ASSUMING THAT THE JC
REM ----  Jc VS H PROFILE IS THE ONE OF DA1. THE FIRST TIME AROUND, DA1
REM ----  IS THE ORIGINAL DATA CONVERTED TO Jc, SUBSEQUENTLY IT IS A
MODIFIED
REM ----  VERSION OF THAT

REM ------------NEW SECTION ----

REM ----  THIS PART CALCULATES THE DEVIATION OF THE APPARENT Jc VS H
(DAPP) CALCULATED FROM THE
REM ----  ARRAY (AFTER THE FIRST TIME THROUGH MODIFIED) AND THE
APPARENT Jc VS H CALCULATED
REM ----  FROM THE ORIGINAL DATA (DA0). THE DIFFERENCE, DEV (I2) IS
ADDED OR SUBTRACTED
REM ----  FROM DA1 AND PUT INTO THE NEW "TRUE" Jc VS H FILE DA2
```

```
TDEV = 0
DEV = 0
IDEV = 0
ITDEV = 0

FOR I2 = 1 TO NP
      DEV = (DAPP(I2, 2) - DA0(I2, 2)) / 2
      DA2(I2, 2) = DA1(I2, 2) - DEV
      TDEV = ABS(DEV) + TDEV
      IDEV = (DA2(I2, 2) - DA1(I2, 2)) / 2
      ITDEV = ABS(IDEV) + ITDEV
NEXT I2

REM ----  END OF THE DEVIATION CALCULATION AND SUBTRACTIO SECTION

REM ----  THIS SECTION LISTS THE ERRORS AND VARIATIONS, AND CHECKS
FOR THE KEY F1, IF NO F1
REM ----  THE FILE DA2 IS FILLED INTO DA1 AND THE NEXT ITERATION
OCCURS
REM ----  IF F1 HAS BEEN HIT, THEN THE FILES 2 AND 3 ARE WRITTEN, ALL
FILES ARE CLOED AND THE
REM ----  PROGRAM ENDS.  IPP SIMPLY KEEPS THE OUTPUT ON THE SCREEN

IPP = IPP + 1
IF IPP = 20 THEN IPP = 0
PRINT "THE INCEMENTRAL CHANGE IN TRUE JC VALUES ITDEV"; ITDEV
PRINT "THE VARIATION FROM THE APPARENT JC VS H       "; TDEV

KEY(1) ON
ON KEY(1) GOSUB 400

REM ----  FILLING THE NEW RESULTS TO THE OLD

FOR I8 = 1 TO NP
      DA1(I8, 2) = DA2(I8, 2)
NEXT I8


GOTO 1078

400 REM PROGRAM WRITES ARRAYS AND STOPS

FOR I3 = 1 TO NP
WRITE #2, DA2(I3, 1), DA2(I3, 2)
WRITE #3, DA0(I3, 1), DA0(I3, 2)
```

```
NEXT I3

CLOSE ALL

END
```

Project Name: **CHARACTERIZATION OF THIN FILM HIGH TEMPERATURE SUPERCONDUCTORS**

Faculty **Dr. Sharmila M. Mukhopadhyay**
Professor, Materials Science & Engineering
Mechanical & Materials Engineering
Wright State University, Dayton, OH 45435.

ABSTRACT

It is well recognized that the quality of HTC films (in both active and passive devices) is strongly dependent on the processing route. "Quality" in terms of physical parameters (Jc, Tc, Transition range etc.) depends on several factors such as microstructure (texture), stoichiometry, chemical states etc. Electron Microscopy and diffraction techniques are used to determine the microstructural factors and X-ray photoelectron spectroscopy (XPS) is suitable for the chemical and compositional investigation of these materials. **In this project, XPS analysis of differently prepared YBCO material as well as of several buffer layers have been performed.**

- This study included several novel substrate materials as well as coated conductors grown by PLD on various substrates.
- The chemical composition and bonding states of outer surface layers as well as the sub-surface region (exposed by ion bombardment) were analyzed. In addition to Dr. Mukhopadhyay, two graduate students (funded independently from the PIs research grants) have worked on these samples. One student has adopted this as her MS thesis topic and has worked on it full time.

INTRODUCTION

The discovery of high temperature superconductivity offered the promise of large-scale application at liquid nitrogen temperatures (e.g., in the range 64 to 77 K), particularly in the electrotechnical area, such as cable, magnet, FCL, MRI, transformer, generator, motor, etc[(1)].

Many techniques have been used to grow $YBa2Cu3O_{7-}$ (YBCO) thin films characterized by high Tc and Jc values. The primary problems in the deposition of 123 thin films are to achieve the correct metallic stoichiometry (Y:Ba:Cu = 1:2:3) and to produce a uniform thickness across the substrate. Also, in order that the deposited thin film has superconducting properties, it has to be ensured that the crystal structure and amount of oxygen in 123 must be correct. The deposition technique, source materials, deposition conditions, and substrates employed need careful study, since they all affect the film composition and/or structure. According to the literature most of the known thin film deposition methods are suitable for the growth of YBCO thin films if the correct experimental conditions are established[(2)].

Three factors influence the properties of complex oxide films deposited on substrates of different materials. They are film composition, film and substrate crystal

structure, and film substrate interactions. The film substrate interactions can further be divided into three groups: reactions between film and substrate, lattice matching and the matching of thermal expansion coefficient between the film and substrate[3]. The film-substrate interactions are important because as-deposited films from most methods are amorphous if the substrate is not heated and require post-deposition annealing in oxygen or air at temperatures of 800 °C and above to form crystalline 123. Since the annealing procedure depends on the starting materials and deposition procedures, the reported annealing times and temperatures vary widely. A long annealing at high temperature (e.g., 10 h at 900 °C) facilitates interface reactions with the substrate, which usually affects the superconducting properties of the film. Therefore a trend towards shorter times and lower annealing temperatures can be found in the literature. It is also found that high substrate deposition temperatures and activated oxygen during deposition make in situ growth possible[2].

Pulsed laser deposition (PLD) is a well-known method for growing high quality YBCO thin films. The process parameter space for PLD includes many variables, such as: substrate temperature (Ts), oxygen deposition pressure P(O2), target-to-substrate distance (ds), laser properties including wavelength, pulsewidth, beam uniformity, fluence and repetition rate, target properties including density and optical absorption, ablation spot size and shape (which affects the plume shape), and substrate parameters such as chemical composition and lattice constant matches[4].

Deposition of YBCO films by PLD was shown to be relatively insensitive to oxygen deposition pressures ranging from P(O2) ~ 400 mTorr to 1200 mTorr. Also, it was found that within this range the Tc and Jc (at 77 K) values were quite high and consistent [5]. In this paper, the film quality of YBCO thin film samples with different substrates and buffer layers are analyzed using XPS technique [6-9]. The results obtained are then correlated to their electrical properties to get an idea of the quality of these films.

INSTRUMENTATION & PROCEDURES:

Fabrication of samples was done at AFRL: mostly by PLD. The composition and chemistry of each sample was measured by X-ray photoelectron spectroscopy (XPS) (Kratos AXIS Ultra). Mono-chromatized AlK X-ray line was used for enhanced spectral resolution. The analysis spot size was about 110 micrometer. An electron flood charge neutralizer was used during analysis to avoid charge build-up differences between different surfaces (if any).

Sputtering was done using a mini-beam ion gun. Ar ions were used at energies of 3-5 KeV.

RESULTS:

Observations on different samples (labeled by AFRL for identification purposes) have been outlined below:

1. YBCO FILM ON TEXTURED METAL: RN36

The aim was to find out whether there is any Zr and Ce diffusion from buffer layers into the YBCO layer. This sample is coated with silver over the YBCO layer. To remove the silver layer on the sample, a part of the sample was etched with 5 cc Ammonium Hydroxide and 1cc water mixture for 3-4 minutes. It was sputtered for 130 minutes. Zr 3d peaks were found as we already missed the YBCO layer due to over etching. Then the sample was sent to WPAFB and the remaining unetched part was etched with 5 cc Ammonium Hydroxide,1 cc hydrogen peroxide and 1cc water to peel off the silver layer. It was then sputtered for 250 minutes+ 235 minutes. But Zr was not found on this part.

(SIDE VIEW)

YBCO sample(RN36 sample but without silver on the top)

The super conductor sample was prepared again without silver on the top. The sample was etched for 695 minutes. After 585 minutes of sputtering, Cu 2p disappeared and after 695 minutes of sputtering Ba 3d is disappeared. But no Zr 3d or Ce 3d was found.

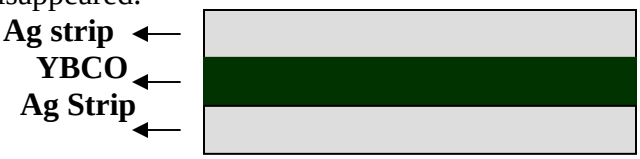

(TOP VIEW)

RN36(with three holes drilled on the YBCO strip)

This sample is covered with silver on all sides. The silver strip is peeled in the black area and three holes of 0.5 μ, 0.85μ and 1.9μ deep are drilled.

Zr is present in the 1.9μ deep holes along with Y, Ba, Cu and O.
Zr is not present in the 0.85μ and the 0.5μ holes.

(TOP VIEW)

2. STUDY OF SUBSTREATES:

YBNO1

This sample is sputtered for 10 minutes. Strong Yttrium, Barium, Niobium and oxygen are found. Carbon is present as contamination, which is removed by sputtering for 5 minutes. There is not much change between 5 minutes and 10 minutes sputtering.

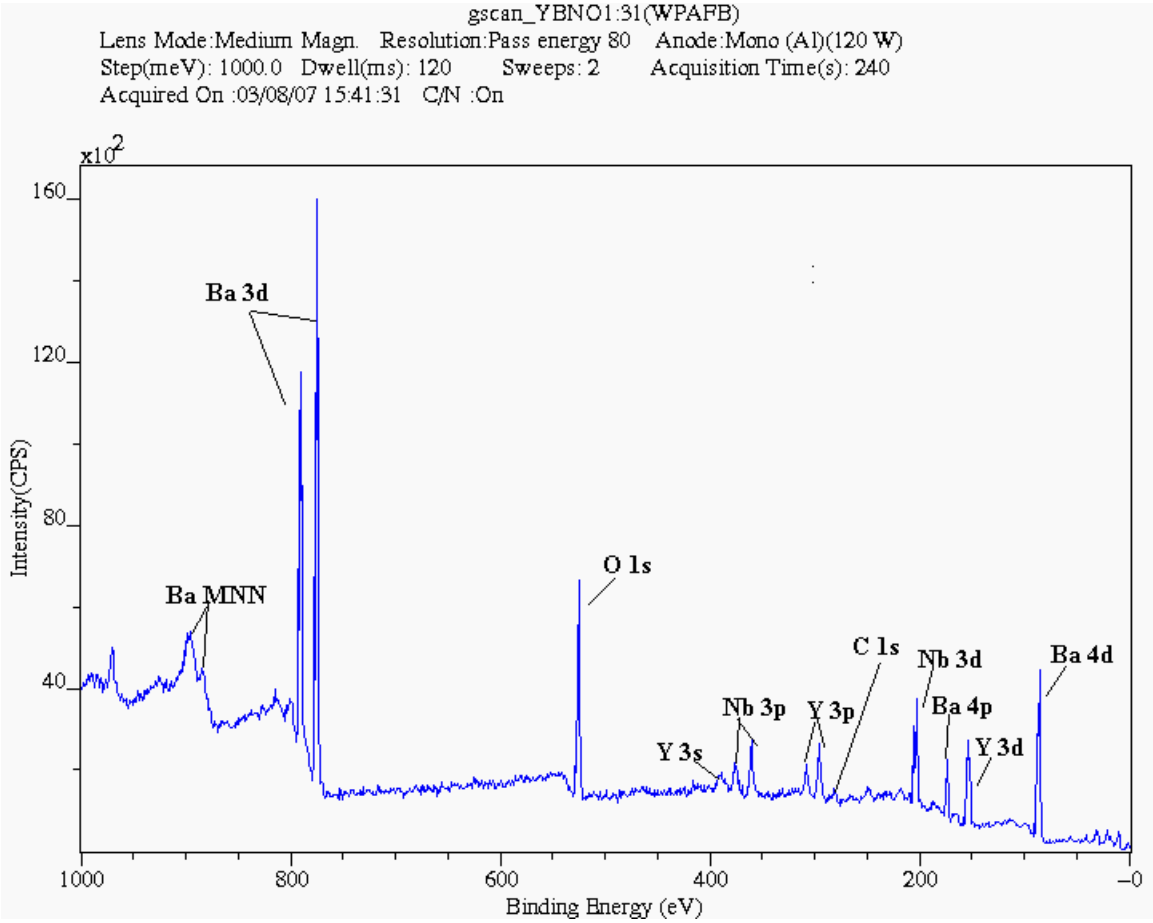

SSMgO2

This sample is sputtered for 5 minutes. Strong Yttrium, Barium, Niobium and oxygen are found. Carbon is present as contamination, which is removed after sputtering for 5 minutes.

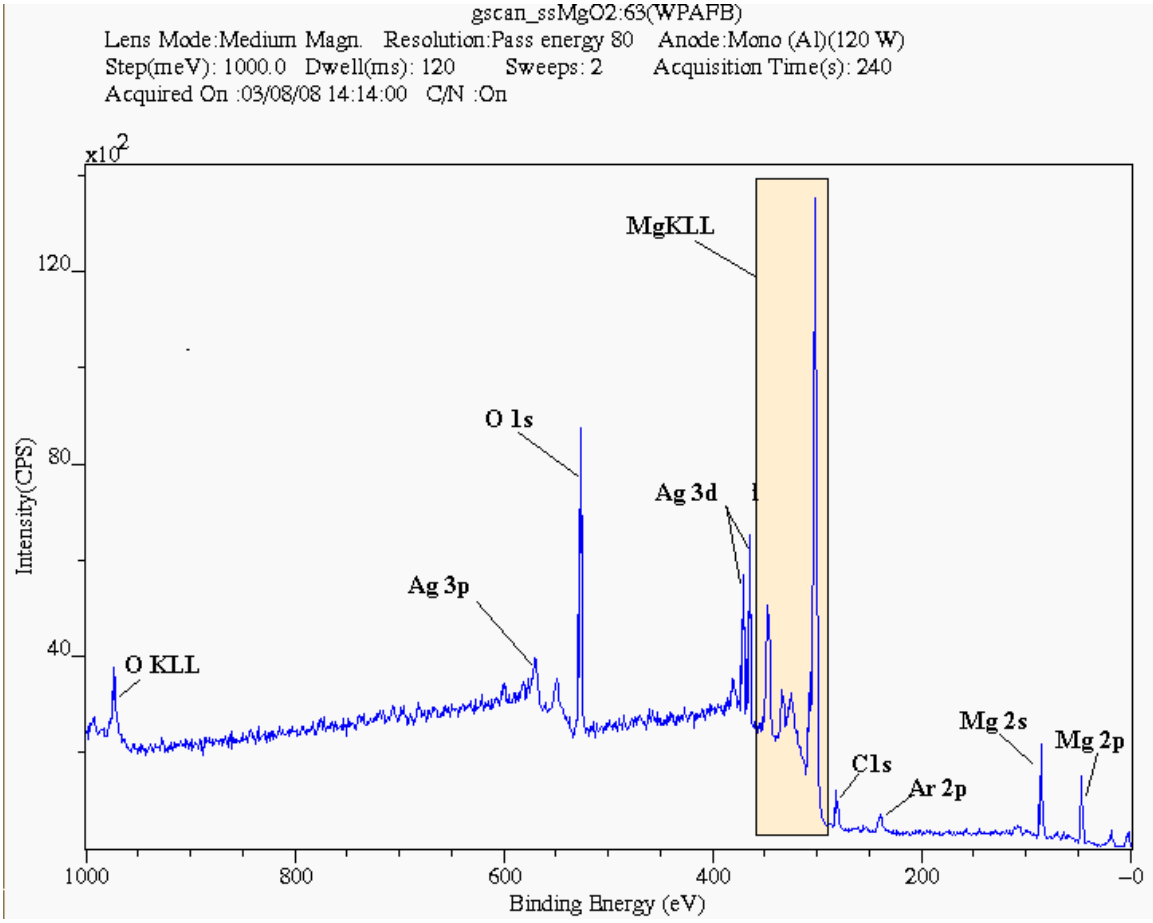

SSMgO4

This sample is sputtered for 5 minutes. Strong Yttrium, Barium, Niobium, Copper and oxygen are found. Carbon is present as contamination, which is removed after sputtering for 5 minutes.

SSNbO9, SSNbO3, SSNbO8, SSNbO5

These samples are YBNO samples with varying percentages of niobium and copper.

These samples are sputtered for 5 minutes. Yttrium, Barium, Niobium, Copper and oxygen are found. Carbon is present as contamination, which is removed after sputtering for 5 minutes.

(Attached are the spectrum peaks for Y3d,Ba3d,Cu2p,Nb3d,O1s,C1s for these 6 samples)

3. STUDY OF DEFECTIVE YBCO SAMPLE WITH THE IDEA OF IDENTIFYING FACTORS LEADIND TO DEGRADED PERFORMANCE:

TJ349 (Tim's bad sample)

This sample is a YBCO sample with strong peaks of Yttrium, Barium, Copper, Oxygen. This is sputtered for 10 minutes and compared with an earlier sample: TJ10. Parameters for this sample were:

Sputtering time	Y 3d/Ba 3d	Cu 2p/Ba 3d	FWHM of Y3d 5/2	FWHM of Y3d 3/2
10 mins	0.3047	0.52456	1.34586	1.56128

CONCLUDING REMARKS:

In summary, a variety of samples have been characterized and analyzed. Several papers are being written based on these results for upcoming conferences next year and for publication in Ceramic Transactions.

REFERENCES

1. Guansen Yuan, Physica C 337 (2000) 91-95
2. M. Leskela et al., J. Vac. Sci. Technol. A 7 (6), Nov/Dec 1989
3. H. Koinuma et al., Jpn. J. Appl. Phys. 26, L 763 (1987)
4. D. Chrisey, G. Hubler, *Pulsed Laser Deposition of Thin Films*, (J. Wiley & Sons 1994)
5. T. Haugan, P. Barnes et al., Air Force Research Laboratory, Wright-Patterson AFB, OH 45433 U.S.A.
6. Handbook of X-ray photoelectron spectroscopy by C.D.Wagner, W.M.Riggs, L.E.Davis, J.F.Moulder, G.E.Muilenberg(Editor) published by Perkin-Elmer corporation
7. Encyclopedia of materials characterization – Surfaces, interfaces and thin films by C.Richard Brundle, Charles A.Evans, Jr. and Shaun Wilson, Manning publications company
8. High performance analytical instrumentation manual by KRATOS ANALYTICAL Inc.
9. Handbook of X-ray and Ultraviolet photoelectron spectroscopy by D.Briggs, ICI Ltd. Corporate laboratory

TEST EQUIPMENT DATA PACKAGE FOR THE MICROGRAVITY SPRAY COOLING EXPERIMENT

Kirk Yerkes

Air Force Research Laboratories, Propulsion Directorate
Wright Patterson Air Force Base
1950 Fifth Street
WPAFB, OH 45433-7251
PH: (937)255-5721
FAX: (937)656-7529
E-mail: kirk.yerkes@wpafb.af.mil

30 August 2004

Paul Kreitzer, WVU
Shannon Glaspell, WVU

Principal Investigator:

Kirk Yerkes
AFRL/PRPS
1950 Fifth Street
WPAFB, OH 45433-7251
PH: (937)255-5721
FAX: (937)656-7529
E-mail: kirk.yerkes@wpafb.af.mil

Experiment Title: Microgravity Spray Cooling

Flight Dates: TBD

Category	Data	See page
Overall Assembly Weight	TBD	22
Assembly Dimensions:	44”×64.5”×44”	61-63
Equipment Orientation Requests:	Lengthwise along axis of aircraft	9
Floor Mounting Strategy	Bolts	21-22
Gas Cylinder Requests	No	---
Overboard Vent Requests	No	---
Power Requirements	115 VAC, 60 Hz	24
Free Float Experiment	No	---
Proposed Researchers	Kirk Yerkes, AFRL Travis Michalak, AFRL John Kuhlman, WVU Donald D. Grey, WVU Charles Hunnell, WVU Paul Kreitzer, WVU Shannon Glaspell, WVU	7

Table of Contents

Table of Contents iii
List of Tables iv
List of Figures iv
Flight Manifest 7
Experiment Background 7
Experiment Description 7
Equipment Description 8
Structural Analysis 9
  Load Factors 10
  Frame Components 10
    FC-72 Reservoir 10
    Component Table 13
  Rig Frame Analysis 13
  Shelves 18
  Pull Testing 21
  Analysis of Microgravity Experiment Rig as One Object 21
Electrical Analysis 24
  Electrical Schematic 24
  Electrical Load 24
  Electrical Emergency Flow Shutdown Switch 24
  Loss of Electrical Power 25
Pressure System 25
  Flow Schematic 25
  Flow Component Listing 25
Laser Certification 27
Parabola Details and Crew Assistance 27
Institutional Review Board 27
KC-135 Hazards Analysis 27
Tool Requirements 40
Photo Requirements 40
Aircraft Loading 40
Ground Support Requirements 40
Hazardous Materials 40
Material Safety Data Sheets 40
Test Procedures 41
  Loading Checklist 41
  Pre-test Checklist 41
  Testing Checklist 41
  Post-test Checklist 42
  Leak Shut Down Procedure 42
  Emergency Shut Down Procedure 42
Appendix A: 80/20 Joint Fastener Testing at WVU 44
Appendix B: Electrical Schematic 52
Appendix C: Experiment Drawings and Flow Schematic 61

Appendix D: Pressure Certification 77
Appendix E: Material Safety Data Sheet 78

List of Tables

Table 1: Flight Manifest 7
Table 2: Bolt Strength Values 12
Table 3: Component Analysis 13
Table 4: Experiment Rig Loads and Moments 14
Table 5: Extrusion Properties 15
Table 6: Joint Strength Values 16
Table 7: Shelf Loading 19
Table 8: Shelf Margins of Safety 21
Table 9: Pull Test Results 21
Table 10: Assembly Weight and Moment Arm 22
Table 11: Component Requirements 24
Table 12: Flow Components 26

List of Figures

Figure 1: Illustration of Test Chamber 8
Figure 2: Equipment Orientation 9
Figure 3: Reactions to 9g Forward Load Factor—FC-72 Reservoir 11
Figure 4: 1010 Extrusion 14
Figure 5: 2020 Extrusion 14
Figure 6: 12 Hole 90º Joining Plate (P/N 4128) 15
Figure 7: 8 Hole Inside Gusset Corner Bracket (P/N 4138) 15
Figure 8: Reactions to 9g Forward Load Factor—Rig Frame 17
Figure 9: 6-Hole Right Inside Corner Bracket (P/N 4121) 19
Figure 10: 6-Hole Left Inside Corner Bracket (P/N 4122) 19
Figure 11: Reactions to 9g Forward Load Factor—Shelf 20
Figure 12: Reactions to 9g Forward Load Factor—Assembly 22
Figure A1: Corner Joint 44
Figure A2: Corner Joint 45
Figure A3: Corner Joint Load Point 45
Figure A4: Loading Versus Time for Corner Section: Test on June 7, 2004 46
Figure A5: Deflection versus Time for Corner Section: Test on June 7, 2004 46
Figure A6: Deflection versus Load for Corner Section: Test on June 7, 2004 47
Figure A7: Corner Joint under Maximum Load: Test on June 7, 2004 47
Figure A8: Corner Joint after Loading: Test on June 7, 2004 48
Figure A9: Tee Joint 48
Figure A10: Tee Joint Point Load 49
Figure A11: Loading versus Time for T Section: Test on June 7, 2004 49
Figure A12: Deflection versus Time for T Section: Test on June 7, 2004 50
Figure A13: Deflection versus Load for T Section: Test on June 7, 2004 50
Figure A14: T Joint under Maximum Load: Test on June 7, 2004 51

Figure A15: T Joint after Loading: Test on June 7, 2004 51
Figure C1: Side View of Rig 61
Figure C2: Top View of Rig 62
Figure C3: Rear View of Rig 63
Figure C4: Three-dimensional View of Rig 64
Figure C5: Three-dimensional View of Rig 65
Figure C6: Three-dimensional View of Rig 66
Figure C7: Three-dimensional View of Rig 67
Figure C8: Three-dimensional View of Chamber with Screen 68
Figure C9: Test Chamber in Mounting Structure 69
Figure C10: Test Chamber 70
Figure C11: Sump for Test Chamber — Side View 71
Figure C12: Sump for Test Chamber — Side View 72
Figure C13: Sump for Test Chamber — Side View 73
Figure C14: Pedestal for Test Chamber — Side View 74
Figure C15: Exploded View of Sump 75
Figure C16: Flow Schematic 76

APPENDIX G

Flight Manifest

Table 1: Flight Manifest

Name	Affiliation	Preferred Days of Flight	Previous Flyer
Kirk Yerkes	AFRL	TBD	Yes, Sept 2004
Travis Michalak	AFRL	TBD	Yes, Sept 2004
John Kuhlman	WVU	TBD	No
Donald Gray	WVU	TBD	No
Charles Hunnell	WVU	TBD	No
Paul Kreitzer	WVU	TBD	Yes, Aug 2003
Shannon Glaspell	WVU	TBD	Yes, Aug 2003

Experiment Background

Two-phase spray cooling is an example of a thermal management technique that may be utilized in high heat flux acquisition and high thermal energy transport concepts. It is one of many possible alternatives to the prevalent passive thermal management technologies, such as heat pipes and capillary pumped loops, which are currently used in space applications. Many researchers have investigated the utility of two-phase sprays for the thermal management of devices generating high heat fluxes. However, there has been little research addressing the physics and ultimate performance and comparison of two-phase spray cooling with and without the effects of an electric field. This fluid management of the spray droplets is hypothesized to enhance heat transfer and/or fluid flow around the heated region in a microgravity environment.

Experiment Description

The experiment consists of two primary components as shown in the equipment drawings. The first component is a spray test chamber containing a spray nozzle, heater, primary condenser surface, and sump configuration to collect the liquid and condensate. The chamber also includes an electromagnetic system to control the fluid management of the working fluid, FC-72 at the heated surface. The second component is the flow loop system which consists of a supply loop and a drain loop to manage the FC-72, and a water loop to cool the spray test chamber. The experiment will be operated by applying electrical power to the Indium Tin Oxide (ITO) heater or thick film resistance heater inside the test chamber generating heat. Under these conditions, the heater will be sprayed with the FC-72 liquid and spray cooling of the heaters can be studied. Data will be collected on the heat transfer performance and thermophysics of spray cooling of the heater in both high-g and micro-g environments. Data will also be collected on the effects of the FC-72 fluid in the presence of an electromagnetic field.

Equipment Description

The spray test chamber is a pressure vessel and will be fixed in one orientation during a flight test (see Figure 1). The spray test chamber consists of a spray nozzle, heater, and sump system. A target heater is mounted on a glass or polycarbonate pedestal. The pedestal is part of a sump system designed to remove unconstrained liquid from the test chamber. An additional drain line is located in one of the viewing ports and is used to speed up the draining process after a period of microgravity, when the sump system is void of fluid. The inside surface of the chamber is lined with a wick structure as the primary condensation surface for the condensate liquid to return to the sump system. Liquid is collected in the sump and returned to the fluid delivery loop. The exterior surface of the chamber is liquid cooled using a separate water loop coupled to liquid-air heat exchangers. Thermocouples mounted in the pedestals are used to determine the heat loss through the heaters. The configuration of the electromagnetic system (which is not yet designed) will be optimized to determine the effects of the fluid management on heat transfer performance.

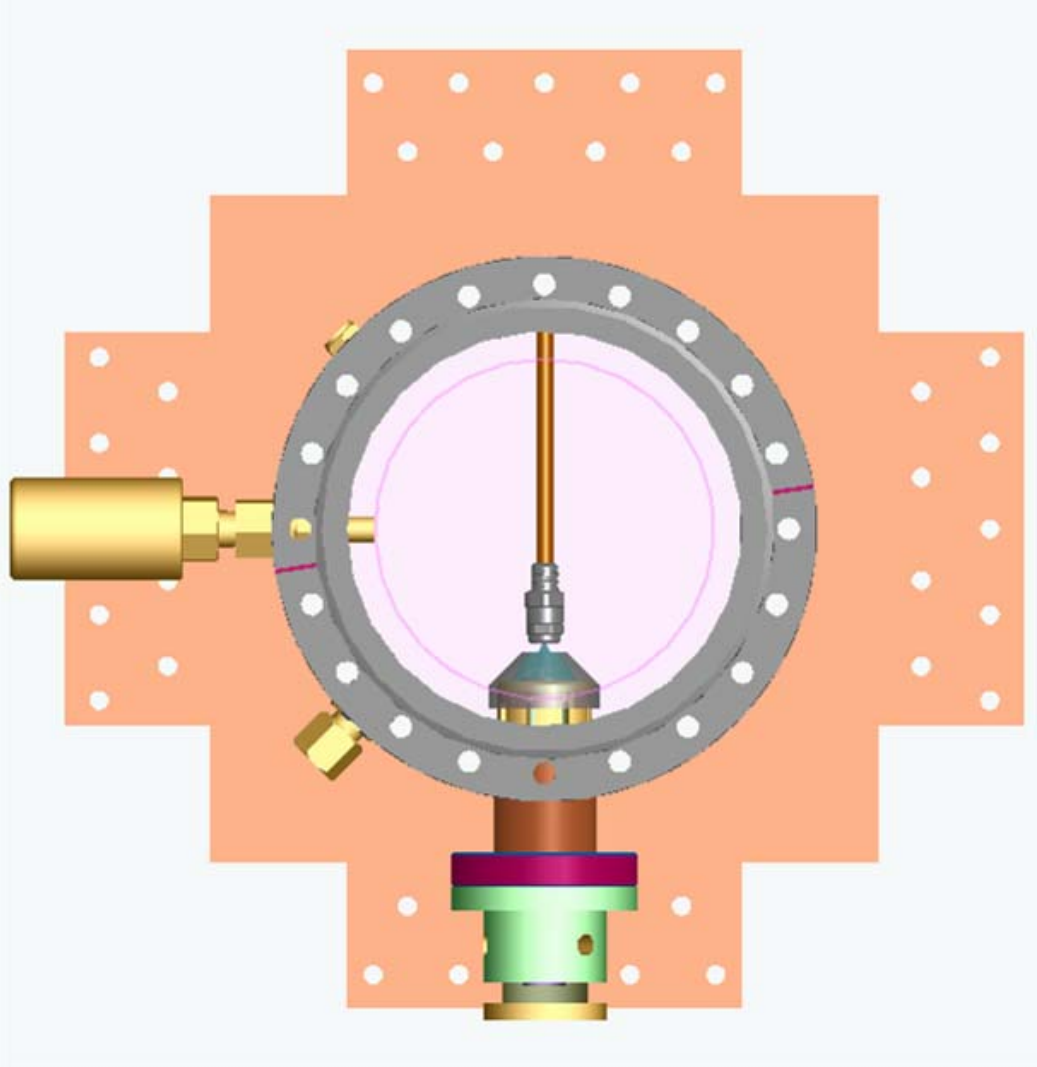

Figure 1: Illustration of Test Chamber

The flow loop section of the experimental apparatus consists of the pumps, flow meters, pressure transducers, pressure relief switches, filters, reservoirs, electrical valves, liquid-air heat exchangers, reheaters, and associated plumbing used to move and control both the FC-72 and cooling water. These components move the two fluids to and from the spray test chamber while monitoring flow rate, temperatures, and pressure. Various power supplies are also mounted on the experimental framework to provide electrical power to those components in the flow loops, heaters, metering equipment, and data acquisition system components. The framework of the experimental rig is comprised of industrial strength 80/20 extrusions mounted to a one half inch thick aluminum plate. The 2020 extrusions are bolted to the base plate and are also secured using caulk to create a containment pan should any fluid leaks occur.

The experiment will be operated and monitored via a control panel and data acquisition system. The data acquisition system consists of a laptop coupled to an HP Data Acquisition/Switch Unit. Various safety features are linked to the emergency shut off control switch and effectively limit the maximum heater temperature and system pressure. This precaution helps to maintain the experiment within the safe operating parameters during the flight test. Both software and mechanical safety features allow for the safe shutdown in the event of a temperature or pressure excursion above allowable limits.

Structural Analysis

The experiment is housed in an 80/20 base which is configured to be mounted inside the KC-135 so that the long axis of the experimental rig is parallel with the longitudinal axis of the aircraft. Figure 2 illustrates the equipment orientation that will be used during the flight on the KC-135.

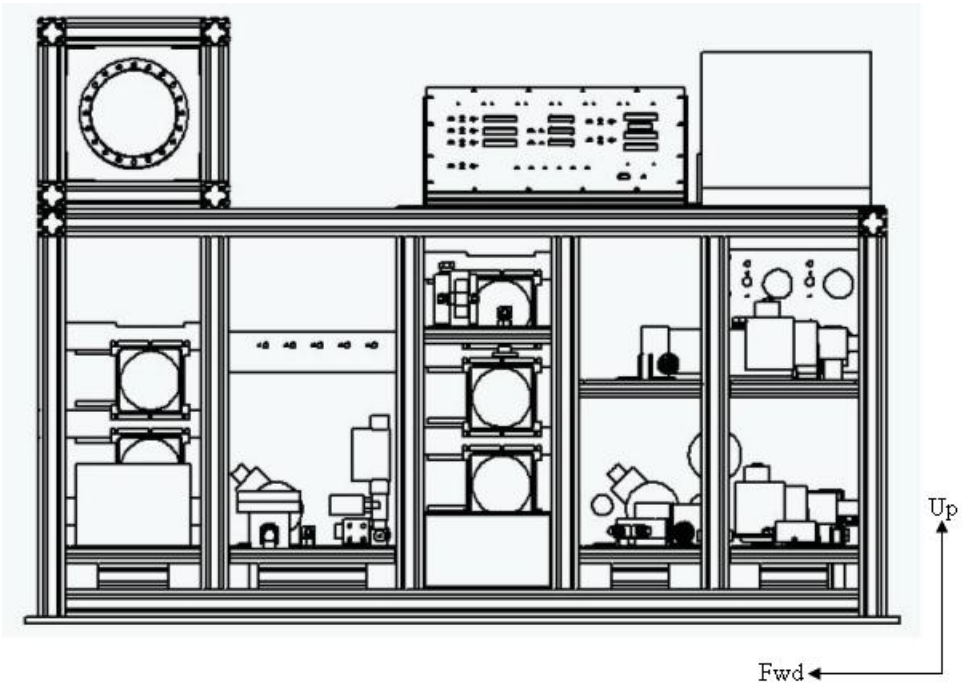

Figure 2: Equipment Orientation

Load Factors

This report analyzes the effects of the emergency load factors specified by the *JSC Reduced Gravity Program User's Guide*. Each component was analyzed under maximum emergency load factors in all appropriate orientations.

Direction	Load Factor
Forward	9g
Aft	3g
Lateral	2g
Up	2g
Down	6g

Frame Components

Provided is a detailed analytical analysis based on the requirements for each component. This will serve as a series of example calculations for all the other components that were analyzed.

FC-72 Reservoir

The FC-72 reservoir is mounted to the base plate and a corresponding shelf with four ¼-20 bolts and weighs 17.66 pounds when filled with FC-72 to its operational level. Figure 3 shows the 9g forward load factor results.

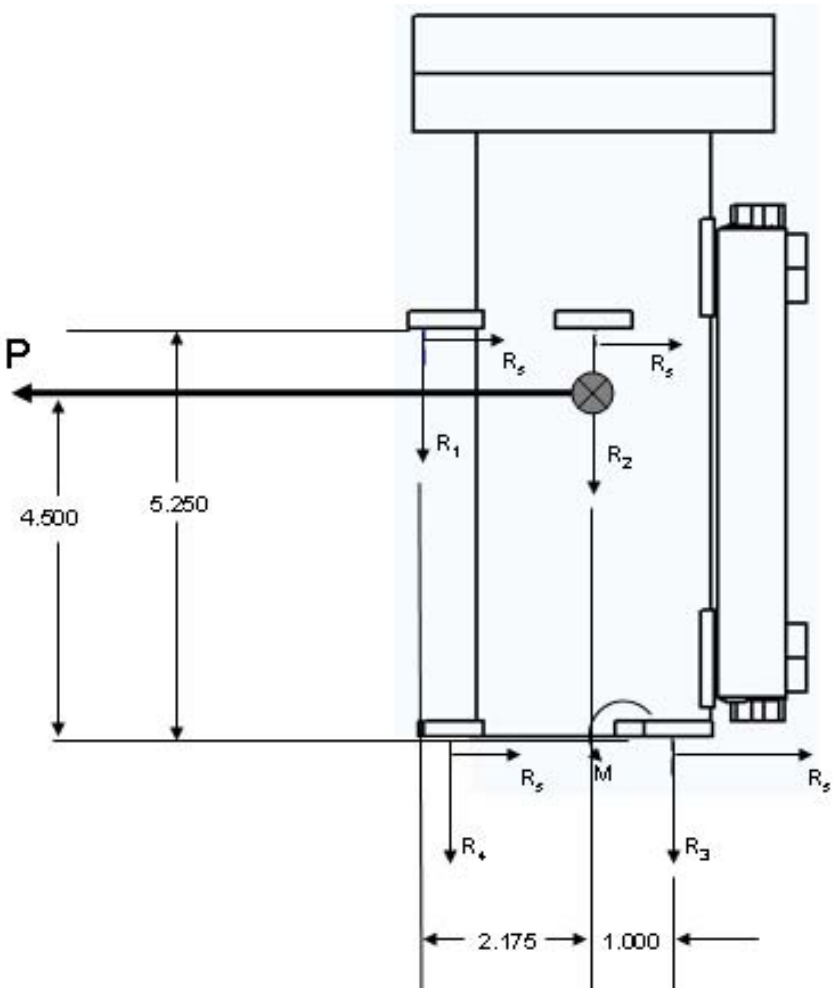

Figure 3: Reactions to 9g Forward Load Factor—FC-72 Reservoir

Applied g loading:

Shown are the loadings in each of the critical directions for the fully filled operational reservoir.

Direction	Load (lbs)
Forward	158.9
Aft	52.98
Up/Lateral	35.32
Down	106.0

Tensile/shear loading: The independent tensile/shear loading per bolt, as shown here, was calculated based on the reservoir being mounted with four bolts. The loads in each of the critical directions were distributed among the bolts mounting the reservoir in place to yield the following numbers:

$$\frac{(applied\ load)}{\#\ of\ bolts}$$

Direction	Number of Bolts	Load (lbs/bolt)
Forward	4	39.75
Aft	4	13.25
Up/Lateral	4	8.83
Down	4	26.49

Margins of Safety: The ultimate tensile margin of safety is calculated using the following equation:

$$MS_{UT} = \frac{F_{UT}}{(applied\ load)(FS)} - 1$$

Where,

F_{UT} = Ultimate tensile failure load (other options include F_{YT} = Yield tensile failure load, F_{SU} = Ultimate shear failure load, and F_{SY} = Yield shear failure load)

FS = Factor of safety

Established NASA factors of safety are 2.0 or greater for all structural or fracture critical elements, unless tested past the ultimate loading point possible under the 9g condition. Table 2 contains data corresponding to the strengths of the different types of bolts used on the flight rig.

Table 2: Bolt Strength Values

	MS51959	AN6	10-32	8 ¼-20	80/20 ¼-20
Sheer Strength (lbs)	1525	8280	1525	2860	3300
Tensile Strength (lbs)	2540	10100	2540	4770	

The ultimate shear margin of safety is calculated using the above equation and the given load limits for the bolts being used, in this case a ¼-20 bolt with a forward loading, to yield:

$$MS_S = \frac{2860}{(39.75)(2)} - 1 = 35$$

When using the largest loading per bolt as shown in the 9g direction, a margin of safety of 35 is calculated. It is clear that the applied g-loads in any direction are small in comparison with the failure or yield loads for the bolts. All tensile/shear loads are two orders of magnitude below the failure loads and thus indicate large margins of safety for any force acting on this component.

Component Table

Table 3 contains all data pertinent to the analysis of the remaining frame components. It is evident from the ultimate tensile margins of safety in the last column that none of the components approach the failure loads of the bolts restraining them and therefore, no further analysis of these components is warranted.

Table 3: Component Analysis

Component	Weight (lbs)	Applied g-load (9g forward – lbs)	Bolt	Tensile/shear loading (lbs/bolt)	F_S (lbs)	MS F_S
Power Supply (480W)	3.85	34.7	Grade 8 ¼-20	8.7	2860	163
Power Supply (100W)	1.60	14.4	Grade 8 ¼-20	3.6	2860	396
Power Supply (chamber)	3.15	28.4	Grade 8 ¼-20	7.1	2860	200
Heat Exchanger Fans	3.35	30.2	10-32	5.0	1525	150
Heat Exchanger Assembly – Water Loop	10.5	94.5	MS51959	3.9	1525	192
Heat Exchanger Assembly – FC-72 Loop	14.2	127.8	MS51959	5.3	1525	142
Water Reservoir	14.0	126.0	Grade 8 ¼-20	25.2	2860	55.8
Ice Point	13.25	119.25	Grade 8 ¼-20	29.8	2860	47.0
High Voltage Power Supply	17.5	157.5	10-32	78.75	1525	8.7
Test Section	70.0	630.0	80/20 ¼-20	26.3	3300	61.9

Rig Frame Analysis

This section will include a detailed analysis of the frame. The loads and moments acting on the rig frame, base, and members are presented in Table 4. The Z distances in the calculations are measured from the top of the base plate.

The rig frame is constructed of 1010 extrusion shelf supports, Figure 4, with a 2020 extrusion frame, Figure 5, from 80/20 Inc. All joints were assembled with their recommended bolt kits and all fasteners were torqued according to their specifications.

Table 4: Experiment Rig Loads and Moments

	Weight (lbs)	Z from bottom of rig (in)	Mz (in-lbs)
Frame	125.18	7.64	1968.86
Shelf Supports	54.67	12.68	693.44
Shelves	109.72	14.13	1550.55
Water Loop	28.07	8.49	238.35
Return Loop	30.41	9.43	286.70
FC-72 Loop	18.08	7.98	144.19
Drain Loop	15.63	19.76	308.74
Test Section	80.00	35.00	2800.00
Power Supplies	33.30	14.76	491.50
Data Acquisition	32.63	17.26	563.14
Optical Mountings	4.00	40.00	160.00
Wiring & Connectors	30.00	10.00	300.00
Plumbing & Fittings	80.00	10.00	800.00
Miscellaneous	10.00	15.00	150.00
Total	**651.69**	**16.04**	**10455.47**

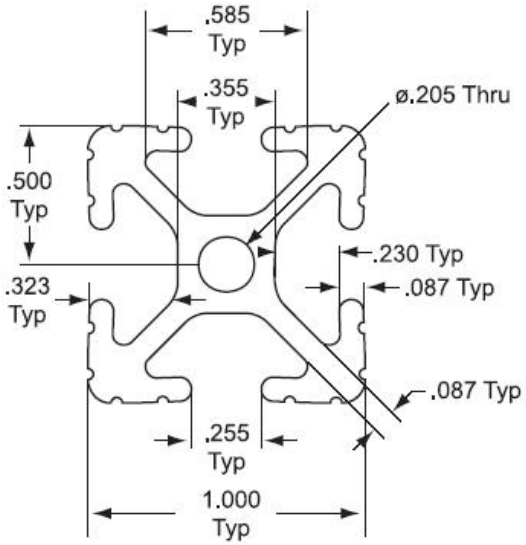

Figure 4: 1010 Extrusion

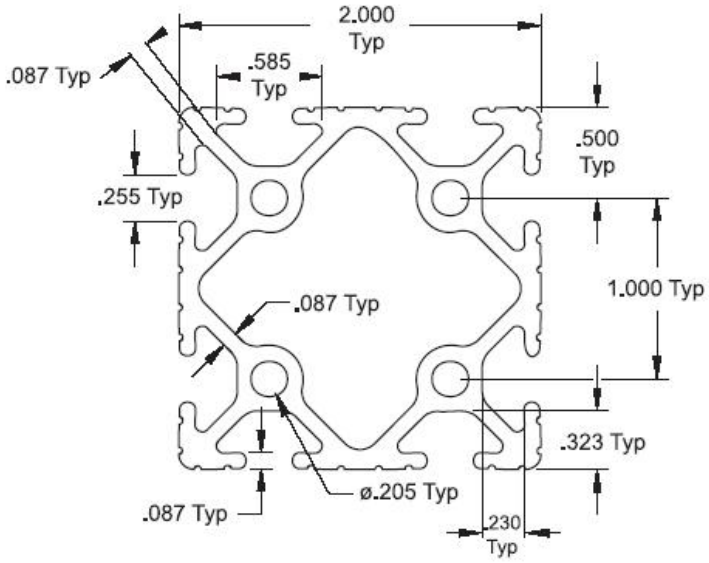

Figure 5: 2020 Extrusion

The corner connections use the manufacturer's 90° joining plates as shown in Figure 6 with two inside corner brackets as shown in Figure 7.

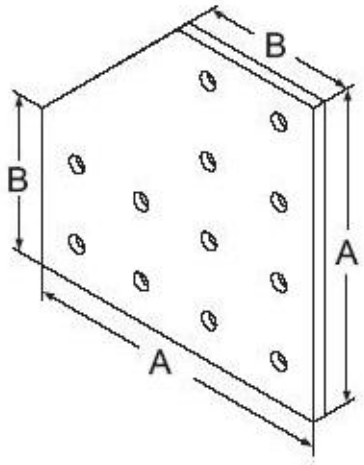

Figure 6: 12-Hole 90º Joining Plate (P/N 4128)

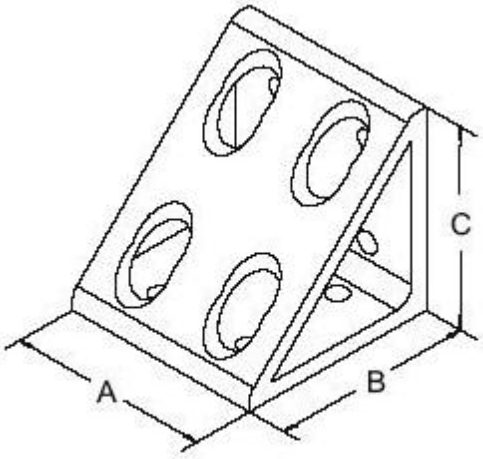

Figure 7: 8-Hole Inside Gusset Corner Bracket (P/N 4138)

Table 5 contains the extrusion properties and Table 6 has the joint strength values for the different 80/20 components. 80/20 has information on how certain joints hold up under different stress conditions. However, documentation was not available for the joint construction with the 2020 extrusions utilized on this apparatus. Therefore, structural testing was performed to develop the appropriate numbers; the results are documented in Appendix A: 80/20 Joint Fastener Testing at WVU. The frame is bolted to the base plate with MS51959-81 screws.

The total moment load, during the maximum loading condition of 9g forward, is distributed over eighteen joints connecting the vertical members to the base members (conservatively ignoring the effects of the eighteen joints at the top of the frame and the bracing that the shelves provide). The total moment load, as determined from the data of Table 4, is:

$$M_{Total} = 9g\left(\sum M\right) = 9(10455) = 94099 \text{ in-lbs}$$

Dividing the total moment, experienced on the flight rig, among the eighteen joints at the base of the frame yields a moment load per joint of 5227 in-lbs. Distributing the loading this way is conservative, since there are two types of joints used and the calculations are performed using the lower failure level for all 18 joints (12,650 pounds as apposed to 18,700 pounds). Comparing this load to the experimentally determined joint ultimate strength, using a margin of safety of 1.5 since the joints have been tested past the calculated maximum loading and no failure occurred, yields:

$$MS_{UT} = \frac{12650}{(5227)(1.5)} - 1 = 0.61$$

This gives a positive margin of safety and catastrophic failure will not occur under the maximum loading conditions.

Table 5: Extrusion Properties

	2020	**1010**
Material	6105-T5 Aluminum	6105-T5 Aluminum
Yield Strength	35000 psi	35000 psi
Tensile Strength	38000 psi	38000 psi
Elastic modulus	10,2000,000 psi	10,2000,000 psi
Moment of inertia (x-x and y-y)	0.5513 in^4	0.04413 in^4
Section area	1.223 in^2	0.435in^2

Table 6: Joint Strength Values

	Double 90° Joining Plate with 90° Corner Brackets – 2020	**Corner Bracket – 1010**
Direct (shear) load	---	325 lb
Moment load	9700.0 in-lbs	225 in-lbs
Torsion load	---	180 in-lbs

Another potential method of failure is the tipping moment under 9gs forward. The tensile load on the bolts in the row farthest from the line of rotation will experience the highest load which can be calculated with the following formula:

$$P_{t,\max} = \frac{FLd_k}{\sum_i nd_i^{\,2}}$$

Where,

F = overturn load

L = vertical distance from overturn line to center of gravity

d_k = distance from overturn line to furthest bolt(s)

n = number of bolts in a row

d_i = distance from overturn line to row

The total rig weighs 651.7 lb and the center of gravity is 16.0 inches from the bottom of the base plate. This will result in the reactions illustrated in Figure 8. Only five of the reactions are shown for clarity in the figure.

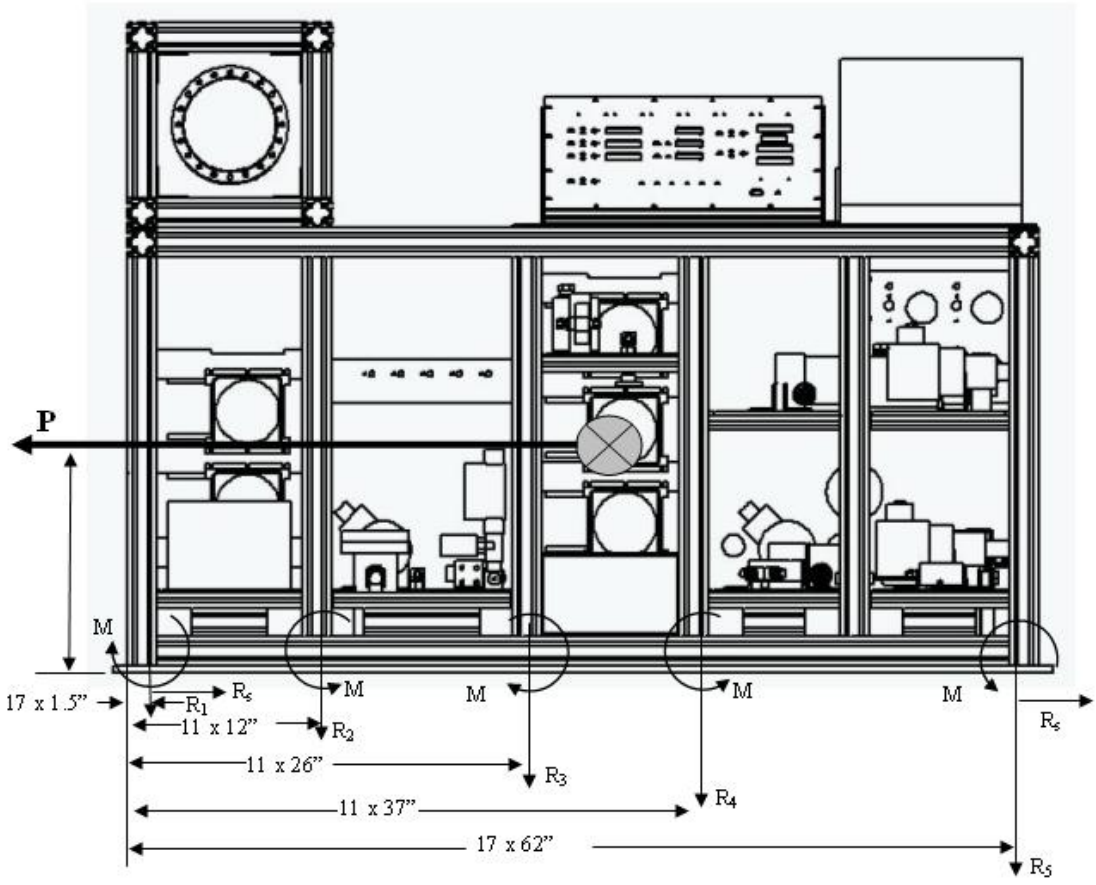

Figure 8: Reactions to 9g Forward Load Factor—Rig Frame

By substituting the known values into the above tensile load formula, a loading for each bolt attaching the flight rig frame to the base plate can be calculated.

$$P_{t,\max} = \frac{(9)(651.7)(16.0)(62)}{\begin{array}{l}17\left(.5^2+61^2\right)+16\left(1.5^2+62^2\right)+11\left(23.25^2+24.25^2+34.25^2+35.25^2+49.25^2+50.25^2\right)+\cdots \\ \cdots+2\left(3.25^2+4.25^2+5.25^2+6.25^2+7.25^2+8.25^2+9.25^2+10.25^2+11.25^2+12.25^2\right)+\cdots \\ \cdots+2\left(13.25^2+14.25^2+15.25^2+16.25^2+17.25^2+18.25^2+19.25^2+20.25^2+21.25^2+22.25^2\right)+\cdots \\ \cdots+2\left(25.25^2+26.25^2+27.25^2+28.25^2+29.25^2+30.25^2+31.25^2+32.25^2+33.25^2\right)+\cdots \\ \cdots+2\left(36.25^2+37.25^2+38.25^2+39.25^2+40.25^2+41.25^2+42.25^2+43.25^2+44.25^2\right)+\cdots \\ \cdots+2\left(45.25^2+46.25^2+47.25^2+48.25^2+51.25^2+52.25^2+53.25^2+54.25^2+55.25^2\right)+\cdots \\ \cdots+2\left(56.25^2+57.25^2+58.25^2+59.25^2+60.25^2\right)\end{array}} = 93.6$$

$P_{t,\max}$ = tipping tensile load = 93.6 lbs/bolt

Margin of Safety: Using the margin of safety calculation stated earlier in this report, the ultimate and yield margins of safety in the tipping tensile load for each bolt in the row farthest from the line of rotation can be calculated by:

$$MS_T = \frac{2540}{(93.6)(2)} - 1 \approx 12.6$$

With the large margins of safety, it is evident that the tensile load on the bolts in the row receiving the most tension during tipping will not be critical for bolt failure.

Combined Shear/Tensile Loading: The combined tipping shear and tensile loading is analyzed with the following formula:

$$\left(\frac{P_S}{F_S}\right)^3 + \left(\frac{P_t}{F_t}\right)^2 \leq 1$$

Where,

P_S = applied shear load

F_S = shear failure load

P_t = applied tensile load (tipping)

F_t = tensile failure load

The combined shear/tensile loadings are analyzed below:

A forward load of 651.7 lbs is multiplied by the 9g loading criteria, which equals 5865 lbs. This load is held in place by 235 screws, and by distribution, the shear loading per screw is 25.0 lbs. From this, the overall load carrying capacity can be determined:

$$\left(\frac{30.5}{1525}\right)^3 + \left(\frac{107}{2540}\right)^2 = 0.0018 = 0.18\% \text{ of load carrying capacity used}$$

Shelves

Table 7 contains all loading data pertinent to the analysis of the shelves.

Table 7: Shelf Loading

Shelf	Weight (including components – lbs)	Applied mass (9g forward – lbs)	Number of Bolts	Shear Loading (lbs/bolt)	Bolt Type	F_S (lbs)
1	50.9	458.2	40	11.45	¼-20	3300
2	21.5	193.9	31	6.25	¼-20	3300
3	18.5	166.9	23	7.25	¼-20	3300
4	37.5	337.8	48	7.04	¼-20	3300
5	7.31	65.79	22	2.99	¼-20	3300
6	45.5	409.6	53	7.73	¼-20	3300
7	24.1	216.9	12	18.08	¼-20	3300

Shear Margin of Safety: The shear margin of safety for the first shelf is calculated using the shear loading per bolt compared to the shear strength with a safety factor of 2 per bolt:

$$MS_S = \frac{3300}{(9.21)(2)} - 1 \approx 143$$

A margin of safety of 143 is obtained, and it is clear that the applied g-loads in any direction are small in comparison with the failure or yield loads for the bolts. All tensile/shear loads are at least two orders of magnitude below the failure loads and thus indicate large margins of safety for any force acting on this shelf.

Shelf Attachment to Frame: The shelves are attached to 1010 extrusions that are attached to the 2020 frame with corner brackets as shown in Figure 9 and Figure 10 (right and left brackets respectively).

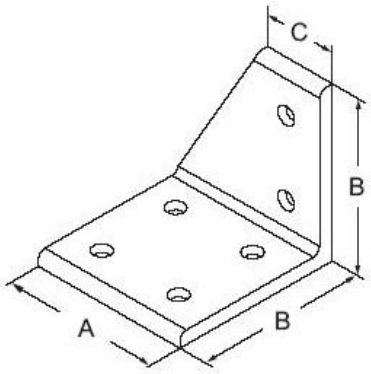

Figure 9: 6-Hole Right Inside Corner Bracket (P/N 4121)

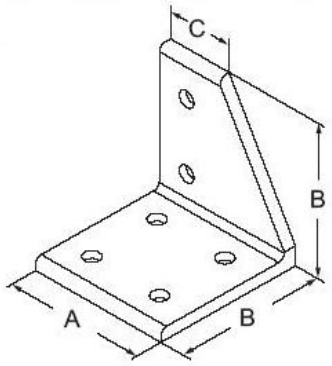

Figure 10: 6-Hole Left Inside Corner Bracket (P/N 4122)

Shelf 1 is used to show the calculations for all other shelves. It is supported by 8 extrusions and the 9g forward load factor results in reactions shown in Figure 11. The 458.2 lb load spread over the 8 joints results in an individual loading of 57.3 lb per joint. With an 80/20 published direct force joint strength value of 325 lb the margin of safety is:

$$MS = \frac{325}{(57.3)(1.5)} - 1 = 2.8$$

The center of gravity of the components on the shelf is at 2.75 in from the top of the base plate. This creates a moment load of:

$$M_{total} = 9g(50.91)(2.75) = 1260$$

Dividing this total moment among the eight joints yields a moment load per joint of 157.5 in-lbs. Using the cantilevered force joint strength values published from 80/20, a margin of safety value is obtained as distributed across the shelf brackets.

$$MS = \frac{375}{(157.5)(1.5)} - 1 = 0.59$$

By symmetry, the 3g aft and 2g lateral load factors are not considered critical for failure in the structure. The results of the calculations for the remaining shelves are shown in Table 8.

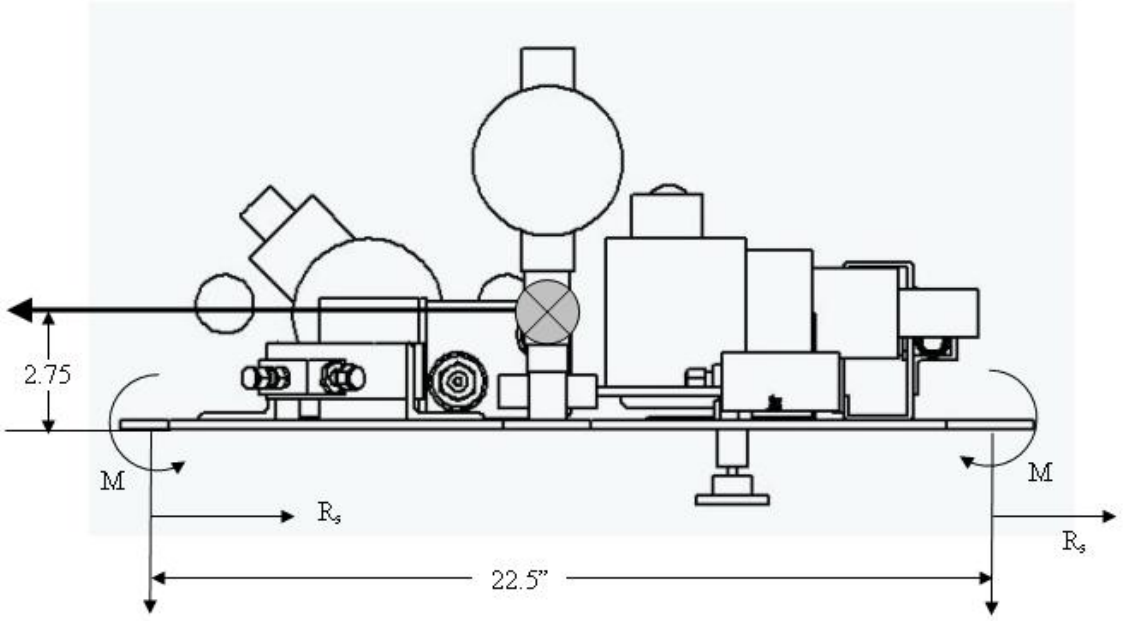

Figure 11: Reactions to 9g Forward Load Factor—Shelf

Table 8: Shelf Margins of Safety

Shelf	Weight (including components – lbs)	Applied mass (9g forward – lbs)	Moment load (in-lbs)	Shear load MS	Moment load MS
1	50.91	458.2	1260	2.8	0.59
2	21.54	193.9	533.1	7.9	2.8
3	18.54	166.9	500.6	9.4	3.0
4	37.53	337.8	928.9	4.1	1.2
5	7.31	65.79	131.6	25	14
6	45.51	409.6	1024	3.2	0.95
7	24.10	216.9	542.3	7.0	2.7

Pull Testing

As the equipment was installed, each component that was not verified by analysis was pull tested. Data gathered from the pull tests is contained in Table 9. All components passed the pull test.

Table 9: Pull Test Results

Component	Location	Weight (lbs)	Forward (lbs)	Aft (lbs)	Left (lbs)	Right (lbs)	Up (lbs)
Pump	Shelves 2,4,5	7.35	(132.3,135)	(44.1,135)	(29.4,135)	(29.4,135)	(29.4,60)
Flow meter	Shelves 2,4,5	3.75	(67.5,80)	(22.5,80)	(15,80)	(15,80)	(15,20)
2-way valve	Shelves 3,4,5	2.55	(45.9,60)	(15.3,60)	(10.2,60)	(10.2,60)	(10.2,15)
3-way valve	Shelves 4,5	2.85	(51.3,60)	(17.1,25)	(11.4,20)	(11.4,20)	(11.4,15)

Note: Format is (target, actual). All hold times are fifteen seconds.

Analysis of Microgravity Experiment Rig as One Object

The weight and moment arm of the entire rig is in Table 10. It was calculated that the vertical center of gravity of the rig is 13.3 in. The base plate of the rig is bolted to the floor of the aircraft with 8 steel AN6 bolts. The independent shear/tensile load on the 8 bolts holding the base plate to the aircraft floor is calculated as:

Forward: 5538 lbs Up/Lateral: 1231 lbs

Table 10: Assembly Weight and Moment Arm

Description	Weight (lbs)	Z from aircraft floor (in)	Moment Arm (lbs-in)
Rig	651.7	16.00	10455
Base Plate	137.0	0.25	34.25
Total	**788.7**	**13.3**	**10489.25**

The normal-gravity load per attach point is computed by dividing the total weight by the number of attaching bolts to be 92.9 lb, which is well below the maximum allowable load of 200 lb per attach point. The 9g forward load factor results in reactions shown in Figure 12.

The tipping tensile load under 9gs forward on the bolts farthest from the line of rotation is calculated as:

$$P_{t,\max} = \frac{(9)(788.7)(13.3)(62.25)}{2\left(2.25^2 + 22.25^2 + 42.25^2 + 62.25^2\right)} = 477.0 \text{ lbs}$$

The shear load per bolt is:

$$P_S = \frac{(9)(788.7)}{8} = 887.3 \text{ lbs}$$

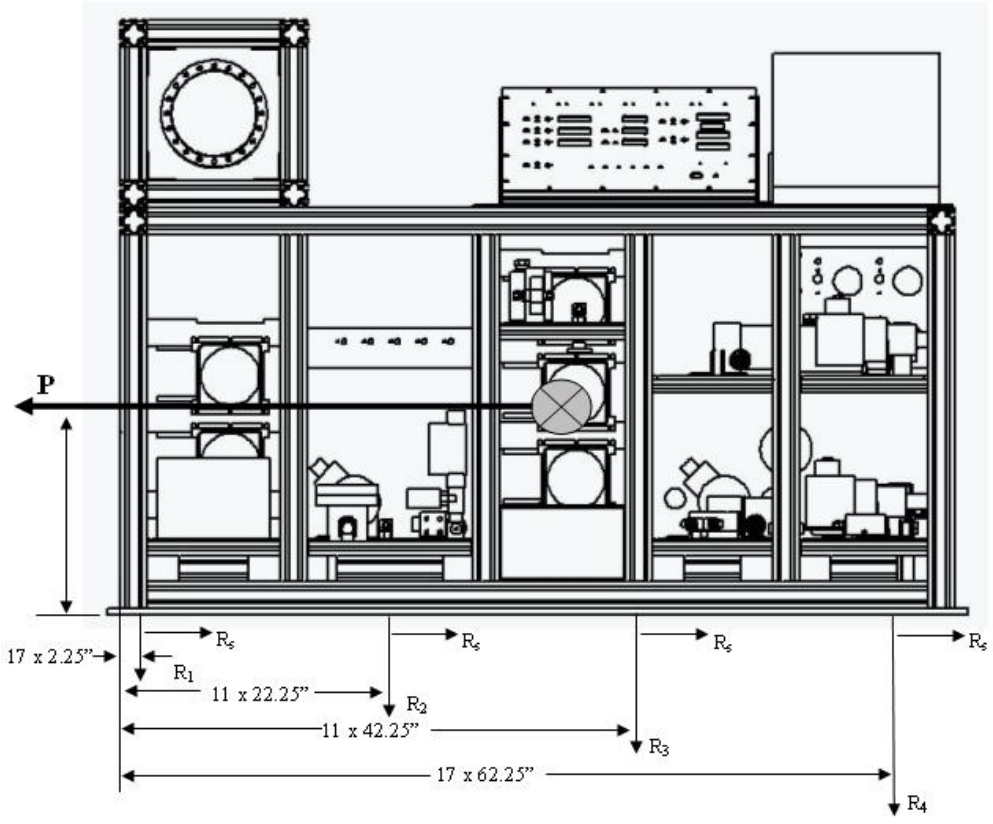

Figure 12: Reactions to 9g Forward Load Factor—Assembly

Margin of Safety: Using the margin of safety calculation stated earlier in this report, the ultimate and yield margins of safety in the tipping tensile load on the bolts in the row farthest from the line of rotation can be calculated by:

For AN6 bolts: F_{UT} = 10100 lbs and F_{YT} = 7740 lbs

$$MS_{UT} = \frac{10100}{(477.0)(2)} - 1 = 10.6$$

$$MS_{YT} = \frac{7740}{(477.0)(2)} - 1 = 8.1$$

The ultimate shear strength for AN6 bolts is: F_{SU} = 8280 lbs. The margin of safety for shear loading is:

$$MS_{UT} = \frac{8280}{(887.3)(2)} - 1 = 3.7$$

With the large margins of safety, it is evident that the tensile load on the bolts in the row receiving the most tension during tipping will not be critical for bolt failure. The margin of safety for shear loading is large too.

Combined Shear/Tensile Loading: The combined tipping shear and tensile loading is analyzed with the following formula:

$$\left(\frac{887.3}{8280}\right)^3 + \left(\frac{477.0}{10100}\right)^2 = 0.00346 \text{ = 0.35\% of load carrying capacity used}$$

With the results above, the combined shear/tensile loading during 9gs forward, including tipping moment, is not critical for bolt failure.

As shown through this structural analysis, the microgravity experiment rig will sustain the 9g forward loading with large margins of safety, indicating large margins in all other directions and planes.

Electrical Analysis

Electrical Schematic

Appendix B: Electrical Schematic contains the electrical schematics for the microgravity experiment and shows the overall power distribution, fuses, and wire sizes.

Electrical Load

The Microgravity Spray Cooling Experiment requires 115 VAC, 60 Hz power for operation. The component requirements are listed in

Table 11.

Table 11: Component Requirements

Circuit	Power	Component	Load (amps)
1	115 VAC, 60 Hz	Water Heater	2
		FC Reheater	6
		Total Circuit 1	**8**
2	115 VAC, 60 Hz	Power Supply	7
		Heater	4.5
		Total Circuit 2	**11.5**
3	115 VAC, 60 Hz	Power Supply	7
		High Voltage Power Supply	1
		Total Circuit 3	**8**
4	115 VAC, 60 Hz	Power Supply	2
		Fans (5)	1
		PID Controller (3)	0.03
		Data Acquisition System	0.5
		Zero-Point Dry Well	1
		Laptop Computer	1.5
		Total Circuit 4	**6.03**

Electrical Emergency Flow Shutdown Switch

In the event that an emergency shutdown is required by any other unforeseen circumstance, there is a large, easily accessible, and clearly marked “emergency flow shutdown” switch that automatically shuts off power to all valves, heaters and pumps. This switch shuts down the fluid flow and electrical components, and the system can only be reset by pulling this button back up. The computer, display, and monitoring instrumentation are not affected by this emergency shutoff and thus permit the monitoring of the experiment if it is necessary.

In addition, individual items can be shut off by shutting off the main power switches on the control panel located on top of the frame.

Loss of Electrical Power

In the event of a loss in electrical power, all valves, pumps, heaters and instrumentation will shut down. There will be no flow.

Pressure System

Flow Schematic

Appendix C contains the flow schematic for the microgravity experiment rig. Hose sizes are specified on the flow schematic.

Relief valve set pressures were determined using the following rationale. Although it is not standard procedure, if the operating pressures are set at ground level, the gauge reading is converted into an absolute reading. Under normal operating conditions, cabin pressure is 11 to 12 psiA. In the event of a rapid cabin depressurization, cabin pressure at altitude can fall to 4 psiA. Therefore, the set pressure (SP) for the relief valves are set using the following function of the working pressure, WP (in absolute pressure):

$$SP = 1.10 \cdot (WP - 4\ \text{psia})$$

The pneumatic pressure (PP) of components is set using the following:

$$PP = 1.25 \cdot 1.1 \cdot (WP - 4\ \text{psia}) + 14.7\ \text{psia}$$

Both the set pressure and pneumatic pressure are differential pressures and the setting/testing occurs at a difference relative to ambient pressure.

The temperature within the test chamber will set the system pressure. The maximum temperature will be at the heater and is 100 °C. The maximum chamber temperature is set for 70 °C, which corresponds to a chamber pressure of 25 psiA. In order to drive flow through the spray nozzle, the pump needs to provide FC-72 at a pressure of 75 psiA.

Pressure switches will be set at 105 psiA and will shut off the heaters and pumps in the event of an overpressure situation. Shutting down the heaters and pumps will serve to remove the heat source and allow the pressure to equalize through the flow loop across the pumps resulting in a system pressure no more than 25 psiA. The volume of the chamber will also act as a fluid overflow reservoir to allow excess expansion of the FC-72.

All water flow components will be pressure tested to 111 psiG. All FC-72 flow components, including the test chamber, will be pressure tested to 132 psiG.

Pressure certification has been completed. Results are available on request.

Flow Component Listing

Table 12 contains a listing of the flow components.

Table 12: Flow Components

Description	MFG	Model Number	Maximum Working Pressure (psiG unless otherwise noted)
Water Loop			
Heat Exchanger	Lytron	6110G1SB	250
Fan	Lytron	MX2A3, 028316	n/a
Heat Exchanger	Lytron	6110G1SB	250
Fan	Lytron	MX2A3, 028316	n/a
Pump	Tuthill	DDS.68PPPV2NN37000	200
Pressure Switch	United Electric	10-B11	12000
Filter	Swagelock	SS-6F-140	2150
Flow Meter	Sponsler	MF90-CB-PH-A-4X-V	5000
Pulse Amplifier	Sponsler	SP711-3V10	n/a
Pressure Transducer	Omega	PX303-100A5V	100 (proof-200) psiA
Drain Valve	Swagelock	SS-4BK	1000
Reservoir/Sight Glass	MDC Vacuum/Lube Devices Inc.	n/a	290
FC-72 Loop			
2-way valve	Hoke/Simco Controls	7115G4Y	6000
Actuator	Hoke/Simco Controls	0172L2	n/a
Heat Exchanger	Lytron	6110G1SB	250
Fan	Lytron	MX2A3, 028316	n/a
Heat Exchanger	Lytron	6110G1SB	250
Fan	Lytron	MX2A3, 028316	n/a
Heat Exchanger	Lytron	6110G1SB	250
Fan	Lytron	MX2A3, 028316	n/a
Pressure Transducer	Omega	PX303-100A5V	100 (proof-200) psiA
Pump	Tuthill	DDS1.3PPPV2NN00000	200
Pressure Transducer	Omega	PX303-200A5V	200 (proof-400) psiA
Filter	Swagelock	SS-6F-40	2150
Reservoir/Sight Glass	MDC Vacuum/Lube Devices Inc.	n/a	290
2-way valve	Hoke/Simco Controls	7115G4Y	6000
Actuator	Hoke/Simco Controls	0172L2	n/a
Pump	Tuthill	DDS.99PPPV2NN00000	250
Drain valve	Swagelock	SS-4BK	1000
Filter	Swagelock	SS-6F-15	2150
Flow Meter	Sponsler	MF90-CB-PH-A-4X-V	5000
Pulse Amplifier	Sponsler	SP711-3V10	n/a
Pressure Transducer	Omega	PX303-200A5V	200 (proof-400) psiA
Pressure Switch	United Electric Cont	10-B11	12000
3-way valve	Hoke/Simco Controls	7673G4Y	6000
Actuator	Hoke/Simco Controls	0172L2F	n/a
Reheater	n/a	n/a	75 psiA

Description	MFG	Model Number	Maximum Working Pressure (psiG unless otherwise noted)
2-way valve	Hoke/Simco Controls	7115G4Y	6000
Actuator	Hoke/Simco Controls	0172L2	n/a
Pump	Tuthill	DDS.99PPPV2NN00000	250
Drain valve	Swagelock	SS-4BK	1000
Filter	Swagelock	SS-6F-15	2150
Pressure Transducer	Omega	PX303-200A5V	200 (proof-400) psiA
Pressure Switch	United Electric Cont	10-B11	12000
Throttling Valve	Swagelock	SS-4BK	1000
Throttling Valve	Swagelock	SS-4BK	1000
Test Section			
Chamber	MDC Vacuum/Lube Devices Inc.	n/a	25 psiA
Pressure Transducer	Omega	PX303-100A5V	100 (proof-200) psiA
Drain Valve	Swagelock	SS-4BK	1000
Drain Valve	Swagelock	SS-4BK	1000
Accelerometer	Columbia	SA307HPTX	n/a

Laser Certification

No lasers will be used with this experiment.

Parabola Details and Crew Assistance

Forty parabolas per flight of 0.01g are requested. No modifications to either the timing between trajectories or the time duration of turns are anticipated.

Institutional Review Board

There are no plans to use human or animal test subjects and these tests are not of a biological nature.

KC-135 Hazards Analysis

This section consists of AOD Forms 70 and 71.

HAZARD SOURCE CHECKLIST

Enumerate or mark N/A

N/A	Flammable/combustible material, fluid (liquid, vapor, or gas)
1	Toxic/noxious/corrosive/hot/cold material, fluid (liquid, vapor, or gas)
2	High pressure system (static or dynamic)
N/A	Evacuated container (implosion)
N/A	Frangible material
N/A	Stress corrosion susceptible material
N/A	Inadequate structural design (i.e., low safety factor)
N/A	High intensity light source (including laser)
TBD	Ionizing/electromagnetic radiation
N/A	Rotating device
N/A	Extendible/deployable/articulating experiment element (collision)
N/A	Stowage restraint failure
N/A	Stored energy device (i.e., mechanical spring under compression)
N/A	Vacuum vent failure (i.e., loss of pressure/atmosphere)
3	Heat transfer (habitable area over-temperature)
4	Over-temperature explosive rupture (including electrical battery)
5	High/Low touch temperature
6	Hardware cooling/heating loss (i.e., loss of thermal control)
N/A	Pyrotechnic/explosive device
N/A	Propulsion system (pressurized gas or liquid/solid propellant)
N/A	High acoustic noise level
N/A	Toxic off-gassing material
N/A	Mercury/mercury compound
N/A	Other JSC 11123, Section 3.8 hazardous material
N/A	Organic/microbiological (pathogenic) contamination source
7	Sharp corner/edge/protrusion/protuberance
N/A	Flammable/combustible material, fluid ignition source (i.e., short circuit; under-sized wiring/fuse/circuit breaker)
8	High voltage (electrical shock)
TBD	High static electrical discharge producer
9	Software error or compute fault
N/A	Carcinogenic material
	Other: _____
	Other: _____
	Other: _____

APPENDIX G
DETAILED HAZARD DESCRIPTION

Use the following format for describing each identified hazard in detail.

Hazard Number: 1

Title:
Toxic fluid – FC-72

Hazard Description:
Water is not a health hazard.
FC-72 is non-toxic and inert; the quantity used in this experiment will not affect the aircraft environment
At room temperature: Eye contact--Contact with the eyes during product use is not expected to result in significant irritation. Skin contact--Contact with the skin during product use is not expected to result in significant irritation. Inhalation--No health effects are expected. Ingestion--No health effects are expected
At temperature >200°C: hydrogen fluoride and perfluoroisobutylene is generated.

Hazard Cause(s):

Leak, spill, or component failure causes release of test fluid from closed experimental system. Over temperature of FC-72 in excess of 200^{o}C.

Hazard Control(s):

Pressure-testing of equipment of at least 1.25 times the operating pressure will ensure adequate containment of fluids.
Safety cut-out measures will monitor heater temperature, to not exceed 100°C, and shut down operation in potentially-hazardous circumstances.
Should a leak occur, the flow system is designed to be able to isolate the FC-72 either in the test chamber or the reservoir.

APPENDIX G
DETAILED HAZARD DESCRIPTION

Use the following format for describing each identified hazard in detail.

Hazard Number: 2

Title:
High pressure system

Hazard Description:
Over pressurization of flow system causes a component to fail; releasing test fluids and possibly injuring nearby personnel.

Hazard Cause(s):

Flow system blockage, or cabin depressurization causes unexpected pressure differential across an experiment component.

Hazard Control(s):

Test chamber: Temperature within the chamber will set the pressure. A maximum working temperature of 70 °C in the chamber will result in a maximum of 25 psiA.
FC-72 Nozzle inlet: Inlet pressure to the spray nozzle will be limited to 75 psiA
Water flow components will be pressure tested to 111 psiG.*
FC-72 flow components, including the test chamber, will be pressure tested to 132 psiG.*
Pressure switches will be set at 105 psiA and will shut off the heaters and pumps in the event of an overpressure situation. Shutting down the heaters and pumps will serve to remove the heat source and allow the pressure to equalize through the flow loop across the pumps resulting in a system pressure no more than 25 psiA. The volume of the chamber will also act as a fluid overflow reservoir to allow excess expansion of the FC-72 or isolation of the FC-72 in the event of a leak.
*All noncommercial components will be pneumatically pressure tested to at least 1.25 times the maximum working pressure. Note: Maximum working pressure for FC-72 system is 100 psiA. Maximum working pressure for water system is 75 psiA.

APPENDIX G
DETAILED HAZARD DESCRIPTION

Use the following format for describing each identified hazard in detail.

Hazard Number: TBD

Title:
Ionizing/electromagnetic radiation

Hazard Description:

Hazard Cause(s):

Hazard Control(s):

DETAILED HAZARD DESCRIPTION

Use the following format for describing each identified hazard in detail.

Hazard Number: 3

Title:

Heat transfer

Hazard Description:

Increase in temperature of habitable area surrounding experiment causes discomfort and/or burning in personnel on board

Hazard Cause(s):

Overheat on one or more components causes an increase in the temperature surrounding the experiment package.

Spill or leak of heated fluid causes an increase in the temperature surrounding the experiment package.

Hazard Control(s):

Maximum expected heater operating temperature of 100 °C and test chamber temperature of 70 °C – minimal heat load, will not significantly alter the environment surrounding the experiment package. This will allow high heat flux testing at the heater without significantly altering the chamber temperature.

Over-temperature controls and safety cut-out measures prevent overheating by shutting down the experiment.

DETAILED HAZARD DESCRIPTION

Use the following format for describing each identified hazard in detail.

Hazard Number: 4

Title:

Over temperature explosive rupture

Hazard Description:

Increase in temperature within the test cell will result in an increase in pressure. Should this increase in temperature result in a pressure exceeding the rating of the viewport to the test chamber, an explosive rupture may occur.

Hazard Cause(s):

The temperature in the chamber is balanced by the heat input from the heaters and the water coil around the chamber walls. The test chamber is controlled at a temperature consistant with a desired pressure. The maximum allowable chamber temperature is 70°C, which will result in a chamber pressure of 25 psiA.

Hazard Control(s):

The test chamber is constructed with 1-inch Lexan viewports mounted to the test chamber. In addition, over-temperature switches will shut off the heaters in the event of a temperature excursion in the test chamber. The Lexan viewports have been structurally analyzed to verify structural integrity in the event of a pressure excursion. The test chamber along with the FC-72 flow components will be tested to 132 psiG.

APPENDIX G
DETAILED HAZARD DESCRIPTION

Use the following format for describing each identified hazard in detail.

Hazard Number: 5

Title:
High touch temperature

Hazard Description:
Components or surfaces feel hot to the touch; may cause minor burns to personnel who come in contact with them.

Hazard Cause(s):

Improperly insulated surfaces expose personnel to hot surfaces.

Hazard Control(s):

High temperature components will be insulated or thermally shielded from the environment.

The test chamber, as well as potentially exposed components and surfaces, will be insulated.

DETAILED HAZARD DESCRIPTION

Use the following format for describing each identified hazard in detail.

Hazard Number: 6

Title:

Hardware cooling loss

Hazard Description:

Planned cooling measures fail, resulting in overheating of hardware, potentially resulting in hazardous temperatures in and around the experimental test package

Hazard Cause(s):

Line blockages

Pump failure

Heat exchanger fan failure

Hazard Control(s):

Safety cutout measures will ensure temperature control, < 70°C, including a manual emergency-shutdown-switch, which will shut down all potentially dangerous components.

APPENDIX G
DETAILED HAZARD DESCRIPTION

Use the following format for describing each identified hazard in detail.

Hazard Number: 7

Title:
Sharp corners

Hazard Description:
Sharp corners or other surfaces on experimental test package cause minor cuts/abrasions to personnel.

Hazard Cause(s):

Unintentional contact with sharp corners may cause minor cuts/abrasions.

Hazard Control(s):

A safety/grab rail will be installed along the perimeter of the experimental test package frame.

Any remaining exposed sharp edges or corners will be padded.

APPENDIX G
DETAILED HAZARD DESCRIPTION

Use the following format for describing each identified hazard in detail.

Hazard Number: 8

Title:
High voltage

Hazard Description:
Potentially lethal voltages will be used to power the experiment.

Hazard Cause(s):

1. Wire breaking and shorting to chassis.
2. Shorting of voltage potential to ground.
3. Breakdown of wire because of high current load.

Hazard Control(s):

1. All power lines are protected using circuit breakers and/or fuses.
2. All voltage potentials are shielded and proper connectors are used.
3. Experiment package is chassis grounded.
4. All wiring is rated for operating currents.

APPENDIX G
DETAILED HAZARD DESCRIPTION

Use the following format for describing each identified hazard in detail.

Hazard Number: TBD

Title:
High static electrical discharge producer

Hazard Description:

Hazard Cause(s):

Hazard Control(s):

APPENDIX G
DETAILED HAZARD DESCRIPTION

Use the following format for describing each identified hazard in detail.

Hazard Number: 9

Title:
Software error

Hazard Description:
Loss of experimental control (ie: temperature/pressure control) due to software error.

Hazard Cause(s):

Computer failure causes software not to work

Aircraft power loss/malfunction.

Hazard Control(s):

Computer operates on battery backup in case of power loss.

All safety cut-out measures will be controlled via hardware, rather than software.

Tool Requirements

Tools supplied by the Reduced Gravity Office should be sufficient for loading and removal of the experiment from the aircraft.

Photo Requirements

None

Aircraft Loading

The experiment can be loaded with a forklift and either directly on its own pallet or the lifting pallet/basket supplied by the Reduced Gravity Office. The experiment assembly contains casters and lifting jacks that are removable.

Ground Support Requirements

It is necessary to have access to 115 VAC, 60 Hz in order to operate the assembly, either for final functional checks or the Test Readiness Review.

Hazardous Materials

FC-72 will be the primary working fluid. Temperatures exceeding 200 °C will result in FC-72 generating hazardous materials, hydrogen fluoride and perfluoroisobutylene. Because the heater temperatures will be limited to 100 °C there will be no hazardous material generation.

Material Safety Data Sheets

See Appendix E for the material safety data sheet (MSDS) for the FC 72.

Test Procedures

Test procedures may change as the electromagnetic system is incorporated into the design.

Loading Checklist

1. Verify that all mounting bolts are tight.
2. Verify power connections, 115 VAC 60 Hz.

Pre-test Checklist

1. Ascertain that the coolant and water systems are filled with sufficient liquids.
2. Plug in cords for the four AC circuits, 20 amp capacity for circuit 1 and 15 amp capacity for circuits 2, 3 and 4.
3. Turn on Breakers 1, 2, 3 and 4, verify green indicators for each.
4. Verify that all toggle switches are in the off (down) position and all potentiometers are at 0 (fully counterclockwise).
5. Press the Start button and verify red indicators for the pumps and target heaters and red and blue indicators for the flow bypass.

Testing Checklist

1. Turn on the laptop computer, log in and start the data acquisition program.
2. Verify system pressures are appropriate for coolant temperature.
3. Turn on the water pump and set the flow rate as indicated on the computer display using the potentiometer; verify green indicator.
4. Turn on the coolant pumps and set the flow rates as indicated on the computer display using the potentiometers; verify green indicators and flow rate on the digital readouts.
5. Switch the bypass toggle switches to the up position and verify spray in the chamber.
6. Set the reheater PID controllers to the desired temperature and set the alarm cutout temperatures.
7. Switch the PID controllers on; verify green indicators.
8. When the fluids are at operating temperature, the reheater indicators will be cycling.
9. Verify that the over-temperature PID controller alarm settings are correctly adjusted.
10. Turn on the video cameras and place them in record mode.
11. Turn on the target heater switches and verify green indicators.
12. Set the target heater wattage using the potentiometers.
13. Take data as appropriate to the flight test plan.

Post-test Checklist

1. Switch off target heaters and set potentiometers to the 0 position.
2. Switch off reheater switches.
3. Switch bypass toggle switches to the down position.
4. Switch off all pumps and set potentiometers to the 0 position.
5. Switch off video cameras.
6. Stop data acquisition and shut down computer.
7. Switch off the four Breakers.

Leak Shut Down Procedure

1. Hit Panic button.
2. Assess source of leak for fixability. If fixable, (e.g., wrong valve is open), seal leak; otherwise, see shutdown procedures.
3. Mop-up leak. Place wet towels into zip lock baggie or vent tank.

Emergency Shut Down Procedure

1. Hit Panic button.
2. Ensure all power is off.
3. Visually verify and contain any leaks.

THIS PAGE INTENTIONALLY LEFT BLANK.

Appendix A: 80/20 Joint Fastener Testing at WVU

The experimental rig is made up of mainly two different joint assemblies. The joint fastener strength values in the 80/20 literature were insufficient for the joint fastener configurations used on the frame. Structural tests using the West Virginia University Civil and Environmental Engineering Department 4000 pound load limit frame, hydraulic ram and load cell were conducted on a test structure made to model the aforementioned joints. The first structure, shown in Figure A1 and Figure A2, was assembled to represent a corner joint and is constructed out of 2020 extrusions, two 90° joining plates (P/N 4128), and three inside gusset corner brackets (P/N 4138). All screws were torqued to recommended limit of 100 in-lbs.

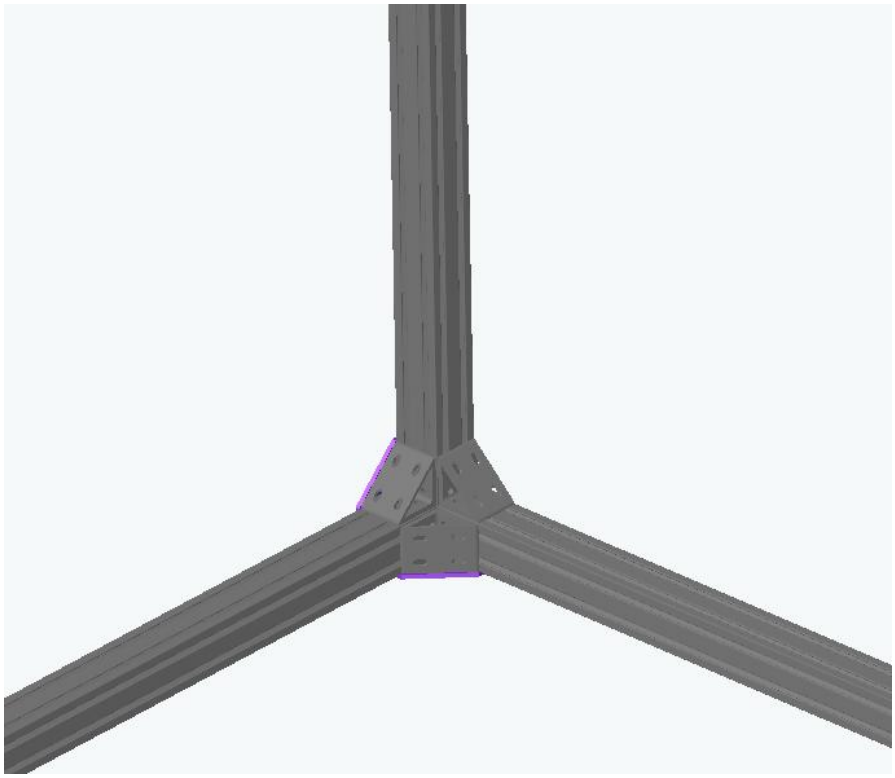

Figure A1: Corner Joint

A 2” LVDT was used to measure the displacement of the extrusion members as the load was applied. Load and displacement data were then recorded versus time using a PC based data acquisition system.

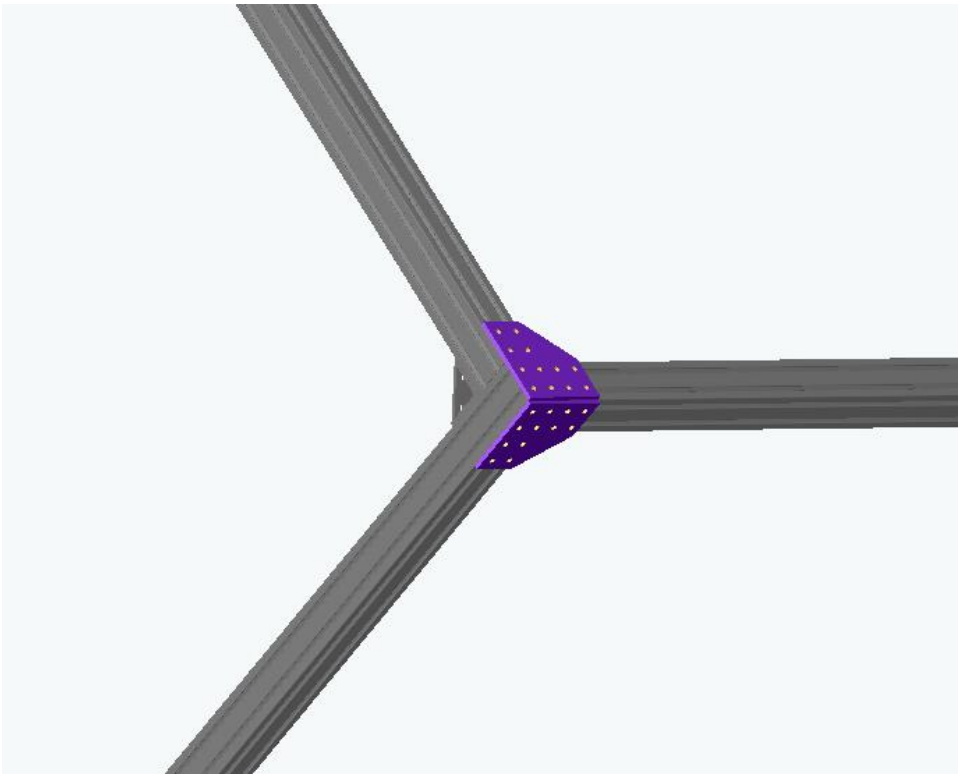

Figure A2: Corner Joint

The corner section, loads were applied at a distance of 23” from the end of the section and displacements were measured 32.25” from the end, as shown in Figure A3.

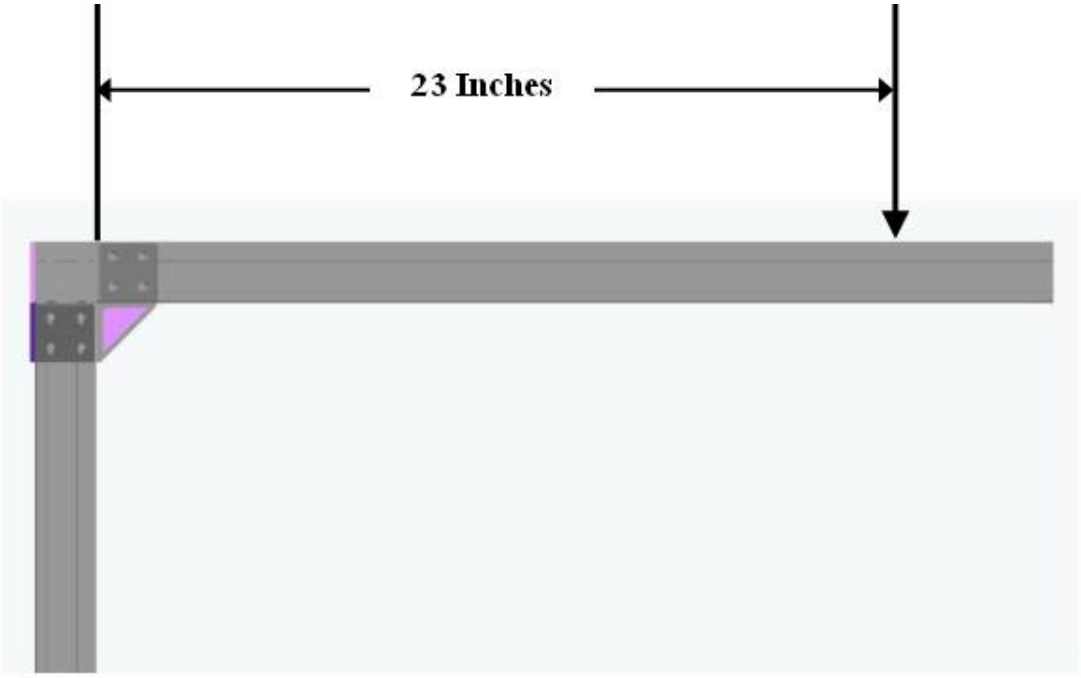

Figure A3: Corner Joint Load Point

For the test of the corner section joint, the plot of the applied load as a function of time is shown in Figure A4. An initial constant loading of 450 lb ±5 lb was applied for 5 minutes. This load was approximately equal to the maximum loading that had been applied to the corner joint during the initial test at WVU on 5/27/2004. This load was followed by 5 minute applied loads of 500 lb ±5 lb and 550 lb ±5 lb. The measured deflection for this loading sequence of the corner joint is shown in Figure A5.

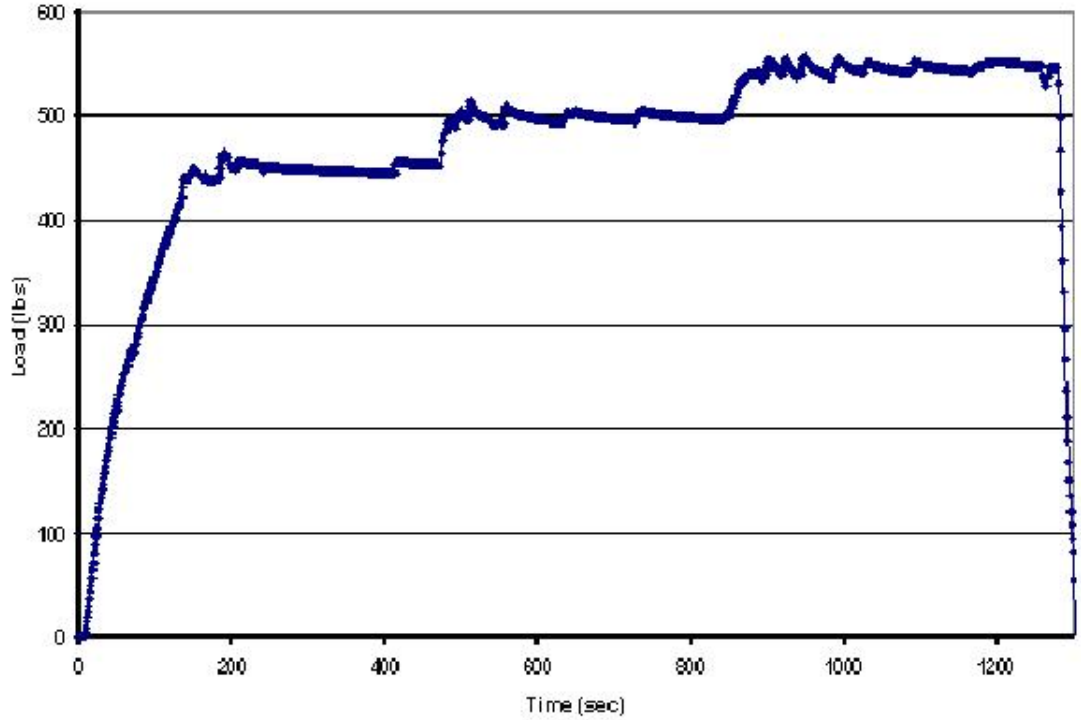

Figure A4: Loading Versus Time for Corner Section: Test on June 7, 2004

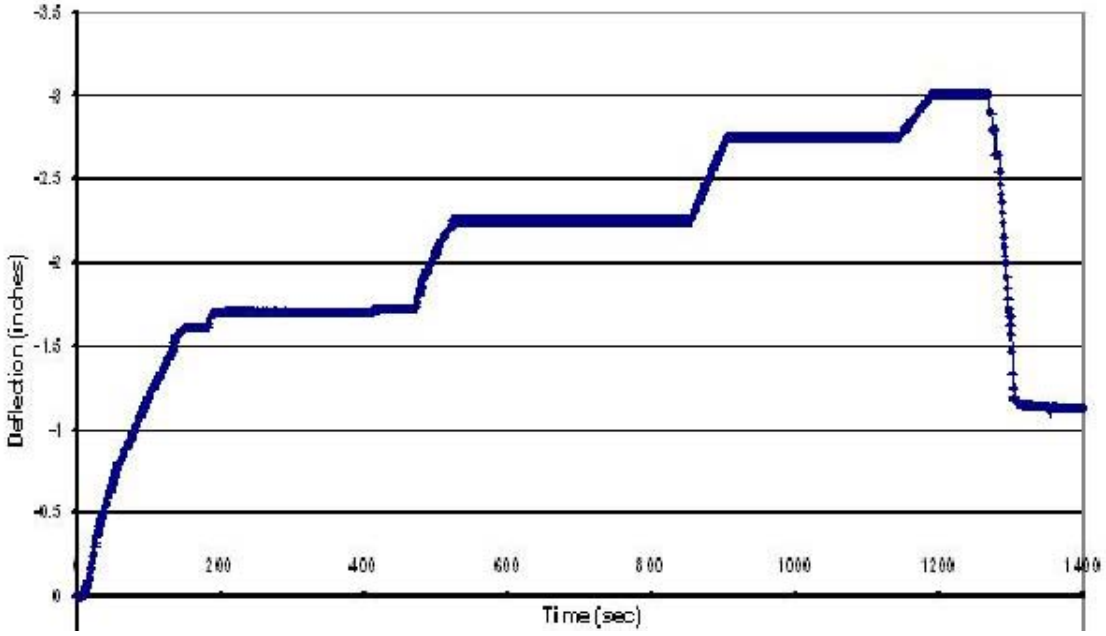

Figure A5: Deflection versus Time for Corner Section: Test on June 7, 2004

Note that deflections larger than 2” have been measured using a tape measure, due to the 2” range of the LVDT. Thus, the small, continual increase in the deflection versus time at fixed loading conditions could not be recorded. For this test of the corner joint, the maximum applied load was 550 lb, resulting in a maximum deflection of 3”. The maximum applied moment about the end of the cantilevered 2020 section was 12,650 in-lbs. A plot of deflection versus applied load for the corner section is shown in Figure A6. Figure A7 shows a photograph of the corner joint under maximum applied loading, while Figure A8 shows the corner joint after loading.

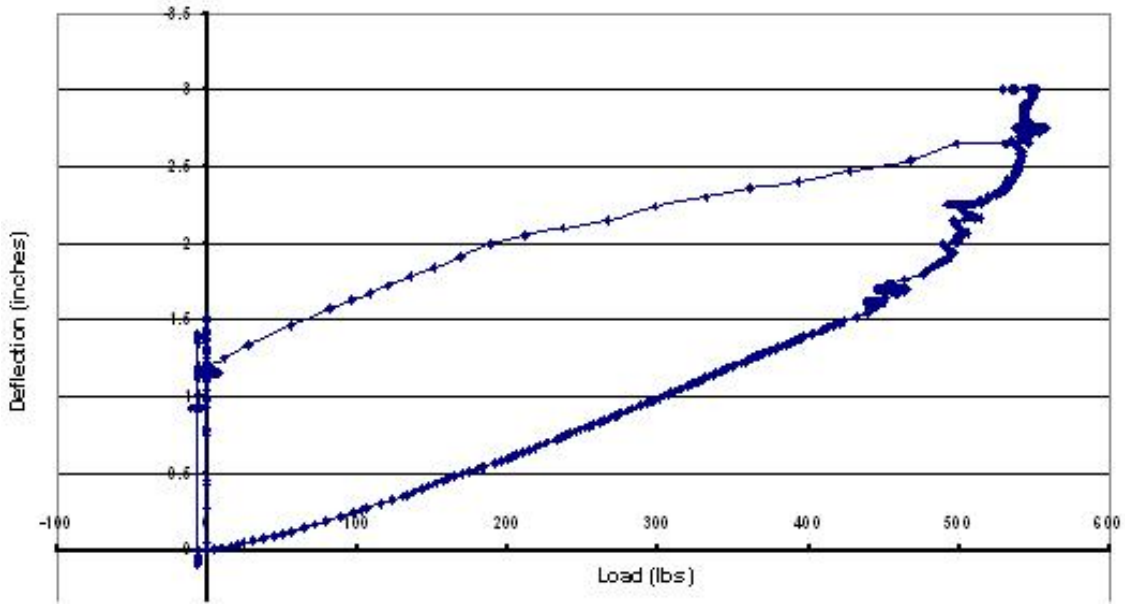

Figure A6: Deflection versus Load for Corner Section: Test on June 7, 2004

Figure A7: Corner Joint under Maximum Load: Test on June 7, 2004

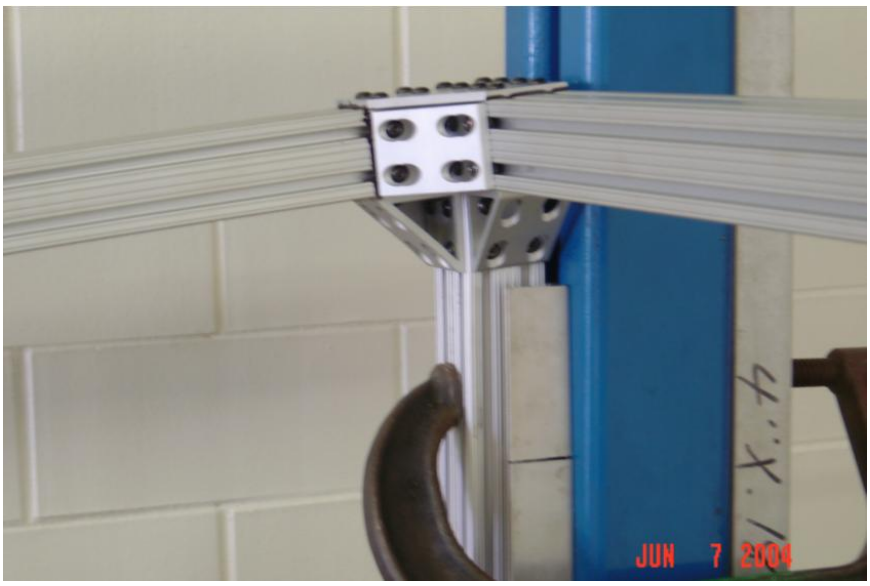

Figure A8: Corner Joint after Loading: Test on June 7, 2004

The joint reached a level of plastic deformation where the joint would not sustain any additional loading. While some of the deflection may be because of the clamping arrangement permanent deflection was defiantly apparent. When the joint was disassembled some deformation was visible in the channels of the 2020 extrusions, as well as in three of the fasteners, but overall critical failure was not obtained.

The second joint tested was the tee joint. It consists of a tee joint (P/N 4125) and two inside gusset corner brackets (P/N 4138). The joint is shown in Figure A9. This configuration was loaded in a similar manner to the corner joint, and the loading is shown in Figure A10.

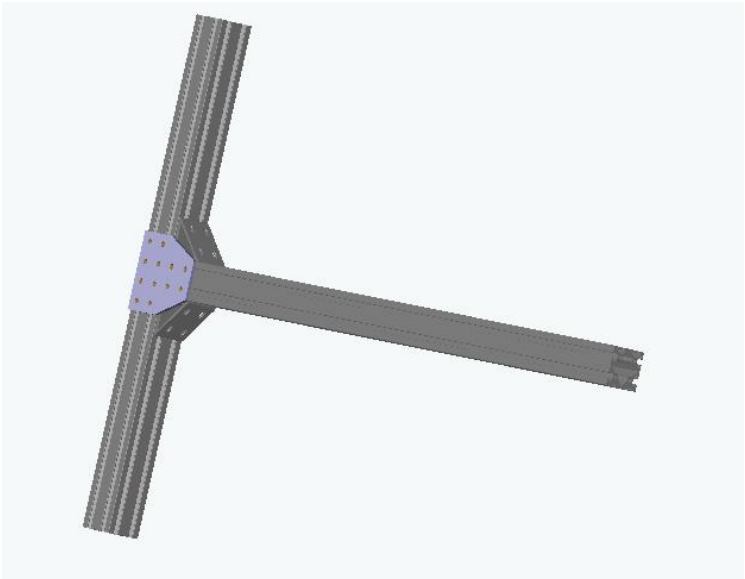

Figure A9: Tee Joint

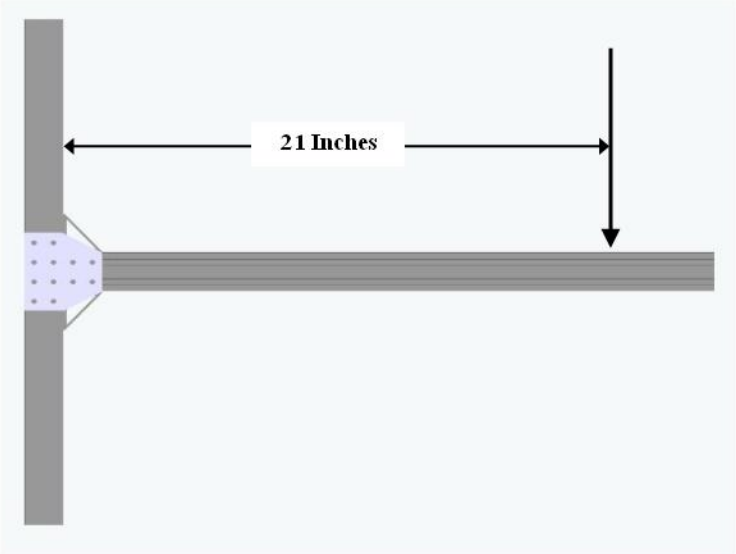

Figure A10: Tee Joint Point Load

This joint was found to be significantly stronger, having smaller deflections under similar applied loading conditions, and having a significantly higher maximum load. Loading versus time for the T section joint is shown in Figure A11**: Loading versus Time for T Section: Test on June 7, 2004**, while the deflection versus time plot is shown in Figure A12.

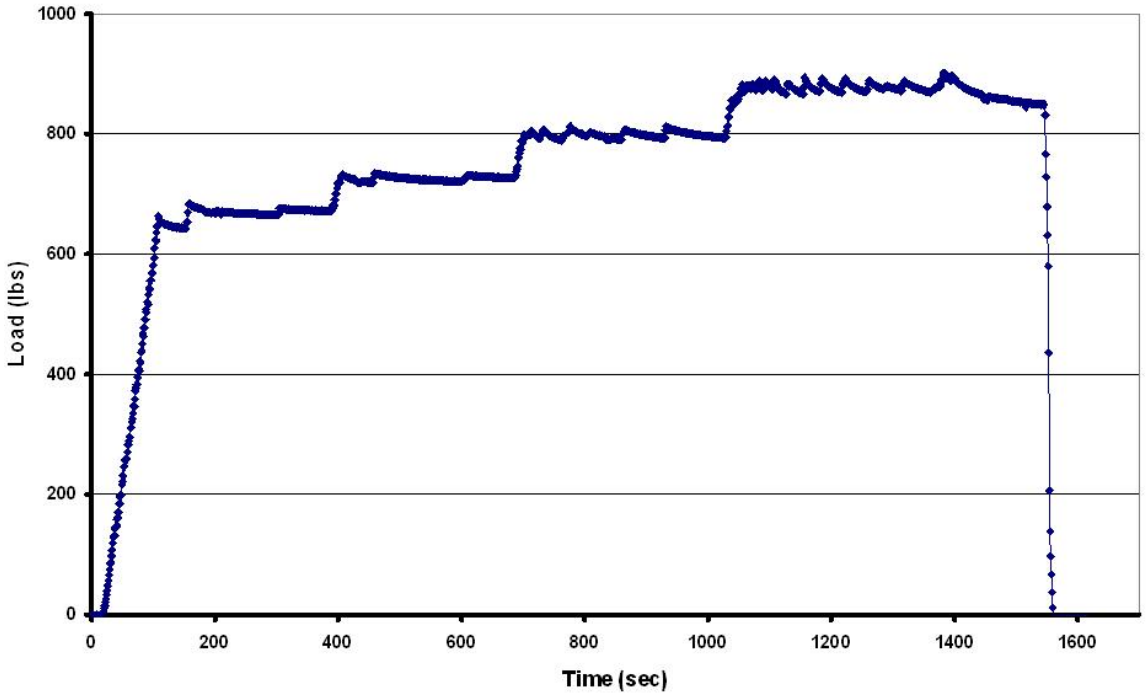

Figure A11: Loading versus Time for T Section: Test on June 7, 2004

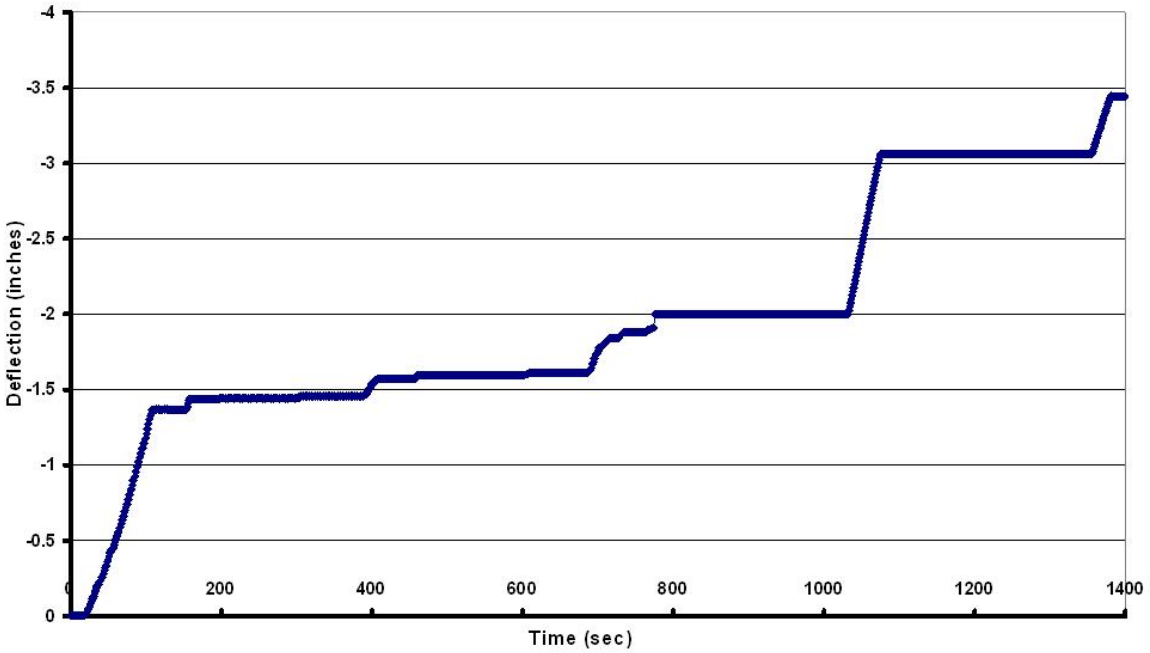

Figure A12: Deflection versus Time for T Section: Test on June 7, 2004

Again, deflections greater than 2" were measured using a tape measure. Also, for the T section test, deflections during unloading conditions were not measured because the LVDT sensor slipped off of the T section cantilever beam. Deflection versus load for the T section test is shown in Figure A13.

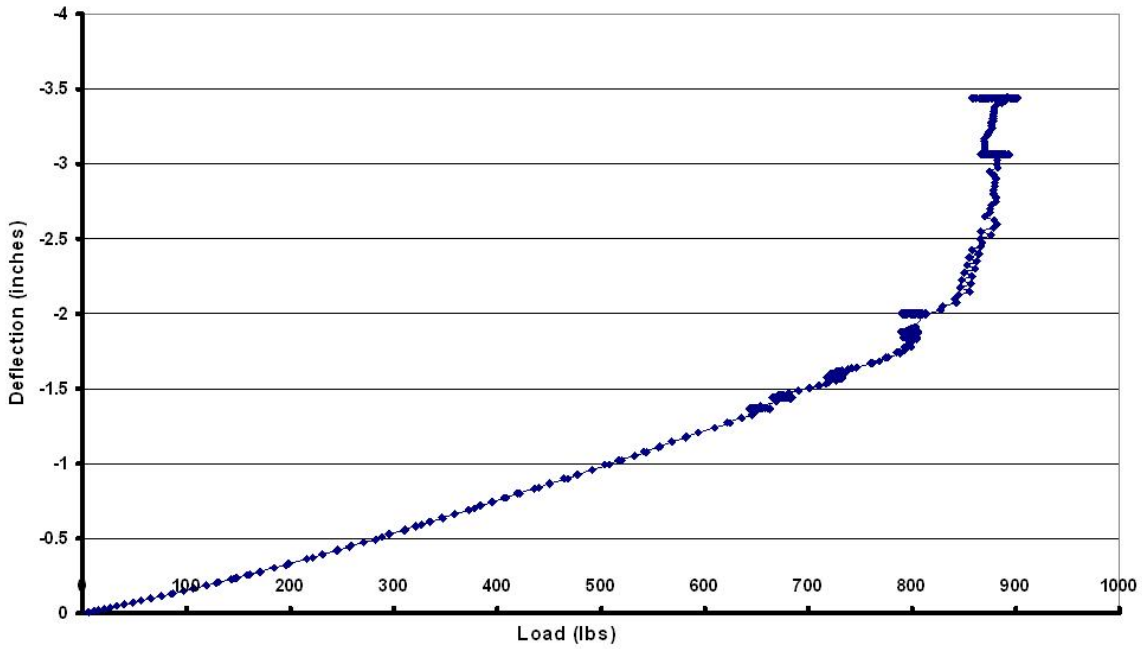

Figure A13: Deflection versus Load for T Section: Test on June 7, 2004

(Note: Deflections for unloading not shown: LVDT sensor slipped)

A picture of the T section joint under maximum loading is shown in Figure A14, while a photo of the section after loading is shown in Figure A15. The maximum applied load for the T section joint was approximately 890 lb, resulting in a maximum deflection of approximately 3.5". The maximum loading corresponded to an applied moment of 18,700 in-lbs.

Figure A14: T Joint under Maximum Load: Test on June 7, 2004

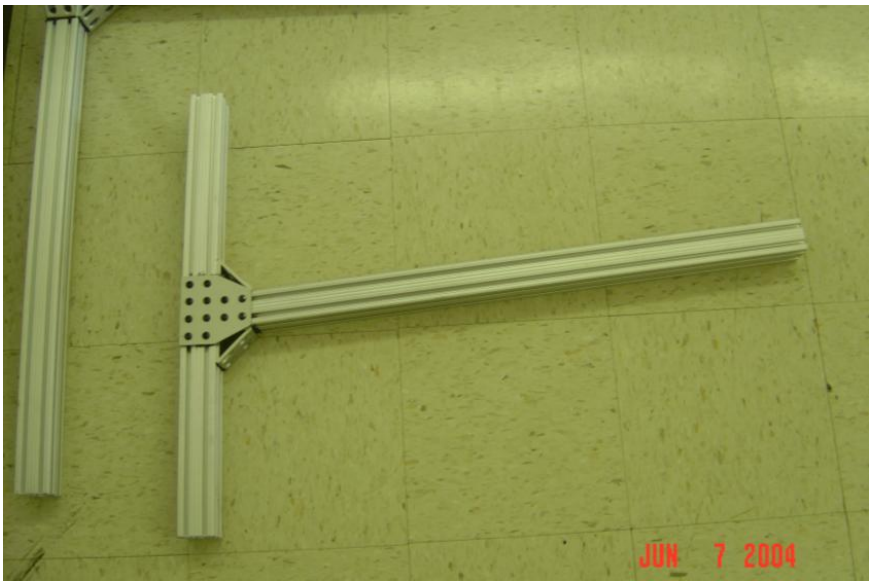

Figure A15: T Joint after Loading: Test on June 7, 2004

The joint reached a level of plastic deformation where the joint would not sustain any additional loading. While some of the deflection may be because of the clamping arrangement permanent deflection was defiantly apparent. When the joint was disassembled some deformation was visible in the channels of the 2020 extrusions but overall critical failure was not obtained.

Appendix B: Electrical Schematic

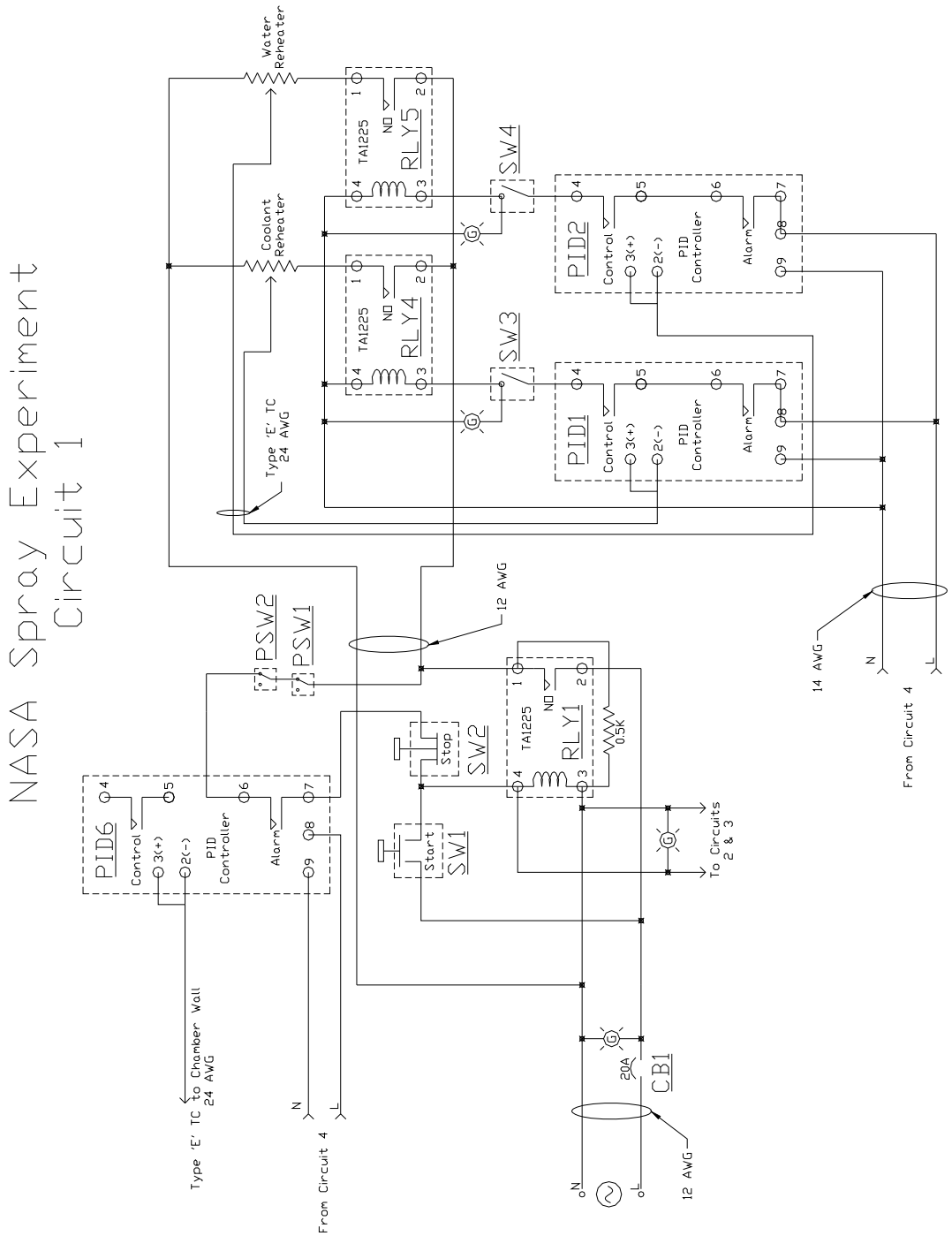
NASA Spray Experiment
Circuit 1
Water Reheater
Coolant Reheater
Type 'E' TC 24 AWG
TA1225
RLY5
RLY4
RLY1
SW4
SW3
SW2
SW1
PSW2
PSW1
PID2
PID1
PID6
Control
PID Controller
Alarm
Stop
Start
0.5k
12 AWG
14 AWG
From Circuit 4
To Circuits 2 & 3
Type 'E' TC to Chamber Wall 24 AWG
20A
CB1
N
L

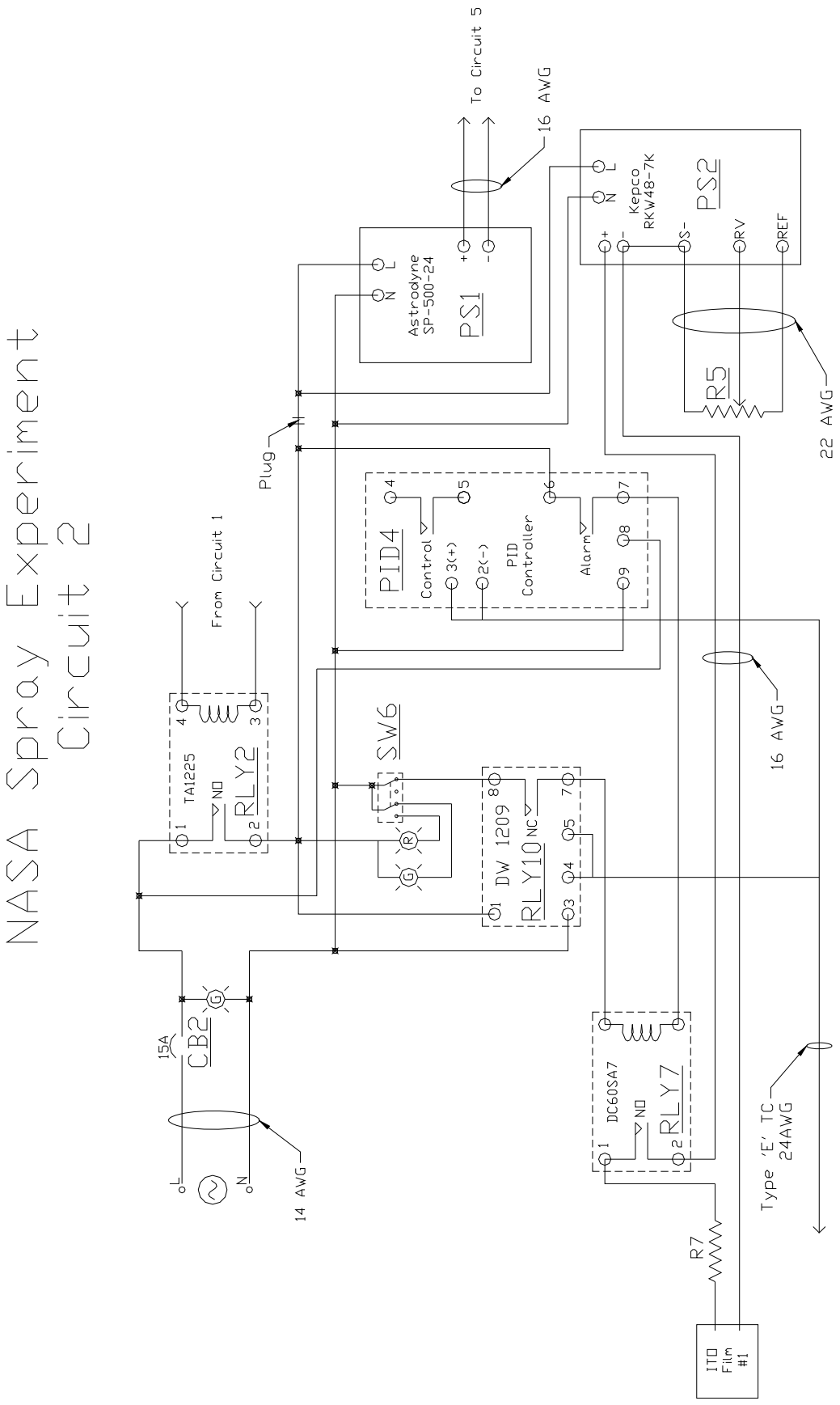
NASA Spray Experiment
Circuit 2
To Circuit 5
16 AWG
Astrodyne
SP-500-24
PS1
L
N
+
-
Kepco
RKW48-7K
PS2
L
N
+
-
S-
RV
REF
R5
22 AWG
Plug
PID4
Control
3(+)
2(-)
PID
Controller
Alarm
From Circuit 1
TA1225
NO
RLY2
SW6
DW 1209
NC
RLY10
16 AWG
15A
CB2
14 AWG
DC60SA7
NO
RLY7
Type 'E' TC
24AWG
R7
ITO
Film
#1

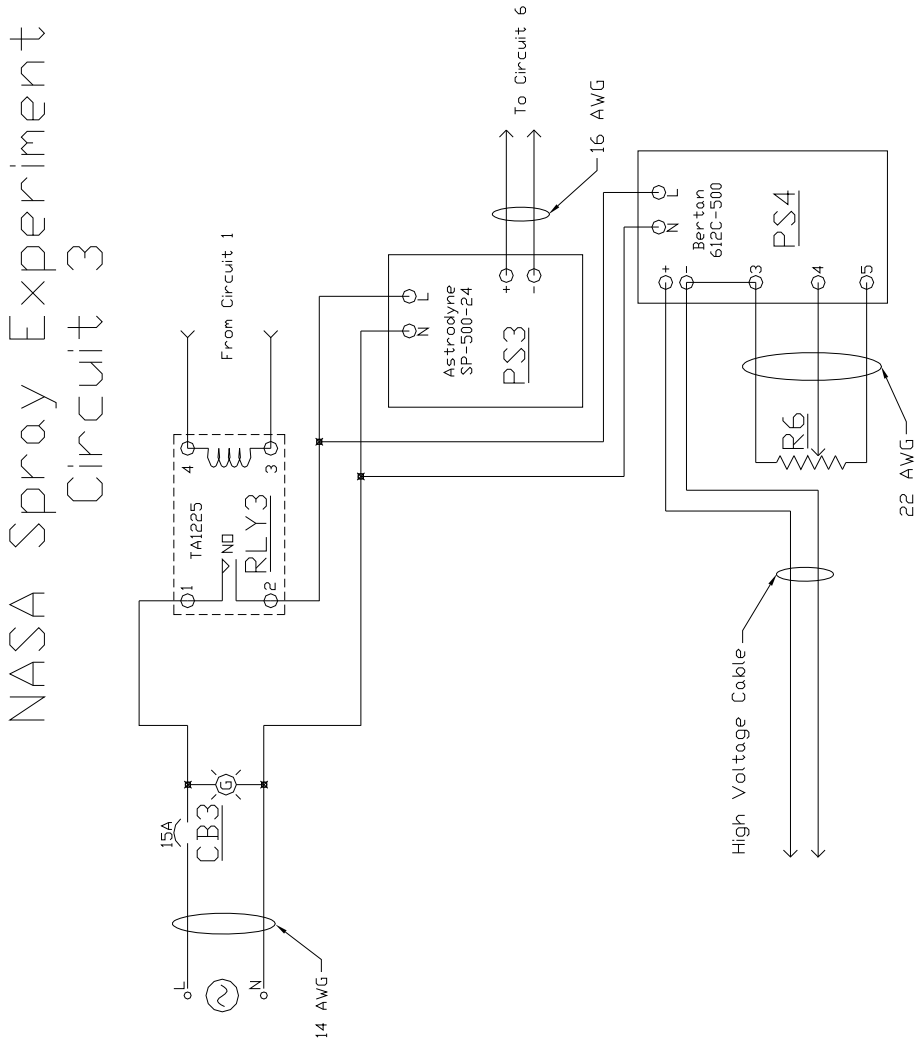
NASA Spray Experiment
Circuit 3
From Circuit 1
To Circuit 6
16 AWG
14 AWG
22 AWG
15A
CB3
TA1225
RLY3
NO
PS3
Astrodyne
SP-500-24
PS4
Bertan
612C-500
R6
High Voltage Cable
L
N
+
-
1
2
3
4
5

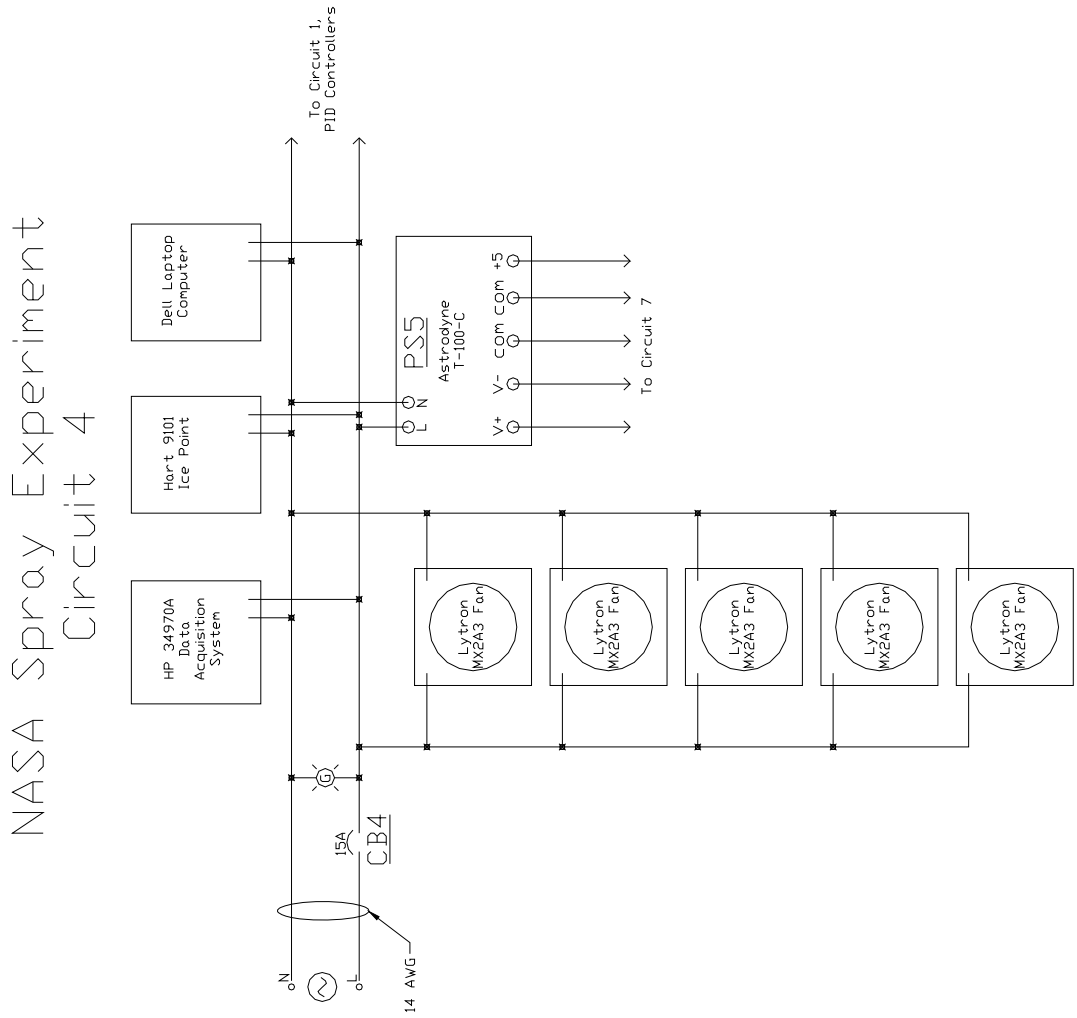
NASA Spray Experiment
Circuit 4
To Circuit 1,
PID Controllers
Dell Laptop
Computer
Hart 9101
Ice Point
HP 34970A
Data
Acquisition
System
PS5
Astrodyne
T-100-C
L N
V+ V- com com +5
To Circuit 7
Lytron
MX2A3 Fan
Lytron
MX2A3 Fan
Lytron
MX2A3 Fan
Lytron
MX2A3 Fan
Lytron
MX2A3 Fan
15A
CB4
N
L
14 AWG

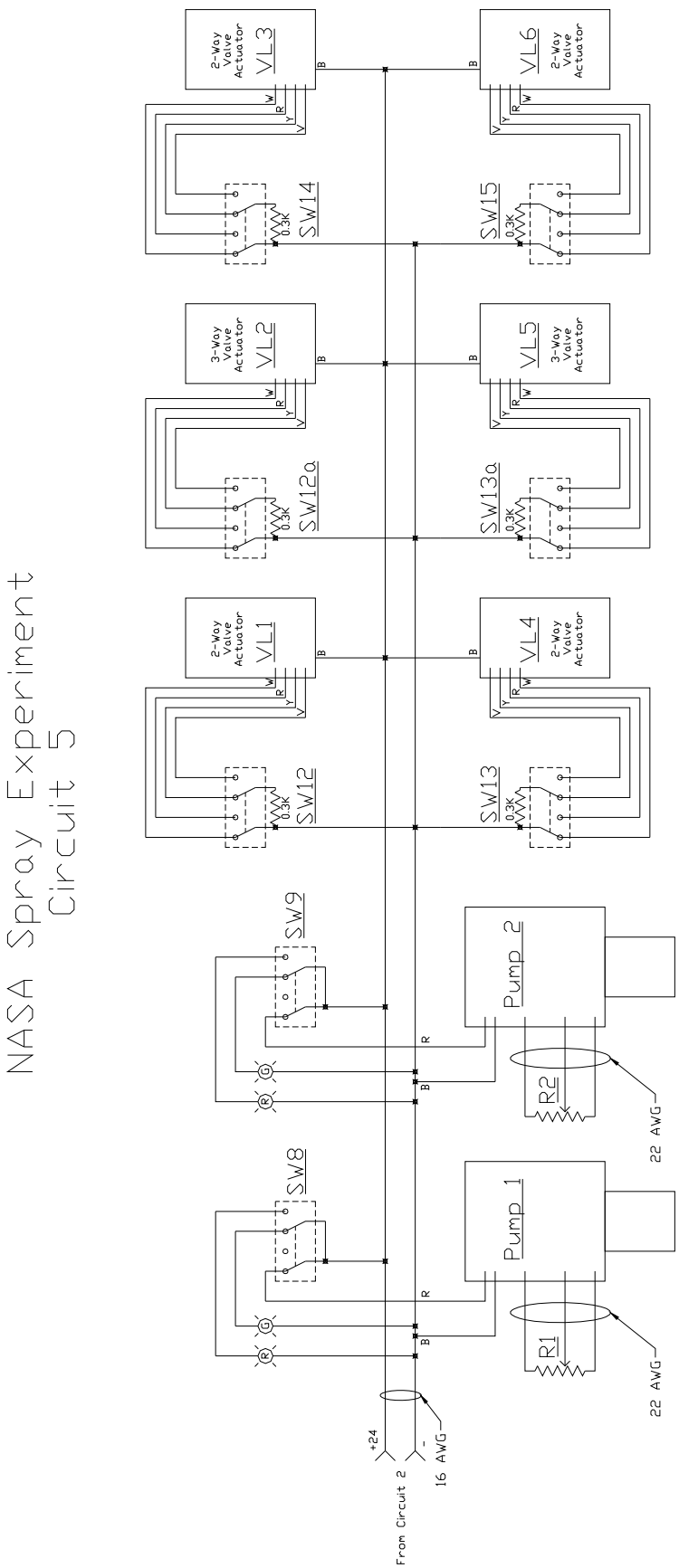
NASA Spray Experiment
Circuit 5
2-Way Valve Actuator
VL3
VL6
3-Way Valve Actuator
VL2
VL5
2-Way Valve Actuator
VL1
VL4
SW14
SW15
SW12a
SW13a
SW12
SW13
0.3K
SW9
SW8
Pump 2
Pump 1
R2
R1
22 AWG
16 AWG
+24
-
From Circuit 2
R
B
G
W
Y
V

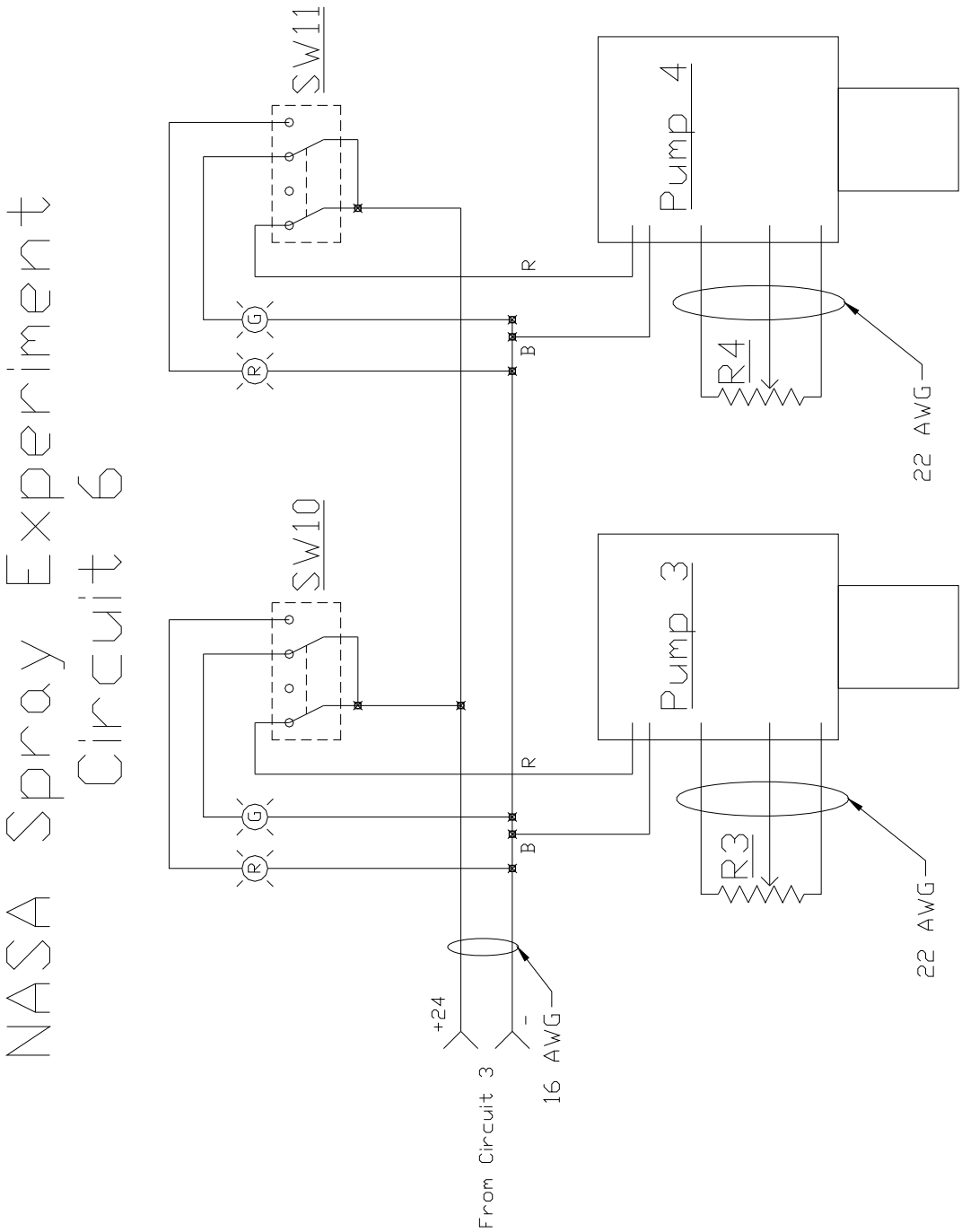
NASA Spray Experiment
Circuit 6
SW11
SW10
Pump 4
Pump 3
R4
R3
R
B
G
R
22 AWG
22 AWG
+24
-
16 AWG
From Circuit 3

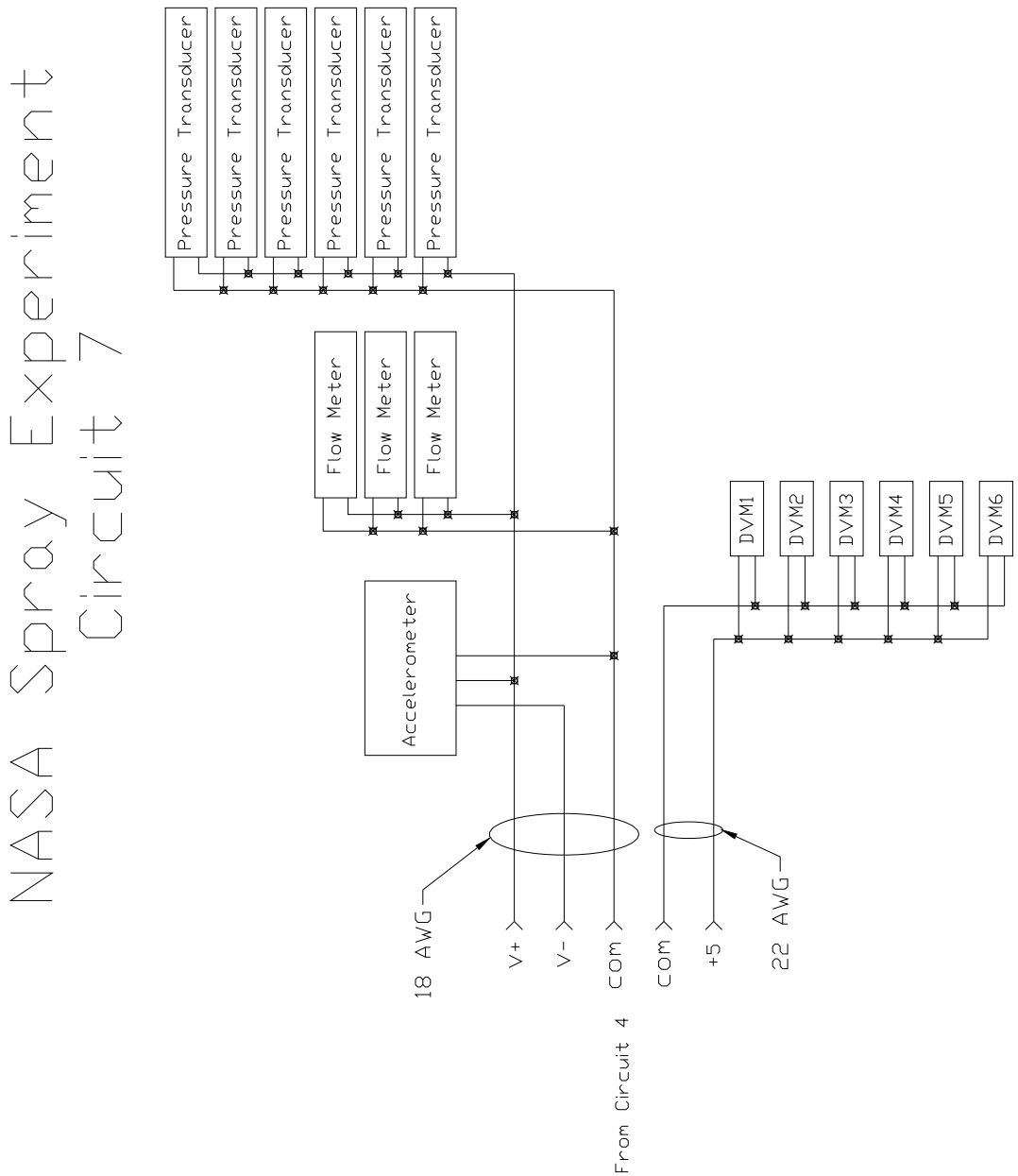
NASA Spray Experiment
Circuit 7
Pressure Transducer
Pressure Transducer
Pressure Transducer
Pressure Transducer
Pressure Transducer
Pressure Transducer
Flow Meter
Flow Meter
Flow Meter
Accelerometer
DVM1
DVM2
DVM3
DVM4
DVM5
DVM6
18 AWG
V+
V-
COM
From Circuit 4
COM
+5
22 AWG

APPENDIX G

Appendix C: Experiment Drawings and Flow Schematic

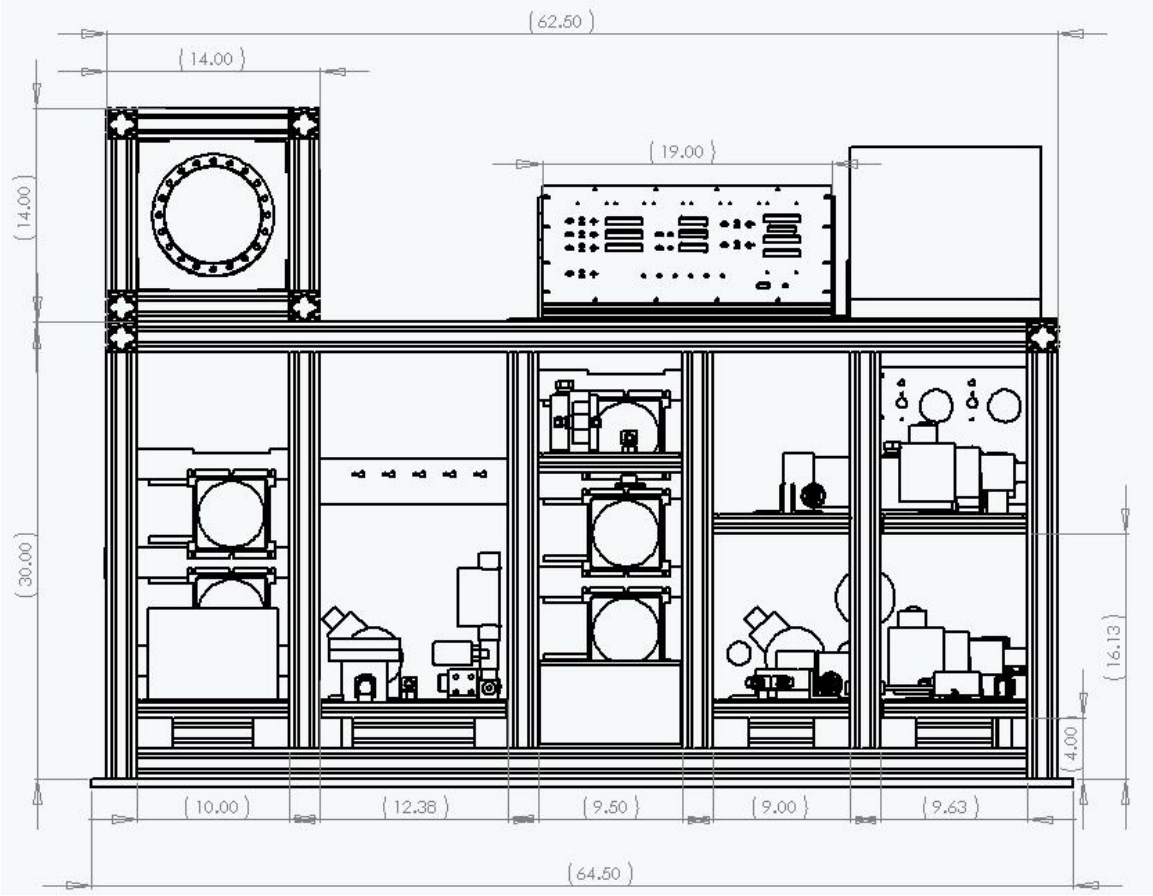

Figure C1: Side View of Rig

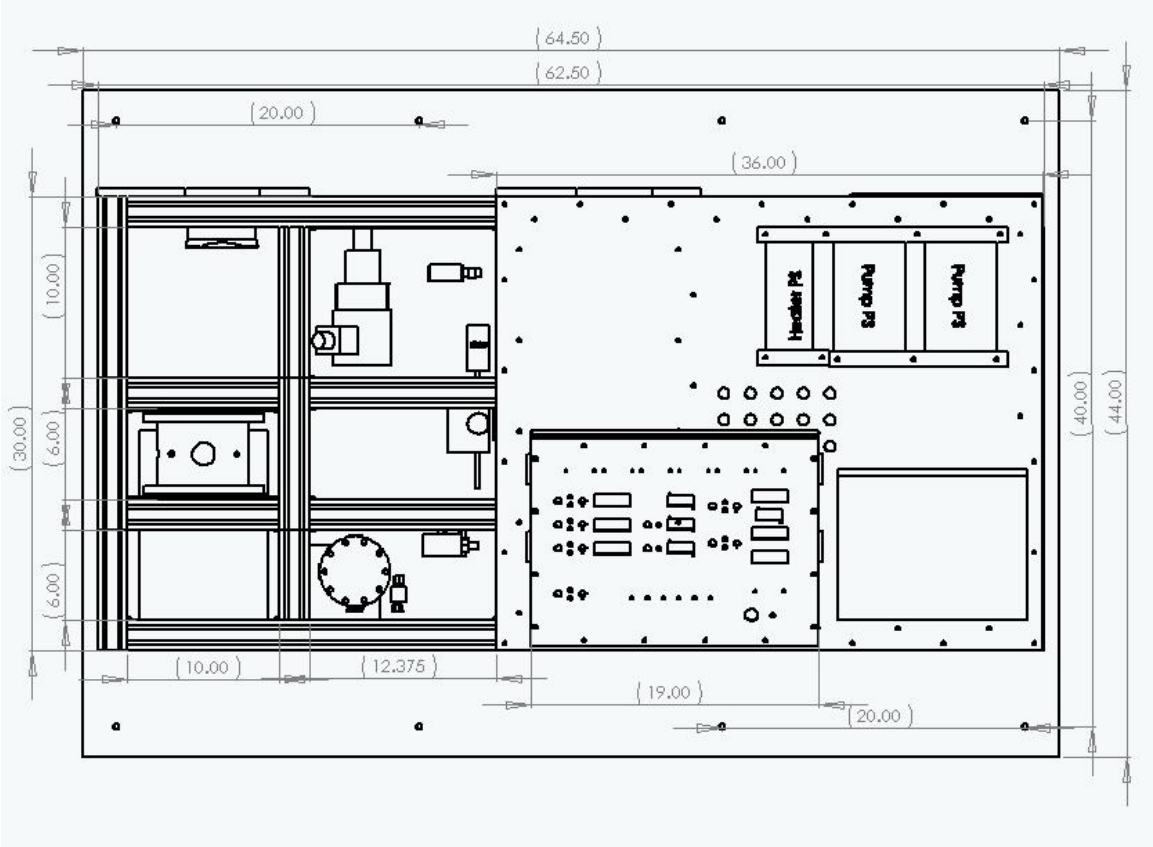

Figure C2: Top View of Rig

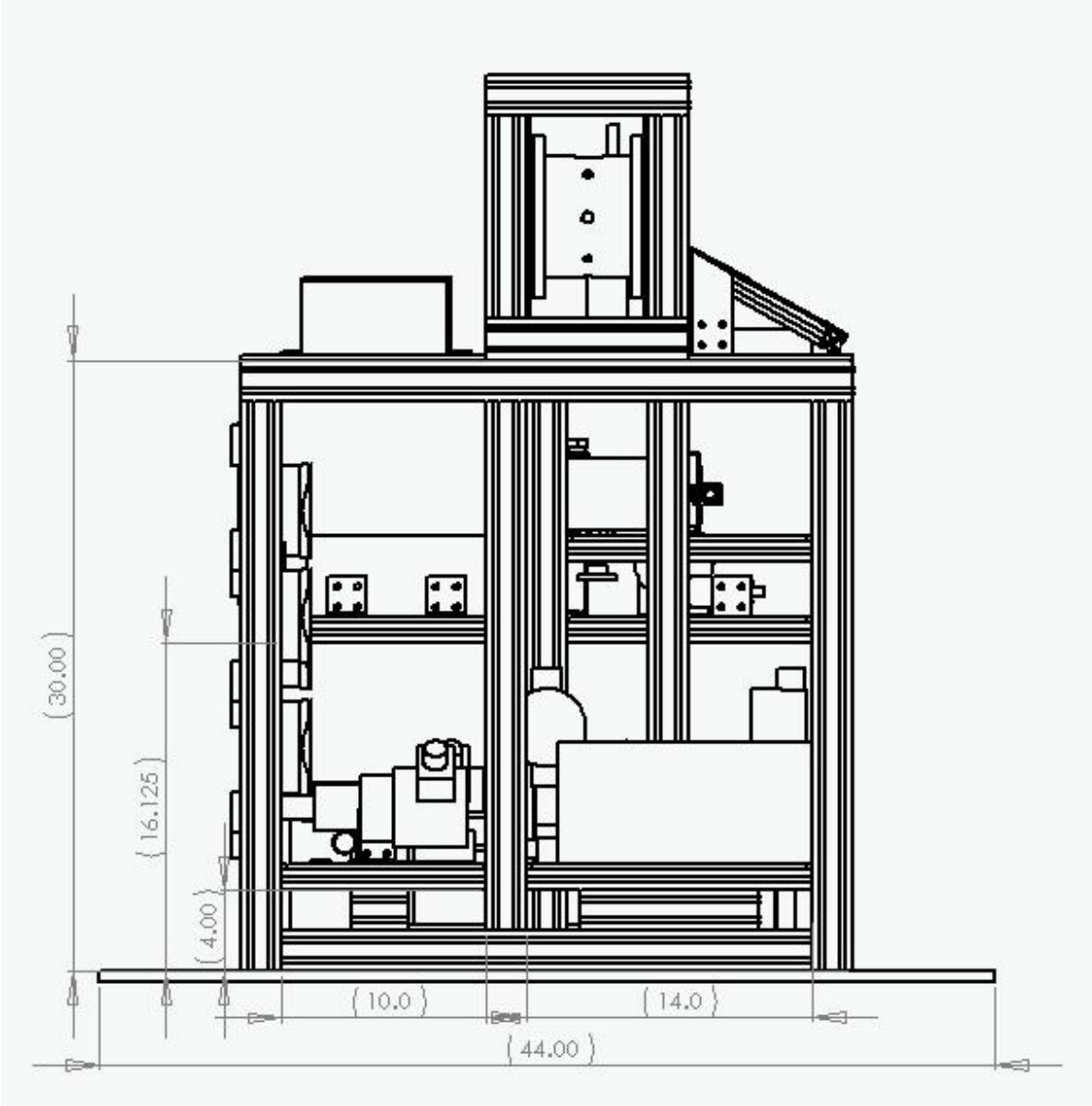

Figure C3: Rear View of Rig

Figure C4: Three-dimensional View of Rig

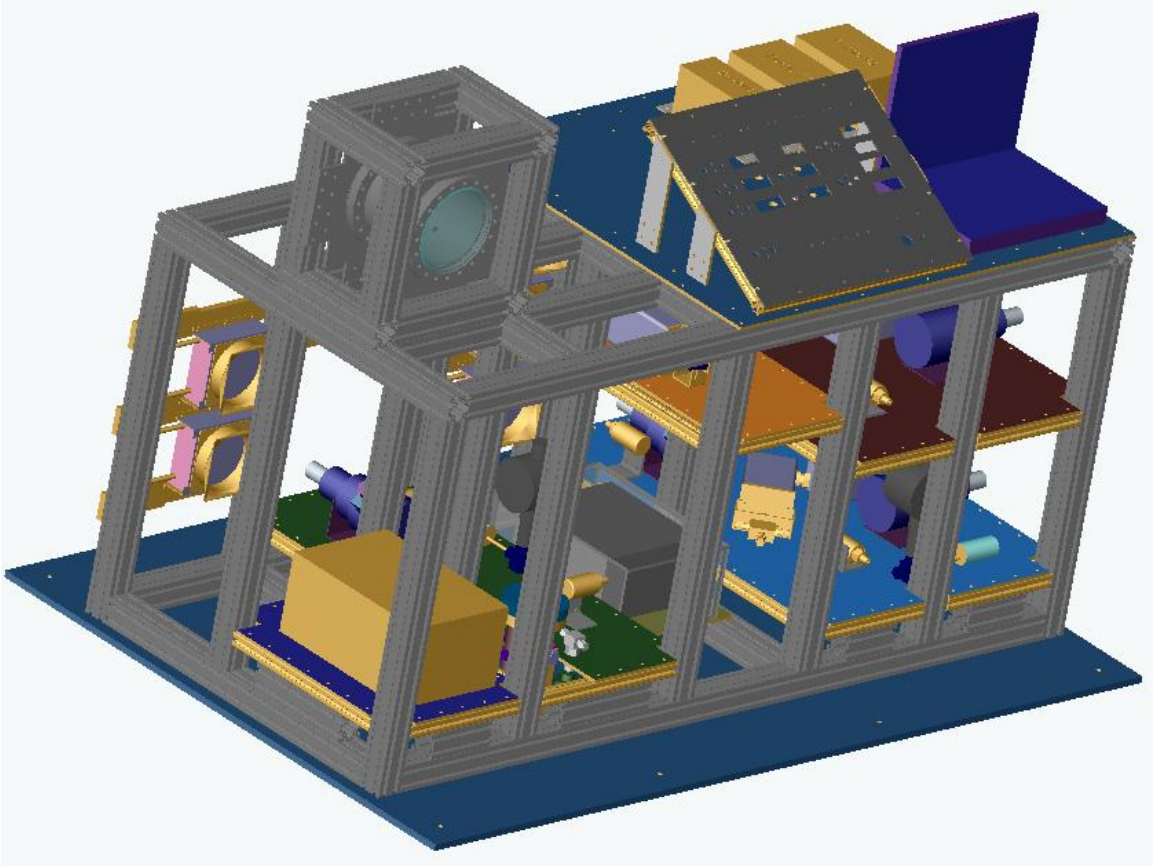

Figure C5: Three-dimensional View of Rig

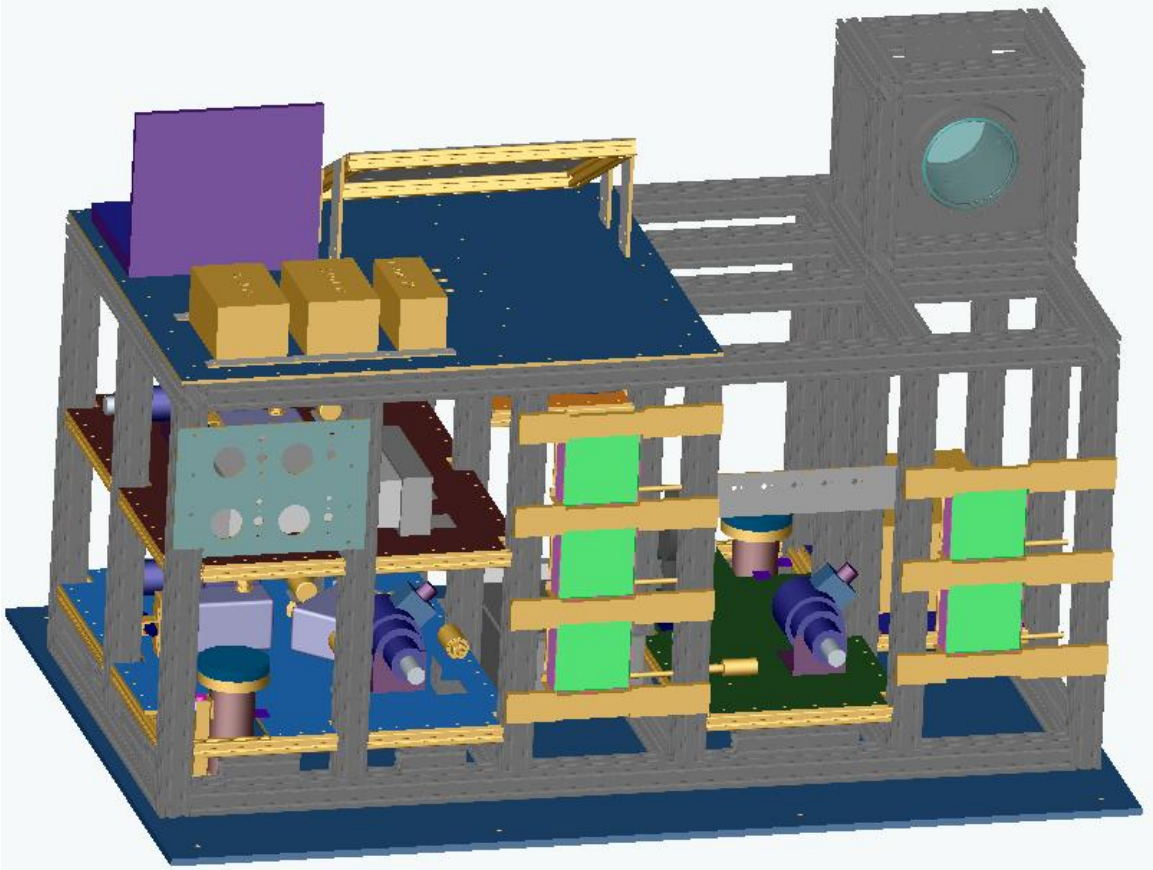

Figure C6: Three-dimensional View of Rig

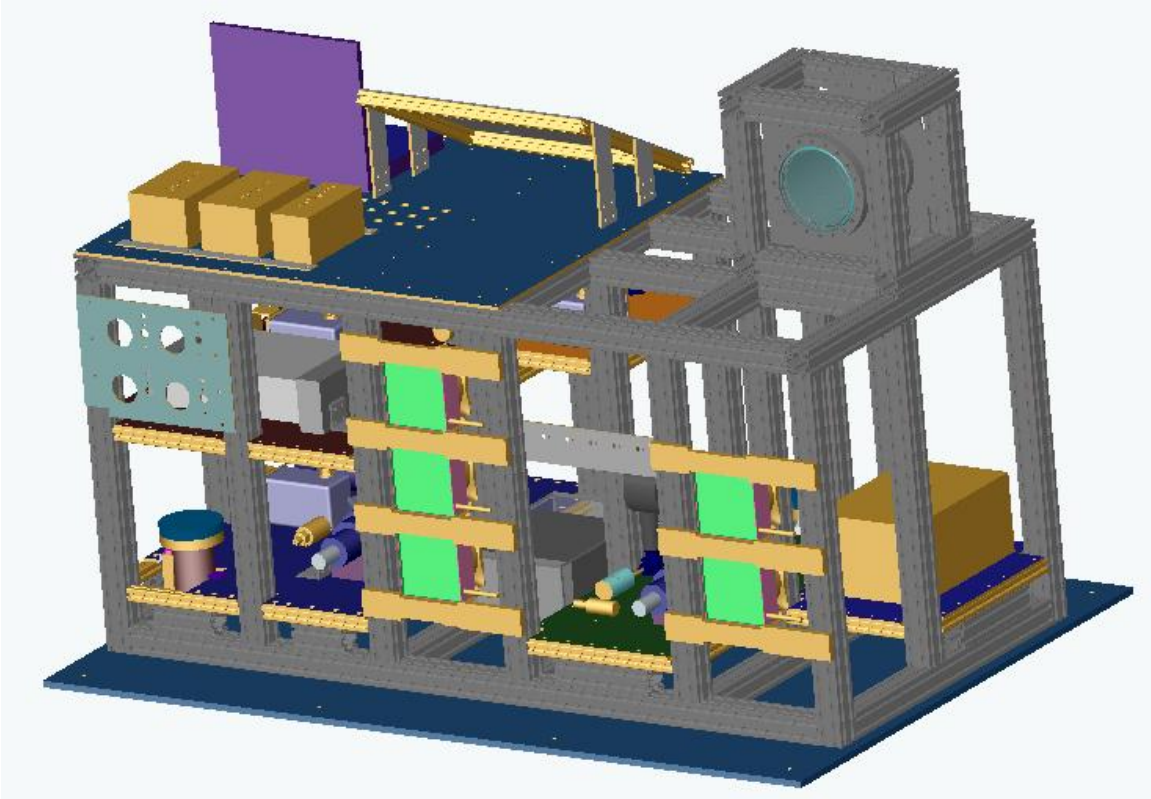

Figure C7: Three-dimensional View of Rig

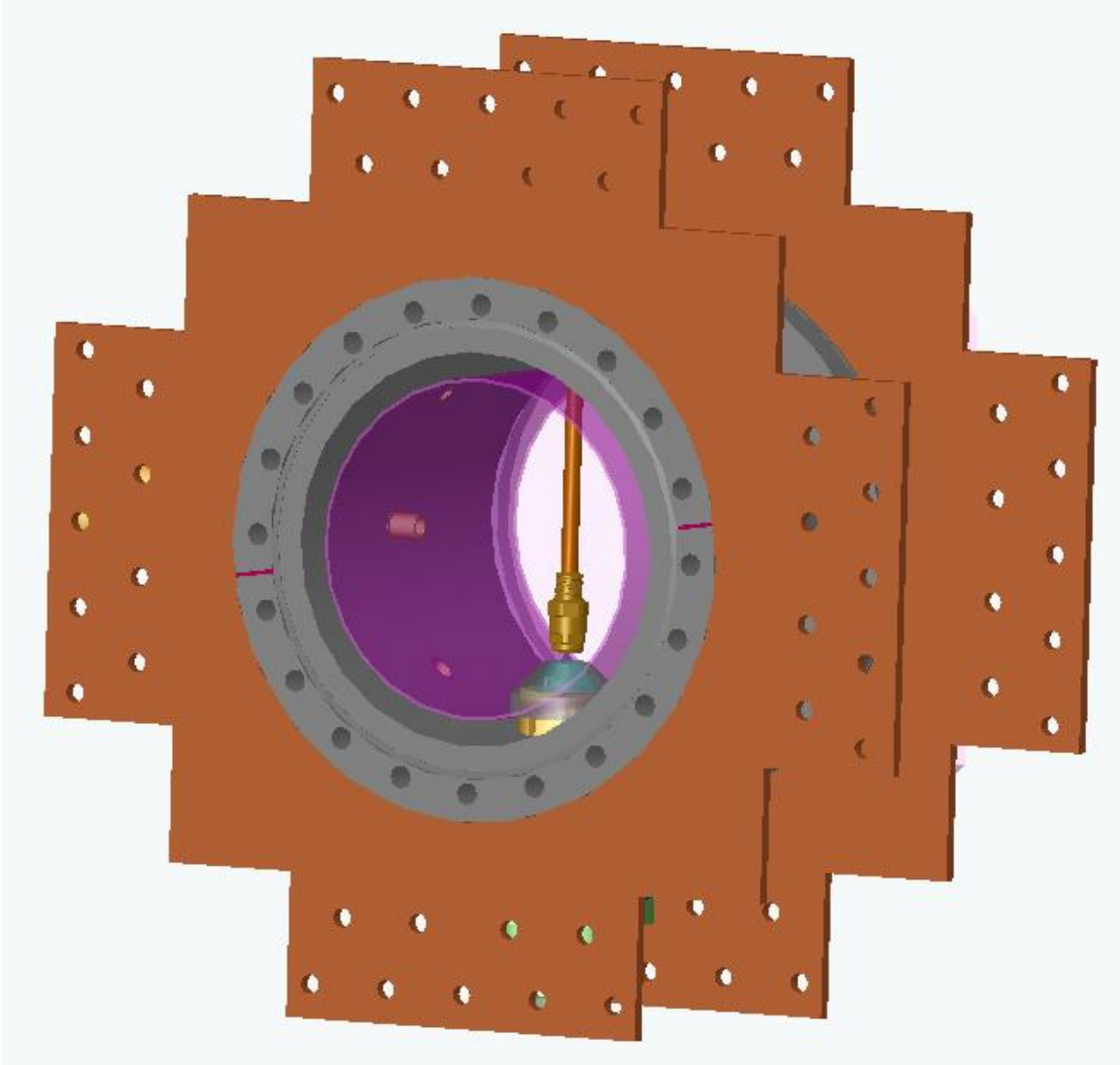

Figure C8: Three-dimensional View of Chamber with Screen

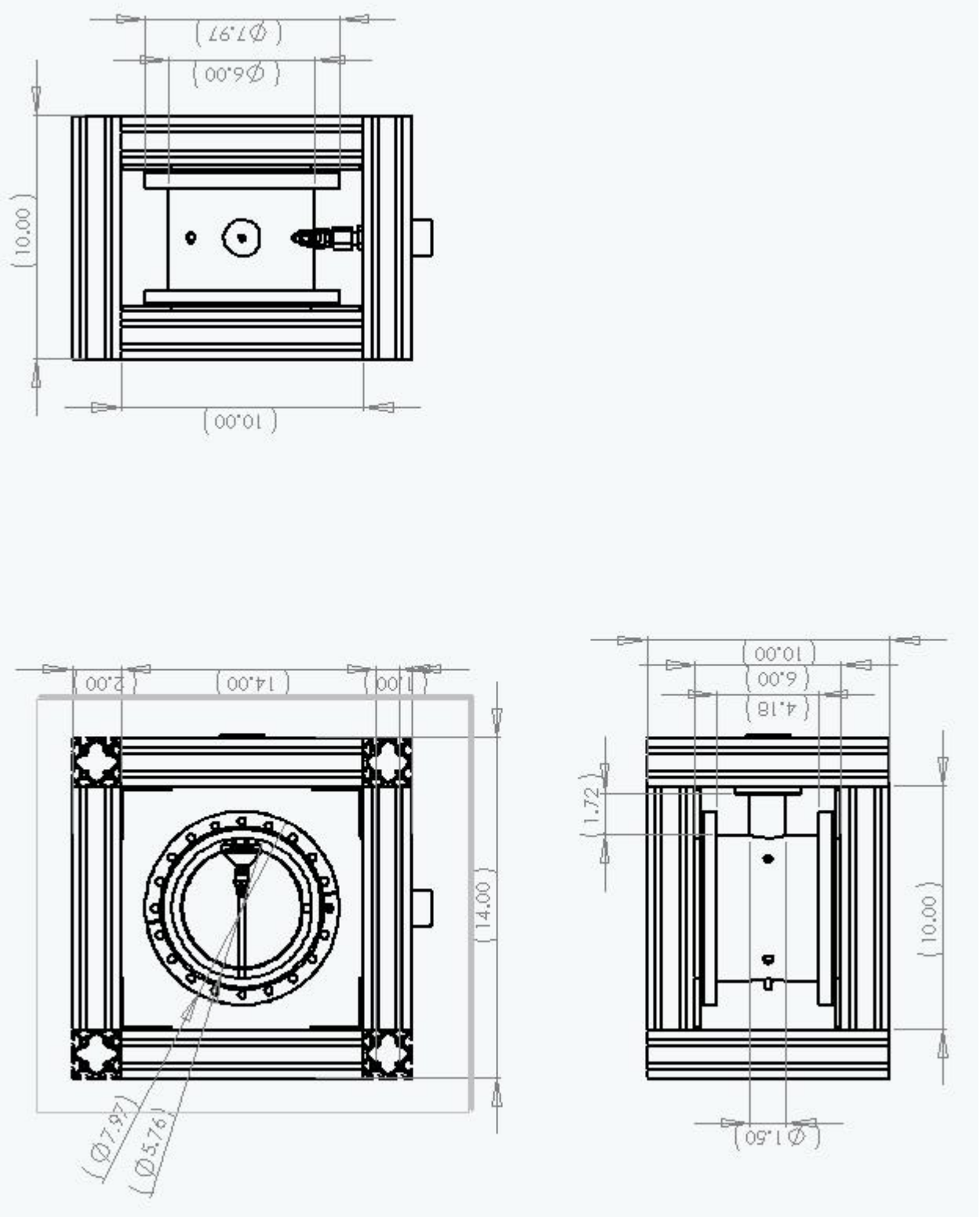

Figure C9: Test Chamber in Mounting Structure

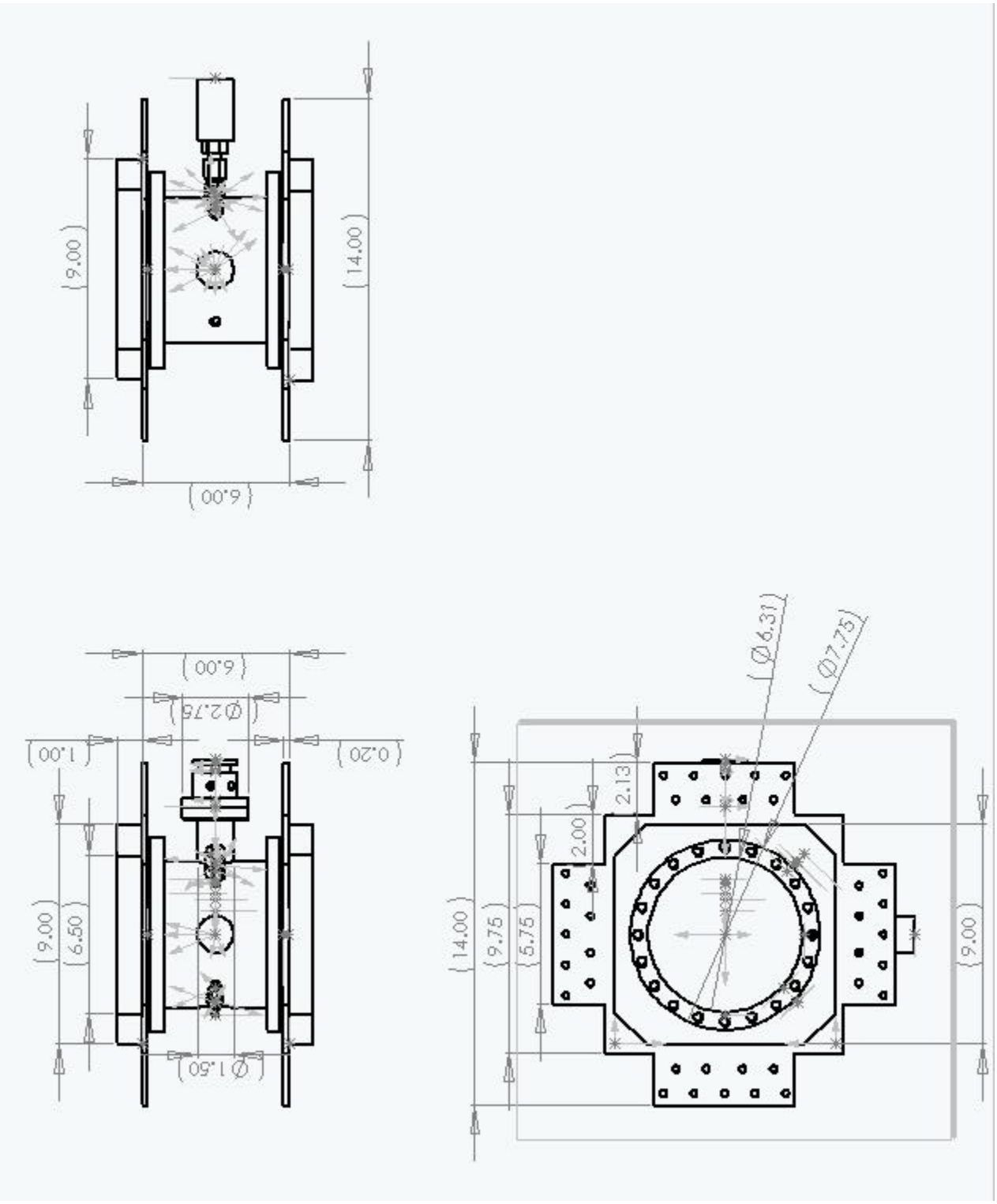

Figure C10: Test Chamber

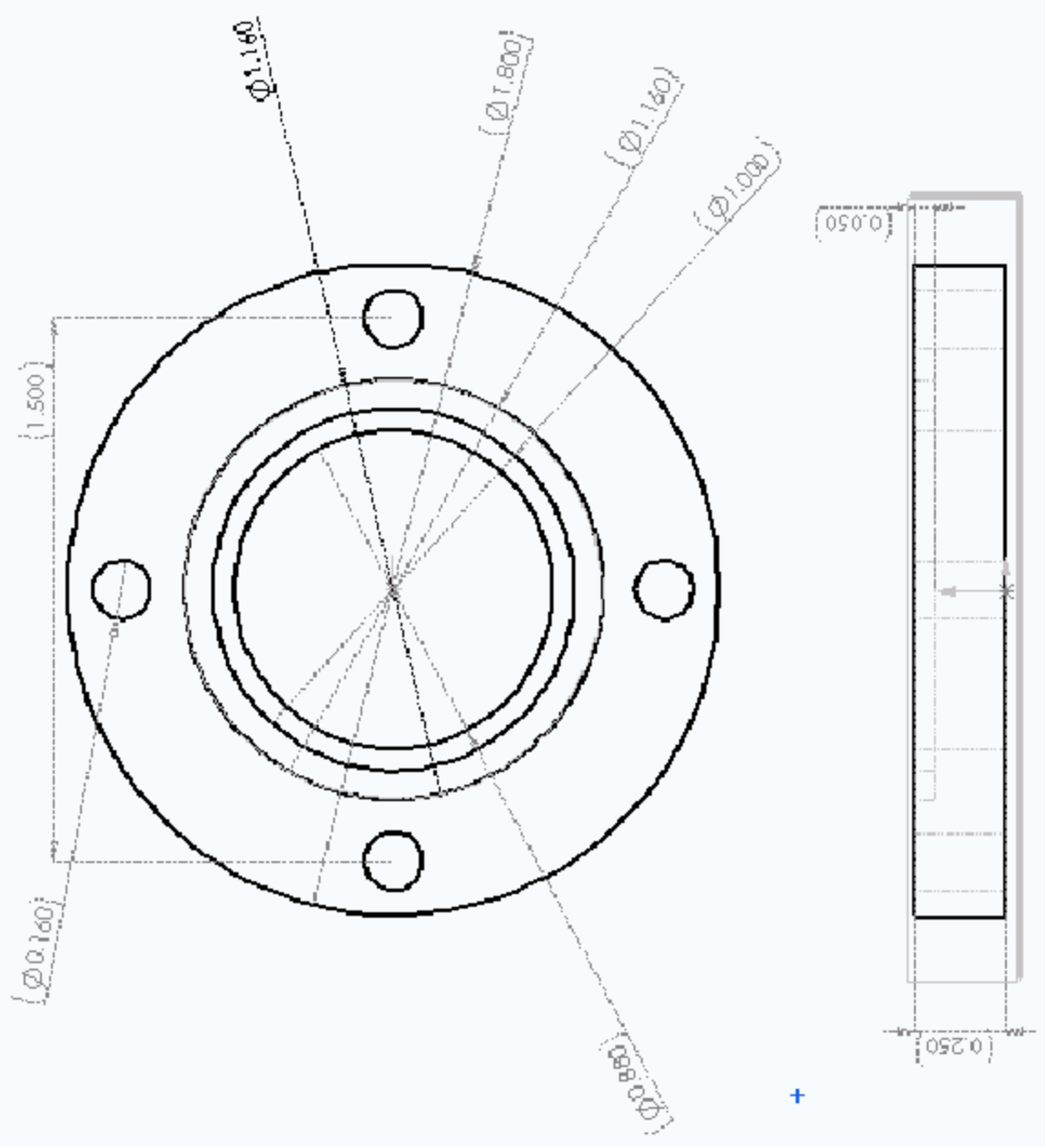

Figure C11: Sump for Test Chamber — Side View

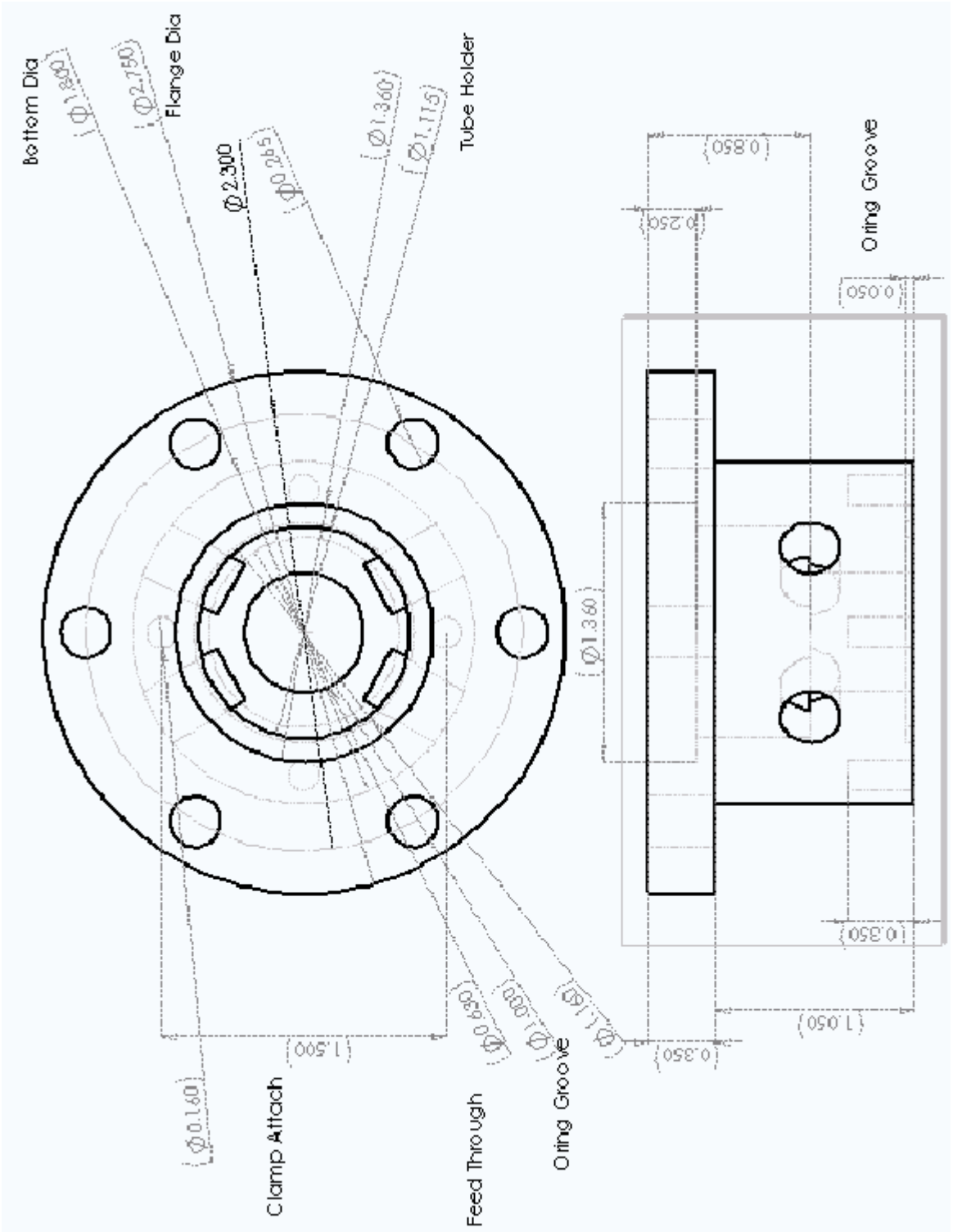

Figure C12: Sump for Test Chamber — Side View

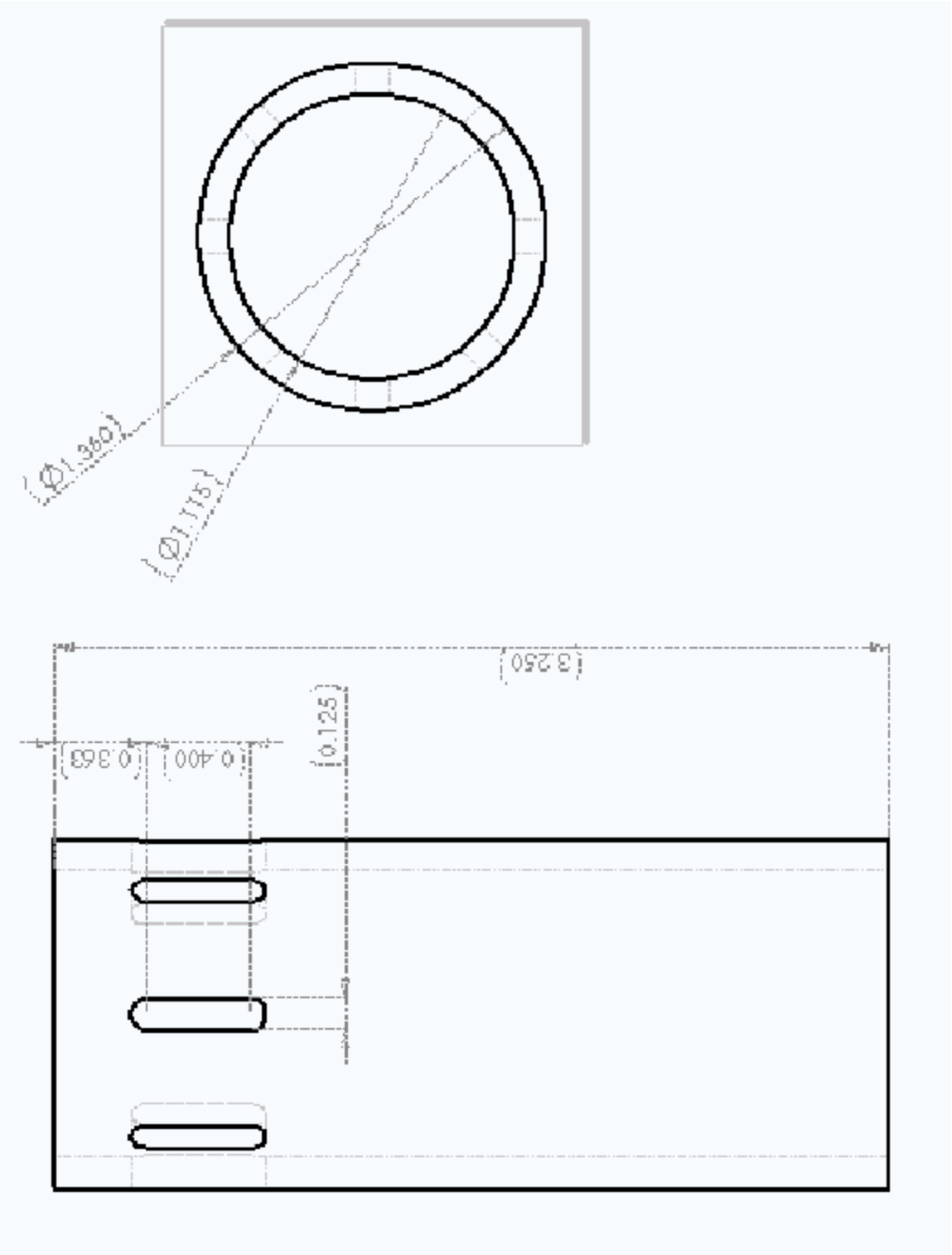

Figure C13: Sump for Test Chamber — Side View

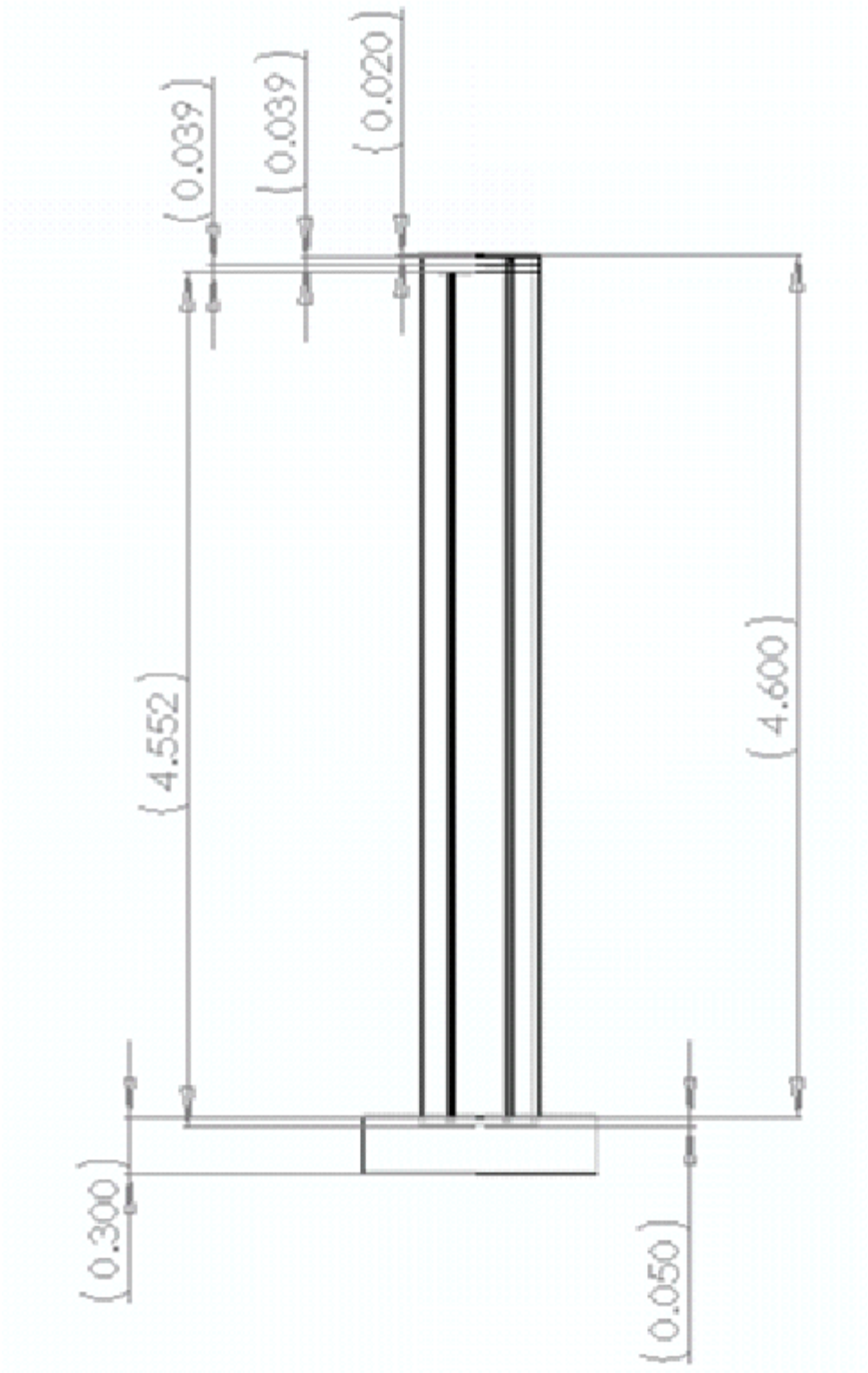

Figure C14: Pedestal for Test Chamber — Side View

Figure C15: Exploded View of Sump

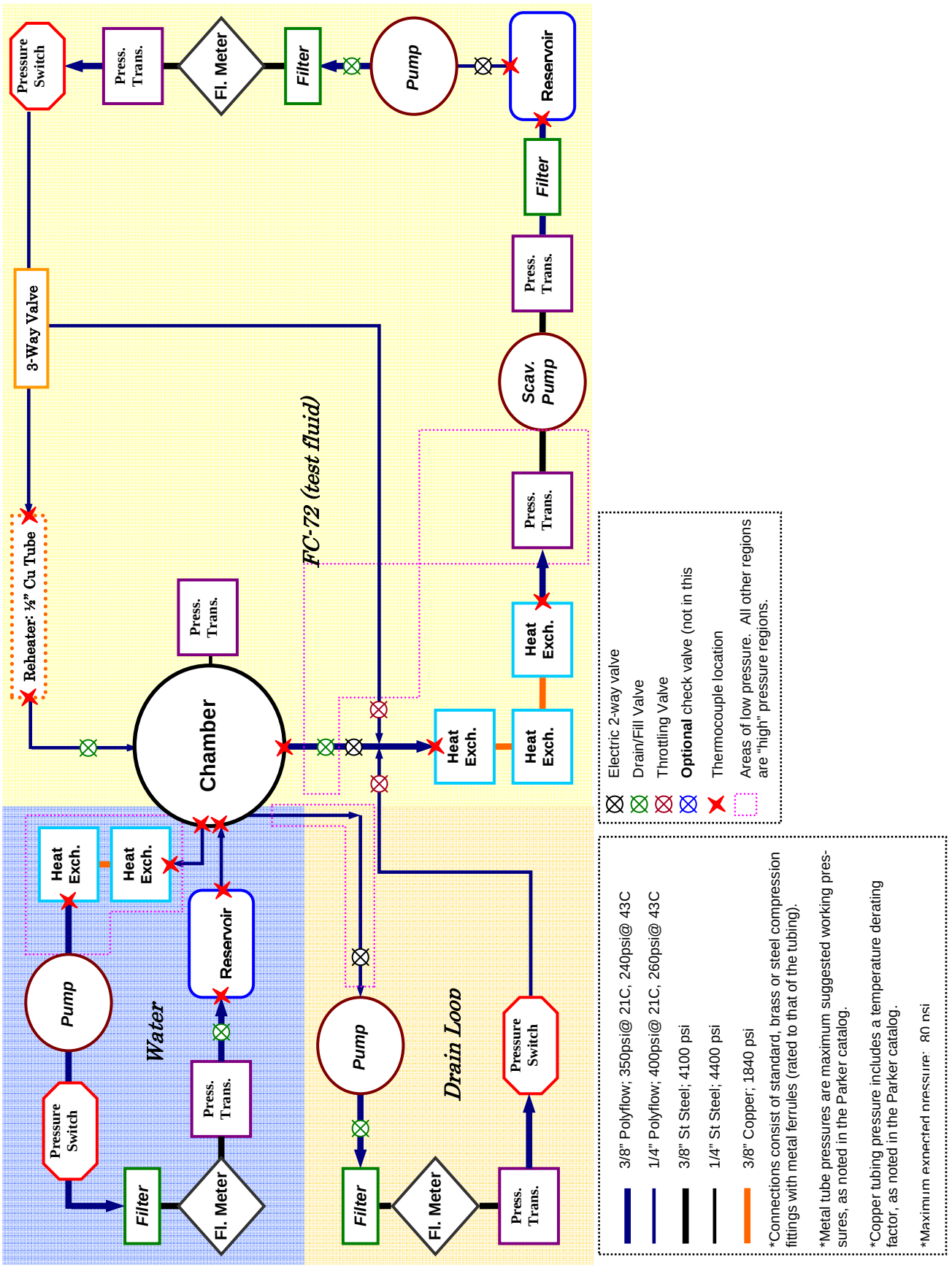

Figure C16: Flow Schematic

Appendix D: Pressure Certification

Results from the pneumatic tests will be presented at or prior to the Test Readiness Review.

The requirements and planned test pressure are in the following table:

Components	Maximum Working Pressure	Planned Pneumatic Test Pressure
Test chamber	100 psiA	132 psiG
FC-72 Nozzle inlet (high pressure side of FC-72 flow system)	100 psiA	132 psiG
Water flow components	75 psiA	111 psiG

Appendix E: Material Safety Data Sheet

APPENDIX G

Material Safety Data Sheet

Copyright, 2002, 3M Company. All rights reserved. Copying and/or downloading of this information for the purpose of properly utilizing 3M products is allowed provided that: (1) the information is copied in full with no changes unless prior written agreement is obtained from 3M, and (2) neither the copy nor the original is resold or otherwise distributed with the intention of earning a profit thereon.

SECTION 1: PRODUCT AND COMPANY IDENTIFICATION

PRODUCT NAME: FC-72 FLUORINERT Brand Electronic Liquid
MANUFACTURER: 3M
DIVISION: 3M Specialty Materials

ADDRESS: 3M Center
St. Paul, MN 55144-1000

EMERGENCY PHONE: 1-800-364-3577 or (651) 737-6501 (24 hours)

Issue Date: 09/05/2002
Supercedes Date: 01/24/2001

Document Group: 10-3789-4

Product Use:
Intended Use: For industrial use only. Not intended for use as a medical device or drug.
Specific Use: Testing Fluid or Heat Transfer Fluid for Electronics.

SECTION 2: INGREDIENTS

Ingredient	C.A.S. No.	% by Wt
PERFLUORO COMPOUNDS, (PRIMARILY COMPOUNDS WITH 6 CARBONS)	86508-42-1	100

SECTION 3: HAZARDS IDENTIFICATION

3.1 EMERGENCY OVERVIEW

Specific Physical Form: Liquid
Odor, Color, Grade: Colorless, odorless liquid.
General Physical Form: Liquid
Immediate health, physical, and environmental hazards: None known.

3.2 POTENTIAL HEALTH EFFECTS

Eye Contact:
Contact with the eyes during product use is not expected to result in significant irritation.

Skin Contact:
Contact with the skin during product use is not expected to result in significant irritation.

Inhalation:
No health effects are expected.

Ingestion:
No health effects are expected.

3.3 POTENTIAL ENVIRONMENTAL EFFECTS

This compound is completely fluorinated (perfluorinated), or it contains perfluorinated portions. Perfluoroalkyl groups resist degradation in most natural environments. This low-solubility substance has insignificant toxicity to aquatic organisms (Lowest LL50 or EL50 is >1000 mg/L). LL50 (Lethal Level) and EL50 are similar to LC50 and EC50, but tests the water phase from incompletely-miscible mixtures. Take precautions to prevent direct release of this substance to the environment.

ATMOSPHERIC FATE:
Perfluoro compounds (PFCs) are photochemically stable and expected to persist in the atmosphere for more than 1000 years. PFCs have high global warming potentials (GWP), exceeding 5000 (100-yr-ITH). The Ozone Depletion Potential (ODP) is Zero.

SECTION 4: FIRST AID MEASURES

4.1 FIRST AID PROCEDURES

The following first aid recommendations are based on an assumption that appropriate personal and industrial hygiene practices are followed.

Eye Contact: Flush eyes with large amounts of water. If signs/symptoms persist, get medical attention.

Skin Contact: Wash affected area with soap and water. If signs/symptoms develop, get medical attention.

Inhalation: If signs/symptoms develop, remove person to fresh air. If signs/symptoms develop, get medical attention.

If Swallowed: No need for first aid is anticipated.

SECTION 5: FIRE FIGHTING MEASURES

5.1 FLAMMABLE PROPERTIES

Autoignition temperature	*Not Applicable*
Flash Point	*Not Applicable*
Flammable Limits - LEL	Nonflammable
Flammable Limits - UEL	Nonflammable

5.2 EXTINGUISHING MEDIA
Material will not burn.

5.3 PROTECTION OF FIRE FIGHTERS

Special Fire Fighting Procedures: Wear full protective clothing, including helmet, self-contained, positive pressure or pressure demand breathing apparatus, bunker coat and pants, bands around arms, waist and legs, face mask, and protective covering for exposed areas of the head. Water may be used to blanket the fire. Exposure to extreme heat can give rise to thermal decomposition.

Unusual Fire and Explosion Hazards: No unusual fire or explosion hazards are anticipated. No unusual effects are anticipated during fire extinguishing operations. Avoid breathing the products and substances that may result from the thermal decomposition of the product or the other substances in the fire zone. Keep containers cool with water spray when exposed to fire to avoid rupture.

Note: See STABILITY AND REACTIVITY (SECTION 10) for hazardous combustion and thermal decomposition information.

SECTION 6: ACCIDENTAL RELEASE MEASURES

Accidental Release Measures: Observe precautions from other sections. Call 3M- HELPS line (1-800-364-3577) for more information on handling and managing the spill. Evacuate unprotected and untrained personnel from hazard area. The spill should be cleaned up by qualified personnel. Ventilate the area with fresh air. Contain spill. Working from around the edges of the spill inward, cover with bentonite, vermiculite, or commercially available inorganic absorbent material. Mix in sufficient absorbent until it appears dry. Collect as much of the spilled material as possible. Clean up residue with an appropriate organic solvent. Read and follow safety precautions on the solvent label and MSDS. Place in a metal container approved for transportation by appropriate authorities. Seal the container. Dispose of collected material as soon as possible.

In the event of a release of this material, the user should determine if the release qualifies as reportable according to local, state, and federal regulations.

SECTION 7: HANDLING AND STORAGE

7.1 HANDLING
Avoid skin contact with hot material. For industrial or professional use only. No smoking: Smoking while using this product can result in contamination of the tobacco and/or smoke and lead to the formation of the hazardous decomposition products mentioned in the Reactivity Data section of this MSDS. Store work clothes separately from other clothing, food and tobacco products. Use general dilution ventilation and/or local exhaust ventilation to control airborne exposures to below Occupational Exposure Limits. If ventilation is not adequate, use respiratory protection equipment.

7.2 STORAGE
Store away from heat. Keep container tightly closed. Keep container in well-ventilated area.

SECTION 8: EXPOSURE CONTROLS/PERSONAL PROTECTION

8.1 ENGINEERING CONTROLS
Provide appropriate local exhaust when product is heated. Provide appropriate local exhaust ventilation on open containers. For those situations where the fluid might be exposed to extreme overheating due to misuse or equipment failure, use with appropriate local exhaust ventilation sufficient to maintain levels of thermal decomposition products below their exposure guidelines.

8.2 PERSONAL PROTECTIVE EQUIPMENT (PPE)

8.2.1 Eye/Face Protection
Avoid eye contact.
The following eye protection(s) are recommended: Safety Glasses with side shields.

8.2.2 Skin Protection
Avoid skin contact with hot material. Wear appropriate gloves, such as Nomex, when handling this material to prevent thermal burns.
Avoid skin contact.
Select and use gloves and/or protective clothing to prevent skin contact based on the results of an exposure assessment. Consult with your glove and/or protective clothing manufacturer for selection of appropriate compatible materials.
Gloves made from the following material(s) are recommended: Nitrile Rubber.

8.2.3 Respiratory Protection
Under normal use conditions, airborne exposures are not expected to be significant enough to require respiratory protection. Avoid breathing of vapors, mists or spray.
Select one of the following NIOSH approved respirators based on airborne concentration of contaminants and in accordance with OSHA regulations: Half facepiece or fullface air-purifying respirator with organic vapor cartridges. Consult the current 3M Respiratory Selection Guide for additional information or call 1-800-243-4630 for 3M technical assistance. If thermal degradation products are expected, use fullface supplied air respirator.

8.2.4 Prevention of Swallowing
Do not eat, drink or smoke when using this product. Wash exposed areas thoroughly with soap and water.

8.3 EXPOSURE GUIDELINES

None Established

SECTION 9: PHYSICAL AND CHEMICAL PROPERTIES

Specific Physical Form:	Liquid
Odor, Color, Grade:	Colorless, odorless liquid.
General Physical Form:	Liquid
Autoignition temperature	*Not Applicable*
Flash Point	*Not Applicable*
Flammable Limits - LEL	Nonflammable
Flammable Limits - UEL	Nonflammable
Boiling point	50 - 60 °C
Density	1.7 g/ml
Vapor Density	Approximately 11.7 [@ 20 °C] [*Ref Std:* AIR=1]
Vapor Pressure	Approximately 232 mmHg [@ 20 °C]
Specific Gravity	Approximately 1.7 [*Ref Std:* WATER=1]
pH	*Not Applicable*
Melting point	*Not Applicable*
Solubility in Water	Nil
Evaporation rate	> 1 [*Ref Std:* BUOAC=1]
Volatile Organic Compounds	Exempt
Percent volatile	Approximately 100 %
VOC Less H2O & Exempt Solvents	Exempt
Viscosity	Approximately 0.42 centistoke [@ 20 °C]

SECTION 10: STABILITY AND REACTIVITY

Stability: Stable.

Materials and Conditions to Avoid: Finely divided active metals; Alkali and alkaline earth metals; Heat(greater than 200 °C)

Hazardous Polymerization: Hazardous polymerization will not occur.

Hazardous Decomposition or By-Products

Substance	Condition
Hydrogen Fluoride	At Elevated Temperatures - greater than 200 °C
Perfluoroisobutylene (PFIB)	At Elevated Temperatures - greater than 200 °C

Hazardous Decomposition: If the product is exposed to extreme condition of heat from misuse or equipment failure, toxic decomposition products that include hydrogen fluoride and perfluoroisobutylene can occur.

Hydrogen fluoride (CAS No. 7664-39-3) has an ACGIH Threshold Limit Value - Ceiling of 3 ppm (as fluoride), an OSHA Permissible Exposure Limit - Time Weighted Average of 3 ppm (as fluoride) and a revoked OSHA Permissible Exposure Limit - Short Term Exposure Limit (which is enforced by some State Right-To-Know programs) of 6 ppm (as fluoride). Hydrogen fluoride may cause respiratory tract irritation, dental or skeletal fluorosis and irritation or burns to the eyes or skin, particularly when dissolved in water (hydrofluoric acid). The odor threshold for HF is 0.04 ppm, providing good warning properties for exposure.

Perfluoroisobutylene(CAS No. 382-21-8) has an ACGIH Threshold Limit Value - Ceiling of 0.01 ppm. Perfluoroisobutylene may cause respiratory tract irritation, pulmonary edema, cyanosis, and effect on the hematopoietic system.

SECTION 11: TOXICOLOGICAL INFORMATION

Product-Based Toxicology Information:

A Material Toxicity Summary Sheet (MTSS) has been developed for this product. Please contact the address listed on the first page of this MSDS to obtain a copy of the MTSS for this product.

Please contact the address listed on the first page of the MSDS for Toxicological Information on this material and/or its components.

SECTION 12: ECOLOGICAL INFORMATION

ECOTOXICOLOGICAL INFORMATION

Test Organism	Test Type	Result
Fathead Minnow, Pimephales promelas	96 hours Lethal Concentration 50%	>1000 mg/l
Water flea, Daphnia magna	48 hours Effect Concentration 50%	>1500 mg/l

CHEMICAL FATE INFORMATION

Test Type	Result	Protocol
20 days Biological Oxygen Demand	Nil	
Chemical Oxygen Demand	Nil	

SECTION 13: DISPOSAL CONSIDERATIONS

Waste Disposal Method: Reclaim if feasible. As a disposal alternative, incinerate in an industrial or commercial facility in the presence of a combustible material. Combustion products will include HF. Facility must be capable of handling halogenated materials. To reclaim or return, check product label for contact.

EPA Hazardous Waste Number (RCRA): Not regulated

Since regulations vary, consult applicable regulations or authorities before disposal.

SECTION 14:TRANSPORT INFORMATION

ID Number(s):
98-0211-0216-9, 98-0211-0217-7, 98-0211-0267-2, 98-0211-1795-1, 98-0211-8068-6, 98-0212-2992-1, ZF-0002-0305-7, ZF-0002-0321-4, ZF-0002-0354-5, ZF-0002-0802-3, ZF-0002-1162-1

Please contact the emergency numbers listed on the first page of the MSDS for Transportation Information for this material.

SECTION 15: REGULATORY INFORMATION

US FEDERAL REGULATIONS

Contact 3M for more information.

311/312 Hazard Categories:
Fire Hazard - No Pressure Hazard - No Reactivity Hazard - No Immediate Hazard - No Delayed Hazard - No

STATE REGULATIONS

Contact 3M for more information.

CHEMICAL INVENTORIES

The components of this product are in compliance with the chemical notification requirements of TSCA.

All applicable chemical ingredients in this material are listed on the European Inventory of Existing Chemical Substances (EINECS),

or are exempt polymers whose monomers are listed on EINECS.

The components of this product are listed on the Canadian Domestic Substances List.

The components of this product are listed on the Australian Inventory of Chemical Substances.

The components of this product are listed on Japan's Chemical Substance Control Law List (also known as the Existing and New Chemical Substances List.)

Contact 3M for more information.

INTERNATIONAL REGULATIONS

Contact 3M for more information.

This MSDS has been prepared to meet the U.S. OSHA Hazard Communication Standard, 29 CFR 1910.1200.

SECTION 16: OTHER INFORMATION

NFPA Hazard Classification

Health: 3 **Flammability:** 0 **Reactivity:** 0 **Special Hazards:** None

National Fire Protection Association Hazard Codes are designed for use by firefighters, sheriffs, or other emergency response teams who are concerned with the hazards of materials under emergency conditions. These NFPA codes are intended to include the hazards of the products of decomposition or combustion in a fire situation.

HMIS Hazard Classification

Health: 0 **Flammability:** 0 **Reactivity:** 0 **Protection:** X - See PPE section.

Hazardous Material Identification System (HMIS(r)) hazard ratings are designed to inform employees of chemical hazards in the workplace. These ratings are based on the inherent properties of the material under expected conditions of normal use and are not intended for use in emergency situations. HMIS(r) ratings are to be used with a fully implemented HMIS(r) program. HMIS(r) is a registered mark of the National Paint and Coatings Association (NPCA).

No revision information is available.

DISCLAIMER: The information in this Material Safety Data Sheet (MSDS) is believed to be correct as of the date issued. 3M MAKES NO WARRANTIES, EXPRESSED OR IMPLIED, INCLUDING, BUT NOT LIMITED TO, ANY IMPLIED WARRANTY OF MERCHANTABILITY OR FITNESS FOR A PARTICULAR PURPOSE OR COURSE OF PERFORMANCE OR USAGE OF TRADE. User is responsible for determining whether the 3M product is fit for a particular purpose and suitable for user's method of use or application. Given the variety of factors that can affect the use and application of a 3M product, some of which are uniquely within the user's knowledge and control, it is essential that the user evaluate the 3M product to determine whether it is fit for a particular purpose and suitable for user's method of use or application.

3M provides information in electronic form as a service to its customers. Due to the remote possibility that electronic transfer may have resulted in errors, omissions or alterations in this information, 3M makes no representations as to its completeness or accuracy. In addition, information obtained from a database may not be as current as the information in the MSDS available directly from 3M.

APPENDIX G

3M MSDSs are available at www.3M.com

APPENDIX H

AC LOSS AND PINNING IN YBCO AND COATED CONDUCTORS

A DRAFT FINAL REPORT

M.D. SUMPTION

Dec 10, 2004

Table Of Contents

1. **Executive Summary**
2. **Measurements of AC Losses in Coated Conductors, Striped and Otherwise**
3. ***N*-factor Studies**
4. **Conductor Design Studies**
5. **Pinning Studies**
6. **Weak Link Studies**
7. **Other Consultation**
8. **Future Challenges**
9. **Presentation, Papers, and Patents at least partially supported by Summer Faculty Effort**

Appendix A: Completed and/or accepted papers

Appendix B: Slides from Presentations

Appendix C: Anti-Cryostat Design

EXECUTIVE SUMMARY

First Segment of the Work

There were two main areas investigated during the first month period: AC Losses in coated conductors and weak link current sharing in coated conductors. During these investigations several papers have been submitted for publication, and also measurements have been performed in preparation for a third publication.

In the area of weak-link conductors, the development of proper geometries for filamentary bridges was considered. It was found that the proper value of critical current for the transverse (filament-to-filament) connections was about 10,000 times smaller than that of the longitudinal direction current. Expressions for the loss of such conductors were developed, and the level of current sharing in such conductors evaluated. A paper based on these studies, "**Low loss striated YBCO coated conductor with interfilamentary current sharing"** was submitted to the Journal of Applied Physics and is under review.

The second topic was the investigation of AC losses in coated conductors. Several samples provided were measured for AC losses at frequencies up to 200 Hz with field amplitudes of up to 140 mT. Hysteretic and eddy current losses were then distinguished by plotting *Q/B* vs *B*f*. A surprising level of eddy currents was observed in the samples, likely indicating only partial laser cutting or perhaps metallic re-deposition. Presently analysis is underway to determine if this have beneficial as well as detrimental effects.

Second Segment of the Work

There were two main areas investigated during the second month period: AC Losses in coated conductors and coated conductor design for incorporation of twisting.

The first area of concentration (AC losses for coated conductors) was a continuation for the first period. Samples with 20 and 40 stripes were measured for AC losses. Hysteretic and eddy current losses were then distinguished by plotting *Q/B* vs *B*f*. Eddy current losses were seen to be much more significant in the 40 stripe sample. The 40 stripe conductor has eddy current losses consistent with interfilament resistivities of several hundreds of micro-ohm cms, the 20 stripe sample had interfilament resistivities much larger.

The second topic was coated conductor design for the incorporation of twisting and J_e improvement. The superconducting fraction, λ, was given for a "simple twisting" structure, as well as an estimate of the minimal possible twist pitch, L_p. This was then compared to three other possibilities, a stacked conductor geometry (which had better λ but similar constraints on L_p) an octagonal conductor (which had much less restriction on L_p and moderately better λ) and a Rutherford type geometry (which had similar L_p and λ characteristics to that of the octagonal conductor). In order to make these comparisons the strain for each geometry was addressed. Of these three architectures, the Rutherford style conductor was suggested to be the best overall compromise between properties (λ and L_p) and manufacturability.

Third Portion of the Work

The work in the third month period involved: VSM measurements of weak-link structures, losses in YBCO coated conductors; estimates for various frequencies and *N*-factor effects, a prototype loss machine analysis, and a stator design and conductor utilization scheme. VSM measurements were made on samples made with specifically induced weak links at 4, 20, 40, 60, 70, and 77 K. The geometry ratio of the samples was used to estimate the weak link strength. *N*-factor effect studies were continued, with SEM analysis used to properly determine and confirm the thickness of filamentarized samples, as part of a study of *N*-factor vs loss for striped samples. The *N*-factor for samples with filaments at low H_m levels was studies, and the results confirm the applicability of *N*-factors (loss reduction factors) for moderately thin filaments. Theoretical estimates have also been made connecting these estimates to those as the samples thickness grows, in order to determine how much loss reduction would be realized in real machines where demagnetization is present. It was found that *N*-factors grow uniformly as thickness grows, thus leading to the conclusion that the thin-strip *N*-factor is a lower limit on loss reduction. Two papers have been prepared on this subject, and will be submitted to the Journal of Applied Physics and Applied Physics Letters (one to each). One paper (partially funded by this program) was accepted for publication in Superconducting Science and Technology, entitled, “AC Loss in Striped (Filamentary) YBCO Coated Conductors Leading to Designs for High Frequencies and Field-Sweep Amplitudes”. A short analysis was performed for a prototype loss machine for a conceptual high frequency, high field large sample coil device. Estimates of limiting parameters were made. Finally a stator concept was outlined for use in combination with YBCO conductor.

Extended Segment

There were three main areas investigated during this period: AC Losses in coated conductors, YBCO thin film measurements aimed at determining ultimate pinning levels, and stator conductor geometry configurations.

The first area of concentration (AC losses for coated conductors) was a continuation for the earlier periods. A series of special geometry samples were measured for loss -- Samples S1-S6. These samples had various weak link patterns etched into them. Losses were measured after various methods of noise reduction were applied to an existing system. 50 data points apiece were taken at 50, 75, 100, 150, and 200 Hz magnetic field frequencies, while the amplitudes ranged from 0 to 140 mT. Loss values were taken, and the influence of various link frequencies observed. Hysteretic and eddy current losses were then distinguished by plotting *Q/B* vs *B*f*.

The second topic was pinning determination in YBCO thin films at very low field amplitudes at a variety of temperatures. Data taken in this way allow the ultimate (depairing) current density to be measured. These values were determined for a set of films, where the measurement temperatures ranged from 4 K to 77 K.

The third area of work was in stator conductor geometry consideration. In this area, the kind of winding geometries needed to limit AC loss development in these type windings was considered, and the effects of coupling to internal fields and external fields was

distinguished. Several possible stator configurations were described, and limiting values of loss components estimated under simplifying assumptions.

Because many of these studies were ongoing throughout the summer period, they are assembled by theme, rather than time, in the detailed report below.

2.0 Measurements of AC Losses in Coated Conductors, Striped and Otherwise

Striped samples were measured for AC loss characteristics. The samples had various patterns, detailed elsewhere. The basic configurations are given in Table 2.1. Here S1 and S2 have 20 and 40 stripes, respectively. S3-S6 have stripes, but also various forms of weak-linkage.

Table 2.1. Sample Parameters

Sample	Description
Unstriped	Unstriped
S1	20 stripes
S2	40 stripes
S3	40 stripes, fish net
S4	40 stripes, brick wall
S5	10 stripes, zipper
S6	20 stripes, well conn

We present the loss data for S2-S5 in Figures 2.1 and 2.2.

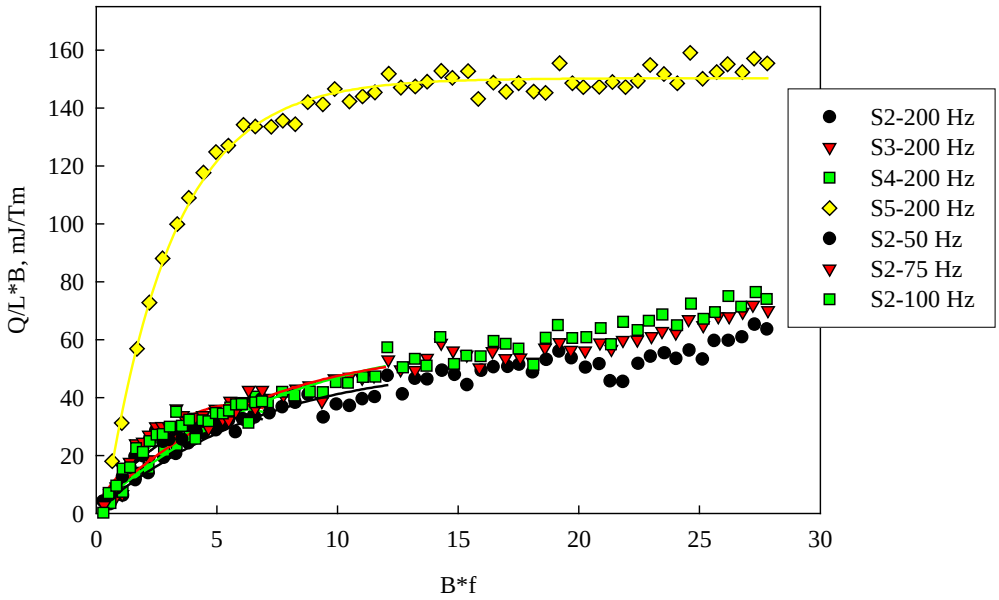

Figure 2.1. Loss data for S2-S5.

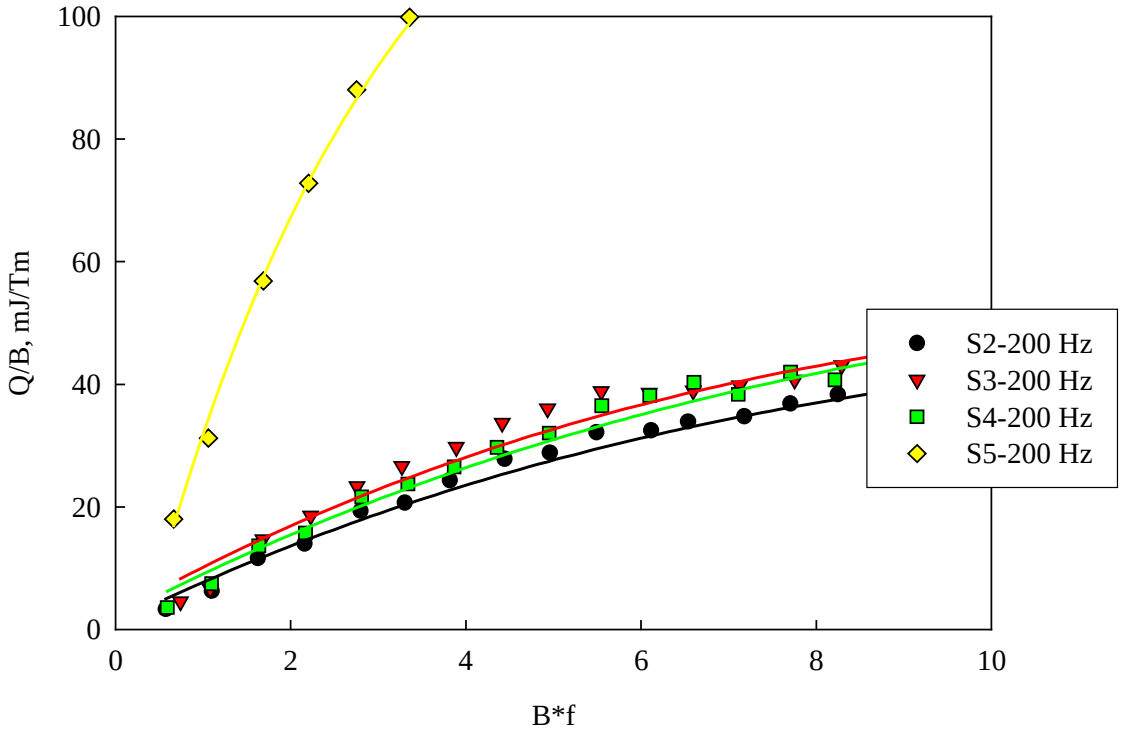

Figure 2.2 Close-up View of loss data for S2-S5.

Immediately obvious is the much larger loss for S5, as might be expected since the filaments are 4 times larger. Indeed, the ratio of losses seems to be about four. Samples S2-S4 are not very different. This may either be because the various linkages are not very different from one another, or it may be because the sample length was insufficient to bring out the differences. Note that we have plotted these graphs after the style of Levin [1], where we have divided the loss by B as well as length. From his analysis we expect that

$$\frac{Q}{LB} = wI_c + Const * B * f \tag{2.1}$$

I_c for these samples is expected to be 120 A. This results in a loss consistent with 0.2 mm. The expected value would be 0.25 mm (based on 40 stripes in a 1 cm wide tape). This difference is most likely do to errors in the value of I_c, either because it is estimated, or because of the reduction associated with the filament area reduction during striping. We can estimate that S5 has a per cycle loss of between 140 mJ/Tm, and that the other samples S2-S4, have an intercept of roughly 25 mJ/Tm. S5, on the other hand, would be consistent with 0.11 cm. This result, however, is influenced by the slope of the intercept line, and if we use only the lower frequencies to extrapolate, may be closer to 0.1 cm.

There may be some slope reduction in this higher loss/higher frequency range because of large amounts of local heat generation. The constant above is given by

$$C = \frac{1}{4\rho_{eff}} L_p^2 wt \tag{2.2}$$

This slope is seen to be about 1.7 mJ/T^{2}mHz for S2-S4. Since we must replace L_p with $2L$, and, assuming that w = 1 cm and t = 25 μm, we would get roughly 25 μΩcm for the resistivity – somewhat over an order of magnitude higher than Cu at room temperature. Of course, this is an "effective" resistivity, and is connected to the real resistivity by the exact geometry of the connecting links. From earlier analysis of G. Levin, this non-infinite resistivity is associated with re-solidification of the metallic materials ablated off in the filamentarization process [2].

REFERENCES

[1] G. Levin, submitted to Phys. Rev. 2004.
[2] G. Levin, private communication, 2004.

3.0 *N*-factor Studies

A series of thin film samples generated at AFRL had been previously measured for VSM based loss in order to see the effects of filamentation. In the process, the application of the Brandt equations was considered for these samples. Further studies on this were performed this year, with the appropriate expressions actually fitted to the Brandt expressions, with no adjustable parameters. Below is an outline of the Brandt equations.

Hysteretic Losses for Simple Slabs and Films

The AC losses of a coated conductor are given by

$$Q = \mu_0 d J_c H_m \tag{3.1}$$

where Q is the loss per cycle per unit volume, μ_0 is the permeability of free space, d is the width of the conductor perpendicular to the applied field, J_c is the critical current, and H_m is the amplitude of the applied field sweep. The field profile is sinusoidal, and the units are SI. This expression is applicable as long as $H_m \gg H_p$, the penetration field. We note that this is essentially the same as the result for a slab with the field aligned parallel, and having a width w perpendicular to the field, because demagnetization effects are negligible. As long as we are well above penetration, we would then expect

FO
$$Q = \mu_0 w J_c H_m \tag{3.2}$$

Or

EO
$$Q = \mu_0 t J_c H_m \tag{3.3}$$

for face-on (FO) and edge-on (EO) conditions, where w is the conductor width and t is the thickness of the YBCO layer. The calculations given above are valid when we are well above full penetration. However, we should note that in the FO orientation the field is determined not by the width perpendicular to the field (as would be the case for the slab parallel to the field) but by [8]

$$H_p = J_c \left[\frac{t}{\pi}\right]\left(\ln\frac{w}{t} + 1\right) \tag{3.4}$$

Here t again is the controlling dimension for H_p. The main import of this is that the system acts relatively similar to a slab at much lower fields that might otherwise be expected. We would estimate a penetration field of 40 mT. However, if the YBCO layer thickness increased, or 20-30 K operation was chosen, this value would probably move into the 100-200 mT range.

For H_m values similar to the penetration field the loss expressions are modified, leading to a prefactor in (1) at lower H_m values, and eventually of course to more complicated expressions, which can be found in Carr in approximate form [8], or Brandt and Muller in fuller form [9][10]. In particular, the prefactor is given by [10]

$$N = \left(\frac{H_m}{H_d}\right) g\left(\frac{H_m}{H_d}\right) \tag{3.5}$$

Here H_{c1} is assumed to be zero, $g(H_m/H_p)$ is given by

$$g\left(\frac{H_m}{H_d}\right) = \frac{H_d}{H_m}\left[\frac{2H_d}{H_m} Ln\left(\cosh\frac{H_m}{H_d}\right) - \tanh\frac{H_m}{H_d}\right] \tag{3.6}$$

and H_d is defined as $0.4J_c t$ (in this particular case about an order of magnitude smaller than H_p). The beneficial impact that this can have on losses has been implicit in recent investigations. In the low H_m limit, $N \rightarrow 0$ as ${H_m}^3$, leading to a $Q_h \propto {H_m}^4$ (as compared to the ${H_m}^3$ of the usual situation). In the high-H_m limit, $N \rightarrow 1$, leading to a recovery of (3.1). Our practical region of interest is not the very high and very low extremes but rather the H_m/H_d range between about 2 and 10. For use in this regime we combine (3.5) and (3.6) into the following approximation for N

$$N\left(\frac{H_m}{H_d}\right) = \left[1 - \frac{2Ln2}{\left(H_m / H_d\right)}\right] \tag{3.7}$$

The take home message here is that filamentation reduces loss, as does reducing the amplitude of the applied field. We can then ask the question, if the applied field amplitude is lower than full penetration, do we still get all of the loss reduction that we expect from filamentation. The above calculations say that we do. The loss is still proportional to d, just with a pre-factor which reflects the lower overall loss because we are below penetration.

We can now test this expression by making a set of samples with fine filaments, and a high aspect ratio, with field amplitudes below the penetration field. Table 3.1 gives these samples. These samples were then measured in a VSM at 4 K for various applied Hm values, and the results are shown in Figure 3.1. Here we can see that the loss is linear with d_f as expected. If we now take the slope (which is related to N) and plot in vs H_m, we should be able to match it to the N expected from Equation 3.7. We do need to know the value of H_d, we can find from measuring the penetration field for these samples. Of course, since magnetic J_c is changing considerably in this region, I must estimate the H_d value at lower fields based on the value of J_c at H_p and the variation of M-H loop height between H_p and 0. Using a linear variation, I obtain an H_d of 500 mT at zero and 250 mT at H_p. These values, and no other assumptions give the fit of Figure 3.2.

Figure 3.3 goes on to calculate the loss reductions that could be seen if the film thickness were further increased. The value of N can be seen at the multiplier for the resulting loss, thus a value of $N = 0.5$ means that the loss would be cut in half.

Table 3.1 PLD samples with various filament sizes cut into them.

Sample Tracer	Sample	N_f	d_f, μm	d_{IF}, μm	Film L x w, cm^2	Film thickness, μm	Vol, 10^{-6} cm^3
TJ216	A	18	82	67.1	0.322 x 1.20	0.627	15.0
TJ205	B	11	254	68.6	0.305 x 1.19	0.422	12.0
TJ209	C	5	492	42.3	0.320 x 1.20	0.344	12.4
TJ199	D	1	3200	--	0.32 x 1.20	0.504	19.4

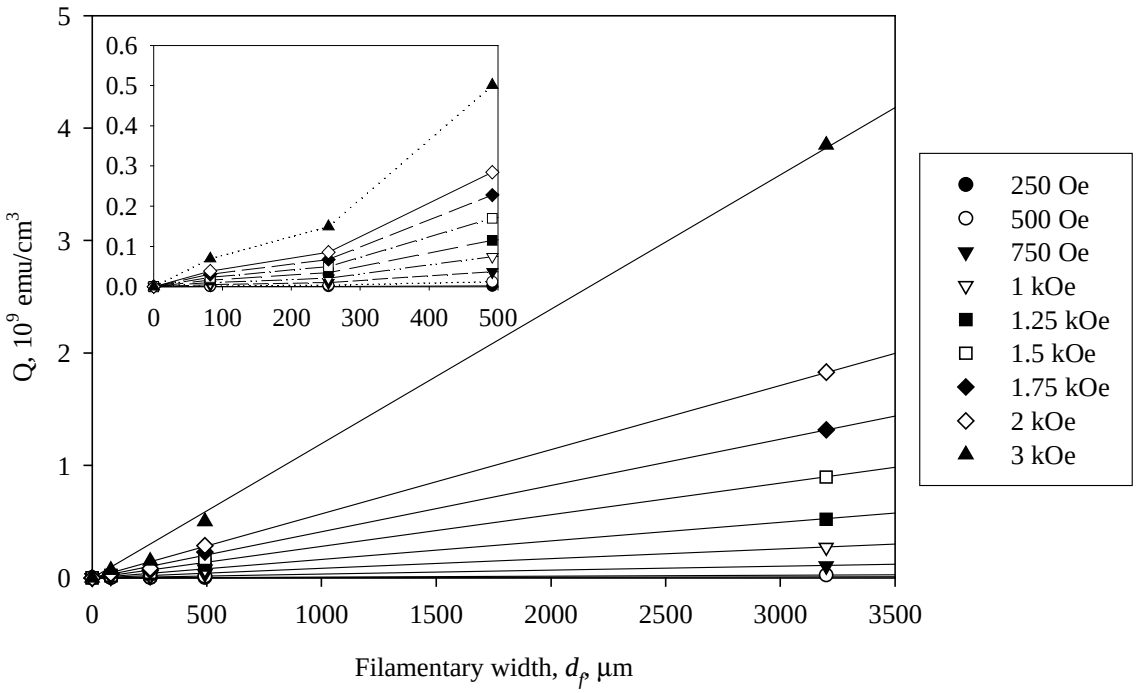

Figure 3.1 Q vs d_f for various amplitude H_m values.

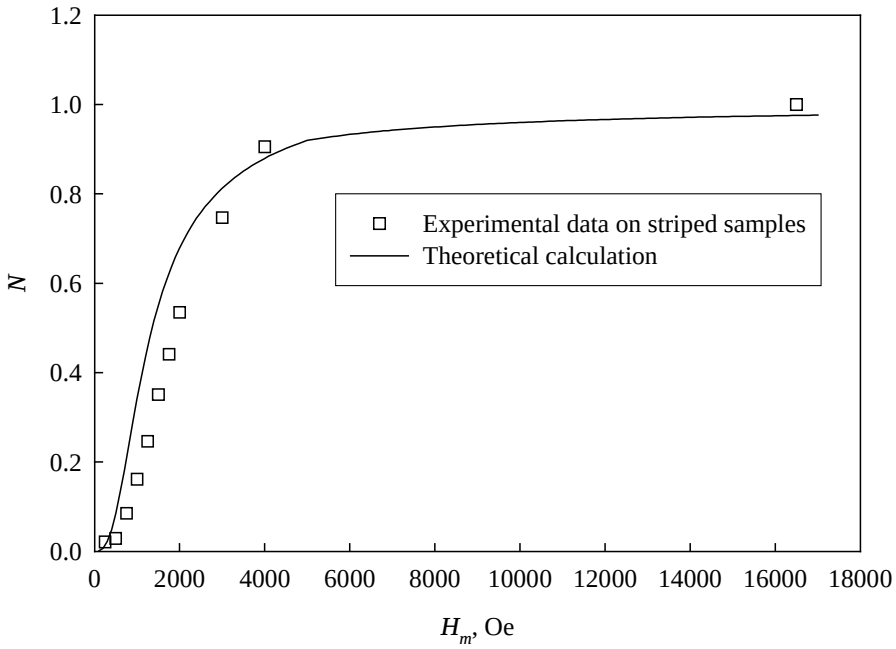

Figure 3.2. N vs H_m from Equation 3.7 and from Experiment (Figure 3.1).

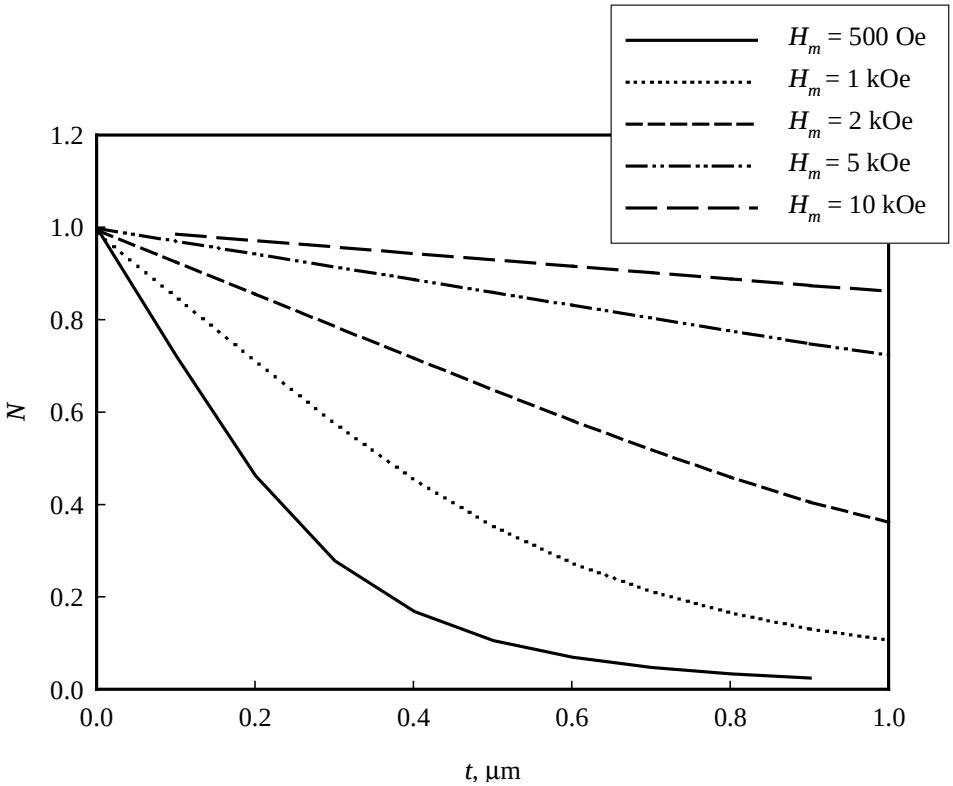

Figure 3.3. Predicted N-values as film thickness is increased (from which we can deduce loss reductions).

THIS REPORT INTENTIONALLY LEFT BLANK.

4.0 Conductor Design Studies

4.1 A YBCO CONDUCTOR PACKAGE WITH FILAMENTED AND TWISTED STRANDS UTILIZING A RUTHERFORD GEOMETRY

Single Conductor with Twisting: Strain and J_e degradation

J_e Reduction

In order to take advantage of the loss reductions offered by striping, transposition of the filaments (typically twisting of the strand) is needed. For a single conductor (strand) which has been striped or filamented, simple twisting the strand leads to very high reductions in J_e (Figure 1). Using λ as the superconductor to total area fraction, we get

$$\lambda \approx \frac{tw}{\pi\left(\frac{w}{2}\right)^2} \approx \frac{t}{w} \tag{4.1}$$

where t is the YBCO thickness and w is the width of the conductor. If t = 2 μm and w = 1 cm, then λ = 1/5000, and J_e = 2 x $10^{-4.}$ This would lead, for instance, to a 1 MA/mm^2 conductor with a J_e of 200 A/mm^2! This is shown schematically in Figure 4.1. This is perhaps an order of magnitude below useful levels.

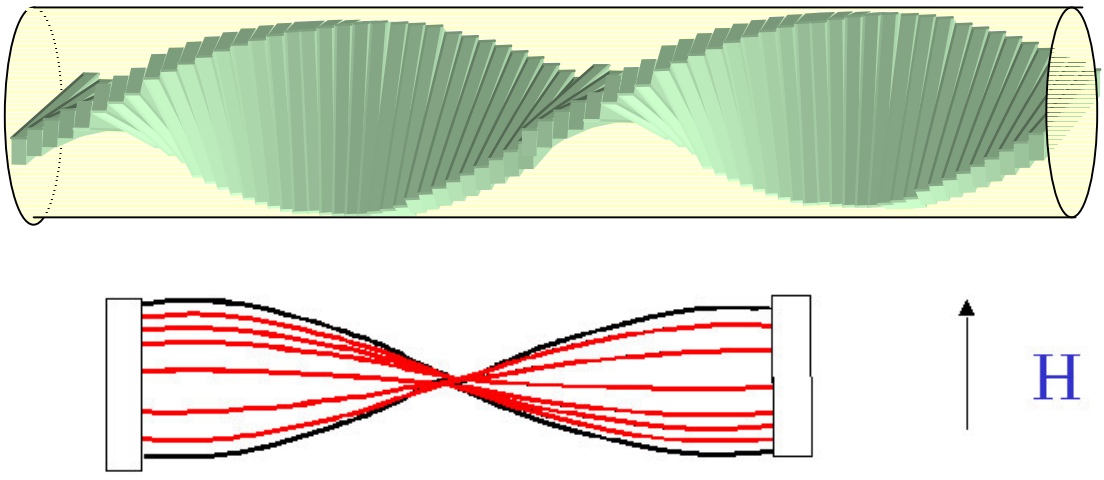

Figure 4.1. Filamented single conductor in twisted geometry. Notice large volume required.

Strain Relationships

The strain for such a conductor is maximized at its edges, and is given by

$$e \approx \frac{1}{2}\left(\frac{2\pi w}{2L}\right) \tag{4.2}$$

If the allowable strain is 0.5%, then this would lead to a minimum L_p of 30 cm or so, assuming a 1 cm wide conductor.

Stacked Conductors with Twisting: Strain limitations

In the case of a stacked, round conductor, the J_e is improved, since it becomes approximately that of the strand itself (Figure 4.2). If t is 2 μm, and the underlayer is 100 μm, the λ = 1/50. If, however, stabilizer is added, this must also be included. If a 1 mm stabilizer is added, then this drops to 1/500. On the other hand, the strain is still determined by the edges of the center conductors, and this thus same minimum L_p limitation is present (30 cm or so for a 1 cm wide conductor).

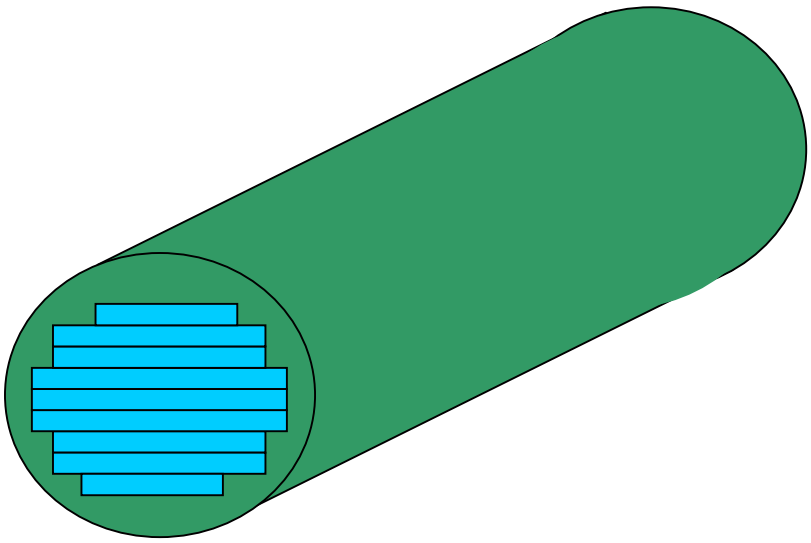

Figure 4.2. A stacked, round, twisted conductor.

Hexagonal (Polygonal) Geometry Conductors

We can imagine vastly reducing the strain using a hexagonal geometry conductor (Figure 4.3). Here there are two strain contributions, that due to in-plane bending, and that due to out-of-plane bending. In plane bending must be carefully controlled, but if the conductor is would onto a shaped inner hex, it can be reduced to very small values. The

out-of-plane bending is very minimal, being approximately given by *t/d*. The L_p of such a conductor is by the overall radius of the hex center region. The λ of such an arrangement is given by

$$\lambda \approx \frac{2\pi tR}{\pi R^2} = \frac{2t}{w} \tag{4.3}$$

This is shown in Figure 4.3 This leads to λ = 1/1000 for one layer of conductor, but this can be reduced to lower values by adding consecutive layers,

$$\lambda_t = \frac{n}{1000} \tag{4.4}$$

where for *n* (layer number) = 10, this can be reduced to 1/100.

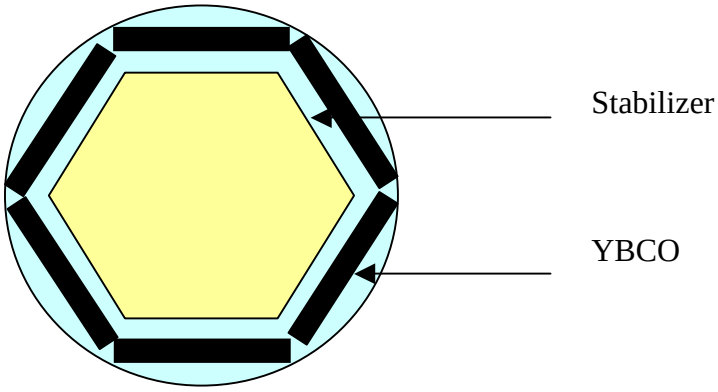

Figure 4.3. Hexagonal Geometry Conductor with internal Cu stabilizer and hexagonal YBCO elements.

Rutherford Geometry Conductors

For Rutherford type geometries, strain will be given by

$$e = \frac{t_{YBCO}}{t_{cab}} \tag{4.5}$$

This gives, for a 0.5% strain limitation and a t = 2μm (and assuming a neutral bending axis for the conductor itself) a limitation not on L_p, but on Rutherford core thickness, in this case to a core no thinner than 1 mm. A one-layer Rutherford cable would then have a λ = 1/500, and the λ would increase linearly with the number of layers, as for the hexagonal geometry conductor. The Rutherford conductor (Figure 4.4) might be easier to manufacture, however, especially while retaining a low in-plane strain.

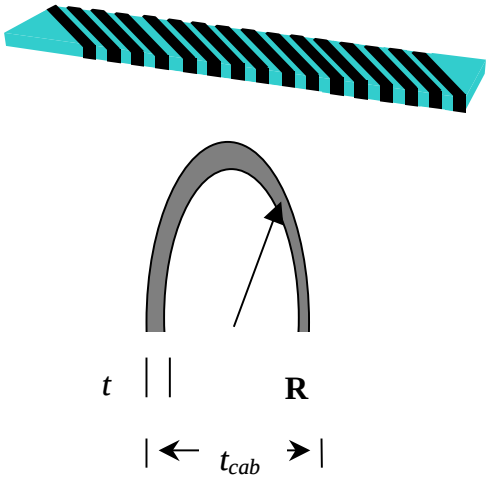

Figure 4.4. Rutherford Geometry Conductors. Top Shows basic Rutherford geometry, bottom shows cross sectional geometry and parameters for strain calculation.

Summary

Coated conductors aimed at low loss applications must be not only twisted, but also must have some field reversal or twisting present. If the fields are to be truly face-on, then twisting will be needed. Several conductor geometries are possible which do this while having lower strain and larger filling factors than the simple twisted single strand geometry. In the case of hexagonal and Rutherford conductors, the filling factor is such that overall J_e values of 2000 A/mm^2 are possible, with acceptable strain on the conductor. These have been outlined above, and overall the Rutherford type geometry seems to be a good compromise for performance and manufacturability.

4.2. YBCO STATOR CONCEPT FOR LOW LOSSES USING STRIPED COATED CONDUCTOR AND MACHINE DESIGN WITH INTRINSIC TRANSPOSITION

INTRODUCTION AND RATIONALE

The objective of the new stator design is to create a stator winding concept which is maximally efficient with respect to power generation, similar to existing diamond pattern stators, feasible to make with YBCO coated conductor, and will, in conjunction with striped coated conductor, have low conductor losses. Figure 4.5 shows a conventional diamond pattern stator. It may be possible to wind YBCO conductors into such a pattern. However, in order to make the flux linkages within the conductor more

balanced (and obvious), we can wind it in a Rutherford-inspired geometry, as seen in Figure 2. In any case, in order to have low losses, patterned tape must be used. In YBCO coated conductor patterned tape, the filaments are striped along their lengths, substantially reducing the hysteretic losses [1]. However, filamentary connections (presumably metallic in nature) are likely, in any case current connections will fuse the filaments together at least at the windings two ends. Thus, in order to keep eddy coupling currents at an acceptable level, the conductor must in some way have transposed filaments. Typically (for example in low temperature superconductors strands or Bi-based strands) by twisting a round wire, or twisting a wire before it is rolled into a tape. However, for YBCO coated conductors this is difficult.

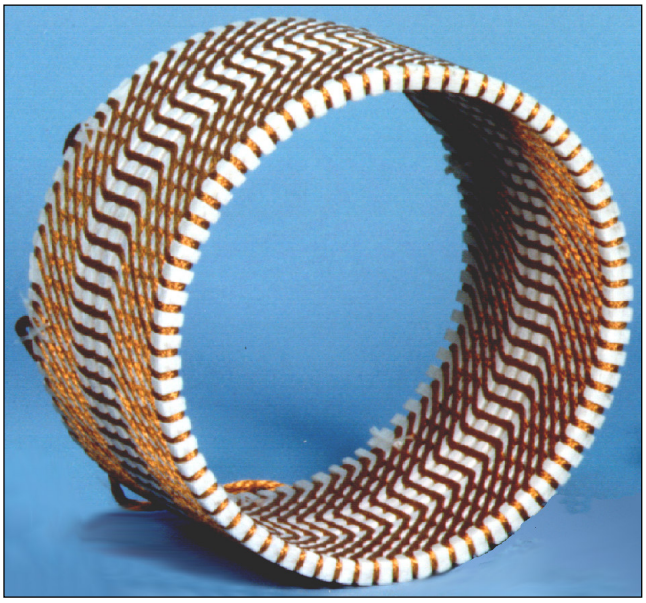

Figure 4.5. A 1 MW cryogenic stator with copper conductors using Diamond Pattern.

EDDY CURRENT LOSSES AND TRANSPOSITION

The losses of patterned YBCO conductors have been considered in detail in Ref [1]. Here, we focus exclusively on coupling loss. Coupling loss, a property of the filamentary (striped) strand is given, at sufficiently low frequencies by:

$$P_{coup} = \frac{1}{4\rho_{eff}}\left[fL\mu_0 H\right]^2 \tag{4.6}$$

and saturates to the hysteretic loss of the hysteretic loss of the unfilamentarized tape. Here P_{coup} represents the volumetric loss of the superconducting layer, f, and H_m have their usual meanings, ρ_{eff} is the "coupling resistivity", and L is the coupling length, either equal to the twist pitch if the conductor is twisted relative to external fields or twice the total length of an untwisted conductor. Usually coupling loss is reduced by twisting and by increasing the interfilamentary resistance; it can also be controlled by limiting the

"active length" of a tape segment (i.e. the length exposed to field of a given orientation) – see below. If however, the conductor is untwisted the losses return to the value of the unstriped conductor – which would be completely unacceptable.

Note here that even if the filaments were fully insulated from one another over the body of the conductor, these filaments are necessarily soldered together at the end so that the current can be introduced. Thus, a truly untwisted conductor, even with insulating filaments, would suffer large losses because of the end connections. Fortunately, however, our present application allows us to get around this difficulty because of the geometry of the machine in which it will be used. This geometry induced an effective active field length, roughly equal to twice the length of the rotor coil. This, in conjunction with appropriately controlled filamentary resistivity, is enough to control the losses.

However, it is also known that oscillations in the direction of the applied field will generate an effective twist. In such cases, The effective twist pitch is similar to the period of oscillation of the field. In general, if a segment of filamentarized conductor is exposed to spatially varying fields, it is the net flux through the segment that will determine the effective active length. While we are unaware of any work specifically related to this in the context of coated conductors, the effect is well known in cables [1-3] and LTSC strands themselves [4-5]. Figure 4.6 displays a schematic of how this effect would operate for a racetrack (e.g. a rotor) coil. The patterned conductor would experience fields which would have a square-wave pattern such that the field experienced on the top and bottom (or side A vs side B) of the coil would have the same magnitude but opposite signs. Figure 4.7 makes this explicit for a particular segment of conductor (in this case a solenoid geometry.

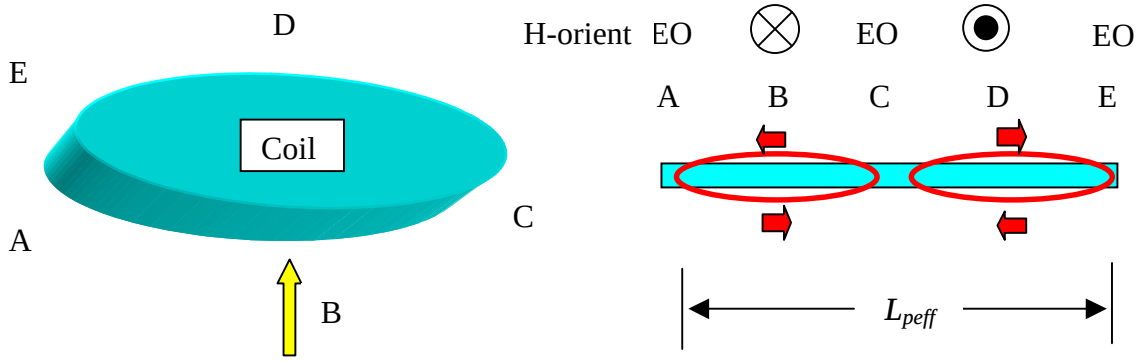

Figure 4.6. Schematic showing the effective twist arising from rotor coil in field applied parallel to plane of racetrack shaped rotor coil. A, B, C, D, and E are positions along a tape conductor used to wind one complete turn of the coil. At left, a field applied along the coil in the least favorable orientation for loss is shown. At right, the resulting field orientations in corresponding sections are shown, along with the resulting coupling eddy current loops that form.

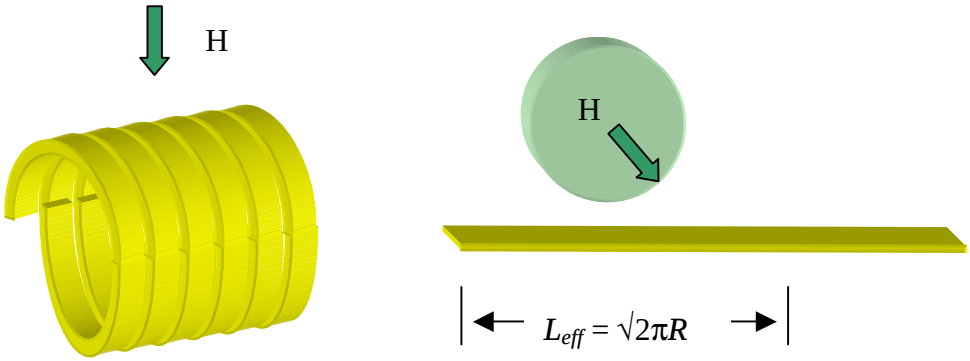

Figure 4.7 Transformation of solenoid winding geometry into rolling field vector.

Since

$$\varepsilon = -\frac{d\Phi}{dt} = -\frac{dB}{dt}A \tag{4.7}$$

the emf, *E*, is induced with a periodicity equal to the radius of a solenoid coil, or the major axis of the racetrack coil. This makes the effective twist pitch equal to twice that length for square-wave field oscillations and something slightly less than the perimeter for solenoid-like windings. Thus, for racetrack coils, $L_{eff} = 2L_{major\ axis}$, while for solenoid-like coils, $L_{eff} = \sqrt{2}\pi R$. Clearly, this can work to our direct advantage for rotor coils; such loss control should also be possible for stator coils. This can be shown to be possible as well, if the conductors can be bent along their easy axis sufficiently. Below we detail one design which should fulfill those requirements.

STATOR CONCEPT

Physical Interference

Because of the need to keep the conductors from physically interfering with one another, there are really two possibilities when winding the stator windings with edge-on YBCO tapes. The first is to put half of the conductor at a different radial position, the other is to twist the conductor into the plane of the coil as it goes into the non-active region of the coil. In the first scheme, part of the conductor may be further or closer to the rotor coils. In the second, significant twisting and bending are needed. The first of these possibilities is outlined below, we can call it the displacement winding.

DISPLACEMENT WINDING: Figure 4.8 shows the concept for a displacement stator design. The winding pattern is in this case inspired by a Rutherford geometry; others are possible.

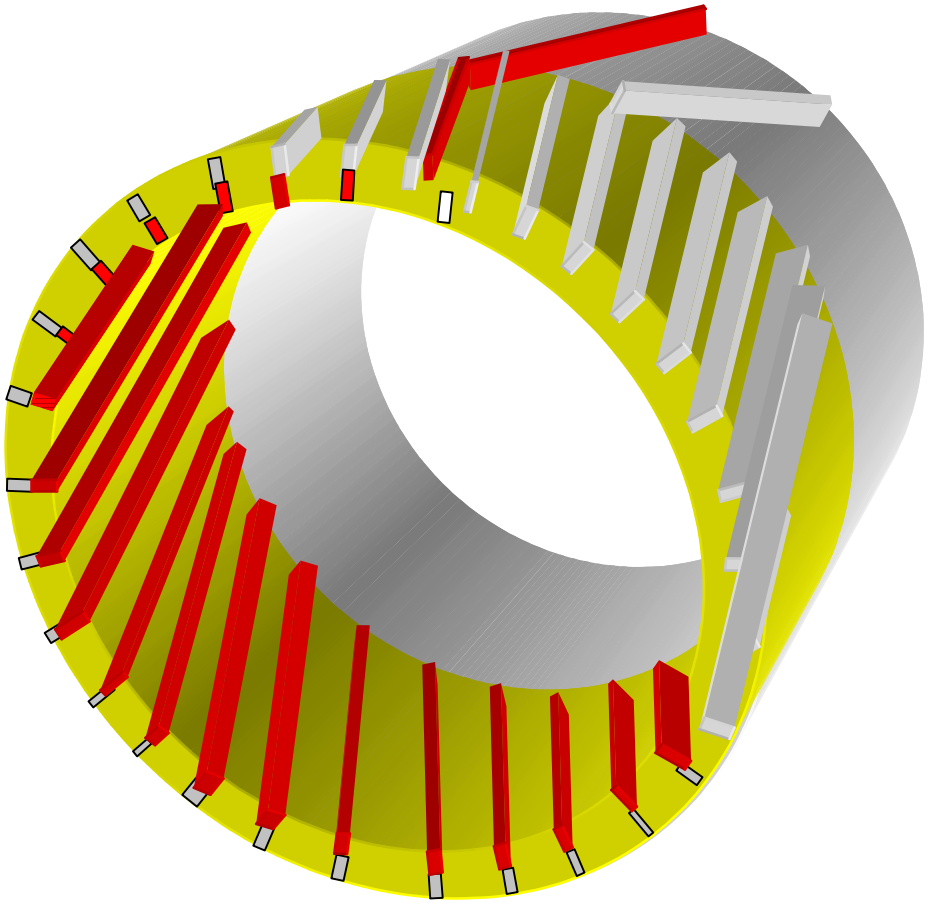

Figure 4.8. A New Stator Design for YBCO Striped Conductors

The central points of the design are that
(A) the conductor is mostly EDGE ON to the applied field

(B) with every wrap of the conductor along the stator length (height of the cylinder) the conductor switches orientation with respect to the stray (FO) field (not externally applied field, but stray field).

The first item is of course central, because the losses for FO oriented tape will be quite large, even for striped conductor. Cryogenic Cu machines operating at liquid hydrogen temperatures would have conductors which, once scaled to a 200 A level, would generate roughly 1.5-3 W/m. While this would be acceptable for an open cycle machine, a closed cycle machine would demand less, certainly below 500 mW/m. Our reference design (one simplified, but basic potential design) for the superconducting stator calls for an AC field amplitude of 1 T. Some designs for *each phase* of a stator call for 150 m of 1000 A conductor, and a loss budget of 100 W. This means 750 m of the "standard" 200 A conductor, with 130 mW/m as its loss target

If we assume that a Gramme-Ring type winding will be used (not shown), then even if we go to 5 micron filaments, with 1 mm wide conductor, the losses are estimated to be roughly 450 mW/m [6]. This is somewhat higher than the goal, and the geometry is not particularly efficient. In addition, 5 μm filament width with be difficult to attain, particularly in a commercially viable way.

On the other hand, these losses can be reduced if we use an edge-on geometry, with the loss reduction being proportional to the fraction of strain-to-main field. Thus, if that ratio is 1/10, the losses can be roughly reduced by 1/10 (although now transport current losses must be added in [6]. Nevertheless, there is a strong incentive to do this. However, we must also account, now that we are talking about long lengths of conductor wound into a machine, for the eddy current losses (coupling eddy currents) that will try to re-couple the filaments, as noted above. In order to keep these low, the conductor must be transposed, as described above. A stator winding can do that by ensuring that item (B) above, is true. In that case the L_{eff} is just twice the length of the stator coil (twice the height of the cylinder). So, the particulars of the design concept are as follows.

PARTICULARS

(1) The YBCO ribbons on the outer surface of the stator have mid-points which are further counterclockwise than their end-points, while ribbons are the inner surface are having midpoints which are clockwise displaced with respect to their end-points.

(2) The ribbons on the inner surface (red) are such that the flux change that they experience is causing eddy currents which flow opposite to those of the gray (outer) strips.

(3) The end crossovers are made in Rutherford-tape-mode (as one would wrap a paper strip about a ruler).

The last point, (3), deserves further comment. For bending geometry, strain will be given by

$$e = \frac{t_{YBCO}}{t_{cab}} \tag{4.8}$$

This gives, for a 0.5% strain limitation and a t = 2μm (and assuming a neutral bending axis for the conductor itself) a limitation on bend radius, in this case to no less than 1 mm. Figure 6 shows the proposed wrapping method about the end-piece. The end piece is a small tab, two for each conductor winding along the length of the stator (one at each end). The small tab redirects tape coming from the outer winding of the stator, bend it about a 1mm tab at a 45 degree angle. The conductor then progresses to the inner winding radius where it is again bent along its easy axis over a 1 mm radius at a 45 degree angle, at which point it flows into the inner stator winding.

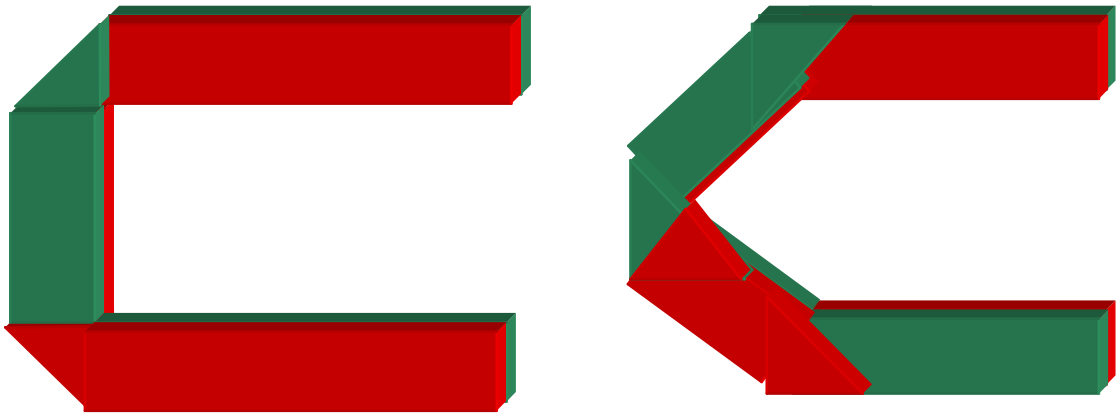

Figure 4.9. (a) Corner-wrap with n = 2. Transposed with respect to “internal fields”. (b) Corner wrap with n = 3, transposed with respect to external field.

We note that 4.9 (a) is transposed with respect to external fields, but note that fir stators, the internal field (coming from the rotor) is more important, thus we will use 4.9 (b). This is not transposed with respect to external fields, but is to “internal fields” of the kind expected to be generated in the stator loops by the rotor. We can see this more clearly if we look at a rotor stator combination, as shown in Figure 4.10. Section A and B, in Figure 4.10, experience mostly EO field, and form a flux containing, emf generating loop useful for generating power in the external circuit. However, in addition to the flux linkage of the larger loop of approximate area RL_{stat} where R is the stator winding radius, and L_{stat} is the length of the stator winding. There is a second loop formed within the strand (assuming striped conductor), of area $wLstat$, where w is the strand width. The flux enclosed by this loop is due exclusively to the face-on (stray) component of the field. This associated emf is the driver of the coupling currents, and must be controlled. If we now consider the whole length of the stator winding, we will have a series of A and B segments “connected together”. Note, however, that the way in which the stray flux linkage and associated emf generated in sections A and B add is quite critical. If they add constructively, then the resulting emf and associated losses are large, if they add destructively, then losses can be controlled.

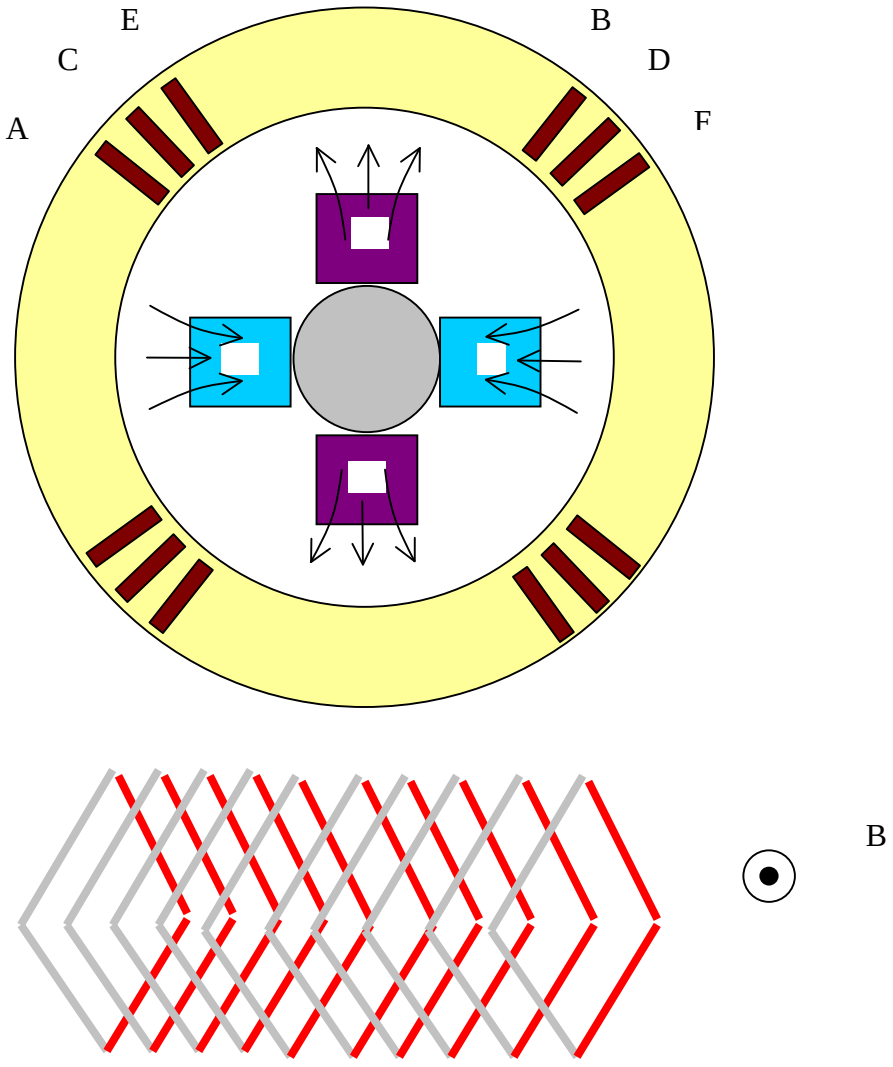

Figure 4.10. A rotor/Stator combination.

We can now consider the case where we have a length of striped conductor exposed to a changing field, in particular, it is a stator winding as depicted in Figure 4.10, above. Let segment A have end points A1 and A2, representing the opposites ends of the active segment A, similar for B1 and B2, and so on. If wound as in Figure 4.10, such that section B follows A, and C follows B, etc., and no twist is introduced into the conductor, then it will be transposed with respect to externally applied fields, ***but not with respect to internally generated stray fields***. We will then have the situation depicted in Figure 4.11, with a large next stray flux. Even if there is no interfilamentary conductivity, except that at the ends conferred by the solder joint used to connect to the outside world, the losses will be large.

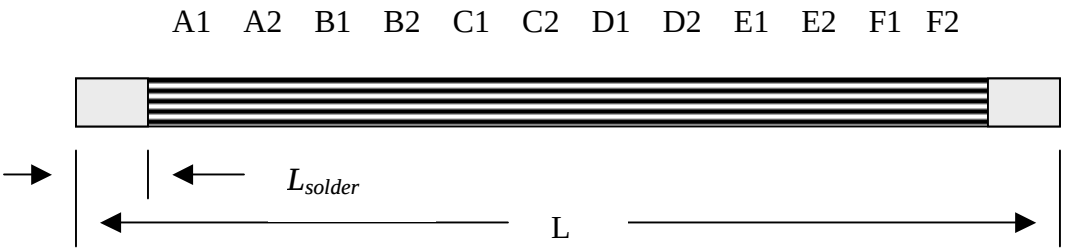

Figure 4.11. Various segments of a stator winding made from a striped coated conductor.

For such a case $\rho_{eff} = \rho_{solder}(L/2L_{solder})$. Of course we must be careful which volumes we normalize to within the loss equations using this expression to make sure they are compatible to the definition of the resistivity. In our case we will use the overall dimensions of the tape for all considerations of this kind.

Imagine a winding the produces (for the sake of simplicity) a square wave pattern of *dB/dt* as experienced by the conductor.

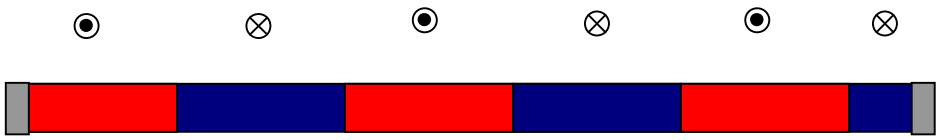

Figure 4.12. Stator winding with unbalanced *dB/dt*.

We know that

$$\varepsilon = -\frac{d\Phi}{dt} = -\dot{B}A \tag{4.9}$$

Also

$$I = \frac{\varepsilon}{R} = \frac{-\dot{B}A}{R_{solder}} \tag{4.10}$$

The $A(dB/dt)$ in question is the net value. This will be controlled the amount of unbalanced loop area exposed to *dB/dt* (as in Figure 4.12). The maximum amount will be proportional to the effective winding pitch, say $L_{winding}$. In that case the coupling current would be

$$I_{\max} = \frac{-\dot{B} w L_{winding}}{R_{solder}} \tag{4.11}$$

The per-unit-length power is then given by

$$P_l = \frac{\dot{B}^2 w^2 L_{winding}^2}{R_{solder} L} \tag{4.12}$$

where L is the length of the whole coil, and w is the conductor width. This of course presumes no interfilamentary contact other than the solder. If such contact is present we will add a term which does not drop as $1/L$ – the traditional loss term.

NON-DISPLACEMENT WINDING: In this case the stator coils is wound as previosu tape conductors have been, with the conductors within the active region all at the same radius. In oder to do that, the winding must have simple quarter twists in the inactive regions, leading to a simple $n = 1$ bend at the stator ends, and, crucially, a "dip" as part of the winding. This "dip" allows the conductors to all be in the same radial position in the active winding, but to avoid physical interference with one another. Characteristic of this dip is the fact that it requires a sharp bend of the conductor along the "hard" axis. This bend should not introduce any transposition. Such a bend is shown in Figure 4.13 – and is denoted an S-bend.

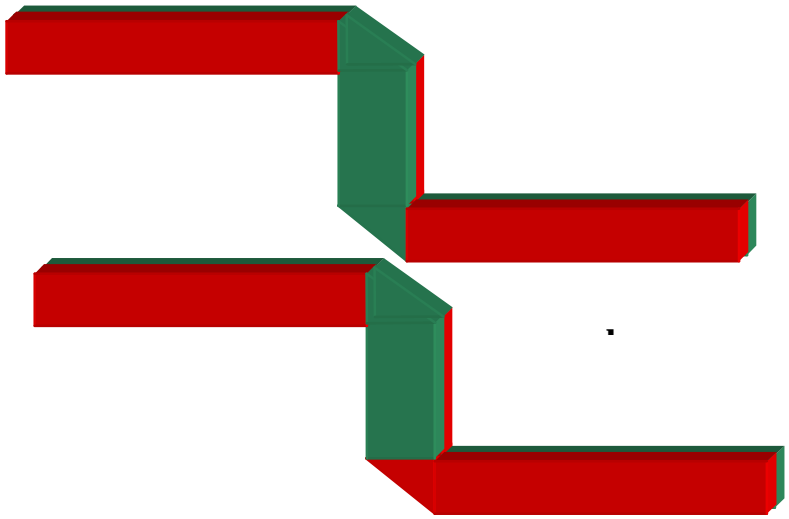

Figure 4.13. S-bends of two kinds ((a)symmetric and (b) nonsymmetric). $n = 2$, and there is no net transposition.

REFERENCES

[1] G. Ries and S. Takács, IEEE Trans. Magn. 17 (1981) 2281-2284.

[2]. S. Takács, N. Yanagi and J. Yamamoto, IEEE Trans. Appl. Supercond. 5 (1995) 2-6.

[3]. A. Verveij, PhD Thesis, University of Twente, Enschede, the Netherlands, 1995.

[4] M.D. Sumption and E.W. Collings, Adv. Cryo. Eng. (Materials) 40 579-587 (1994).

[5] K.R. Marken. A.J. Markworth, M.D. Sumption, E.W. Collings, and R.M. Scanlan, Effy Current Effects in Twisted and Wound SSC Strands, IEEE Trans. Magn. 27 (1991) 1791.

[6] M.D. Sumption, E.W. Collings, and P.N. Barnes, AC Loss in Striped (Filamentary) YBCO Coated Conductors Leading to Designs for High Frequencies and Field-Sweep Amplitudes, to be published in *Superconducting Science and Technology*.

5.0 Pinning Studies

In this segment supplemented earlier studies of magnetic J_c and pinning force [1,2] for a 211 inclusion-pinned sample and a control sample with studies of the pinning potential. The object was to interpret the earlier evidence for strong pinning enhancement in terns either of increases in pinning well depth, or increases in the number of pinning sites. First, however, we must look again to the magnetic J_c and pinning force results. The two samples were TJ127C, one of the best of the samples with 211 inclusions, and sample TJ360, a typical control sample. Previous experiments had shown TJ360 and TJ127C to be a useful comparison, and also showed significant enhancement at 77 K for TJ127C, as compared to TJ360 [1,2].

The samples were mounted in a vibrating sample magnetometer, and measured at temperatures from 10 K to 77 K, with varying ramp rates. The 10 minute loops are displayed below. The temperature was measured by a Si-diode placed near the sample. The field was applied perpendicular to the wide face of the sample, and thus the currents measured were ***a-b*** type. The resulting ***M-H*** loops were volume normalized, and then the magnetic J_c was extracted via

$$J_c = \frac{30\Delta M}{d} \tag{5.1}$$

The magnetic J_c results are shown in Fig. 5.1 and 5.2.

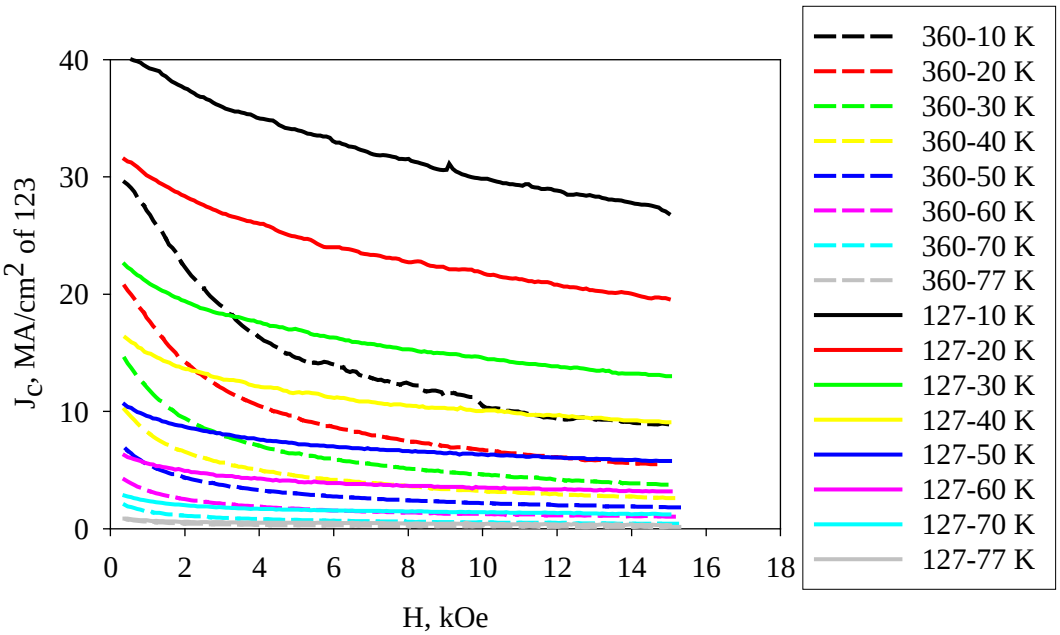

Figure 5.1. Magnetic J_c for samples TJ360 and TJ127C at temperatures 10 to 77 K.

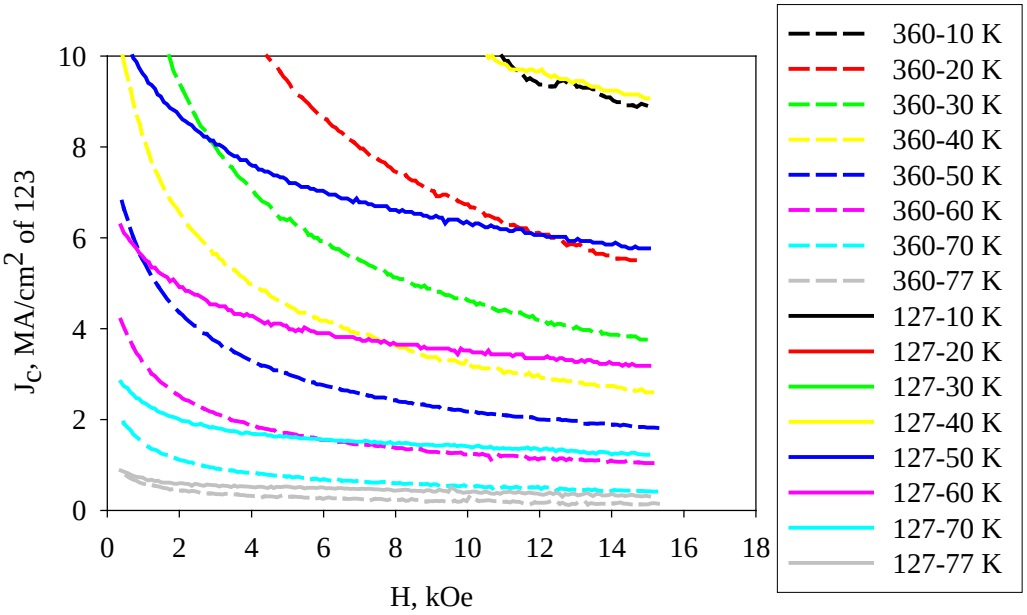

Figure 5.2. Magnetic J_c for samples TJ360 and TJ27C at temperatures from 10 K to 77 K – high temperature values.

Clearly, the values at low temperatures are very much greater for TJ127C – a much larger improvement than is evident at 77 K. This confirms the flux pinning advantages conferred by the 211 inclusions. Figures 5.3-5.5 show this in terms of the pinning force curves. Here $F_p = J_cB$ was used, and the force is in GN/m^2. The results are comparable to those of Foltyn et al [3].

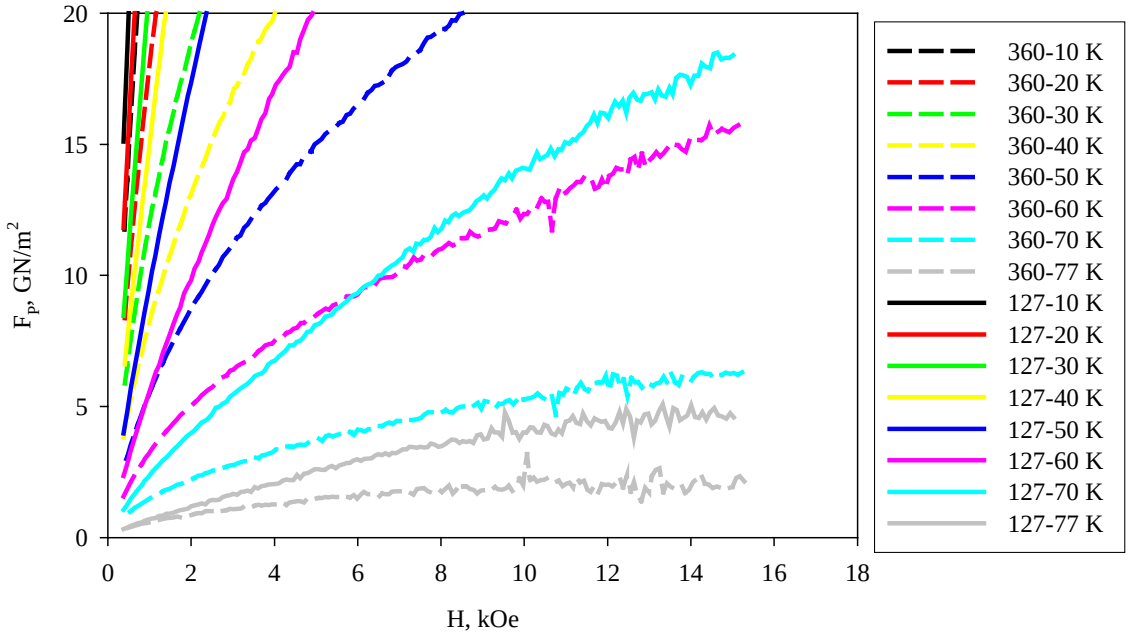

Figure 5.3. F_p vs H for samples TJ127C and TJ360 at high temperatures.

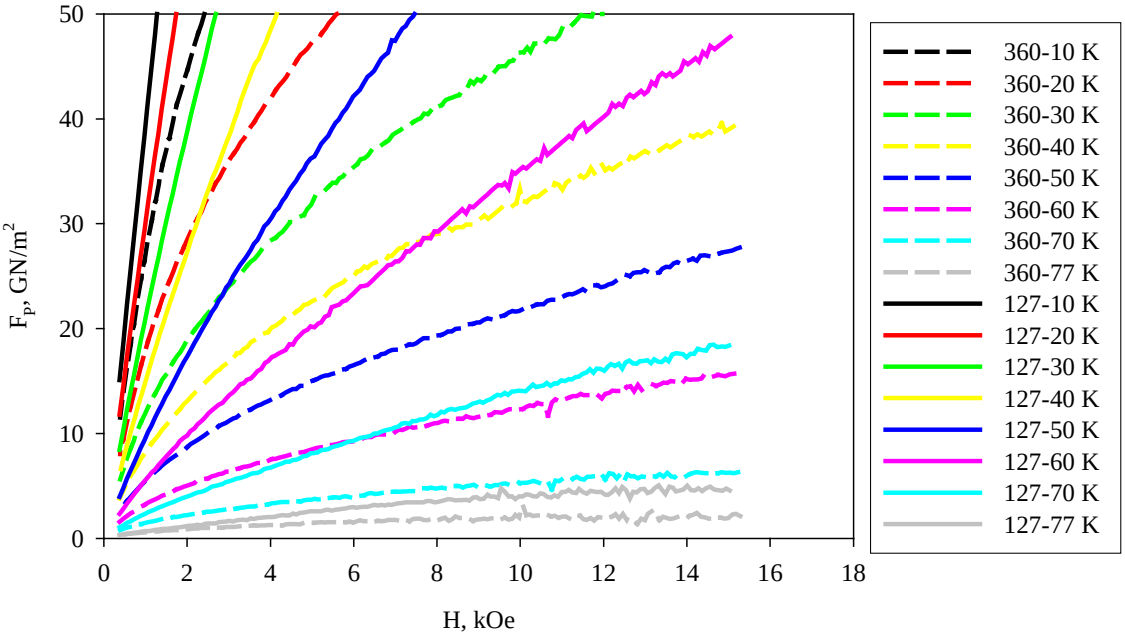

Figure 5.4. F_p vs H for samples TJ127C and TJ360 at intermediate temperatures.

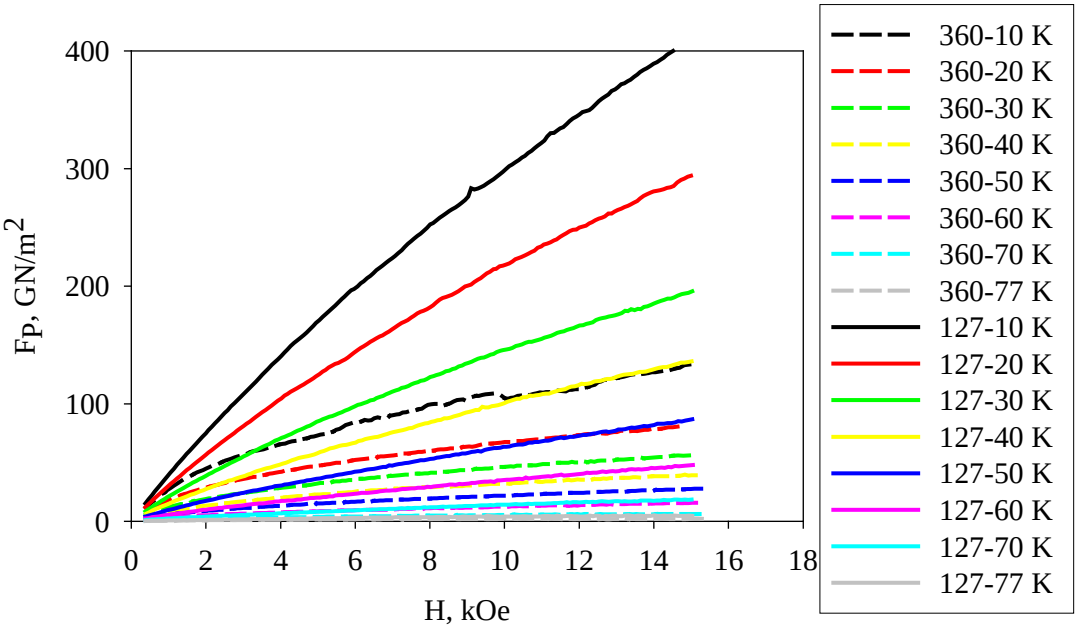

Figure 5.5 F_p vs H for samples TJ127C and TJ360 at temperatures from 10-77 K.

The addition of 211 inclusions significantly enhances YBCO thin film performance. The direct extraction of F_p conclusively demonstrates that this is so, and underscores the large increases in low temperature J_cs which are seen.

Ramp Rate Results and Pinning Strength in YBCO Coated Conductors

The *M-H* response of samples with 211 inclusions (nano-pinning) (TJ127C) and control (TJ360) samples were measured at various fields and temperatures, as described below. The response was plotted as a function of ln(*dH/dt*), since

$$M = M_0 + SLn\left(\frac{dH}{dt}\right) \tag{5.2}$$

This can be connected to the more standard expression for magnetization decay

$$M = M'[1 - R\ln(t)] \tag{5.3}$$

by $R = S/M_0$. We note then that $R = k_B T/U_{eff}$, where U_{eff} is the uncorrected apparent pinning potential. If we use k_B = 8.617 x 10^{-5} eV/K, then U_{eff} can be obtained in eV. Below (Figures 5.6-5.17) we display the ramp rate dependence of the nano-pinned sample side-by-side with that of the control sample at various temperatures. The increase in M_0 for the nano-pinned sample is immediately obvious. Closer inspection shows that the drift rate at lower temperatures is lower for the nano-pinned sample as compared to the control sample, however, this is not true a higher temperatures where the drift rates are similar. Figure 5.18 summarizes these results using Eq 5.2 and 5.3 to obtain U_{eff} for the two samples at various temperatures and field values. Note that while these graphs (5.6-5.17) are displayed on a common-log scale the slopes used in obtaining U_{eff} were taken from a natural log scale, as Eq 5.2 dictates.

Figure 5.18 is in the style of Maley et al [4], who elucidated the variation of U_0^* ($U_{0,apparent}$) stemming from the variation of apparent pinning strength with J_c (and thus M_0). We can understand, of course, that the effective pinning force would be reduced by the Lorentz force. In general, this would not necessarily be a linear function, however, the quite-often used linear approximation is that $U_{eff} = U_0 - JBV_c a$, where B is the field, V_c is the correlation volume, and a is a hop distance. It is clearer to insert U_0* here in place of U_0, defining U_0* as the U_0 generated from a linear approximation. Maley, on the other hand, plotted U_{eff} vs ΔM ($\propto J_c$) , finding a non-linear function which could be extrapolated to $J_c = 0$. The U value of the extrapolation is the true U_0.

In Figure 5.18, we have plotted U_0 and $U_{apparent}$ for these samples. The U_0 is similar for the nano-doped and control samples. However, it seems that $U_{apparent}$ is less dependent upon J_c than for the control sample. The most reasonable way to look at this system is that there are pinning sites being added by the nano-pinning, therefore we have the old pinning sites in additions to new ones. These new sites have similar U_0 values at 77 K, but are less influences by strong flux gradients (see also Figure 5.19). This may be due to a different topology of pinning center. We notice, on the other hand, that the F_p value is enhanced by a factor of 2-3 (2 at 77 K and 3 at 10 K) by the nano-inclusions. Thus, overall we can say that the nano-inclusions seem to be increasing the number of pinning sites, rather than their intrinsic U_0 values. However, it must also be noted that for whatever reason they are less influenced by flux gradients.

We include for completeness a study of the drift-determined U_{eff} values for the nano-pinned sample. Here, the sample was subjected to a static field and the magnetization was allowed to decay. Equation 5.3 was used to determine $U_{apparent}$. In addition to this, however, we went back to the approach of using Maley's approach for drift measurements. Here $U = k_B T \ln(dM/dt)$ locally (plus a constant). Figure 5.21 shows this expression plotted, and 5.22 shows the resulting $U_{apparent}$ values (and a U_0). Note here that the pinning energies derived in this way are higher than those from ramp rate experiments because the electric fields are lower, and we are probing a different part of the critical state.

Overall, we conclude that the nano-inclusions seem to be increasing F_p and J_c by increasing the ***number*** of pinning sites, rather than their ***intrinsic*** U_0 values. There are presumably two classes of pinning site, those present in the control sample, and the new ones generated by the nano-defects. These new sites seem to be similar in number and strength to the original sites. However, it must also be noted that for whatever reason they are less influenced by flux gradients (i.e., the pinning wells are just as effective at high flux gradients (low temperatures) as they are at lower ones (high temperatures).

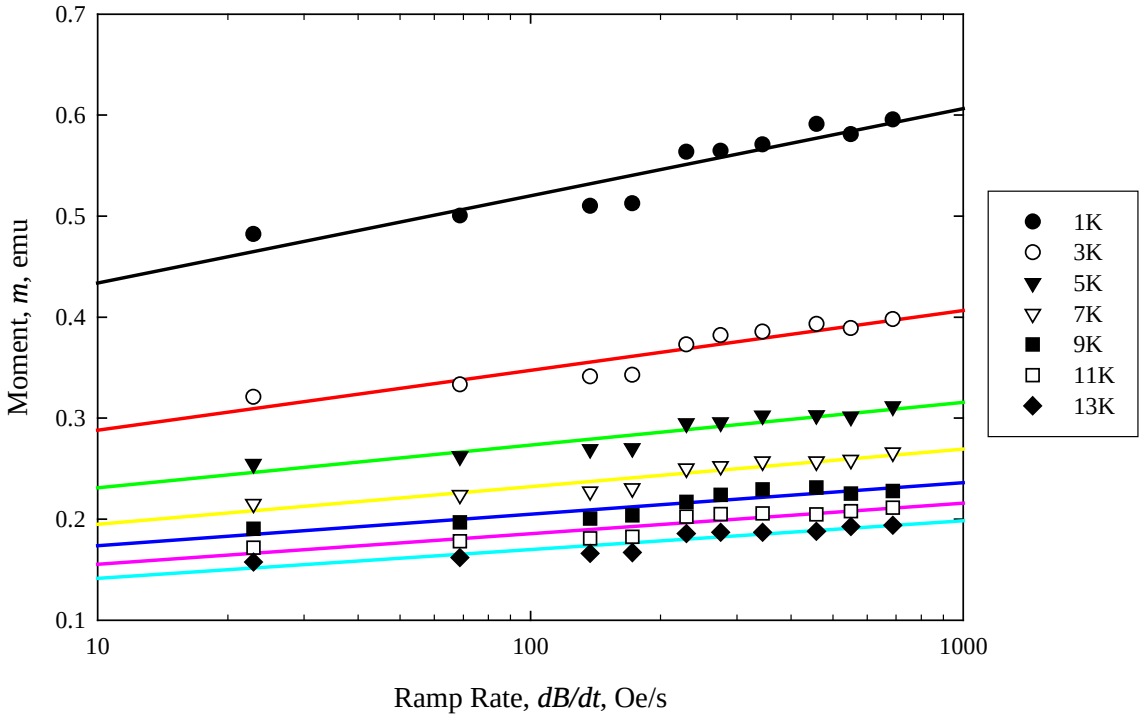

Figure 5.6. Control Sample at 20 K.

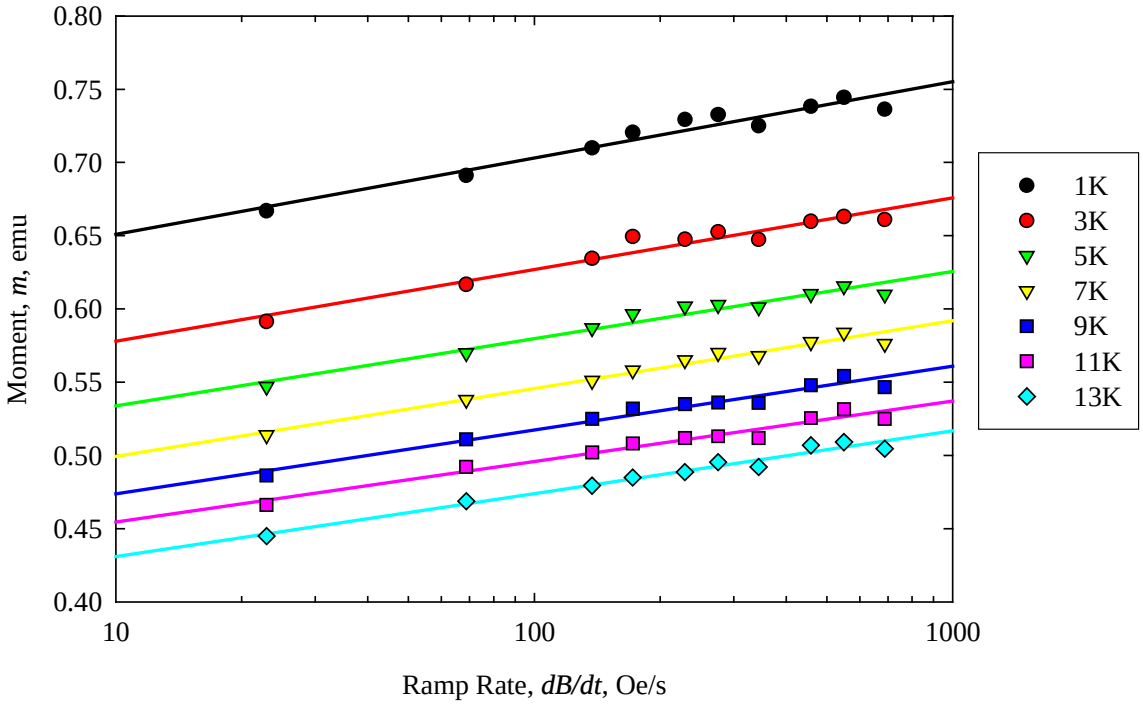

Figure 5.7. Nano-pinned sample at 20 K.

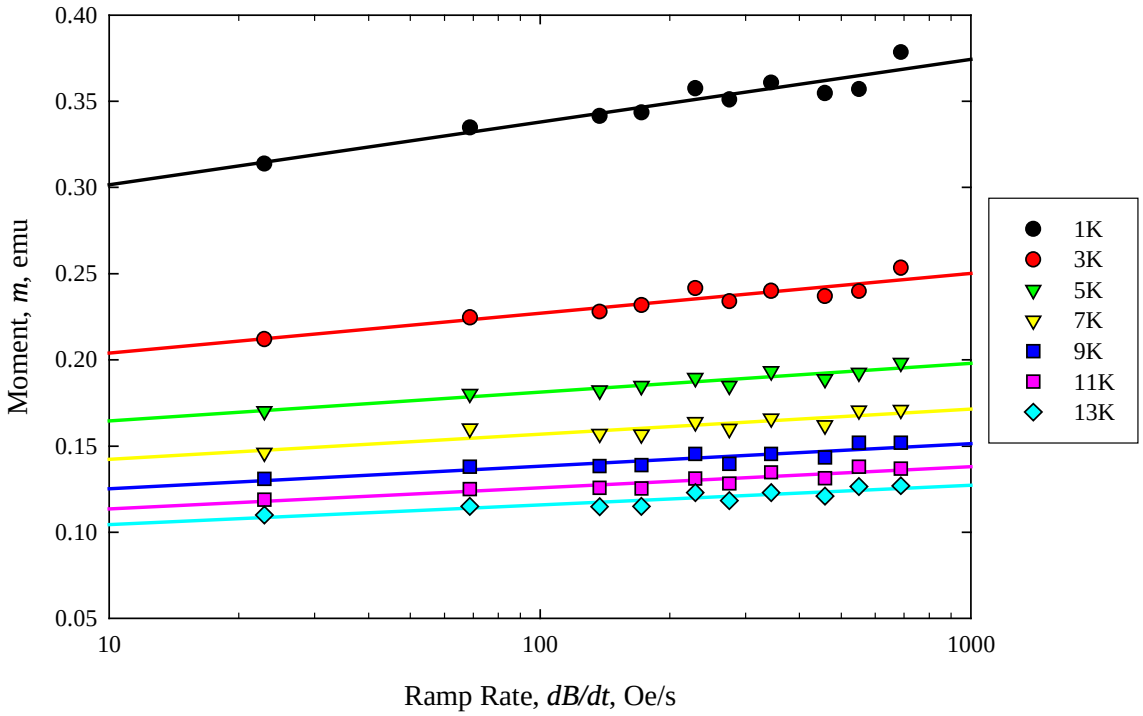

Figure 5.8. Control sample at 30 K.

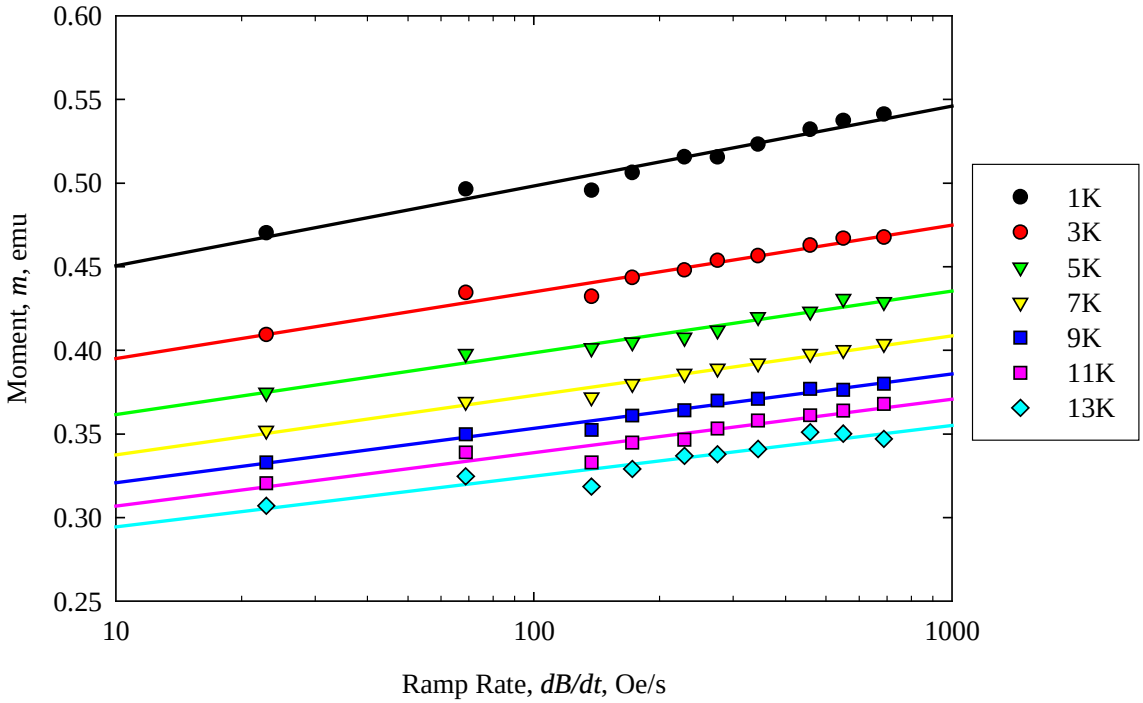

Figure 5.9. Nano-pinned sample at 30 K.

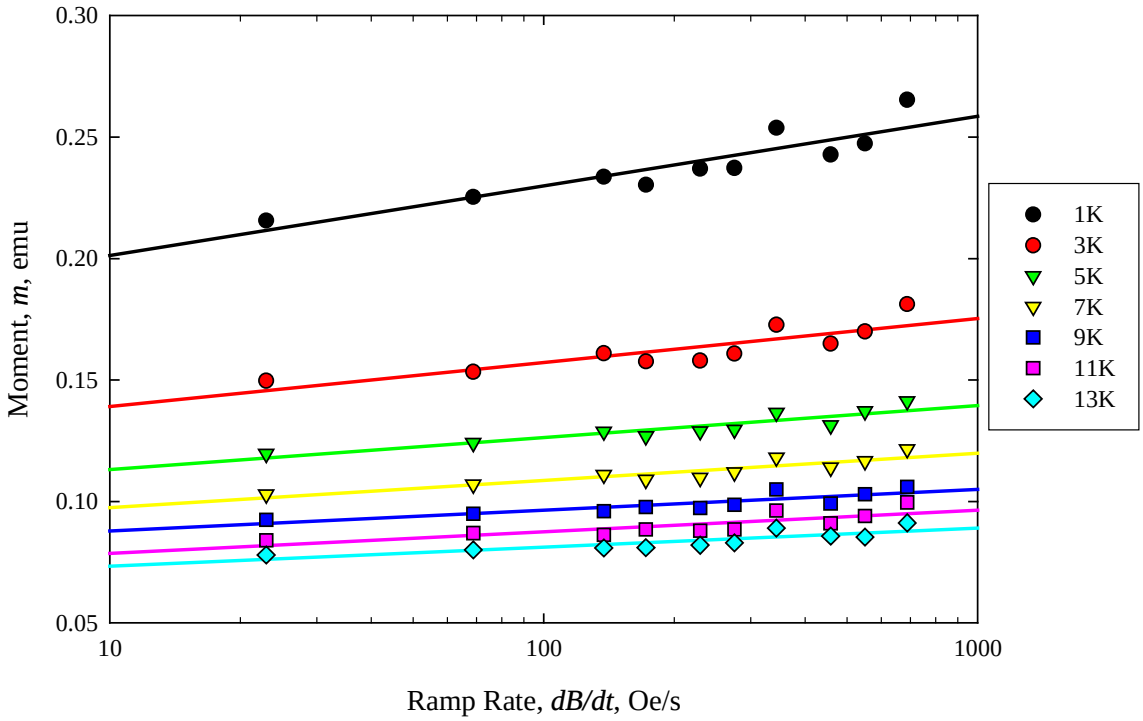

Figure 5.10. Control sample at 40 K.

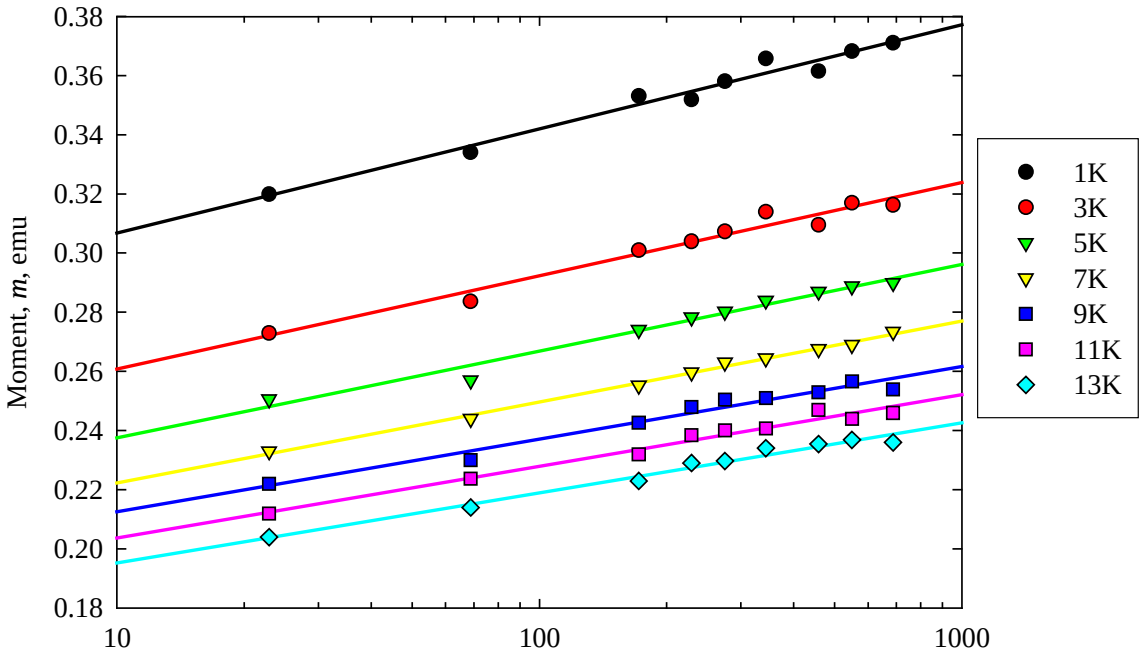

Figure 5.11. Nano-pinned sample at 40 K.

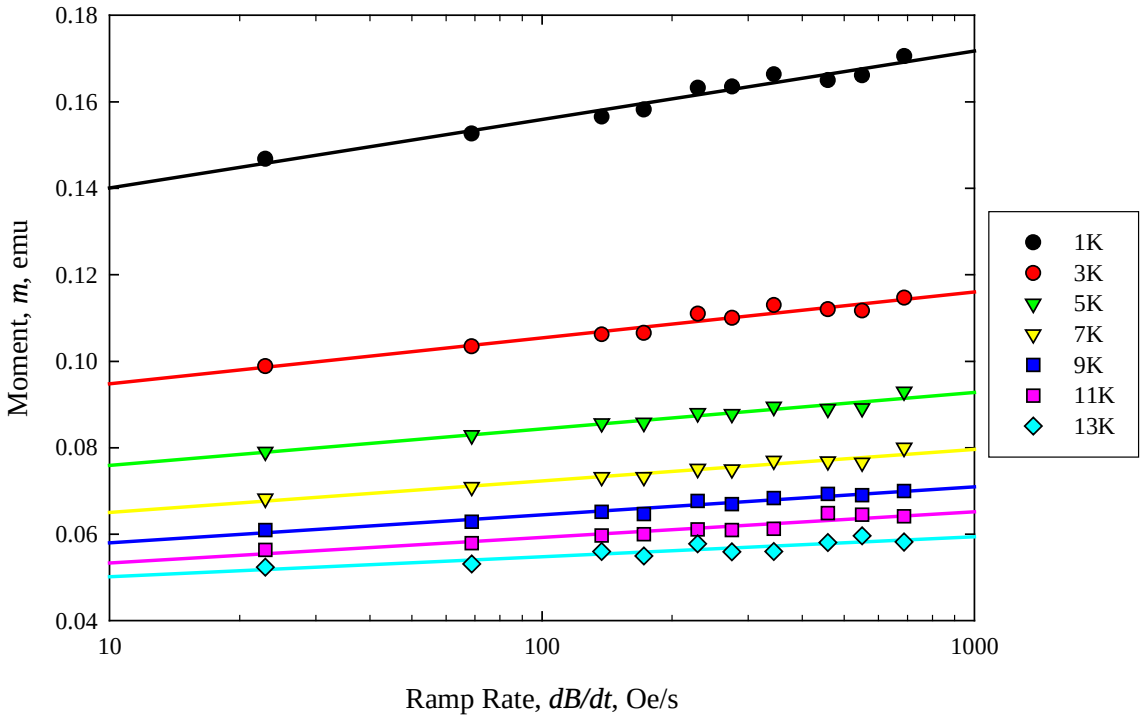

Figure 5.12. Control sample at 50 K.

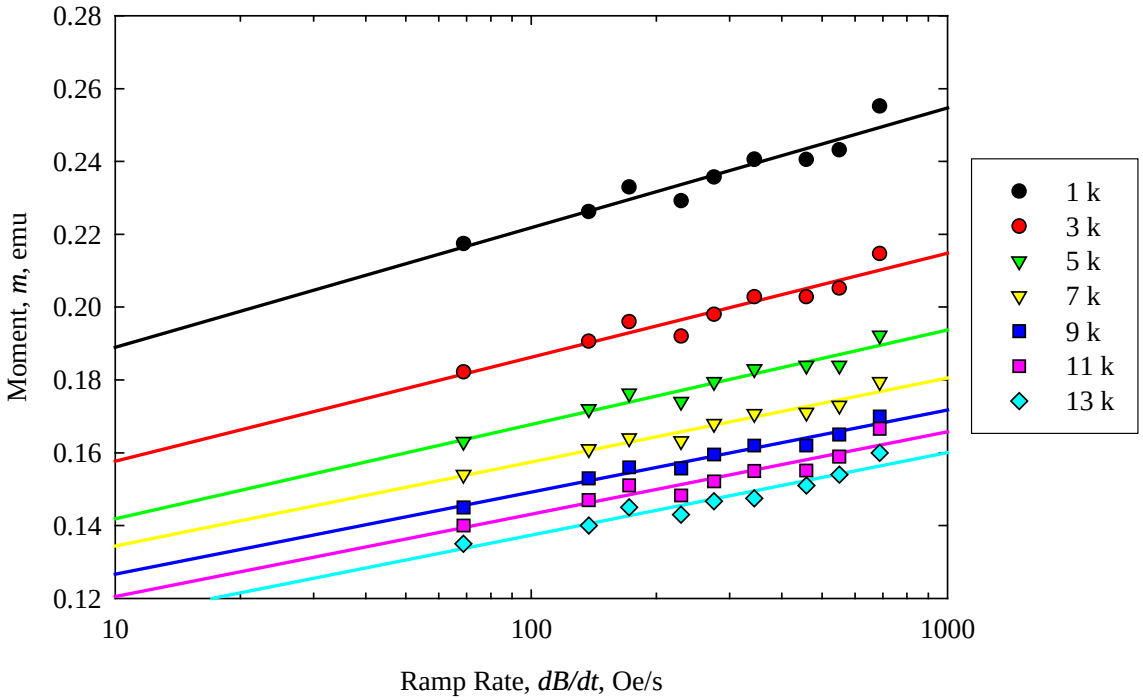

Figure 5.13. Nano-pinned sample at 50 K.

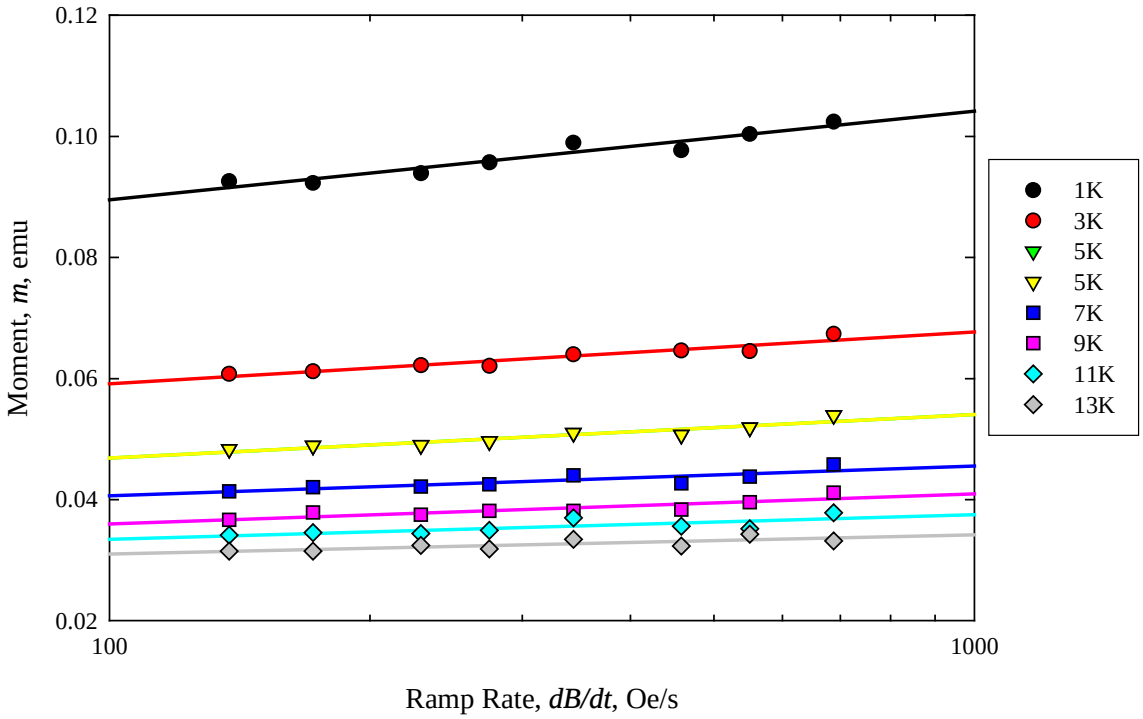

Figure 5.14. Control sample at 60 K.

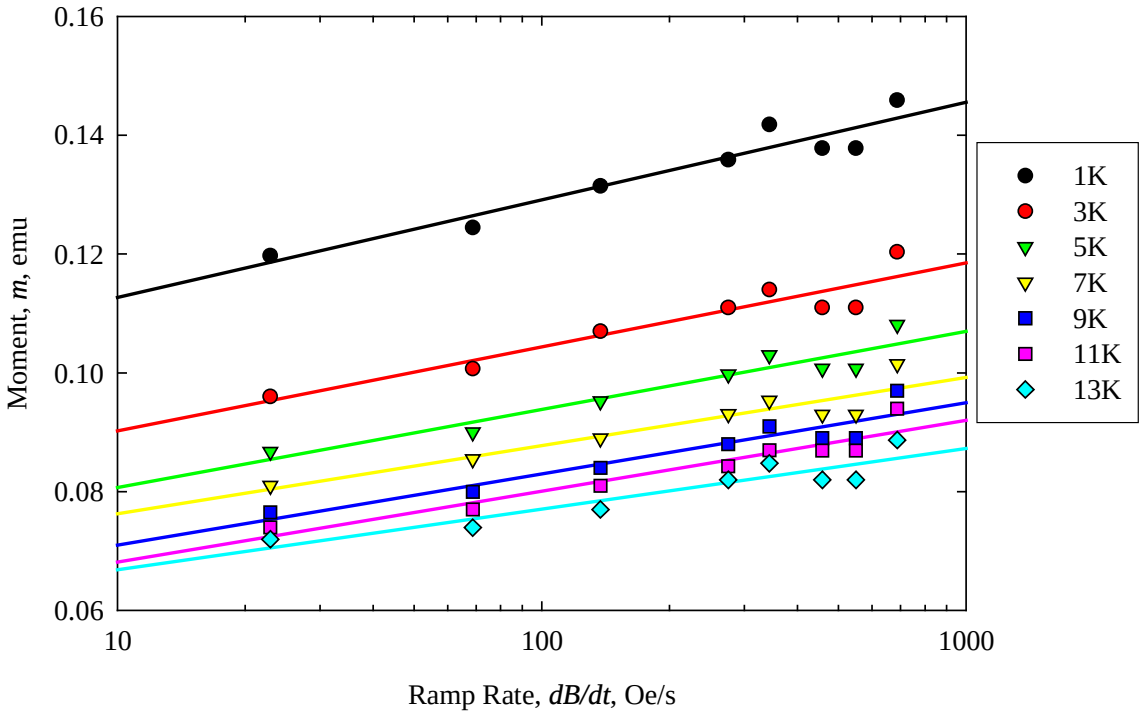

Figure 5.15. Nano-pinned sample at 60 K.

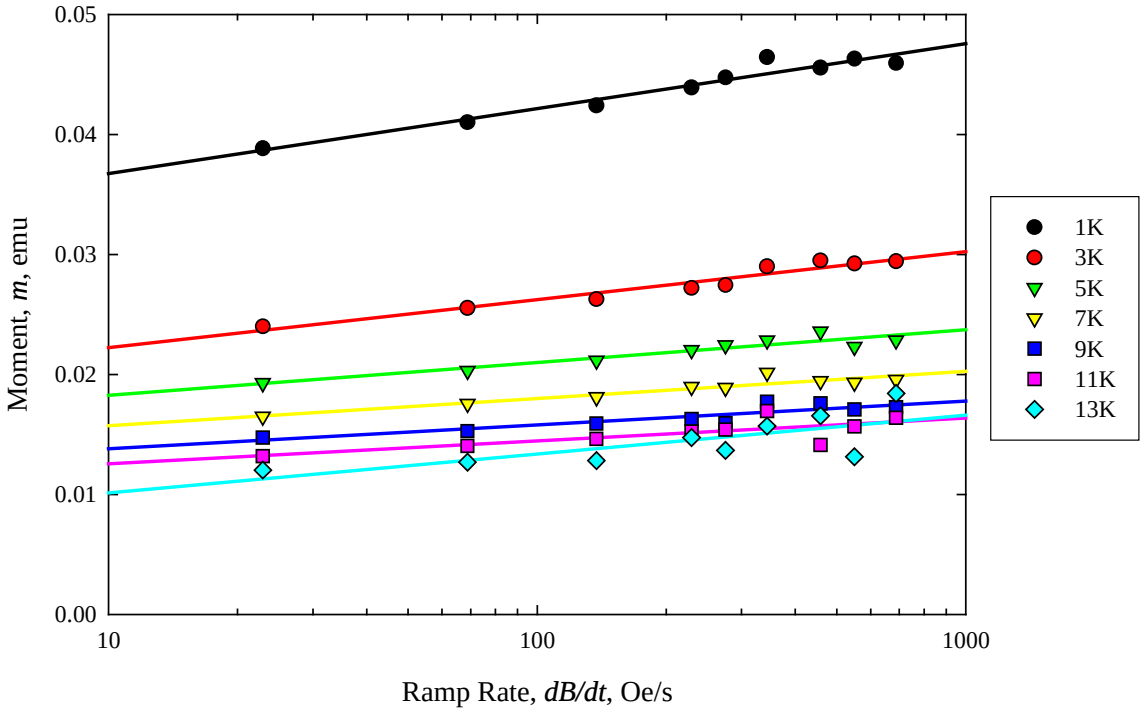

Figure 5.16. Control sample at 70 K.

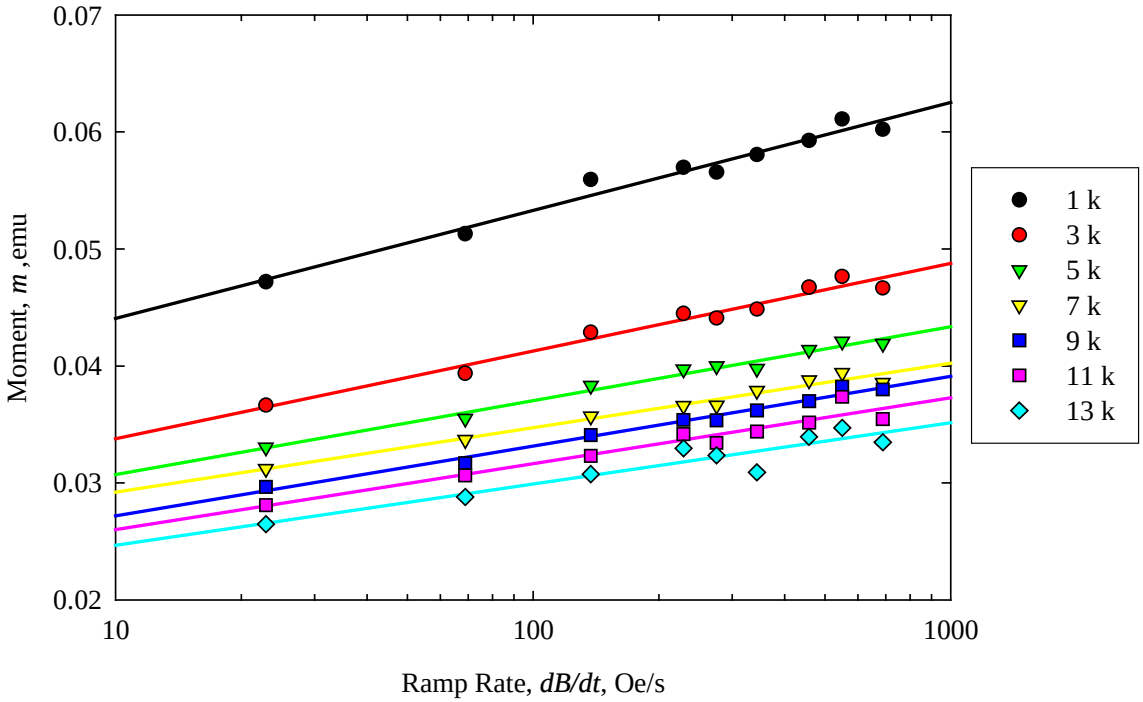

Figure 5.17. Nano-pinned sample at 70 K.

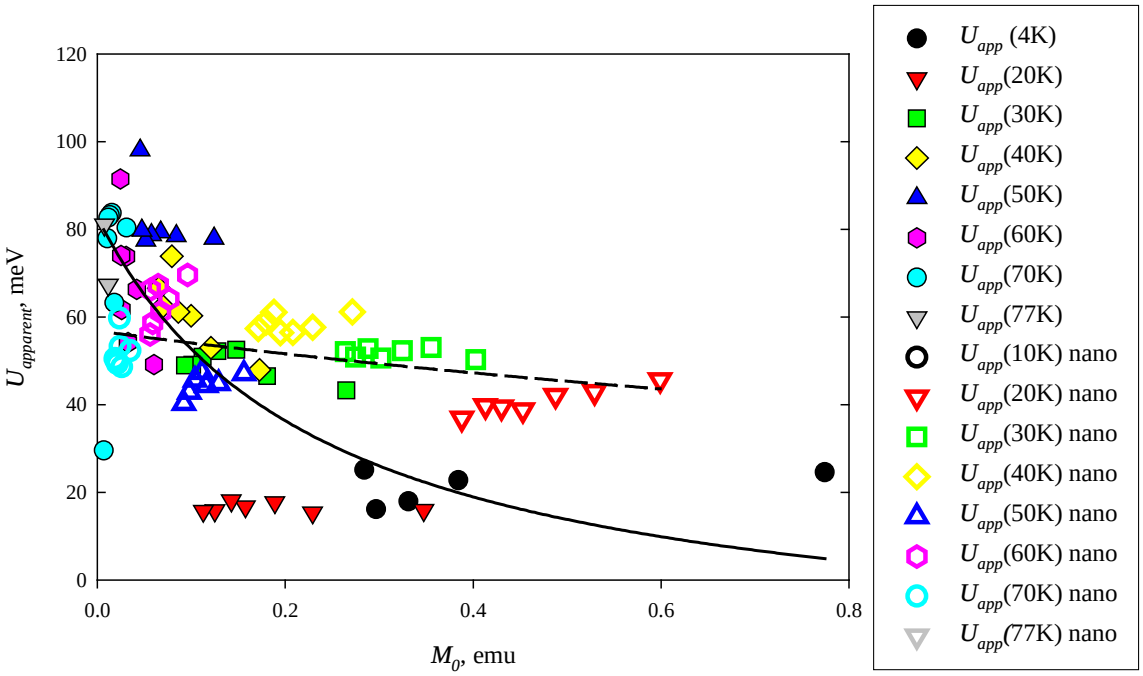

Figure 5.18. Summary of $U_{apparent}$ and U_0.

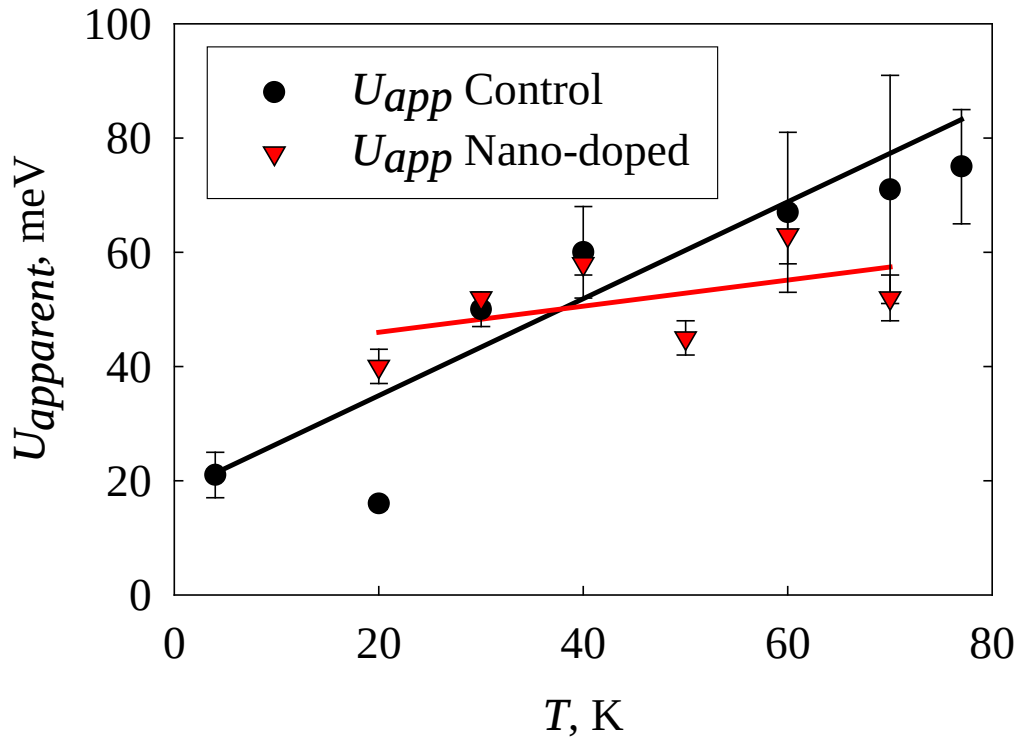

Figure 5.19. U_{app} vs T – to show lower temperature independence of U_{app} for nano-pinned sample.

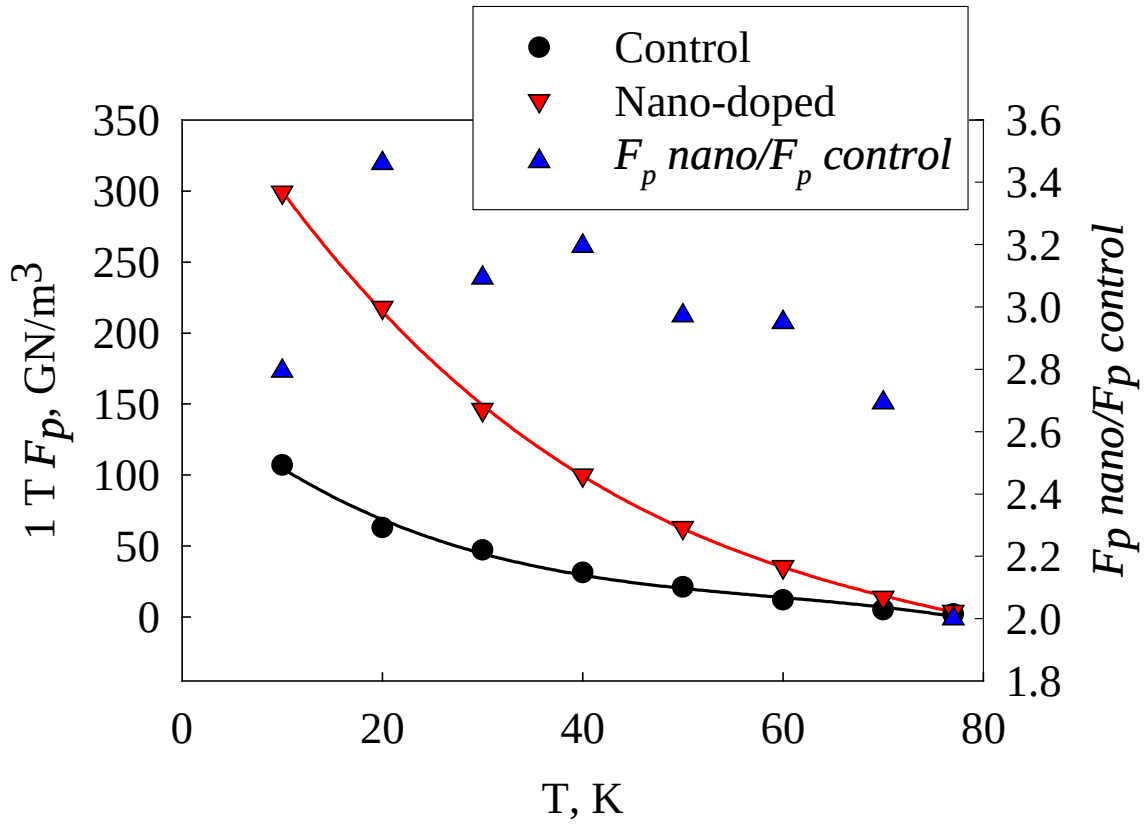

Figure 5.20. Temperature dependence of 1 T F_p for nano-pinned sample and control sample.

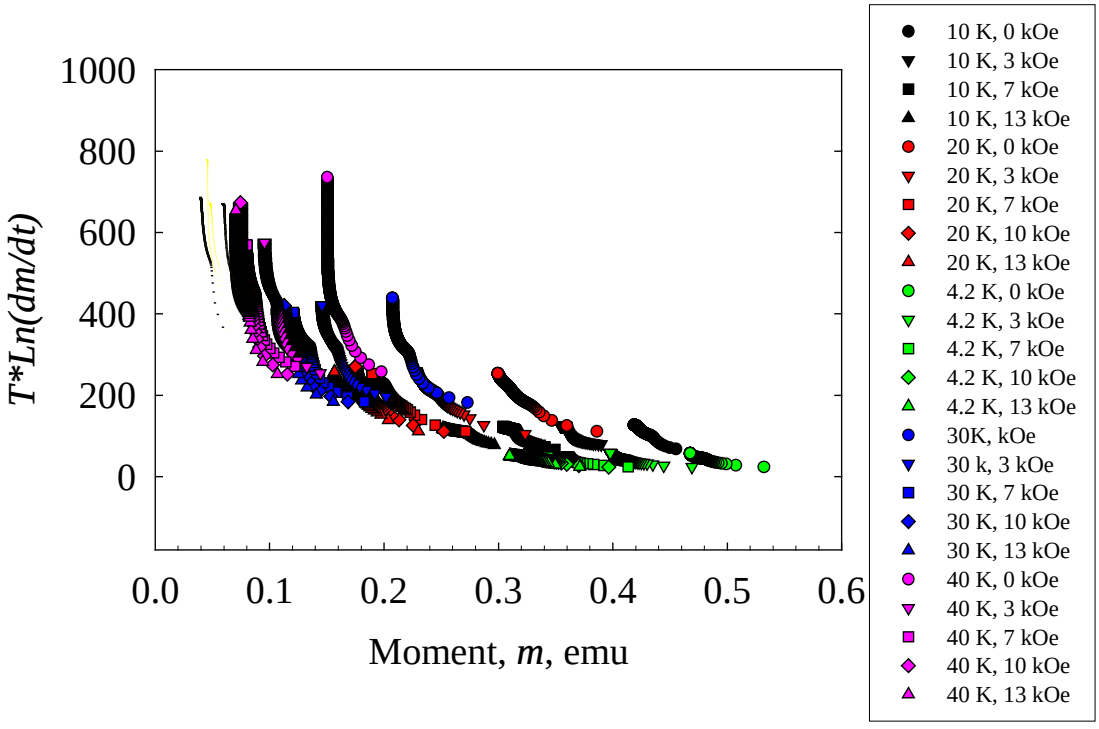

Figure 5.21. Decay (drift) measurements made at various temperatures and fields, al-la Maley plot [4].

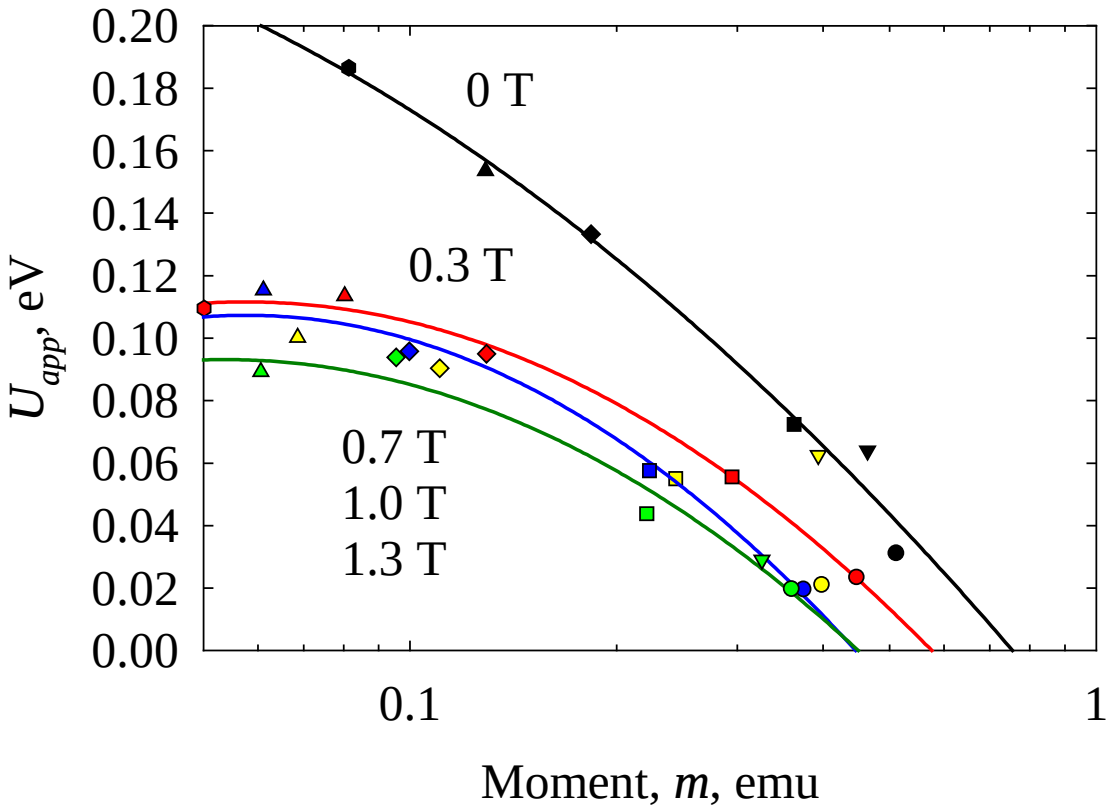

Figure 5.22. $U_{apparent}$ from Drift measuremnts. Note U_{app} is significantly higher than for ramp rate experiments due to higher electric field.

REFERENCES

[1] P. Barnes and M.D. Sumption, Submitted to ASC 2004.

[2] M.D. Sumption, Pinning Force and U_0 In YBCO Thin Film Conductors With and Without Artificial 211 Inclusions, Report, 2003.

[3] Folytn et al., LANL (1996) YBCO/Ni/YSZ 1 micron microbridge.

[4] M.P. Maley, J.O. Willis, H. Lessure, and M.E. McHenry, "Dependence of Flux-Creep Activation Energy upon Current Density in Grain-Aligned YBCO", Phys. Rev B 42 (1990) 2639.

6.0 Weak Link Studies

Three samples were fabricated of YBCO PLD conductor. The first had no stripe, the second one stripe, and the third two stripes. The purpose was to see how effective laser striping could be at reducing magnetization, and if the strength of the resulting weak line could be could be controlled. The magnetization for the one stripe and no stripe are shown below.

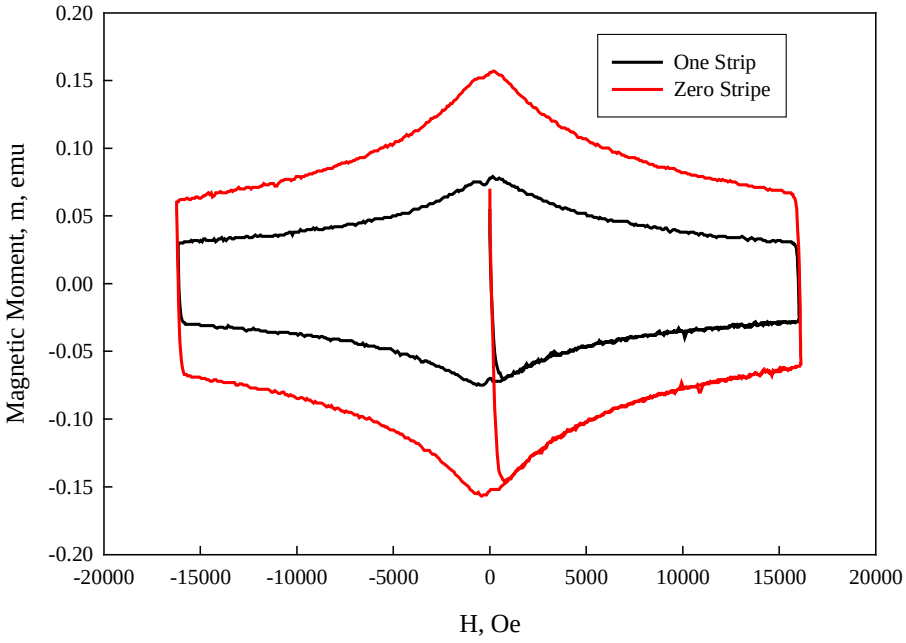

Figure 6.1. *M-H* at 4.2 K for one-strip and no-stripe sample.

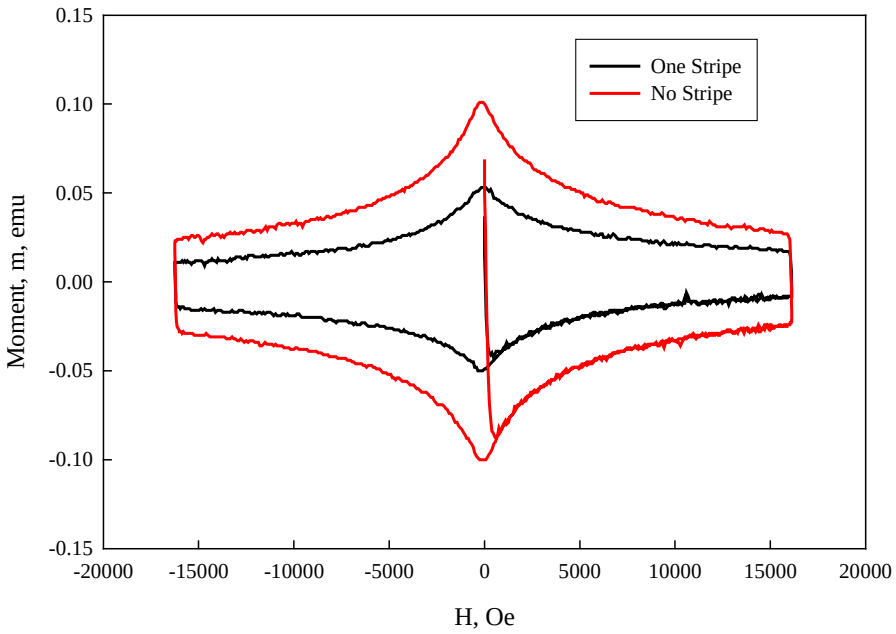

Figure 6.2. *M-H* at 25 K for one-stripe and no-stripe sample.

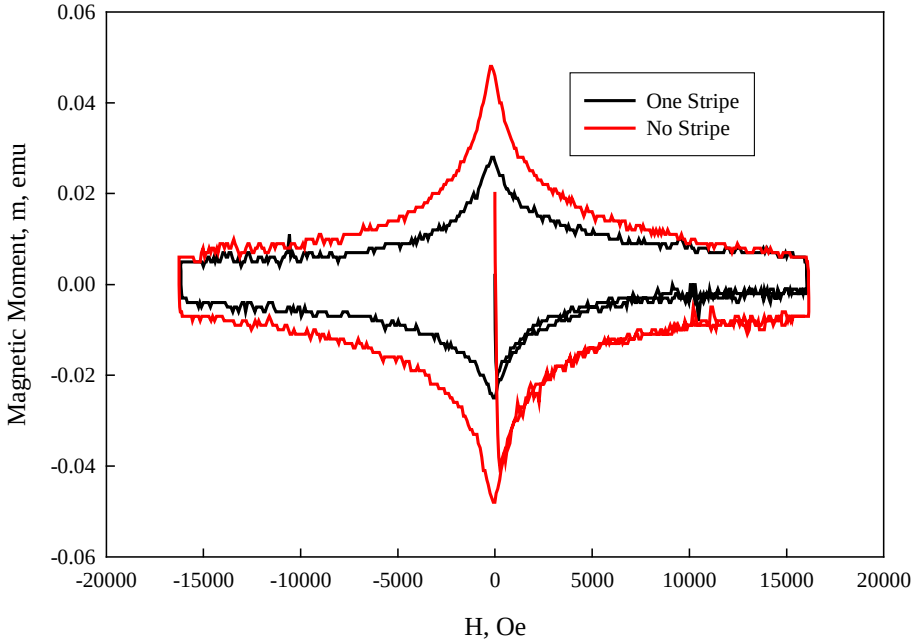

Figure 6.3. M-H at 50 K for one-stripe and no-stripe sample.

7.0 Other Consultation

7.1.0. Large Current Measurements for YBCO (J. Murphy Discussions)

In order to perform large current J_c measurements for any superconductor, the heat balance must be kept in mind. A rough rule of thumb is that for samples carrying less than 300 A, a 3 cm short sample measurement can be acceptable, for 1000 A measurements, 10 cm^2 is roughly sufficient. ***This presumes immersion in liquid cryogen, the limits are much smaller for gas-cooled samples***. Figure 7.1 below shows the heat removal possible for liquid helium from a sample surface. Here we see the larger difference as we go from the nucleate to film boiling conditions. Of course, the temperature axis is expanded greatly for potted samples. Similar data is available for liquid nitrogen. In this case, the per area heat dissipation which becomes unstable (50 mW/cm2 for He) is 500 mW/cm2. However, the temperature difference is larger too – roughly in the 1 K range. This helps greatly, however, and is should be possible to push relatively big currents through a 1 cm^2 well-soldered contact for YBCO, presuming the Ag-YBCO contact is good. Pb-Sn solder in liquid helium dissipates about 20 mW/cm^2 at 1000 A for a 10 cm^2 solder joint. This would seem to suggest a 1 cm^2 contact area would be sufficient, as long as the sample was in liquid nitrogen. However, the situation would be quite different for gaseous cryogens, where much more stringent A limitations would be present. A similar curve for LN_2 is shown in Figure 7.2.

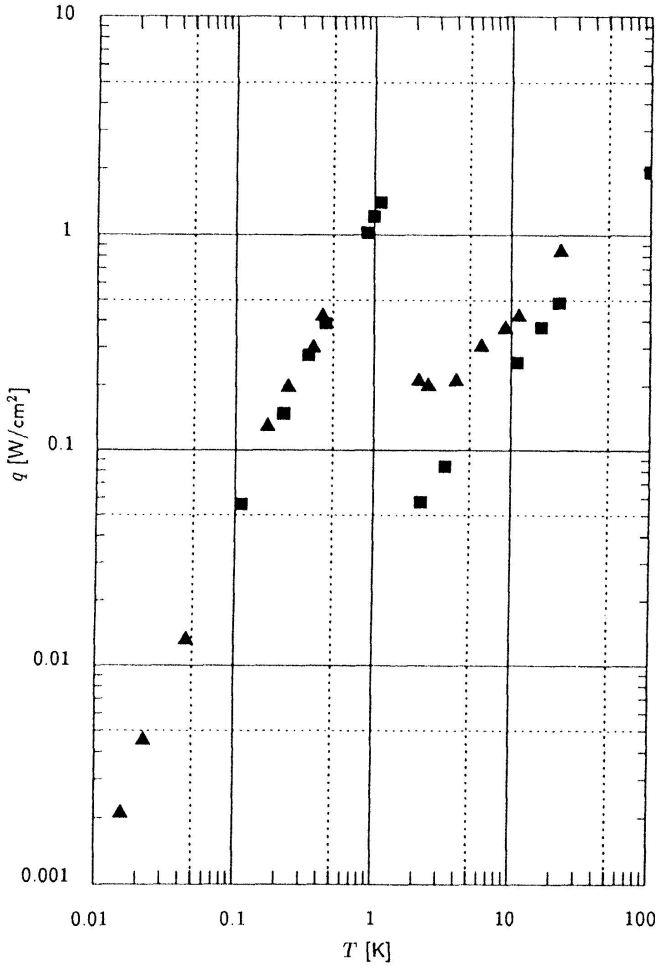

Figure 7.1. Heat dissipation by pool-boiling liquid helium – Iwasa [1].

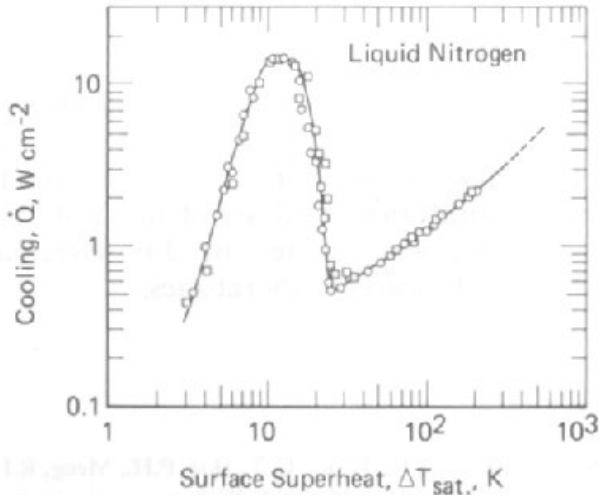

Figure 7.2 Q vs Surface dissipation for LN2.

Design Consultation on Large Rotating Machine (J. Murphy)

Several different machine designs for reaching large *B*dB/dt* values have been under consideration at the AFRL. They can be divided into two different approaches. In the first, the approach is direct, a static sample is immersed in a magnet with a given *B*dB/dt*. In the second, *B* is constant for the magnet, but there is a relative motion between the sample and the coil. For the first approach, the main problem is the winding. The power supply must also be properly designed, but because the system is assumed either to be wound with superconductors or cryogenic Cu, the actual resistance of the coils is much lower than their reactance, thus a proper resonant circuit design can made the power supply requirements manageable. The coil, on the other hand, is more difficult. The two main issues are the heat generated, and the breakdown voltage at the terminals.

If the coil is to be wound with superconductor, the superconductor required is the very conductor under development. That is, no conductor with sufficiently small losses yet exists. On the other hand, if cryogenic Cu is to be used, we must dissipate the ohmic losses. As we can see from the above discussion, this will be much more difficult for Helium, even though the resistance is smaller. While the losses will be an order of magnitude lower, (resistivity is 10 times lower) the boiloff will be quite large. In any case, Nitrogen is much less costly, and so it must be the cryogen of choice. We note that even at 150 mT and 200 Hz, the boiloff of Nitrogen is significant [Sumption, unpublished report]. Thus, any system made to run continuously would have to deal effectively with this issue. Beyond this, voltages on the terminals of such a magnet would be large. The present system at OSU has terminal voltages of about 2 kV. Running to 500 Hz and 1 T would push this up into a range where special techniques would be needed to prevent arc-over.

A possible modification of this route would be to use a pulse system. We can consider a room T system as a pulse system in order to investigate the feasibility. The idea here was to remove the difficulty of designing a rotating cryogenic system by operating a

system in a pulse mode at room temperature. The sample would be static, but the coil system would rotate.

Considering the system shown in Figure 7.3, we have to calculate B. Using $B = \mu NI/L$, we find that to get a 1 T field, we must have roughly 2000 turns, assuming 20 A in the wire. If we can push to 40 A, this would be reduced to 1000 turns, and fit in a 50 mm x 20 mm pack winding for 1 mm OD wire. The mass of such of winding (Cu only) would be approximately 2.7 kg. The length of Cu would be 32 m, and the resistance of such a winding would be (assuming 1.75 μΩcm for Cu at RT), roughly 65 Ω. The power generation would then be 1040 W.

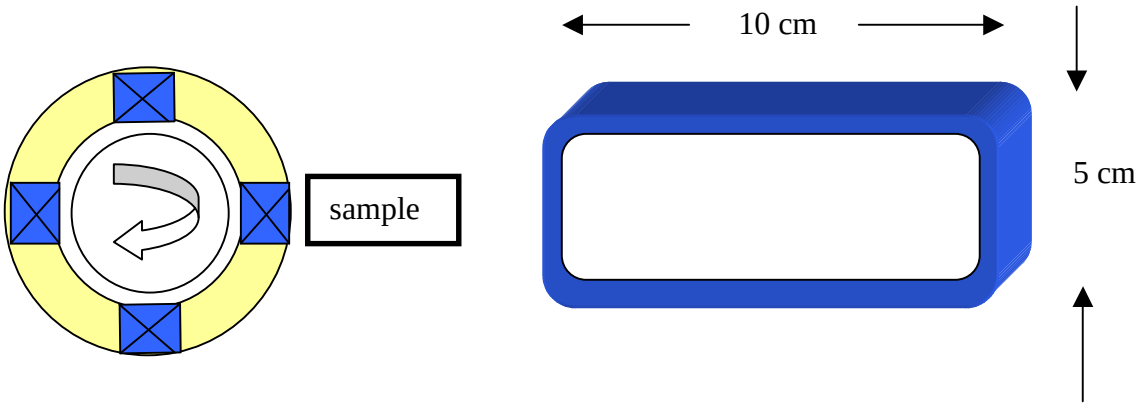

Figure 7.3. Schematic of pulse-Rotating system.

Using ΔT = 0.385 J/g x 2700 g x 1040 W * τ, where τ is the pulse time, we find that if we allow ΔT to be 300 K, the allowable time for measurement is 2 msec. Clearly, then, the Cu must be cooled, either by oil (as would be done for more typical generators) or by cryogen. In addition, such a system would require large voltages to ramp up the current for such a short pulse. The inductance is such a system would be roughly 50 mH, which would require $\varepsilon = d\phi/dt\ N$ = 2.5 kV. This latter value is possible, as we have seen before. However, the measurement time is very limited, making the overall design unattractive. This brings us back to a rotating cryogenic system or a mock up of a noncryogenic generator with force-flow oil.

Comments on Noise in Magnetometer Measurements

Noise is apparent in some of the *M-H* loops taken at the AFRL. Questions have arisen as to what the origin of this noise is, and, most importantly, whether it invalidates the data, or just makes it less pretty. Attention was given to putting the powders in something to affix them, this did not solve the problem. Sample rod rubbing could be another potential noise source. However, two things can be noticed which point to a different origin. The first is that the noise only occurs for small moment measurements on samples which have a significant baseline. The second is the regularity of these “bumps”. The most likely explanation is some kind of digitations noise. Figure 7.3 shows a loop which has had a baseline tilt removed (the tilt can occur for a number of reasons, including response of the powders and/or sample holder). Figures 7.4 and 7.5 show in more detail the jump. This jump seems regular in size, and occurrence. However, its size does not exactly correspond to the stated resolution of the machine.

In general, the large moment present as a baseline (either the reversible magnetization of the SC, or other signals) is causing the machine to need a given moment setting in order to take measurements. The smaller moment changes corresponding to the measurement of interest (the irreversible part) therefore has digitations noise. However, this digitations noise seems larger than would be possible from the manufacturer specification. This specification is somewhat vague, however, and the averaging process used is not clear. Plans were made for AFRL personnel to contact the manufacturer to investigate this possibility.

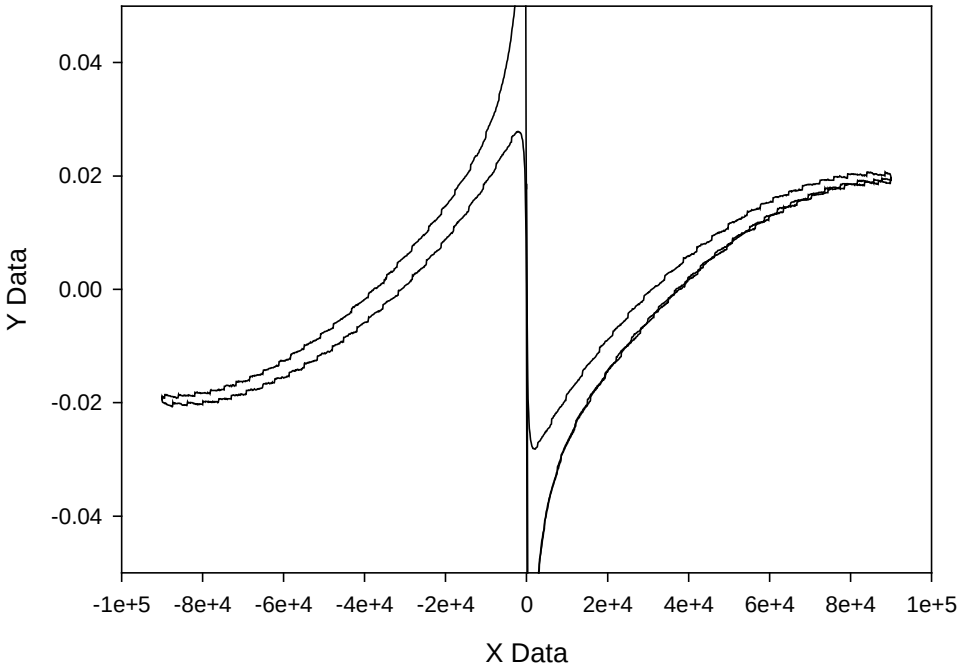

Figure 7.3 Larger view of sweep data. Tilt corrected, digitations noise already evident.

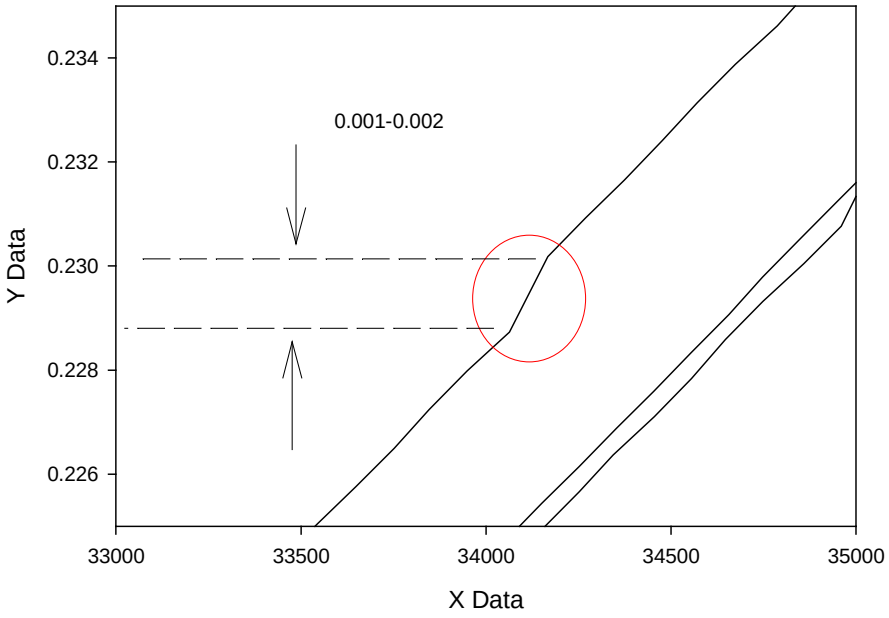

Figure 7.4. Close-up of digitations noise.

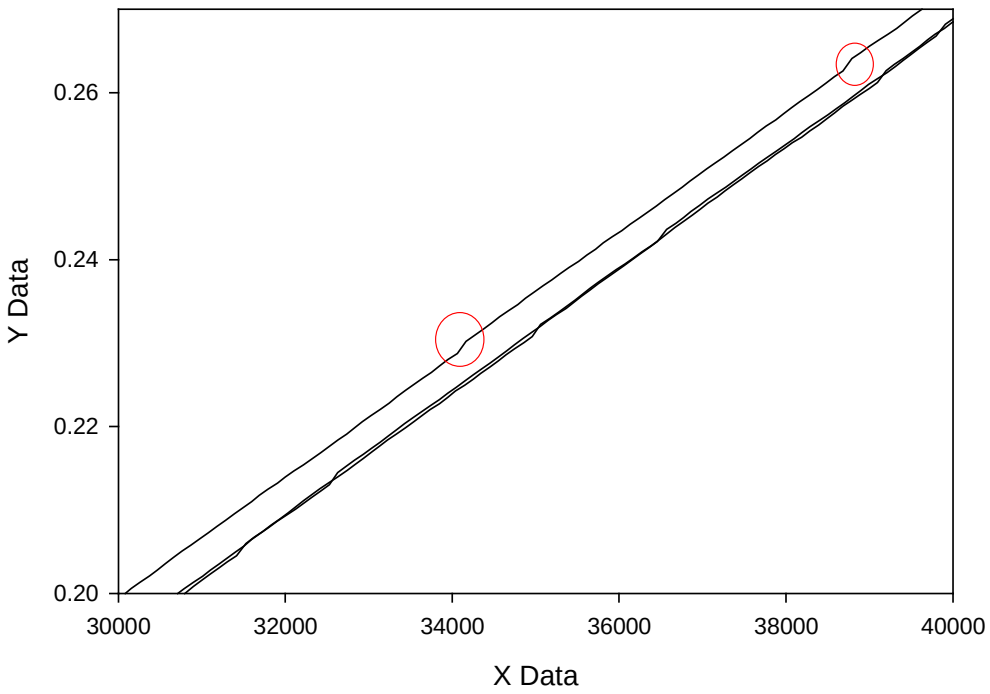

Figure 7.5. Regularity of digitations noise.

8.0 Future Challenges

1. **Completion of various papers in the works, specifically one on N-effects**
2. **Finalization of AC loss measurements on a set of S1-S6 like samples**
3. **Generation of a pinning-related paper**
4. **Completion of an AC loss/Generator paper**
5. **Further Investigation of weak link measurements**
6. **Proper Understanding of AC Susceptibility Measurements for YBCO films**
7. **Deeper Understanding of Pinning Effects in layered structures**
8. **Direct Measurement of J_c out to higher fields at 77 and 65 K**

9. 9.0 Presentation, Papers, and Patents at least partially supported by Summer Faculty Effort

PAPERS

1. ***Paper and presentation to*** the Applied Superconductivity Conference, accepted, to be published in IEEE Trans Supercon. June 2005: "**AC Losses of Coated Conductors in Perpendicular Fields and Concepts for Twisting"** Mike D. Sumption, Paul N. Barnes, and Edward W. Collings.
2. ***Paper in Preparation***, (Cryogenics) "**Review of High Power Density Generators: Present State and Prospects for Incoporating YBCO Windings**", Paul N. Barnes, Michael D. Sumption, Gregory L. Rhoads.
3. ***Paper in Preparation*** (Applied Phys Lett.) "**Filament Width and Conductor thickness Influence on YBCO Coated Conductor Loss**", M.D. Sumption, M. Bhatia, and E.W. Collings, P. Barnes, T. Haugan, J. Tolliver.
4. ***Paper, published in Superconductor Science and Technology*** "**AC Loss in Striped (Filamentary) YBCO Coated Conductors Leading to Designs for High Frequencies and Field-Sweep Amplitudes**", M.D. Sumption, E.W. Collings, and P.N. Barnes.

PRESENTATIONS

1. ***Presentation (Oak Ridge) AC Loss in Striped (Filamentary) YBCO Coated Conductors* – Some items we know, Some we would like to,** M.D. Sumption, E.W. Collings.
2. ***Presentation at the Applied Superconductivity Conference, "J_c, F_p,* and U_0 Enhancements for YBa2Cu3O7-d Thin Films with Y2BaCuO5 Nanoparticulates",** M. Sumption, Timothy J. Haugan, and P.N. Barnes.

PATENTS

1. ***Patent Application #1:* "A YBCO Conductor Package with Filamented and Twisted Strands Using a Rutherford Geometry",** P.N. Barnes, M.D. Sumption
2. ***Patent Application #2:* "Armature Winding Methodology for High Temperature Superconducting Machines",** P.N. Barnes, M.D. Sumption, and L. Long.

APPENDIX A: COMPLETED AND/OR ACCEPTED PAPERS

AC Losses of Coated Conductors in Perpendicular Fields and Concepts for Twisting

Mike D. Sumption, Paul N. Barnes, and Edward W. Collings

***Abstract*—AC losses for striped and unstriped YBCO coated conductors are presented. The loss for a sample subdivided into 10 filaments is shown to be reduced by the expected factor of 10. Various concepts for introducing strand twisting are investigated, and some estimates are given for their superconductive filling factors and the resulting twisting-induced strain. Additionally, the concept of winding induced effective twist is described, and the effective induced twist pitch is shown to be approximately two times the length of the winding. The influence of end-soldering of the strands is described, and simple estimates of the coupling losses are given for a striped strand with soldered ends in conjunction with an effective induced twist.**

***Index Terms*—AC losses, striping, twisting, YBCO.**

I. Introduction

THE emerging availability of high performance YBCO coated conductor is stimulating the design of superconducting machinery based on YBCO coated conductor capabilities. Numerous applications are being envisioned, one which is based on a US Air Force (USAF) desire for a high frequency (f), high field amplitude (H_m), generator with HTS field—and (eventually) stator windings. The need for hundreds of Hz (up to 500 Hz), a $B_m = 1$ T, and acceptable AC loss/m of conductor pushes the properties of striped coated conductor to the very limit of attainability.

Under such conditions, especially the higher frequency end of the spectrum, it will be essential to determine and minimize AC losses. AC magnetic field losses are greatest when the field is normal to the wide face of the tape (face-on, FO) and least in when it is parallel to that face (edge-on, EO). In practice it will generally not be possible to engineer the pure EO condition. Some FO component of the applied field (the so-called "stray field") will always be present and will call for special conductor designs to minimize that loss. Stray field loss components are expected for transformers and inductors, as well as all-superconducting generators and motors, which represent extreme examples.

To combat FO loss in general the conductor is subdivided into N_f parallel filaments running down the length of the tape. To prevent magnetic re-coupling of these filaments it is necessary to limit the effective length over which these filaments are exposed to a field of a given direction. With round multifilamentary (MF) strands, twisting is routinely applied. But for coated conductors, which are high aspect ratio tapes, the feasibility of twisting has been questioned. Certainly, simple twisting, as proposed by Oberly and Carr [1] is more conceptual than directly applicable, for two primary reasons. In the first instance there are physical limits to twist pitch reduction for a coated conductor tape because of the significant strain induced. Not only this, but if simple helical twisting is used, the conductor "envelope" occupies a large volume and severely reduces the engineering critical current density. Even so it is important to recognize that some kind of twisting or transposition will be needed in a conductor of respectable length with its required low resistance current contacts at each end. In practice the twisting, if not performed on the conductor itself as part of the processing sequence (as in round LTS MF strands), may occur naturally during the winding of the superconducting machine. In any case, in order to control loss, both filamentary subdivision and twisting are needed. In this paper we describe and compare several possibilities for incorporating twist, and offer rough estimates of induced strain and possible filling factors. First, however, we will show some results on the loss reductions which have been achieved by striping.

Manuscript received October 5, 2004. This work was supported by the Air Force under an SBIR subcontract from Hyper Tech Research, Inc., and by a Summer Faculty Research Program of the AFRL.

M. D. Sumption and E. W. Collings are with the LASM, Materials Science and Engineering Department, OSU, Columbus, OH 43210 USA (e-mail: mdsumption+@osu.edu).

P. N. Barnes is with the Air Force Research Laboratory, Wright-Patterson AFB, OH 45433 USA.

Digital Object Identifier 10.1109/TASC.2005.848233

II. AC Loss in Striped Conductors

A. Loss Measurements

Two segments of IBAD-based coated conductor from Superpower were measured in this study. The first was as-received. Ten laser cuts were made in the second to filamentarize the sample. Segments 4 cm long were then measured in an integration magnetometer type AC loss rig. Details of sample laser machining, AC loss rig set-up, further experiments, and a study of loss components for higher frequencies are given in [2]. The results of AC-loss measurements on the Superpower striped and unstriped tapes are given in Fig. 1, where loss reduction with striping is seen. In an AC field of amplitude B_m we note that the per cycle loss per unit volume in SI units is given by [4]

$$Q = wJ_cB_m + \frac{1}{4}\frac{f}{\rho}L_p^2B_m^2 \tag{1}$$

where w is the conductor width, and L_p is a twist pitch (which can be replaced by $2L$ for untwisted samples of length L). We expect then, that the striping of the strand into ten filaments should reduce the loss by factor of ten, which it does. However, looking at the second (coupling loss) term it can be seen that we will re-introduce loss as we go to the longer conductors required for real use, unless we induce a twist pitch. The other apparent alternative, making the transverse resistivity, ρ, very

1051-8223/$20.00 © 2005 IEEE

Authorized licensed use limited to: AFRL Technical Library. Downloaded on April 29, 2009 at 11:29 from IEEE Xplore. Restrictions apply.

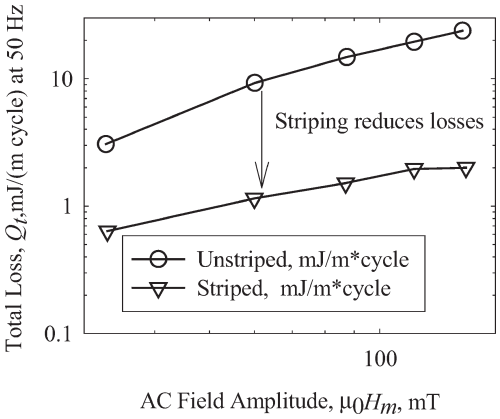

Fig. 1. AC losses in striped and unstriped coated conductors.

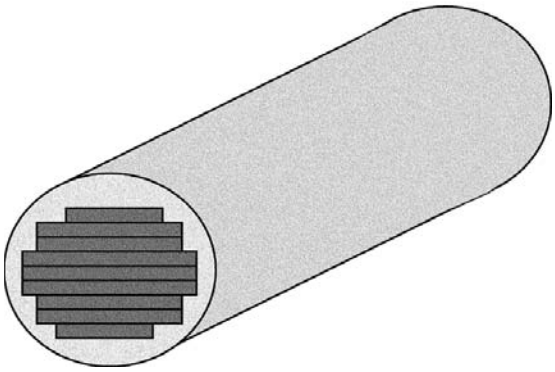

Fig. 2. A stacked, round, twisted conductor assembled from several coated conductor tapes of different widths.

large, has its limits because of the needed low resistivity, current-introducing end-connections.

III. Introducing Filamentary Twist

A. Simple Twist

In order to take advantage of the loss reductions offered by striping, transposition of the filaments (typically twisting of the strand) is needed. An initial concept for twist introduction was originally proposed by Carr and Oberly [2]. However, for a single conductor (strand) which has been striped or filamented, simple twisting leads to very high reductions in J_e. Defining λ as the superconductor-to-total area fraction, we get

$$\lambda \approx \frac{tw}{\pi\left(\frac{w}{2}\right)^2} \approx \frac{t}{w} \tag{2}$$

where t is the YBCO thickness and w is the width of the conductor. If $t = 2\ \mu\mathrm{m}$ and $w = 1\ \mathrm{cm}$, then $\lambda = 1/5000$, and $J_e = 2\times10^{-4}\, J_c$. This would lead, for instance, to a $1\ \mathrm{MA/cm^2}$ conductor with a J_e of $200\ \mathrm{A/cm^2}$. This is perhaps an order of magnitude below useful levels. The strain for such a conductor is maximized at its edges, and is given approximately by [4]

$$e \approx \left(\frac{\pi w}{2L_p}\right) \tag{3}$$

If the allowable strain is 0.5%, then this would lead to a minimum L_p of 30 cm or so, assuming a 1 cm wide conductor.

B. Stacked Twisted Conductors

In the case of a stacked, round conductor, the J_e is improved, since it becomes approximately that of the strand itself, as shown schematically in Fig. 2. If t is 2 μm and the underlayer is 100 μm, the $\lambda = 1/50$. If, however, stabilizer is added, this must also be accounted for. If a 1 mm thick stabilizer is added, then $\lambda \approx 1/500$ (equal to that of the strand). After twisting, the strain is still determined by the edges of the center conductors, and thus the same minimum L_p limitation is present (30 cm or so for a 1 cm wide conductor).

C. Hexagonal (Polygonal) Geometry Conductors

We can imagine vastly reducing the twisting-induced strain using a hexagonal geometry conductor, as shown in Fig. 3. Here there are two strain contributions, that due to in-plane bending, and that due to out-of-plane bending. In plane bending must be carefully controlled, but if the conductor is wound onto a shaped hexagonal central element, the in-plane can in theory be reduced to very small values. The out-of-plane bending is minimal, being approximately given by (again assuming a neutral axis conductor)

$$e \approx \frac{t}{\frac{L_p^2}{4d} + d} \tag{4}$$

which becomes t/d in the limiting case of very tight twist, where d is the effective diameter of the central hexagonal element. The L_p of such a conductor has no serious lower limit, at least any stemming from strain considerations. The λ of such an arrangement is given by

$$\lambda \approx \frac{2\pi t\left(\frac{d}{2}\right)}{\pi\left(\frac{d}{2}\right)^2} = \frac{4t}{d} \tag{5}$$

This leads to $\lambda \approx 4/5000$ for one layer of conductor, but this can be increased by adding n consecutive layers, thus

$$\lambda_t \approx \frac{4n}{5000} \tag{6}$$

which for $n = 10$, increases to 1/100.

D. Rutherford Geometry Conductors

For Rutherford type geometries (see also [3]), strain per bend will be given by

$$e = \frac{t_{YBCO}}{t_{cab}} \tag{7}$$

This gives, for a 0.5% strain limitation and a $t = 2\ \mu\mathrm{m}$ (and assuming a neutral bending axis for the conductor itself) a limitation not on L_p, but on Rutherford core thickness, in this case to a core no thinner than 1 mm. A one-layer Rutherford cable

Authorized licensed use limited to: AFRL Technical Library. Downloaded on April 29, 2009 at 11:29 from IEEE Xplore. Restrictions apply.

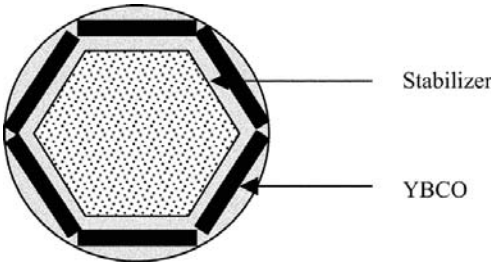

Fig. 3. Hexagonal geometry conductor with internal Cu stabilizer and hexagonal YBCO elements.

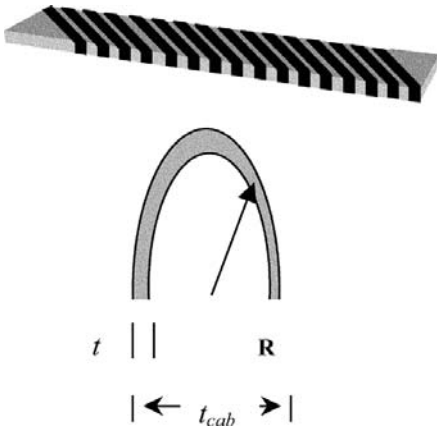

Fig. 4. Rutherford geometry conductors. Top shows basic Rutherford geometry, bottom shows cross sectional geometry and parameters for strain calculation.

would then have a $\lambda = 1/250$, and the λ would increase linearly with the number of layers, as for the hexagonal geometry conductor. The Rutherford conductor might be easier to manufacture, however, especially while retaining a low in-plane strain (Fig. 4).

IV. Effective Twist

The losses of patterned YBCO conductors have been considered in detail in [1]. Let us assume for the moment that we will stripe the conductor reducing hysteresis loss, and focus now on coupling loss, which in the nonsaturated regime (second term in (1)) is proportional to L_p^2/ρ. Usually coupling loss is reduced by reducing L_p and by increasing the interfilamentary ρ. It can also be controlled by limiting the "active length" of a tape segment (i.e. the length exposed to field of a given orientation)—see below. If however, the conductor is untwisted the losses return to that of the unstriped conductor as conductor length, L, becomes large (assuming noninfinite ρ).

Note here that even if the filaments were fully insulated from one another over the main section of the conductor, these filaments are necessarily soldered together at the end so that transport current can be introduced in a practical way. Thus, a truly untwisted conductor, even with insulating filaments, would suffer large losses because of the end connections. The use of a simple twist [3] is difficult, and vastly reduces the filling factor of the coil pack. Fortunately, it is also known that

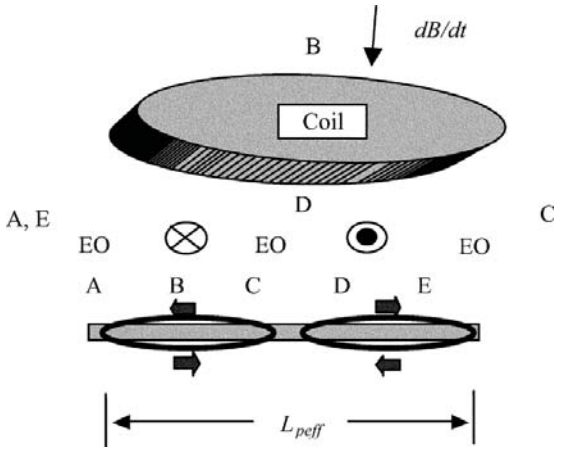

Fig. 5. Top: racetrack coil with externally applied fields and winding geometry induced effective "twist". Bottom: tape is shown "unwound" with spatial variation of field given and induced coupling currents shown to have spatial extent $L_{peff}/2 \times w$. Corresponding positions on tape as wound on coil and "unwound" are tagged with letters A–E.

oscillations in the direction of the applied field will generate an effective twist. In such cases, the effective twist pitch is similar to the period of oscillation of the field. In general, if a segment of filamentarized conductor is exposed to spatially varying fields, it is the net flux through the segment that will determine the effective active length. Related effects have been seen in low temperature SC based cables [5], [6] and LTSC strands themselves [8], [9]. Fig. 5 displays a schematic of how this effect would operate for a racetrack (e.g. a rotor) coil exposed to an in-plane magnetic field. The patterned conductor would experience fields which would have a periodic variation (in this case approximated as a square-wave) such that the field experienced by opposite sides of the coil would have the same magnitude but opposite signs.

Imagine the coil in Fig. 5 to be wound with striped conductor. A, B, C, D, and E are positions along a tape conductor used to wind one complete turn of the coil. Above, a field applied in the plane of the coil (the least favorable orientation for loss) is shown. Below, the resulting field orientations in corresponding sections are shown, along with the resulting coupling eddy current loops that form.

Since

$$\varepsilon = -\frac{d\Phi}{dt} = -\frac{dB}{dt}A \tag{8}$$

the emf, ε, is induced with a periodicity equal to the major axis of the racetrack coil. This makes the effective twist pitch equal to twice that length for square-wave field oscillations and something slightly less than the perimeter for solenoid-like windings. Thus, for racetrack coils, $L_{eff} = 2L_{major\ axis}$, while for solenoid-like coils of radius R, $L_{eff} = \sqrt{2\pi R}$. We will then have the situation depicted in Fig. 6, with a field oscillation that can be described as a square wave, and a resulting net stray flux. Even if there is no interfilamentary conductivity, except that at the ends conferred by the solder joint used to connect to the outside world, the losses will be large if there is no field reversal (a long length of tape in free space). However, for our coil, this is

Authorized licensed use limited to: AFRL Technical Library. Downloaded on April 29, 2009 at 11:29 from IEEE Xplore. Restrictions apply.

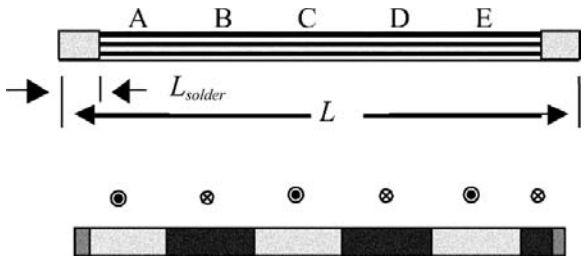

Fig. 6. Striped coated conductor with soldered ends in a spatially changing field.

not the case. Let us assume for simplicity that the filaments are totally insulated from one another except at the very ends. For such a case $\rho_{eff} = \rho_{solder}(L/2L_{solder})$. Of course we must be careful which volumes we normalize to within the loss equations using this expression to make sure they are compatible to the definition of the resistivity. In our case we will use the overall dimensions of the tape for all considerations of this kind.

Using (8) above, along with ohms law, we get the coupling current, I, as

$$I = \frac{\varepsilon}{R} = \frac{-\dot{B}A}{R_{solder}} \tag{9}$$

The $A(dB/dt)$ referred to is the net value. This will be controlled by the amount of unbalanced loop area exposed to dB/dt (as in Fig. 6). The maximum such area will be proportional to the effective winding pitch, hence $wL_{winding}$. In which case, the coupling current is

$$I_{\max} = \frac{-\dot{B}wL_{winding}}{R_{solder}} \tag{10}$$

The per-unit-length power is $P_l = (I_{max}^2 R_{solder})/L$, which becomes

$$P_l = \frac{\dot{B}^2 w^2 L_{winding}^2}{R_{solder} L} \tag{11}$$

where L is the length of the whole coil, and w is the conductor width. This of course presumes no interfilamentary contact other than the solder. If such contact is present we will add a term which does not drop as $1/L$—this is analogous to the traditional loss term coming from coupling currents.

V. Conclusion

Coated conductors aimed at low loss applications where significant time varying external fields are present must be not only striped, but also must have some field reversal or twisting present. Several conductor geometries are possible which do this while having lower strain and larger filling factors than the simple twisted single strand geometry. In the case of hexagonal and Rutherford conductors filling factor improvements and much lower effective twist pitch lengths are possible. Overall the Rutherford type geometry seems to be a good compromise for performance and manufacturability.

It is also possible to limit loss in situations where the fields experienced by the conductor are oscillating spatially as well as in time. In these cases the losses will be proportional to the square of an effective twisting length (a length similar to twice the winding length of the coil). Finally, the influence of end-soldering is described in this context.

Acknowledgment

The authors would like to thank V. Selvamanickam from SuperPower for YBCO coated conductor samples.

References

[1] W. J. Carr and C. E. Oberly, "Filamentary YBCO conductors for AC applications," *IEEE Trans. Appl. Supercond.*, vol. 9, pp. 1475–1478, Jun. 1999.

[2] M. D. Sumption, E. W. Collings, and P. N. Barnes, "AC loss in striped (filamentary) YBCO coated conductors leading to designs for high frequencies and field-sweep amplitudes," *Supercond. Sci. Technol.*, vol. 18, pp. 122–134, Jan 2005.

[3] W. J. Carr and C. E. Oberly, "Possibilities for use of coated superconductors in AC applications," *Adv. Cryo. Eng.*, pp. 773–780, 2004.

[4] W. J. Carr, *AC Loss and Macroscopic Theory of Superconductors*, 2nd ed: Taylor and Francis, 2001.

[5] G. Ries and S. Takács, "Coupling losses in finite length of superconducting cables and in long cables partially in magnetic field," *IEEE Trans. Magn.*, vol. 17, pp. 2281–2284, Sep. 1981.

[6] S. Takács, N. Yanagi, and J. Yamamoto, "Size effect in AC losses of superconducting cables," *IEEE Trans. Appl. Supercond.*, vol. 5, pp. 2–6, Mar. 1995.

[7] A. Verveij, "Electrodynamics of Superconducting Cables in Accelerator Magnets," PhD Thesis, University of Twente, Department of Low Temperature Physics, Enschede, The Netherlands, 1995.

[8] M. D. Sumption and E. W. Collings, "Influence of cable and twist pitch interactions on eddy currents in multifilamentary strands calculated using an anisotropic continuum model," *Adv. Cryo. Eng. (Materials)*, vol. 40, pp. 579–587, 1994.

[9] K. R. Marken, A. J. Markworth, M. D. Sumption, E. W. Collings, and R. M. Scanlan, "Eddy current effects in twisted and wound SSC strands," *IEEE Trans. Magn.*, vol. 27, pp. 1791–1795, 1991.

Authorized licensed use limited to: AFRL Technical Library. Downloaded on April 29, 2009 at 11:29 from IEEE Xplore. Restrictions apply.

INSTITUTE OF PHYSICS PUBLISHING SUPERCONDUCTOR SCIENCE AND TECHNOLOGY
Supercond. Sci. Technol. **18** (2005) 122–134 doi:10.1088/0953-2048/18/1/020

AC loss in striped (filamentary) YBCO coated conductors leading to designs for high frequencies and field-sweep amplitudes

M D Sumption[1], **E W Collings**[1] **and P N Barnes**[2]

[1] Laboratories for Applied Superconductivity and Magnetism, Materials Science and Engineering Department, The Ohio State University, OH 43210, USA
[2] Propulsion Directorate, Air Force Research Laboratory, Wright-Patterson AFB, OH 45433, USA

Received 17 June 2004, in final form 18 August 2004
Published 23 November 2004
Online at stacks.iop.org/SUST/18/122

Abstract
AC losses of YBCO coated conductors are investigated by calculation and experiment for the higher frequency regime. Previous research using YBCO film deposited onto single-crystal substrates demonstrated the effectiveness of 'striping' or filamentary subdivision as a technique for AC loss reduction. As a result of these studies the idea of subdividing YBCO 'coated conductors' (YBCO, overlayer, and even underlayer) into such stripes suggested itself. The suggestion was implemented by burning grooves into samples of coated conductor using laser micromachining. Various machining parameters were investigated, and the striping and slicing characteristics are presented. Loss measurements were performed on unstriped as well as striped samples by the pick-up coil technique at frequencies from 50 to 200 Hz at field sweep amplitudes of up to 150 mT. The effect of soft ferromagnetic Fe shielding was also investigated. The results of the experiments form a starting point for a more general study of reduced-loss coated conductor design (including hysteretic, coupling, normal eddy current, and transport losses) projected into higher ranges of frequency and field-sweep amplitude with transformer and all-cryogenic-motor/generator applications in mind.

1. Introduction

1.1. Background

Advances in the processing of multifilamentary (MF) superconducting strand particularly during the late 1960s and early 1970s [1] were accompanied by a burgeoning interest in large-scale applications of superconductivity [2]. Both DC (high field magnets for particle acceleration, magneto-hydrodynamic-based power, fusion, etc) and AC applications were being engineered. Among the AC applications being considered worldwide were generators, power transmission lines, transformers, and motors. Accompanying the development of AC applications the study of AC loss in superconductors was being actively pursued, particularly by a group at the then Westinghouse Research and Development Center. With MF composite strand as a model system in some cases, the Westinghouse group analysed loss due to: (i) an external AC magnetic field, (ii) the self field of an AC transport current, (iii) AC field and DC current, (iv) AC field and AC current. Although based on low temperature superconductors (LTS) at the time the theoretical findings of that group (as detailed by Carr in the first edition of his book [3] and elsewhere) are closely adaptable to the AC loss problems of high temperature superconductors (HTS) as explained in the second edition of Carr's book [4].

Now, just as before, the emerging availability of high performance strand is again stimulating the design and eventual construction of superconducting machinery but this time with HTS superconductors. Reaching maturity as HTS conductors

are the 'first generation' Ag-clad powder-in-tube composites based on Bi(Pb)–Sr–Ca–Cu–O, referred to as Bi:2212/Ag and Bi:2223/Ag. Under development and also being considered for energy and power applications are the 'second generation' HTS coated conductors based on epitaxial $YBa_2Cu_3O_x$ (Y:123, or YBCO). The particular conductor design goal being approached here is based on a US Air Force desire for a high frequency (f), high field amplitude (H_m), generator with HTS field- and stator windings. The need for hundreds of Hz (up to 500 Hz), a $\mu_0 H_m = 1$ T, and acceptable AC loss m^{-1} of conductor pushes the properties of striped coated conductor to the very limit of attainability.

1.2. The coated conductor

The coated conductor is a multilayer composite tape in which textured YBCO is supported on a strong metallic underlayer and protected in most cases by an Ag overlayer. Buffer layers, typically oxides, are sandwiched between the YBCO and substrate. Three major processing methods are in use, their designations referring to the techniques used to texture, or apply texture to, the underlayer creating an epitaxial template for the subsequent growth of the biaxially textured YBCO layer. They are known as the rolling-assisted-biaxially-textured-substrate (RABiTS) method, the ion-beam-assisted-deposition (IBAD) method, and the inclined-substrate-deposition (ISD) method [5]. In the RABiTS approach the biaxially textured template is induced in a metallic foil, typically an Ni alloy, by a series of deformations followed by a heat treatment. With IBAD and ISD the epitaxial template is created in an initial oxide buffer layer by controlled depositions using either ions (IBAD) or angular deposition (ISD) to induce the texture. Numerous oxides are available for buffering including CeO_2, YSZ, MgO, GdZO, $SrRuO_3$, $LaNiO_3$, and $(La, Sr)MnO_3$. The final tape is generally coated with a protective layer of Ag, and a Cu layer may be added for stabilization.

1.3. Conductors for AC applications

There is a need for an AC-tolerant YBCO coated conductor for 60–500 Hz applications. Under such conditions, especially at the higher frequency end of the spectrum, it will be essential to determine and minimize the AC losses. AC magnetic field losses are greatest when the field is normal to the wide face of the tape (face-on, FO) and least when it is parallel to that face (edge-on, EO). In practice it will generally not be possible to engineer the pure EO condition. Some FO component of the applied field (the so-called 'stray field') will always be present and will call for special conductor designs to minimize that loss. Stray field loss components are expected for transformers and inductors, as well as all-superconducting generators and motors, which represent extreme examples.

To combat FO loss in general the conductor is subdivided into N_f parallel filaments running down the length of the tape. To prevent magnetic re-coupling of these filaments it is necessary to limit the effective length over which these filaments are exposed to a field of a given direction. With round multifilamentary (MF) strands, twisting is routinely applied. But for coated conductors, which are high aspect ratio tapes, the feasibility of twisting is questionable. For tape there are physical limits to twist pitch reduction. But even if twisting is achievable the tape would assume a helix-like profile, occupying a large volume and severely reducing the engineering critical current density. Even so it is important to recognize that some kind of twisting or transposition will be needed in a conductor of finite length with its required low resistance current contacts at each end. In practice the twisting, if not performed on the conductor itself as part of the processing sequence (as in round LTS MF strands), may occur naturally during the winding of the superconducting machine. To control loss both filamentary subdivision and twisting are needed. In this study, however, we focus on the filamentary subdivision of a coated conductor and its effectiveness in loss reduction.

1.4. Organization of the paper

We begin the paper by referring to some of our previous studies of striped YBCO films in which the effects of filamentary subdivision on hysteretic loss were studied using vibrating sample magnetometry (VSM) at 4.2 K in slow ramp-rate fields of amplitudes as high as 9 T, and in which insights were developed concerning the loss-controlling properties of *stripe width* and *film thickness*. We then move on to describe the striping of some YBCO coated conductor samples and a series of measurements performed inductively on them using pick-up-coil magnetometry at 4.2 K in AC magnetic fields of frequencies ranging from 50 to 200 Hz and amplitudes of up to 150 mT. The effects of ferromagnetic partial shielding are also described. Then recognizing that these measurements:

(1) are just part of a planned more extensive research program involving much higher frequencies and fields, and
(2) point the way towards the design of low loss conductors for machine applications,

we use the results as a starting point for a design study of low loss coated conductors for use over a range of frequencies of up to 500 Hz and field amplitudes of up to 1 T. The collected results of the design study are tabulated and discussed, and conclusions are offered.

2. Experimental details

2.1. Patterning (striping) of YBCO films

As mentioned above, filamentary subdivision is routinely applied to LTS round strands in order to suppress flux-jumping (under all conditions) and hysteretic loss (under AC field conditions). Filamentary subdivision of first generation HTS strands (which become fully bridged after reaction heat treatment) is applied for entirely different reasons—crack suppression and increase of the Ag/HTS interface surface area. With second generation HTS (coated) conductors we return to one of the original motivations—if not flux-jump suppression, then certainly AC loss reduction. Carr has been a long time contributor to the theory of loss reduction by filamentary subdivision, first in the context of LTS conductors [3] and later with regard to second generation HTS [4, 12].

Numerous techniques have been used to pattern YBCO, including wet chemical etching, ion beam etching, and laser ablation. In some cases the aim is to completely remove

material, in others to merely degrade the superconductivity of the interstripe region. Laser ablation has been used to form stripes in some cases by totally removing material, and in other cases to cause it to react in an oxygen-rich environment to degrade the SC properties. Other methods used have been: (i) ion implantation [6] or (ii) inhibition- or reactive-patterning [7] which locally degrades the properties of the YBCO film by destroying its crystalline structure or, while retaining the structure, lowers its electrical conductivity [6, 7]. In this latter case stripe patterns made were typically 10 μm wide, with interface transitions of about 0.1 μm. Another striping technique used masking and Ar-ion-beam etching [8]. These earlier studies of YBCO patterning have been made in the pursuit of electronic applications. But with regard to 'large-scale applications' some recent studies have focused on the striping of conductors as a way of reducing their AC losses.

We have demonstrated the utility of patterning or striping the conductor (at least from a short-sample standpoint) using YBCO films deposited on single crystal substrates [9, 10]. The striping was performed in one case by laser ablation, where the already deposited YBCO was fully removed (ablated) from the target interfilamentary zones. In this work the results of T_c and DC susceptibility measurements performed on the striped YBCO films revealed almost no degradation in the filamentary areas remaining. Magnetization (M–H) loops were measured and their areas shown to follow the expected dependence on filamentary width. Furthermore, detailed analysis of the results indicated that the proportionality of loss to stripe width was superimposed on a general reduction of loss in response to decrease in stripe *thickness* under appropriate conditions. Filaments have also been formed mechanically [11] and the expected loss reductions seen.

Based in large part on the insights developed in studying striped YBCO/LaAlO coupons we went on to pattern several samples of YBCO coated conductor and study their AC loss properties.

2.2. Sample preparation

2.2.1. Conductor and patterning. The coated conductor specimens were fabricated elsewhere. The YBCO layer was an IBAD-deposited buffer layer on a Hastelloy-type ribbon (the substrate, or underlayer). Sputtering was used to deposit an overlayer of Ag to a thickness of 3–4 μm. The finished tapes, 0.125 mm thick and 1 cm wide, were then sent to Mound Laser Photonics Inc. for patterning (or striping) by laser micromachining (following the work of the Air Force Research Laboratory on the patterning of YBCO/LaAlO coupons [9]). The striping was done using the third harmonic of a Nd:YVO_4 diode-pumped solid-state laser at 355 nm whose beam was focused using a simple lens. The coated conductor, mounted on a vacuum stage attached to a translation stage, was positioned at the focal plane of the lens. The stripe was machined by translating the conductor through the focused beam. Typically, the incident average power was less than 1 W and the translation (scan) rate was 10 mm s^{-1}. Currently, the attainable stripe and slice widths are approximately 25–30 μm.

The desired structure is shown schematically in figure 1, where the patterning is seen to separate not only the YBCO layer but also the Ag overlayer into stripes. Figure 2 shows the actual results of the laser patterning on a sample of coated conductor. The top micrograph shows that in this particular case the tape was patterned with several groove width and depth values, achieved by proper choice of laser power and scan speed. The lower figure shows a detail in the vicinity of a stripe. Figure 3 is taken looking down on the same set of experimental stripes (intentionally made with varying widths); it depicts one of the two 'test' samples which were made to determine the proper laser striping and slicing parameters (here we use stripe to denote cutting into the filaments, and slicing to denote cutting very deeply into, and in many cases all the way through, the sample). Table 1 describes the (more complete) second set of striping tests which were performed. Several power levels and scan speeds were used, resulting in various stripe depths. Additionally, either Ar or air was passed over the sample during laser processing to clean away debris. We also investigated slicing all of the way through the samples; these experiments are described in table 2. Figure 4 (from table 1) displays groove widths and depths as functions of scan rate and beam power. Here we see a very sensible trend for the depth of the stripe from the 0.5 W beam in air, plotted as a function of scan speed (i.e., depth decreasing with increasing scan speed). This trend is still present, although not as smooth, for the 0.75 W beam, and the 0.5 W beam in Ar. It should be noted at this point that the depths recorded in figure 4 are the final stripe depths, and not the depths of the initial melt. Inspection of the SEM micrographs suggests that much of the time for the

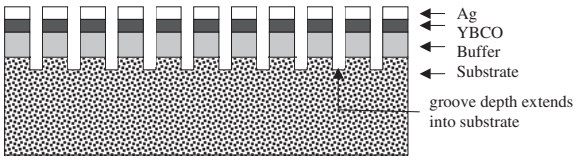

Figure 1. Schematic of striped coated conductor geometry.

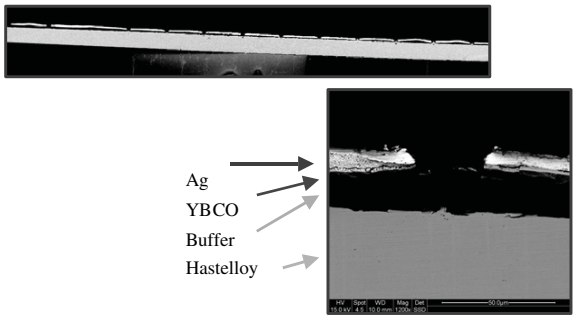

Figure 2. Cross-sectional views of striped YBCO conductor.

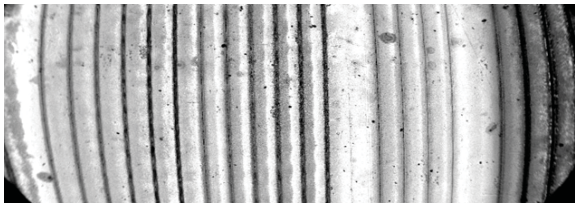

Figure 3. Top view of laser-induced stripes (wide angle shot).

Table 1. Striping parameters.

Stripe name	Speed (mm min^{-1})	Width at Ag (μm)	Width at YBCO (μm)	Depth (μm)	Beam power at tape (W)	Atm	No. pass
G	250	36	28.70	37.60	0.75	Air	1
F	300	24	23.65	33.00	0.75	Air	1
E	350	34	27.69	28.10	0.75	Air	1
D	400	39	30.95	31.59	0.75	Air	1
C	450	30	30.16	27.93	0.75	Air	1
B	500	36	29.04	31.60	0.75	Air	1
M	250	29	26.82	36.82	0.50	Ar	1
L	300	32	26.65	36.02	0.50	Ar	1
K	350	35	26.99	30.63	0.50	Ar	1
J	400	34	23.48	28.87	0.50	Ar	1
I	450	30	26.67	29.90	0.50	Ar	1
H	500	35	24.28	31.90	0.50	Ar	1
S	250	31	25.08	49.03	0.50	Air	1
R	300	39	25.08	42.23	0.50	Air	1
Q	350	32	21.97	38.57	0.50	Air	1
P	400	36	27.14	36.83	0.50	Air	1
O	450	34	23.95	31.59	0.50	Air	1
N	500	34	21.27	26.97	0.50	Air	1
T	550	33	23.65	31.27	0.50	Air	1
U	600	32	26.18	29.04	0.50	Air	1
V	650	39	30.46	30.78	0.50	Air	1

Table 2. Slicing parameters.

Slice name	Speed (mm min^{-1})	Width at Ag (μm)	Width at YBCO (μm)	Depth (μm)	Beam power at tape (W)	Atm	No. pass
W	700	27.46	23.65	31.89	0.50	Air	1
X	700	26.92	22.80	30.16	0.50	Air	2
Y	700	36.83	28.73	50.15	0.50	Air	5
Z	700	33.99	27.61	88.87	0.50	Air	10
ZA	700	37.45	29.83	118.0	0.50	Air	15
ZB	700	58.09	51.75	117.8	0.50	Air	20
ZC	700	53.64	47.30	132.1	0.50	Air	30
ZD	700	50.17	46.66	132.0	0.50	Air	40

0.75 W beam there is a difference in these two depths; this may also induce scatter in the data. Such effects are probably also present to a lesser degree in the 0.5 W sample. This is probably also responsible for the differences seen at 0.5 W for Ar versus air environments for the samples. Figure 5 (from table 2) shows the slice depths and widths for various numbers of passes. After the initial series of experiments, a nominal stripe depth of 25 μm was chosen to guarantee filament separation, and all samples measured for AC loss had stripes of that depth.

2.2.2. Ferromagnetic foils. In preparation for 'shielding effect' measurements Fe strips were incorporated into some of the YBCO coated conductor sample packs; see table 3. The Fe strips were 99.9975% pure, stock number 10 866 from Alfa Aesar, and had dimensions 0.025 × 10.0 × 50.0 mm^3.

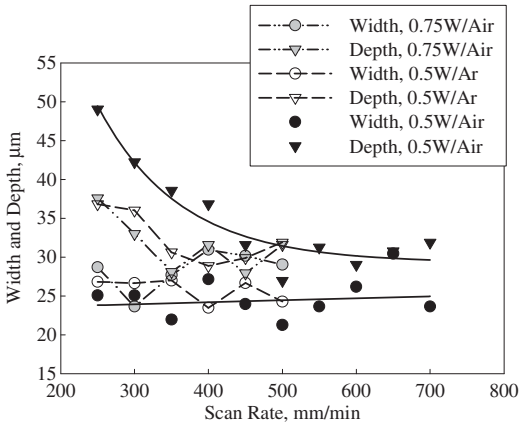

Figure 4. Width and depth of groove versus scan rate and beam power.

2.3. Measurements

AC loss was measured using a pick-up coil magnetometer immersed in boiling liquid nitrogen. The field was applied by a solenoidal primary with a clear bore of 76 mm and a length of 186 mm. It was wound with 1510 turns of 1 mm OD Cu wire. The applied frequency ranged from 50 to 200 Hz with a maximum amplitude of 150 mT. The pick-up coil consisted of two single-layer racetrack-like windings (6 cm × 1 cm) each with 238 turns. The wire diameter was 100 μm and the inductance of the coil was 0.98 mH. The compensating coil was nominally matched to the pick-up coil, the two being

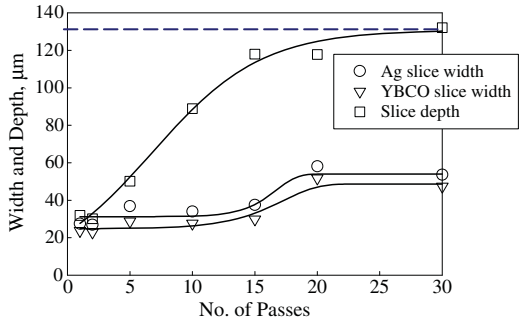

Figure 5. Slice width and depth versus number of passes. (This figure is in colour only in the electronic version)

Table 3. Sample pack specifications.

Sample pack	Striped YBCO	Unstriped YBCO	Fe strips	Total length YBCO (m)	Fe/tape vol ratio
A	—	6	0	0.3	0.0
B	—	6	4	0.3	0.063
C	2	—	0	0.1	0.0
D	2	—	2	0.1	0.167

placed at positions symmetrically displaced from the centre of the primary coil (along the axial direction of the solenoid). The pick-up coils were designed for 5–6 cm long samples. The system is configured to take the data as M–H loops which were then integrated to find the total loss. Calibration was performed in terms of the magnetization of high purity Fe as determined by measurement on a sample of the same material in a calibrated VSM. The VSM was calibrated at higher fields using Ni spheres and cylinders. Sample packs assembled for measurement are listed in table 3.

3. Results

3.1. Unmodified coated conductor

Figure 6 depicts a typical set of M–H loops, in this case for sample pack A (table 3) which consists of six unstriped YBCO tapes, each 5 cm long, stacked on top of one another. The measurements were performed at 77 K and, in this case, under 50 Hz applied fields of up to 150 mT in amplitude oriented perpendicular to the tape faces (the FO orientation). The magnetic moment, M, expressed in SI units m^{-1} leads directly to statements of the AC loss in the useful units J m^{-1} per cycle and hence W m^{-1} or subsequently W kA^{-1} m^{-1} if desired. The M–H loop is featureless with no evidence of flux-jumping.

3.2. Fe/YBCO multilayer results

Magnetometer measurements under the above conditions were made on samples surrounded by Fe strips; see figure 7. Four strips of Fe each having about the same surface dimensions as the YBCO were placed two above and two below the central YBCO pair to form sample pack B (table 3). This is probably not an optimal configuration for shielding, but does in fact show some suppression of loss for lower field amplitudes. The Fe response tends to rotate and change the character of the loops—the former due to the simple addition of Fe magnetization, the latter to influences of the Fe shielding on field distributions and thus YBCO magnetization.

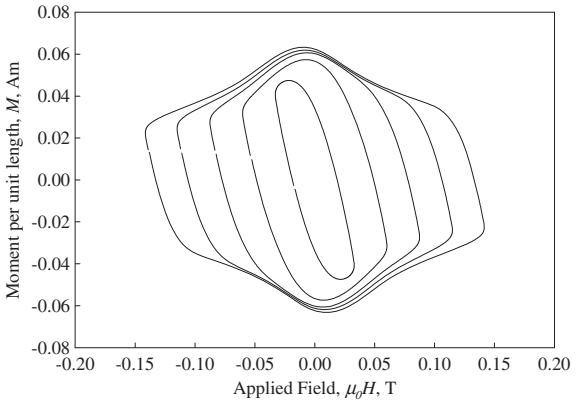

Figure 6. M–H loops at 50 Hz at various applied field amplitudes for sample pack A.

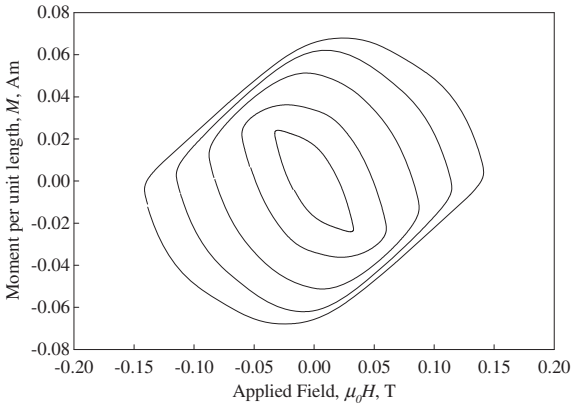

Figure 7. M–H loops at 50 Hz at various applied field amplitudes for sample pack B.

3.3. Comparisons of striped and non-striped conductors, with and without Fe multilayers

Magnetometer measurements under the above conditions, and with and without the included Fe layers, were made on coated conductor tapes that had been striped by laser into ten filaments. These were sample packs C and D (table 3). The results, expressed in the format mJ m^{-1} per cycle, are displayed in figures 8 and 9, along with data from unstriped samples (figures 6 and 7, also integrated to obtain the total per-cycle loss m^{-1}).

3.3.1. Striping without Fe. Referring to figure 8, we notice that the striping into ten filaments reduces the loss by a factor of about ten, as expected from the standard expression for per-cycle hysteretic loss—see equation (1) below (which of course is valid only for H_ms well above the penetration field, H_p). We notice also that striping is uniformly effective at all field-sweep amplitudes, H_m. This agrees with the principle that loss reduction scales with filament-width reduction at

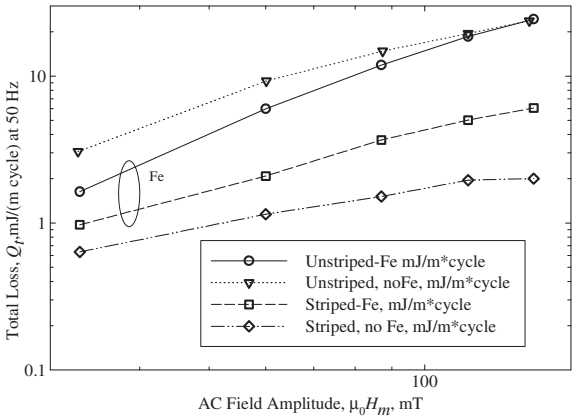

Figure 8. Loss at 50 Hz versus $\mu_0 H_m$ for striped and unstriped samples, with and without Fe (A–D).

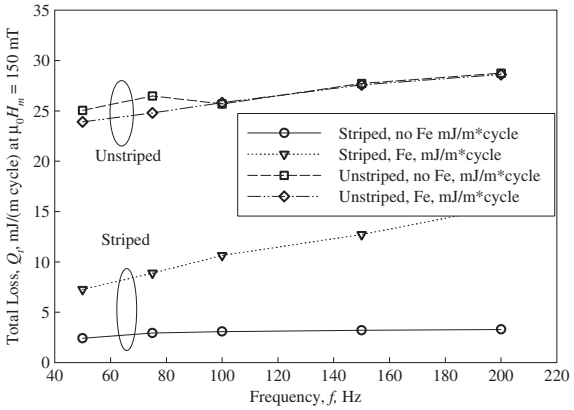

Figure 9. Loss for striped and unstriped samples with and without Fe as a function of frequency (A–C).

all H_m—even as H_m approaches H_p, according to arguments associated with equations (2) and (3) below. Figure 9 displays the per-cycle loss (at fixed $H_m = 150$ mT) as function of frequency. The per-cycle hysteretic loss of the YBCO is of course independent of frequency—equation (1) below. The very slight frequency dependency observed in the striped tape is presumably coming from eddy currents in the Hastelloy underlayer with perhaps a small contribution from the Ag overlayer (depending on the strength of its electrical connectivity to the YBCO layer).

3.3.2. Striping with Fe. We notice in figure 8 that at 50 Hz, the presence of the Fe reduces the loss of the unstriped sample, but increases it for the striped sample. When Fe strips are incorporated into the conductor pack three mechanisms operate to influence the total loss: (1) eddy currents (f^2-dependent); (2) hysteretic loss (f-dependent); and (3) partial shielding of the YBCO (ineffective at saturation field strengths). Differences in their internal layouts (see table 3) complicate a direct comparison between the Fe effects in the striped and unstriped sample packs. Nevertheless some useful observations can be made. With regard to striped-conductor loss, figures 8 and 9 suggest that any beneficial magnetic influence of the Fe (shielding or field tailoring) is masked by loss due to its eddy currents and the fact that the striped YBCO loss is relatively small to begin with. On the other hand, when the YBCO loss is large, as in the unstriped conductor, the presence of Fe can reduce it slightly (see in particular figure 8). This observed reduction is evidence that in this case loss reduction by shielding or field tailoring is greater than loss augmentation by hysteresis and eddy currents.

3.4. Comparison with theory

How does the measured total loss of our coated conductor sample (dominated by the hysteretic loss of the YBCO layer) compare with standard theory? Four-terminal measurements of the 1 cm wide conductor's self field critical current gives a J_c of 2.5×10^9 A m^{-2} (based on an I_c of 50 A and a layer thickness of 2 μm). Figure 8 suggests then that J_c averaged over the whole 150 mT cycle is just under 1/2 of this. Standard theory—equation (1) below—then predicts an energy loss per 150 mT cycle of about 38 mJ m^{-1}. As for the experiment, figure 9 indicates an f-independent loss per cycle at $H_m = 150$ mT of 25 mJ m^{-1}. The effect of striping into N_f 'filaments' (with negligibly thin grooves) is to divide this loss by about N_f, as shown in figure 9.

3.5. Implications for striped conductor design

Experiments performed initially on YBCO/LaAlO films set the stage for a much more detailed study of coated conductor patterning techniques. Close control of the focused laser beam enables grooves to be cut not only through the overlayer and YBCO layer but also into the underlayer (see table 1) and through it (see table 2). Measurements, first by VSM, and later using pick-up-coil magnetometry at 50–200 Hz, demonstrate the effectiveness of striping in the reduction of hysteretic loss. Furthermore, since eddy current loss goes as sample width squared, the possibility of cutting the overlayer along with the YBCO, and also of cutting through the underlayer as well, offers the possibility of drastically reducing the normal metal eddy current losses. With these observations, among others, as a starting point, we go on to analyse the loss components that would be operative in a composite coated conductor. In the following design study we estimate these losses first for 500 Hz/1 T (by way of example) and go on to extend the range of these estimates to other frequencies and field amplitudes; see table 4.

4. Conductor design for AC applications

4.1. Outline

After considering the relative magnitudes of applied field and self field losses experienced by coated conductors, the present paper focuses on the dominant source of AC loss (external field) and its reduction by striping, the control of the resulting coupling component of loss, and the overall design of striped conductors. After demonstrating that for a simple coated conductor in the presence of AC transport current, the hysteretic component is the dominant source of loss, we go on to consider the reduction of that loss by striping, the resulting coupling loss mediated by resistive paths between the stripes and end contacts, and eddy current loss in the normal metal

layers. Also explored is the effect of ferromagnetic shielding on the applied-field loss. In most cases we consider the losses generated by fields applied normal to the tape surface (face-on, FO, orientation) and parallel to it (edge-on, EO, orientation).

We arbitrarily set the operating temperature at 77 K and tape specifications (arbitrarily but realistically) at critical current density, J_c, 10^{10} A m^{-2}; total width, w, 1 cm; stripe width, d, various; thickness, t, 2 μm. We express the 500 Hz AC losses of the tape's various components in the units W m^{-1}; although not taken here, a small additional step would enable the loss to be expressed in terms of another useful unit, W kA^{-1} m^{-1}.

4.2. Flux-jump stability

In designing a superconducting wire the first consideration has always been its flux-jump stability. A sample of superconductor of unspecified size in the virgin state will acquire sufficient energy to initiate magnetothermal instability when an applied field exceeds a critical value H_{fj}. However, the available energy can be metered by reducing the width of the sample 'seen' by the field; thus a superconductor of finite width will never acquire enough energy to flux-jump provided the applied field reaches penetration (at H_p) before the estimated H_{fj}. Initially intended to eliminate flux-jump instability, and subsequently to control hysteretic loss, the idea of flux metering by width reduction has guided the design of MF strand since the 1960s [13]. Returning to HTS superconductors, adiabatic flux-jumping in bulk YBCO has been described by several authors [14, 15]. The simple criteria they developed indicate flux-jump immunity for tapes of the kind under consideration especially in the light of the thickness-suppressed H_p generally exhibited by tapes [4, p 182]; see below. Indeed flux-jumping is completely absent from the hysteresis loops depicted in the following figures.

Of course a topic of more relevance to the design of coated conductors exposed to AC fields is the 'dynamic stability of films', a subject recently treated theoretically by Mints and Brandt [16] and awaiting adaptation to the present conductors and conditions.

4.3. Hysteresis loss for tapes

4.3.1. The FO orientation. The per-cycle hysteretic loss per unit volume of a superconducting slab of width w perpendicular to an applied sinusoidal AC field of amplitude H_m is given in SI units by [4, p 182]

$$Q_h \approx \mu_0 w J_c H_m \tag{1}$$

where μ_0 is the permeability of free space, and J_c is the critical current density. This expression is applicable as long as $H_m \gg H_p$, which in the case of a slab of thickness t is given by

$$H_p \approx J_c \left(\frac{t}{\pi}\right)\left(\ln\frac{w}{t}+1\right) \tag{2a}$$

or

$$H_p \approx \left(\frac{5}{2\pi}\right) H_d \left(\ln\frac{w}{t}+1\right) \tag{2b}$$

in which H_d is defined as $H_d = 0.4 J_c t$. For our model coated conductor ($J_c = 10^{10}$ A m^{-2}, $w = 10^{-2}$ m, $t = 2$ μm), $\mu_0 H_p$ is about 76 mT and $\mu_0 H_d$ is 10 mT. We conclude that in an FO field of amplitude 1 T applied perpendicular to w equation (1) holds and that our model conductor would experience a hysteretic power loss ($P = Q_h f$) at 500 Hz of 5×10^4 MW m^{-3}—equivalent to 1.0 kW m^{-1} using the conversion factor 2×10^{-8} m^3 m^{-1}. The assumption $H_m \gg H_p$ will be valid for high field applications but not for small H_m applications, e.g. transformers. In case $H_m < H_p$, the hysteretic loss, Q_h, is modified by a prefactor $N < 1$—a rapidly decreasing function of H_m/H_p, as detailed in [10]; see also below. The parameter N may be expressed in the form [17, 18]

$$N = 2\left(\frac{H_d}{H_m}\right)\mathrm{Ln}\left(\cosh\frac{H_m}{H_d}\right) - \tanh\left(\frac{H_m}{H_d}\right)$$
$$\approx \left(1 - \frac{1.4}{(H_m/H_d)}\right). \tag{3}$$

The behaviour of N in the high-H_m and low-H_m limits is conveniently discussed in terms of the ratio (H_m/H_d): referring to the exact expression for N, in the high-H_m limit (e.g. $H_m \rightarrow 1$ T) $N \rightarrow 1$ leading to the recovery of equation (1). But in the low-H_m limit, $N \rightarrow 0$ as H_m^3, leading to $Q_h \propto H_m^4$ (as compared to the H_m^3 of the usual unpenetrated critical state situation).

The beneficial impact of reduced N on hysteretic loss is implicit in the results of recent investigations [10, 19–21]. Clearly hysteretic loss can be lowered by reducing the prefactor $N(H_m/H_d)$ to well below unity. For a given H_m this can be accomplished by bringing H_d (=$0.4J_c t$) closer to H_m by increasing the YBCO layer thickness. With a $\mu_0 H_d$ in the present case of 10 mT there is scant possibility of accomplishing this for generator stator windings with their large values of H_m. On the other hand, for rotor windings and transformers with FO stray fields of order 20 mT, meaningful H_m/H_d reduction can be accomplished by increasing the YBCO coating thickness, t, beyond the 2 μm considered here. This approach is based on the assumption that the effect described remains valid when the conductor is wound into a device; in reality interaction among neighbouring strands needs to be considered.

4.3.2. The EO loss and striping. In the EO orientation, equation (1) holds but with w replaced by the strip thickness, t. In a strictly EO field the power dissipation would be only 200 mW m^{-1}. Of course it would be impossible to build a machine that experienced *only* EO loss. At best, the broad face of the conductor will be exposed to 'stray field' from various sources, including EO-field misalignment. For example, a field misalignment of only 1.15° would provide an FO component equal to 2% of the 'EO' main component. Such a relative stray field due to this or other sources could be expected in an air core transformer designed for mostly EO field at the windings. In terms of loss, the effect of the stray field is magnified by the aspect ratio (w/t) of the YBCO—5000 in the present example of an unstriped conductor. Thus a '2% stray field' could generate loss 100 times as great as the pure EO loss.

Clearly it is essential to reduce the conductor's FO loss, not only in response to fields deliberately directed normal to the conductor's broad face, but stemming from stray fields.

The way to do this is to reduce the conductor width to the micrometre level by striping. A multiplicity of such stripes, now of width d, is needed to maintain current carrying capacity following the fine-MF concept of hysteretic loss reduction that guided the design of composite NbTi/CuNi AC strands during the 1970s. This will be the most practical route for AC loss reduction for strand intended for EO field orientations—and it will be absolutely essential for those intended for FO orientations.

Provided the filaments are 'decoupled' (see below) the hysteretic power loss per unit volume of the MF assembly is given by equation (1) with the symbol w replaced by d, the width of an individual filament. Picture for example our 1 cm wide superconducting tape, 2 μm thick, subdivided into 100 stripes 50 μm wide and 50 μm apart. At 500 Hz, 1 T, this would dissipate 2.5 W m^{-1}—400 times less than the unstriped value (not forgetting of course that the current carrying capacity, I_c, of the conductor has been reduced by the striping from 200 to 100 A). Such loss reduction is probably not yet sufficient for generator stator applications [22], but may be satisfactory for transformers. For generators, even smaller filaments are needed to control the hysteretic loss, but beyond this other losses must be considered.

4.4. Loss in the presence of transport current

4.4.1. AC transport current in zero applied field. In the self field of an AC transport current of amplitude I_m a strip experiences a power *loss per unit length* given, according to Norris [23] (see also [4, p 192]), by

$$[P_{sf}]_L = \frac{f\mu_0 J_c (wt)^2}{\pi}[(1-i)\ln(1-i)+(1+i)\ln(1+i)-i^2]. \quad (4)$$

Here we leave P normalized to unit conductor length, $i = I_m/I_c$ (in which the critical current, I_c, is 200 A for our model strip), and there is no applied field. If we pick $i = I_m/I_c$ at 0.9, and $f = 500$ Hz, then $P = 1.44$ W m^{-1}. Dropping the relative transport current density to 0.5 reduces this loss by a factor of 16 to 88 mW m^{-1}. Equation (4) indicates that $[P_{sf}]_L$ decreases with reduction of strip width. In fact if a tape of width w is subdivided by negligibly narrow grooves into many stripes each of width d, the self field loss is reduced by the factor w/d. The subdivision is effective only when the stripes are decoupled—which is accomplished in the presence of an applied field.

4.4.2. AC transport current in AC applied field. The losses are modified significantly when the tape is exposed to an AC field while carrying AC transport current. This condition has been considered by Carr [24], [4, p 98], for the special cases of an AC current in-phase with a transverse field, applied to a round wire and a tape in the EO orientation. The analysis does not yet deal with an FO applied field which is the condition of most practical interest as explained above in connection with stray field effects. Nevertheless the round wire result would be closely applicable to the individual stripes of a field-uncoupled MF tape. At relatively high AC field amplitudes, $H_m \gg H_p$, the EO-tape- and round-wire results coalesce and allow us to compute the transport current contribution to the total loss using $(1/3)i^2 Q_h$, where Q_h is now the FO loss for an uncoupled tape.

4.4.3. Combined loss and filamentarization. As just pointed out, for $H_m \gg H_p$, the relative combined loss, Q_{hi}/Q_h, for the round wire coincides with that for the EO tape. But when $H_m < H_p$, as might be the case for the ripple field experienced by a rotor, Carr's analysis shows, for a given i, that $[Q_{hi}/Q_h]_{(wire)}$ is very much less than $[Q_{hi}/Q_h]_{(tape)}$. In this regard filamentarization has a double benefit: it not only reduces the FO Q_h but allows the round-wire approximation to be applied to the AC-field/AC-current condition. However, for the present purposes, we can take the high H_m limit, where the combined hysteretic and transport current loss is given by $Q_{hi} = Q_h(1 + i^2/3) \equiv Q_h + Q_i$. In this case the 'additive factor' due to transport current loss (when the applied field is large enough to decouple the filaments) is between 8 and 33% of the hysteretic loss, as i ranges from 0.5 to 1. Thus striping, in this case, reduces both hysteretic and transport current loss.

In large H_m applications the dominant loss experienced by an AC tape is the FO hysteretic component. It is essential to suppress Q_h—filamentarization is the standard remedy, in this case subdivision of the superconductor into strips. But filamentarization ('striping') embodies serious problems of its own—coupling loss due to induced currents that flow along the filaments and across the normal paths between them either the intervening matrix or, in the case of fully insulated filaments, their common end current-contacts.

4.5. Coupling loss

The power loss per unit volume due to coupling currents in a conductor with filamentary subdivision is given by

$$P_{coup} = \frac{1}{n\rho_{eff}}[fL(\mu_0 H)]^2 \quad (5)$$

where $n = 2$ for a round MF strand [4, p 127] and $n = 4$ [4, p 188] for a striated flat tape. In both cases coupling loss saturates to the hysteretic loss of the monolithic conductor. In equation (5), f, and H_m have their usual meanings, and ρ_{eff} is the 'coupling resistivity'. The coupling length, L, is equal to the twist pitch if the conductor is twisted relative to external fields or twice the length of an untwisted conductor. Usually coupling loss is reduced by decreasing L (by twisting) and increasing ρ_{eff}. As suggested it can also be controlled by decreasing the 'active length' of a tape segment (i.e. $L/2$) that is exposed to field of a given orientation.

4.6. Twisting and related issues

4.6.1. Interfilamentary resistance. According to equation (5), if sufficient L-reduction cannot be attained, we must look to ρ_{eff} as a means of reducing coupling loss [25]. How much coupling loss is acceptable, and what is the corresponding ρ_{eff}? A useful estimate of it can be made by requiring that the coupling loss be equal to the hysteretic loss, which for a *twisted* tape is $(2/\pi)$ times the untwisted value, equation (1) (where $w \to d$) [4, p 189]. Accordingly the 'reference' ρ_{eff} is given by

$$\rho_{eff} = \left(\frac{\pi}{8}\right)\frac{f\mu_0 H_m}{J_c}\left(\frac{L^2}{d}\right). \quad (6)$$

Note that this simple relationship differs from Carr's expression for ρ_{eff} [4, p 191] by a factor 2.4, close enough

given that the criterion has been arbitrarily chosen. With regard to limitations on L, present estimates are that YBCO coated conductors can support a 0.4% tensile strain without degradation. For a tape conductor this leads to an $L \sim 30w$. If L is to be 10 cm, as it might be for a Gramme ring, then w must be about 1/3 cm, less than that of our reference 1 cm wide tape, but one that we will adopt for the moment. Taking as before $\mu_0 H_m = 1$ T, $f = 500$ Hz, $J_c = 10^{10}$ A m^{-2}, assuming L = 10 cm and a stripe width, d, of 50 μm, we find that $\rho_{eff} = 4 \times 10^{-6}$ Ω m (400 $\mu\Omega$ cm). *The most important thing to note here is that this value shows that the notion of unstriped metallic layers connecting striped filaments is untenable at 500 Hz and 1 T—the loss penalty would be prohibitive*. Thus, from this point forward we will assume that the overlayer is striped along with the filaments.

It is difficult to envision a practical method of applying twist to a coated tape. As pointed out by Carr [4, p 183], Oberly's suggestion of a spiral-patterned coating on a cylindrical tube would result in a relatively large diameter conductor. Carr himself has suggested applying the twist directly to a tape bearing a striped coating [4, p 183]. Again the twisted tape will occupy much more space than the untwisted one. But spatial issues aside, the above analysis indicates that the needed ρ_{eff} would be out of the range of metallic conductivity. Taken at face value equation (5) indicates that coupling loss vanishes for insulated filaments for all L no matter how large. But in a real conductor, since the filaments are all joined together at the ends of the winding by their low resistance contacts to the current source, at least one twist is needed to zero out the net flux threading the conductor. In practice as many twists as possible should be introduced. This line of reasoning leads us to a twisted group of insulated filaments with no coupling loss. The price for this outcome is an absence of current sharing; the alternative is obvious.

4.6.2. The composite tape. The composite tape possesses metallic underlayers and overlayers. The underlayer is separated from the YBCO by a buffer layer which can only weakly couple the filaments (see below). On the other hand, the overlayer usually of pure Ag may be in direct contact with the YBCO filaments, and hence will couple them very strongly unless they are striped along with the YBCO. Thus the Ag coating must be striped along with the filaments themselves.

4.7. Reduction of coupling loss—further practical details

4.7.1. Field oscillations. It should be kept in mind that it is possible to reduce the coupling current significantly by reversing the field direction within a given length of conductor. In any case, such oscillations must be taken into account when calculating the actual AC loss of a given configuration. In general, if a segment of multifilamentary conductor is exposed to spatially varying fields, it is the net flux through the segment that will determine the effective active length. While we are unaware of any work specifically related to this in the context of coated conductors, the effect is well known in cables [26–28] and LTSC strands themselves [29].

4.7.2. Interaction effects and calculation limitations. The presence of significant oscillating field complicates the detailed calculation of the losses. However, for a first-order estimate, we can in fact expect the dynamic resistance effect to suppress the transport current loss substantially, and hence we need consider only the external magnetic field losses. Some rough estimates for these effects (based on round wire models in various limits) were given above in section 4.4.3. However, further refinement of these effects are in order.

4.7.3. Effective interfilamentary resistivity of the composite tape. We consider a model striped composite coated conductor of width w in which the interfilamentary spacing is taken to be the same as the filament width, d. The particular choice was made for our model calculations and for comparisons to test samples; in fact the results will be generally valid, even as the interfilamentary spacings get small. The YBCO is deposited on a buffer layer of thickness t_{buf} and resistivity ρ_{buf}. The substrate is of thickness t_{sub} (later $t_{sub} \cong d$) and resistivity ρ_{sub}. We will show that although ρ_{buf} is generally very high its contribution to ρ_{eff} is reduced by a factor $2(t_{buf}/w)$, which in practice could be of order 10^{-4}. The analysis proceeds as follows.

The resistance (per unit length of conductor) of a current path from one outside filament to the other including two passages through the buffer layer is

$$R_l = \rho_{sub}\left(\frac{w}{t_{sub}}\right) + 2\rho_{buf}\left(\frac{t_{buf}}{d}\right). \tag{7}$$

The effective resistivity is of course

$$\rho_{eff} = R_l \frac{t_{sub}}{w} \tag{8}$$

which becomes

$$\rho_{eff} = \rho_{sub} + 2\rho_{buf}\frac{t_{buf}}{d}\frac{t_{sub}}{w} \tag{9}$$

and with $t_{sub} \cong d$ becomes

$$\rho_{eff} = \rho_{sub} + 2\rho_{buf}\left(\frac{t_{buf}}{w}\right). \tag{10}$$

The lowered effective resistivity is a natural consequence of the fact that the high buffer layer resistivity is localized and 'widely separated' by the width of the strand. The effect of the buffer layer in this case is in some ways analogous to that of the resistive barrier that surrounds the filaments in some LTS and HTS MF conductors.

4.7.4. Loss in the normal metal components of a composite tape conductor.

Ferromagnetic loss. A requirement of the RABiTS process is the need for a textured Ni or Ni alloy substrate with the accompanying ferromagnetic-hysteresis loss. The loss per unit volume of a ferromagnetic substrate is given by [30]

$$P_{Fe} = 4\mu_0 H_c M_s f \tag{11}$$

where H_c is the coercive field and M_s is the saturation magnetization. For an Ni substrate with M_s = 485 kA m^{-1}

and a published $\mu_0 H_c$ of 7×10^{-5} T [31], we find P (at $f = 500$ Hz) to be 6.8×10^4 W m^{-3}. This leads to a hysteretic loss in an Ni strip 1 cm wide and 50 μm thick of 34 mW m^{-1}. In practice a textured and slightly work-hardened Ni strip has been stated to have a measured $\mu_0 H_c$ of 7×10^{-4} T [5] resulting in a loss that is ten times greater, about 340 mW m^{-1}. The ferromagnetic-hysteresis loss can be reduced by alloying the Ni with W or Cr, which reduces both M_s and H_c. For example, use of Ni–7 at.% Cr with an M_s of 195 kA m^{-1} and a $\mu_0 H_c$ of 4×10^{-4} T reduces the loss by a factor of four. Under the above conditions such a ribbon would dissipate a ferromagnetic loss of 78 mW m^{-1}. A better choice (from the standpoints of both magnetic properties and buffer-layer compatibility [32]) would be an Ni–W alloy, e.g. Ni–5 at.% W with hysteretic loss (when annealed at 1000 °C) of about 270 J m^{-3}-cycle [32] and hence an alloy-strip loss of 67 mW m^{-1}.

How significant is this 67 mW m^{-1} compared to the composite's other loss components? It is certainly small compared to the FO loss of a model striped conductor (2.5 W m^{-1} for 50 μm wide stripes) but comparable to its pure EO loss (100 mW m^{-1}, or 50% of the unstriped value due to the correspondingly lower fraction of superconductor present). Furthermore, as noted above, a significant loss contribution by a nominally EO-oriented tape is expected to be the stray (FO) field component. At an amplitude equal to 2% of the EO H_m (e.g. 2% of 1 T in this case) the stray field would contribute $(2/100) \times (1/2) \times 100$ mW m^{-1} = 50 mW m^{-1} of loss (cf section 4.3.2). The total 'EO loss' in this case would therefore be 150 mW m^{-1}. Thus the ferromagnetic loss in the alloyed Ni, at a little less than 1/2 of the total EO loss, must be regarded as significant and hence a candidate for elimination.

Eddy current loss in normal metal underlayers and overlayers. Eddy current loss can be expected from the two normal metal components of the composite ribbon—the underlayer (substrate) and the overlayer(s). This loss, on a volumetric basis, is given by [30]

$$P_e = \frac{\pi^2}{6\rho_n}[(\mu_0 H_m) w f]^2. \tag{12}$$

It is useful to compare this with the coupling loss as in

$$\frac{P_e}{P_{coup}} = \left(\frac{2}{3}\right)\left(\frac{\pi}{L}\right)^2 \left(\frac{\rho_{eff}}{\rho_n}\right) w^2. \tag{13}$$

Since, as already indicated, ρ_{eff} can be very much larger than any normal metal resistivity, ρ_n, the eddy current loss P_e can be greater than P_{coup} unless the underlayer and overlayer contributions can be reduced by each of two approaches. (1) The ρ_n of the underlayer should be increased. (2) Since the ρ_n of the overlayer(s) will generally be low, their eddy current loss contribution (again, per unit volume) can be reduced by striping them along with the superconductor; in other words by replacing w^2 by d^2. Thus subdivision into 100 stripes 50 μm wide would reduce the unit-volume overlayer loss by a factor 4×10^4. This reduces the pure-Ag full width (1 cm) FO eddy current loss of 425 W m^{-1} down to 5.3 mW m^{-1} after allowing for the gaps between the stripes.

(a) The underlayer. Underlayers for the RABiTS process are Ni alloys. Likewise, that for the IBAD process is usually an Ni alloy (Hastelloy type). At a resistivity 0.6 $\mu\Omega$ cm at 77 K a pure Ni substrate of standard dimensions (1 cm × 50 μm) would contribute an eddy current loss at $f = 500$ Hz, $H_m = 1$ T of 3.4 kW m^{-1}. This unacceptably large loss can be significantly reduced by alloying with Cr or preferably W (RABiTS) or about 30 wt% Mo or Cr + Mo (Hastelloy, IBAD). The resistivities of these Ni alloys are an almost temperature independent 50–125 $\mu\Omega$ cm [33, 34]. Even so such alloys at a nominal resistivity of 100 $\mu\Omega$ cm would provide eddy current losses of about 20 W m^{-1}. But this is still an order of magnitude greater than the FO hysteretic loss of the striped conductor (2.5 W m^{-1}). Taken together, these results again emphasize the importance of arranging for an EO orientation of the applied field.

(b) The overlayer. The primary overlayer is a protective film of Ag (77 K resistivity 2.9×10^{-7} Ω cm [35]). At a thickness of 3 μm, and if insulated from the YBCO, this would contribute 425 W m^{-1} to the total loss, 20 times greater than that of the Ni alloy underlayer. Apart from the 'EO solution' there are two ways around this problem:

(1) Alloy the Ag with Au to raise the 77 K resistivity into the range of 3.88×10^{-6} Ω cm [35, 36] and reduce the loss to 32 W m^{-1}, comparable to that of the Ni alloy underlayer.
(2) Place the Ag film in intimate electrical contact with the YBCO layer to completely eliminate the eddy current.

By the same token a superposed pure Cu 'stabilization' layer in electrical contact with the Ag and hence the YBCO will not contribute to the eddy current loss. Assuming that we have already agreed upon the necessity of striping the YBCO coating, the overlayer must not be permitted to connect the filaments. The result of so doing would be very large coupling loss. To prevent this, the overlayer should be striped along with the YBCO coating.

4.8. Implications for the conductor and loss mitigation

4.8.1. Eddy current, coupling, and hysteretic losses in the composite tape. We have shown the need for striping the YBCO layer in order to control the FO hysteretic loss. Overlayers applied *after* the striping fill the interfilamentary spaces with high conductivity metal and reintroduce large coupling loss. But striping performed after a well-bonded coating has been applied maintains the benefit of zero eddy current loss in the overlayer and reduced FO hysteretic loss in the superconductor. An underlayer alloy having been chosen, apart from thickness reduction, nothing can be done to reduce its eddy current loss per metre; it is insulated from the YBCO and is unable to be striped.

4.8.2. Ferromagnetic shielding. As pointed out in connection with research on Fe-clad MgB_2 strands, some interesting loss properties accompany the shielding of a superconductor by a thin layer of Fe [37–39]. The hysteretic loss is in some cases reduced, and the field lines through the superconductor may be modified by the presence of the Fe. But a *fully shielded* superconductor will not be able to perform its function in an

Table 4. AC loss component estimates under various conditions.

Condition/ loss (mW m^{-1})		500 Hz, 1 T	500 Hz, 0.2 T	500 Hz, 0.02 T	500 Hz, 0.002 T	200 Hz, 1 T	200 Hz, 0.2 T
(1a)	P_h[a]	2500	500	50	5	1000	200
Face-on	$P_{e,sub}$[b]	20 000	800	8	0.08	3200	128
$w = 1$ cm	$P_{e,over}$[c]	5.3	0.212	0.002	—	0.85	0.034
$d_f = 50\ \mu$m	P_c[d]	—	—	—	—	—	—
	P_{Fe}[e]	68	68	??	?	27	27
(1b)	P_h	250	50	5	0.5	100	20
Face-on,	$P_{e,sub}$	20 000	800	8	0.08	3200	128
$w = 1$ cm	$P_{e,over}$	0.053	0.002	—	—	0.009	—
$d_f = 5\ \mu$m	P_c	—	—	—	—	—	—
	P_{Fe}	68	68	??	?	27	27
(1c)	P_h	250	50	5	0.5	100	20
Face-on	$P_{e,sub}$	200	8	0.08	0.001	32	1.28
10 strips	$P_{e,over}$	0.053	0.002	—	—	0.009	—
$w = 1$ mm	P_c	—	—	—	—	—	—
$d_f = 5\ \mu$m	P_{Fe}	68	68	??	?	27	27
(2)	P_h	100	20	2	0.02	40	8
	$P_{e,sub}$	0.5	0.02	—	—	0.08	0.003
Edge-on	$P_{e,over}$	0.019	0.001	—	—	0.003	—
	P_c	—	—	—	—	—	—
	P_{Fe}	68	68	??	?	27	27
(3a)	$P_{sf}(1a, b)$[f]	88	88	88	88	35	35
AC current/ self field	$P_{sf}(1c)$	8.8	8.8	8.8	8.8	3.5	3.5
$i = 0.5$							
(3b)	$P_i(1a)$[g]	208	41.6	4.16	0.416	83	16.6
AC current/	$P_i(1b)$	20.8	4.16	0.416	0.042	8.3	1.66
AC field FO	$P_i(1c)$	20.8	4.16	0.416	0.042	8.3	1.66
$i = 0.5$							

[a] P_h = Superconductor hysteretic loss (YBCO layer, 2 μm thick). No N-factor applied here.
[b] $P_{e,sub}$ = Normal metal eddy current loss for substrate (Hastelloy-type alloy, 50 μm thick, $1 \times 10^{-6}\ \Omega$ m).
[c] $P_{e,over}$ = Normal metal eddy current loss for overlayer (pure Ag, 3 μm thick, $2.9 \times 10^{-9}\ \Omega$ m. The overlayer is assumed to be striped. Values do not include the influence of the SC on the electric field).
[d] P_c = Coupling current loss.
[e] P_{Fe} = Ferromagnetic substrate hysteretic loss (Ni–5% W here, but could be zero if nonmagnetic substrate was used).
[f] P_{sf} = Transport current loss, self field.
[g] P_i = Transport current loss, in the presence of AC field.

electromagnetic device. In the interest of loss minimization, EO operation is desirable but not necessarily fully attainable in practice, as explained in section 4.3.2. Even a one degree misorientation of the EO field would activate some FO loss to the extent of some 100 times the pure EO value. This could to some extent be alleviated by suitably engineering an FE layer to redirect the stray field closer to the EO direction.

4.8.3. Coated composite tapes for AC applications—design summary. First we need to choose a non-magnetic substrate with sufficiently high resistance. Beyond this, we must be careful with our choice of buffer layers, such that the interfilamentary resistance is sufficiently high. Then we must sparingly apply the conductive overlayer, using an alloy such as Ag–Mg. This overlayer should also be striped, along with the YBCO layer. There are several potentially important components to the loss: hysteretic loss of the YBCO coating, coupling loss of the striped composite, ferromagnetic loss in an Ni alloy underlayer if present, and normal metal eddy current losses in the underlayer and overlayer. For large-H_m applications it will be necessary to introduce filamentary subdivision of the YBCO, to reduce the hysteretic loss. It will then be desirable to use very resistive underlayers and overlayers (excepting in the latter case when a stabilization function is required). It is important to note that the eddy current loss from an unstriped normal metal layer in intimate contact with an unstriped YBCO coating would be low even in FO fields. The same would also be true for a comparable striped conductor provided that the striping were performed after the overlayer had been applied. The converse would lead to large coupling loss if the overlayer were in good electrical contact with the superconductor, or large eddy current loss if it were insulated from it, for example by a buffer layer.

5. Discussion

Table 4 lists various loss contributions for a number of coated conductor designs and orientations, all with striped filaments

and overlayers. In all cases $I_c = 200$ A before striping, and 100 A after striping. The underlayer is 50 μm thick Hastelloy-type (100 $\mu\Omega$ cm). The overlayer is 3 μm thick Ag, and is assumed to be striped along with the filaments. The striping is assumed to remove 50% of the filamentary region. This is too pessimistic for 50 μm filaments—even now better superconducting fractions can be achieved and this will continue to improve. However, a 50% superconducting fraction is probably realistic (for now) for 5 μm filaments and so for consistency of comparison we choose this value. All values are calculated for 77 K operation. In generating the data for table 4 we have used the expressions from section 4, above. Thus, table 4 gives a first-order approximation (estimate) of the values for each of these loss components. Hysteretic loss is calculated using the field independent J_c. Normal metal eddy currents are calculated using equation (12) directly, thus any suppression of this loss in the overlayer due to its close connection to the YBCO (caused by electric field suppression due to physical proximity and high electrical connectivity to the overlayer) is ignored. Based on our discussions above regarding the futility of normal-metal-connection-enabled current sharing at 500 Hz, the filaments are assumed to be connected to one another only via the buffer layers to the substrate. In addition, the influence of end-connections on P_c is ignored (a point of view valid for a long twisted sample); taken together with the highly resistive buffer layer connections this makes the coupling term negligible. Ferromagnetic loss, P_{Fe}, is calculated for an Ni–5% W underlayer, and can be deleted for Hastelloy or other non-magnetic underlayers (e.g., higher Cr content Ni–Cr alloys). Transport current losses are also shown in table 4. Here row (3a) assumes no applied field. The real contribution of this term will be less than that shown as the fields become large enough to decouple the filaments with respect to their self field. We have estimated those results for the regions of the conductor experiencing large fields (from our discussions above) and they are listed in row (3b). Below, the data of table 4 are discussed with reference to the stator and rotor requirements of an all-superconducting generator operating at 500 Hz.

The stator

Cryogenic Cu machines operating at liquid hydrogen temperatures would have conductors which, once scaled to a 200 A level, would generate roughly 1.5–3 W m^{-1}. While this would be acceptable for an open cycle machine, a closed cycle machine would demand less, certainly below 500 mW m^{-1}. Our reference design (one simplified, but basic potential design [22]) for the superconducting stator calls for an AC field amplitude of 1 T. Some designs for *each phase* of a stator call for 150 m of 1000 A conductor, and a loss budget of 100 W. This means 750 m of the 'standard' 200 A conductor, with 130 mW m^{-1} as its loss target.

The rotor

For a rotor, the situation is different. Fortunately, the AC fields to which it is exposed are relatively small. The rotor is a DC magnet which experiences just a ripple field by inductive coupling to the stator—for example, one with an amplitude of only 2% of the stator field amplitude (assumed to be 1 T). Of this only about 10% would be FO oriented. Thus on this basis the FO field experienced by the rotor has an H_m of about 2 mT. It is estimated that for the rotor some 4000 m of 150 A wire would be needed, with a loss budget of 0.5 mW m^{-1} as the target.

With these targets in mind we are now in a position to examine table 4 in some detail. Consider first the stator requirements. Several possible conductor geometries are listed, denoted (1a), (1b), and (1c). Geometry (1a) is a 1 cm wide tape with 50 μm filaments. Here the losses for FO oriented fields (as might be expected for stator coils using a Gramme ring geometry) are far too high. In going to (1b) we reduce the filament width by an order of magnitude. This reduces the hysteretic component, but the substrate losses are still much too high. Only by going to (1c) can we reduce the loss to 450 mW m^{-1} which is getting close to the goal. But we have not yet taken into account the duty cycle of the winding. We have (as a first-order approximation) assumed that all sections of the Gramme ring conductor would be experiencing the 1 T AC field at all times. The loss requirement needs to be down-rated because:

(1) only the inner portions of the winding (those nearest the rotor) experience the full field, and
(2) only some fraction of the Gramme ring winding experience the full field at any given time in the cycle.

The reduction factor associated with these effects (unpublished to our knowledge) might result in a factor of two for each effect separately. The final loss estimate of 112 mW m^{-1} puts the Gramme ring stator, wound with Option-(1c) conductor, within range of the target. The Gramme ring might be regarded as a 'worst-case scenario'. That winding geometry can be used as a means to keep the bending radius of the conductor as large as possible—but it can be argued that bending the conductor is less damaging than twisting it. Indeed, YBCO coated conductor has been demonstrated to have almost double the strain tolerance of BSCCO HTS conductor and can tolerate a smaller bend radius [40]. A simple conception of twisting, on the other hand, would tend to reduce J_e considerably, and might be difficult to do in practice for any device winding. If, alternatively, we go to a more traditional diamond-geometry stator it should be possible to avoid twisting and to additionally align the conductors mostly EO. At 2% stray field they would be exposed to an equivalent FO field amplitude of 0.02 T; allowing for somewhat greater misorientation we might consider a larger $\mu_0 H_m$, somewhere between 0.02 and 0.2 T, and hence a specific loss close to the 130 mW m^{-1} target and with a more easily fabricable conductor geometry—option (1b).

As for the rotor, which would be exposed FO to an AC field component of only 2 mT, conductor (1c) will satisfy the 0.5 mW m^{-1} loss requirement. Note that we have assumed no shielding for the rotor. A shield can be included, in which case the loss is transferred to it in the form of eddy currents.

6. Concluding summary

AC losses for coated conductors have been investigated by calculation and experiment. Based on previous studies the utility of striping as a way of reducing hysteretic loss was verified. A suggested YBCO striping geometry which

includes striping the stabilizer was described. Such striping was then performed on segments of coated conductor using laser micromachining. Various machining parameters were investigated, and the stripe and slicing characteristics were presented. Typical stripe and slice widths were 25 μm at the level of the YBCO layer, and the depth of the slice could be controlled, sometimes through the use of multiple passes. Some simple striping patterns were selected and packs of coated conductor (some including strips of Fe for partial shielding) were prepared for AC loss measurement. For the ten-filament samples measured the loss reduction was consistent with the factor of ten expected. Fe shielding lowered the loss for unstriped samples, but increased the loss of striped samples (or rather, striped YBCO/Fe sample packs had greater loss than those without Fe). An eddy current component was seen only for the samples with Fe; this contribution was the normal metal eddy current within the Fe itself. In general, striping was shown to be very effective for loss reduction, while ferromagnetic shielding was only partially effective. Based on the outcome of what might be regarded as preliminary experiments at AC field frequencies of 50–200 Hz and amplitudes of up to 150 mT, detailed calculations were made of losses at 500 Hz and 1 T. Then by way of a Conductor Design exercise, values were estimated for various components of the total loss, including hysteretic, normal metal eddy current, coupling eddy current, and transport loss. In the high frequency/moderate field regime the dominant contributions are shown to be hysteretic losses and eddy currents in FO applied fields. The conductor design study concluded with a tabulation of loss contributions from all anticipated sources for two frequencies (200 and 500 Hz) and several AC field amplitudes (1, 0.2, 0.02, and 0.002 T) and an indication as to how the various cells of the table describe conductors for use in particular large-scale applications.

Acknowledgments

We thank the supplier for the YBCO coated conductor and Ken Hix from Mound Laser Photonics for laser striping these samples. We also appreciate helpful discussions with Larry Long of LEI. This research was funded by an AFOSR STTR (via Hyper Tech Research) and an AFSOR summer faculty program.

References

[1] Foner S and Schwartz B B (ed) 1981 *Superconductor Materials Science, Metallurgy, Fabrication, and Applications* (New York: Plenum)
[2] Foner S and Schwartz B B (ed) 1974 *Superconducting Machines and Devices, Large Systems Applications* (New York: Plenum)
[3] Carr W J Jr 1983 *AC Loss and Macroscopic Theory of Superconductors* (London: Gordon and Breach)
[4] Carr W J Jr 2001 *AC Loss and Macroscopic Theory of Superconductors* 2nd edn (London: Taylor and Francis)
[5] Thompson J R *et al* 2002 *Physica* C **370** 169–76
[6] Kuhn M *et al* 1998 *Physica* C **294** 1–6
[7] Ma Q Y *et al* 1994 *Supercond. Sci. Technol.* **7** 294–7
[8] Elsner H *et al* 1998 *Microelectron. Eng.* **41/42** 407–10
[9] Cobb C B *et al* 2002 *Physica* C **382** 52–6
[10] Sumption M D *et al* 2003 *IEEE Trans. Appl. Supercond.* **13** 3553–6
[11] Polák M *et al* 2002 *Physica* C **372–376** 1830–4
[12] Carr W J Jr and Oberly C E 1999 *IEEE Trans. Appl. Supercond.* **9** 1475–8
[13] Wilson M N *et al* 1970 *J. Phys. D: Appl. Phys.* **3** 1517–83
[14] Müller K-H and Andrikidis C 1994 *Phys. Rev.* B **49** 1294–306
[15] Collings E W and Sumption M D 1995 *Advances in Superconductivity VII* ed K Yamafuji and T Morishita (Tokyo: Springer) pp 605–8
[16] Mints R G and Brandt E H 1996 *Phys. Rev.* B **54** 12421–6
[17] Brandt E H and Indenbom M 1994 *Phys. Rev.* B **48** 12893–906
[18] Muller K-H 1997 *Physica* C **281** 1–10
[19] Amemiya N, Nishioka T, Jiang Z and Yasuda K 2004 *Supercond. Sci. Technol.* **17** 485–92
[20] Suenaga M *et al* 2004 *J. Appl. Phys.* **95** 208–13
[21] Suenaga M *et al* 2003 *J. Appl. Phys.* **94** 502–6
[22] Long L 2004 LEI private communication
[23] Norris W T 1970 *J. Phys. D: Appl. Phys.* **3** 489
[24] Carr W J Jr 1979 *IEEE Trans Magn.* **15** 240–3
[25] Oberly C E *et al* 2002 *Adv. Cryog. Eng.* **48** 621–30
[26] Ries G and Takács S 1981 *IEEE Trans. Magn.* **17** 1281–4
[27] Takács S, Yanagi N and Yamamoto J 1995 *IEEE Trans. Appl. Supercond.* **5** 2–6
[28] Verveij A 1995 *PhD Thesis* University of Twente, Enschede, The Netherlands
[29] Sumption M D and Collings E W 1998 *Adv. Cryog. Eng. (Mater.)* **40** 579
[30] Carr W J Jr 1998 *Adv. Cryog. Eng. (Mater.)* **44** 593–600
[31] Bozorth R M 1951 *Ferromagnetism* (Princeton, NJ: Van Nostrand-Reinhold)
[32] Goyal A *et al* 2002 *Physica* C **382** 251–62
[33] Smith T F *et al* 1975 *J. Phys. F: Met. Phys.* **5** L96–9
[34] Clark A F, Childs G E and Wallace G H 1970 *Cryogenics* **10** 295–305
[35] Collings E W and Sumption M D 1995 *Appl. Supercond.* **3** 551–7
[36] Yoo J *et al* 1996 *Physica* C **269** 109–14
[37] Sumption M D *et al* 2002 *Physica* C **378** 894–8
[38] Sumption M D *et al* 2002 *Physica* C **382** 98–103
[39] Sumption M D *et al* 2002 *Adv. Cryog. Eng. (Mater.)* B **48** 824–31
[40] Cheggour N, Ekin J W, Clickner C C, Verebelyi D T, Thieme C L H, Reenstra R and Goyal A 2003 Reversible axial-strain effect and extended strain limits in Y-Ba-Cu-O coatings on deformation-textured substrates *Appl. Phys. Lett.* **83** 4223

APPENDIX B: SLIDES FROM PRESENTATIONS

Available from mdsumption+@osu.edu

APPENDIX H

APPENDIX C: NEW ANTI-CRYOSTAT

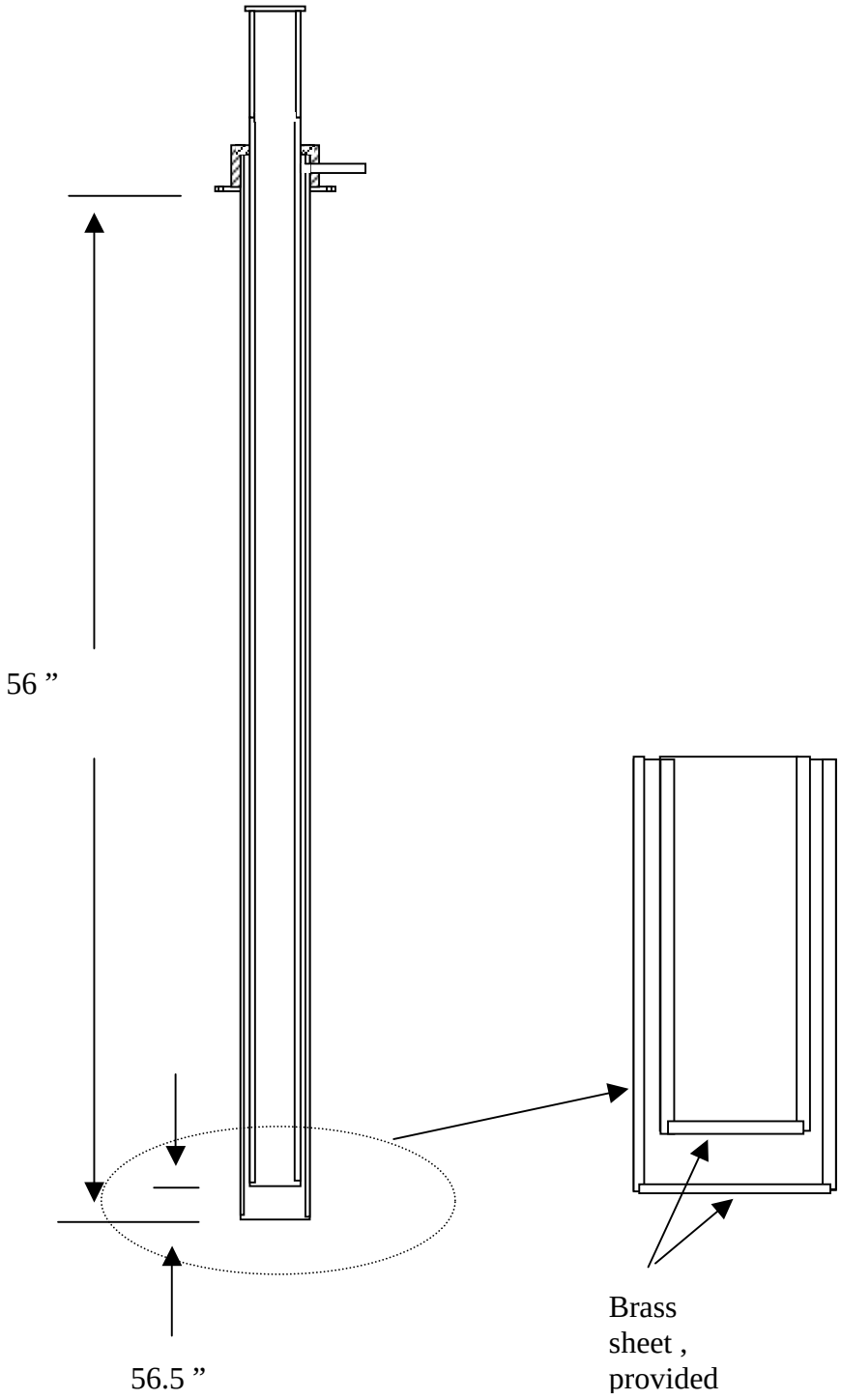

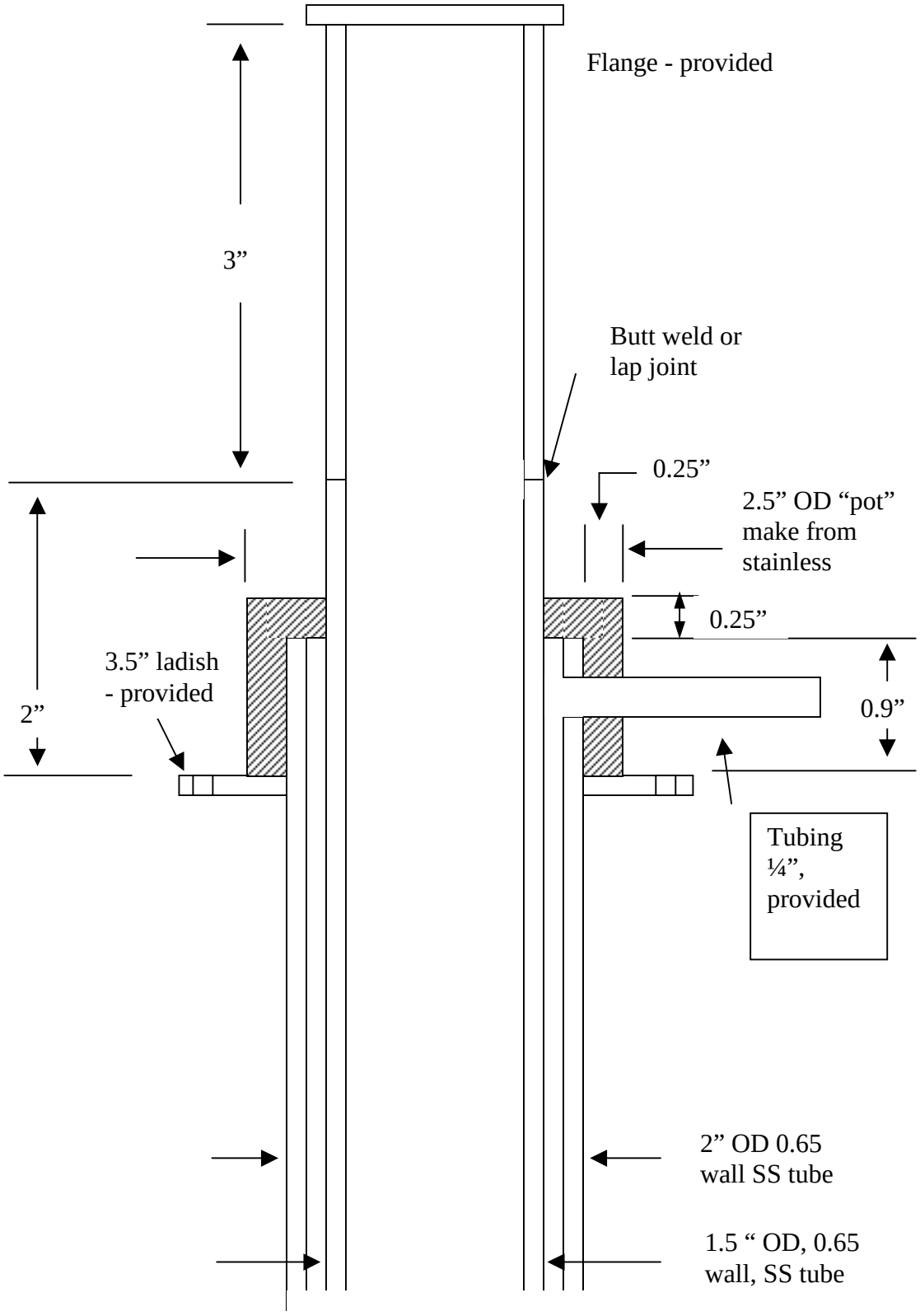
Flange - provided
3”
Butt weld or
lap joint
0.25”
2.5” OD “pot”
make from
stainless
0.25”
3.5” ladish
- provided
2”
0.9”
Tubing
¼”,
provided
2” OD 0.65
wall SS tube
1.5 “ OD, 0.65
wall, SS tube

Air Force Summer Faculty Fellowship Program Final Report
Summer 2004

A NEW ENERGY APPROACH FOR HIGH CYCLE AXIAL AND BENDING FATIGUE LIFE PREDICTION

by

Dr. M.-H. Herman Shen, Professor
Onome Scott-Emuakpor, Graduate Student
Department of Mechanical Engineering
The Ohio State University
206 W. 18th Ave.
Columbus, Ohio 43210
Tel: (614) 29-2280; Fax: (614) 292-8290
E-mail: shen.1@osu.edu

Host Adviser:
Dr. Charles Cross
Turbine Engine Division
Propulsion Directorate
Air Force Research Laboratory
1950 Fifth Street, Bldg. 18
Wright-Patterson AFB, OH 45433-7251

Tenure: [May 23, 2004] to [August 27, 2004]

Submitted [August 27, 2004] to:
Air Force Research Laboratory
SFFP Point of Contact (John Horner, AFRL/PROP) and
Adviser (Dr. Charles Cross, AFRL/PRTS)

Final Report, AFRL/PR Summer Research Fellowship Program 2004
Dr. Herman Shen & Onome Scott-Emuakpor

I. EXECUTIVE SUMMARY

This report summarizes the research and scholarly activities on the 14 weeks summer research assignment at Turbine Engine Fatigue Facility (TEFF), AFRL/PR under the Summer Research Fellowship Program. In the summer research period, the faculty from OSU (Prof. Herman Shen) and his graduate research assistant (Onome Scott-Emuakpor) in collaborating with Dr. Charles Cross and Dr. Tommy George of AFRL/PRTS were conducting research at the Turbine Engine Fatigue Facility (TEFF) at Wright-Patterson AFB. The objective of the summer research is to extend the research activities of Prof. Shen's multiaxial high cycle fatigue research programs previously funded by AFRL/ML, AFRL/PR, and DAGSI (The Dayton Area Graduate Studies Institute). The overall concept of the research approach is to accumulate fatigue energy on a base-excited plate specimen at high frequency resonant modes and to complete a multiaxial fatigue test in a few hours at very low cost. The performance of the approach, so-called vibration-based multiaxial fatigue testing methodology, had been demonstrated [1-5] by the experimental results from steel, 6061-T6 aluminum, and Ti-6Al-4V plate specimens subjected to fully reversed uniaxial and biaxial bending stress states. Results were compared with those produced using traditional fatigue test machines. Additionally, this vibration-based fatigue method has the advantage of being able to produce a fatigue crack in the test specimen while it is still in the initiation stage [2-3]. Furthermore, a technique has been also developed [4] to produce residual stress, enabling vibration-based fatigue testing at various stress ratios.

In order to extrapolate the results from the experience accumulated under the previous projects and foresee the needed directions of the fully realized implementation of this new technology, recently, our efforts has been focused on the development of an integrated computational-experimental approach for prediction and estimation of total fatigue life to damage (crack initiation) and final failure (crack growth to a critical size) of aircraft gas turbine materials and components. The approach consists of the following elements: (1) development of a vibration based fatigue testing procedure to achieve low cost bending fatigue experiments and (2) development of a life prediction and estimation implementation scheme for calculating effective fatigue cycles.

The vibration-based fatigue testing procedure is capable to produce bending fatigue data at greatly reduced savings in both time and cost. This testing procedure can be further extended, through proper specimen geometrical design and a yielding process, to generate fatigue data at various stress ratios, so that assessment of material fatigue properties can be achieved at greatly reduced savings in both time and cost. The resulting fatigue data from 6061-T6 aluminum under fully reversed bending and axial stresses have been used to construct S-N curves for comparison. A significantly higher fatigue limit in bending was observed. Finally, an improved energy-based criterion was developed for fatigue life prediction. The comparison between the life prediction and the experimental results clearly indicates that the criterion provides reasonable life estimations.

The scope of the approach is quite significant and complex and the completion of all the issues addressed in this research exceeded the 14 weeks timeframe of the summer faculty research program scope, therefore, during this summer, we aimed to explore all the possibilities that this new methodology can achieve and lay down a solid theoretical and experimental foundation for the follow-up research. The accomplishments during this summer tenure are summarized as follows:

- **Construction of S-N Curves – Fully Revised Axial and Bending:** In our recent investigations [5], a series of fully reversed bending fatigue tests were carried out using a vibration-based testing procedure to investigate the effects of bending stress on fatigue limit. The results indicate that the fatigue limit for 6061-T6 aluminum is approximately 20% higher (see Figure 1 or Figure 2) than the respective limit in fully reversed tension-compression (axial).

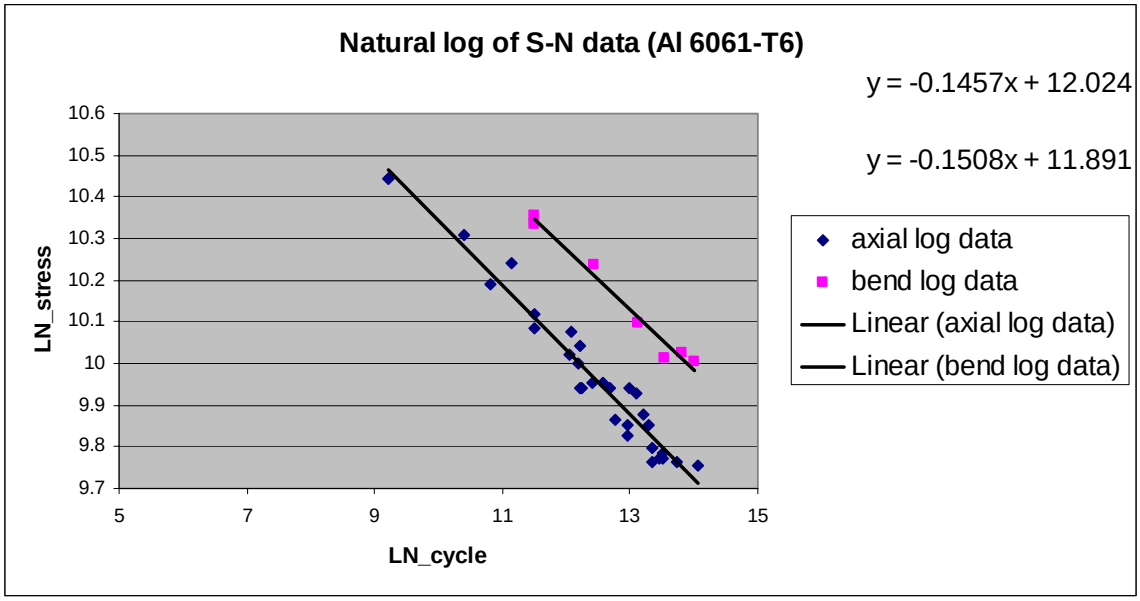

Figure 1. Natural log of stress versus natural log of cycle plot – linear scale

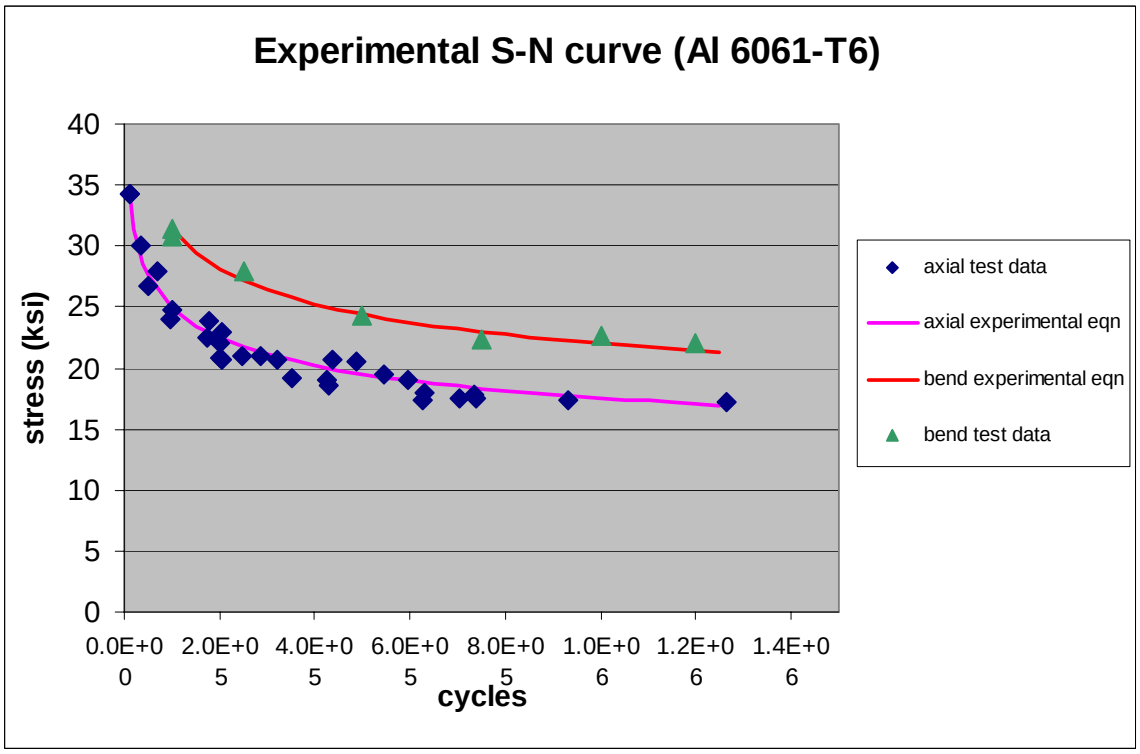

Figure 2. Linear S-N curves – tension/compression, bending

- **Energy-based Fatigue Criterion – Fully Revised Axial:** To validate the experimental observations and further evaluate the possibility of prediction of fatigue life, an improved high cycle fatigue criterion has been developed, which allows one to systematically determine the fatigue life based on the amount of energy loss per fatigue cycle. A comparison between the prediction and the experimental results was conducted and shows (see Figures 3&4) that the criterion is capable of providing accurate fatigue life prediction.

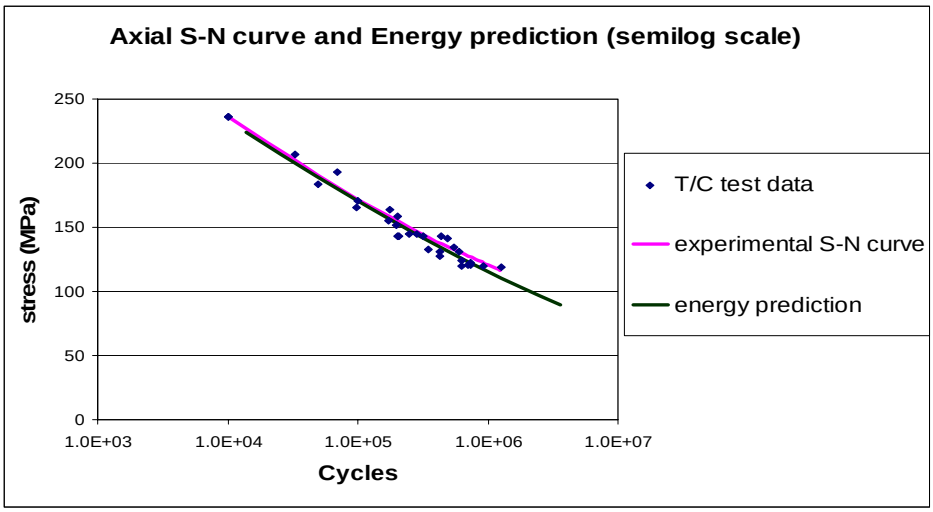

Figure 3. Comparison of the energy prediction and experimental S-N curve Linear-Logrithmic scale.

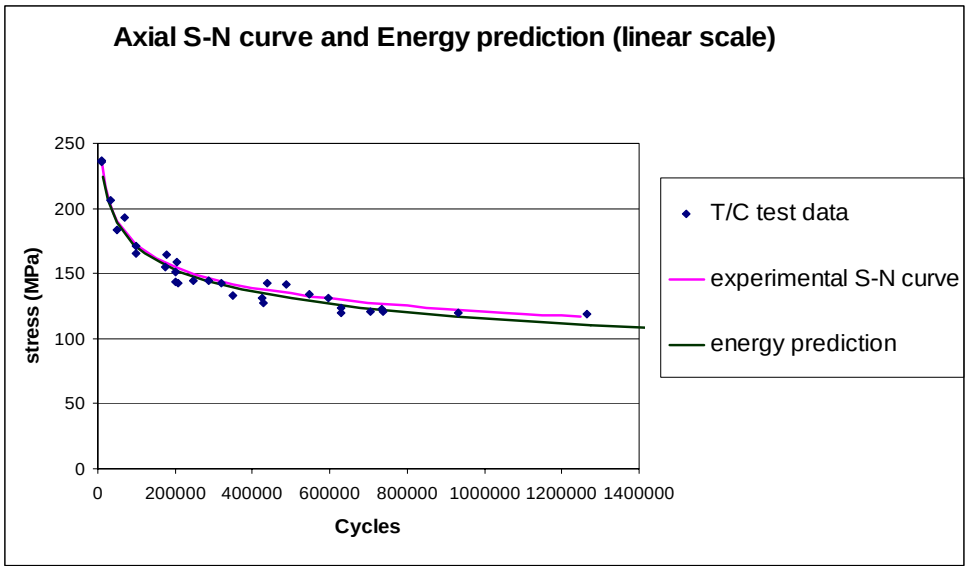

Figure 4. Comparison of the energy prediction and experimental S-N curve Linear-Linear scale.

- **A New Total Energy-based Fatigue Criterion – Fully Reversed Bending:** In order to extend the energy-based criterion to the bending case, the stress gradient effect through the thickness of the specimen has been evaluated. The above fatigue criterion for fully reversed axial cannot be used, in its current state, to accurately calculate fatigue life cycles for the bending case. Therefore, a new total energy-based fatigue criterion was developed which incorporates the evaluation of the strain energy through the thickness of the specimen (so-called total effective strain energy). A comparison between the prediction and the experimental results was conducted and shows (see Figure 5) that the new total energy-based fatigue criterion is capable of providing accurate fully reversed bending fatigue life prediction.

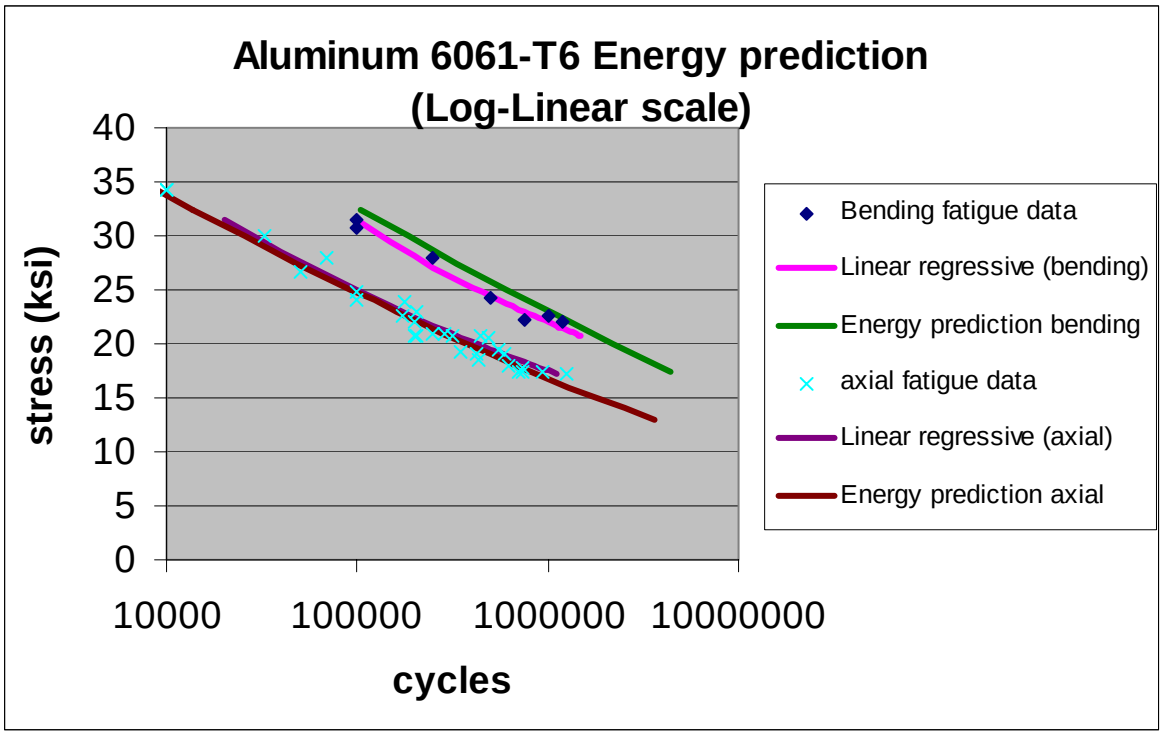

Figure 5. S-N test data and energy-based prediction results (bending, and tension/compression)

- **A New Energy-based Fatigue Criterion – Axial with Various Stress-Ratios:** When mean stress is included in a fatigue procedure, it dissipates residual energy and increases the plastic strain per cycle, thus reducing the amount of cycles required for fatigue. In order to evaluate the effects of mean stress during a cyclic procedure, a new criterion for mean stressed fatigue life assessment was developed. The performance of the criterion was demonstrated by the experimental results from 6061-T6 dog-bone specimens subjected to axial stress at two mean stress levels (10.2ksi and 20ksi) in the range of failure cycles from 10000 to just over 3 million. Results were used to construct a fatigue stress versus cycle, or S-N, curve as shown in Figure 6. In Figure 6, a comparison between the prediction and the experimental results was also conducted and clearly shows that the criterion is capable of providing accurate fatigue life prediction.

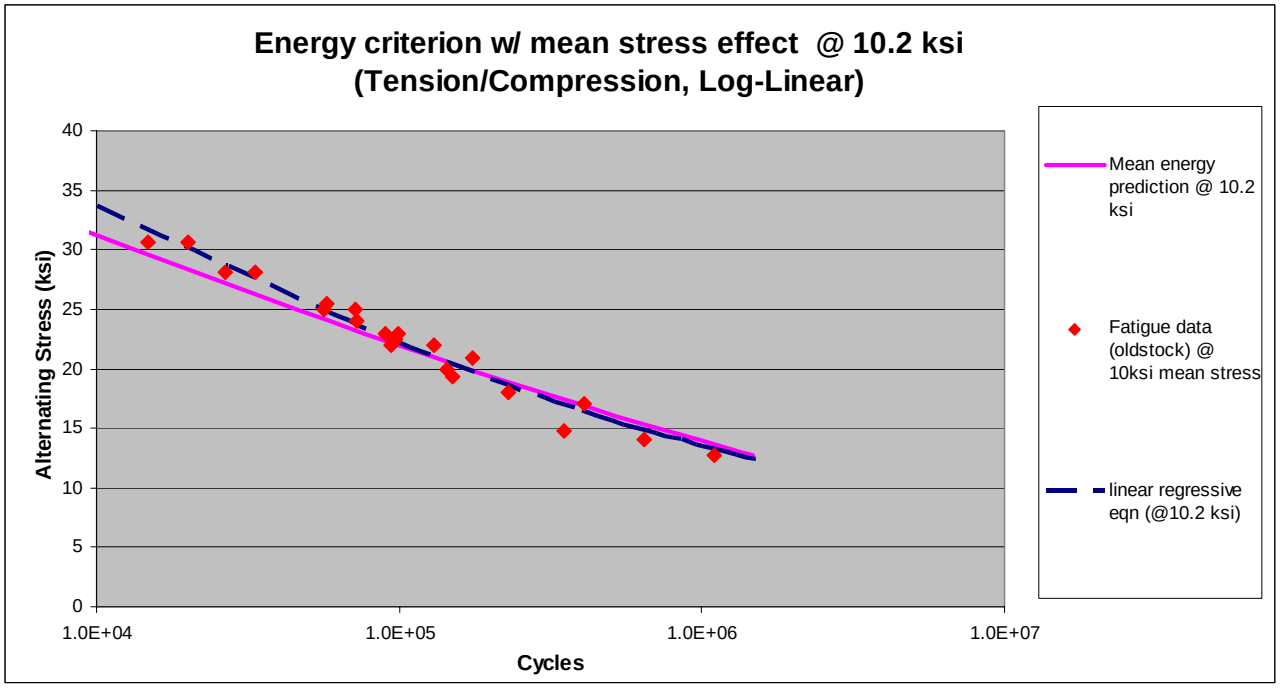

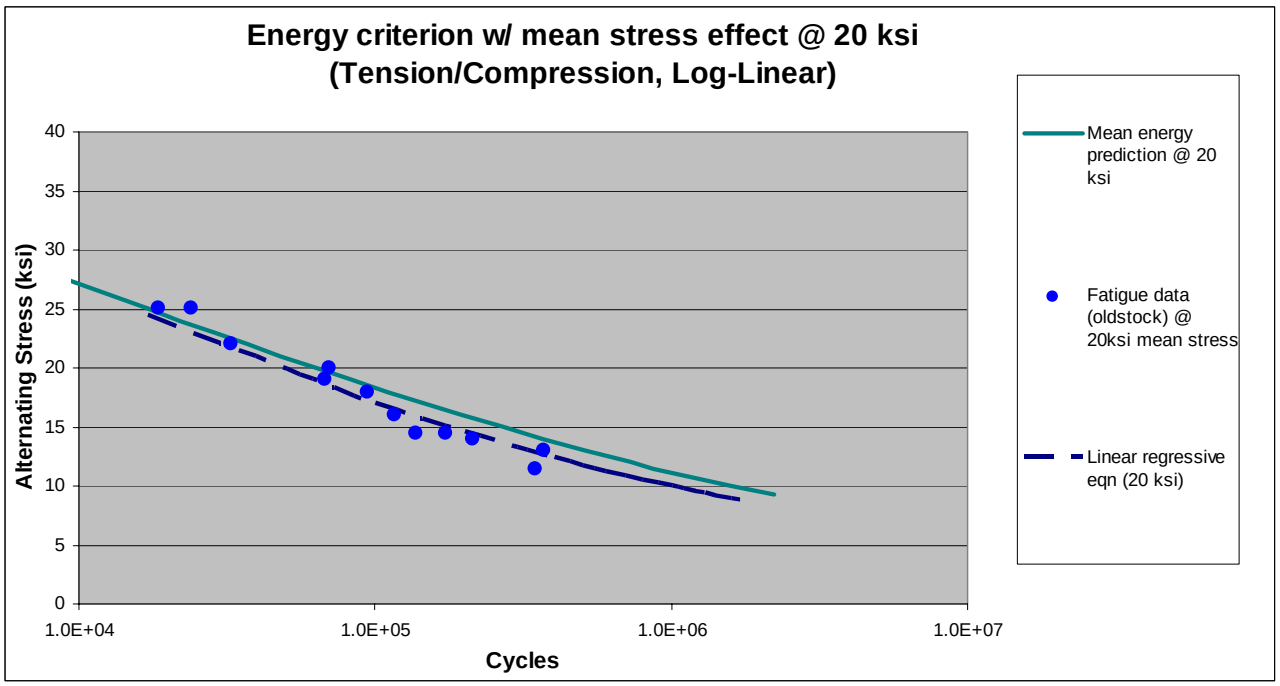

Figure 6. Semi-log S-N plots for fatigue data with mean stresses of 10.2 and 20 ksi

ACKNOWLEDGMENTS

The summer faculty (Dr. Herman Shen) and his student (Onome Scott-Emuakpor) would like to thank the Air Force Research Labs, specifically the TEFF Lab of AFRL/PRTS, for their financial support, facility and equipment access, and encouragement of this summer research.

II. INTRODUCTION

Structural components subjected to high frequency vibrations, such as those used in rotating parts of gas turbine engines, are usually required to be designed using a lifetime failure-free criterion for a very large number of cycles, or an endurance limit. Tools, such as the Goodman diagram [6] and the modified Goodman diagram [7] are often used, but these diagrams are usually constructed using uniaxial fatigue data only, and the design is based on uniaxial stresses. The Goodman (or Haigh) diagram is a constant life diagram in the form of a plot of alternating stress (half of the cyclic stress range) vs. mean stress, and represents the fatigue strength of a given material for a very large number of cycles. A typical Goodman diagram for Ti-6Al-4V forged plate, corresponding to a constant life of 10^7 cycles, is shown in Figure 1 [7, 8]. While it is desirable to have data at many values of mean stress, or equivalent stress ratio, R, as shown in Figure 7, there are many cases in design where data at a single value of R=-1, fully reversed loading with zero mean stress, are the only data available. Such data, often obtained from vibratory tests on a specimen or component, are then used to construct a Modified Goodman diagram using a straight line extrapolation from the zero mean stress data point to the yield or ultimate strength of the material which is considered as zero alternating stress (see Fig. 7). Alternate approaches can be used to construct a Goodman diagram by using an equation to represent behavior at all values of mean stress or stress ratio, but data for at least one value of R are needed to establish the constants. An example of such a formulation is presented by Nicholas and Maxwell [9] using a modification of the constant energy density formulation due to Jasper [10]. The modified Jasper equation fit to the data is shown in Figure 7.

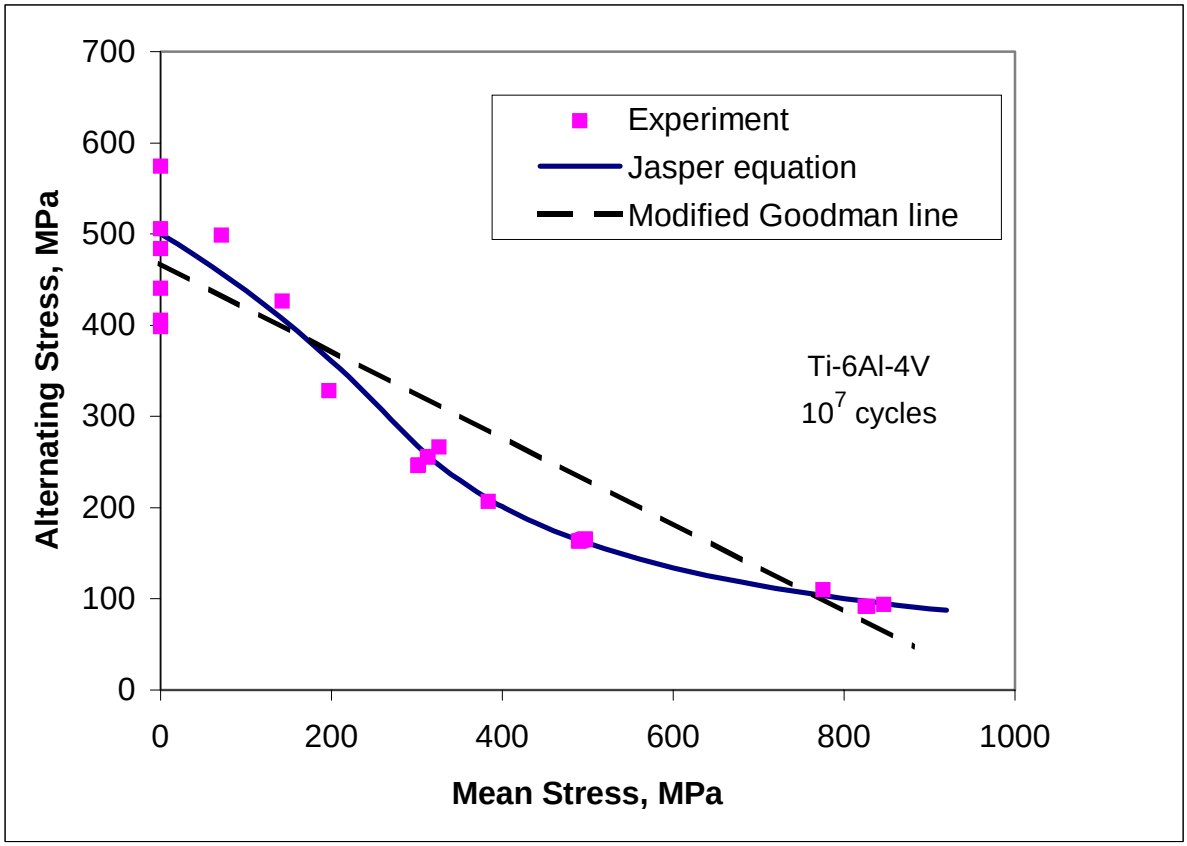

Figure 7. Typical Goodman (or Haigh) Diagram [7, 8]. The straight line represents a Modified Goodman diagram. The modified Jasper equation is also shown.

Uniaxial fatigue tests on conventional test machines require long time periods to achieve a large number of cycles approaching the endurance limit. Even a servo-hydraulic test machine operating at 60 Hz requires approximately 46 hours to accumulate 10^7 cycles for a point on an S-N curve. Additionally, for each value of mean stress or stress ratio, several data points are needed in order to interpolate the value of stress at the desired life (10^7 in this example) to get a point on the Goodman Diagram. Therefore, significant amounts of time are required to characterize the uniaxial fatigue properties of a material. While newer machines are available which can achieve higher frequencies, and ultrasonic machines that operate at 20 kHz have been developed [11], these tests are typically limited to uniaxial tension. Uniaxial fatigue data are insufficient for assessing high cycle fatigue limit stresses which often occur in components that are subjected to biaxial loading over a wide range of cyclic frequencies. In turbine blades, for example, fatigue failure often occurs under high

order bending or combined bending and twist modes that produce short wave length stress states at very high frequencies. Unfortunately, the current capability to conduct biaxial fatigue tests, especially under bending as well as axial stress states, is adversely affected by the high cost of development of such testing methods and the lack of existing equipment to conduct the necessary tests at anything other than very low frequencies. In turn, the development of a basic understanding of the effects of frequency, biaxial stress state, and stress gradient in bending on the high cycle fatigue strength of complex geometries has been hampered. Hence, current U.S. Air Force HCF research efforts to develop new design methodologies for HCF under realistic stress states have been significantly hindered due to lack of ability to obtain sufficient fatigue data for a meaningful fatigue strength assessment of actual components.

Resonant fatigue testing procedures have been in existence for over a century. It is of interest to note that in the time period from 1879 to 1925, no fewer than 35 journal articles appeared describing new test procedures and methods for fatigue testing [12]. The earliest test methods involved coupling a specimen and a driver in order to obtain a resonance or near resonance condition to decrease the power requirements. It was recognized early on that “working in or near the resonance (unstable dynamic equilibrium) demands special controlling devices” [13]. These early machines were only able to achieve frequencies up to approximately 100 Hz and were confined to either pure axial or torsion modes under either resonant or non-resonant conditions [14]. Among the early test machines that operated on the resonance principle were those built by Sontag that produced a constant force at 30 Hz. The Schenck machines, of the 1930’s and later [15], operated in a fairly stable manner by using a very large spring coupled to a much smaller specimen and could run continuously under constant load at approximately 30 Hz. Later on, such machines were controlled with automatic feedback from a load cell to correct for any deformation of the specimen during the test such as creep or initiation of a fatigue crack. A very large version of a Schenck machine [16] was used in the Messerschmitt factory during World War II to test large components, but the loading was still uniaxial. It is of interest to note that electromagnetic resonant fatigue test machines are currently advertised on the Internet having high test frequencies of 40-300 Hz and boast of the same advantage of the first machines, namely low power consumption. One of the advantages of a resonant machine where the specimen is part of the mechanical system is that upon incipient failure, the spring constant of the specimen changes and throws the system off

resonance which is a warning of impending failure if it is desired to examine the specimen before total destruction of the sample [17]. In addition to mechanically driven machines, magnetic excitation to drive a machine/sample combination into resonance dates back to prior to World War II (see, for example, [18]).

Tests of structural components and full-scale structures conducted under both resonant and non-resonant conditions [19] date back to the 1860's [20]. Because of the expense of the test articles as well as the test machines, such tests are normally limited to very few components and are not very useful for extracting fatigue properties of the material, even though the stress state at a failure point may be complex. Whatever information is extracted is limited to the specific number of cycles to failure due to the applied loading condition. Fatigue limit strengths of the structure or the material are rarely obtained for cycle numbers near the endurance limit.

Recently, the use of a variation of a step-test procedure that dates back many years [21] has been shown to produce fatigue limit data that are consistent with those obtained from interpolation of S-N curves at fixed values of mean stress or stress ratio [22]. With a limited number of samples, since each sample produces a fatigue limit stress data point, a Haigh diagram (see Fig. 7) can be constructed in a reasonable amount of time.

To achieve the goal of determining the fatigue limit stress under uniaxial or biaxial bending, stress states that are commonly achieved in turbine blades under resonance conditions, a combination of the concepts described above were utilized and expanded to develop a new testing procedure. A novel vibration-based fatigue testing concept was developed by the authors and his AFRL partners [1-5] where a base-excited plate specimen is driven into a high frequency resonant mode. Using the step-testing procedure [22] and finite element analysis of the vibrating specimen, we are able to determine the loads and stresses to produce high cycle fatigue failure corresponding to a fixed number of cycles (10^6 or 10^7 in this case). Our previous studies [1-5] clearly showed it is possible: (1) to accomplish fatigue testing in only a few hours compared to the tens of hours required of typical fatigue test machines, (2) to generate both uniaxial and biaxial bending fatigue data through proper specimen geometrical design, and (3) to identify the presence of fatigue crack in the test specimen while it is still in the initiation stage. Further development and modifications to this

technique are in progress which will allow generation of multiaxial fatigue data at various stress ratios as well as estimation/prediction of fatigue life via energy approaches.

III. ENERGY-BASED RESEARCH SCOPE

Previous research conducted in this area reveals a correlation between the fatigue life of a material and the strain energy dissipation during the process. It is understood that the strain energy required to fracture a material, monotonically, is the same as the strain energy during a cyclic fatigue procedure. Due to this belief, an energy-based criterion has been developed to allow one to systematically determine fatigue life based on the amount of energy loss per fatigue cycle.

Prior to the development of this criterion, a number of uniaxial fatigue test were conducted under tension/compression (axial) and bending loads (Each procedure is discussed in section IV). The fatigue results were observed and analyzed on a stress versus cycle, or so-called S-N, plot. A comparison between the resulting uniaxial fatigue data illustrates that the fatigue limit of bending is approximately 20% higher than tension/compression at each respective fatigue life (number of cycles). The difference in the uniaxial results is, believed to be, due to the effect of the stress gradient through the thickness of each respective uniaxial procedure. In a tension/compression specimen, as shown in Figure 8, the distribution of the normal stress along the thickness of the specimen is constant, therefore implicating the stress gradient is zero. In the case of bending, the normal stress decreases from the surface to the neutral axis, thus creating a stress gradient. Based on this observation, intuitively, it is natural to assume that at the same fatigue life, the alternating fatigue stress level, or fatigue limit, of a bending specimen must be higher than that of a tension/compression specimen to compensate for the severe discrepancy in plastic deformation through the thickness at the fatigue zone. Therefore, under the same stress level, the number of cycles to failure for a bending specimen is expected to be higher.

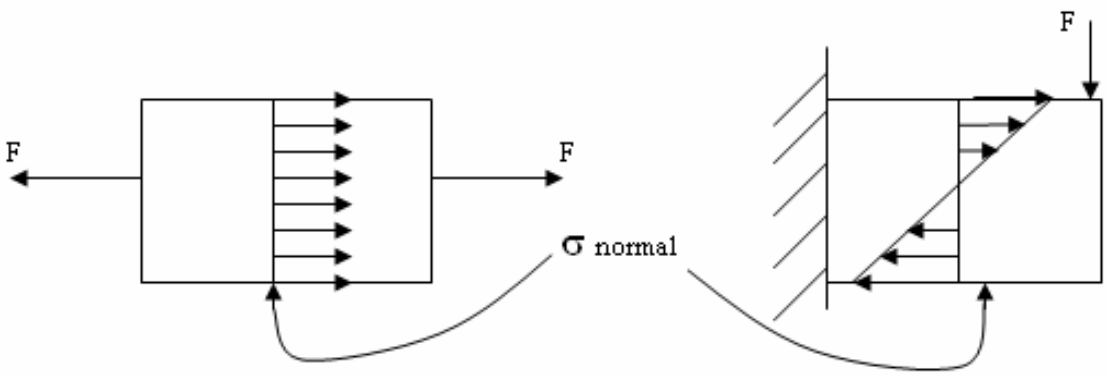

Figure 8. Stress distributions of axial and bending

Several energy-based methods for predicting fatigue life have been developed. However, an improved criterion with the capability to, easily, incorporate stress gradient effect was essential. Hence, an improved energy-based criterion was developed for tension/compression fatigue life prediction, as a benchmark for the bending case. The criterion was developed with the concept that fatigue life can be systematically determined by dividing the total strain energy density dissipated during a monotonic process by the strain energy density for one cycle. This impression is the foundation of the energy-based criterion, which is calculated with the expression shown by Equation 1 [5].

$$N = C\frac{\sigma_f\left(\varepsilon_f - \frac{\sigma_f}{2E}\right) - \sigma_o\varepsilon_o\left(\cosh\frac{\sigma_f}{\sigma_o} - 1\right)}{2\sigma_o\varepsilon_o\left[\frac{\sigma}{\sigma_o}\sinh\frac{2\sigma}{\sigma_o} - \left(\cosh\frac{2\sigma}{\sigma_o} - 1\right)\right]} \quad (1)$$

The parameters are defined as follows: C, ε_o, and σ_o are material properties acquired through the analysis of tension/compression fatigue data, σ_f and ε_f are the monotonic failure stress and strain respectively, σ is the fatigue stress, and E is the modulus of elasticity [5]. E, σ_f, and ε_f can be obtained from experimental monotonic fracture results. Figures 3 and 4 show the comparison between the energy criterion, experimental S-N curve (linear regressive equation), and

tension/compression test data. Each figure shows that the energy prediction compares well with experimental data for cycles higher than 10^5, thus proving that the criterion provides reasonable life estimations.

IV. EXPERIMENTAL PROCEDURES

To assess the fatigue life or fatigue limit of materials, a stress versus cycle plot, so-called S-N curve, was created to display the relationship between the number of cycles to failure and the alternating fatigue stress for aluminum 6061-T6 specimens under axial (tension-compression) and bending stress states.

S-N curve construction – tension/compression:

Axial (tension-compression) loading data was acquired from the ASTM standard fatigue dog-bone (coupon) specimen in Figure 9. To assure accuracy in the cross-sectional area, the specimen was cut from a 0.122 in sheet of aluminum using a water jet procedure. This procedure provided a maximum variance of 2 percent for a specimen with a 0.0305 square inch cross-sectional area.

All the tests were conducted at the room temperature using a MTS Systems Corporation servo hydraulic load frame [4]. The dog-bone specimen is held in place with hydraulic controlled diamond wedges (Figure 10), and a cyclic axial force, at a frequency of about 40 hertz (Hz), is applied. The fatigue limit strength in the tests is determined as the stress for the number of total cycles at which complete failure occurs. Thirty dog-bone tests were completed and the data is acquired using a TestStar II control system [4].

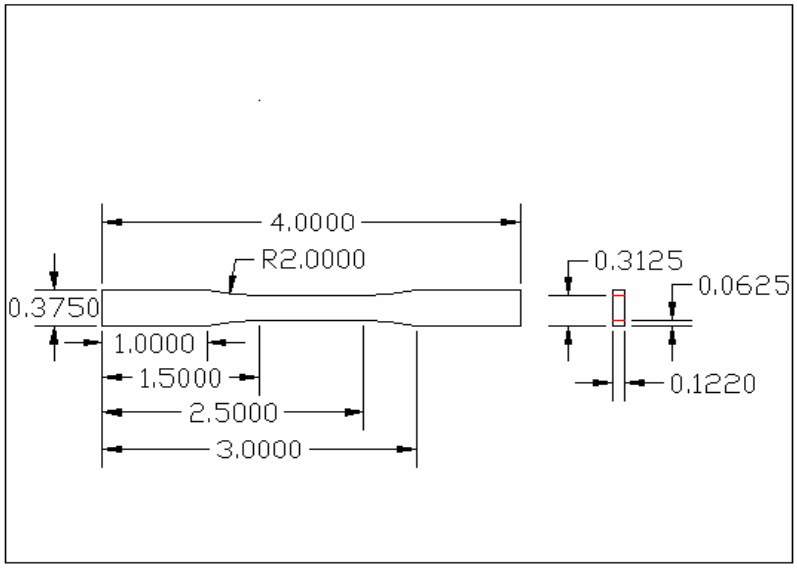

Figure 9. Dimensions of the ASTM fatigue dog-bone specimen

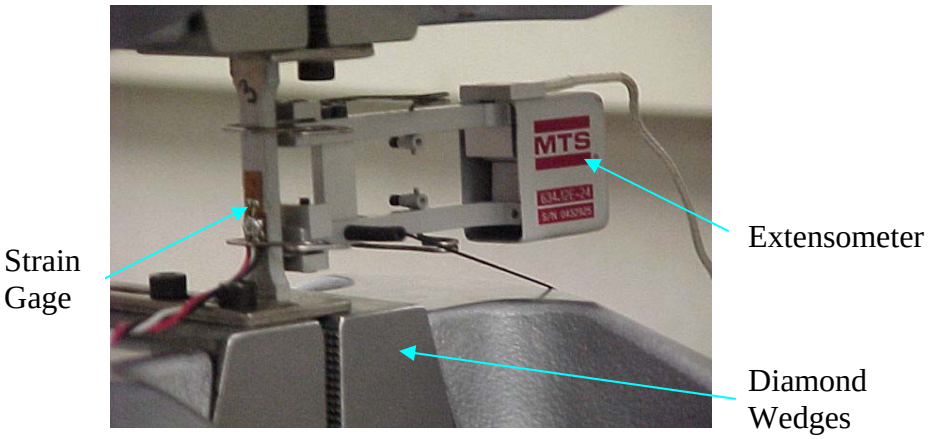

Figure 10. MTS clamping and measurement devices

The results acquired, thus far, for tension-compression fatigue tests can be viewed on the summarized S-N plot in Figures 1-6. In order to reduce the effect due to the machine instability at different frequencies, all the tests are conducted at 40Hz. The scatter in each plot is typical in S-N data, therefore the results can be observed as consistent.

S-N curve construction – bending:

Bending fatigue data was acquired from the uniaxial fatigue specimen in Figure 11 [1]. The specimen is 4.5 by 6.5 inches with a clamp area of 2 by 4.5 inches and was sheared from the same 0.122 in thick sheet of aluminum 6061-T6 as the dog-bone specimens.

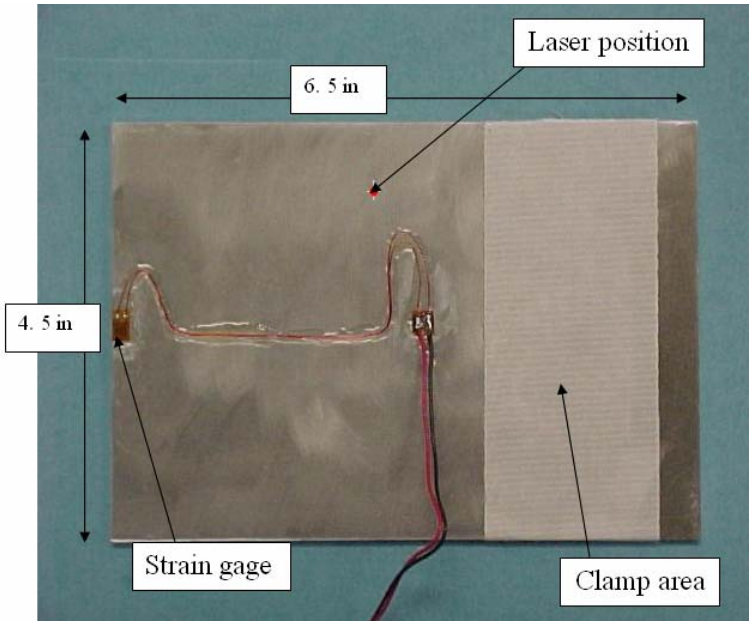

Figure 11. Bending fatigue specimen

Bending tests were conducted with an Unholtz Dickie 6000 lb electrodynamic shaker (Figure 12) located in the Turbine Engine Fatigue Facility (TEFF) of the Air Force Research Laboratory (AFRL) in the Propulsion Directorate at Wright-Patterson Air Force Base. As shown in Figure 12, the test specimen is mounted cantilevered to the shaker head. A forced vibration is then conducted on the specimen at two-stripe mode (the mode shape that contains with two nodal lines with frequency range: 1500 Hz – 1600 Hz). The Vibratory displacement of the plate during two-stripe mode, analyzed with the finite element software ABAQUS, is shown in Figure 13 [5]. The test specimen is sufficient for acquiring bending data due to the behavior at the free edge being similar to a free-free bending analysis.

The measurement instruments used consist of an accelerometer, a laser-vibrometer for measuring the velocity or displacement of a point on the specimen, and strain gages. The finite element (FEM) study, from Figure 13, was conducted before the tests to locate the instrumentation on the plate specimens and to determine the frequency at which two-stripe mode occurred [1].

Due to strain gages experiencing internal failure at cycles fewer than the total at the anticipated fatigue limit, the fatigue tests were conducted using the laser vibrometer for measurement. This provides the only non-intrusive technique of the available instrumentation as well as an accelerometer for monitoring the shaker input force. However, the velocity signal from the laser must first be calibrated to the corresponding strain in the fatigue region of the plate. This was achieved by running a calibration test with the plate specimen instrumented with a strain gage placed in the expected maximum strain region or the fatigue region, the mid-point at the free edge of the plate.

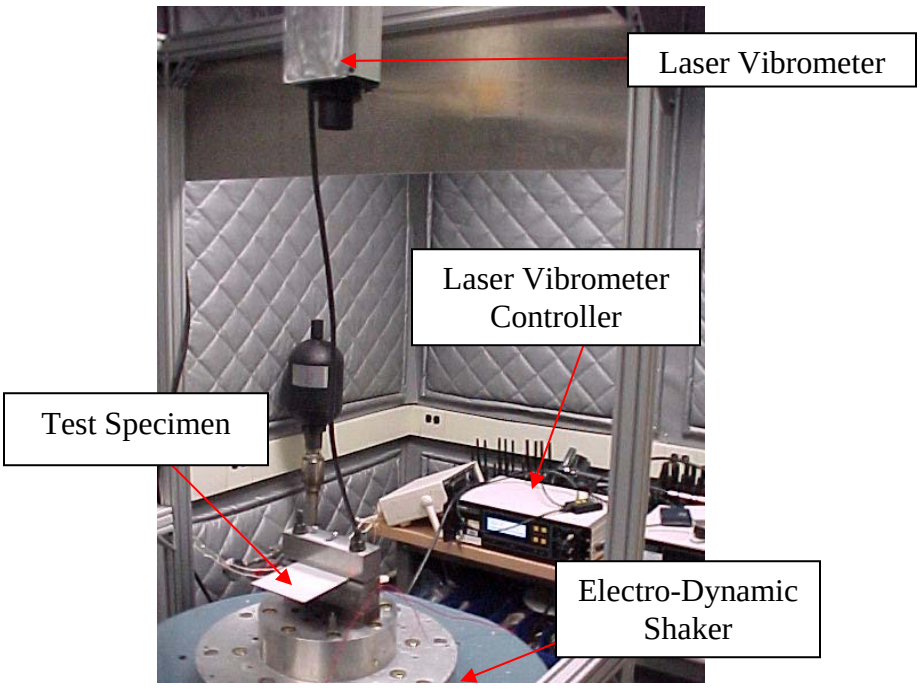

Figure 12. Vibration-based fatigue experiment set-up

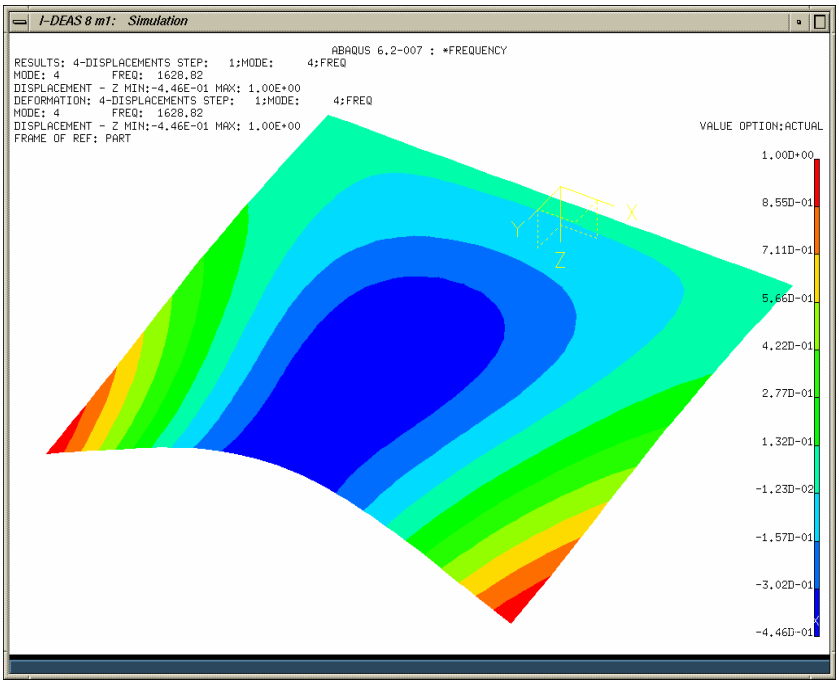

Figure 13. FEM two-stripe mode shape of the plate specimen

During the calibration process, data were taken from both the strain gage and from the laser vibrometer while the specimen was in resonance at various shaker power settings, or in other words, for various strain levels in the specimen which allows for the construction of a strain-laser calibration curve. Once a relationship between the strain in the fatigue region and the velocity/displacement at the laser position is established, which is approximately linear as shown in Figure 14, a fatigue test may be conducted. It is important to note that the linear relationship between strain and velocity is not the same for all tests. Minimal change in the natural frequency of a test specimen, which is caused by slight changes in the clamping fixture and precision of the specimen's geometry, can alter the slope between velocity and strain data. Therefore, the calibration must be done for each bending fatigue test.

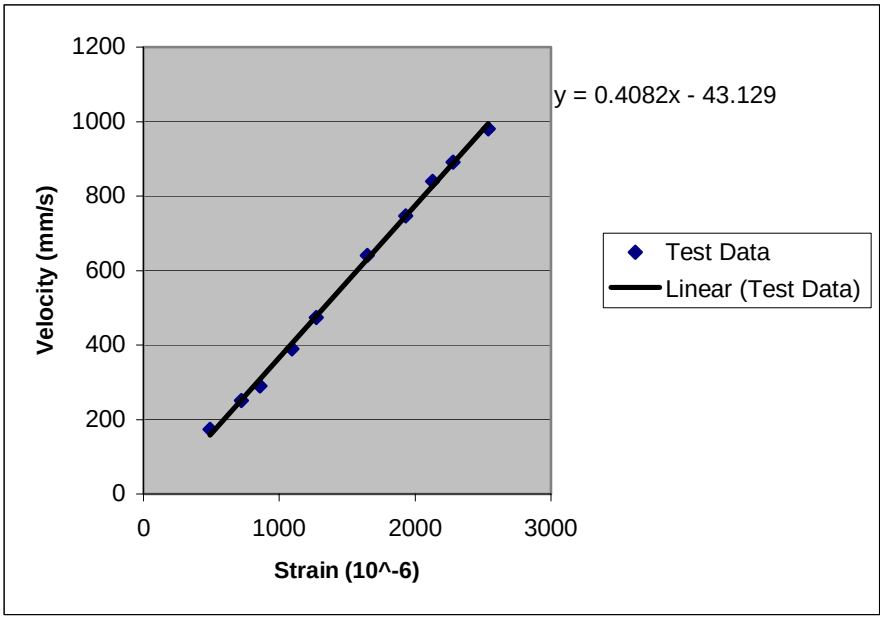

Figure 14. Laser-strain gage correlation

All the bending fatigue tests were conducted in accordance with the step-test method developed by Maxwell and Nicholas [6]. This step-test technique uses a single specimen to generate a fatigue limit from multiple incremental loading steps. Each step corresponds to the number of cycles considered to be necessary to reach the fatigue limit. In the bending fatigue tests, the fatigue limit was assigned a life in the range between 10^4 to $2\text{x}10^6$ cycles. The step-test method has been utilized in our previous studies [1-3] and shown to produce fatigue limit stresses that are consistent with those obtained using conventional S-N test results [6]. The fatigue limit stress is determined using the following equation

$$\sigma_A = \sigma_{pr} + \frac{N_f}{N_t}\left(\sigma_f - \sigma_{pr}\right) \tag{2}$$

where σ_A is the (max) alternating stress, σ_{pr} is the (max) stress level of the step prior to failure, N_f is the number of cycles to failure in the final step, σ_f is the (max) stress level of the final (failure) step, and N_t is the number of cycles of each complete step. The test is begun at a stress level below that of the anticipated fatigue crack initiation stress at the number of cycles of interest for the particular test specimen material. After completing the specified number of cycles in a step without a failure,

the stress level is increased incrementally for the next step. The procedure is repeated until failure occurs. Then, using the above equation, the fatigue limit stress of the material at the desired number of cycles can be determined.

The fatigue limit strength in typical tension/compression tests is determined as the stress at which complete failure occurs at the required number of cycles. Total life, where the fatigue crack propagates through the specimen and failure occurs, was not distinguished from crack nucleation or crack initiation life. Computations have shown that the fatigue crack propagation life is only a small fraction of total life when testing at stress levels near the HCF limit defined at 10^6 cycles. In the case of vibration-based bending fatigue testing under resonance conditions, however, there does not exist a definitive phenomenon such as abrupt failure. Therefore, in all bending tests the fatigue limit is defined at the instance corresponding to a sudden change in the dynamic response of the plate associated with the initial stage of fatigue crack development. At this point, an approximately 0.5mm to 1 mm long series of microcracks were developed and identified. The development of a crack or microcracks in the specimen changes its stiffness and hence its resonant frequency. The initiation or development of the fatigue crack in the plate specimens was observed by the onset of a rapid decrease in the measured velocity for a given shaker driving frequency and amplitude and it is at this point that the fatigue limit stress, the stress in the crack location, was determined via finite element calculation in conjunction with the laser readings. This technique was developed and has been verified in our previous studies [1-3].

Experimental bending data is acquired from test specimens fatigued at the two-stripe mode with a natural frequency around 1600 Hz. Recall that, typical tension-compression fatigue tests on a MTS tensile test machine operate at 40 Hz, requiring approximately 7 hours to accumulate 10^6 cycles for each step during the step-test. Therefore, significant amounts of time can be saved to characterize the bending fatigue properties via the vibration-based fatigue testing procedure [1, 2]. The fatigue data from the bending tests can be seen in Figures 1-6. The number of cycles to failure range from 10^5 to 1.2×10^6. Similar to tension/compression S-N results, bending fatigue result displays some scatter which is common in a majority of published fatigue data.

V. TOTAL EFFECTIVE ENERGY-BASED BENDING FATIGUE CRITERION

In order to extend the energy-based criterion to the bending case, the stress gradient effect through the thickness of the specimen was evaluated. The current fatigue life prediction method (Equation 1) cannot be used, in its current state, to accurately calculate fatigue life cycles for the bending case. Therefore, the evaluation of the strain energy through the thickness of each fatigue specimen (total effective strain energy) was incorporated. The total effective strain energy is, essentially, strain energy per unit area (length and width). Due to the constant alternating stress through the thickness of a specimen under tension/compression fatigue, integrating the total effective strain energy analysis to this case would produce fatigue life predictions identical to those previously calculated with Equation 1 and shown on Figures 3 and 4. In the case of bending, the alternating stress through the thickness is not constant, thus Equation 1 can be written as a function of the specimen thickness. Figure 15 shows the stress distribution of a typical specimen in bending, where σ_A is the alternating stress and y_t is the distance from the neutral axis.

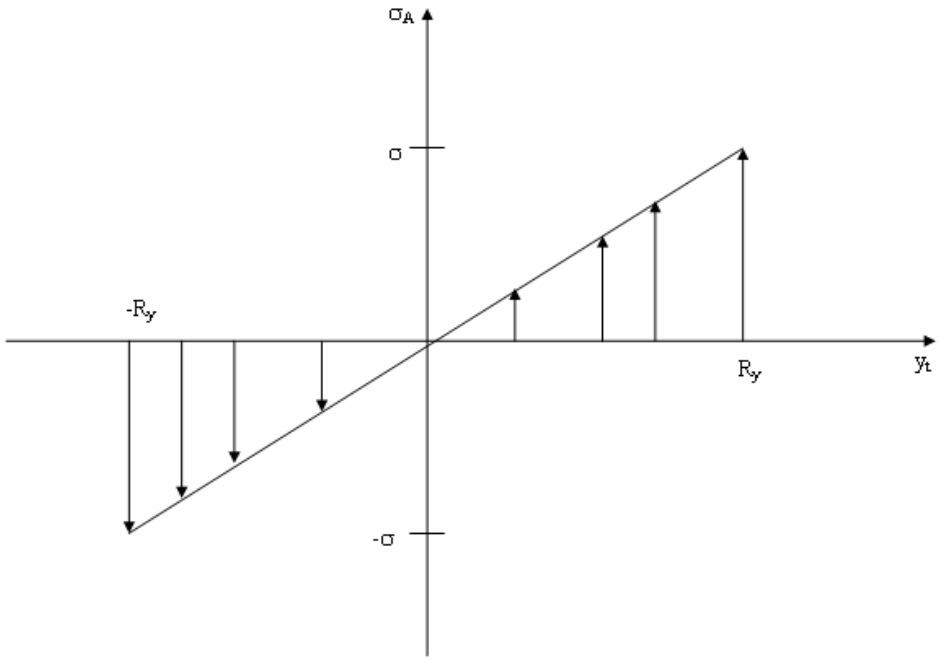

Figure 15. Bending stress distribution

As a result of evaluating the slope in Figure 15, the alternating stress at any point through the thickness of the specimen can be determined by Equation 3.

$$\sigma_A = \frac{\sigma}{R_y} y_t \tag{3}$$

The strain energy density dissipated per cycle (W_{cycle}) and during monotonic failure (W_f) is expressed as followed:

$$W_{cycle} = \frac{2\varepsilon_o \sigma_o}{C}\left[\frac{\sigma_A}{\sigma_o} Sinh\left(\frac{2\sigma_A}{\sigma_o}\right) - \left(Cosh\left(\frac{2\sigma_A}{\sigma_o}\right) - 1\right)\right] \tag{4}$$

$$W_f = \sigma_f\left(\varepsilon_f - \frac{\sigma_f}{2E}\right) - \varepsilon_o \sigma_o\left(Cosh\left(\frac{\sigma_f}{\sigma_o}\right) - 1\right) \tag{5}$$

In order to calculate the total effective strain energy during cyclic and monotonic failure, each equation is integrated with respect to the distance from the neutral axis. Due to the inability to acquire sufficient, or useful, monotonic bending data, it is assumed that the tensile (monotonic) strain energy density value is the same for bending. Therefore, the total effective strain energy per cycle and during monotonic failure is expressed by Equation 6 and 7:

$$W_{cycle,ev} = \int_{-R_y}^{R_y} W_{cycle} dy_t \tag{6}$$

$$W_{f,ev} = W_f\left(2R_y\right) \tag{7}$$

Where R_y is the maximum distance from the neutral axis. After substituting Equation 3 into Equation 6 and integrating the expression, the resulting equation represents the total effective strain energy dissipated per bending cycle (Equation 8).

$$W_{cycle,ev} = \frac{2\varepsilon_o \sigma_o}{C}\left[R_y Cosh\left(\frac{2\sigma}{\sigma_o}\right) - \frac{3\sigma_o R_y}{2\sigma} Sinh\left(\frac{2\sigma}{\sigma_o}\right) + 2R_y \right] \quad (8)$$

The approximate fatigue life of a specimen at a stress level of σ is systematically determined by the energy-based criterion for bending fatigue life prediction, which is represented by Equation 9.

$$N = C \frac{\sigma_f\left(\varepsilon_f - \frac{\sigma_f}{2E}\right) - \varepsilon_o \sigma_o\left(Cosh\left(\frac{\sigma_f}{\sigma_o}\right) - 1\right)}{\varepsilon_o \sigma_o\left[Cosh\left(\frac{2\sigma}{\sigma_o}\right) - \frac{3\sigma_o}{2\sigma} Sinh\left(\frac{2\sigma}{\sigma_o}\right) + 2\right]} \quad (9)$$

No parameters were altered from the original values, acquired from the tensile/compressive case [5], to facilitate the exactitude between the experimental versus theoretical comparison. The prediction results from Equation 9 were plotted and compared with the bending experimental data, tension/compression test data, and the energy-based prediction results for tension/compression (Equation 1). These results are shown in Figure 16. The results show that the energy-based criterion for bending compares well to previous test data as well as the energy-based prediction for tension/compression.

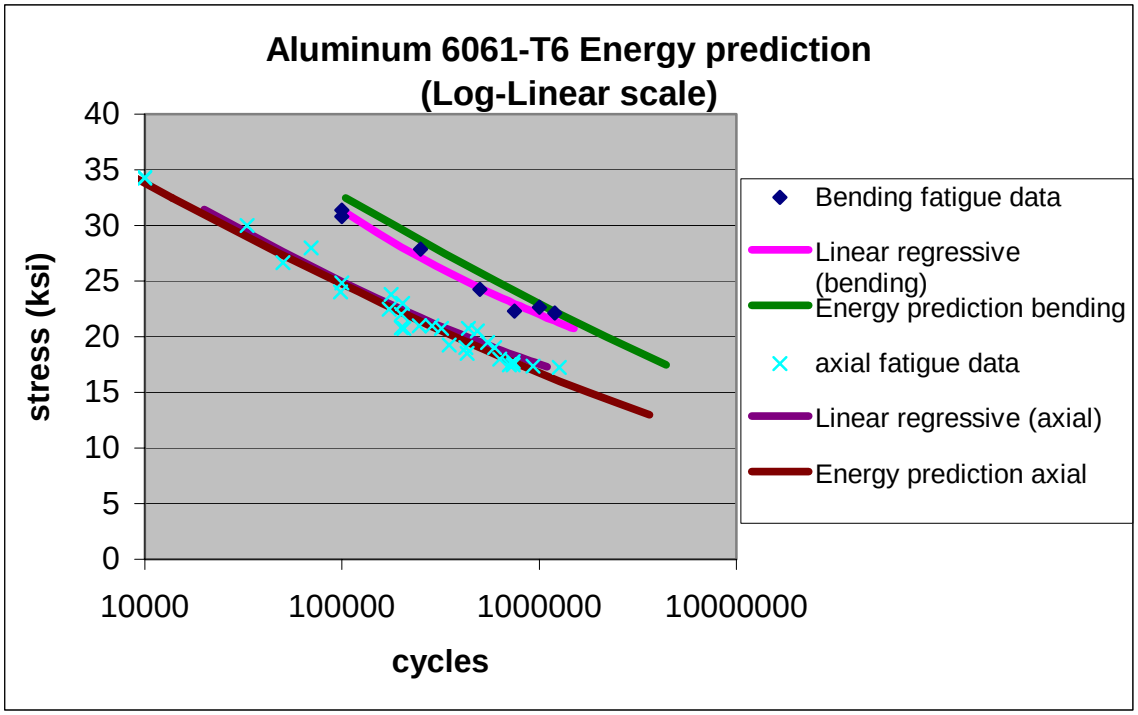

Figure 16. S-N test data and energy-based prediction results (bending, and tension/compression)

VI. MEAN-STRESS EFFECT ON FATIGUE LIFE

When mean stress is included in a fatigue procedure, it dissipates residual energy and increases the plastic strain per cycle, thus reducing the amount of cycles required to fatigue a specimen. Figure 17 shows an illustration of the residual strain energy density via mean stress, which is represented by Equation 10. The gray region represents the mean strain energy. The total strain energy density is defined by the area underneath the stress-strain curve, which is essential both the gray and yellow regions. Therefore, the remaining energy required for fatigue is represented by the yellow region of Figure 17 and the expression of Equation 11.

$$W_{mean} = \sigma_{mean}\left(\varepsilon_{mean} - \frac{\sigma_{mean}}{2E}\right) - \varepsilon_o \sigma_o \left(Cosh\left(\frac{\sigma_{mean}}{\sigma_o}\right) - 1\right) \qquad (10)$$

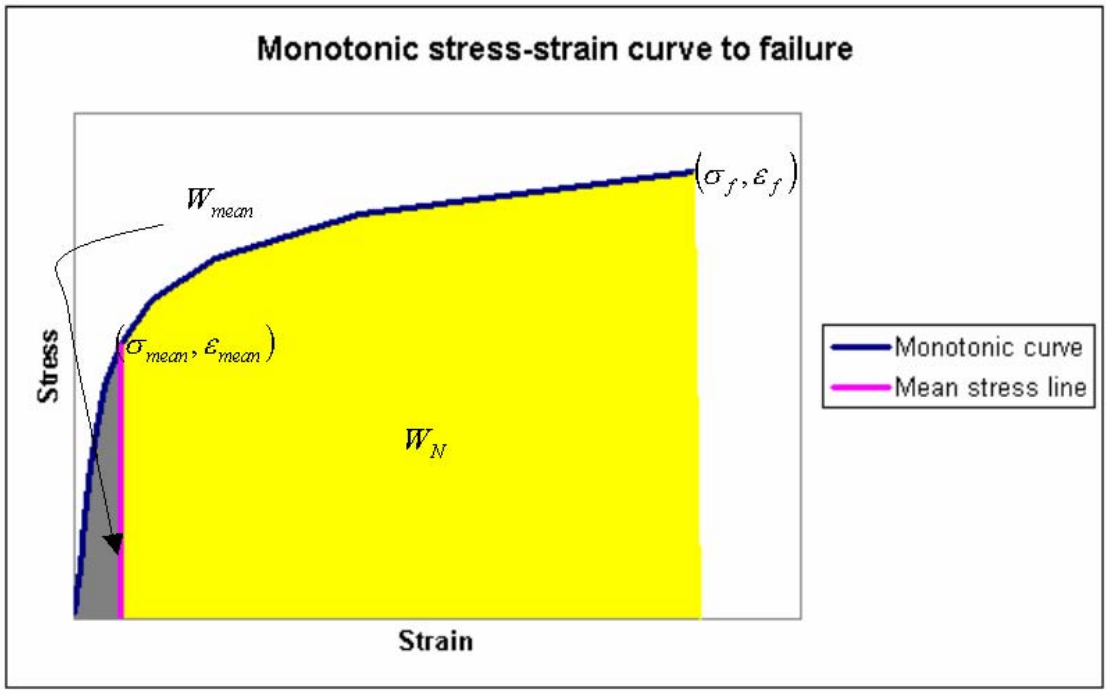

Figure 17. Monotonic stress-strain relation with mean stress illustration

$$W_N = W_f - W_{mean} \tag{11}$$

When evaluating the fully reversed tension/compression cyclic behavior, two assumptions were set in place. It is considered that a significant amount of strain damage is caused by plastic deformation, and the tensile cyclic curve (from zero applied stress to peak-to-peak stress) is a slight modification of the true strain equation, which defines the stress-strain relation of a monotonic procedure [5]. In order to incorporate mean stress effect, both of these assumptions should still be in place. Meaning, each cycle, regardless of the mean stress value, should be plotted on the same axis and evaluated with the same cyclic strain equation, for tensile loading, as the fully reversed cycle. However, unlike the fully-reversed case, it cannot be assumed that the compressive behavior of the Hysteresis loop (stress strain plot for one complete cycle) is identical to the tensile curve. Meaning, the curve from zero applied stress to peak-to-peak is not the same as the curve from peak-to-peak to zero. This assertion is, indubitably, proven by the experimental results displayed in Figure 18. The compressive curve is shown to be reasonably linear, thus this would be a rather fair assumption when analytically characterizing it.

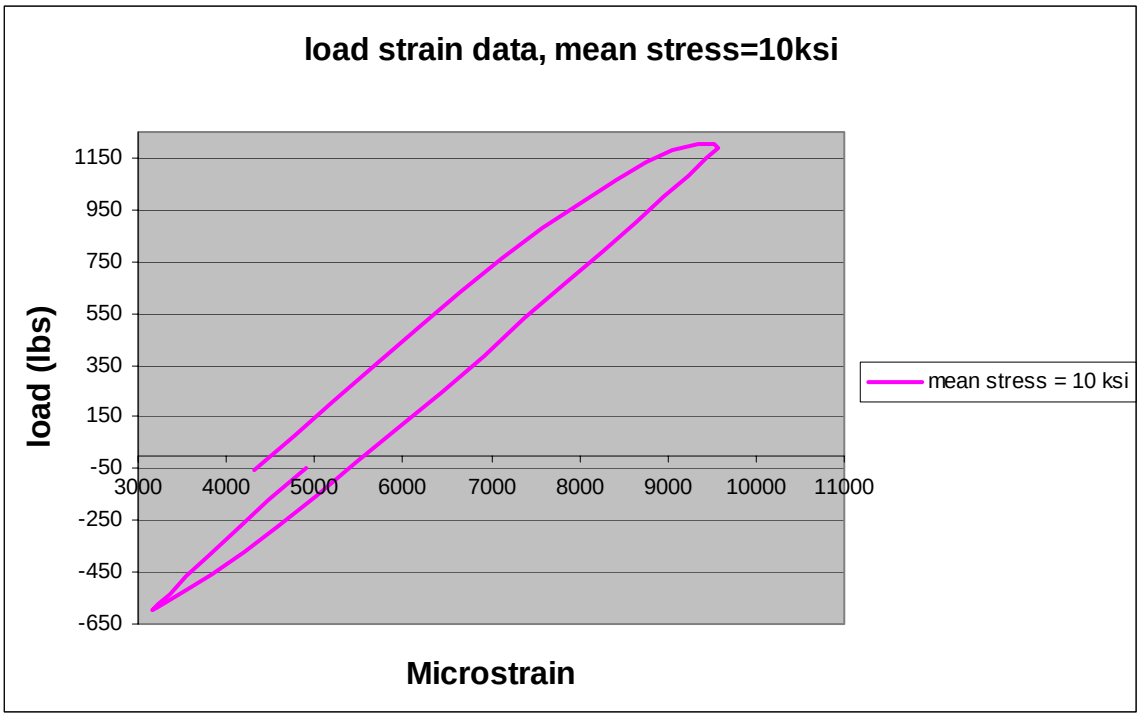

Figure 18. Hysteresis loop for loading with mean stress.

Figure 19 shows the plastic Hysteresis loop for both fully reversed loading and varying stress ratio loading (σ_{mean} is not zero), where σ_{pp} is the peak-to-peak stress (essentially 2σ), σ_{mean} is the applied mean stress, ε_p is the total plastic strain generated per cycle, ε_{mean} is the mean strain, and ε_{pt} and ε_{pc} represents the tensile and compressive curve, respectively, of the loop with varying mean (Equation 12 and 13). As stated earlier, and illustrated in Figure 19, the effect of the mean stress increases the amount of plastic deformation per cycle. This effect, as well as the residual mean strain energy, will reduce the fatigue life of materials with stress ratios greater than negative one.

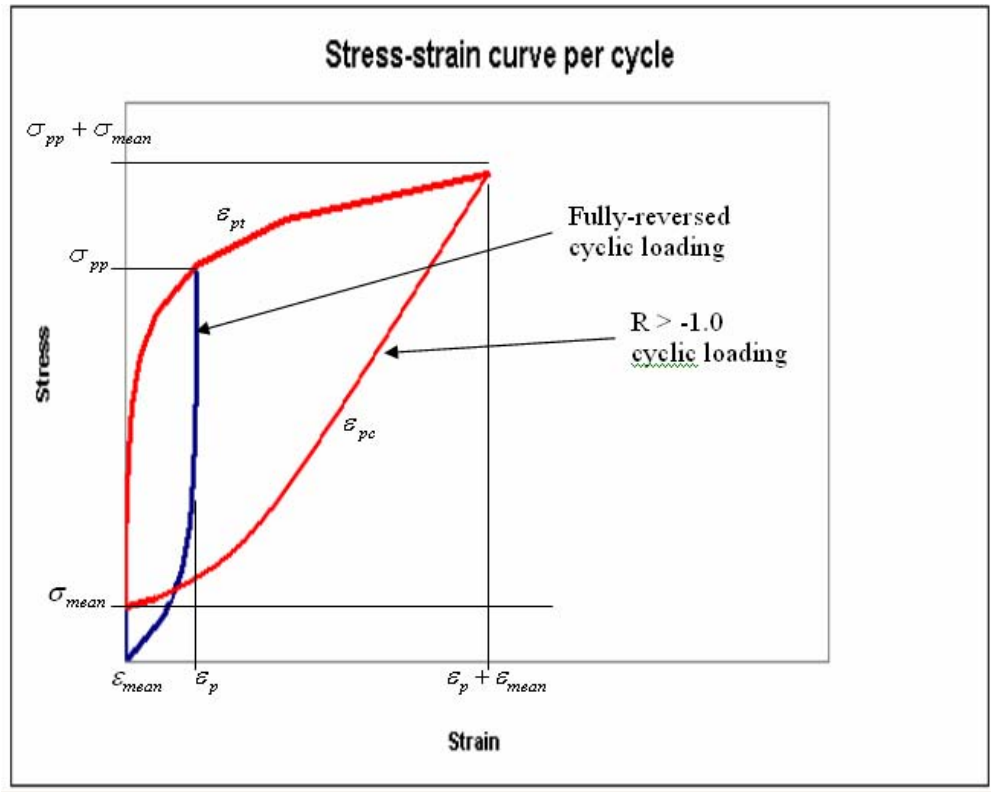

Figure 19. Hysteresis loop with mean stress effect

$$\varepsilon_{pt} = \frac{\varepsilon_o}{C} Sinh\left(\frac{\sigma_{pp}}{\sigma_o}\right) \tag{12}$$

$$\varepsilon_{pc} = \frac{\varepsilon_o}{2C} Sinh\left(\frac{\sigma_{pp}}{\sigma_o}\right) \tag{13}$$

The strain energy density for the hysteresis loop, where R > -1.0, is calculated by the following equation.

$$W_{cycle,mean} = \left[\sigma_{pp}\right]_{\varepsilon_{mean}}^{\varepsilon_p+\varepsilon_{mean}} \left[\varepsilon_{pt}\right]_{\sigma_{mean}}^{\sigma_p+\sigma_{mean}} - \int_{\sigma_{mean}}^{\sigma_p+\sigma_{mean}} \varepsilon_{pt} d\sigma_{pp} - \left[\sigma_{pp}\right]_{\varepsilon_{mean}}^{\varepsilon_p+\varepsilon_{mean}} \left[\varepsilon_{pt}\right]_{\sigma_{mean}}^{\sigma_p+\sigma_{mean}} + \int_{\sigma_{mean}}^{\sigma_p+\sigma_{mean}} \varepsilon_{pc} d\sigma_{pp} \tag{14}$$

As illustrated by Figure 18, the value of ε_{mean} is very close to zero, but cannot be implicated as zero. Consequently, Equation 14 can be rewritten as Equation 15.

$$W_{cycle,mean} = \frac{\sigma_o \varepsilon_o}{C}\left\{\frac{2\sigma}{\sigma_o}\left[Sinh\left(\frac{2\sigma+\sigma_{mean}}{\sigma_o}\right) - Sinh\left(\frac{\sigma_{mean}}{\sigma_o}\right)\right] - \left[Cosh\left(\frac{2\sigma+\sigma_{mean}}{\sigma_o}\right) - Cosh\left(\frac{\sigma_{mean}}{\sigma_o}\right)\right]\right\}$$
$$-\frac{\sigma_o \varepsilon_o}{C}\left\{\frac{\sigma}{\sigma_o}\left[Sinh\left(\frac{2\sigma+\sigma_{mean}}{\sigma_o}\right) - Sinh\left(\frac{\sigma_{mean}}{\sigma_o}\right)\right] - \frac{1}{2}\left[Cosh\left(\frac{2\sigma+\sigma_{mean}}{\sigma_o}\right) - Cosh\left(\frac{\sigma_{mean}}{\sigma_o}\right)\right]\right\} \quad (15)$$

Incorporating Equation 11 and 15 into the energy-based fatigue criterion leads to this equation, which calculated the number of cycles required to fatigue a material with an applied stress of σ and a mean stress of σ_{mean}.

$$N = \frac{W_N}{W_{cycle,mean}} \quad (16)$$

Fatigue results were acquired from several aluminum 6061-T6 dog-bone specimens using a 22 kip MTS uniaxial load frame. Fatigue test were conducted at mean stresses of 10.2 and 20 ksi, with stress ratios ranging from –0.5 to 0.3. The results were compared to the mean energy-based criterion and plotted on figures 20, 21, and 22.

Figure 20. Semi-log S-N plot for fatigue data with mean stresses of 10.2 and 20 ksi.

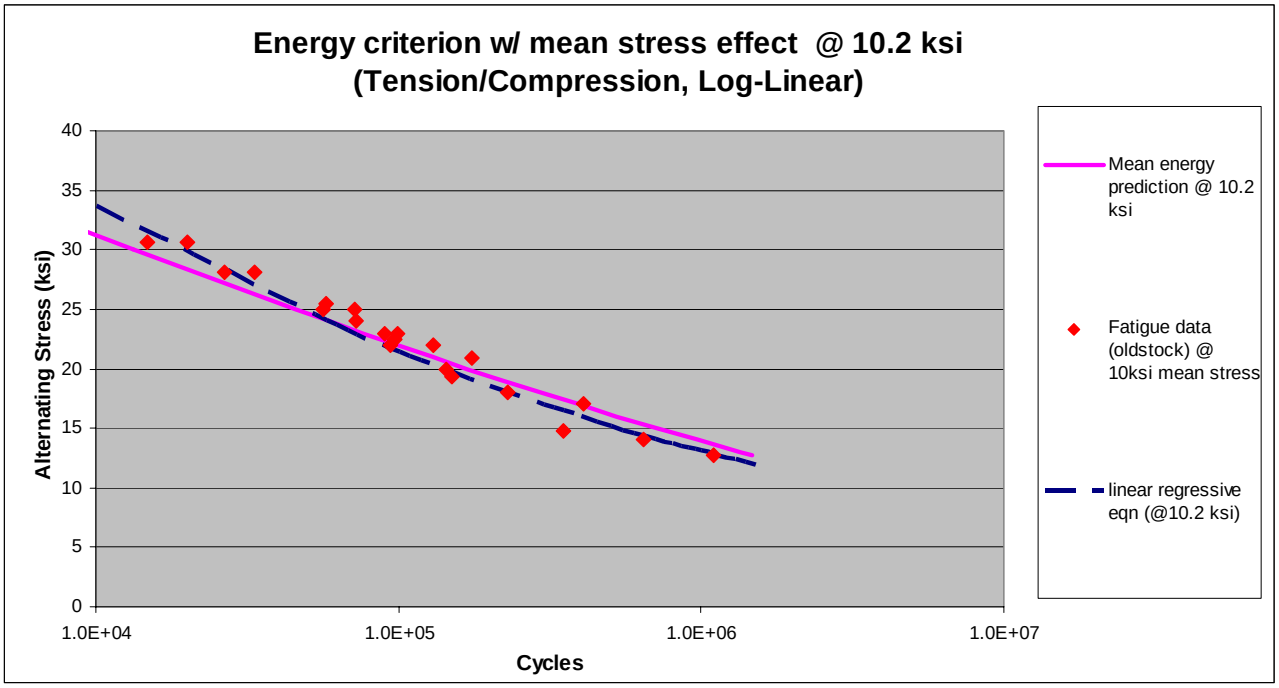

Figure 21. Semi-log S-N plot for fatigue data with mean stresses of 10.2.

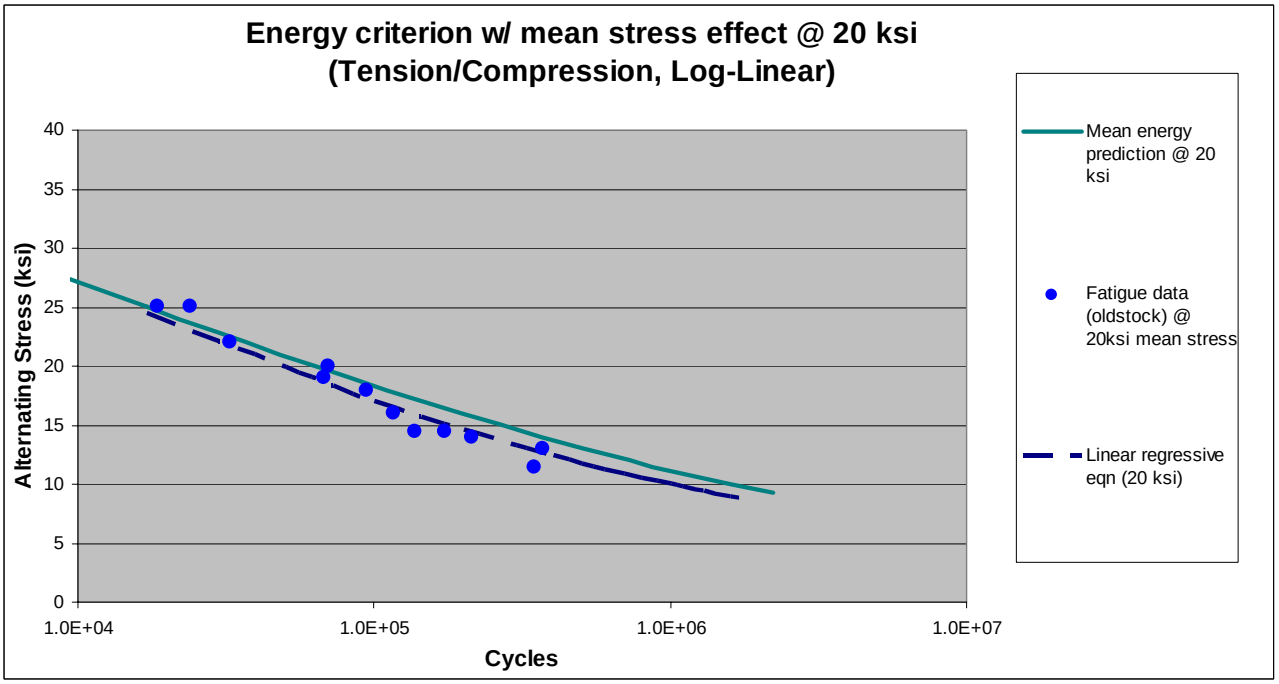

Figure 22. Semi-log S-N plot for fatigue data with mean stresses of 20 ksi.

The figure shows commendable comparison at approximately 10^5 cycles. The minimal variations at lower and higher cycles could be a result of factors such as, approximating the slight non-linearity in the cyclic compressive curve as a linear behavior, the inconsistency of the MTS actuators at large tensile loads, slipping between the wedges of the hydraulic grips and the dog-bone at high tensile loads, or excess applied pressure by the wedges on the dog-bone, which causes supplementary axial loading, at lower applied loads. Nevertheless, the modification of the energy-based criterion provides a sufficient method for fatigue life estimation and prediction for tension/compression specimens under various stress ratios.

VII. REFERENCES

[1]. M.-H. H. Shen, J. Seidt, T. George, C. Cross, P. W. Whaley, and T. Nicholas, 2001, " Development of A Novel Method for Evaluating Material Behavior under Turbine Engine Operating Conditions, Part I: Design of Accelerated HCF Testing Procedures", 6th National Turbine Engine High Cycle Fatigue Conference. M.-H. H. Shen, T. George, J. Seidt, T. Nicholas, and C. Cross, 2001, " Development of A Novel Method for Evaluating Material Behavior under Turbine Engine Operating Conditions, Part II: An Empirical Vibration-Based Fatigue Assessment Framework", 6th National Turbine Engine High Cycle Fatigue Conference.

[2]. T. George, J. Seidt, M.-H. H. Shen, C. Cross, and T. Nicholas, 2004, "Development of A Novel Vibration-Based Fatigue Testing Methodology", International Journal of Fatigue, Vol. 26, Issue 5, pp. 477-486.

[3]. T. George, M.-H. H. Shen, C. Cross, and T. Nicholas, "A New Multiaxial Fatigue Testing Method for Variable-Amplitude Loading and Stress Ratio", ASME/IGTI TURBO Expo 2003 and accepted for publication, ASME Journal of Engineering for Gas Turbines and Power.

[4]. T. George, M.-H. H. Shen, O. Scott-Emuakpor, T. Nicholas, C. Cross, and J. Calcaterra, "Goodman Diagram Via Vibration-Based Fatigue Testing ", accepted for publication, Journal of Engineering Materials and Technology.

[5]. Scott-Emuakpor O, Shen M, Cross C, Calcaterra J, and George T, ``Development of An Improved High Cycle Fatigue Criterion'', GT2004-53851, proceeding of 2004 ASME/IGTI Turbo Expo.

[6]. Goodman J, Mechanics Applied to Engineering, Longmans, Green, and Co., London, 1899.

[7]. Nicholas T and Zuilker JR, “On the Use of the Goodman Diagram for High Cycle Fatigue

Design", Int. Journal of Fatigue 1996; 80: 219-235.

[8]. Shen M, "Reliability Assessment of High Cycle Fatigue Design of Gas Turbine Blades using the Probabilistic Goodman Diagram", Int. Journal of Fatigue; 21: 699-708.

[9]. Nicholas T and Maxwell D, "Mean Stress Effects on the High Cycle Fatigue Limit Stress in Ti-6Al-4V", Fatigue and Fracture Mechanics: 33rd Volume, ASTM STP 1417, W.G. Reuter and R.S. Piascik, Eds., American Society for Testing and Materials, West Conshohocken, PA, pp. 476-492.

[10]. Jasper TM, "The Value of the Energy Relation in the Testing of Ferrous Metals at Varying Ranges of Stress and at Intermediate and High Temperatures," Philosophical Magazine, Series. 6, Oct. 1923; 46: 609-627.

[11]. Mayer H, "Fatigue crack growth and threshold measurements at very high frequencies" International Materials Reviews 1999; 44: 1-34.

[12]. Sendeckyj GP, Bibliography on the History of Fatigue, Air Force Research Laboratory, Materials Directorate 1997 (unpublished).

[13]. Bernhard RK, "Testing Materials in the Resonance Range," Proc. ASTM 1941; 41: 747-757.

[14]. Nowack H, "Fatigue Test Machines," in Fatigue Test Methodology, AGARD Lecture Series No. 118, North Atlantic Treaty Organization, October 1981: 3-1 – 3-23.

[15]. Memmler K and Laute K, "Dauerversuche an der Hochfrequenz-Zuf-Druck-Maschine, Bauer Schenck [Fatigue tests with the Schenck high frequency tension-compression machine]," *Forschungsarbeiten a. d. Gebiete d. Ingenieur-wesens*, No. 329, 1930: 32; Abstract: Z. *Ver. dtsch. Ing*, Feb. 8, 1930; 74: 189-190; Z. *Metallk.*, July 1930; 22: 249-250.

[16]. Herzog A, "Six ton Schenck fatigue testing machine," *Tech. Rep. U.S. Army Air Force,* No. 5623, Aug. 15, 1947: 24

[17]. Rawlins RE, "Fatigue Tests at Resonant Speed," Metal Prog. 1947; 47: 265-267.

[18]. Fehr RO and Schabtach C, "Resonant Vibration Testing," Steel 1941; 109: 64-65, 96, 102.

[19]. Symposium on Large Fatigue Testing Machines and Their Results, ASTM STP 216, American Society for Testing and Materials, Philadelphia, 1958.

[20]. Fairbairn W, "Experiments to Determine the Effect of Impact Vibratory and Long-Continued Changes of Load on Wrought-Iron Girders," Phil. Trans. Roy. Soc., London, 1864: 311.

[21]. Prot M, "Un Nouveau Type de Machine D'Essai des Metaux a la Fatigue par Flexion Rotative," Rev. Métall., Vol. 34, 1937, p. 440: see also: Prot, M., "Fatigue Tests under Progressive Load. A New Technique for Testing Materials," Rev. Métall. 1948; 45: 481-489.

[22]. Nicholas T., "Step Loading for Very High Cycle Fatigue," Fatigue Fract. Engng. Mat.. Struct. 2002; 25: 861-869.

ELECTRIC-FIELD-INDUCED FLAME SPEED MODIFICATION

S. D. Marcum
Department of Physics, Miami University
Oxford, OH 45056

B. N. Ganguly
Air Force Research Laboratory
Wright-Patterson AFB, OH 45433

Abstract

The effects of pulsed and continuous DC electric fields on the reaction zones of pre-mixed propane-air flames have been investigated using several experimental diagnostics. Electrical measurements facilitated efforts to provide effective coupling of the external bias voltage to the flame. The observed effects require minimal input electrical power (< 1 W for a 1 kW burner) and, due to the much better electric field coupling achieved in the present experiments, the magnitude of the externally applied voltage necessary to significantly perturb the reaction zone geometry is substantially smaller than those used in previous studies. Electrical measurements that are reported include bulk current and voltage characteristics, and vertical and horizontal variations of the floating potential within the flames. All observed effects on the flame are dependent upon the applied voltage polarity, indicating that negatively charged flame species do not play a role in the perturbation of the reaction zone. Experiments designed to characterize the electric-field-induced modifications of the shape and size of the inner cone, and the concomitant changes in the temperature profiles of flames with equivalence ratios between 0.8 - 1.7, are also reported. High-speed two-dimensional imaging of the flame response to a pulsed DC voltage shows that the unperturbed conical flame front (laminar flow) is driven into a wrinkled laminar flamelet (cellular) geometry on a time scale of the order of 5 ms. Temperature distributions derived from thin filament pyrometry (TFP) measurements in flames perturbed by continuous DC fields show similar large changes in the reaction zone geometry, with no change in maximum flame temperature. All measurements are consistent with the observed flame perturbations being a fluid mechanical response to the applied field brought about by forcing positive flame ions counter to the flow. The resulting *electrical pressure* decreases Lewis numbers of the ionic species and drives the effective flame Lewis number below unity. The observed increases in flame speed and the flame fronts' trend toward turbulence can be described in terms of the flame front wrinkling and concomitant increase in reaction sheet area. The effect is a potentially attractive means of controlling flame fluid mechanical characteristics.

Introduction

A rather large amount of work has been reported on the various effects of electric fields on a wide variety of flames[1-10]. However, the mechanism(s) responsible for the rather dramatic field-induced effects on the size and shape of the inner cone of some hydrocarbon flames is still not well understood. Bradley[1] provides a good overview of the subject, as well as a thorough review of the literature in this general area up to the date of that text's publication.

Electric-field-induced modifications of flame geometry have been known for some time, the first report being published by Chattock[2] in 1899. Since then, many aspects of the effects of externally applied fields on flames have been investigated. For example, increases in flame blowoff flow rates due to the application of external fields in both diffusion[3] and premixed[4] methane-air flames have been

measured. Similar increases in flame stability have also been observed at fields sufficient to produce a corona discharge[5] within the flame. Improved heat transfer to solid surfaces[6] due to externally applied fields has been reported. Increased burning velocities for hydrocarbon flames in DC fields[7] and elevated electron temperatures for flames in microwave fields[8] have been similarly established. It has also been shown that soot formation in diffusion flames is diminished[9] by application of both DC and AC external fields. Flame extinction limits in pre-mixed flames are also perturbed[10] by DC fields. More recently, a reaction kinetics model[11] simulating the effects of electric fields in premixed methane flames has been published, and electric fields have been used to counterbalance natural convection and simulate microgravity[12] in small diffusion flames.

This work demonstrates that close coupling of the externally applied voltage to pre-mixed propane/air flames with the electric field directed generally counter to the flow, can produce significant flame front perturbations with relatively small ratios[8] of voltage to the electrode separation. Bulk flame current/voltage measurements, and intrusive floating potential measurements within the flames, were performed to measure improved coupling of the externally applied voltage to the flame. The degree and time scale of the dynamic response of the flame to a pulsed voltage is documented using high-speed two-dimensional imaging. Non-intrusive measurements of DC electric-field-induced changes in the temperature profiles of the flames using thin filament pyrometry (TFP) are also reported. Spectroscopic measurements of the CH(A-X) emission bands and a CARS-based measurement confirm the TFP results.

Together, the measurements reported here provide direct evidence of significant increases in flame speed (of the order of a factor of 2 and greater) when an externally applied voltage is effectively coupled to premixed propane air flames. Modest applied voltages are capable of driving the flame from laminar (stable, conical flame geometry) to a wrinkled laminar geometry (cellular; multiple laminar flamelets), with some evidence of the approach to higher intensity turbulence regimes. High-speed two-dimensional imaging of the flame response to a pulsed voltage also shows that the characteristic time required to complete the field-induced flame stretch is on the order of 5 ms, somewhat more rapid than that found in previous work[9], but still indicative of the fluid mechanical nature of the flame response to the external field. Temperature distribution measurements offer a complementary view of the significant modification of the flame front and indicate *no change* in adiabatic flame temperature, suggesting no overall change in the flame chemistry. Further, the temperature measurements indicate that increased flame temperature is not the cause of the observed flame speed increases.

In much of the previous work[1], the effects of DC electric fields on flames was described in terms of the body force known as the ionic wind, which has been shown to be capable of providing a maximum pressure difference across the flame[1,11] of only 0.0004 atm. The effects reported here differ sufficiently in magnitude that an alternative explanation of the observed effects must be considerd. Under otherwise quiescent laminar flow conditions where Fick's law applies and strong temperature gradients give rise to significant thermal diffusion[13], imposition of an external electric field gives rise to an additional *electric pressure* induced diffusion effect. The electric field acts directly on the highly localized, chemiionization-derived positive ions in the flame reaction zone, significantly increasing their mass diffusivities and thereby lowering the Lewis numbers of the ionic species. The observed result is a diffusive-thermal instability[14,15], typical of flames with global Lewis numbers less than one. The increased differential diffusional velocity of the reaction zone positive ions strongly affects the bulk flame speed[14,15], and the instability results in the flame front collapsing toward the burner head and taking on a wrinkled laminar geometry. Such indications of the onset of turbulence suggest that electrically stressed hydrocarbon flames can be quite sensitive to the *electric pressure* effect.

Experimental Apparatus and Procedures

The principal experimental flame diagnostics used to gauge the efficacy of externally applied voltage-to-flame coupling, measure temperature distributions, and quantify the degree and time scale associated with the flame dynamic response to a pulsed bias voltage with rise time ~ 0.2 msec, are shown in Figure 1.

The burner used was a commercial atomic absorption type (Perkin-Elmer) with a modified cylindrical (44-mm diameter x 50 mm) stainless steel head. The premixed gas inlet orifices consisted of five concentric rings of close spaced 0.8-mm diameter holes, the largest ring having a 17-mm diameter. The hollow, 25-mm diameter portion of the burner head is filled with multiple layers of fine mesh wire screen in series with the standard burner body to ensure complete fuel/air mixing. The lower electrode evolved from a section of perforated stainless steel sheet positioned over the orifice array, to a patch of 100-mesh stainless steel wire cloth stretched across the inlet array. Both array/electrode arrangements produce axially symmetric flows, as evidenced by the highly symmetric conical laminar flame fronts produced at moderate flow speeds (~1 m/s). The wire cloth electrode was somewhat more flow restrictive, and thus required higher overall fuel/air flow rates to provide the same gas flow speed, but provided superior bias voltage-to-flame coupling and reproducibility than the perforated sheet electrode.

The dc current/voltage characteristics of the electrically stressed flames were recorded with the burner grounded and the upper electrode biased up to $\pm$ 3 kV (Hewlett-Packard Model 6516A, 0-3 kV, bipolar). Such measurements were used to quantify the voltage-to-flame coupling of the various electrode arrangements, and thus guide efforts to improve the coupling efficiency. The first upper electrode arrangement used was a copper tubing (51-mm o.d x 1-mm thick x 64-mm height) placed between 30 and 40 mm above the burner head. The large diameter of the electrode compared to the extent of the burnt gas plume, as well as its large radiative area and thermal conductivity (thus low temperature), combine to provide poor voltage-to-flame coupling, and minimal observable effect on the flame front geometry. Changing the upper electrode to a stainless steel ring geometry (44-mm o.d. x 3-mm thick x 18-mm height) provided much better coupling and enhanced flame front modifications. Still better coupling is achieved by stretching a coarse-mesh, woven stainless steel screen (0.85-mm diameter wire, 6-mm square grid) across the ring electrode. This last iteration of upper electrode geometry provides a simple parallel-plate-like electrode geometry at the cost of perturbing the burnt gas flow field. The bulk of the results reported here were derived from the latter electrode geometry, and the improvement in bias voltage-to-flame coupling is documented in the next section.

Intrusive flame electrical characterizations that can easily be performed are floating potential measurements. Such measurements were made along the axis of an electrically stressed flame, as well horizontally as across the flame at various heights above the burner. The voltage probe consisted of a 0.75-mm diameter chromel wire housed in 1-mm inner diameter aluminum oxide tube. The length of the wire protruding through the end of the insulating housing exposed to the electrically biased flame was 1 mm. Floating potentials were measured at 1-mm intervals both horizontally and vertically. However, the relatively large size of the voltage probe disturbed and cooled the flame flow field somewhat, especially near the surface of the inner cone. Nevertheless, the general features of the horizontal and vertical floating potential profiles were recorded.

The apparatus used to record high-speed (100 μs exposures) two-dimensional images of the flame's response to a pulsed high voltage as functions of applied voltage, fuel-to-air ratio and flow rate is shown schematically in Figure 1. Pulsed DC fields were applied to the flames by adding a high-voltage transistor (IGBT) switch (up to 2.1 kV) and shunt to ground to the same power supply circuit used for the

continuous DC flame bias studies. The images used to document the flame's dynamic response to a pulsed DC bias were made using an intensified, gateable CCD camera (Princeton Instruments Model ICCD-576). A series of one-hundred microsecond exposures spaced 1 ms apart were recorded after both the rise and fall of the pulsed-DC field.

The detection setup used to make spatially resolved temperature measurements within a flame by thin filament pyrometry[16,17] (TFP) is also shown schematically in Figure 1, and consists of a simple lens, filter and detector combination. In this case, the power supply was operated in a continuous DC mode. Flame temperatures were sampled using the blackbody emission from commercially available silicon carbide fibers, nominally 15 μm in diameter, which were suspended under slight tension horizontally across the flame. The glowing fiber was imaged onto a filter detector combination using a 30-cm focal length, 75-mm diameter lens. The filter used was a long-pass type that transmitted wavelengths greater than 780 nm, and was used to prevent bright visible flame emissions from reaching the detector. The detector was a silicon PIN diode with a 1-mm^2 active area and the detector current was measured by an electrometer working in the current mode. The nano-ammeter was in turn interfaced to a PC that was used for experimental control and data reduction.

The burner was mounted on translation stages so that temperature measurements at different locations within the flame could be accomplished simply by repositioning the burner. Temperature measurements were made along the length of the SiC fiber at 1-mm intervals. The glowing fiber was observed at a number of locations along its length sufficient to span the width of the flame. Vertical translation of the burner allowed horizontal temperature profile measurements to be made at different distances above the burner head. Such temperature profile measurements were performed at 3-mm intervals starting 3 mm above the burner head and continuing to locations above the peak of the inner cone. The total number of horizontal profiles measured for each flow condition studied thus depended on the height of the inner cone.

The fuel and air flow rates were set and monitored by simple ball-float type flow meters (rotameters, Cole Parmer) capable of flow rates up to 2.7 standard liters per min (slm) for propane, and up to 66 slm for air. Typical flow rates used for results reported here were between 5 and 25 slm for air, with the corresponding flow rates for propane varied to provide the desired equivalence ratio. The total range of equivalence ratios used during this study was between 0.8 and 1.7. The propane used was a standard commercial grade, and the air was supplied by a small, portable compressor.

Spectroscopic measurements of bright flame emissions from the CH($A^2\Delta$ -$X^2\Pi$) band at 431 nm provided a check on the TFP measurements. For those measurements the camera system shown in Figure 1. was replaced with a CCD-based spectroscopy camera (Photometrics Model CCD9000) mounted on a 0.27-m spectrometer (Jarrel-Ash MonoSpec 27). A simple lens system imaged portions of the surface of the inner cone onto the spectrometer's entrance slit. The spectral resolution of the rotational structure of the CH radical was sufficient to extract the gas temperature from the Boltzman plot of the rotational quantum number dependent spectral intensity.

Results and Discussion

Electrical Measurements

To enhance an electrically driven process it is advantageous to provide effective coupling of the power source to the load. Here, bulk circuit current/voltage (I/V) characteristics are the most straightforward electrical measurements that can be made to assess the efficacy of external bias voltage-to-flame coupling. I/V characteristics for a flame with total pre-mixed fuel/air flow rate of 16 slm, an equivalence ratio of 1.2, and two different upper electrode geometries are shown in Figure 2. The

forward (reverse) bias case is for a grounded burner head and the upper electrode biased positively (negatively), and the burner-upper electrode separation was 40 mm. Independent of the upper electrode geometry, both I/V curves show a diode-like behavior. Not surprisingly, noticeable flame front geometry modifications occur only when the upper electrode is positively biased, indicating that only positive ions play a significant role in the observed reaction zone perturbations. The difference in voltage-to-flame coupling between the two electrode geometries is readily apparent from the forward I/V curves. The screen electrode, which is in much more intimate contact with the burnt gas plume than the ring electrode, allows a roughly 50 % higher current through the flame than the ring electrode for the same applied voltage.

Although the diode-like behavior has been noted previously[1,3,4], the magnitude of the current drawn with the screen anode is better than an order of magnitude higher than previously reported for electrically biased pre-mixed hydrocarbon flames. All subsequent results reported here are derived from experiments that use the grounded burner, screen anode (forward bias) arrangement. Another significant feature of the I/V curves of Figure 1 is that a small amount of electrical input power is required to produce the significant flame front modifications observed during this study. The largest current drawn under the conditions cited above is approximately 300 μA at 3 kV forward bias, or slightly under 1 W of electrical input power applied to a burner that is generating heat at the rate of roughly 1 kW. Also of note is that although the general trend is towards some saturation current, saturation is not reached up to the limit of the power supply output voltage (+3 kV).

As discussed previously, floating potential measurements within an electrically biased flame represent a much more intrusive electrical diagnostic. Though the absolute values of the measured floating potentials are accurate only for the probe-disturbed flame, the general shape of the floating potential profiles provide some insight into the flame front geometry modifications detailed below. Horizontal and vertical floating potential profiles were also measured for each flow condition and electrode geometry as described above. Figure 3 shows a typical set of horizontal and vertical floating potential profiles measured during this study. The data shown is for an equivalence ratio of 1.35 and overall flow rate of 16 slm, 1.5 kV bias, and 35 mm anode-burner head separation.

The upper plot in Figure 3 shows the vertical floating potential profile measured along the flame axis at locations separated by 1 mm for an overall bias of 1.5 kV. As indicated, the bulk of the voltage drop occurs near the anode. More significantly, the slope of the floating potential profile slope changes sign near the applied-field-modified surface of the reaction zone. The lower plot in Figure 3 shows the measured horizontal floating potential profiles at two locations above the burner head. At 21 mm above the burner head, well above the field-modified reaction zone, the floating potential profile is flat, indicating a relatively small electric field in that region. However, the profile at 15 mm above the burner head, near the surface of the modified reaction zone, shows a much larger floating potential gradient (electric field) that is directed toward the burner head and inward toward the flame axis. The shape of the electric field suggested by the floating probe measurements would tend to force the positive ions in the flame front downward toward the burner head and inward toward the flame axis. The time evolution of the geometry of the reaction zone shown and discussed below is consonant with these results.

High-Speed Two-Dimensional Imaging

The typical dynamic flame response to a pulsed electric field is shown in Figure 4. The total flow rate was once again 16 slm and the equivalence ratio used was 1.25. The bias potential for that set of two-dimensional images was a 2.1-kV square pulse. The rise time of the voltage pulse was less than 0.2 ms, and the fall time was in the 10's of microseconds range. The figure shows two sets of individual 100-μs exposures of the flame's inner cone spaced 1 ms apart after the rise (top set) and fall (bottom set) of the voltage pulse for an equivalence ratio of 1.2.

In the top set, the unperturbed conical flame front (laminar flow) is driven by the field into a strongly curved, wrinkled cellular geometry on a time scale of roughly 5 ms. The acceleration of the reaction zone begins with a symmetric constriction of the inner cone at its base, followed by rapid decrease in the height of the deformed flame front as the flame channel that remains at t = 5 ms closes. The sequence of flame front deformation is consistent with the floating probe measurement which suggest that the electric field points inward toward the flame axis and down toward the burner head. After collapse, the flame front maintains a highly wrinkled, somewhat unstable geometry for as long as the bias voltage is maintained. When the bias pulse is terminated (bottom set), recovery to laminar flow proceeds first by a symmetrical expansion of the flame front at its base, followed by increase in height back to the normal zero field, symmetric inner cone. The time scale for the flame front recovery is also ~ 5 ms.

Although different in the details of the time sequence of flame front modifications, the sequence shown in Figure 4 is qualitatively similar to the collapse of the flame front in the well known singing flame[18]. Analogous to the singing flame's response to oscillating ambient pressure, the electric-field-driven positive ions localized in the flame front are able to exert an effective dynamic pressure on the flame front, causing it to collapse inward toward the flame axis, the resulting channel rapidly closing as the flame propagates essentially radially inward. The imaging results suggest that the effective fluid mechanical response of the flame is altered by the applied field, resulting in an increased flame speed. Using the frames for t = 0 and t = 7 ms from the upper portion of Figure 4, and approximating the flame front shown in the latter as a cone, gives a conservative estimate of the flame speed increasing by roughly a factor of 2. From the cone angle of the t = 0 frame, the flow speed for that data set was approximately 110 cm/s (propane laminar flame speed[13], S_L = 44 cm/s). Larger flame speed increases were observed given that at nearly 50 % higher overall flow rate than that used for the results of Figure 4, the taller laminar cone was still collapsed near the burner head by similar applied voltages. To achieve such a flame speed increase by preheating[13] the gas mixture would require a temperature increase of 150 K. Assuming a volume flow rate of 16 slm, effecting such a temperature change would require approximately 50 W of electrical power – greatly in excess of the maximum electrical power input of slightly less than 1 W shown by the I/V curves of Figure 2. By comparison with the preheating the gas mixture to increase flame speed, the electric-field-induced flame speed modifications observed here are a factor of 50 more energy efficient than preheating the gas.

Temperature Measurements

The horizontal temperature profiles measured by the TFP procedure, describe above, for the case of the equivalence ratio of 1.35 are shown in Figure 5 for the screen anode geometry. In that Figure, results are shown for the normal flame (no applied field) by solid lines and for the electric field-modified flame by dashed lines. The total voltage drop across the flame was 1500 V, and the anode-burner head gap was 35 mm. The vertical lines shown at each data point location are $\pm$ 80 K error bars.

The horizontal profiles in the top-most plot of Figure 5 are for a location just above the peak of the inner cone in the unperturbed flame. It is clear that the effect of the applied voltage on this portion of the flame is negligible. Temperature profiles measured at locations successively closer to the burner head show markedly different electric field-induced effects. Between 18 and 6 mm above the burner head, the horizontal temperature profiles with and without an applied field are radically different. The temperature profile measured at 3 mm above the burner head again shows only slight differences between the applied field and the no applied field cases.

A general comment is in order at this point. As the applied field is increased, the reduction of the inner cone height shown in Figure 5 is accompanied by significant wrinkling and increasing fluctuation of the flame front. Voltage probe measurements also show increased voltage amplitude fluctuations at frequencies higher than natural flame flicker frequencies. The surface of the inner "cone" has its shape altered significantly by the applied field and the surface oscillates at essentially the same frequency

observed with the voltage probe. The depressed inner "cone" typically appears as multiple, oscillating small cones. Additionally, the depressed inner "cone's" surface was observed to substantially alter its shape occasionally, and oscillate about a new quasi-stable shape, without any noticeable perturbation that could be taken as the cause for the change. Such changes in overall inner cone shape occurred between data recording for the horizontal profiles at 12, 9 and 6 mm above the burner head. Those changes are reflected in the temperature profiles for those locations that appear in Figure 5.

The observed flame speed increase, the strong wrinkling of the flame (large negative curvature), and the sudden dramatic shifts in reaction zone geometry observed under otherwise quiescent laminar flow conditions, all point to the onset of turbulent flow induced by the external field's effect on the flame front. The final experimental observation presented in Figure 6, unburned pocket formation, suggests the onset of even more intense turbulence conditions. Chen et. al.[21] have published an extensive numerical study of pocket formation, and among their findings they note that pocket formation, channel closing and pocket burnout correspond to strongly curved flames.

For the same fuel/air flow conditions as those just discussed, similar field-induced effects on the temperature profiles were found for the initial experiments that used a ring anode geometry. However, the ring anode geometry required a 2500 V bias for the production of the same general level of field-induced flame perturbations shown in Figure 5, which used only a 1500 V total drop across the flame. The reduction in applied voltage necessary to produce a given modification of the reaction zone with the screen anode is easily understood in terms of the much better coupling of the electric field between the screen electrode and the flame, as suggested earlier by the I/V curves of Figure 2. Producing the same field-induced flame perturbations with a lower applied voltage has obvious advantages in any practical application of the effects described here. Additionally, the compression of the inner cone toward the burner head when an electric field was applied occurred to varying degrees over the entire range of equivalence ratios studied (0.8 - 1.7), and flow rates up to 20 slm.

It is again significant to note that *none* of the field-induced temperature profile modifications described above occurs for any flame condition investigated if the polarity of the applied voltage is reversed. Additionally, other than reducing the height of the flame front, no measurable difference in flame temperature was observed either at, or outside the surface of the inner cone. CARS temperature measurements were also performed with and without an applied voltage at locations just above the tip of the unperturbed reaction zone for each case described above. All CARS-based temperature measurements agreed with the TFP measurements within experimental error. Additionally, emission spectra of the CH 431 nm band allow rotational temperatures[18] to be determined. The rotational temperatures measured for all cases were essentially equal to the gas temperature at a given equivalence ratio. In addition to indicating that CH(A-X) rotational temperature measurements also provide a good indicator of the temperature of electrically stressed propane flames, the results also provide an additional independent verification of the TFP measurements.

Conclusions

Under the flow conditions studied here, with the upper electrode in place but no potential difference applied to the flames, stable laminar pre-mixed propane/air flames with highly symmetric right circular cone geometries result. Clearly under such conditions Fick's law applies, strong temperature gradients give rise to significant thermal diffusion[13], and stable conical flame fronts result. Such a stable laminar flame has small negative curvature everywhere on the flame front, with the largest curvature at the apex of the laminar inner cone. The primary results of this study shows that with effective voltage-to-flame coupling, normal bias of such flames at modest voltages rapidly converts (within ~ 5 ms) the stable flame to one that is quite unstable and unable to support a laminar combusting flow. The flame speed is

substantially increased, and the resulting wrinkled laminar flame exhibits strong negative curvature. One way to interpret the destabilizing effect of the external electric field is that it gives rise to an additional *electric pressure* induced diffusion effect which significantly increases the flame speed. A possible mechanism by which such a minority flame constituent as the flame ions (1 part in roughly 10^7 in terms of overall density) can effect such a dramatic change in flame geometry follows.

The electric field can act directly and effectively only on the highly localized, chemiionization-derived positive ions in the flame reaction zone. The resulting force on the flame ions could significantly increases their mass diffusivities and thereby lowers the ionic species Lewis numbers. The observed result is a diffusive-thermal instability[14,15], typical of flames with global Lewis numbers less than one and negative curvatures[19-21]. The electric-field enhanced differential diffusional velocity of the reaction zone positive ions toward the burner head strongly affects the bulk flame speed[14,15,19-21], and the instability causes the burning speed of the negatively curved[19] reaction zone to increase and collapse toward the burner head taking on a wrinkled laminar geometry. In some cases pocket formation results with clear indications of turbulence, suggesting that electrically stressed hydrocarbon flames can be quite sensitive to the *electric pressure* effect.

That such increases in flame speed can occur without concomitant increases in flame temperature can be understood from two points of view. Considering that the input electrical power to the flame in the experiments reported here is on the order of one-one thousandth of rate at which chemical energy is converted to heat in the flame, conservation of total energy would certainly speak against the possibility of any global temperature increase for the flame. Essentially, since the flame ions are present in such minor concentrations in hydrocarbon flames, even though they could be forced to diffuse by the field into regions where reactant concentrations differ significantly from those of laminar flow, their total contribution to the enthalpy of the mixture may be insufficient to produce any modification in the flame temperature. From the point of view of observed flame structure changes, Echekki and Chen[20] note that for similar flames the net enhancement in the volumetric heat release and fuel consumption rates is primarily due to the increase in flame surface area by wrinkling. They note that the heat release and fuel consumption per unit flame area is reduced relative to the laminar flame.

Acknowledgement

The authors would like to thank Dr. Larry Goss for his advice on the TFP techniques and also for performing the CARS temperature verification measurement.

References

1. Bradley, D., in *Advanced Combustion Methods*, F.J. Weinberg, Ed., Academic Press, New York (1986)
2. Chattock, A.P., Phil. Mag **48**, 401 (1899).
3. Calcote, H.F. and Pease, R.N., Ind. Eng. Chem. **43**, 2726 (1951).
4. Calcote, H.F. and Berman, C.H., in Fossil Fuels Combustion Symposium PD-Vol. 25, S.N. Singh, Ed., 25 (1989).
5. Bradley, D. and Nasser, S.H., Combust. Flame **55**, 53 (1984).
6. Bradley, D. and Ibrahim, S.M.A., 15th Symposium (International) on Combustion, The Combustion Institute, Pittsburgh, PA, 1974, p 1023.
7. Jaggers, H.C. and von Engel, A., Combust. Flame **16**, 275 (1971).

8. Maclatchy, D.S., Clements, R.M. and Smy, P.R., Combust. Flame **45**, 161 (1982).
9. Kono, M., Carleton, F.B., Jones, A.R. and Weinberg, F.J., Combust. Flame **78**, 357 (1989).
10. Gulyaev, G.A., Popkov, G.A. and Shebeko, Yu.N., Phys. Combust. Explosion **21**, 25 (1985).
11. Pedersen, T. and Brown, R.C., Combust. Flame **94**, 433 (1993).
12. Strayer, B.A., Posner, J.D., Dunn-Rankin, D. and Weinberg, F.J., Proc. R. Soc. Lond. A, Math. Phys. Eng. Sci. **458**, 1151 (2002).
13. Turns, S.R., *An Introduction to Combustion*, 2nd Edition, McGraw-Hill, Singapore (2000), p 86, pp 450-470.
14. Williams, F.A., *Combustion Theory: The Fundamental Theory of Chemically Reacting Flow Systems*, 2nd Edition, The Benjamin/Cummings Publishing Company, Menlo Park, CA (1985), pp 357-365, pp 429-440.
15. Linan, A. and Williams, F.A., *Fundamental Aspects of Combustion*, Oxford University Press, New York (1993), pp 32-37, 111-151.
16. Goss, L.P., Vilimpoc, V., Sarka, B and Lynn, W.F., Jour. Engr. Gas Turb. Pwr. **111**, 46 (1989).
17. Vilimpoc, V., Goss, L.P., and Sarka, B., Optics Lett. **13**, 93 (1988).
18. Gaydon, A.G. and Wolfhard, H.G., *Flames: Their Structure, Radiation and Temperature*, 4th Edition, Chapman and Hall, London (1979), pp 182-186, plate 14, p 359.
19. Chen, J.H. and Im, H.G., 27th Symposium (International) on Combustion, The Combustion Institute, Pittsburgh, PA, 1998, p 819.
20. Echekki, T. and Chen, J.H., Combust. Flame **106**, 184 (1996).
21. Chen, J.H., Echekki, T., and Kollmann, W., Combust. Flame **116**, 15 (1999).

Figure Captions

Figure 1. Experiment configurations for high-speed two-dimensional imaging, current/voltage and TFP temperature measurements.

Figure 2. Typical current/voltage characteristics measured for field-modified flames using different upper electrode geometries. The diode-like behavior is obvious, and the screen anode configuration clearly provides significantly better coupling to the flame. Also note that the total electrical power input is quite small (< 1 W at the highest bias).

Figure 3. Typical vertical (upper plot) and horizontal floating potential profiles measured using a screen anode configuration for the upper electrode.

Figure 4. High-speed two-dimensional images (100 μs exposures) of the flame response to a pulsed bias.

Figure 5. Horizontal flame temperature profiles measured for the screen anode geometry.

Figure 6. Images showing unburned pocket formation.

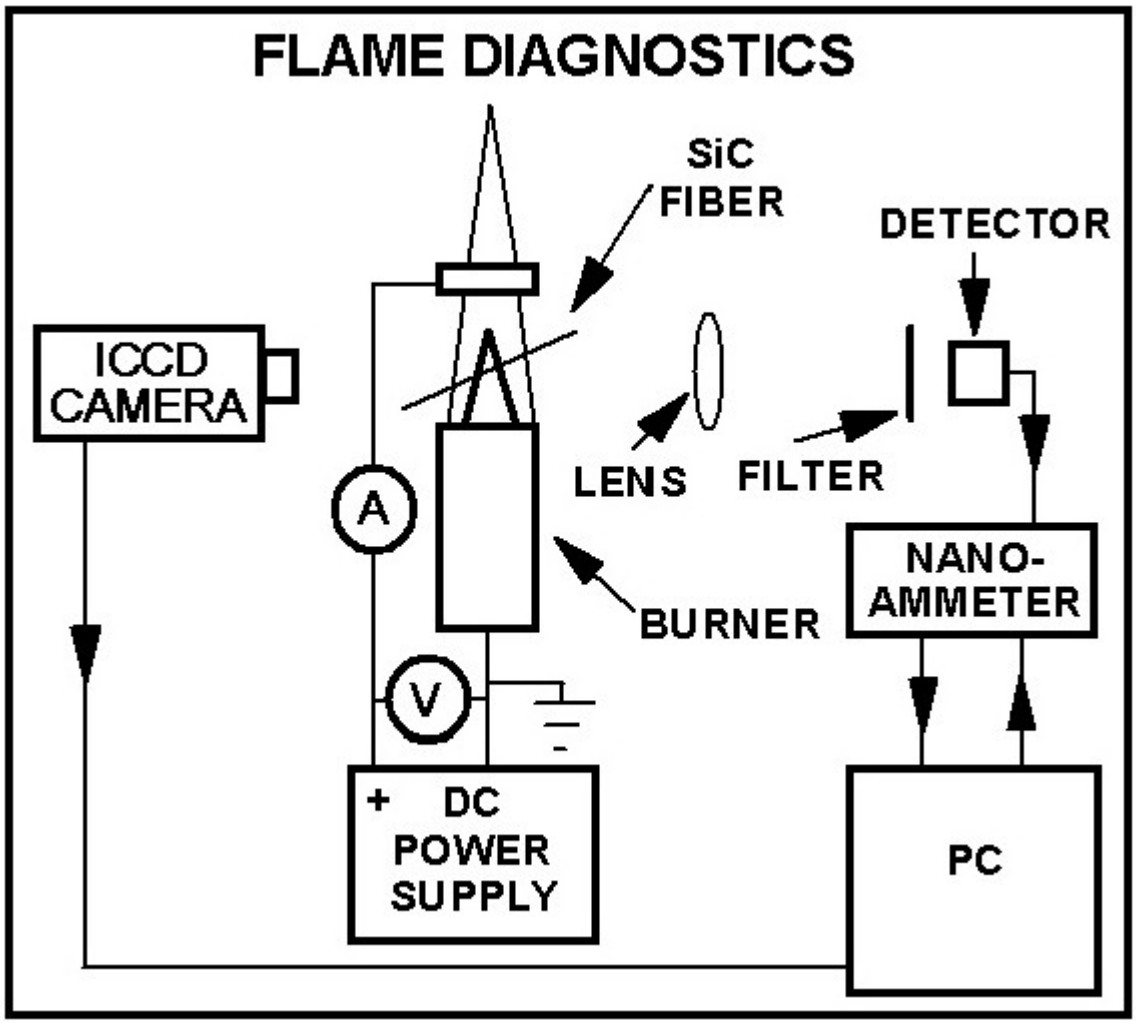
FLAME DIAGNOSTICS
SiC
FIBER
DETECTOR
ICCD
CAMERA
LENS
FILTER
A
NANO-
AMMETER
BURNER
V
+ DC
POWER
SUPPLY
PC

Figure 1.

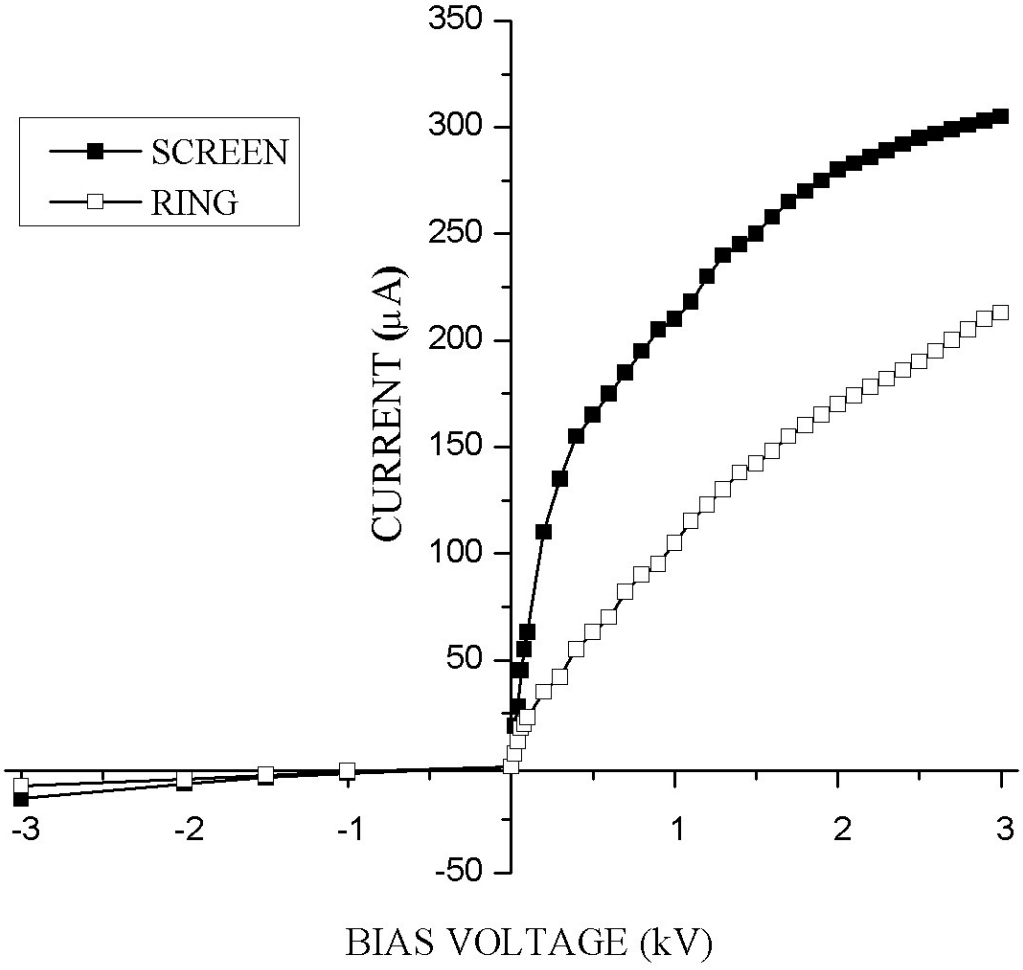
SCREEN
RING
CURRENT (μA)
350
300
250
200
150
100
50
-50
-3
-2
-1
1
2
3
BIAS VOLTAGE (kV)

Figure 2.

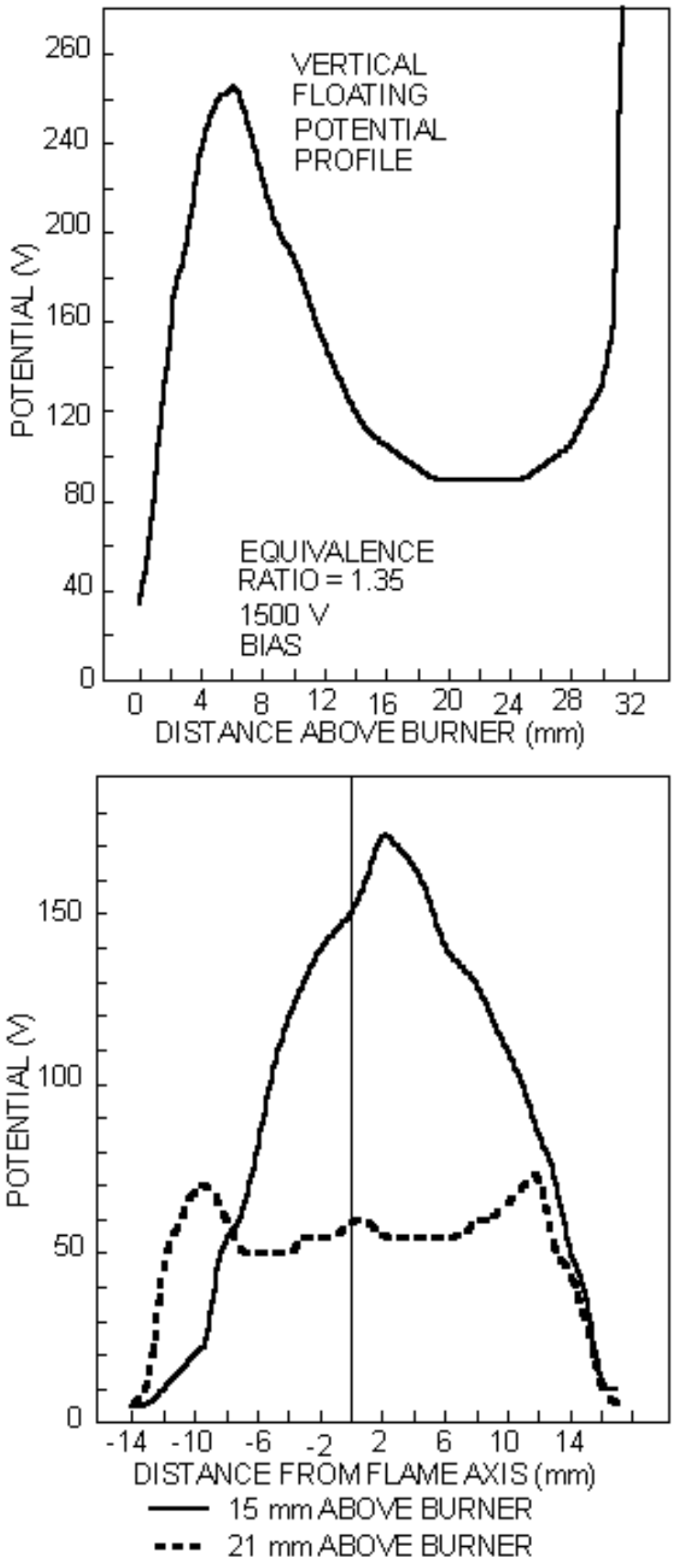
VERTICAL
FLOATING
POTENTIAL
PROFILE
EQUIVALENCE
RATIO = 1.35
1500 V
BIAS
POTENTIAL (V)
DISTANCE ABOVE BURNER (mm)
DISTANCE FROM FLAME AXIS (mm)
15 mm ABOVE BURNER
21 mm ABOVE BURNER

Figure 3.

VOLTAGE RISE

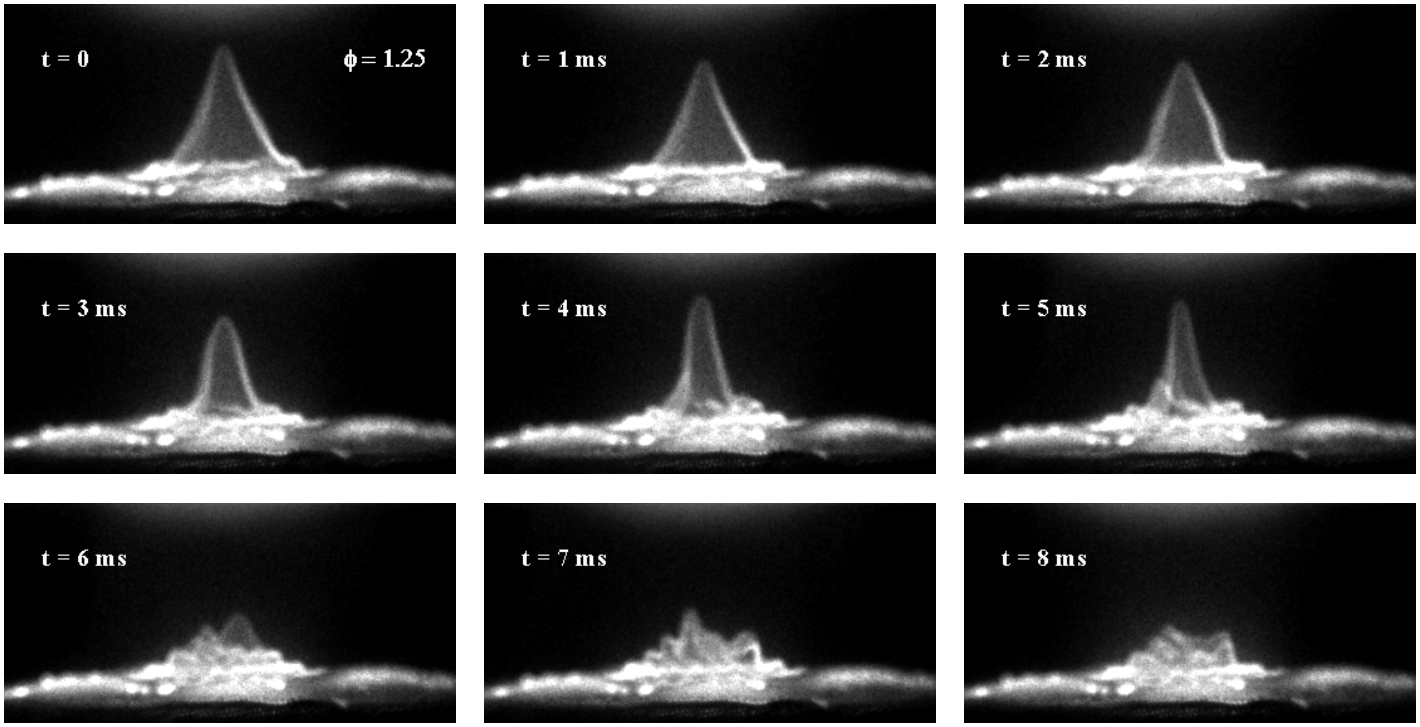

VOLTAGE FALL

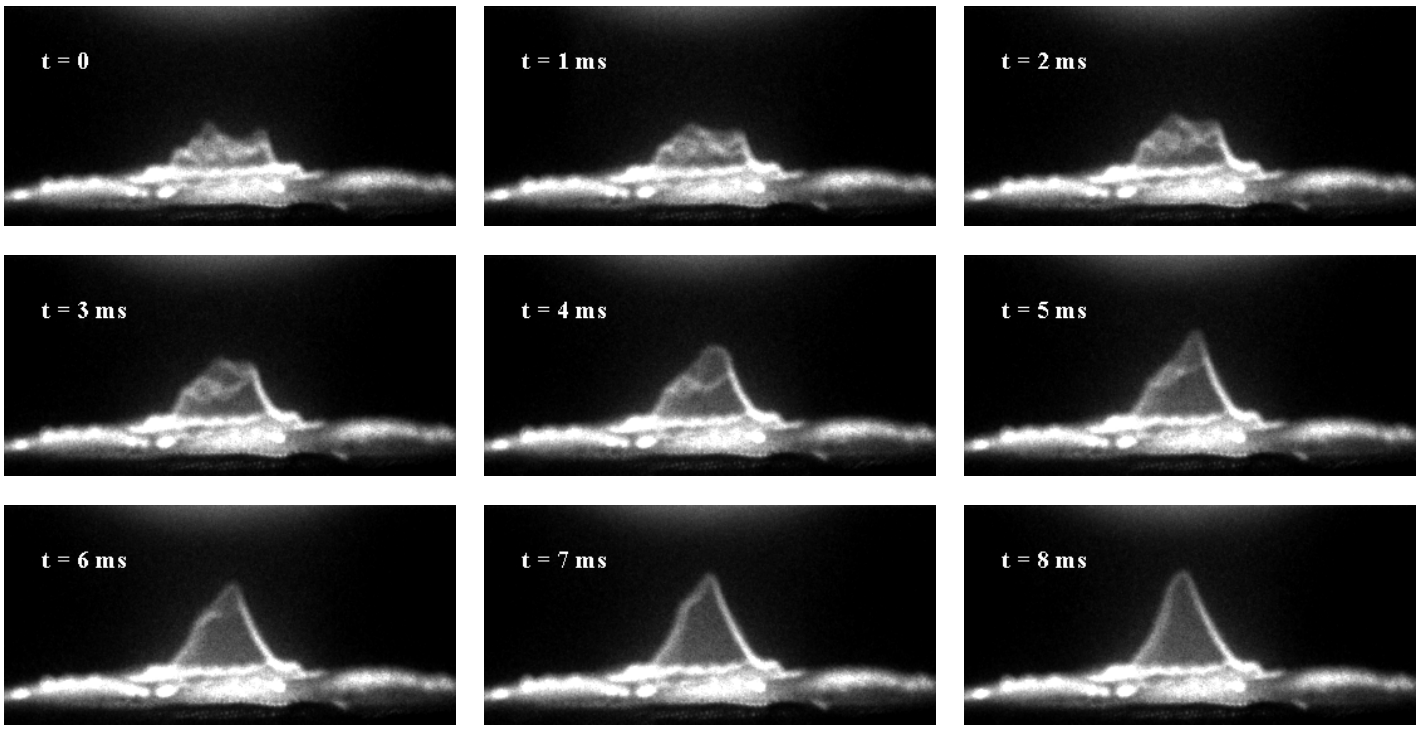

Figure 4.

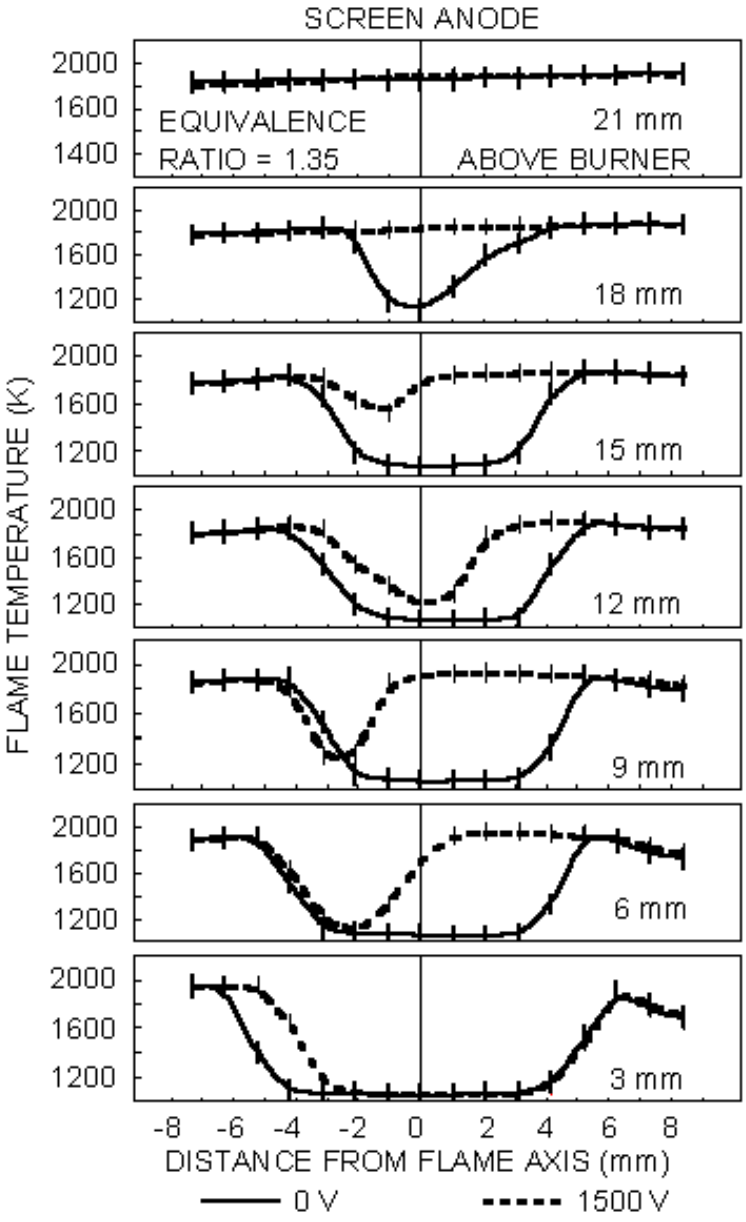
SCREEN ANODE
EQUIVALENCE RATIO = 1.35
21 mm ABOVE BURNER
18 mm
15 mm
12 mm
9 mm
6 mm
3 mm
FLAME TEMPERATURE (K)
2000
1600
1400
1200
-8 -6 -4 -2 0 2 4 6 8
DISTANCE FROM FLAME AXIS (mm)
0 V
1500 V

Figure 5.

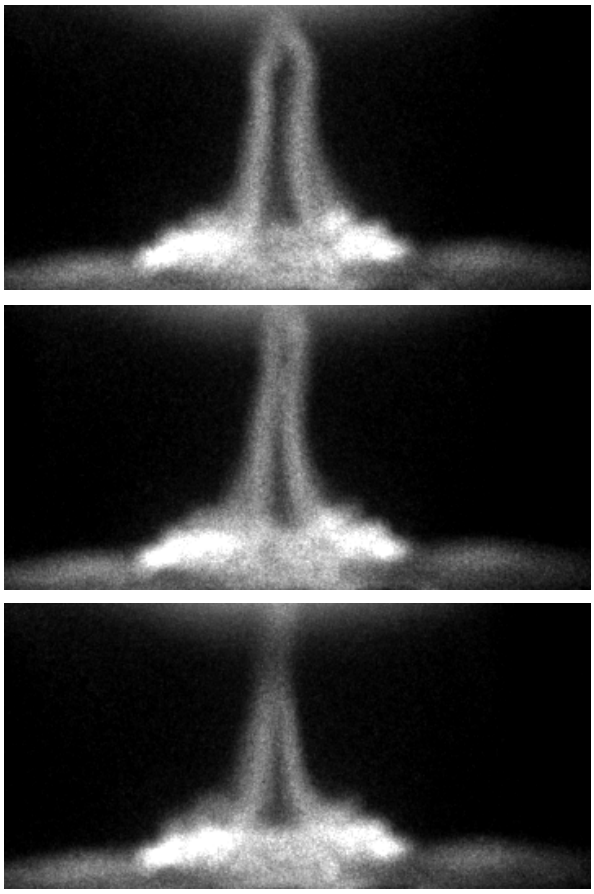

Figure 6.

Numerical Modeling of Spray Cooling Phenomena for Thermal Management of High Power Systems

Final Report to

Universal Technology Corporation
1270 N. Fairfield Rd
Dayton, OH 45432-2600
P.C: F33615-02-D-2299
May 2004 – Aug. 2004

Submitted by

R. Panneer Selvam
Professsor & Director of Computational Mechanics Lab.
Department of Civil Engineering
BELL 4190 University of Arkansas
Fayetteville, AR 72704
ph.: 479-575-5356, fax: 479-575-7168
email: rps@engr.uark.edu

Numerical Modeling of Spray Cooling Phenomena for Thermal Management of High Power Systems

R. Panneer Selvam [1]

[1] Professsor & Director of Computational Mechanics Lab., BELL 4190 University of Arkansas, Fayetteville, AR 72704, ph.: 479-575-5356, email: rps@engr.uark.edu

Abstract: A survey on the current status of computational modeling of spray cooling is reported. From the survey, it is concluded that modeling heat transfer of the spray effect on thin liquid film in the range of 70 μm on a hot surface will help us to understand and improve the performance of spray cooling. The computer modeling of multiphase flow using the level set method to identify the interface of vapor and liquid is presented. Computer modeling of growth of vapor bubble in thin film on a hot wall, growth of vapor bubble at a distance from the wall and merging of a growing vapor bubble with the vapor layer above the thin film are reported. The variations of Nusselt number with time are reported. The computed velocity and temperature variation in time are also reported. From this study the importance of transient conduction in the liquid film leading to high heat flux in a short time is identified. The mechanics of spray cooling is explained from the modeling study. Further research topics are identified.

1. Introduction

Spray cooling is a high flux heat removal technique considered for high power systems such as advanced lasers. The spray cooling with phase change takes advantage of relatively large amount of latent heat vaporization release. Heat fluxes up to of 1000 W/cm^2 have been demonstrated by Yang et al. (1996). Several experiments have been conducted using spray cooling in recent years (Chow et al. 1997, Mudawar, 2001, Rini et al. 2002, Lin and Ponnappan, 2003 & and references there in) and various designs of spray cooling devices are emerging. Theoretical understanding of the spray cooling heat acquisition phenomena is still in its infancy and a focused effort to develop a comprehensive numerical model is a prime importance to this field.

Even though spray cooling is used in the industry for several years the overall theoretical understanding is limited due to complex nature of the problem. Only limited work is available in the area of bubble dynamics, nucleate boiling and film boiling literature published in recent years. In the present study, the modeling issues involved in the spray cooling starting from the event of fluid discharge from the nozzle as spray, droplet interaction and their dynamics, splashing of the droplets on hot surface, the interaction of the droplets with hot surface and finally to the convection of the spent fluid from the hot surface will be discussed. The current literature dealing with computer modeling of each of these physical phenomena and the numerical methods employed will be surveyed and reported. The depth of this problem can be realized only when we try to establish applicable rules of physics such as the interaction of a subcooled liquid droplet to form a super heated vapor. Recently, a few numerical works on nucleate boiling have appeared.

The task of combining all these individual complex phenomena together to model the spray cooling is a great challenge at this time. Some of the key individual phenomena which pose strong impact on modeling the spray cooling will be addressed specifically in this work. Time taken for a thin liquid film to evaporate during nucleate boiling will be modeled using multiphase flow. The details of the numerical model and the computed results will be reported with illustration.

2. Theoretical Issues in Spray Cooling

From the efficient design of jets to convert the liquid into spray and finally the process of removing the heat from the hot surface there are several theoretical challenges at this time. There is no comprehensive theoretical model available at this time for spray including phase change. Complete modeling the heat removal of micro jet array system using finite difference method for single fluid was reported by Selvam and Elshabhini (2000). Similar models for spray cooling will be a valuable tool for the design of spray system. Tryggvason et al. (2001) gives a general review on multiphase flow modeling and specific development in front-tracking method. They discussed the application of the model to bubbly flows, atomization of liquid for combustion, secondary breakup of drops, primary breakup of a jet, solidification and boiling flows. They also discussed the current limitations in those applications. This is a good survey paper for some one to start in this area. Dhir (2001) gives a summary of their numerical simulation of pool boiling heat transfer work including some micro gravity environment.

2.1 Flow in Spray Nozzle: Rahman et al. (2004) analyzed the flow in a swirling jet using finite element method for optimum design. Here the flow is a single phase flow. The numerical simulation predicts the jet cone angle and pressure drop across the nozzle. Further work is needed to consider the formulation of spray and its effect in the design of jets.

2.2 Atomization of droplet: Tryggvason et al. (2001) gives a survey on computer modeling of atomization of droplets. The classified into two groups: primary breakup and secondary breakup. Few searchers including their group work is reported. General survey on drop and spray formation from a liquid jet is provided by Lin and Reitz (1998) including the status of experiment and modeling.

2.3 Droplet and Surface Interaction: Kizito et al. (2004) used the Tryggvason's front tracking model to study the splashing droplet on a hot plate. They found that maximum heat is transferred on the substrate when the droplet has the widest extent of spread. Pasandideh-Fard et al. (2001) used VOF method for similar work. In the above works the fluid is below the range of boiling and they both used 2 mm diameter droplet.

2.4. Liquid and Vapor Interaction or Bubble Dynamics: Extensive computer modeling work is done in this area. The survey of Tryggvason et al. (2001) and Sussman et al. (1994) are notable work. Here surface tension and gravity have impact on the dynamics of bubble in the liquid. Depending upon which dominates the shape of the

bubble can change. There is extensive knowledge available in this area. This is part of the boiling flows and spray cooling when vapor grows as a bubble and moves in the liquid.

2.5. Liquid, Vapor and Surface Interaction on a Hot Surface or Boiling Flows: The phenomenon of nucleation during boiling and the growth of vapor bubble on the hot surface are not well understood and only few modeling work is initiated in the recent years. The modeling work can be classified into two categories: 1. Multiphase flow modeling considering conduction, convection and phase change phenomena 2. Simplified procedures where in only conduction and phase changes are considered. Welch and Wilson (2000), Son and Dhir (1998) and Juric and Tryggvason (1998) have computed the film boiling stage using multiphase flow model. Even though this occurs after nucleate boiling this problem is modeled earlier may be because the density ratio is far less compared to nucleate boiling situations. Few works are done in nucleate boiling and will be reported below.

2.5.1 Film Boiling: Welch and Wilson (2000) used the Volume of fluid (VOF) method to model the film boiling. Juric and Tryggvason (1998) used the front-tracking method to study the film boiling in 2D grids and Shin and Juric (2002) used it for 3D grids. They could consider only for low density ratios. The numerical method couldn't allow them to apply for high density ratio occurring in nucleate boiling flows. Son and Dhir (1998) used the level set method to compute the film boiling. The level set procedure is similar to the Sussman et al. (1994). The computed results are in reasonable agreement with experimental results.

2.5.2 Nucleate Boiling: Lee and Nydhal (1989) computed the single bubble growth in nucleation boiling by considering only the liquid region and assuming the bubble to be spherical. Then Son et al. (1999) applied their film boiling model to compute bubble growth during nucleation boiling. The computed bubble size is around 1 mm and the computed size is in comparison with their experimental result. The bubble growth during nucleation in their model is mainly due to the micro region model which is based on a one dimensional model close to the dry out area on the hot wall. The macro region where NS equations are used the contribution to phase change is very small. Bai and Fujita (1999) and Yoon et al. (2001) also computed the nucleated pool boiling using Lagrangian method of tracking the interface and considering only the liquid region for computing. This is similar to Lee and Nydhal except the meniscus model in Bai and Fujita is close to Son et al. (1999). Kunugi (2001) used VOF method for boiling and condensation problem with out much detail on the numerical implementation or the problems that is considered.

2.5.3 Simplified Models: Di Marzo et al. (1993) model a single water droplet on hot surface., other two groups. He et al. (2001) proposed a model of boiling heat transfer based on numerical macrolayer model. Here the boiling curve is reproduced numerically by determining the macrolayer thickness. The explained that the evaporation due to the growth of vapor stem is the main contribution to the total heat flux. They combined this model with conduction model for transient analysis. Stephan and Hammer (1994) and Kern and Stephan (2003) used a micro and macro region for modeling the nucleation boiling heat transfer. In the micro region a one dimensional complex fourth order

equation is solved to determine the thickness and width of the region. The macro region they only considered conduction. They compared their computed results with experimental results.

2.6 Spray Cooling: From the above discussions one can conclude that several different works were done to understand different phases of boiling and most of them were for pool boiling. None of them can be directly applicable for the understanding of spray cooling. In the case of spray cooling which is of interest to electronic cooling, conduction of heat from the hot wall into liquid, nucleation and growth of vapor bubble on the hot surface due to phase change, convection of liquid and vapor bubble in the liquid film, impact of spray droplet on thin liquid film and vapor bubble all happens simultaneously as shown in Figure 1. The above process happens in the midst of surface tension and micro or macro gravity.

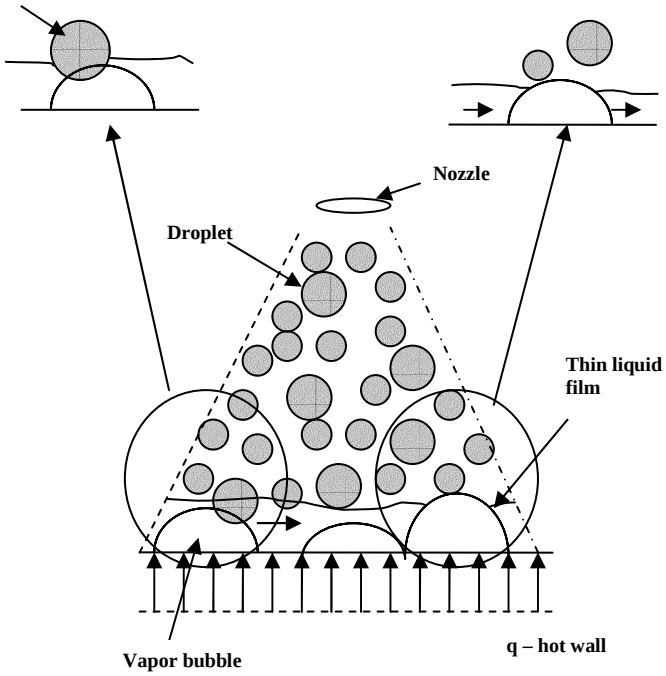

Figure 1. Spray cooling phenomena

In spray cooling it is very rare to have liquid film thickness more than couple of millimeters. Son et al. (1999) could grow bubble diameters more than 1.25 mm and moved them smoothly into 7.5 mm pool of liquid above. Also in their work most of the phase change happened in the micro region. Where as in the case of spray cooling designed for high heat flux, liquid film on the hot surface will be in the range of 50 μm to 150 μm. Usually the thickness can be about 20% of the diameter of the spray as observed by Kizito et al. (2004) in their experimental and computer modeling work. Lin and Ponnappan (2003) reported around 40 μm and Rini et al. (2002) reported in the range of 200 μm.

Theoretical understanding of the nucleate boiling in thin film in the range of 40 μm to 200 μm is not available at this time. As a start to understand the spray cooling phenomena a thin liquid film in the range of 70 μm is considered for study. The growth of vapor bubble and their impact on heat removal on the hot surface will be investigated first. Then the effect of partially grown bubble merging with the vapor on the top of the film will be computed and its impact on heat flux on the wall will be investigated.

3. Methods to Solve Multiphase Flow

The major classifications of methods to solve multiphase flow are the Lagrangian method, Arbitrary-Lagrangian-Eulerian method and Eulerian method. Some of the application of multiphase flow modeling using these methods will be discussed below with advantages and disadvantages of each method. Tryggvason et al. (2001) gives a comprehensive survey and Scardovelli and Zaleski (1999) gives survey on VOF with discussions on numerical techniques. In the same journal volume of Tryggvason et al. (2001), several other review papers on multiphase flow are available and are very informative. The equations are solved using either finite difference method (FDM) or finite element method (FEM). Of the two the most popular is finite difference method.

3.1 Lagrangian method. This method is fairly complex as reported by Tryggvason et al. (2001). The method is used for vapor bubble growth by Welch (1998) using FEM and Lee and Nydhal (1989) for nucleate boiling using FDM on a body-fitted grid system.

3.2 Arbitrary-Lagrangian-Eulerian method (ALE): Yoon et al. (2001) applied the ALE procedure to study the bubble growth and departure from the heated surface. They used mesh free method which is a recent development in engineering for the Eulerian calculations. The implementation may be complex compared to FDM or FEM.

3.3 Eulerian methods: Front capturing methods, separate boundary-fitted grids for each phase, front tracking method and the hybrid of front tracking and front capturing are the methods available at this time for multiphase flow calculations as reported by Tryggvason et al. (2001) . The primary methods in front capturing method are Marker and Cell (MAC) method, Volume of Fraction (VOF) method, Level set method and the combination of VOF and level set method. The separate boundary-fitted grid procedure is suitable for simple geometry.

The primary numerical procedure used here is FDM or FEM on equal grid spacing. Of the methods mentioned above VOF method and level set methods are applied extensively in the literature for multiphase flow. Discussions on VOF and level set methods are available from Ferziger and Peric (2002) and good discussion on different applications of level set method is discussed in Osher and Fedkiw (2003). In the VOF method sharp differentials have to be calculated between the interfaces. The color function in the VOF method is solved using a time dependent convection equation. This is similar to computing shock flow in compressible flow.

To alleviate this problem in the level set method a distance function is introduced which will be varying gradually in each phase. The equation to be solved is same as VOF method except use a distance function instead of color function. Once the distance function is solved the color function is recovered from the sign of distance function. The level set method is good for calculating interfacial curvature accurately but mass conservation is not satisfied. Combining with VOF method this error is eliminated as reported by Son and Hur (2002). In the level set method it is easy to handle breaking and merging of the interface. Also implementation for three dimensional problems is a straight forward extension. In this research level set technique is selected for interface capturing.

4. Numerical Formulation for Multiphase Flow Using Level Set Method

For computer modeling of the multiphase flow region of liquid and vapor during nucleate boiling the level set formulation introduced by Sussman et al. (1994) for bubble dynamics which is modified by Son and Dhir (1998) to accommodate the effect of phase change is used. The interface separating the two phases is captured by φ which is defined as a signed distance from the interface. Similar to Son and Dhir (1998) and Son et al. (2002) the negative sign is chosen for the vapor phase and the positive sign is chosen for the liquid phase. For more details on the level set method and it application one can refer to recent books on Sethian (1999) and Osher and Fedikw (2003). The extensive application of the level set method in various areas of science and engineering are illustrated with their basic development in the above two books.

4.1 Governing Equations

In this model the fluid properties, including density, viscosity and thermal conductivity, are constant in each phase and the flow is assumed to be incompressible. The Navier-Stokes equations considering the effect of surface tension, gravity and phase change at the interface are as follows:

$$\rho(\partial_t \mathbf{u} + \mathbf{u}.\nabla \mathbf{u}) = -\nabla p + \rho \mathbf{g} - \sigma\kappa\nabla H + \nabla.\mu\nabla \mathbf{u} + \nabla.\mu\nabla \mathbf{u}^T \quad (1)$$

$$\rho c_{pl}(\partial_t T + \mathbf{u}.\nabla T) = \nabla.k\nabla T \quad \text{for } H>0 \quad (2)$$

$$T=T_{sat}(p_v) \text{ for } H = 0$$

$$\nabla.\mathbf{u} = \mathbf{m}.\nabla\rho/\rho^2 \quad (3)$$

$$\text{where : } \rho = \rho_v + (\rho_l - \rho_v)H. \quad (4)$$

The value of μ and k are calculated using the similar relation in Eq. (4). Here:

$$\begin{aligned} H &= 1 \text{ if } \varphi \geq 1.5\,h \quad (5)\\ &= 0 \text{ if } \varphi \leq -1.5h \\ &= 0.5 + \varphi/(3h) + \sin[2\pi\varphi/(3h)]/(2\pi) \text{ if } |\varphi| \leq 1.5h \end{aligned}$$

where h is a grid spacing. The Eq. (5) implies that the interface separating two phases is replaced by a transition region of finite thickness. The volume source term included in the continuity equation (3) due to liquid-vapor phase change is derived from the conditions of mass continuity and energy balance at the interface:

$$m = \rho(\mathbf{u}_{int}-\mathbf{u}) = k\nabla T/h_{fg} \quad (6)$$

In the level set formulation, the level set function φ, is advanced and reinitialized as:

$$\partial_t \varphi = -\mathbf{u}_{int} . \nabla \varphi \quad (7)$$

$$\partial_t \varphi = \varphi_o (1- |\nabla \varphi|) /\sqrt{(\varphi_o^2+ h^2)} \quad (8)$$

where φ_o is a solution of Eq. (7).

The surface tension effect is considered in the momentum equation by using a step function H (H=0 in the vapor and 1 in liquid) and κ is the interfacial curvature expressed as:

$$\kappa = \nabla_\circ (\nabla \varphi/|\nabla \varphi|) \quad (9)$$
$$= (\varphi_y^2 \varphi_{xx}- 2 \varphi_y \varphi_y \varphi xy + \varphi_x^2 \varphi_{yy})/(\varphi_x^2+ \varphi_y^2)^{3/2} \text{ for 2D}$$

Here subscripts are differentiation with respect to φ. The surface tension force, $-\sigma\kappa\nabla H$ is implemented in the volume form to avoid the need for explicit description of the interface (Brackbill et al. 1992).

4.2 Nondimensional Form of the Governing Equations

The nondimensional form of the equation is derived using the characteristic length l_r, velocity u_r, time t_r and dimensionless temperature T^*. They are defined as follows:

$$l_r = \sqrt{\sigma/g(\rho_l- \rho_v)},\ u_r = \sqrt{g l_r},\ t_r = l_r / u_r \text{ and } T^* = (T-T_{sat})/(T_w-T_{sat}). \quad (10)$$

The reference values are taken in such a way that the gravity force becomes unity that is Froude number equal to 1 and the Weber number We is just above 1.0 if the density ratio of the liquid to vapor is larger. In addition considering ρ, k, μ and c_p of liquid as reference values and the nondimensional equation with out their superscripts are expressed as follows:

$$\rho(\partial_t \mathbf{u} +\mathbf{u}. \nabla \mathbf{u}) = -\nabla p+ \rho g_y - \kappa\nabla H/We + (\nabla.\mu\nabla \mathbf{u} + \nabla.\mu\nabla \mathbf{u}^T)/Re \quad (11)$$

$$\rho c_{pl}(\partial_t T +\mathbf{u}. \nabla T) = (\nabla.k\nabla T)/Pe \quad \text{for } H>0 \quad (12)$$

$$\nabla_\circ \mathbf{u} = Ja\ k\ \nabla T . \nabla\rho/ (Pe\ \rho^2) \quad (13)$$

$\mathbf{u}_i = \mathbf{u} + Ja\ k\ \nabla T/ (Pe\ \rho)$ (14)

where: $Re = \rho_l u_r l_r / \mu_l$, $We = \rho_l u_r^2 l_r / \sigma$, $Ja = c_{pl} \Delta T / h_{fg}$, $Pr = c_{pl} \mu_l / k_l$ and $Pe = Re\ Pr = \rho_l u_r l_r c_{pl} / k_l$. Here g_y represents unit gravitational force in the y direction. In the equations 11 to 14, ρ, k, μ and c_p are dimensionless with respect to reference value.

4.3 Boundary Conditions

The boundary conditions for the governing equations are shown in Figure 2 and also given below:

At the wall (y=0): $u = v = 0$, $T = T_w$, $\varphi_y = 0$

At the plane of symmetry (x=0 and x= xmax): $u = v_x = T_x = \varphi_x = 0$

At the top of the computational domain (free surface, y= ymax): $u_y = v_y = \varphi_y = 0$, $T = T_{sat}$

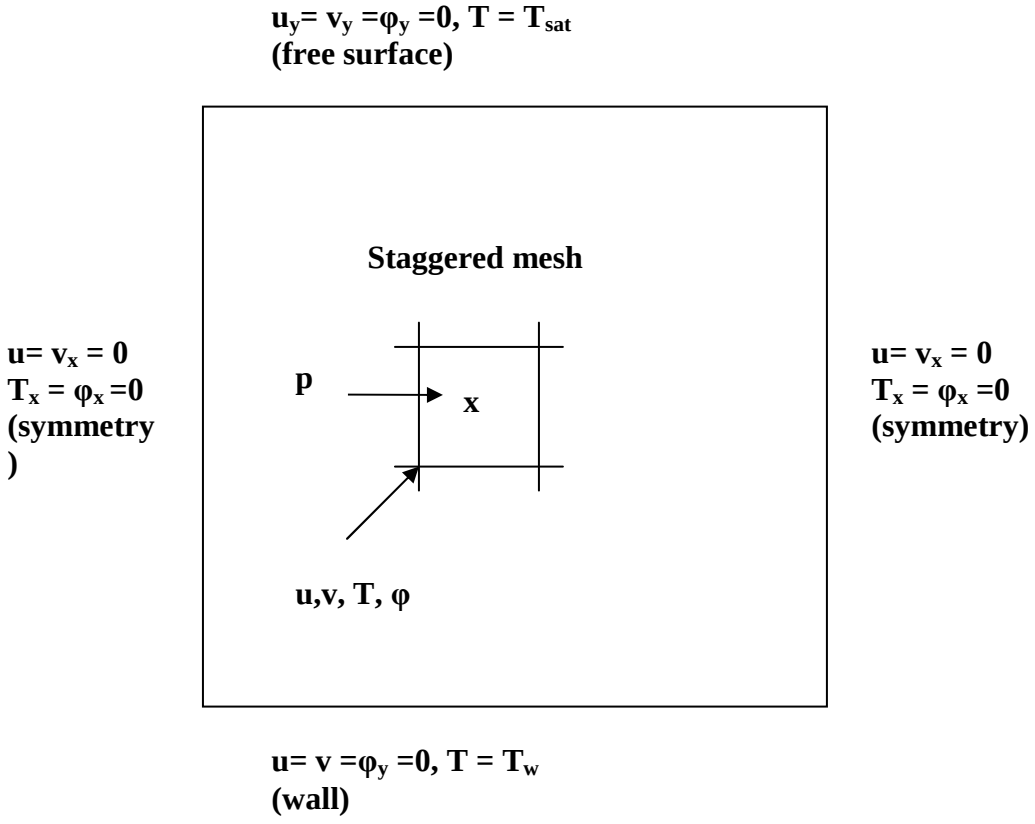

Figure 2. Boundary conditions and the location of the variables stored in staggered grid system.

4.4 Numerical Solution

The governing equations Eq. (1), (2), (3), (7) and (8) combined together are highly nonlinear. The equations are discretized using finite difference method on a staggered grid system in which the all the variables except pressure are stored at the grid points and pressure alone stored at the cell center as shown in Figure 2. The diffusions terms are considered implicitly and the convection and source terms are considered explicitly in time. For spatial approximations all terms are considered using second order central difference and the convection term by a second-order ENO method described by Chang et al. (1996) to prevent numerical oscillations. The pressure and velocity are solved in a sequential manner by the procedure described in Selvam (1997).

The discretized equations from the momentum, energy and pressure equations are symmetric and they are solved by the preconditioned conjugate gradient procedure (Ferziger and Peric, 2002) in an iterative form. The iteration is done until the average residue for each node reduced less than 10^{-9}. This amount of accuracy is needed because of high density difference between liquid and vapor.

After assuming initial position for distance functions, at each time step the equations are solved sequentially in the following order:

1. Solve the momentum equations Eq. (1) for velocities.
2. Correct the velocity to take the pressure effect.
3. Solve the pressure Poisson equation to satisfy continuity.
4. Update the velocities to include the new pressure effect.
5. Solve temperature equation Eq. (2).
6. Solve the distance function Eq. (7)
7. Reinitialize the distance function as per Eq. (8) and go to next time step

During the computation, time steps were chosen to satisfy the CFL condition, $\Delta t \leq \min (h/(|u|+|v|), 10^{-6})$. This was done because of the explicit treatment of the convection terms and the condition that the numerical results should not change if the time steps are halved.

5. Results and Discussions

Lin and Ponnappan (2003) conducted spray cooling experiments using FC-72 for different T_{sat}. As an example T_{sat} = 53 ° C case is considered. For the temperature the computed reference values are: reference length l_r =736.2 μm, reference velocity u_r = 85 mm/s, reference time t_r = 8.66 ms and ΔT = 10 ° C. The density ratio of liquid to vapor (ρ_l/ρ_v) is 138 and other nondimensional numbers are: Re= 218, We=1.0, Pe = 2050 and Ja =0.127. For initial study the parameters considered are: ρ_l/ρ_v = 20 to 90, Re= 200, We=1.0, Pe = 1000 and Ja =0.1. Low density ratios are considered to reduce computer time and to avoid numerical instability. The computed results for higher density ratio has similar trend as low density ratio but the time step needs to be much smaller. Further study in the future will consider higher density ratios in detail.

Time steps considered are $5.x10^{-6}$ (43.3 ns) and $1.x10^{-6}$ (8.66 ns) nondimensional time. The computational domain considered are 0.1 units x 0.1 units which is equal to 73.62

μm x 73.62 μm. The computational domain is discretized by 51x51 and 101x101 mesh at this time. The 101x101 mesh is considered to compare the results from 51x51 mesh and to evaluate the convergence. Most of the runs are made using 51x51 mesh. The smallest grid size varied from 7.362 μm to 14.724 μm.

5.1 Vapor Bubble Growth

The whole computational domain is assumed to have liquid and the vapor is assumed to grow at the origon. The initial bubble size is assumed to have a radius of 0.02 units which is about 10 grid points. The temperature is assumed to be T_{sat} every where except at the wall T= T_w to start and the model is allowed to run for 80,000 time step (692.8 μs) with a time step of $1.x10^{-6}$ (8.66 ns) nondimensional time. The velocity vector and the temperature distribution in the computational domain at the end of 692.8 μs is shown in Figures 3 and 4.

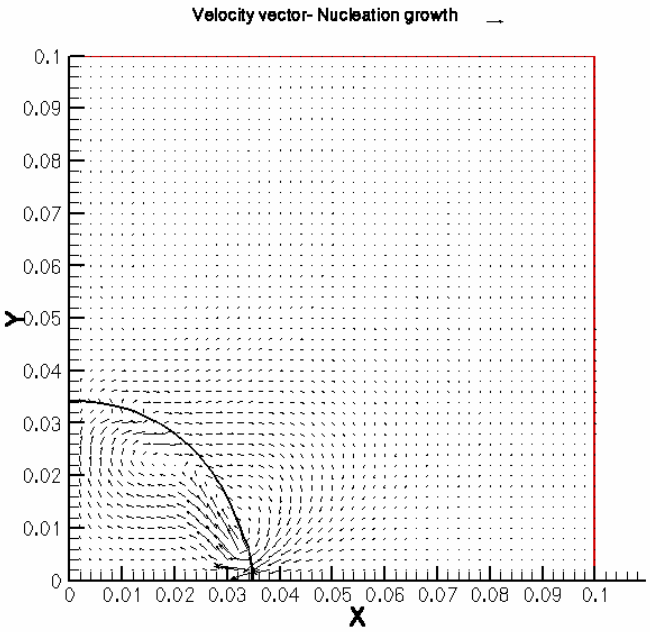

Figure 3. Veocity vector diagram for nucleation growth of vapor bubble in FC-72 after 692.8 μs.

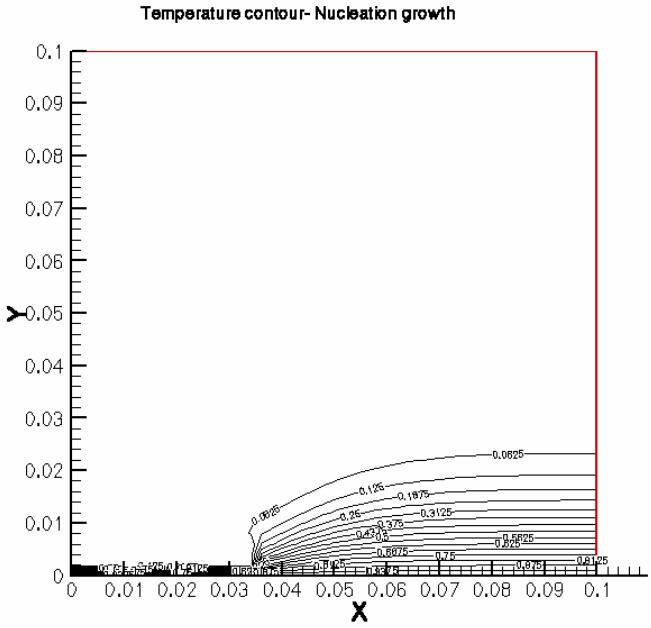

Figure 4. Temperature contour diagram for nucleation growth of vapor bubble in FC-72 after 692.8 μs.

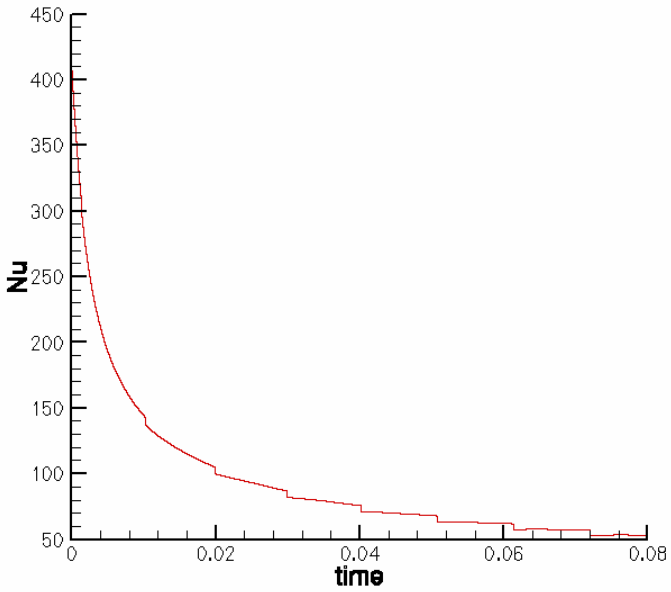

Figure 5. Variation of Nusselt number with time for up to 692.8 μs.

It can be seen from Fig. 3 that the bubble grew with radius about 0.035 units. The shape of the bubble looks more circular. Several test runs with different angle of contact at the base were contacted. Finally they came to the same shape. This may be due to the dominance of surface tension effect in the thin film of liquid. The velocity is higher at the interface close to the wall because that is the region where high temperature gradient

occurs as shown in Fig. 4 between vapor and liquid and hence the phase change is high. In Fig. 5 the variation of the average Nusselt number with respect to time at the wall is reported. Since the temperature is assumed to be Tsat initially in the liquid, the Nu decreases from 420 to 52. As the bubble grows the Nu decreases because the area to conduct heat is reduced. The analytical solution of transient conduction in semi infinite region with constant temperature at the wall as reported in Kreith and Bohn (1986) is:

$$q = k\Delta T / \sqrt{(\pi \alpha t)} \qquad (15)$$

From this one can explain that at the initial stages when t is small the q is very high and hence the Nu is high. In this case the grid spacing is 0.002 units and the dimensionless temperature difference between the wall and the next grid point is 1.0 unit and the maximum possible Nu is 1.0/0.002 = 500. The value 420 is close to this because there is no heat flux with in the 0.02 unit of bubble assumed to start with.

5.2 Mechanics of Spray Cooling

From the above observation in section 5.1 one can say that if the liquid is moved from the wall as quick as possible (in this case in about 9 ns) and replace it with cooler liquid whose temperature is T_{sat} then high heat flux can be achieved. This is what happens when the liquid droplets impact the wall and the old liquid gets moved away. In addition the collapse and movement of the bubble away from the wall also brings cooler liquid close to the wall and hence high Nu. The movement of the bubble away from the wall creates a sharp thermal boundary layer and that increases the Nu. This can be viewed as artificial creation of convection boundary layer due to bubble created by phase change. The whole phenomena involves simultaneous interaction of conduction, convection, phase change and liquid droplet impact on thin film of liquid and vapor bubble as shown in Figure 1. Hence all of these phenomena interact in spray cooling to achieve high heat flux or Nu. To engineer spray cooling each of its effect needs to be understood clearly.

5.3 Modeling a Bubble at a Distance From the Wall

When considering nucleate boiling in a liquid thin film of 73.62 μm in gravity there is not much room for the vapor bubble to grow and depart in to liquid. Son et al. (2002) reported that the bubble diameter to be varying from 2.5 mm to 3 mm from both experiment and computer modeling. In a thin liquid film there is not enough space for a vapor bubble to grow to its fullest extent. Before that the bubble burst and merge with vapor on the top of the liquid layer on its own or due to the impact of a spray droplet. Hence to show the increase in Nu when the bubble is little away from the wall; modeling study is done when a small vapor bubble is at a distance from the wall.

In the same computational domain of 0.1x0.1 dimensionless unit, a bubble with radius of 0.04 units is kept at 0.05 units from the wall as initial condition. Temperature is assumed to be Tsat every where except the wall as initial condition. Computation is done for the same duration of time and time step as before. The final velocity vector diagram and temperature contour plot are plotted in Fig. 6 and 7.

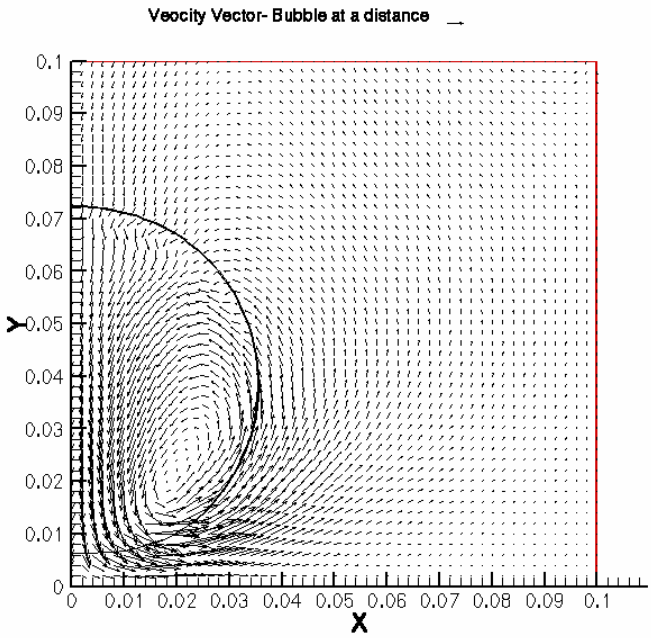

Figure 6. Veocity vector diagram for bubble at a distance from the wall after 692.8 μs.

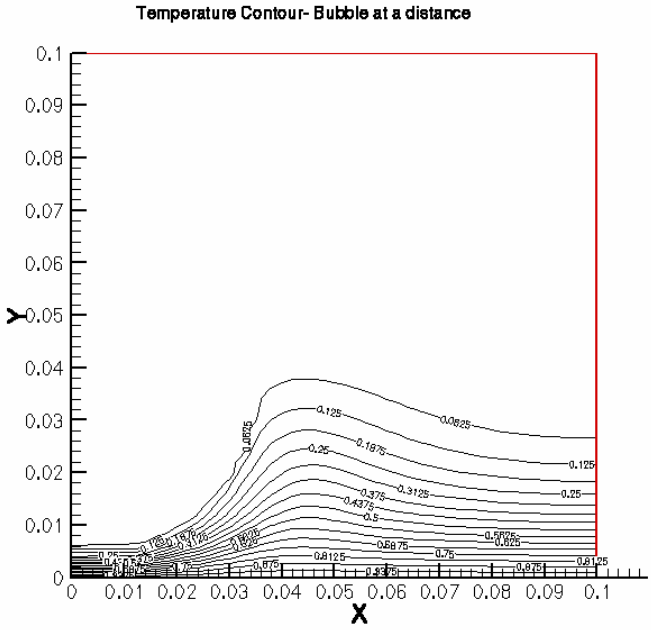

Figure 7. Temperature contour diagram for bubble at a distance from the wall after 692.8 μs.

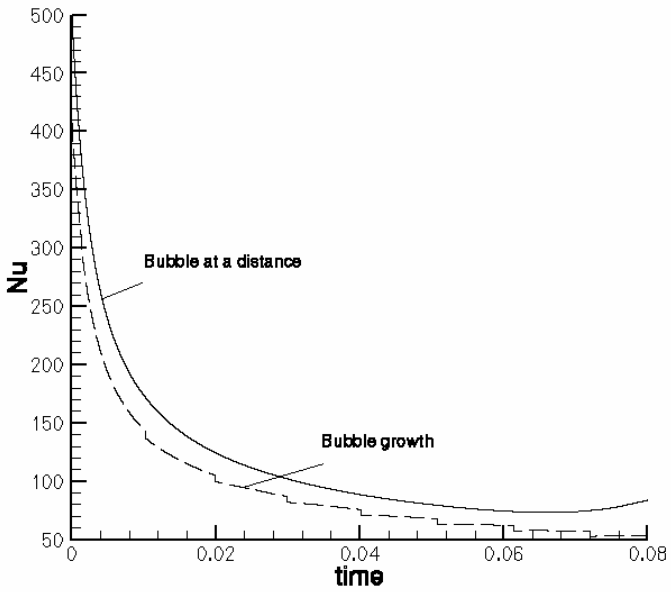

Figure 8. Variation of Nusselt number with time for up to 692.8 μs

The bubble in Fig. 6 has a radius close to 0.35 units which is less than 0.4 units to start with. Initially it is assumed that the velocity in most of the domain is zero. Hence the flow evaluation in time with temperature to satisfy the governing equation could have caused this change. The temperature boundary layer propagates in time and the depth reached about 0.03 units as shown in Fig. 7. This depth is similar to Fig. 4 for the previous case at the same place. At the same time close to bubble one can see clearly a thin boundary layer of 0.006 units. The Nu at the wall for the case in previous section and this section is shown in Fig. 8. Here one can see that the Nu for this case is higher than the previous case. When the bubble is away the minimum Nu is about 70 where as for bubble growth it is 50. The similar trend is reported by Son et al. (2002) when a bubble grows and departs. Ways to collapse and move the bubble from the nucleation site and bring cooler liquid close to the wall can only achieve higher heat flux.

5.3 Nucleation Growth and Merging of the Vapor Bubble

In a thin liquid film a growing bubble will merge with vapor on the top of the liquid layer when the size is larger than the thickness of the film. In this section the process of growth and merging of vapor bubble is modeled. During the process the heat flux at the interface of liquid, vapor and wall is computed. For this case in the same computational domain of 0.1x0.1 dimensionless unit 0.05 unit of vapor layer is considered above the 0.05 unit of liquid layer as shown in Fig. 9. The total thickness of 0.1 units is equivalent to 73.62 μm. Grid sizes 51x51 and 101x101 are considered here for convergence study. The process of vapor bubble mixing with vapor on the top of the liquid film is a complex phenomenon where surface tension, phase change due to evaporation and gravity are interacting.

To accelerate the merging of the vapor bubble with vapor on the top layer an initial bubble radius of 0.03 to 0.04 units is considered for nucleation boiling. The liquid layer is considered up to 0.05 units depth and beyond is assumed to be vapor. The distance function is assumed to have constant value at the middle of the distance between the bubble and top of the liquid layer. The temperature is assumed to be varying linearly from T_w to T_{sat} in the 0.01 units from the wall. Computation is done for 0.2 dimensionless time or 1.732 ms. Time steps considered are $5.x10^{-6}$ (43.3 ns) and $1.x10^{-6}$ (8.66 ns) nondimensional time. Total time steps varied from 40,000 for 43.3 ns to 200,000 for 8.66 ns.

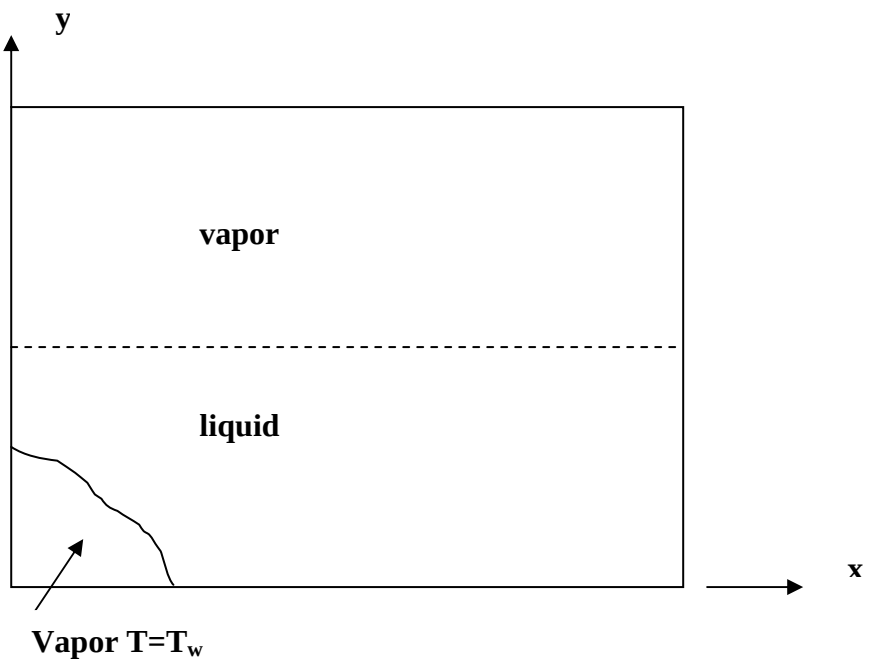

Figure 9. Sketch showing the vapor bubble growing and vapor layer on the top of the liquid layer

The computed average Nu and the maximum velocity in the computational region with time are plotted in Fig. 10 and Fig. 11. The average Nu decreases initially from 90 to 35 (until 0.1 dimesnionless time) during nucleate boiling of the bubble growth. After that the bubble merges with outside vapor. During this process the average Nu increases up to 106 sharply and then decreases to 30 in 0.02 dimensionless time (3.464 μs). After that also there are few jumps which are not as sharp as this one. At the same time in Fig. 11 one can see that the maximum velocity in the region increase from 3 to 36 units and comes back to 3 units. Hence when the vapor bubble merges with vapor on the top and the liquid finds its equilibrium position; the flow changes simultaneously in a very short time due to the interaction of the surface tension, viscosity, gravity and temperature. During this time the liquid spreads in the dry areas and hence there is an increase in average Nu. This is illustrated in time sequence using the velocity vector and temperature

contour diagram for seven instant of time. The time, average Nu and maximum velocity at which plots were made are reported in Table 1.

The velocity vector and temperature contour diagrams for the corresponding time in Table 1 are reported in Fig. 12 and the variation of Nu along the wall for the same times is reported in Fig. 13. The maximum velocity in the computational region varies from 2 to 38 as plotted in Fig. 11 and it is very difficult to show such variations with same reference velocities in plots Fig. 12. In Fig. 12 (a), (b) and (g) has same reference velocity for the plots and the rest of the figures the reference velocities are 10 times less than the reference velocity used in Fig. 12 (a), (b) and (g). It can be seen that the maximum average Nu is 92.91 at 927.53 μs and the maximum velocity is 11.16 at 891.16 μs which are less than the maximum reported in Figures 10 and 11. The maximum velocity occurs when the bubble merges with the vapor layer around 0.102 (883.32 μs) dimensionless time and the maximum Nu occurs around 0.106 (917.96 μs) dimesnionless time. The Fig. 12 (f) is close to the time of maximum Nu occurs. During this time it can be seen that the liquid is spread more than 0.07 units of the wall. Before the merger the liquid is spread less than 0.05 units. It is expected at 917.96 μs that the liquid could have spread more than 0.07 units and the thin layers could have evaporated. From Fig. 12 (d) to Fig. 12 (f) one can observe that the thermal boundary layer at the right boundary (x=0.1 units) is almost similar. At the interface of liquid and vapor the thermal boundary layer is very thin in Fig. 12 (f) and spread for 0.02 units more than Fig. 12 (d). This is because the cooler liquid is slowly heated by conduction as explained in Eq. 15.

Table 1. Average Nu and maximum velocity for various times

Dimensionless time (μs)	Average Nu	Dimensionless max. velocity
0.018905 (163.72)	66.	2.93
0.092405 (800.23)	39.18	2.97
0.100805 (872.97)	40.81	10.21
0.102905 (891.16)	44.93	11.16
0.105005 (909.34)	88.14	10.72
0.107105 (927.53)	92.91	9.86
0.199505 (1727.71)	31.96	3.02

In Fig. 13 one can see that maximum Nu is about 200 in Fig. 13 (a), (b) and (c) and once the bubble merges and liquid configuration changes it reaches as high as high as 450 in Fig. 13 (e) and also peak value is spread much larger area than other plots. In other plots the Nu varies very sharply close to the maximum. When the liquid is spreading with cooler liquid on the hot wall the Nu is high and distributed for some area. The sharp peaks are due to phase change on the side and the wider spread is due to phase change in the vertical direction. The maximum Nu reported in Fig. 13 are not the maximum occurring in the computation because we did not capture the time of maximum average Nu. This can be more than 500.

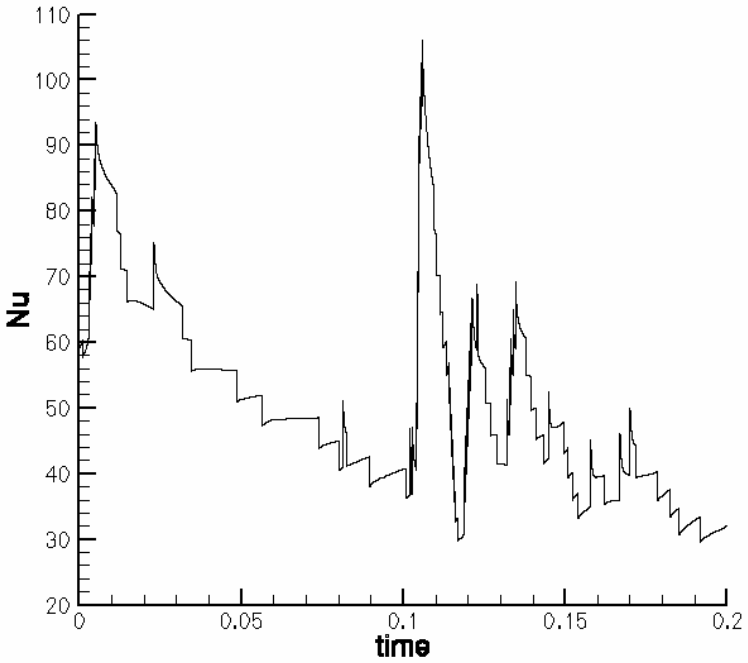

Figure 10. Variation of Nusselt number with time for up to 1.732 ms

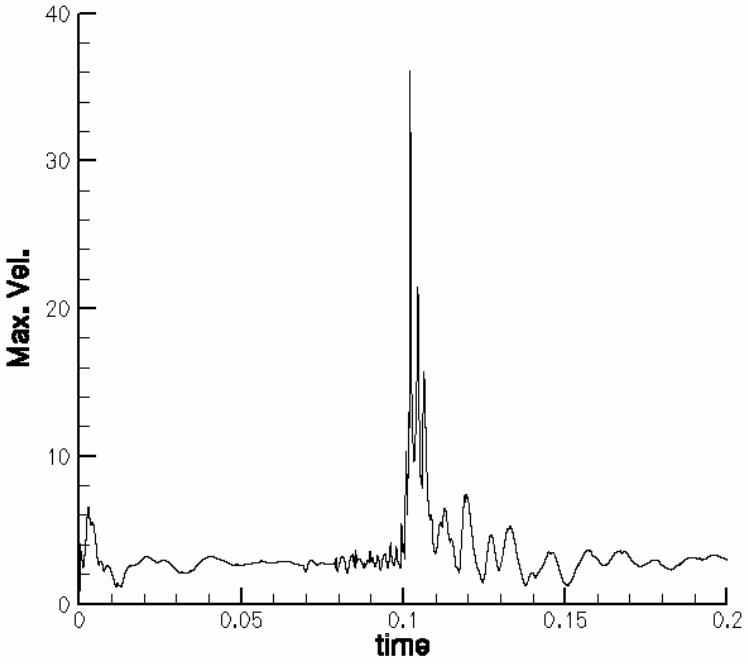

Figure 11. Variation of maximum velocity in the computational region with time for up to 1.732 ms

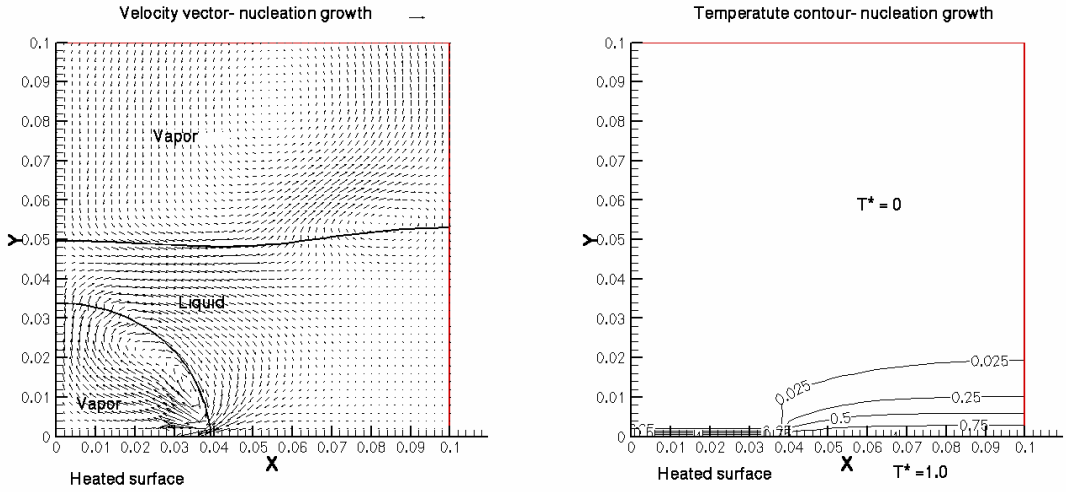

Figure 12 (a) Plot at 163.72 μs

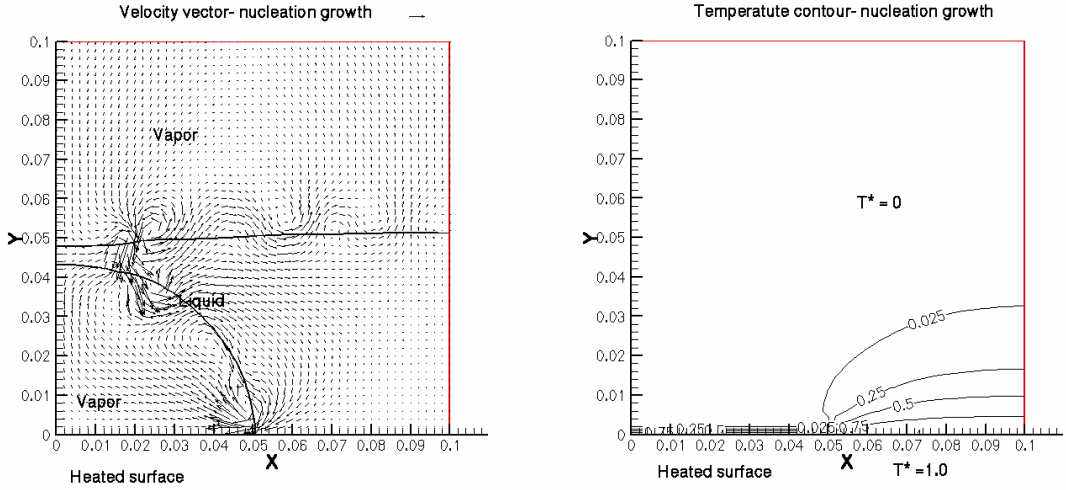

Figure 12 (b) Plot at 800.23 μs

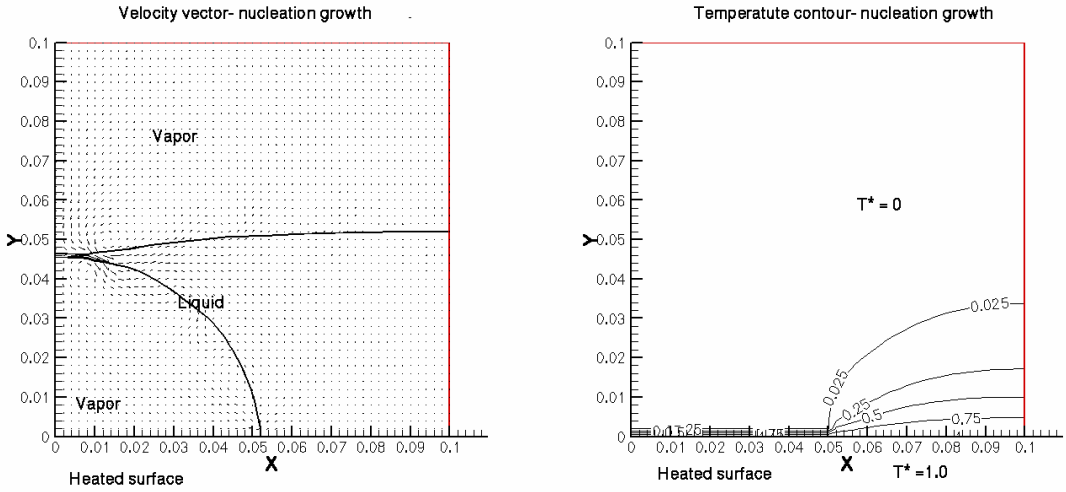

Figure 12 (c) Plot at 872.97 μs

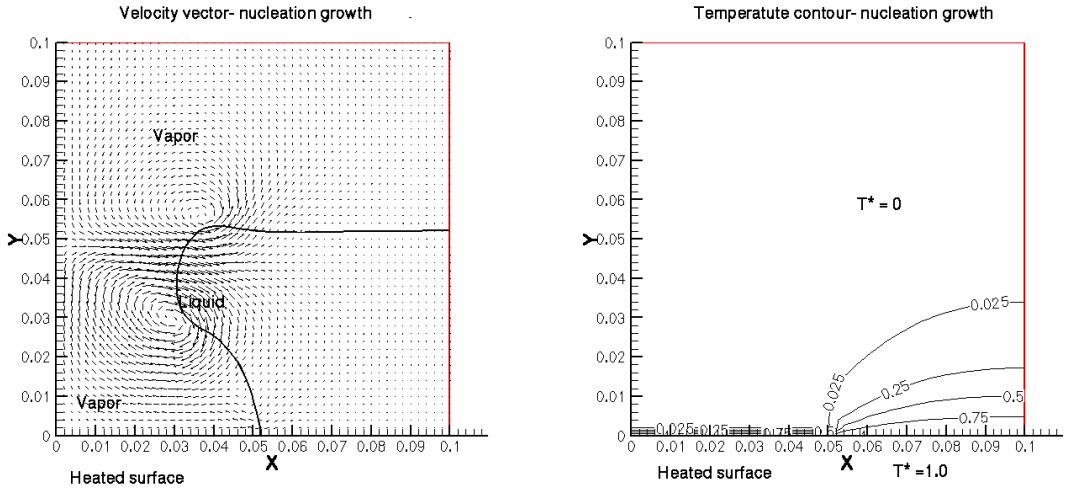

Figure 12 (d) Plot at 891.16 μs

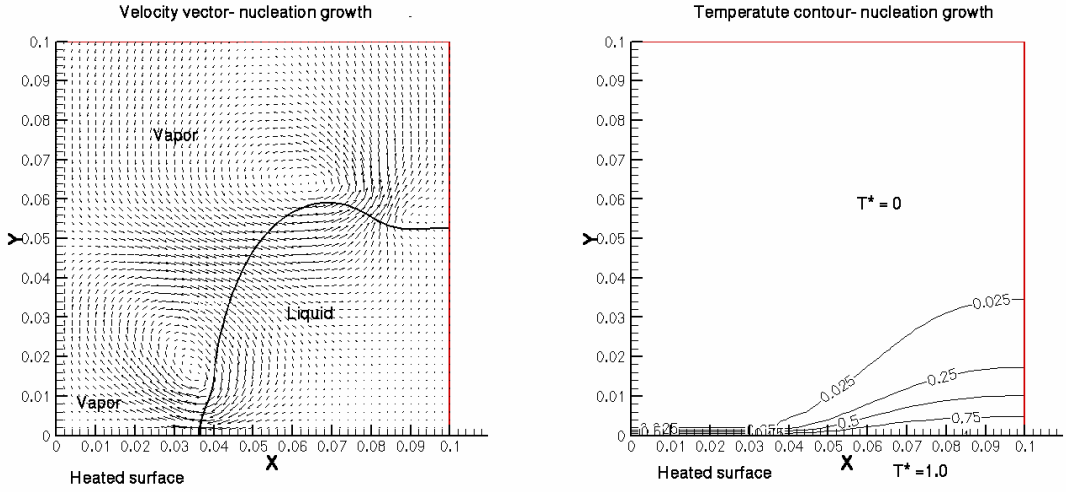

Figure 12 (e) Plot at 909.34 μs

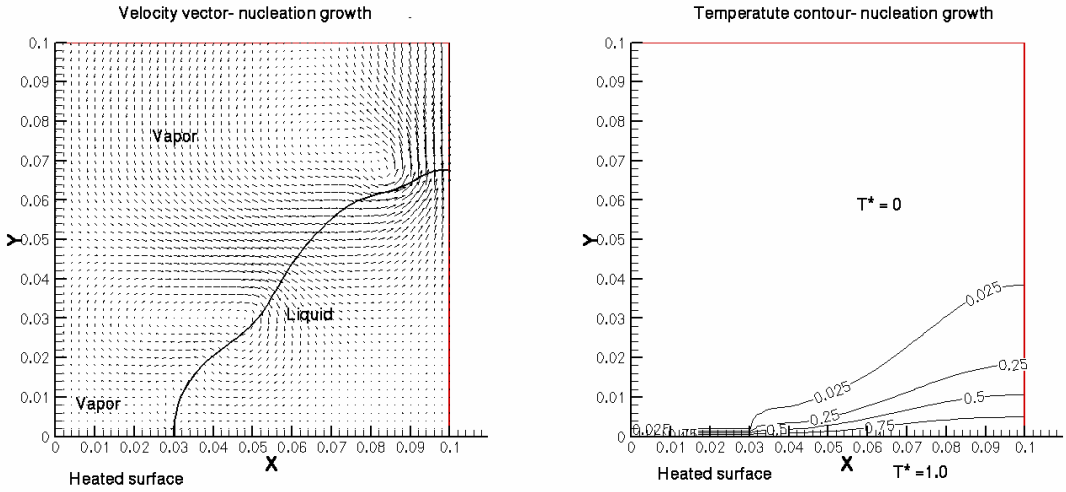

Figure 12 (f) Plot at 927.53 μs

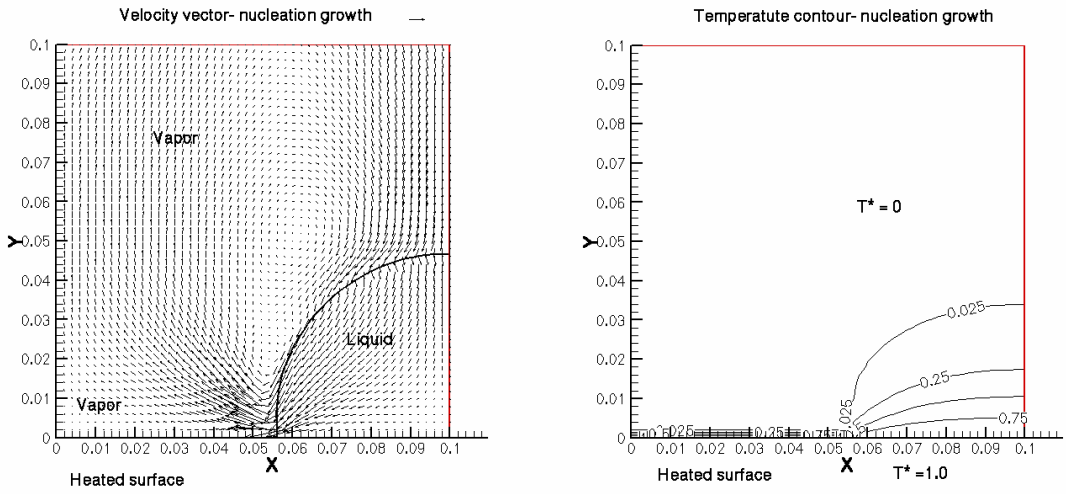

Figure 12 (g) Plot at 1727.71 μs

Figure 12. Velocity vector and temperature contour diagrams during the merging of vapor bubble with vapor layer

Using a 101x101 mesh the same computation is done in the same region of 0.1x0.1 units with a time step of $5.x10^{-6}$ (43.3 ns). The computed maximum average Nu and velocity came to be 147.4 and 26.32 units compared to 106.1 and 36.11 units using 51x51 mesh. The grid spacing has impact on maximum Nu when transient conduction is considered for a fresh liquid occupying a hot wall; it is difficult to consider the convergence study on Nu. The maximum velocity decreased due to grid refinement because there is more grid point available for the liquid and vapor interaction. Over all the flow features and variation of Nu with time have similar trend. When a time step of $1.x10^{-6}$ (8.66 ns) is used on the 51x51 mesh the maximum Nu is 111.1. This is about 5% increase in the Nu.

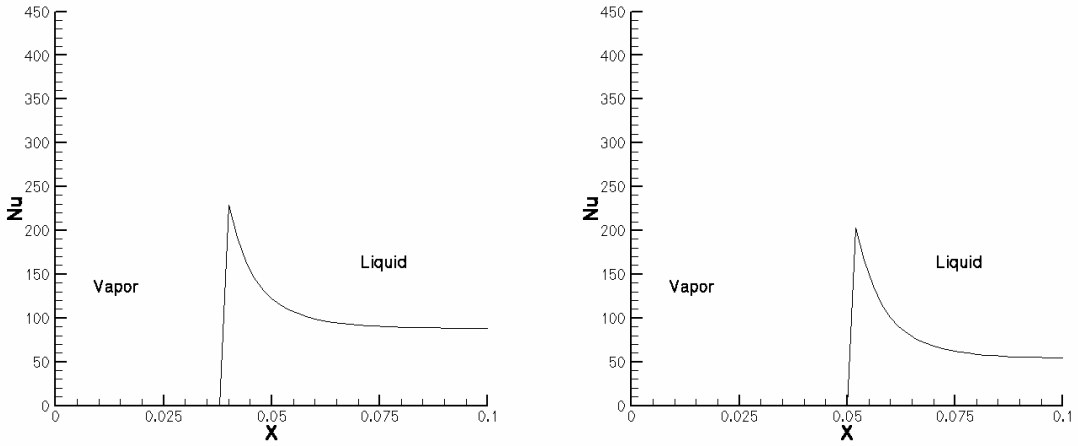

Fig. 13. (a) and (b)

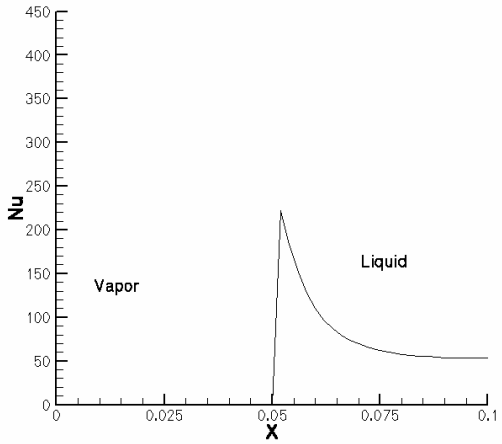

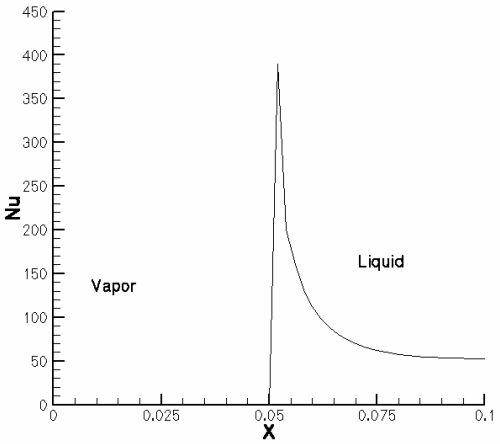

Fig. 13. (c) and (d)

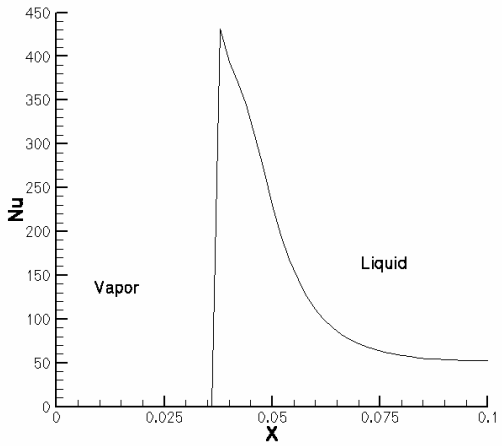

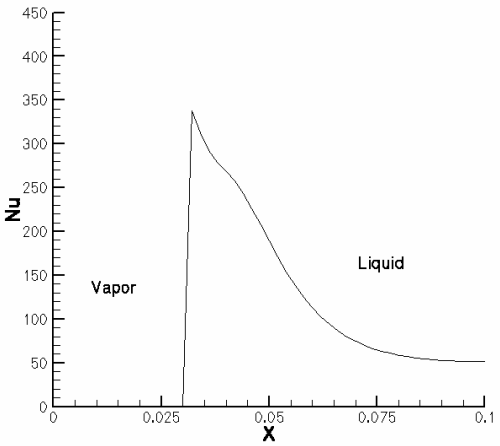

Fig. 13. (e) and (f)

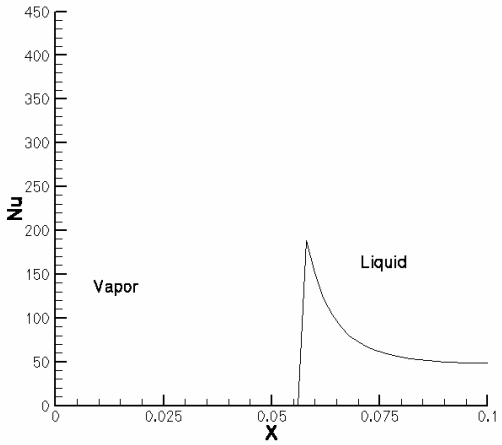

Fig. 13. (g)

Figure 13. Variation of Nusselt number along the hot surface for different times in Table 1

The computed maximum Nu and velocity using a 51x51 mesh with same time step for a liquid to vapor density ratio of 90 are 106. and 49.8. So this maximum Nu is the same as for density ratio of 20. On the other hand the velocity increased from 36.11 units to 49.8 units when the density ratio is increased. This is expected as the density ratio is increased the resistance due to vapor gets decreased.

This study illustrates the importance of how the collapse of the vapor bubble in a rapid way helps to increase the heat transfer on the wall. The maximum average Nu reported in Fig.10 is 106 where as Lin and Ponnappan (2003) reported more than 200. Here the collapse of the bubble due to merging with vapor layer is considered. In the actual spray cooling merging of vapor bubble with top layer, collapse of vapor bubbles due to impact of liquid droplet and convective flow of the liquid in the thin film all happens simultaneously in various proportions at different regions. Further work is underway for more detail studies including the impact of liquid droplet on vapor bubble. For sure this will increase the heat transfer mechanism.

Further detailed studies are underway to consider the effect of grid resolution, high density ratio of liquid to vapor and to extend the model for three-dimensional problem.

6. Conclusions

1. Current survey on spray cooling modeling and the complexities are addressed in modeling. Especially the importance of liquid-vapor-solid interaction identification
2. For high heat flux spray cooling the thin film on the surface and its interaction with liquid droplet is very important.
3. The collapse of vapor bubble either by liquid droplet hitting at high speed or the vapor bubble breaks during merging of vapor on the top of the thin film has major impact on spray cooling heat transfer. The merging of vapor bubble with vapor on the top of the liquid layer is computed and related to spray cooling.
4. The influence of conduction and convection during the collapse of vapor bubble are explained from the computed average Nu at the bottom of the wall.
5. The importance of moving the fluid quickly to get dry surface and moving fresh liquid over them to get high heat flux. This can be explained from transient conduction in short time.
6. Development of multiphase flow model to solve the thin film nucleate boiling and studying the merging of vapor bubble with vapor on the top of the liquid. This phenomenon causes high heat flux.
7. Future study on spray dynamics on thin film with vapor bubble and its impact on heat transfer mechanism close to the hot surface.

Acknowledgements

I would like to acknowledge the partial support received from AFRL/WPAFB through Universal Technology Corporation as a summer faculty and ONR/DEPSCoR support to perform this work. I thank Dr. R. Ponnappan for encouraging me to visit AFRL/WPAFB for the summer of 2004 and for all the interesting discussions with me during the course of my stay. Several discussions on spray cooling experiment with Dr. Lancho Lin were very fruitful for the modeling work. I would like to thank the colleges Mr. Roger Carr and Mr. Dick Harris for helping me in several aspects during my visit at the Thermal Science group, Propulsion Power division for summer. I thank the encouragements and support provided by Dr. Juan Balda, Professor of Electrical Engineering to visit WPAFB during the summer of 2004.

Nomenclature

c_p = specific heat at constant pressure
g = gravity vector
H = step function
h = grid spacing
h_{fg} = latent heat of evaporation
Ja = Jacob number = $c_{pl}\,\Delta T/\,h_{fg}$
k = thermal conductivity
l_r = characteristic length $\sqrt{\sigma/g(\rho_l-\rho_v)}$
m = mass flux vector
Nu = Nusselt number $q\,l_r\,/(\Delta T\,kl)$
p = pressure
Pe = Peclet number = $\rho_l\,u_r\,l_r\,c_{pl}\,/k_l$
Pr = Prandtl number = $c_{pl}\,\mu_l\,/k_l$
q = heat flux
Re = Reynolds number = $\rho_l\,u_r\,l_r\,/\mu_l$
T = temperature
T^* = dimensionless temperature $(T-T_{sat})/(T_w-T_{sat})$
ΔT = temperature difference $T_w - T_{sat}$
t = time
t_r = characteristic time $l_r\,/\,u_r$
u = velocity vector (u,v)
$\mathbf{u}_{int}$ = interface velocity vector
u_r = characteristic velocity $\sqrt{gl_r}$
We = Weber number = $\rho_l\,u_r^2\,l_r\,/\,\sigma$
α = thermal diffusivity
κ = interfacial curvature
μ = dynamic viscosity
ρ = density
σ = surface tension
φ = level set function

Subscripts
int = interface

l, v = liquid , vapor
sat, w = saturation, wall

References

1. Q. Bai and Y. Fujita (1999), Numerical simulation of the growth for a single bubble in nucleate boiling, Thermal Science & Engineering, 7, 45-53.
2. J.U. Brackbill, D.B. Kothe and C. Zamach (1992), A continuum method for modeling surface tension, *J. Comp. Physics*, 100, 335-354.
3. Y.C. Chang, T.Y. Hou, B. Merriman and S. Osher (1996), A level set formulation of Eulerian interface capturing methods for incompressible fluid flows, *J. Comp. Physics*, 124, 449-464.
4. L.C. Chow, M.S. Sehembey and M.R. Paris (1997), High heat flux spray cooling, *Ann. Rev. Heat Transfer*, 8, 291-318.
5. V. K. Dhir (2001), Numerical simulation of pool-boiling heat transfer, *AIChE Journal*, 47, 813-834.
6. M. DiMarzo et al. (1993), Evaporative cooling due to a gravity deposited droplet, *Int. J. Heat Mass Transfer*, 36, 4133-4139.
7. J.H. Ferziger and M. Peric (2002), *Computational Methods for Fluid Dynamics*, Springer, New York.
8. Y. He, M. Shoji and S. Maruyama (2001), Numerical study of high heat flux pool boiling heat transfer, *Int. J. Heat Mass Transfer*, 44, 2357-2373.
9. D. Juric and G. Tryggvason (1998), Computations of boiling flows, *Int. J. Multiphase Flow*, 24, 387-410.
10. S.G. Kandlikar, M. Shoji and V.K. Dhir (Eds) 1999, *Handbook of phase change: Boiling and condensation*, Taylor & Francis, New York.
11. J. Kern and P. Stephan (2003), Theoretical model for nucleate boiling heat and mass transfer of binary mixtures, *Journal of Heat Transfer*, 125, 1106-1115. [Micro amd macro region. Evaporation and bubble growth but no movement of the bubble]
12. J.P. Kizito, et al. (2004), Numerical and experimental studies of splashing droplets, AIAA-2004-0960, 42nd AIAA Aerospace Science Meeting and Exhibit. [splashing & thermal]
13. F. Kreith and M.S. Bohn (1986), *Principles of heat transfer*, Harper & Row Publishers, New York.
14. T. Kunugi (2001), MARS for multiphase calculation, *CFD Journal*, 9, 563-571.
15. R.C. Lee and J.E. Nydahl (1989), Numerical calculation of bubble growth in nucleate boiling from inception through departure, *Journal of Heat Transfer*, 111, 474-479.
16. L. Lin and R. Ponnappan, (2003), Heat transfer characteristics of spray cooling in a close loop, *Int. J. Heat Mass Transfer*, 46, 3737-3746
17. S.P.Lin and R.D.Reitz (1998), Drop and spray formation from a liquid jet, *Annu. Rev. Fluid Mech*, 30, 85-105.
18. R. Monti (Ed.) (2001), *Physics of fluids in microgravity*, Taylor & Francis, New York.
19. I. Mudawar (2001), Assessment of high heat-flux thermal management schemes, *IEEE Transactions on Components and Packaging Technologies*, 24, 122-141
20. S. Osher and R. Fedkiw (2003), *Level set methods and dynamic implicit surfaces*, Springer, New York. Applies Mathematical Sciences: Vol. 153.

21. M. Pasandideh-Fard, S.D.Aziz, S. Chandra and J. Mostaghimi, (2001), Cooling effectiveness of water drop impinging on hot surface, *Int. J. Heat Mass Transfer*, 22, 201-210. [droplet dynamics- impact- shape of the film etc- thermal modeling & experiment]
22. M.M. Rahman, R. Mead, C.T. Hong, L. Lin and R. Ponnappan, (2004), Numerical analysis of a spray nozzle for predictions of cone angle and pressure drop, IECEC 2004: Proceedings of the 2nd International Energy Conversion Engineering Conference, Rhode Island, Aug. 16-19.
23. D.P. Rini, R.H. Chen and L.C. Chow (2002), Bubble behavior and nucleate boiling heat transfer in saturated FC-72 spray cooling, *Journal of Heat Transfer*, 124, 63-72.
24. R. Scardovelli and S. Zaleski (1999), Direct numerical simulation of free-surface and interfacial flow, *Annu. Rev. Fluid Mech*, 31, 567-603.
25. R. P. Selvam (1997), Computation of pressures on Texas Tech building using large eddy simulation, *J. Wind Engineering and Industrial Aerodynamics*, 67 & 68, 647-657.
26. R.P. Selvam, and A.Elshabini (2000), Nonlinear thermal stress and flow modeling in various electronic packages, *International Journal of Microcircuits & Electronic Packaging*, 23, 224-233.
27. J.A. Sethian (1999), *Level set methods and fast marching methods: Evolving interfaces in computational geometry, fluid mechanics, computer vision and materials science*, Cambridge University Press, Cambridge, UK.
28. S. Shin and D. Juric (2002), Modeling three-dimensional multiphase flow using a level contour reconstruction method for front tracking without connectivity, *J. Comp. Physics*, 180, 427-470.
29. G. Son, and V.K. Dhir (1998), Numerical simulation of film boiling near critical pressures with a level set method, *Journal of Heat Transfer*, 120, 183-192.
30. G. Son, N. Ramanujapu and V.K. Dhir (2002), Numerical simulation of bubble merger process on a single nucleation site during pool nucleate boiling, *Journal of Heat Transfer*, 124, 51-62.
31. G. Son and N. Hur (2002), A coupled level set and volume-of-fluid method for the buoyancy-driven motion of fluid particles, *Numerical Heat Transfer, B*, 42: 523-542.
32. P. Stephan and J. Hammer (1994), A new model for nucleate boiling heat transfer, *Heat Mass Transfer*, 30, 119-125
33. M. Sussman, P. Smereka and S. Osher, (1994), A level set approach for computing solutions to incompressible two-phase flow, *J. Comp. Physics*, 114,146-159.
34. G. Trggvason et al. (2001), A front-tracking method for the computations of multiphase flow, *J. Comp. Physics*, 169, 708-759.
35. S.W.J. Welch (1998), Direct simulation of vapor bubble growth, *Int. J. Heat Mass Transfer*, 41, 1655-1666.
36. S.W.J. Welch and J. Wilson (2000), A volume of fluid based method for fluid flows with phase change, *J. Comp. Physics*, 160, 662-682.
37. J. Yang, L.C. Chow and M.R. Paris, Nucleate boiling heat transfer in spray cooling, *Journal of Heat Transfer*, 118, 668-671, 1996
38. H.Y. Yoon, S. Koshizuka and Y. Oka (2001), Direct calculation of bubble growth, departure, and rise in nucleate pool boiling, *Int. J. Multiphase Flow*, 27, 277-298.

Final Report H.T.V. Using an ArF Excimer Laser

Michael Lahr

Introduction

The focus of this summer's research at Wright-Patterson Air Force Base was to apply HTV (Hydroxyl Tagging Velocimetry) to the high speed scramjet facilities available at the base. Working with Dr. Cam Carter, Dr. Robert Pitz, Dr. Mark Hsu, Zach Douglas, and the system engineers in Test Cell 19, velocity measurements at different conditions and locations were obtained on four different test dates. I was at Wright-Patterson from May 17, 2004 – August 6, 2004.

Overview

Hydroxyl flow tagging is a non-intrusive way to measure the velocity of an air or fuel/air mixture in either a high or low temperature environment. This process uses two lasers. An ArF excimer laser at ~ 193nm uses the natural moisture in the air to produce OH and H photoproducts through a single-photon photo dissociation. Utilizing optics and most importantly grid optics at the entrance to the test section, a grid can be created of this OH. The OH can then be revealed throughout its displacement in a flowfield by fluorescence caused by OH excitation using a pulsed frequency-doubled dye laser (~ 282 nm). A CCD camera is then utilized to take the images of the displaced grid. Although two different setups were utilized, the following figure shows the main configuration of the two lasers, CCD camera, and optics.

Figure 1. Experimental Setup

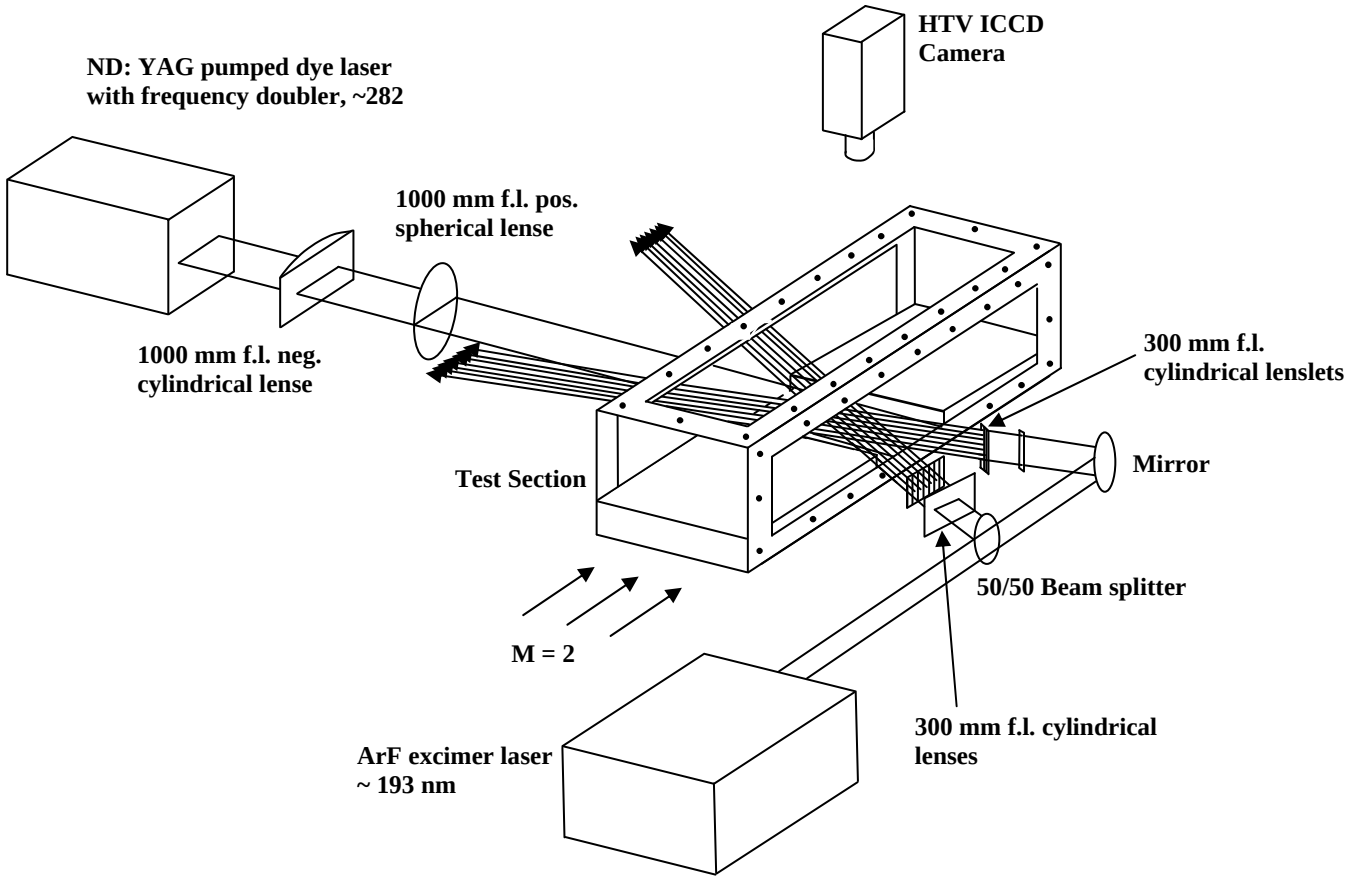

The main focus of the flow tagging work this summer was to investigate the flameholding region of a combustor test section. Using this technique the shear layer and subsequent change in velocities throughout the depth of the cavity could be seen. Figure 1 shows a schematic of the setup including the test section with the cavity. The following figure shows the dimensions of this flame holder.

Figure 2. Cavity

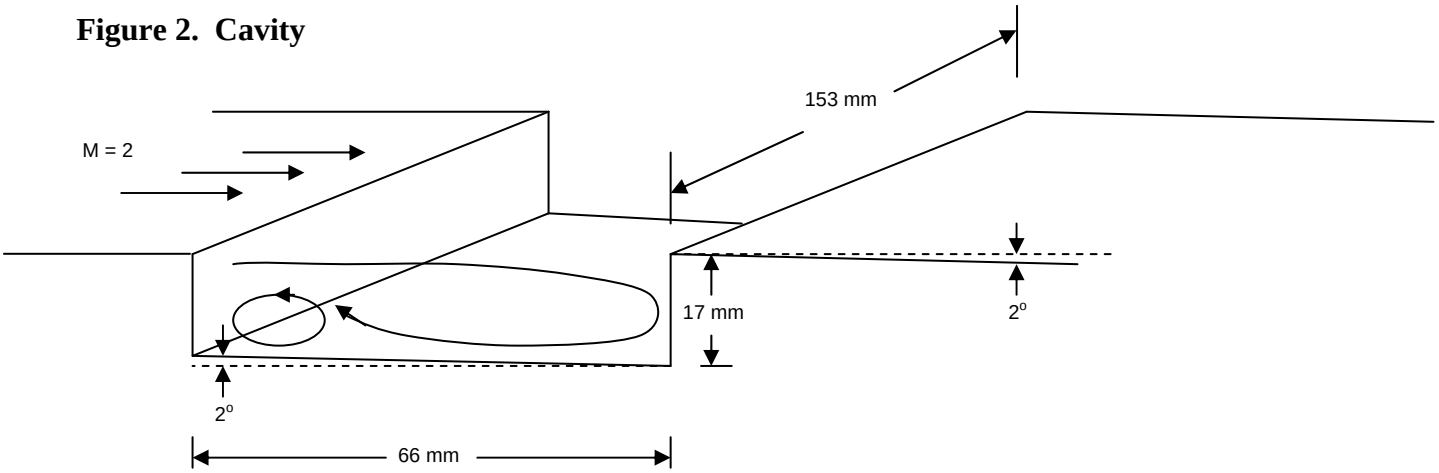

Tests

Zach and I spent countless hours setting up for each test. From making sure the laser was in tune to setting up the grid optics, the preparation for each test was extensive. On each test date there was a main objective. The following is a breakdown of what was accomplished on each of the four dates.

- Test 1 (June 22) - For the first test, we all decided to hold off on actual combustion in the test section and just analyze the effects of moving the grid up and down, in and out of the flameholder cavity. This vertical adjustment showed many facets of the flow including the freestream above the cavity and the evidence of the turbulent shear layer and recirculation zone as the grid was brought more towards the top of the cavity and then actually into it.

- Test 2 (June 29) - This test continued with the trend of moving up and down throughout the freestream and shear layer. One difference in the testing was the introduction of combustion. After testing the images in just the flow of air, an ethylene flame was created inside the flame holder to see the effects the flame had on the reading of OH. This was at zero back pressure. There was a lot of OH produced by the flame and the grid got very hard to see while sitting directly in the most intense part of the flame.

- Test 3 (July 7) - Still investigating some combustion, the main focus of this test was to analyze velocity fields while adjusting the back pressure in the test section. This creates a shock wave propagating down the section and can be controlled utilizing the valve adjustment.

- Test 4 (July 13) - A different setup was used on this date. The camera was positioned horizontally on the table to view the grid lines in a vertical manner across the cavity. This configuration was very complicated in regards to the optic alignment and covered a longer

distance than the first setup. Due to the long distance and the lack of a narrowband beam, the power dissipated greatly by the time the beam got to the final grid optic. With 1 mJ and 3 mJ in the two grid optics the OH was very hard to see. However, when combusting in the cavity, more OH could be seen using this setup. This configuration was advantageous because this view could show more characteristics of the shear layer and recirculation zone.

Results

From each test, thousands of images were taken characterizing the movement of the grid in the cavity and freestream. Using PD View and LaVision Davis software, Zach and I analyzed all of the data. The following figures are representative of the data obtained throughout the summer tests. These are averages of single shots taken during each collection of data from the camera. So, each image shown here is the average of 100 images.

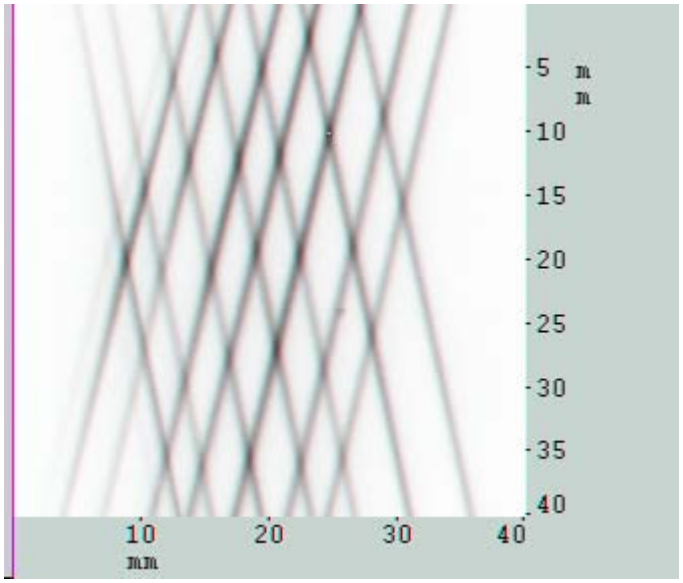

.516" above the top of the cavity (freestream) at t = 0.

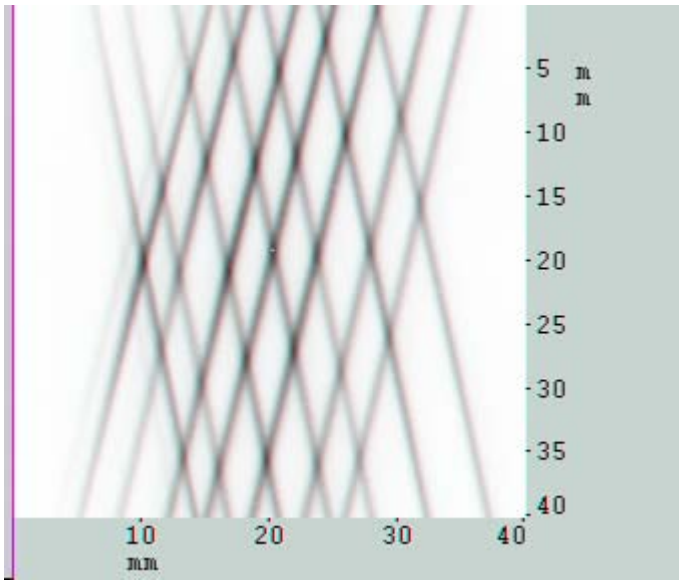

.516" above the top of the cavity (freestream) at t = 2 μs

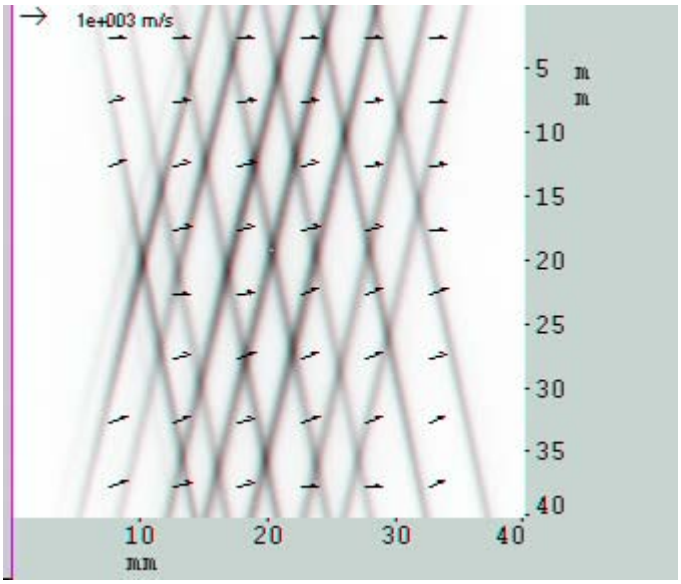

Vector image at .516” above the top of the cavity (freestream) with a 2 μs delay.

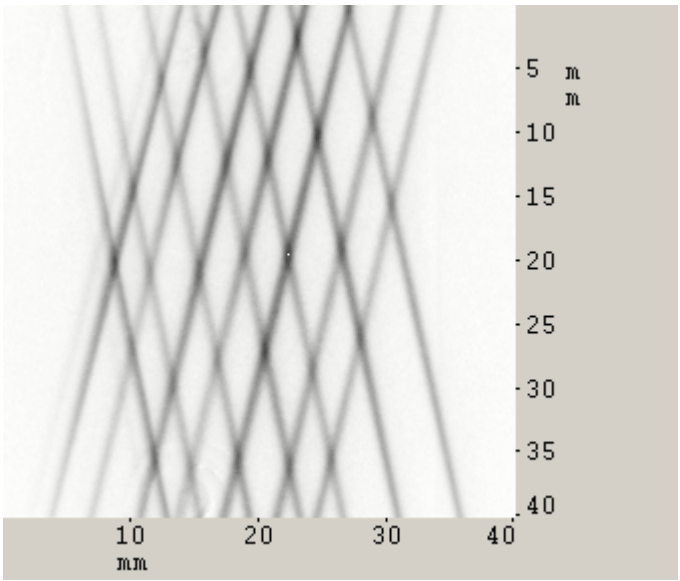

.216” below the top of the cavity (shear layer) at t = 0.

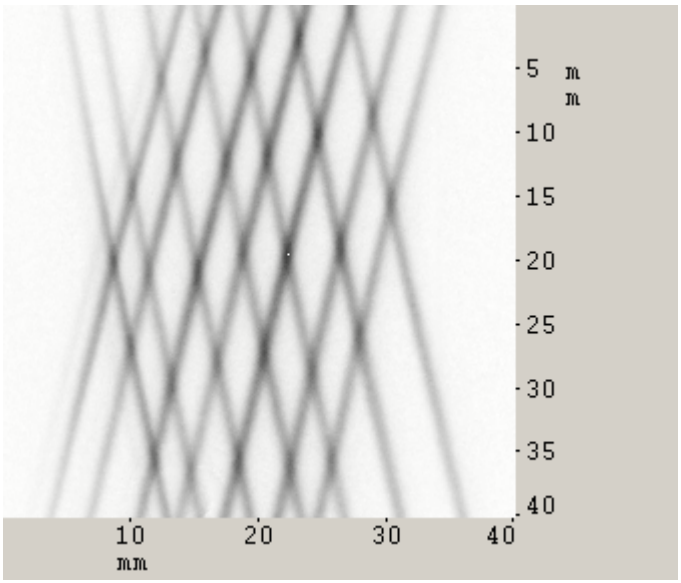

-.216” below the top of the cavity (shear layer) at t = 2 μs.

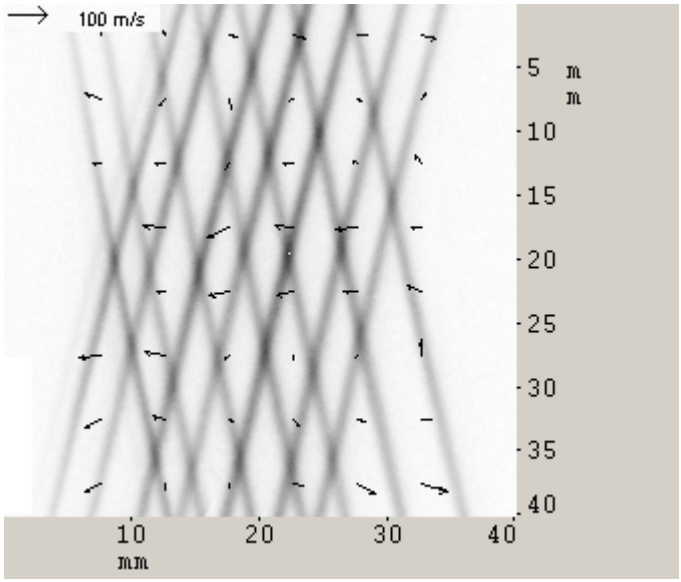

Vector image at .216” below the top of the cavity (shear layer) with a 2 μs delay.

To show how each single shot within these averages varies, some single shot vector images were also created. These used the average of the zero displacement grid as the initial image. The following figures are examples of these.

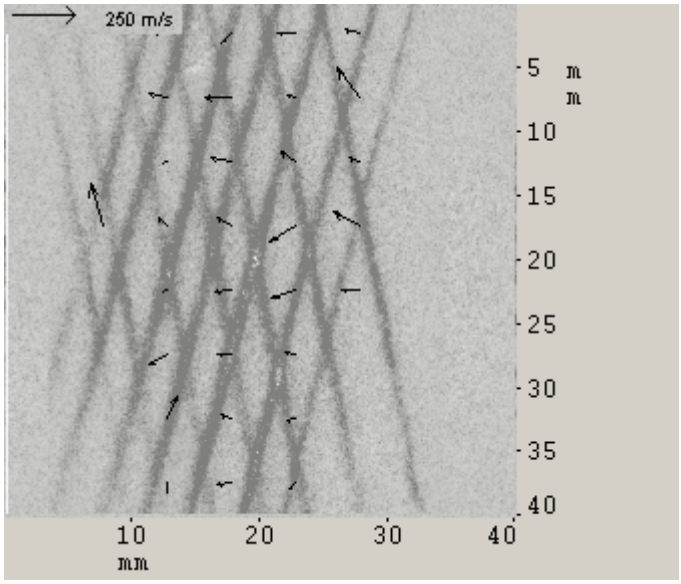

-.216 in. below the cavity (2 microsec delay)

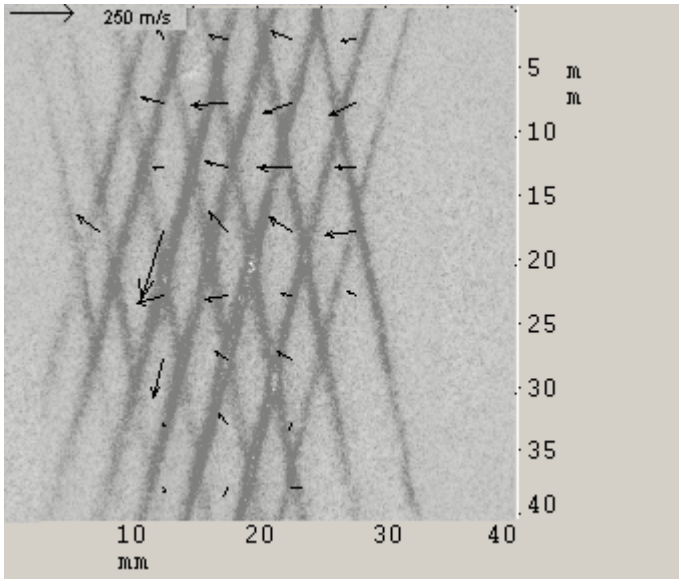

-.216 in. below the cavity (2 microsec delay)

These two single shots show the change from shot to shot and can be used in a movie format to show the actual change in the grid throughout the time of the imaging.

The main objective of this research this summer, as stated before, was to explore the flame holder cavity and the velocity that results when the Mach 2 flow is passed through the combustor region. A profile from all of the single shots was created to show how the velocity changed as the air advanced into the cavity. Since the grid was only 20 mm wide, the steps on each side of the cavity did not play a part in the profile data. Therefore, along the length of the grid the trend is very much the same in accordance with each of the test's conditions. The trends can be seen in the following graphs for low and high back pressure.

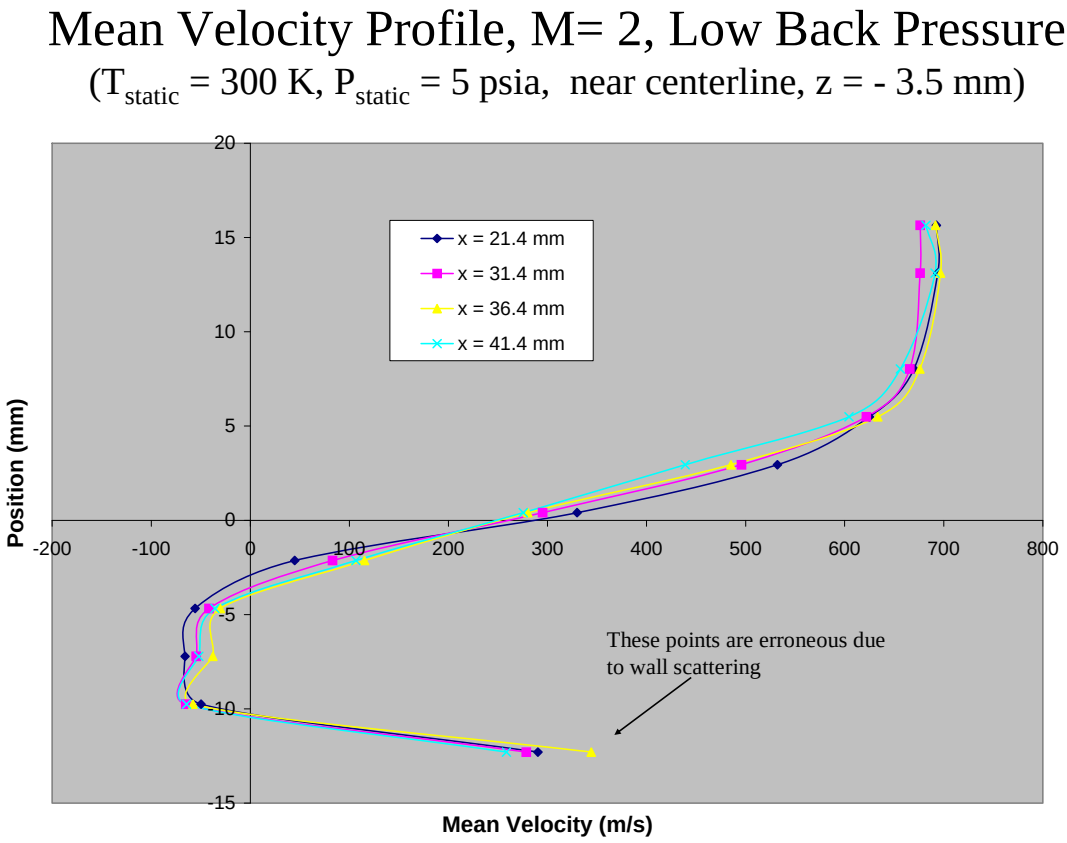

Mean Velocity Profile, M= 2, High Back Pressure

(T_{static} = 300 K, P_{static} = 10 psia, near centerline, z = - 3.5 mm)

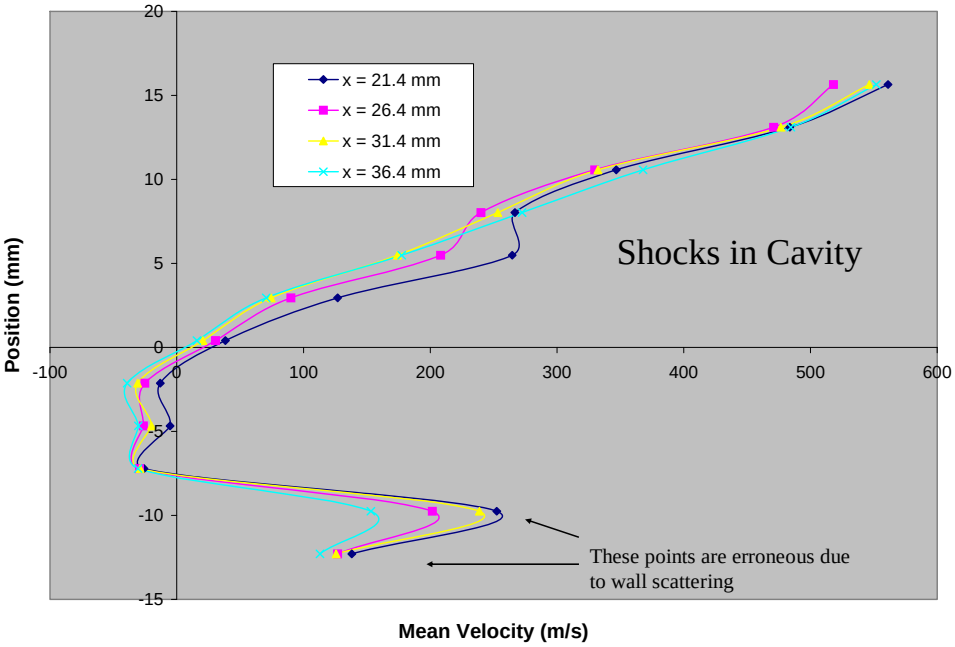

These graphs are useful in showing how the velocity changes as we investigate further into the cavity. The recirculation zones are also evident. However, there are a few erroneous points towards the bottom of the cavity due to wall scattering. The following two graphs show the deviation associated with these measurements.

RMS Velocity Profile, M= 2, Low Back Pressure

(T_{static} = 300 K, P_{static} = 5 psia, near centerline, z = - 3.5 mm)

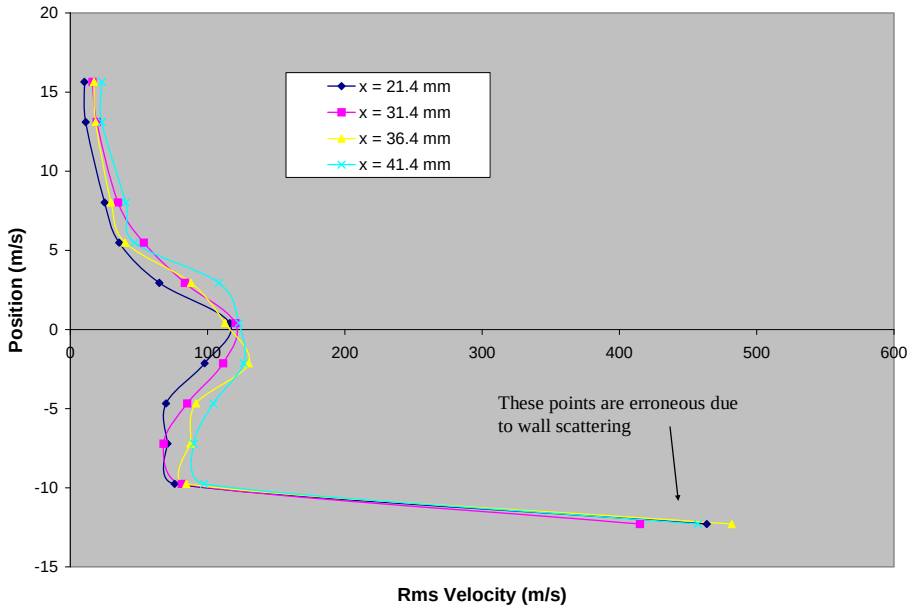

RMS Velocity Profile, M= 2, High Back Pressure

(T_{static} = 300 K, P_{static} = 10 psia, near centerline, z = - 3.5 mm)

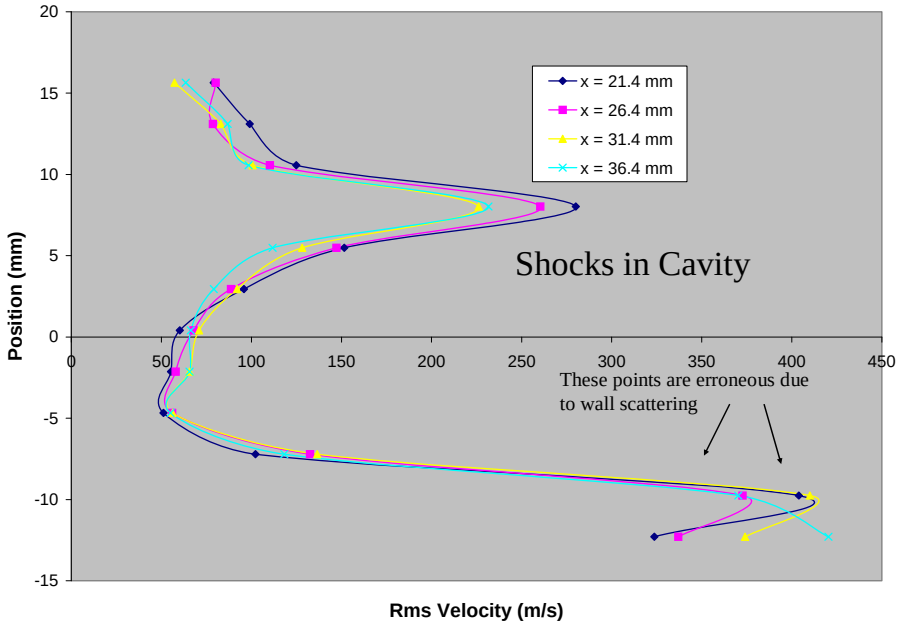

These RMS graphs show a trend of increasing deviation as there is progression through the shear layer to the bottom of the cavity. This is what should be expected due to the turbulence and recirculation zone present. Again, erroneous points have a very large deviation.

Conclusion

The work this summer was very enjoyable and proved to show some great results. Dr. Pitz is now working on writing a paper in conjunction with Cam, Zach, and myself to be presented in January at an AIAA conference in Reno. Then, hopefully it will be published in a journal.

I again want to thank UTC and Wright-Patterson for the great opportunity I had to gain experience and an unbelievable amount of knowledge as a mechanical engineer. In the future, I definitely hope to stay in touch and possibly continue to do research.

Ruth Hinde
Summer Summary – **Behavior of an RF-Pulsed, Inductively Coupled Argon Plasma**
12 August 2004

This summer I again worked in the Propulsion Directorate with Dr. John Horwath, electrical engineer, and Dr. Charles DeJoseph, plasma physicist. I spent two days with Dr. DeJoseph each week, and the other three with Dr. Horwath. I kept a fairly regular schedule regarding which days I spent working in the two labs, which helped me to really get involved with the projects.

Dr. DeJoseph and his colleagues are currently studying the behavior of an RF-pulsed, inductively coupled argon plasma when given voltages are applied to the plasma. Depending on the pressure the plasma is under, as well as the width and frequency of the RF pulse and the voltage applied to the pulse, the light emitted by the plasma exhibits widely varying properties. Most of the work I did for Dr. DeJoseph involved running tests, and recording the emission spectra of the plasma. This was similar to the work I did last summer for Dr. DeJoseph, but slightly more in-depth. Also, this summer I learned a great deal more about the setup of the experiment and the way the whole system works. I also wrote and submitted an abstract on our experiment to the American Physical Society's Division of Plasma Physics and have been working on putting together a presentation, with the possibility of presenting our studies at an undergraduate research poster session during the division's November meeting in Savannah, Georgia.

The work I did for Dr. Horwath was not quite as focused as the work I did for Dr. DeJoseph, which enabled me to learn a bit about a lot of things. There were two major projects that Dr. Horwath has had running throughout the summer, which I and the other summer hires worked on with him. The first is the Lifetime Test. I worked on this experiment with Dr. Horwath last summer as well. We are testing samples of epoxy under high voltages to see how long they will last before dielectric breakdown occurs. Some of the samples are control samples, while others contain nano-particles, in order to study the effect of the presence of nano-particles on the dielectric strength of the material. A second major project we worked on this summer was the Corona Test. This test measures the partial discharge off a high-voltage AC power supply. I spent some time working on this experiment, because it we had a lot of trouble calibrating it and isolating the signal from electrical noise, but I did not do as much work on this experiment as some of the other summer hires did. Outside of these two projects, I also spent time doing research and editing technical papers for Dr. Horwath and his colleagues.

Tuskegee University
Kenita Shaw – Fuel Cell Study
6 August 2004

The technical support rendered while at Wright Patterson Air Force Base was informative, educational, and useful.

The first couple of days were used to obtain identification and security information for the base. Becoming comfortable with the base and locations that would be needed throughout the summer we achieved.

The opportunity to have a more formal knowledge of the fuel cell was introduced. The fuel cell is defined as an electrochemical device that directly converts the electrochemical reaction to electrical energy continuously, without producing heat, known as cold combustion. A fuel cell converts the chemicals hydrogen and oxygen into water, and in the process it produces electricity.

The other electrochemical device that we are all familiar with is the battery. A battery has all of its chemicals stored inside, and it converts those chemicals into electricity too. This means that a battery eventually "goes dead" and you either throw it away or recharge it. With a fuel cell, chemicals constantly flow into the cell so it never goes dead -- as long as there is a flow of chemicals into the cell, the electricity flows out of the cell. Most fuel cells in use today use hydrogen and oxygen as the chemicals.
The fuel cell will compete with many other types of energy conversion devices, including the gas turbine in your city's power plant, the gasoline engine in your car and the battery in your laptop. Combustion engines like the turbine and the gasoline engine burn fuels and use the pressure created by the expansion of the gases to do mechanical work. Batteries converted chemical energy back into electrical energy when needed. Fuel cells

should do both tasks more efficiently. A fuel cell provides a DC (direct current) voltage that can be used to power motors, lights or any number of electrical appliances.

There are several different types of fuel cells, each using a different chemistry. Fuel cells are usually classified by the type of electrolyte they use.

The six major types of fuel cells

1. Alkaline Fuel cell (AFC)
2. Phosphoric Acid Fuel Cell (PAFC)
3. Solid Polymer Electrolyte Fuel Cell (SPEFC)
4. Molten Carbonate Fuel Cell (MCFC)
5. Solid Oxide Fuel Cell
6. Direct methanol Fuel Cell

There are several types of fuel-cell technologies are being developed for possible commercial uses:

- Alkaline fuel cell (AFC): This is one of the oldest designs. It has been used in the U.S. space program since the 1960s. It is also very expensive, so this type of fuel cell is unlikely to be commercialized.
- Solid oxide fuel cell (SOFC): These fuel cells are best suited for large-scale stationary power generators that could provide electricity for factories or towns.

Fuel cells could be used in a number of applications. Each proposed use raises its own issues and challenges.

Experiments were assigned that led to work with the Prototype Smart Fuel Cell. The Prototype Smart Fuel Cell is a Direct Methanol Fuel Cell. Tests were run to determine the

amount of methanol that would be required for a 72- hour mission on average consuming 20 Watts. The energy density for the total system was also calculated.

A fuel cell, like an ordinary battery, provides dc electricity from two electrochemical reactions. These reactions occur at electrodes (or poles) to which reactants are continuously fed. The negative electrode (anode) is be maintained by supplying a fuel such as hydrogen or methanol, whereas the positive electrode (cathode) is maintained by the supply of oxygen or air.

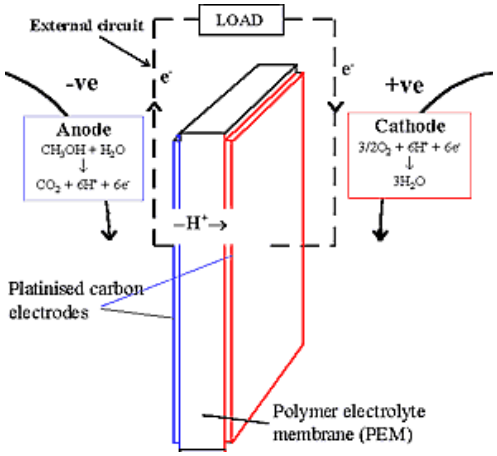

The figure above shows a diagram of the operating principles of fuel cell utilizing methanol as fuel, i.e., a Direct Methanol Fuel Cell (DMFC). When providing current, methanol is electrochemically oxidized at the anode electro catalyst to produce electrons which travel through the external circuit to the cathode electro catalyst where they are consumed together with oxygen in a reduction reaction. The circuit is maintained within the cell by the conduction of protons in the electrolyte.

The overall reaction occurring in the DMFC is the same as that for the direct combustion of methanol,

i.e; $CH_3OH + 3/2O_2 \rightarrow CO_2 + 2H_2O$

APPENDIX N

Assistance was given to a Wright State University student pursuing a Master's Degree within the Chemistry field. Support was rendered by proofreading her final thesis, formatting diagrams to be used within an upcoming published work, measuring and plotting of the conductivity of the HClO4 at different temperatures, which all led to a further understanding of the material within this writings. Also calibrating of a Gas Chromatography was attempted to help complete the research. Gas chromatography is a chromatographic technique that can be used to separate volatile organic compounds. A gas chromatograph consists of a flowing mobile phase, an injection port, a separation column containing the stationary phase, and a detector. The organic compounds are separated due to differences in their partitioning behavior between the mobile gas phase and the stationary phase in the column.

Many pieces of new laboratory equipment were acquired. In doing so these pieces were researched and presented with the capabilities and price ranges to ensure a full adequacy within the lab. Also new timelines were created within in the office to created more organization within each research venture. Assists was given with formatting and the designing of a reader friendly overview of the intended progression.

Working on base and dealing with chemicals, RCRA Hazardous Waste Training Course was required. RCRA is Resource Conservation and Recovery Act of 1976 and the Solid Waste Amendments (HSWA) to RCRA of 1974. RCRA Oversees permits for treatment, storage, and disposal of hazardous wastes and the amendments introduced corrective action component to RCRA, required cleanup of treatment, storage and disposal facilities after they are closed.

Simulation Software Technology for Turbine Engine Research in Engine Controls and Health Management

AFRL Summer Research Program Final Report[1]

Submitted by
Dr. Jeffrey S. Dalton, Mechanical and Aerospace Engineering, University of Missouri-Rolla
September 1, 2004

Abstract

There has been a parallel increase in sophistication for turbine engine technology, the simulation technology used to model behavior of turbine engine systems and controls, and the computing technology available for research and development of engine technology. The use of simulation software for engine design and development and the development of control systems for turbine engines has enabled progressive increases in engine performance. This capability is a critical part of our nations defense capability and also plays an important role in the advancement of civil air propulsion. We have progressed from the early days of engine simulation development in traditional computer programming languages to an environment that is much more advanced, utilizing object oriented software development technology to incorporate reusable component based simulation capability into today's simulation models. Research and facilities available in the Air Force Research Laboratories and in other research institutions now make it feasible to conduct real-time engine and control system technologies on high performance reconfigurable hardware. The benefits of the use of this relatively new technology include the ability to conceptualize advanced turbine engine systems, there, control systems and to research the incorporation of engine health management systems into the engine control. The end result is a more efficient design process, significant improvements in engine performance for current and next generation engines, and a reduction in total cost of ownership for turbine engines. In this study a survey of past and present engine simulation capability has been completed. The accomplishments of recent engine model development are highlighted and progress toward the development of reusable Simulink models for augmented turbofan engine simulation in real-time are described in the context of current and future research in the Intelligent Controls facility at AFRL on Wright Patterson Air Force Base.

1. Introduction

Mathematical modeling in various forms has been used in engineering during the entire history of its development and has played an important role in the understanding and development of turbine engine technology. Various levels of computing capability have existed during most of the history of the development of turbine engines. The use of computer modeling and simulation has played an especially important role as a tool for understanding the complex interaction of many subsystems that exist and as a tool for predicting engine performance and behavior. As

[1] AFRL/PRTS Summer Research, Prime Contract: F33615-02-D-2299, ICA: 04-S530-0010-01-C21, Supervised by Dr. Al Behbahani.

advances in computing technology have made higher computing performance readily available to engine developers, the sophistication of computer simulation models has increased. Current engine developers depend on high level engine simulation studies to further improve engine performance and to balance the many constraints that exist in the production of today's advanced engines for both military and commercial uses. Early simulation models based on the use of FORTRAN language computer programs have been used by engine manufacturers to describe and model the thermodynamic flow characteristics as air and fuel flow through engine. More recent advancements in both computing hardware and software technology are changing the way that engineers can approach the engine modeling problem. Simulation technology will continue to provide engineers with modeling resources that can be exploited for technology improvements. In this study a survey of past and emerging simulation technologies is presented. A summary of the use of modern simulation techniques is included and the context for the use of simulation techniques for development of future commercial and military turbine engine technology is established. This report details the results of simulation technology study, use and advancement undertaken as a part of a summer research program conducted by the author in the propulsion directorate, controls and engine health management branch of the Air Force Research Laboratory (AFRL) at Wright Patterson Air Force Base.

In 1987 the United States Air Force initiated a three phased development program, the Integrated High Performance Turbine Engine Technology Program (IHPTET), aimed at significantly improving turbine engine performance through advanced technology. Phase I goals have been met, phase II goals are currently under test and phase three goals are scheduled for completion in 2005. Computer simulation has played an important role in the development and testing of turbine engine designs during the IHPTET programs. Further performance advancements beyond the IHPTET goals have been established for next generation engine designs. The Versatile Advanced Affordable Turbine Engine (VAATE) program will incorporate advance control and health monitoring technologies to develop engine designs with prognostic and diagnostic capabilities to reduce the number of unscheduled engine removals and thereby significantly decrease maintenance costs over the life of the engine. VAATE establishes a goal for a 10x improvement in propulsion affordability and a 2x improvement in propulsion capability beyond that achieved with the IHPTET program. On-board modeling and simulation capability built into engine control and health monitoring systems may provide a way to achieve these goals. Development of intelligent engine control technology using advanced simulation techniques will further improve performance and reduce implementation costs for future engines. The intelligent engine concept is one of the core focus areas for VAATE program development. Development of self-diagnostic, and performance optimizing capabilities along with mission adaptability will required detailed engine modeling and analysis technology.

Key focus areas for the VAATE program include an intelligent engine area, a durability area and a versatile core area. Emphasis within the intelligent engine are targets the use of active control technology, health management diagnostics and prognostics and integration with other aircraft systems to create a propulsion system that can adapt to changes in mission and engine life cycle in order to provide optimal performance with minimal maintenance cost. The durability area is concerned with engine readiness and calls for the development of a protocol for the understanding of high cycle fatigue as well as other protocols for robust engine performance understanding and the validation of design methods through testing. The versatility goals

established in the VAATE program assure that future engine technology can be reused both for new engine designs and also for retrofitting existing engines in order to reduce the development and maintenance costs associated with the life of an engine.

In this work the author presents a brief history of the development and use of computer simulation tools specifically for the understanding of turbine engine systems. We are most interested in turbine engines used in aerospace applications and focus our study there. However, many of the same tools may also be applied to industrial gas turbine engine research and development. In the following section a brief survey outlines the development of turbine engine simulation technology. Section 3 contains a description of recent technology developments in the Propulsion Directorate within the Air Force Research Laboratory at Wright Patterson Air Force Base and also identifies summer research accomplishments. Section 4 contains an outline of near term future research objectives that directly extend work described here. Section 5 sets the context for the use of these developments in current research in engine control and health monitoring within the Air Force. We conclude with a summary of this work in sections 6.

2. Brief History of Turbine Engine Simulation

A constant progression from relatively simple simulation capabilities suitable for computing technologies of the 1970s and 1980s to more advanced techniques that exploit computational power of the workstations of today can be observed in the literature. Most recent work in turbine engine design and control system design takes advantage of the use of real-time control processors. The technology exists today for the use of high level computer languages to develop sophisticated models that execute in real-time on flexible, high speed processors. Future advances in computing technology will add increasing real-time modeling capability including the use of three dimensional flow simulation. In this section a sketch of the development of turbine engine simulation technology is given and representative work during this history of development cited. The references contained here are not exhaustive. However they provide a picture of the development of the technology and set the stage for current and future work in engine control and health monitoring research.

Simulation using Computational Fluid Dynamics

The increasing computational power available for computer simulation technology has been used to advance the field of computational fluid dynamics. Using this technique engineers can perform three dimensional flow, pressure, and temperature studies in engine components and use results to perform analysis and design optimization for turbine engine components. One might expect this technology to play an increasing role in the control of turbine engines. However, the computing capability required to perform calculations in real-time for the purpose of engine control and health monitoring does not yet exist. Off-line analyses are possible using computational fluid dynamics and results obtained using computational fluid dynamics approaches can be compared with results of thermodynamics based modeling and simulation technologies discussed below.

Simulation Based on Thermodynamic Models

Early engine simulation work using thermodynamics models was based on the FORTRAN programming language. A considerable effort has been expended in the development and validation of FORTRAN subroutines to support engine simulation and development. As a result of this effort, a great deal of legacy computer code based on FORTRAN is still in use. The DYNAGEN program is a well known early example of the use of FORTRAN simulation code for both transient and steady-state performance analysis of turbojet and turbofan engines [Sellers75]. Other simulation codes based on conventional programming languages have been produced and are commonly available. Jack Mattingly has included simulation programs used for turbine engine design and coded in QuickBASIC with several text books [Mattingly87, Mattingly95, Mattingly02].

Aircraft engine original equipment manufacturers typically provide detailed thermodynamic performance simulation programs in support of their own product development efforts. These simulation programs are typically run in a batch processing mode with an input file formed to define the parameters of the simulation and results produced in an output file that must be analyzed by engine design engineers, analysts, and control system developers. These simulations are typically very specialized, difficult to use and can not be extended to other engine models. Such simulation codes provided as customer decks to engine customers have been used as a baseline of engine performance for research in engine control technology [Lamber91, Simon03]. Differences among engine manufacturers in the production of customer decks for engine model simulation and the text based, batch processing approach used requires a significant continuing effort for customer and partner use of these programs in the research and development of engine control systems.

Researchers have realized the need for general purpose, generic codes for thermal analysis and simulation of turbine engine performance. This study is necessary for steady-state operating conditions at the engine design point, steady-state off-design analysis and also for transient analysis of engines. Kong, et. al. present a brief survey of simulation technology efforts [Kong03]. The GASCAN code developed by El-Masri facilitates thermodynamic performance simulation using a dimensionless formulation [Kong03, Masri88]. The GETRAN simulation code provides generic simulation capabilities for analyzing dynamic behavior of gas turbine engines.

In the mid to late 1980s the use of an object oriented approach to software development emerged as a way to reduce the effort required to develop new software. Object oriented software development methodology is based on three primary concepts: encapsulation, inheritance, and polymorphism. In an object oriented approach to software development, software objects are coded in a modular way such that the details (properties and methods of the object) required to use each module are encapsulated within the module. Objects are also structured in a hierarchy so that specific objects can inherit properties and methods for interrelating with other objects from their more general parent objects. For example one could consider an object called *EnginePart* which contains properties like *Name* and *LastMaintenanceAction.* Having defined the *EnginePart* class one could then create objects such as *Fan*, *Compressor*, and *HPTurbine* that

inherit the common structure of each part from their parent class, *EnginePart*, and refine the behavior of *EnginePart* in a way that is specific to the component. Polymorphism is a concept in object oriented programming that provides a way for objects to inherit common methods for dealing with other objects from their parent and yet refine the behavior so that it is specific to the new object. To illustrate this consider the example above. We may define a general method called *SelfTest* that is associated with the *EnginePart* class and refine the specific behavior of the method for each member of the class.

The main objective of object oriented programming is to decompose the software development task in such a way that the common structure that exists between software components can be defined and maintained in a single place and reused rather than repeatedly rewritten in each context where it is needed. This approach, if applied correctly, greatly reduces software development cost, time and effort. The development of object oriented programming methodologies is important in the history of simulation and modeling for turbine engines.

In his master's thesis, John Reed developed an interactive graphical propulsion system simulation based on object orient design techniques [Reed93]. This simulation was developed using the Java programming language standardize by Sun Microsystems Inc. The vision of Sun Microsystems founders was to provide Java as a programming environment that is portable across platforms. Reed later converted the Java simulator program into a Java applet that could be served across the internet as a turbine engine design and analysis tool [Reed97]. The Java Gas Turbine Simulator is currently available on the web. Reed, Follen, and Afjeh, describe the use of the world-wide-web for collaborative design of aircraft engines in [Reed00].

The Gas turbine Simulation Program (GSP) developed and used by the National Aerospace Laboratory in the Netherlands is an example of on object oriented approach to turbine engine modeling and simulation. GSP provides for both transient and steady-state analysis of engine models and features component based models. GSP can be used for both design point analysis and off design analysis of turbine engines. Visser and Broomhead describe GSP modules that are structured into a class hierarchy based on both control components and gas path components. The object oriented approach is also used in developing engine simulations and in the user interface [GSP01].

The Matlab and SIMULINK products sold by MathWorks Inc. have been used extensively in the development of turbine engine simulation models. The original version of Matlab was developed by Cleve Moler during his tenure at the University of New Mexico to assist students in their understanding of linear algebra and matrix computations. Cleve Moler and John Little formed MathWorks Inc. in 1983 to market and further develop a professional version of Matlab [MatFaq]. In the early 1990's MathWorks introduced the Simulink product built as a graphical user interface built on top of the existing Matlab product. The company has continued to develop the Matlab and Simulink products as well as extensions through add-on toolboxes and blocksets. Current versions of Matlab and Simulink include limited support for object oriented software development principles. Matlab provides supports for structured arrays of abstract object types and operator overloading. Simulink features allow the user to create libraries of reusable block objects that can be interconnected and incorporated into simulation models. Models can be built up in a hierarchical structure so that implementation details of subsystems

can be encapsulated. It is possible to “drill down” into subsystems in order to see increasing levels of model detail.

Many examples of the use of Matlab and Simulink for turbine engine modeling exist in the literature. Bettrocchi, et. al. use Simulink to model the dynamics of a Single-Shaft industrial gas turbine engine [Bett96]. Crosa, et. al. use Simulink to model a heavy duty gas turbine plant [Crosa98]. Kong, Roh and Lim describe the development of a Simulink model for a Pratt and Whitney PT6A-6s turboprop engine [Kong03]. Their model is a component level model of the engine with subsystems defined for the intake, compressor, burner, compressor turbine, power turbine, and nozzle. Design point calculations, steady-state installed and uninstalled results were verified using a GASTURB model and acceptable modeling errors observed. The authors also compare Simulink results with FORTRAN simulations of the engine for part load performance and transient state performance analysis.

Object oriented software design technologies have lead to the development of standards for distributive computing environments. The Common Object Request Broker Architecture (CORBA) developed by the Object Modeling Group (OMG) is one implementation of this idea. Distributive Common Object Model developed by Microsoft Inc. is a second example. These technologies have a direct bearing on the future development of advanced turbine engine and engine control technology because the industry involves, by its very nature, a large distributive collaborative effort. CORBA and DCOM are enabling technologies for the development of secure collaborative development environments.

Object oriented program design technologies and the use of distributed computing environments have been used by researchers in turbine engine design and control at the NASA Glenn Research Center (GRC). GRC researchers are developing the Numerical Propulsion System Simulation (NPSS) program in an effort to support the development of turbine engine system and engine control systems. NPSS provides a slightly different, more extended approach to the development of simulations. The zooming capabilities that are inherent in the Simulink environment have been extended through the use of CORBA to provide simulation capabilities that can vary in modeling fidelity based on the particular needs of the simulation customer. NPSS loosely couples the thermodynamic simulation capabilities that have emerged in Matlab and Simulink with other 3-D simulation and modeling tools to add for example, computational fluid dynamic studies in support of dynamic system simulations [Ashleman98, Evans98, Foollen99].

The thesis work done by van Oosterhout at Delft Technical University in 1996 describes a generic real-time thermodynamic turboshaft simulation model [Oost96]. This work was further developed at the National Aerospace Laboratory (NRL) in the Netherlands and is now a key component in their turbine engine simulation capability [TERTS02]. The Turbine Engine Real-Time Simulator (TERTS) features a generic real-time simulation environment capable of component based thermodynamic engine model simulation. TERTS is developed using Simulink and Real-time Workshop for rapid prototyping of engine simulation and control code. Personnel at the National Simulation Laboratory at NRL use TERTS to perform real-time, pilot-in-the-loop simulations of engine and integrated controls system/airframe studies. The development of TERTS models is based on simulations completed using the NRL GSP engine modeling tool described above. Visser, Broomhead and van der Vorst present results of a real-time, twin spool,

afterburning turbofan engine with low bypass ratio, maximum thrust of 110 kN, and overall pressure ratio of approximately 25. The simulation includes separate models for Digital Electronic Engine Control (DEEC) that includes nozzle control and actuation, and afterburner fuel control. The model was validated against installed performance data at MIL power with errors within 5%. The real-time simulations were completed with integrated flight control and engine control with 10 ms time steps on a 4 processor Silicon Graphics Challenge L computer [TERTS02].

Recent efforts at the NASA Glenn Research Center in Cleveland OH has resulted in the development of the Modular Aero-Propulsion System Simulation (MAPPS) [MAPPS04]. MAPSS is a flexible turbofan engine simulation environment based on the use of Matlab and SIMULINK that provides a graphic simulation environment capable of being used for the development of advanced engine control systems. MAPSS can be used to do both steady-state and transient analysis of a generic, high-pressure ratio, dual spool, low bypass variable cycle turbofan engine. Development of the MAPSS system is described in [Parker03].

The MAPSS system is a multi-rate system simulation that integrates both engine control and a physics based engine model. MAPSS was developed using existing FORTRAN code developed at NASA Glenn Research Center. Curry and Behbahani have used MAPSS as a starting point in conjunction with the Real-Time Workshop software product from Mathworks, Inc. to produce a high fidelity, real-time system simulation running on dSPACE using state-of-the-art software and hardware from dSPACE Inc [Curry04]. Developed in the Intelligent Control Facility (ICF) in the Propulsion directorate at Wright Patterson Air Force Base, the real-time system simulation provides a more realistic approach to real time control system development.

Curry and Behbahani partitioned the MAPSS simulation into engine and controller subsystems each running on a separate embedded dSPACE processors. The Rapid Control Prototyping (RCP) processor executes control system functions. The Hardware-In-the-Loop (HIL) processor executes the engine model. A realistic control environment is achieved by including physical sensors and actuators with-in the hardware. Curry and Behbahani compared results of the real-time implementation with the original MAPSS model and found average percentage errors for key engine states less than 1 percent [Curry04].

The establishment of realistic real-time simulation development using rapid prototyping tools as a means for study of turbine engine system and control system integration is an important step toward the goal of improving both engine technology and technology for integrated control and health monitoring systems. The development of engine control technology in the past has been conservative and based on rigid simulation models. Validation of control systems technology in the past using either fixed engines operating in a test stand or in-flight testing has been extremely expensive, time consuming and at substantial risk to original equipment manufacturers.

The facilities available to Air Force Research Laboratory (AFRL) researchers within the ICF provide a platform for research and development in engine control and health management systems that is much more realistic than prior development environments based solely on simulation and at a substantially lower cost. Rapid prototyping technology using object oriented software approaches enables much faster technology conception, development, test and evaluate

cycles. Detailed physics based engine models composed of reusable components enable the development of control and engine health management systems that achieve higher engine performance while maintaining safe, environmentally sound engine operation. In the following section we describe recent achievements at the ICF in the Air Force Propulsion Directorate.

3. Air Force Turbine Engine, Control System, and Health Management Simulation

The Intelligent Control Facility (ICF) within the Air Force Research Laboratory Propulsion Directorate at Wright Patterson Air Force Base is a state of the art facility for the study of modern turbine engine design and the development of advanced turbine engine control concepts through real-time simulation. The ICF provides an in-house capability for the independent evaluation, verification, and integration of advanced turbine engine control system concepts into turbine engine systems. The combination of both reconfigurable hardware and reusable software simulation components available to researchers enables rapid prototyping of systems at a substantially reduced cost when compared to previously used development methods. The facilities include 1) generic engine models and engine component library, 2) Generic control system models and control system component library, 3) dSPACE real-time processors and associated analog and digital I/O and communication buses, 4) Simulation development workstations and support software, 5) An intranet interconnecting ICF laboratory computers and other computing facilities in other development laboratories. Each of these items is described in more detail below.

Generic Engine Model Components

The generic engine simulation model developed under contract for the Air Force Research Laboratory is a high fidelity, physics based, modular, non-augmented, twin-spool, turbofan engine model developed using Simulink. Requirements for the model include the ability to perform real time engine simulation for an aircraft propulsion system operating over the entire flight envelope, accurate steady state behavior specifically at the design point but also for off design point operation, and credible transient behavior [Mink04]. The modularity built into the engine and control model design enables the engine to be customized to accurately model other turbofan engines. To the extent possible with Matlab/Simulink, object oriented design techniques have been used to develop the generic engine model. A brief description of the engine components and simulation design is presented below.

The generic engine model is constructed by interconnecting component models based on thermodynamic flow continuity through the engine. Top level engine component models in a design library include general modeling blocks for modeling the thermodynamic and mechanical behavior of inlet, compressor, combustor, turbine, mixer, nozzle, shaft and cooling subsystems. Subsystems are instantiated where necessary for modeling related components in the engine and inherit top-level design properties from these parent objects. Instances of the objects can be customized through parameter specification in the underlying Matlab workspace and addition of subsystem models where necessary using the Simulink development interface.

The primary input functions for the engine model are related to the operating environment (ambient pressure and temperature based on altitude and the standard atmospheric model and Mach number) and fuel mass flow derived from the engine control system. Component models derived from the compressor base component include fan hub, fan tip, high pressure compressor, and low pressure compressor. Turbine derived components include the high pressure and low pressure turbines. Fan and core shafts are derived from the base shaft model. The generic engine model contains single inlet, by pass flow, combustor, mixer and nozzle subsystem blocks. High and low pressure turbine and combustor cooling blocks are included. In addition, the generic model is capable of modeling the operation of variable inlet guide vane angles and compressor variable stator guide vane angles. For all engine component blocks, the primary interface between blocks consists of downstream demanded thermodynamic flow properties including temperature, pressures, mass flow, and fuel-air ratio as block input signals and subsystem thermodynamic flow properties on the component downstream side as block outputs. Specific additional block input and output signals are added where required.

The structure of the engine model takes advantage of the hierarchical modeling capability in Simulink. The high power turbine contains, among others, a block for turbine thermodynamic calculations, which in turn contains a subsystem for table lookups and a further hierarchical level for a temperature ratio calculation. Customization of these components is accomplished by relating them back to variables within the Matlab workspace. Thus, model variations are easily investigated by modifying the underlying workspace variables. This modeling framework also allows researchers to alter engine behavior during a simulation run so that advanced control and engine health management systems can be evaluated.

Generic Engine Control System Model Components

Two turbine engine controller models currently exist in the ICF. The simplified controller receives engine feedback signals that sense the operating speeds of both engine spools, N1 and N2 for the fan and core speeds, respectively, exit temperarture, T2 and pressure, P2 from the engine inlet, inter turbine temperature, T45 from between the high and low pressure turbines, and the pilot controlled position of the power lever angle, PLA. The controller calculates a set-point for N1 using T2, P2, and PLA and a proportional plus integral control to calculate required fuel flow. Embedded control logic within the controller prevents fuel flow rates that cause excessive T45 in the engine.

A more advanced propulsion control system model for the generic engine has been developed recently [Mink04]. This digital electronic engine control (DEEC) model uses more extensive sensor feedback from the engine and is capable of producing control signals for inlet guide vane angles, compressor stator vane angles, main burner and augmenter fuel flows. The DEEC model is derived from the MAPSS propulsion control system model and exceeds the capabilities of the generic engine model. Additional propulsion control system components that have been developed include engine sensor and signal conditioning, actuator dynamics, and a preliminary engine health management system for engine trending.

The Simulink model blocks that comprise the propulsion control and health management functions are decoupled from the generic engine model but feature a similar object oriented structure. As a result, control system components can be modified, developed and tested independently from the engine model. The currently available engine control system modes demonstrate the utility of rapid prototyping of performance enhancing, life extending and active engine control concepts. The graphic modeling language approach is easily understood and modified by control system researchers. These are important considerations for the development and study of advanced engine control concepts.

Real-Time Simulation Processors

The generic engine and control system models described above are decomposed into two independent models for simulation of the engine model and control system model each on dedicated real-time processors available in the ICF. Both real time processing units were developed for engine control research by dSPACE Inc [dSPACE02]. Both units communicate via serial port connection to individual workstations used for off-line model development. The Real-time Control Processor (RCP) runs engine control system models in real-time and the Hardware-In-the-Loop processor executes the engine model. The RCP and HIL processor units combine analog and digital sensing and control circuitry to accurately model real-time interfaces with engine thermocouples, strain gages, torque motors, linear variable differential transformers (LVDT), Resistor Temperature Devices (RTD) and speed sensors. The RCP and HIL processor units feature front panel interfaces for direct connection to one another during integrated propulsion system simulations. Technical specification summaries for the RCP and HIL processors are provided in the following paragraphs.

The RCP features a dSPACE 480 MHz power pc processor board. The board is capable of communication with a host workstation during the model build process and during real time simulation execution. The processor board communicates with additional interface cards at 20 megabytes/second. Other interface boards included in the RCP include 32 channel multiplexed analog to digital converter (ADC) programmable for 4-16 bit resolution, 32 channel digital to analog convert (DAC) at 14 bits resolution, and 96 bi-directional discrete I/O lines. Signal condition hardware is provided for driving 10 torque motors, 10 LVDT and other sensor signal conditioning hardware. The HIL also uses a power pc processing board and has similar analog and digital I/O capabilities. The HIL processor executes the engine simulation. It is controlled by analog actuation signals provided by the RCP and provides simulated sensor feedback to the RCP through front panel interface cables during real-time simulations.

Custom Simulink block libraries for both RCP and HIL signal interfaces are provided in the development environment to facilitate the development of real-time simulation code. The HIL library contains simulated strain gauge, RTD, LVDT, thermocouples, wheel speed, and a torque motor input block. The RCP library contains input blocks for reading thermocouple, strain gauge, speed sensor, RTD, and LVDT signals as well as an output block for producing torque motor drive signals.

Computing Infrastructure

Workstations exist within the ICF for Matlab/Simulink model development and interfacing to the real-time hardware. Control Desk software from dSPACE is used to display engine and control system parameters in real-time on an integrated display system as simulations proceed. The NASA MAPSS propulsion system, NPSS modeling system, and other engine modeling simulation software is also available to support propulsion system, engine control and health monitoring system development. An intranet exists to connect the ICF real-time environment with other test facilities in the AFRL Propulsion Directorate so that tests performed in other facilities can be integrated into ICF driven propulsion system simulations.

Role of the ICF in VAATE Program Development

The current developments in the Intelligent Control Facility relate directly to the VAATE durability goals as follows. First, the ICF serves as a platform for high speed, detailed modeling of high cycle fatigue concepts and can be used in the development of the HCF protocol. Through the development of detailed engine system models one might easily investigate the sensitivity of engine performance to changes in hundreds of engine system and control system design parameters and use this analysis as a basis for the study of engine robustness with respect to disturbances due to modeling errors as well as uncontrollable environmental factors. The flexibility for integrated real time software modeling and hardware testing built into the ICF makes it uniquely suitable for independent testing of component technology and the validation of design methods.

The intelligent engine focus area serves as a means for the accomplishment of many of the technologies and goals for the VAATE program. Factors in the intelligent engine include adaptive component performance, integrated propulsion and power, real-time life tracking, and proactive health management. The concept of adaptive component performance is that individual engine components should be aware of changes in their own performance characteristics and of changes in other interrelated components. The engine should be capable of continuous improvement and optimization of performance both locally at the component level and globally at the system level during the life of the engine. The monitoring of component performance is very closely related to real-time life tracking. Current component life models are based on the concept of an assumed standard mission. Individual aircraft engine stresses may vary widely from this standard due to variations in mission, operating environment, and the specific pilot operating the aircraft. A life model that is based on continuous monitoring of the operational history of an aircraft is demanding in terms of the required data analysis and reduction but could reduce maintenance cost by avoiding unnecessary maintenance actions that have been scheduled conservatively in the past in order to reduce the risk of catastrophic system failure. A proactive engine system will be able to detect small changes in performance and adjust operational parameters for extending component life in a way that is not detectable by the pilot and such that survivability constraints are not violated. If realized, this capability satisfies VAATE goals for proactive health management.

Four key elements in Engine Health Management (EHM) have been identified. Of these four elements, maintenance process control and diagnostics are involved in the reduction of maintenance effort. Prognostics and active control are involved in the reduction of unscheduled removals. Key definitions for these four elements are as follows. Maintenance process control consists of the optimization of the maintenance process through information management. Maintenance process control includes the use of data mining and integration techniques, autonomous logistics and training, large scale data warehousing with continuous contributions from every engine. Diagnostics capability that will be embedded within the engine includes the ability to detect crack and structural fatigue, advanced vibration diagnostic techniques, oil condition monitoring, temperature and emissions monitoring, bearing health monitoring and advanced inspection capability. Engine prognostics capabilities are targeted for advanced mission analysis and will include comprehensive engine trending, physics based component life models, information fusion, knowledge modeling and advanced reasoning. The controls element in engine health management features active and adaptive component control using nonlinear model based control methods. Control systems will use electric actuation, high temperature power conversion and will be capable of continuous life tracking. A certain degree of commonality exists between three of the four EHM elements. The diagnostics element relates to state awareness and life usage. The prognostic element deals with the prediction of remaining life and methods for extending component life and active control of engine components provides the means for accomplishing these tasks.

There are three technical challenges that must be overcome in order to address the objectives of improved average time on wing and reduce maintenance man hours per maintenance action. First it is challenging to monitor health and life of engine components due to uncertainty in their operating conditions. To overcome this challenge, program architects propose developments in robust and virtual sensors, and embedded lifing models. It is implied through earlier concepts that these technologies be adaptive. The second challenge is that it is difficult to prevent operating exceedences due to current direct control limitations. The proposed approach to this challenge includes the use of condition based performance through active control, learning algorithms, data trending, fusion and reasoning. The third challenge is that it is difficult to proactively manage health on-line due to poor information gathering, distribution and interpretation. To address these concerns, VAATE architects have proposed the use of engine level information fusion, and model based diagnostics.

Summer Research Program Accomplishments

Previous sections of this report have surveyed briefly the history of the use of computer simulation in the design and performance prediction of turbine engines. Objectives of current engine development programs provide the setting and motivation for engine, control system, and engine health management system study. The Intelligent Control Facility capability has also been described briefly. As a part of the summer research program I was able to review past work and accomplishments in turbine engine control and health monitoring research conducted by members of the controls and health monitoring branch. I also had the opportunity to participate in the planning of future research efforts. In this section I describe how current software

methods were used in the study of engine simulation technology and describe accomplishments resulting from these efforts.

The summer research efforts focused on the modeling of twin spool low bypass ratio augmented turbofan engines. The GE F110 and Pratt & Whitney F100 engines were selected for study and customer cycle decks that model steady state engine behavior were used as a baseline for the study of the operation of these engines. The cycle decks are based on FORTRAN code produced by OEM analysis groups for modeling the thermodynamic cycle associated with the operation of these engines. These programs accept as input, a text file containing parameters that describe the ambient inlet and exhaust conditions and operating constraints for installed and/or uninstalled engines. They produce an output text file that contains engine variable/value pairs describing engine steady state behavior for the corresponding input case. In order to use these programs I created text file processing scripts capable of producing the input case files in the required format and scripts capable of extracting variables from output files and importing these into a Matlab workspace for further analysis.

Low pressure and high pressure compressor maps containing data sampled from engine cycle deck models were used to model these components. Further processing was required to create the data structures required for this study and the following approach to modeling high pressure compressor map data was taken. Data points containing pressure ratio, corrected mass flow, efficiency and corrected speed were fitted to polynomial functions representing the speed lines of the compressor map. These speed lines were then re-sampled at equally spaced points along the speed line to create grid points used in the models. The stall line and primary operating line as well as other run lines for off design operation were identified from this data. Further processing scripts were developed to format the data for use with both Simulink engine component models and NPSS component models.

The generic engine model described in previous sections of this report consists of a library of engine components that include inlet, compressor, bypass duct, combustor, mixer and nozzle as well as associated pumps, valves actuators and engine sensors. The primary engine components modify the thermodynamic properties of air (and fuel where appropriate) between component input streams and output streams. Demanded flow required from down stream components is fed back to prior engine components in order to establish a continuity of flow between the various engine stages. The generic engine model does not contain an after burner or provisions for variable area nozzle as is present in the F100 and F110 engines. The generic model also contains separate subsystems for fan hub and fan tip flows which are create the core and bypass flow streams, respectively. Because of the nature of the map data available for modeling the fan, it was necessary to combine these two subsystems into a single fan subsystem and then create a splitter subsystem on the output side of the fan to split core and bypass flows for the F100 and F110 engines. In order to understand the operation of each of the engine components, I created a series of Simulink models that consisted only of the individual component and constant block representing input parameters for the subsystems. I also created separate Simulink models for the combinations of core (high speed shaft), inlet-fan-high pressure compressor, and low pressure turbine, afterburner and nozzle to understand interactions between these separate groups of subsystems. Most of the work required to model new engines is performed by tuning Matlab workspace variables that are used in the engine component models.

In order to further compare the results of simulations I also created a similar set of component models using the NPSS system for engine models. The basis of this work was a single NPSS model for the F110 engine produced by George Mink of Scientific Monitoring Incorporated (SMI). Data structures embedded within the NPSS model were modified based on engine data supplied by AFRL and simulation data obtained from the engine customer decks. The primary engine components from the original engine model were split out into self contained NPSS component models with configurable component inlet conditions and parameters so that these NPSS component models could be compared with the Simulink component models. The NPSS reporting system for these models was also configured to produce variable names and values in a format that could easily be compared with output from the OEM customer decks.

Due to time constraints imposed by the summer research program, this work is not yet complete. However, key steps have been taken to establish agreement of simulations based on three separate simulation technologies: the existing customer deck simulation that has been traditionally used by engine manufacturers and their customers, object oriented simulation techniques available in newer NPSS based approaches, and the object oriented and graphical simulation capability provided by Simulink and Matlab based approaches. Completion of this work is a key for the study of advanced engine controls and health monitoring system design in a real-time simulation environment. Progress toward the goals established during the summer research assignment is on-going.

4. Turbine Engine Simulation Research Directions

In this section research directions in turbine control and engine health management that can be pursued as an immediate consequence of prior work and infrastructure development in the Air Force Propulsion Directorate Intelligent Control Facility at Wright Patterson Air Force Base are discussed. The ICF is a unique facility within the Air Force. The facility infrastructure has been specifically designed for supporting mixed hardware, software, and integrated systems development and testing. The flexibility of the ICF is a starting point for software algorithm development, real-time studies and hardware-in-the loop testing. By using the modeling and analysis capabilities within the laboratory, researchers can investigate and characterize current and planned prototypes for control system algorithms, actuators, sensors, and FADEC hardware. Simulated engine system tests can be performed safely at the systems level without the time and expense needed to assemble actual test cells and demonstrator engines.

The generic engine model that has been developed and described in this paper is comprehensive and its flexible structure facilitates reuse in the development of models for existing and future turbine engine technology. There are several areas where continuing development is needed and development in these areas is in progress. The generic engine control system and engine model do not fully implement the control of variable inlet guide vane angles or compressor stator vane angles. Addition of these controlled variables will enable more realistic simulation of actual engine. Progress toward the modeling of afterburning engines has been noted but further development, testing and validation is required. Addition of the afterburner and associated control systems is an important step toward the development of more versatile and realistic

turbofan engine models. Completion of the work to map the engine model to specific engines that has been begun during the summer research program needs to be completed and a procedure for repeating this for other specific engine types established so that the Simulink engine model can be fully utilized for further control system and health management system research and development. By accomplishing this mapping task and validating engine models against OEM customer decks provided for specific engines we will be able to demonstrate the approach and prove rapid prototyping concepts that underlie the research approach. This also provides a basis for the study of engine design optimization and what-if analysis to support decisions for future engine designs at a cost that is significantly lower than that used currently in the design process.

The intelligent engine concept envisioned for VAATE engine development programs is expected to provide a means for achieving desired increases in the mean time between unscheduled engine removal and reduction in the number of man-hours per maintenance action. Key elements of the intelligent engine include active component control for engine components, inclusion of a real-time engine health manager in the control loop and auto adaptive control capable of optimizing engine performance in the presence of uncertainties. Research in areas that support the concept of the intelligent engine will result in improved prognostic and diagnostic capabilities within the propulsion system. Research in support of the intelligent engine depends on advances in model based non-linear control system design, real-time performance and life management and engine information fusion and understanding.

Continuing control system model development is also needed and even though the generic control system model is comprehensive there are several areas where additional detail will provide better insight into the improvement of engine performance. Current FADEC systems incorporate a limited amount of airframe data in the control loop. This is not currently supported in the generic engine control system and developments in this area are needed. Current FADECs also provide control logic that sets engine operational limits based on sensor feedback to avoid operation of the engine that would be damaging or limit the life of the engine. The generic engine model above includes some of this logic that is independent of engine types. However, additional work is needed to increase the level of modeling detail for specific engines.

A universal FADEC capable of easy and possibly automatic adaptation for a wide range of engines and operating conditions is an ultimate goal for engine control research. A universal FADEC may use predictive control techniques and thus may need to include an intelligent or adaptive engine model within the control system. Control systems that include engine health information in the control loop and the ability to optimize engine performance relative to changing performance criteria are being studied in Air Force research programs.

The current propulsion system simulation models in the ICF contain four operator controlled inputs for adjusting the engine operating environment. These include specification of the operating pressure altitude from which ambient temperature and pressure are derived using a standard atmospheric model, the free stream mach number, and the power lever angle setting. For engine health management and life studies we would like to be able to generate standard mission sorties which exercise propulsion system models in more realistic settings than are currently available. The incorporation of an airframe model in a system simulation provides an additional level of modeling detail to the ICF. Generation of aircraft motion including angle-of-

attack and side slip angle and their rates provides additional information to the FADEC from which to generate engine control sequences. A modular approach to airframe integration will also enable comparison between actual and simulated engine performance if mission data is available.

A number of state-of-the art research laboratories exist within the propulsion directorate for the purpose of facilitating the study and understanding of all facets of turbine engine operation, control, and performance over the life time of the engine. Examples include the Turbine Engine Fatigue Facility, laboratories for compressor and combustor study, bearings research facilities, and others. Modeling and simulation capabilities available in the ICF serve as an integrating function within the propulsion directorate. Research in collaboration and integration between the various laboratories involved in turbine engine propulsion are currently in progress.

5. Areas for Further Research and Development

Many opportunities exist for further research and development in the simulation of turbine engine and engine health management systems. Suggestions for some of these are offered in this section.

Collaboration tools and distributed simulation are used but many issues remain before wide spread use is possible. The turbine engine business remains very competitive. A considerable level of effort and commitment is required of the primary engine original equipment manufacturers. Incremental advances in engine design and control involve research and development that is proprietary. A means for collaboration among engine manufacturers in a way that protects the business share of each manufacturer may be required to foster the team environment that is required for additional engine technology improvements.

Currently existing simulation and modeling tools have maintained a separation between low dimensional analysis based on thermodynamic flows and higher dimensional results based on computational fluid dynamics. More effort is required to reconcile simulation data obtained through CFD simulations, the results of thermodynamic flow simulation studies, and data obtained through experimentation on physical engine components. The level of understanding that could be achieved through this integration of technologies may play a significant role in future development of engine and control technology.

Recent achievements in object oriented simulation technology and the exploitation of advances in readily available, low cost and high performance computing equipment have enabled recent advancements in turbine engine technology and control. New simulation tools should integrate the best features of existing software. Further developments in object oriented programming techniques in graphical simulation tools are needed. Newly developed tools should integrate additional discrete event system simulation techniques as well as hybrid system capabilities. Managing the integration of these additional technologies in a way that is easily understood and used by developers remains a challenge and will require cooperation between software engineering professionals and domain experts in engine technology.

The complexity that is involved in design and development tasks is ever increasing. More effective utilization of existing systems engineering technology and the development of new tools, possibly including simulation and process modeling, must be considered. Ways to design simulation experiments and to understand and interpret their results are needed. Very few of the tools considered in this study fully utilize integration standards based on, for example, XML. Since it is unlike that any one simulation tool will be able to deal with the complexity of turbine engine design and control technology, newly developed tools must keep integration standards in mind for interoperability among tools.

6. Conclusions

Turbine engine technology is pervasive through out the international civil and military aviation industry. Continuing improvements in engine technology, engine control technology and health management are required in order to achieve goals for improved performance, lower development and maintenance costs, and reduction of the impact of engine usage to the environment. In this paper we have outlined a brief history of the use of simulation as a research tool in engine technology research and development directed at achieving the goals stated above. Recent advances in embedded real-time system development, modeling technology and the ability to do rapid prototyping with the option to use hardware in the simulation loop have improved our ability to develop and evaluate advanced engine control and health management systems at substantially reduced cost and risk. We have discussed how this technology is being applied at the Intelligent Control Facility in support of the development of versatile and affordable engines with improved performance.

The ICF, state-of-the-art research facility that exists can be used for independent evaluation, validation and verification of vendor developed hardware and software to ensure that products developed meet performance specifications and to integration issues early in a development program so that they may be addressed in a cost effective manner. The research focus within the Air Force Propulsion Directorate has been described briefly and we have suggested areas where further research should be addressed. The development and application of advance simulation capabilities applied to turbine engine systems and control will lead to further improvements in engine performance and reduced impact on our environment.

7. Acknowledgments

I would like to sincerely thank staff members in the controls and health management branch, AFRL/PRTS for their assistance during the summer research program. Thanks to Dan Tasch for program guidance and encouragement, thanks to Ken Semega for numerous interesting discussions on diverse topics related to engine technology and health management, and thanks to Rick Wade for discussions and ideas related to sorte generation and mission analysis. Gary Smith’s willingness to share and quickly apply knowledge and experience related to engine diagnostics that has kept me on the road to (and from) engine control research and health management. A very special thanks to Al Behbahani for his research guidance, mentoring and efforts to provide this research opportunity for me. I’d also like to thank members of PRTA for

their assistance in engine modeling and Roger Rucker of UTC for his help in the transition to the Dayton area and contract support during the summer.

8. References

[Ashleman98] Ashleman, Russell H., Jr. “The National Cycle Program--A Flexible System Modeling Architecture for Aircraft Engine Simulation. AIAA Paper 98-3114, 1998.

[Balwin] M. G. Balwin, “A high fidelity real-time simulation of a small turboshaft engine,” NASA TM-1000991.

[Bett96] R. Bettocchi, P.R. Spinna, et. al., “Dynamic modeling of single shaft industrial gas turbine,” ASME 96-GT-332, 1996.

[Crosa98] G. Crosa, F. Pittaluga, et.al., “Heavy-duty gas turbine plant aerothermodynamic simulation using SIMULINK,” Transactions of the ASME, 1998.

[Cury04] T. Curry and A. Behbahani, “Propulsion Directorate/Control and Engine Health Management (CEHM): Real-Time Turbofan Engine Simulation,” IEEE AC paper #1291, January 2004.

[dSPACE02] “RCP and HIL System for Wright Patterson Air Force Base Dayton Ohio,” Technical Manual, dSPACE Incorporated, Novi, MI, 2002.

[Douglas86] L.E. Douglas, “Development of a generalized computer program for gas turbine performance simulation,” PhD Thesis, Cranfield University, UK, 1986.

[Evans98] Evans, A.L., et al.: Numerical Propulsion System Simulation's National Cycle Program. AIAA Paper 98-3113, 1998.

[Foollen99] Follen, G.J.; and auBuchon, M.: Numerical Zooming Between the NPSS Version 1 and a 1-Dimensional Meanline Design Analysis Code. ISABE 99-7196, Proceedings of the 14th International Symposium on Air Breathing Engines, 1999.

[French] M. W. French, “Development of a compact real-time turbofan engine dynamic simulation,” SAE Paper 821401.

[GSP01] W.P.J. Visser and M.J. Broomhead, “GSP, A generic object-oriented gas turbine engine simulation environment,” Technical Report NLR-TP-2000-267, National Aerospace Laboratory, NLR, Netherlands, www.nlr.nl, 2001.

[Kim99] S. Kim “Gas turbine dynamic simulation using SIMULINK,” MSc Thesis, SME, Cranfield University, 1999.

[Kong00] C. Kong, J. Ki, et.al. “Propulsion system integration of turboprop aircraft for basic trainer,” ASME 00-GT-100, 2000.

[Kong01] C. Kong, J. Ki, et.al. “Performance simulation of turboprop engine for basic trainer,” ASME Turbo Expo 2001, ASME 01-GT-391.

[Kong03] C. Kong, H. Roh, and K. Lim, “Steady-state and transient simulation of turboprop engine using SIMULINK model,” Proceedings of the ASME Turbo Expo 2003 Power for Land, Sea, and Air, June 16-19, 2003 Atlanta GA, pp. 151-161, GT2003-381881.

[Kurzke98] J. Kurzke, “GASTURB Program Manual Version 8.0, 1998.

[Lambert91] H. H. Lambert, “A Simulation Study of Turbofan Engine Deterioration Estimation Using Kalman Filtering Techniques,” NASA Technical Memorandum 104233, June 1991.

[MAPSS04] K.I. Parker and K. J. Melcher, “The modular aero-propulsion system simulation (MAPSS) users’ guide,” NASA technical report TM-2004-212968, March 2004.

[Masri88] M.A. El-Masri, “GASCAN-An interactive code for thermal analysis of gas turbine systems,” Journal of Engineering for Gas Turbines and Power, Vol. 110, pp. 201-209, April 1988.

[MatFaq] Matlab Frequently Asked Questions at the University of Texas-Austin. http://www.utexas.edu/math/Matlab/Manual/faq.html

[Mattingly87] J. D. Mattingly, W. H. Heiser, D. H. Daley, “Aircraft Engine Design,” AIAA Education Series, AIAA, New York, 1987.

[Mattingly95] J. D. Mattingly, “Elements of Gas Turbine Propulsion,” McGraw Hill, 1995.

[Mattingly02] J. D. Mattingly, “Aircraft Engine Design,” 2nd Ed., AIAA Education Series, AIAA, New York, 2002.

[Mink04] G. Mink, “ICF Generic Engine Model Documentation,” Version 3.0.0, Scientific Monitoring Incorporation, June 2004.

[Oost96] W.W.P.J. van Oosterhout, “Development of the generic thermodynamic turboshaft engine real-time simulation (TERTS) model,” Delft Technical University, Faculty of Aerospace, thesis report, Delft 1996.

[Ouzts93] Ouzts, P.J.; Lorenzo, C.F.; and Merrill, W.C.: Screening Studies of Advanced Control Concepts for Airbreathing Engines. NASA TM-106042, 1993.

[Parker03] K.I Parker and T. H. Guo, “Development of a turbofan engine simulation in a graphical simulation environment,” NASA TM-2003-212543, August 2003.

[Reed93] J. A. Reed, “Development of an Interactive Graphical Aircraft Propulsion System Simulator,” MS Thesis, The University of Toledo, Toledo OH.

[Reed97] J. A. Reed, and A. A. Afjeh, “A Java-based Interactive Graphical Gas Turbine Propulsion System Simulator,” AIAA Paper No. 97-0233, 1997.

[Reed98] J. A. Reed, “Onyx: An object oriented framework for computational simulation of gas turbine systems,” PhD Dissertation, University of Toledo, Toledo OH, 1998.

[Reed00] J. A. Reed, G. J. Follen, and A. Afjeh, “Improving the Aircraft Design Process Using Web-Based Modeling and Simulation,” ACM Transactions on Modeling and Computer Simulation, Vol 10, No. 1, January 2000, pp. 58-83.

[Schobeiri94] M.T. Schobeiri, M. Attia and C. Lippke, “GETRAN: A generic modularly, structured computer code for simulation of dynamic behavior of aero and power generation gas turbine engines,” Journal of Engineering for Gas Turbines and Power, Vol. 116, pp. 483-494, July 1994.

[Sellers75] J. F. Sellers and C.J. Daniele, “DYNAGEN-A program for calculating steady-state and transient performance of turbojet and turbofan engines,” NASA TN 0-7901, 1975.

[Simon03] D. Simon and D. L. Simon, “Kalman Filtering with Inequality Constraints for Turbofan Engine Health Estimation,” NASA Technical Memorandum, TM-2003- 212111, February 2003.

[Southwick95] Southwick, R.D., et al.: High Stability Engine Control (HISTEC) Phase I: Algorithm Development, Volume I: Final Report and Appendix A. NASA CR-198399, 1995.

[TERTS02] W.P.J. Visser and M.J. Broomhead, and J. van der Vorst, “TERTS A generic real-time gas turbine simulation environment,”Technical Report NLR-TP-2002-069, National Aerospace Laboratory, NLR, Netherlands, www.nlr.nl, 2002.

[Visser04] W. Visser, M. Oostveen, and O. Kogenhop, “A generic approach for gas turbine adaptive modeling,” Proceedings of the ASME Turbo Expo June 14-17, 2004, ASME GT2004-53721.

ELECTRIC-PRESSURE-INITIATED INSTABILITIES IN PREMIXED PROPANE-AIR FLAMES

S. D. Marcum & D. L. Wisman
Department of Physics, Miami University
Oxford, OH 45056

Abstract

The effects of closely-coupled DC electric fields on the reaction zones of pre-mixed propane-air flames have been investigated using several types of experimental measurements. Experiments designed to characterize the electric-pressure-induced modifications of the geometry and of the reaction zone and the stability of the resulting turbulized flame are reported. The former is quantified by combustion intensity enhancement measurements derived from high-speed two-dimensional imaging. Such images also clearly depict highly unstable combustion arising from the electric pressure effect, and Fourier transforms of oscillatory current and flame-front optical signals are used to quantify observed self-excited oscillatory combustion modes. Results using the range of equivalence ratios between 0.8 - 1.3, flow velocities up to 1.7 m/s, and applied potentials up to 5 kV (40-mm gap) are presented and discussed. At bias voltages above 2 kV, improved electrical coupling to the flame is shown to drive a stable conical flame front (laminar flow) into first a wrinkled laminar flamelet (cellular) geometry, and further toward either a distributed flamelet regime or a collective large-amplitude oscillation of the flame front. The flame fluid mechanical response to the applied field brought about by forcing positive flame ions counter to the flow and the resulting electric pressure decreases Lewis numbers of the ionic species and drives the effective flame Lewis number below unity, even near stoichiometric conditions. This effect is a potentially attractive means of controlling flame fluid mechanical characteristics and validating combustion instability models. Various electrical measurements are also described which establish that minimal input electrical power is required to produce the observed flame instabilities (~ 1 W for a 1 kW burner).

Introduction

A rather large amount of work has been reported on the various effects of electric fields on a wide variety of flames[1-10]. However, the mechanism(s) responsible for the rather dramatic field-induced effects on the size and shape of the inner cone of some hydrocarbon flames is still not well understood. Bradley[1] provides a good overview of the subject, as well as a thorough review of the literature in this general area up to the date of that text's publication.

Electric-field-induced modifications of flame geometry have been known for some time, the first report being published by Chattock[2] in 1899. Since then, many aspects of the effects of externally applied fields on flames have been investigated. For example, increases in flame blowoff flow rates due to the application of external fields in both diffusion[3] and premixed[4] methane-air flames have been measured. Similar increases in flame stability have also been observed at fields sufficient to produce a corona discharge[5] within the flame. Improved heat transfer to solid surfaces[6] due to externally applied fields has been reported. Increased burning velocities for hydrocarbon flames in DC fields[7] and elevated electron temperatures for flames in microwave fields[8] have been similarly established. It has also been shown that soot formation in diffusion flames is diminished[9] by application of both DC and AC external fields. Flame extinction limits in pre-mixed flames are also perturbed[10] by DC fields. The most extensive efforts to construct and test theoretical models sufficient to predict the maximum practical

effects of electric fields on flames are contained in a series of publications by Lawton and Weinberg.[11-13] (The principal results of those models are summarized in Reference 1.) More recently, a reaction kinetics model[14] simulating the effects of electric fields in premixed methane flames has been published, and electric fields have been used to counterbalance natural convection and simulate microgravity[15] in small diffusion flames.

This work demonstrates that close coupling of the externally applied voltage to pre-mixed propane/air flames with the electric field directed generally counter to the flow, can produce significant flame front perturbations with relatively small ratios[8] of voltage to the electrode separation. The close coupling provides current densities comparable to those previously produced using applied voltages sufficient to produce near-breakdown[1,11-13] electric fields. All work reported here used applied voltages roughly an order of magnitude smaller (1 - 5 kV). Bulk flame current/voltage measurements were performed to measure improved coupling of the externally applied voltage to the flame. The nature and degree the dynamic response of the flame to the applied voltage is documented using high-speed two-dimensional imaging.

Together, the measurements reported here provide direct evidence of significant increases in flame speed and the combustion intensity (of the order of a factor of 2 and greater) when an externally applied voltage is effectively coupled to premixed propane air flames. Modest applied voltages are capable of driving the flame from laminar (stable, conical flame geometry) to a wrinkled laminar geometry (cellular; multiple laminar flamelets). Voltages between 2 – 5 kV produced higher intensity turbulence regimes, and for some combinations of flow velocity, equivalence ratio and applied voltage, a large-scale collective (audible) oscillation of the flame front.

In much of the previous work[1], the effects of DC electric fields on flames was described in terms of the body force known as the ionic wind, which has been shown to be capable of providing a maximum pressure difference across the flame[1,11-14] of only 0.0004 atm. The effects reported here differ sufficiently in magnitude that an alternative explanation of the observed effects must be considered. Under otherwise quiescent laminar flow conditions where Fick's law applies and strong temperature gradients give rise to significant thermal diffusion[16], imposition of a closely coupled external electric field on the flame gives rise to an additional *electric pressure* induced ionic molecular diffusion effect. The electric field acts directly on the highly localized [14,17], chemiionization-derived positive ions in the flame reaction zone, significantly increasing their mass diffusivities and thereby lowering the Lewis numbers of the ionic species. The observed result is a diffusive-thermal instability[18,19], typical of flames with global Lewis numbers less than one. The increased differential diffusional velocity of the reaction zone positive ions strongly affects the bulk flame speed[18,19], and the instability results in the flame front collapsing toward the burner head and taking on a wrinkled laminar geometry. Strikingly similar responses of flames to variations in ambient pressure[22] well above the maximum predicted for the ionic wind, suggested the term *electric pressure* would be an appropriate label for the observed effects. The strong wrinkling of the flame front and other indications of the onset of turbulence detailed below suggest that electrically stressed hydrocarbon flames can be quite sensitive to the *electric pressure* effect.

Experimental Apparatus and Procedures

The principal experimental flame diagnostics used to gauge the efficacy of externally applied voltage-to-flame coupling and quantify the degree and time scale associated with the flame dynamic response to a DC bias voltage are shown in Figure 1. The burner used was a commercial atomic absorption type (Perkin-Elmer) with a modified cylindrical (44-mm diameter x 50 mm) stainless steel head. The premixed gas inlet orifices consisted of five concentric rings of close spaced 0.8-mm diameter holes, the largest ring having a 17-mm diameter. The hollow, 25-mm diameter portion of the burner head is filled with multiple layers of fine mesh wire screen in series with the standard burner body to ensure

complete fuel/air mixing. The lower electrode was a patch of 100-mesh stainless steel wire cloth stretched across the inlet array. Both array/electrode arrangements produce axially symmetric flows, as evidenced by the highly symmetric conical laminar flame fronts produced at moderate flow speeds (< 2 m/s).

The dc current/voltage characteristics of the electrically stressed flames were recorded with the burner grounded and the upper electrode biased up to + 5 kV (Glassman, Model 6516A). Such measurements were used to quantify the voltage-to-flame coupling of the various electrode arrangements, and thus guide efforts to improve the coupling efficiency. The anode used for all work reported here was a perforated, stainless steel disk suspended 40-mm above the burner, and always above the tip of the unperturbed inner come. This version of upper electrode geometry provides a simple parallel-plate-like electrode geometry at the cost of perturbing the burnt gas flow field downstream of the flame front

The apparatus used to record high-speed (100 μs exposures) two-dimensional images of the flame's response to as functions of applied voltage, fuel-to-air ratio and flow rate is shown schematically in Figure 1. DC fields were applied to the flames through a 500 kΩ ballast resistance connected between the bias supply and the anode, and a 100 kΩ current sense resistor was placed between the floating burner and ground. The images used to document the flame's dynamic response to the DC bias were made using an intensified, gateable CCD camera (Princeton Instruments Model ICCD-576). Direct (broadband) images, and images produced by the major flame emitting species (chemiiexcited CH, OH and C2) were recorded with the aid of interference filters (10 nm bandpass).

Flame front motions were monitored by imaging the reaction zone onto the end of an optical fiber (0.5-mm diameter) using the simple single lens system shown. Either broadband, or spectrally filtered signals entering the fiber were detected using a photomultiplier tube (RCA 9265). Variations in light signals, as well as any fluctuations in the bias circuit current were digitized and processed using an oscilloscope (LeCroy Waverunner).

The fuel and air flow rates were set and monitored by simple ball-float type flow meters (rotameters, Cole Parmer) capable of flow rates up to 2.7 standard liters per min (slm) for propane, and up to 66 slm for air. Typical flow rates used for results reported here were between 5 and 25 slm for air, with the corresponding flow rates for propane varied to provide the desired equivalence ratio. For most data reported here, the flow velocity was approximately 1.7 m/s, and the range of equivalence ratios used during this study was between 0.8 and 1.3. The propane used was a standard commercial grade, and the air was supplied by a small, portable compressor.

Results and Discussion

Electrical Measurements

To enhance an electrically driven process it is advantageous to provide effective coupling of the power source to the load. Here, bulk circuit current/voltage (I/V) characteristics are the most straightforward electrical measurements that can be made to assess the efficacy of external bias voltage-to-flame coupling. I/V characteristics for a flame with total pre-mixed fuel/air flow rate of 21 slm (flow velocity = 1.7 m/s, and an equivalence ratio of 1.2, is shown in the upper plot of Figure 2. The points marked A, B and C refer to bias potentials near which major modifications of the reaction zone geometry occurred. Point A locates the potential needed to cause the inner cone to be reduced in height and be made even more stable than the low velocity laminar flow inlet stream allows. For the conditions used to produce the IV curve of Figure 2, the cold flow Reynolds number was near 2000. Point B indicates the potential needed to cause the inner cone to distort noticeably from cone shape and begin large amplitude (audible) oscillation. Point C denotes the potential that must be applied to depress the reaction zone close to the burner head and induce more random motion of the reaction sheet typical of strong turbulence.

Another significant feature of the IV characteristic is that there is no indication of reaching a saturation current up to the maximum applied potential of 5 kV. Also note that the maximum electrical power input is on the order of a few watts.

The effect of varying the fuel flow rate at a fixed air flow rate of 20 slm (essentially the same flow velocity of 1.7 m/s) and a fixed bias of 3 kV is shown in the bottom plot of Figure 2. The data shown essentially maps the combined variation in flame conductivity and coupling to the external circuit as a function of equivalence ratio. The peak power input occurs at an equivalence ratio slightly above 1.1. If the bias potential is reversed, the current drawn at a 3 kV bias is less than 10 μA indicating a diode like response of the flame to external bias. Points marked A, B and C here mark equivalence ratios for which the flame front is collapsed near the burner head, undergoing significant collective oscillation, and recovering from collapsed near the burner head, respectively.

Although the diode-like behavior has been noted previously[1,3,4], the magnitude of the current drawn with the disk anode is better than an order of magnitude higher than previously reported for electrically biased pre-mixed hydrocarbon flames. All results reported here are derived from experiments that use the grounded burner, disk anode (forward bias) arrangement. Another significant feature of the I/V curve of Figure 1 is that a only a small amount of electrical input power is required to produce the significant flame front modifications observed during this study. The largest current drawn under the conditions cited above is approximately 600 μA at 5 kV forward bias, or roughly 3 W of electrical input power applied to a burner that is generating heat at the rate in excess of 1 kW. Also of note is that although the general trend is towards some saturation current, saturation is not reached up to the maximum voltage (+5 kV).

High-Speed Two-Dimensional Imaging

The typical flame response to an applied electric field is shown in Figure 3. The total flow rate was once again 21 slm and the equivalence ratio used was 1.2. The effect of a bias potential of 5 kV is compared to the unperturbed laminar flame in each set of high-speed images shown in Figure 3. Figure 3a shows a direct image of the flame using an exposure time of 500 μs. That time exposure is sufficiently short to essentially freeze all motion of the turbulent flame front in the case of the field-perturbed flame. Adjacent to each photo is a set of intensity profiles that correspond to the emission intensity as a function of distance from the flame axis for the six horizontal bands marked in the corresponding image. The increase in combustion intensity is clearly indicated by comparison of the plots.

The following three sets of images and intensity plots, Figures 3b, 3c and 3d, correspond images taken through 10-nm bandpass filters that select for CH, C_2 and OH emissions respectively. The exposure times used for those images were 10 ms for each of the CH and C_2 image sets, and 20 ms for the OH images. Note that the flame front is sharply imaged in all cases (a-d) for the unbiased flame. However, the 10- and 20-ms exposure spectral images show increasing blurring due to the rapid turbulent motion of the cellular reaction sheet. The corresponding emission intensity profiles show that *all* major chemiluminescent flame emission have the same response to the applied field, i.e. they all indicate a strongly enhanced combustion intensity as the applied field induces a strong instability in the normally laminar flame front.

Although different in the details of flame front modifications, the images shown in Figure 3 are similar in magnitude to the collapse of the flame front in the well known singing flame[22]. Analogous to the singing flame's response to oscillating ambient pressure, the electric-field-driven positive ions highly localized[14,17] in the flame front are able to exert an effective dynamic pressure on the flame front, causing it to collapse inward toward the flame axis, the resulting channel rapidly closing as the flame propagates essentially radially inward. The pressure variation required to produce a singing flame response[22] is sufficiently in excess of the maximum pressure difference across the flame available from ionic wind effects (0.0004 atm)[1,11-14] that an alternative source is required. The effective dynamic pressure on the

flame front due to the closely coupled applied electric field is given the label *electric pressure.* In the experiments reported here, the effects of electric pressure on the flame front are clearly sufficient to seriously distort the flame front relative to that produced by the normal balance between concentration-driven, and thermally-driven diffusion (i.e. stable conical flame front and laminar flow driven to a wrinkled cellular geometry and increasingly turbulent flow by the applied field).

The pressure difference across a flame due to the ionic wind[1,11-14] has been shown to be proportional to the current density (j) through the flame, and to depend upon the mobilities of the charged flame species according to,

$$\Delta p \propto j\left(\frac{1}{\mu_+} - \frac{1}{\mu_-}\right),$$

where $\mu_{\pm}$ represent the mobilities of the respective charge carriers. Model assumptions include a minimum distance[1,11-13] between the flame and the cold biasing electrodes sufficient to eliminate quenching of the flame at their surfaces. Predictions of the maximum practical effects of the ionic wind include a maximum current density of 250 $\mu A/cm^2$ and a resulting maximum pressure change of 0.0004 atm, using an applied electric field of 30 kV/cm. In the experiments reported here, current densities of the order the maximum predicted for the ionic wind are achieved using substantially smaller fields. Additionally, the observed flame front modifications are in excess of the maxima predicted for the ionic wind effect. The close coupling of the field to the flame achieved here gives rise to the observed large response of the flame front (Figure 4), similar in magnitude to those observed for the singing flame[22], and in excess of those predicted for the ionic wind. This is not surprising since the close coupling of the electrodes to the flame violates the aforementioned quenching distance separation assumption of the ionic wind analysis. The electrical effects on flames reported here are ascribed to an *electric pressure* effect which is larger, and which requires a substantially smaller potential to implement, than the ionic wind.

The imaging results suggest that the effective fluid mechanical response of the flame is altered by the applied field, resulting in an increased flame speed. To achieve the conservatively estimated doubling of the flame speed shown in Figure 3 by preheating[16] the gas mixture would require a temperature increase of 150 K. Assuming a volume flow rate of 16 slm, effecting such a temperature change would require approximately 65 W of electrical power – greatly in excess of the maximum electrical power input of roughly 3 W shown by the I/V curve of Figure 2. By comparison with the preheating the gas mixture to increase flame speed, the electric-field-induced flame speed modifications observed here are better than a factor of 20 more energy efficient than preheating the gas.

Flame Oscillation Characterizations

The final data reported here are derived from measurements of the current and flame front optical signal oscillations. Figure 4 shows a series of fast Fourier transforms (FFTs) of broadband and spectrally filtered flame front emissions, as well as the FFT of the oscillating current drawn from the external bias supply. Again, the experimental conditions are the same as those used for the imaging data shown in Figure 3 (21 slm overall flow and equivalence ratio of 1.2) except that the bias used was only 4 kV (corresponding to point C in the IV curve of Figure 2).

The top left FFT of Figure 4 shows the very low amplitude, featureless power spectrum of the flame's broadband emissions under zero bias. It indicates stable laminar flow. With a 4 kV bias the flame front is driven into a large amplitude resonate-like oscillation with a fundamental frequency near 300 Hz and harmonics ranging up to 1.8 kHz. Essentially the same responses are seen again from broadband emissions and those corresponding to chemiexcited CH, C_2 and OH. Further, the current passing through the flame exhibits a power spectrum that is essentially identical to that of the flam front

emissions. The details of the cause(s) of the observed oscillatory response of the flame to and externally applied *DC bias* are currently unknown.

Conclusions

Under the flow conditions studied here, with the upper electrode in place but no potential difference applied to the flames, stable laminar pre-mixed propane/air flames with highly symmetric right circular cone geometries result. Clearly under such conditions Fick's law applies, strong temperature gradients give rise to significant thermal diffusion[16], and stable conical flame fronts result. Such a stable laminar flame has small negative curvature everywhere on the flame front, with the largest curvature at the apex of the laminar inner cone. The primary results of this study shows that with effective voltage-to-flame coupling, normal bias of such flames at modest voltages rapidly converts (within ~ 5 ms) the stable flame to one that is quite unstable and unable to support a laminar combusting flow. The flame speed is substantially increased, and the resulting wrinkled laminar flame exhibits strong negative curvature. One way to interpret the destabilizing effect of the external electric field is that it gives rise to an additional *electric pressure* induced diffusion effect which significantly increases the flame speed. A possible mechanism by which such a minority flame constituent as the flame ions (1 part in roughly 10^7 in terms of overall density, or a peak density in the range[14,17] of $10^{10} - 10^{11}$ cm^{-3}) can effect such a dramatic change in flame geometry follows.

The electric field can act directly and effectively only on the highly localized, chemiionization-derived positive ions in the flame reaction zone. The resulting force on the flame ions significantly increases their mass diffusivities and thereby lowers the ionic species Lewis numbers. The observed result is a diffusive-thermal instability[18,19], typical of flames with global Lewis numbers less than one and negative curvatures[23-25]. The electric-field enhanced differential diffusional velocity of the reaction zone positive ions toward the burner head strongly affects the bulk flame speed[18,19,23-25], and the instability causes the burning speed of the negatively curved[23] reaction zone to increase and collapse toward the burner head taking on a wrinkled laminar geometry. Analogous to very similar flame front modifications produced by changes in ambient air pressure[22], the overall process is labeled an *electric pressure* effect. In some cases pocket formation results with clear indications of turbulence, suggesting that electrically stressed hydrocarbon flames can be quite sensitive to *electric pressure*.

That such increases in flame speed can occur without concomitant increases in flame temperature can be understood from two points of view. Considering that the input electrical power to the flame in the experiments reported here is on the order of one-one thousandth of the rate at which chemical energy is converted to heat in the flame, conservation of total energy would certainly speak against the possibility of any global temperature increase for the flame. Essentially, since the flame ions are present in such minor concentrations in hydrocarbon flames, even though they could be forced to diffuse by the field into regions where reactant concentrations differ significantly from those of laminar flow, their total contribution to the enthalpy of the mixture may be insufficient to produce any modification in the flame temperature. From the point of view of observed flame structure changes, Echekki and Chen[24] noted that for similar flames the net enhancement in the volumetric heat release and fuel consumption rates is primarily due to the increase in flame surface area by wrinkling. They noted that the heat release and fuel consumption per unit flame area is reduced relative to the laminar flame.

Future work will focus on the scaling effects of the increased applied voltage to the flame to determine the extent to which the laminar flame speed could be increased by increasing the electric pressure to the propane/air flame.

References

1. D. Bradley, in Advanced Combustion Methods, F.J. Weinberg, Ed., Academic Press, New York, 1986, p. 331.
2. A.P. Chattock, Phil. Mag **48** (1899) 401-403.
3. H.F. Calcote and R.N. Pease, Ind. Eng. Chem. **43** (1951) 2726-2731.
4. H.F. Calcote and C.H. Berman, in Fossil Fuels Combustion Symposium PD-Vol. 25, S.N. Singh, Ed., ASME Book No. H00453, 1989, p. 25.
5. D. Bradley and S.H. Nasser, Combust. Flame **55** (1984) 53-58.
6. D. Bradley and S.M.A. Ibrahim, Proc. Combust. Inst. **15** (1974) 1023-1029.
7. H.C. Jaggers and A.von Engel, Combust. Flame **16**, (1971) 275-285.
8. D.S. Maclatchy, R.M. Clements and P.R. Smy, Combust. Flame **45**, (1982) 161-169.
9. M. Kono, F.B. Carleton, A.R. Jones and F.J. Weinberg, Combust. Flame **78** (1989) 357-363.
10. G.A. Gulyaev, G.A. Popkov and Yu.N. Shebeko, Phys. Combust. Explosion **21** (1985) 23-25.
11. J. Lawton and F.J. Weinberg, Proc. Roy. Soc. **A227** (1964) 468-497.
12. J. Lawton, P.J. Mayo and F.J. Weinberg, Proc. Roy. Soc. **A303** (1968) 275-298
13. J. Lawton & F.J. Weinberg, Electrical Aspects of Combustion, Clarendon Press, Oxford, 1969, pp. 285-336.
14. T. Pedersen and R.C. Brown, Combust. Flame **94** (1993) 433-448.
15. B.A. Strayer, J.D. Posner, D. Dunn-Rankin and F.J. Weinberg, F.J., Proc. R. Soc. Lond. A, Math. Phys. Eng. Sci. **458** (2002) 1151-1166.
16. S.R. Turns, An Introduction to Combustion, 2nd Edition, McGraw-Hill, Singapore, 2000, p 86, pp 450-470.
17. J.M. Goodings, D.K. Bohme and Chun-Wai Ng, Combust. Flame **36** (1979) 45-62.
18. F.A. Williams, Combustion Theory: The Fundamental Theory of Chemically Reacting Flow Systems, 2nd Edition, The Benjamin/Cummings Publishing Company, Menlo Park, CA, 1985, pp 357-365, pp 429-440.
19. A. Linan and F.A. Williams, Fundamental Aspects of Combustion, Oxford University Press, New York, 1993, pp 32-37, 111-151.
20. L.P. Goss, V. Vilimpoc, B. Sarka and W.F. Lynn, Jour. Engr. Gas Turb. Pwr. **111** (1989) 46-52.
21. V. Vilimpoc, L.P. Goss and B. Sarka, Optics Lett. **13** (1988) 93-95.
22. A.G. Gaydon and H.G. Wolfhard, Flames: Their Structure, Radiation and Temperature, 4th Edition, Chapman and Hall, London, 1979, pp 182-194, plate 14, p 359.
23. J.H. Chen and H.G. Im, Proc. Combust. Inst. **27** (1998) 819-826.
24. T. Echekki and J.H. Chen, Combust. Flame **106** (1966) 184-202.
25. J.H. Chen, T. Echekki and W. Kollmann, Combust. Flame **116** (1999) 15-48.

Figure Captions

Figure 1. Experiment configurations for high-speed two-dimensional imaging, current/voltage and flame oscillation measurements.

Figure 2. Typical current/voltage characteristic measured for field-modified flames (upper plot). Note that the total electrical power input is quite small (~ 3 W at the highest bias). The lower plot shows the variation of flame current with equivalence ratio for fixed air flow rate and external bias.

Figure 3. High-speed two-dimensional images of the flame response to a 5 kV bias taken using broadband and spectrally filtered flame front light emissions. The corresponding intensity profile plots show the degree of combustion intensity enhancement that is achieved.

Figure 4. Current and flame front optical signal oscillations quantified by computing the power spectrum of the time-varying signal.

APPENDIX R C. Tong

Scalar Filtered Density Function for Improving Large Eddy Simulation

Work performed

Experimental study of three-stream mixing was performed. The research focus on scalar filtered density function for improving large eddy simulation of turbulent flames.

A nozzle was made for the study. We used a flow configuration in which two scalars issue from a jet nozzle and mix with air in a co-flow (the third scalar). The three-stream flow consists of a co-annular jet of ethylene and acetone-doped air issuing into an air co-flow. Measurements were performed using Rayleigh scattering (ethylene) and planar laser-induced fluorescence (acetone) in collaboration with Dr. Cam Carter (AFRL/PRAS) at the Air Force Research Laboratories (AFRL).

We set up a measurement system for Rayleigh scattering (ethylene) and planar laser-induced fluorescence (acetone). Tests were performed to determine the spatial resolution and the signal to noise ratio of the measurement system. Extensive data sets were collected for a range of flow conditions and downstream locations. The data will be analyzed to study the filtered density function in tree-stream mixing.

Design and Development of a High Temperature DC-DC Power Converter Utilizing SiC Power Devices

Final Report
Summer Faculty Research Fellowship Program
AFRL Propulsion Directorate

AFRL Contact:
Dr. James D. Scofield
AFRL/PRPE

UTC Contact:
Mr. Roger Rucker

Prepared by:

Biswajit Ray
Dept. of Physics & Engineering Technology
Bloomsburg University of Pennsylvania
400 East Second Street
Bloomsburg, PA 17815

August 4, 2006

Table of Contents

Abstract			1
1.0	JFET driver design		2
2.0	BJT/MOSFET driver design		3
3.0	High temperature power converter using SiC power devices		4
	3.1	Design of the power converter	4
	3.2	Design calculations	6
	3.3	Experimental setup and testing	12
	3.4	Future work	14
4.0	PPU for Hall thruster		15
5.0	Summary		16
6.0	References		17

Abstract

During the eight weeks of summer work, driver circuits for BJTs, JFETs, and MOSFETs have been developed and tested. A 180 W, 100 kHz, 270 V/28 V two-transistor forward power converter has been designed and successfully tested for operation from room temperature (25^{o}C) to 200^{o}C. This design included the use of SiC BJTs and Schottky rectifiers and high temperature powdered ferrite based cores. There is a critical need for developing high temperature capacitors with reasonable leakage current and dissipation factor. Specifications and power/control architecture development of a 6 kW Hall thruster PPU was also undertaken during the final week of the summer experience at AFRL. Overall, it was an excellent research experience, and I thank you all for the opportunity!

1.0 JFET driver design

A driver circuit for normally-on SiC JFETs was designed with the requirement that the gate-to-source voltage should be in the 3-5 V range during the device on period and a negative voltage of 25-30 V range is needed during the device off period. Another objective was to keep the drive circuit power consumption to the minimum possible level.

Figure 1 below shows the schematic of the designed driver circuit. The 0V/5 V PWM logic signal is converted to -15 V/0V level using a high current and high speed optocoupler (HCPL-3180). This unidirectional signal is then isolated, stepped up, and level shifted using capacitors, resistors, and zener diodes. The generated gate drive signals have a level of +5 V/-30V. This circuit has been successfully tested in driving high side and low side JFETs switching a 60 V/3 A load at 30 kHz.

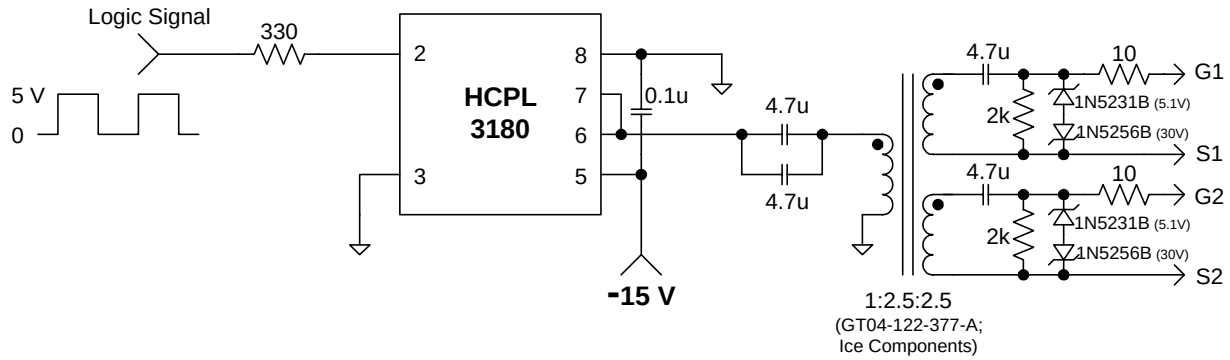

Figure 1: Schematic of the JFET gate driver circuit.

2.0 BJT/MOSFET driver design

Driver circuit for MOSFETs does not need to supply much of a steady state current; however, the driver circuit for BJTs needs to supply a significant amount of steady state current. The design shown in Figure 2 is based on a 9 A (peak) high speed MOSFET driver IC (TC-4422A/TO-220) with a capability of delivering 2 A of steady state current. The output of the driver IC is level shifted, isolated, and stepped down for driving BJTs. It is recommended that a unity ratio (1:1:1) isolation transformer be used for driving MOSFETs. This circuit has been successfully tested to drive high side and low side BJTs and MOSFETs switching a 60 V/6 A load at 30 kHz.

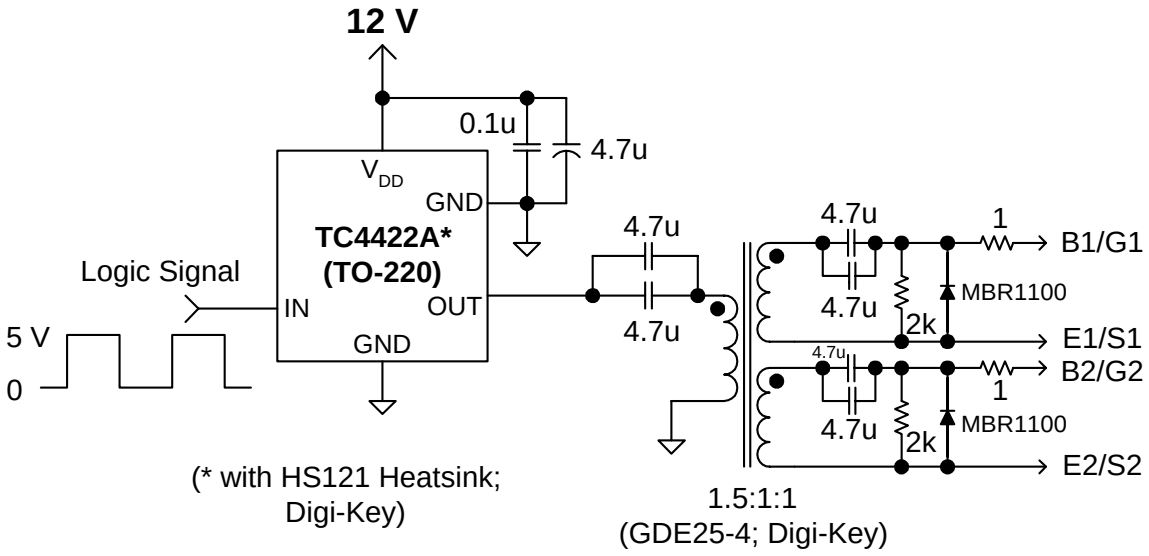

Figure 2: Schematic of the BJT/MOSFET driver circuit.

3.0 High temperature power converter using SiC power devices

Design, operation, and performance evaluation of a 180 W, 100 kHz, 270 V/28 V two-transistor forward dc-dc power converter are reported for elevated temperatures up to 200°C. Use of SiC power semiconductor devices, and high temperature powdered ferrite (for magnetics design), and characterization of ceramic (X7R) capacitors' leakage current over temperature are presented as well.

High temperature electronics is becoming increasingly important in a multitude of applications [1] including automobiles (on-engine and in-transmission environments), well drilling (instrumentation for oil and gas recovery), and aircraft and spacecraft (turbine engines, motor drives, and space propulsion systems). Advances in silicon-on-insulator (SOI) technology and the steady development of wider band semiconductors such as silicon carbide (SiC) are enabling the practical deployment of high temperature electronics in the near future. As temperature increases in a semiconductor, intrinsic carrier density increases thereby increasing the leakage current. Additionally, device parameters vary, electromigration of interconnection traces increase, dielectric breakdown strength decreases, and TCE mismatches stress the die mechanically. Even with the use of SOI technology [2,3], these effects limit the maximum ambient use temperature of Si power devices to 200°C. Above 200°C, use of wider bandgap semiconductor materials become imperative [4,5] since they produce a smaller concentration of intrinsic carriers than Si at elevated temperatures. Among the wide bandgap materials, SiC technology is far ahead of GaN and diamond technologies. SiC Schottkys are commercially available, and the use of SiC BJTs, JFETs, and MOSFETs has been reported at the developmental level. In the passive components domain, high temperature ferrite magnetic material has been developed recently, [6,7] and the development of high temperature high frequency capacitors with acceptable drop in capacitance value and decrease in leakage currents is in progress [8]. Previous studies [9-12] have reported high temperature operation of SiC diodes, JFETs, and MOSFETs as well as power converters utilizing these devices. This paper presents the operation of a 180 W, 270 V/28 V, 100 kHz two-transistor forward dc-dc converter at elevated temperatures up to 200°C, utilizing SiC power devices and high temperature magnetics.

3.1 Design of the power converter

A 180 W, 270 V/28 V, 100 kHz two-transistor forward converter was designed to operate with a minimum load power of 15 W under continuous conduction mode and a peak-to-peak output ripple of 140 mV (i.e., 0.5% of the output voltage). The two-transistor forward converter [13] power stage is shown in Figure 3. This converter goes through three different modes of operation within a switching cycle: energy transfer mode (S_1 and S_2 are on, and D_1 conducts), transformer reset mode (RD_1 and RD_2 conduct applying reverse input voltage to the transformer winding, and output inductor current freewheels through D_2), and dead time mode (all primary switches are off while the output inductor current is freewheeling through D_2). Because of the way the transformer core reset is achieved, the maximum duty cycle is limited to 0.5. For this design, a maximum duty cycle of 0.45 is used. Key advantages of this topology are: transformer leakage inductance energy is fed back to the input capacitor via RD_1 and RD_2, and maximum voltage stress on the primary switches is limited to the input voltage level requiring no primary-side snubber circuits. Additionally, voltage shoot-through is absent in this topology since S_1 and S_2 are turned on and off at the same time.

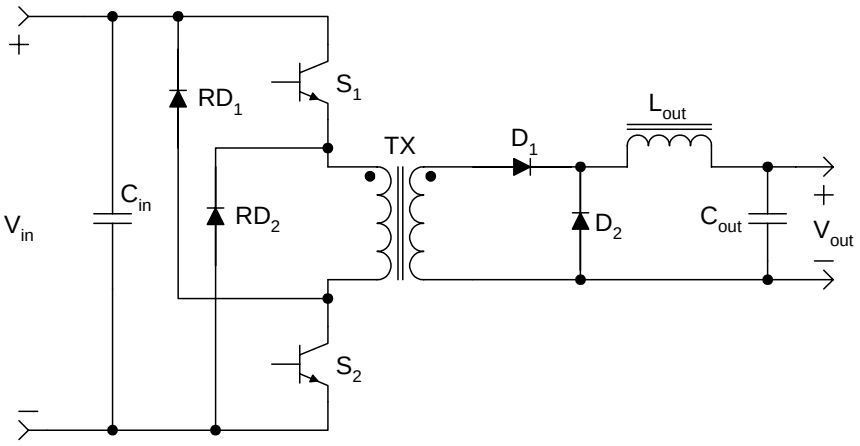

Figure 3: Power stage of the two-transistor forward dc-dc converter.

SiC power semiconductor selection: The power semiconductors used in the power stage design are shown in the table below. All three devices are from Cree Incorporated.

Device ref. designator	**Device type**	**Part #**	**Key specifications**
S_1, S_2	BJT	---	1000 V, 5 A, Tj,max >300°C, TO-257
RD_1, RD_2	Schottky	CSD10060	600V, 10 A, V_F=2.0 V @ 10 A/Tj = 175°C, TO-220
D_1, D_2	Schottky	CSD20030	300V, 20 A, V_F=1.4 V @ 10 A/Tj = 175°C, TO-247

Development of 4H-SiC BJTs with high dc current gain and associated high temperature current-voltage characteristics have been recently reported [14]. These 1000 V/30 A devices show fast switching properties and a sharp avalanche behavior at a collector-emitter voltage of 1000 V. The switching devices used in the two-transistor forward power converter implementation are from the same family of devices reported in [14], and are currently not available commercially. SiC Schottky rectifiers, however, are commercially available with 600 and 1200 V blocking voltage ratings and current handling capabilities of up to 20 A. The positive temperature coefficient of V_F makes these devices very amenable to paralleling in order to achieve high current handling capability. Figure 4 below shows the V_{BE} and V_{CE} variation with temperature for the BJT used in the design, and Figure 5 shows the forward voltage drop variation of the 300 V Schottky used in the output rectifier design.

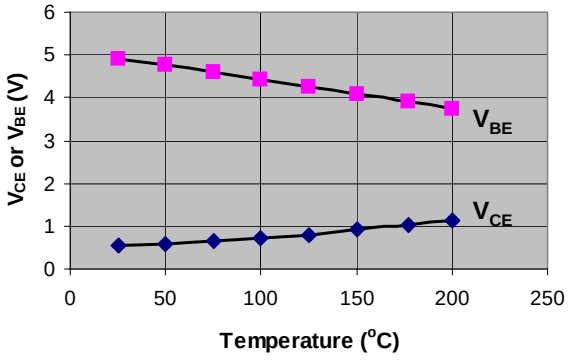

Figure 4: SiC BJT junction voltages for a dc current gain of 10 (I_B = 0.2 A; I_C=2 A).

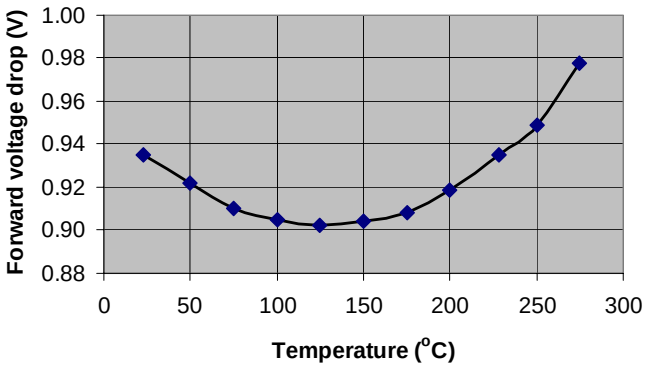

Figure 5: SiC Schottky diode (CSD20030) forward voltage drop for a dc forward current of 6.5 A.

Transformer design: A planar core of E46410 configuration made of Fe-Mn-Zn ferrite material with a Curie temperature in excess of 300°C [6,7] was used in designing the transformer. Key magnetic properties of this high temperature material are: relative permeability of 500-1000 at 25°C, saturation flux density of 0.48 T at 25°C and 0.3 T at 200°C, coercive force of 0.5 Oe at 25°C and 0.35 Oe at 200°C, power loss of less than 1 W/cc @200 kHz/0.08 T, and a resistivity of 100-200 Ω-cm. A transformer with a primary-to-secondary turns ratio of 3.5 was designed with 28 turns in the primary and 8 turns in the secondary. The design assumed a peak flux density of 0.08 T, avoiding magnetics saturation of the core for up to 300°C. The primary winding used one strand of #24 copper wire with Fluorene Polyester (FPE) coated insulation. The breakdown strength of FPE is approximately 10 kV/mil for up to 300°C. The secondary winding was implemented with one strand of 0.3125"x0.003" copper foil using Kapton polyimide film tape, rated for operation up to 260°C, as the insulating material.

Output inductor design: The E46410-shaped high temperature core was also used in designing the inductor. An air gap of 1.8 mm (70 mils) was used in the center leg for energy storage purpose. Based on the minimum load current requirement of 0.54 A, the calculated value of required inductance is 150 μH. A peak flux density of 0.1 T was used in the design with a peak-to-peak ac flux density of only 15 mT. In winding the inductor, 24 turns of six strands of FPE-coated #24 wire were used.

Capacitor selection: For higher dielectric constant capacitors such as ceramics, capacitance generally decreases and leakage current increases with increasing temperatures [8]. For low capacitance values, C0G (Class I) ceramic capacitors are likely the best choice due to lower dissipation factor and stable temperature characteristics. However, due to the need of capacitance in the range of 10-30 μF for this power converter design, X7R (Class II) ceramic capacitors are the next best alternative. For this design, the input capacitance of 10 μF consisted of two 5 μF/ 300V/X7R (AVX) capacitors. The output capacitance of 45 μF, however, consisted of three 15 μF/25V Class-II high temperature (200°C) capacitors from Novacap. It shall be noted that the capacitance of high temperature capacitors from Novacap drops significantly in value between 150°C and 200°C.

3.2 Design calculations

The following five pages show the power converter design calculations for the input and output filter sizing, transformer design, output inductor design, and power semiconductor current and voltage stresses.

$nH := 10^{-9} \cdot H$ $mW := 10^{-3} \cdot W$ $\mu m := 10^{-6} \cdot m$

Two Transistor Forward Converter Design (175 W)
June 28, 2006

$Pout := 175W$

$Vin_max := 290V$ $Vin_nom := 270V$ $Vin_min := 250V$

$Vout := 28V$ $Iout := \frac{Pout}{Vout}$ $Iout = 6.25A$

$freq := 100kHz$ $Dmax := 0.45$

==========

Primary turns: N1; Secondary turns: N2; Turns_ratio = N2/N1

==========

$Turns_ratio := \frac{Vout}{Vin_min \cdot Dmax}$ $Turns_ratio = 0.249$

$Turns_ratio_reqd := 1.1 \cdot Turns_ratio$ $Turns_ratio_reqd = 0.274$

$Dmin := \frac{Vout}{Vin_max \cdot Turns_ratio_reqd}$ $Dmin = 0.353$

==========

Core: E46410 (high temp core)

$Ae := 516mm^2$ $Vcore := 41400mm^3$ $Bmax_goal := 0.08T$

$AL := 5660nH$ $Avg_length_turn := 8in$

$area_foil := 0.375in \cdot 0.0035in$ $I_density := 5\frac{A}{mm^2}$

$temp_C := 250$

$\rho_cu_\Omega cm := 1.724 \cdot [1 + 0.0042(temp_C - 20)] \cdot 10^{-6}$ $\rho_cu_\Omega cm = 3.389 \times 10^{-6}$

$R_foil := \frac{\rho_cu_\Omega cm}{area_foil} \cdot \Omega \cdot cm$ $R_foil = 0.04 m^{-1} \Omega$

==========

$Np := \frac{Vin_min \cdot Dmax \cdot \left(\frac{1}{freq}\right)}{Ae \cdot Bmax_goal}$ $Np = 27.253$

$Np_used := ceil(Np)$ $Np_used = 28$

$Ns_used := ceil(Np_used \cdot Turns_ratio_reqd)$ $Ns_used = 8$

==========

$Is_rms := Iout \cdot \sqrt{Dmax}$ $Is_rms = 4.193A$

$Ip_rms := Is_rms \cdot Turns_ratio_reqd$ $Ip_rms = 1.148A$

$strands_sec := ceil\left(\frac{Is_rms}{I_density \cdot area_foil}\right)$ $strands_sec = 1$

==========

$Lm := AL \cdot Np_used^2$ $Lm = 4.437mH$

$Im_peak := \frac{Vin_min \cdot Dmax \cdot \left(\frac{1}{freq}\right)}{Lm}$ $Im_peak = 0.254A$

$Im_rms := Im_peak \cdot \sqrt{Dmax}$ $Im_rms = 0.17A$

$Ip_rms_TOTAL := \sqrt{\left(Ip_rms^2 + Im_rms^2\right)}$ $Ip_rms_TOTAL = 1.16A$

$strands_pri := ceil\left(\frac{Ip_rms_TOTAL}{I_density \cdot area_foil}\right)$ $strands_pri = 1$

==========

$\Delta B := \frac{Vin_min \cdot Dmax \cdot \left(\frac{1}{freq}\right)}{Ae \cdot Np_used}$ $\Delta B = 0.078T$

$core_loss_pu_vol := \frac{700}{5}\frac{mW}{cm^3}$

$Core_loss := core_loss_pu_vol \cdot Vcore$ $Core_loss = 5.796W$

$Aw_reqd := 3(Np_used \cdot area_foil \cdot strands_pri + Ns_used \cdot area_foil \cdot strands_sec)$

$Aw_reqd = 91.451 \times 10^{-6} m^2$

$Awindow := 22.5mm \cdot 10mm$

$$Window_utilization_factor := \frac{Aw_reqd}{Awindow} \qquad Window_utilization_factor = 0.406$$

$$R_pri := Avg_length_turn \cdot R_foil \cdot \left(\frac{Np_used}{strands_pri} \right) \qquad R_pri = 0.228\Omega$$

$$R_sec := Avg_length_turn \cdot R_foil \cdot \left(\frac{Ns_used}{strands_sec} \right) \qquad R_sec = 0.065\Omega$$

$$P_Cu_pri := Ip_rms^2 \cdot R_pri \qquad P_Cu_pri = 0.3W$$

$$P_Cu_sec := Is_rms^2 \cdot R_sec \qquad P_Cu_sec = 1.144W$$

$$Copper_loss := P_Cu_pri + P_Cu_sec \qquad Copper_loss = 1.444W$$

$$Total_loss := Copper_loss + Core_loss \qquad Total_loss = 7.24W$$

==========

Power Semiconductor Voltage/Current Ratings

$$MOSFET_Vpk := Vin_max \cdot 1.2 \qquad MOSFET_Vpk = 348V$$

$$MOSFET_Ipk := Iout \cdot 1.1 \cdot Turns_ratio_reqd + Im_peak \qquad MOSFET_Ipk = 2.136A$$

$$Reset_Diode_Vpk := 1 \cdot Vin_max \cdot 1.2 \qquad Reset_Diode_Vpk = 348V$$

$$Reset_Diode_Ipk := Im_peak \qquad Reset_Diode_Ipk = 0.254A$$

$$Output_Diode1_Vpk := 1.2 \cdot Vin_max \cdot Turns_ratio_reqd \qquad Output_Diode1_Vpk = 95.275V$$

$$Output_Diode1_Ipk := Iout \cdot 1.1 \qquad Output_Diode1_Ipk = 6.875A$$

$$Output_Diode2_Vpk := 1.2 \cdot Vin_max \cdot Turns_ratio_reqd \qquad Output_Diode2_Vpk = 95.275V$$

$$Output_Diode2_Ipk := Iout \cdot 1.1 \qquad Output_Diode2_Ipk = 6.875A$$

==========

Output Filter Inductor Design

$\Delta I := 0.2 \cdot Iout$ $\Delta I = 1.25A$

$Iout_min := \frac{\Delta I}{2}$ $Iout_min = 0.625A$

$Lf_min := \frac{Vout \cdot (1 - Dmin)}{freq \cdot \Delta I}$ $Lf_min = 145.003\mu H$

$Lf_used := 1.01 \cdot Lf_min$ $Lf_used = 146.453\mu H$

$ILf := 1.01 \cdot \left(Iout + \frac{\Delta I}{2} \right)$ $ILf = 6.944A$

==========

Core: 46410 (high temp core)

$AL_g := AL \cdot \frac{42}{700} \cdot 0.8$ $AL_g = 271.68nH$

$u0 := 4 \cdot \pi \cdot 10^{-7} \cdot T \cdot \frac{m}{A}$

$Bmax_goal_L := 0.1T$

$Lg_reqd := \frac{u0 \cdot Lf_used \cdot ILf^2}{Bmax_goal_L^2 \cdot Ae}$ $Lg_reqd = 1.72mm$

$Lg_used := 1.8mm$

$Lg_used = 70.866 \times 10^{-3} in$

$Bmax_used := \sqrt{\frac{u0 \cdot ILf^2 \cdot Lf_used}{Ae \cdot Lg_used}}$ $Bmax_used = 0.098T$

$Nturns := \sqrt{\frac{Lf_used}{AL_g}}$ $Nturns = 23.218$

$Nturns_used := ceil(Nturns)$ $Nturns_used = 24$

$strands_ind := ceil\left(\frac{ILf}{I_density \cdot area_foil} \right)$ $strands_ind = 2$

$$\Delta B_L := \frac{Vout \cdot \frac{(1 - Dmin)}{freq}}{Nturns_used \cdot Ae} \qquad \Delta B_L = 0.015T$$

$$core_loss_L := core_loss_pu_vol \cdot Vcore \cdot \left(\frac{\Delta B_L}{\Delta B} \right) \qquad core_loss_L = 1.089W$$

$$AwL_reqd := 3(Nturns_used \cdot area_foil \cdot strands_ind) \qquad AwL_reqd = 1.219 \times 10^{-4} m^2$$

$$Window_UF_L := \frac{AwL_reqd}{Awindow} \qquad Window_UF_L = 0.542$$

$$R_L := Avg_length_turn \cdot R_foil \cdot \left(\frac{Nturns_used}{strands_ind} \right) \qquad R_L = 0.098\Omega$$

$$Copper_loss_L := Iout^2 \cdot R_L \qquad Copper_loss_L = 3.813W$$

$$Total_loss_L := core_loss_L + Copper_loss_L \qquad Total_loss_L = 4.902W$$

==========

Capacitor Requirement Calculations

$$C_out := \frac{Vout \cdot (1 - Dmin)}{8 \cdot (0.005 Vout) \cdot Lf_used \cdot freq^2} \qquad C_out = 11.05\mu F$$

$$C_out_used := 30\mu F$$

$$C_in := \frac{2A \cdot \frac{(1 - Dmin)}{freq}}{2V} \qquad C_in = 6.473\mu F$$

$$C_in_used := 30\mu F$$

==========

3.3 Experimental setup and testing

Power stage of the converter was built using two pieces of FR-4 board and 5 mils copper strips, high temperature wire (260°C; MIL-W-25038/1), and high temperature solder (240°C liquidus temperature; 95Sn/5Sb). Figure 6 shows a pictorial view of the power stage of the converter placed outside the oven. The power semiconductor devices are located on the bottom side of FR-4 boards. The complete power stage was placed inside an oven with the control board placed outside. This necessitated long wires out of the oven to be able to feed base-emitter signals to the BJTs. The control circuit used to drive the BJTs is shown in Figure 7. Additionally, long wires out of the oven were needed for connecting to the input source and output load, and for monitoring voltages at various points of the converter. The converter was tested for ambient (board) temperatures of 25°C to 200°C, in steps of approximately 25°C. The measured power stage efficiency of the converter, shown in Figure 8, remained between 90% and 91% in the 25°C to 175°C range. However, the converter efficiency dropped from 90% at 175°C to 88.3% at 200°C.

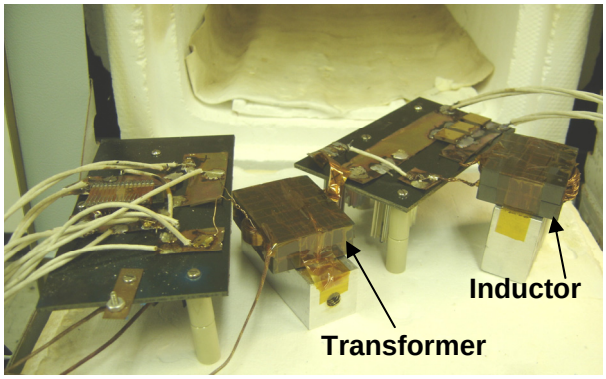

Figure 6: Pictorial view of the converter power stage (outside the oven).

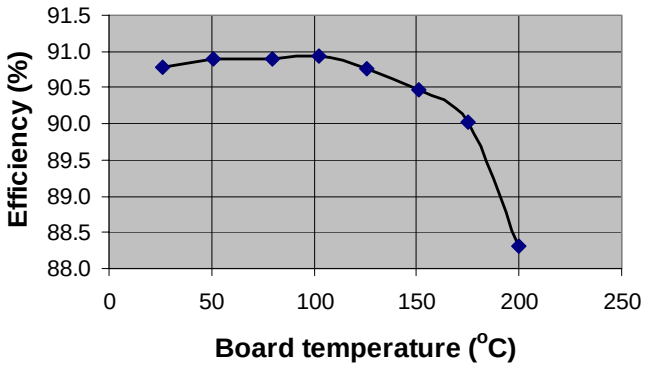

Figure 8: Efficiency of the converter as a function of temperature (P_{out} = 180 W).

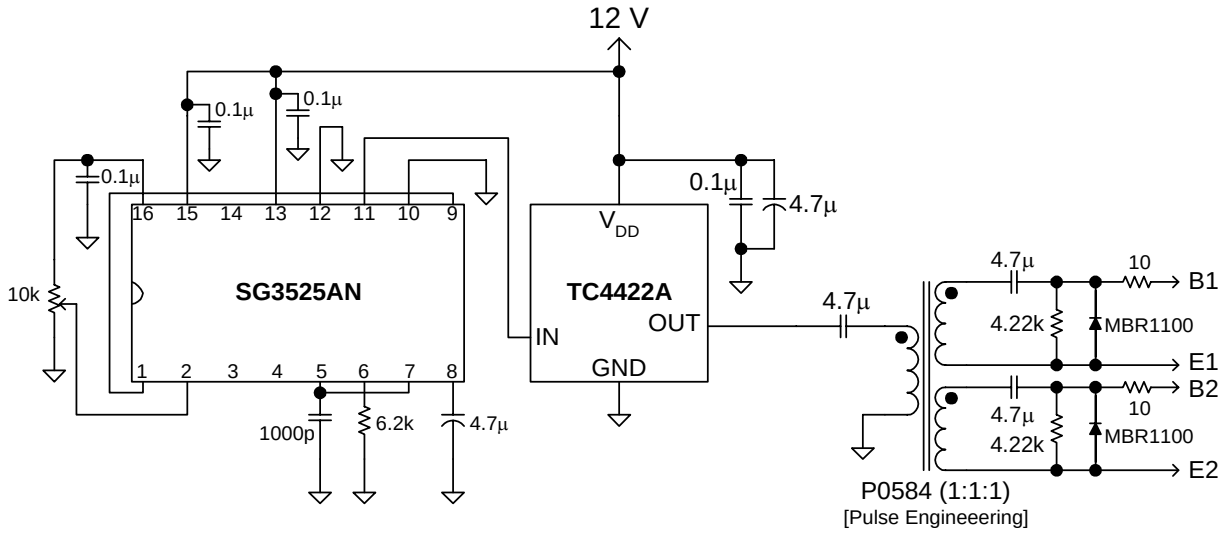

Figure 7: Control circuit used to drive the BJTs.

Figure 9 below shows the base-emitter and collector-emitter voltages of the primary switch (S_2), output diode (D_2) voltage, and transformer (TX) primary voltage waveforms at 26°C and 200°C. The V_{BE2} waveform looks noisy primarily due to lead inductance of long wires used to connect the control board outside the oven to the BJT inside the oven. The V_{D2} waveform shows the high frequency ringing at primary switch turn-on due to resonance between the transformer leakage inductance and the output diode capacitance. This ringing can be reduced significantly by the use of a snubber circuit in the secondary side of the converter. The $V_{XFMR,PRI}$ waveform clearly shows the complete demagnetization of the core and the associated dead time. Most importantly, it shall be observed that the waveforms shown in Figure 6 clearly demonstrate that the operation of BJTs, Schottkys, and the transformer are practically unchanged over the wide temperature range of 26°C to 200°C. This led to testing the converter in excess of 200°C. However, the converter failed shorted at 215°C.

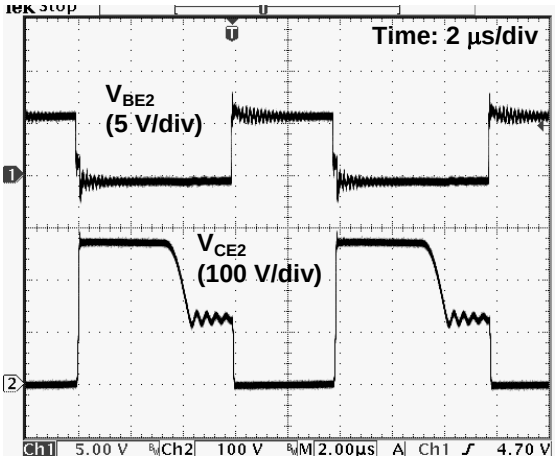

(a) Primary switch (S_2) voltage waveforms at **26°C**

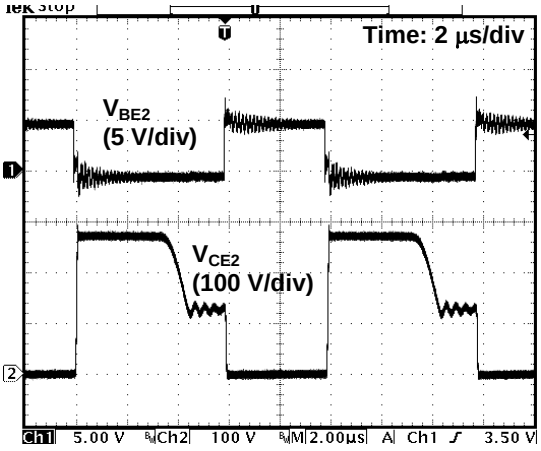

(c) Primary switch (S_2) voltage waveforms at **200°C**

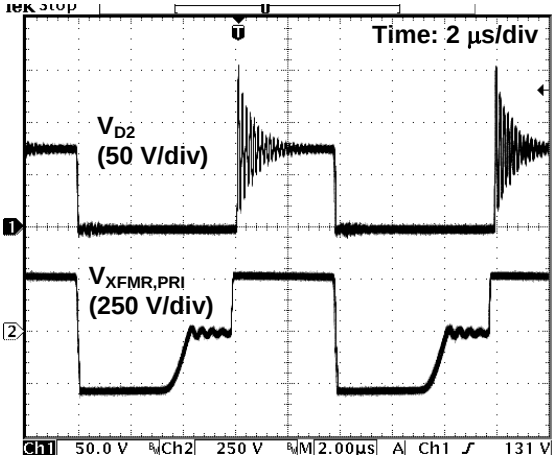

(b) Output diode (D_2) and transformer (TX) primary voltage waveforms at **26°C**

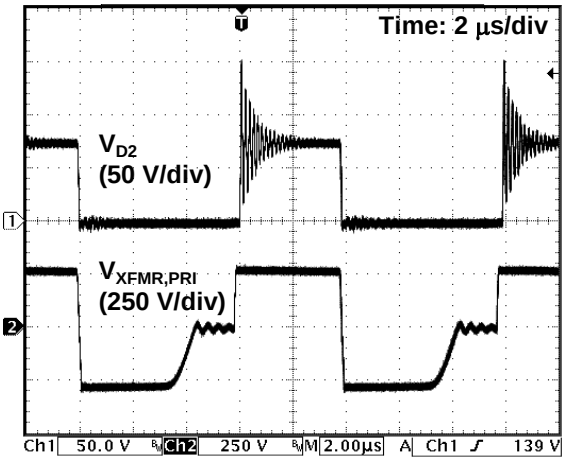

(d) Output diode (D_2) and transformer (TX) primary voltage waveforms at **200°C**

Figure 9: Power converter voltage waveforms under full load at 26°C (left) and 200°C (right).

Upon removing the converter from the oven, it was noticed that the input capacitor (2*5 μF/300V; X7R) cracked; and the power converter ran successfully once the cracked input capacitor was removed. Further testing of this capacitor revealed the fact that the converter failed shorted due to shorting of this capacitor (contributed by excessive leakage current and self-heating/thermal runaway). This led to testing of various X7R and Class-II capacitors for leakage current over temperature under dc condition. Figure 10 shows that leakage current of X7R capacitors (30 μF/300V and 5 μF/300 V) starts to increase exponentially above 175°C. The 5 μF/300V capacitor (used in the power converter design) seems usable to approximately 200°C; however, its reliability will definitely be questionable under ac ripple current excitation. The high temperature Class-II capacitor (15 μF/25 V from Novacap) shows almost no increase in leakage current up to 225°C, and is definitely usable for 200°C design. A pictorial view of the high temperature cracking of X7R capacitors is shown in Figure 11. This experimental study does explain the failure of the power converter at 215°C due to a short created by the leaking X7R input capacitor leading to significant decrease in converter efficiency from 175°C to 200°C.

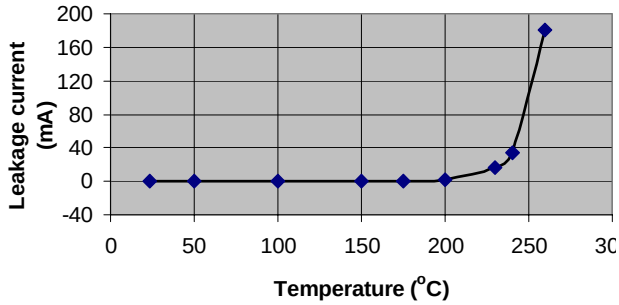

(a) 30 μF/300 V ceramic (X7R) capacitor

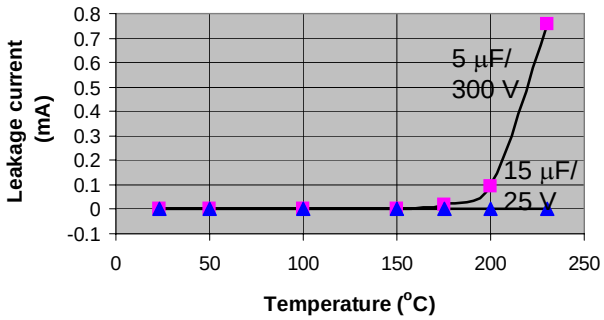

(b) 5 μF/300 V ceramic (X7R) and 15 μF/25 V ceramic (Class-II) capacitors

Figure 10: Measured leakage current of ceramic capacitors as a function of temperature.

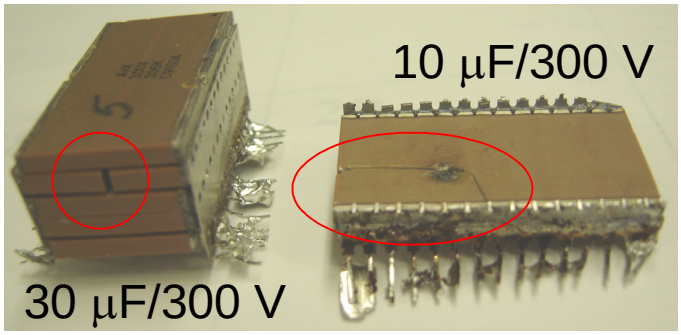

Figure 11: Pictorial view of the high temperature cracking of X7R capacitors.

3.4 Future work

Successful operation of the power converter at elevated temperatures up to 200°C has been reported. Replacing the 300 V/X7R input capacitor with high temperature Class-II or C0G ceramic capacitor would likely permit the operation of the converter to at least 250°C, and this change will be incorporated in the next design update. Implementation of a higher power version (e.g., 1 kW) of the converter using a full-bridge topology is under consideration now. The use of SiC JFETs and MOSFETs as power switch, in place of SiC BJTs, will be studied in the near future as well.

4.0 PPU for Hall thruster

Hall thrusters [15] are becoming increasingly important for commercial and military satellite applications. During the last week of the summer tenure, several power converter topologies [16-19] were reviewed for 5 kW class Hall thrusters. Specifications and design considerations for a 6 kW power processing unit (PPU) were considered for a Hall thruster system. Figure 12 below shows the required voltage-current characteristics of the PPU output.

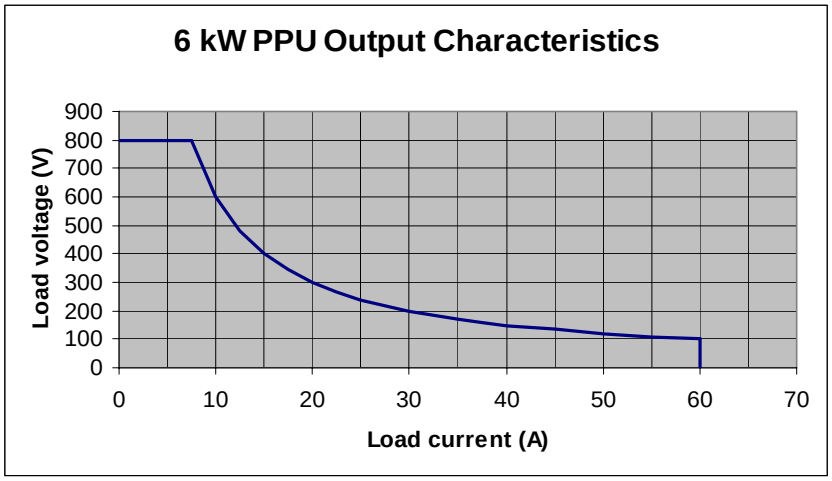

Figure 12: Voltage-current characteristics of the 6 kW PPU for Hall thrusters.

A phase-staggered/phase-shifted full-bridge topology with zero-voltage switching and PWM control is planned to be used in designing the converter. Figure 13 in the next page shows the preliminary power architecture of the PPU. The parallel connection in the input will reduce the size of the input filter and series connection in the output will reduce the voltage rating and reverse recovery time of the output rectifiers by about 50%. Current-mode PWM control will be used to provide inherent cycle-by-cycle short circuit protection. Additional protection features will include UVLO and overcurrent shutdown.

Several power MOSFETs and ultrafast rectifiers are to be used in parallel to reduce conduction loss; however, this would potentially increase the switching loss. In order to maintain a balance between high efficiency and high power density (kW/kg), a switching frequency of 50 kHz will likely be selected. Zero-voltage switching technique will be used to keep the switching loss within acceptable limit.

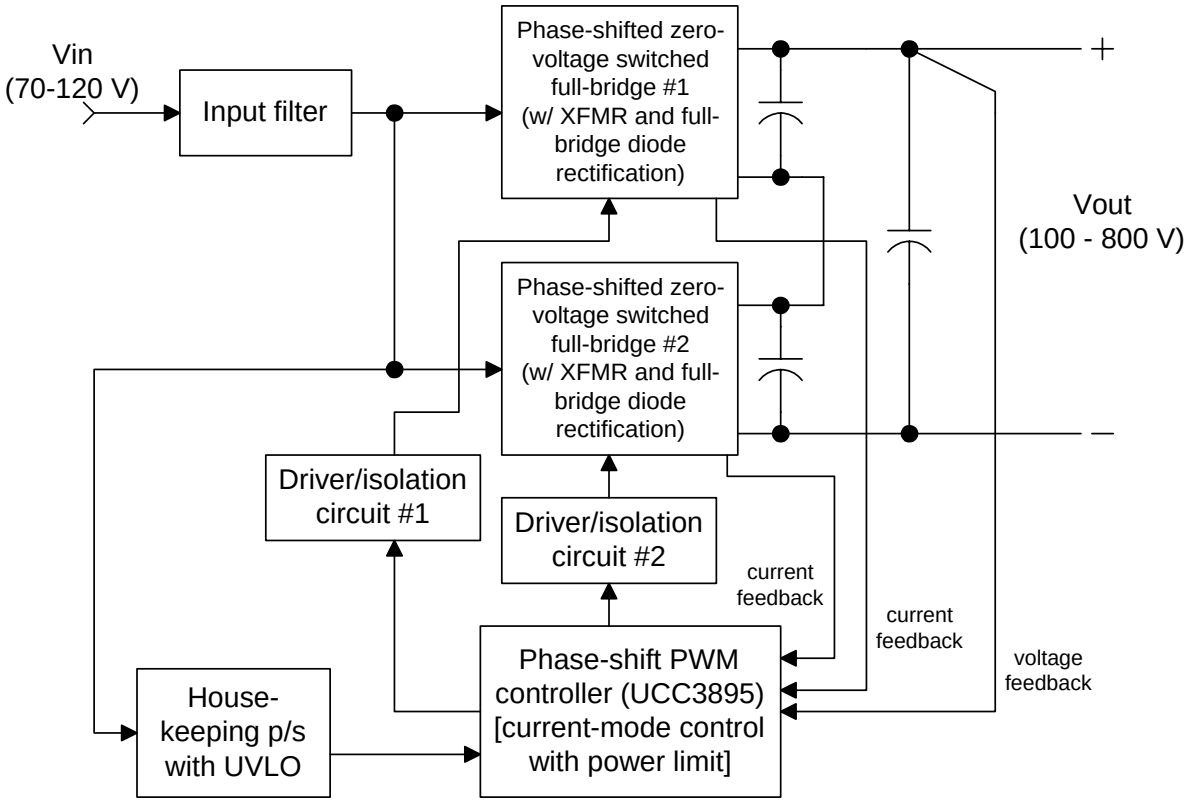

Figure 13: A block diagram representation of the proposed power converter architecture.

5.0 Summary

This report presents the work carried out as a faculty fellow during summer-2006. A total of eight weeks (June 12 through August 4) of effort included design of driver circuits for MOSFETs, BJTs, and JFETs. However, main focus of the summer effort was designing, constructing, and testing a 180 W, 270 V/28 V, 100 kHz two-transistor forward dc-dc converter for operation up to 200^{o}C. Results of the successful operation of this high temperature power converter have been submitted for possible publication and presentation at the 22nd Annual IEEE Applied Power Electronics Conference to be held in February 2007. During the final week of the summer tenure, specifications finalization and development of the power converter architecture were completed for a 6 kW power processing unit for Hall thruster applications.

6.0 References

1. H. Alan Mantooth et al., “Emerging capabilities in electronics technologies for extreme environments, Part I: High temperature electronics,” IEEE Power Electronics Soc. Newsletter, Vol. 18, No. 1, pp. 9-14, Jan. 2006.
2. J. Goetz, “High temperature electronics for sensor interface and data acquisition,” Sensors Expo, 1998.
3. J. M. O’Connor, “225 C High temperature silicon-on-insulator (SOI) ASICs for harsh environments,” Proc. IEEE Int. Workshop on Integrated Power Packaging, pp. 2-5, Sept. 1998.
4. A. Hefner et al., “Emerging silicon-carbide power devices enable revolutionary changes in high voltage power conversion,” IEEE Power Electronics Soc. Newsletter, Vol. 16, No. 4, pp. 10-12, Oct. 2004.
5. P. G. Neudeck et al., “High-temperature electronics – A role for wide bandgap semiconductors?”, Proc. IEEE, Vol. 90, No. 6, pp. 1065-1076, June 2002.
6. R. Spyker et al., “300C Ferrite material for high temperature magnetics,” Proc. IEEE Power Electronics Specialists Conf. Rec., pp. 155-160, June 2004.
7. R. Spyker et al., “300C High temperature magnetics,” Proc. IEEE Applied Power Electronics Conference, pp. 1275-1280, Feb. 2005.
8. J. S. Bowers, “Comparative characterization of capacitors used in high temperature electronics applications,” Proc. IEEE High Temperature Electronics Conf. (HiTEC), pp. 184-190, June 1998.
9. G. Spiazzi et al., “Performance evaluation of a Schottky SiC power diode in a boost PFC application,” IEEE Trans. Power Electronics, Vol. 18, No. 6, pp. 1249-1253, Nov. 2003.
10. B. Ozpineci and L. M. Tolbert, “Characterization of SiC Schottky diodes at different temperatures,” IEEE Power Electronics Letters, Vol. 1, No. 2, pp. 54-57, June 2003.
11. B. Ray et al. “High temperature operation of a dc-dc power converter utilizing SiC power devices,” Proc. IEEE-APEC, pp. 315-321, Feb. 2004.
12. R. M. Nelms et al. “200^{o}C operation of a 500 W dc-dc converter utilizing power MOSFETs,” IEEE Trans. Industry Applications, Vol. 33, No. 5, pp. 1267-1272, Sept./Oct. 1997.
13. R. W. Erickson and D. Maksimovic, “Fundamentals of Power Electronics,” 2nd edition, ISBN: 0-7923-7270-0, Springer, 2001.
14. S. Krishnaswami et al., “1000-V, 30-A 4H-SiC BJTs with high current gain,” IEEE Electron Device Letters, Vol. 26, No. 3, pp. 175-177, March 2005.
15. J. A. Haas et al., “Performance characteristics of a 5 kW laboratory Hall thruster,” Proc. 34th Joint Propulsion Conf., Paper #98-3503, AIAA, July-1998.
16. G. N. Drummond et al., “Ion and plasma thruster test console based on three-phase resonant conversion power modules,” Proc. 42nd Joint Propulsion Conf., Paper #2006-4339, AIAA, July-2006.
17. F. Dong Tan et al., “An optimum power processing unit for the Hall-effect thruster,” Proc. 33rd IECEC, Paper #98-224, August 1998.
18. L. R. Pinero et al., “High performance power module for Hall effect thrusters,” Proc. 38th Joint Propulsion Conf., Paper #2002-3947, AIAA, July-2002.
19. L. R. Pinero et al., “Multi-kilowatt power module for high-power Hall thrusters,” Proc. 40th Joint Propulsion Conf., Paper #2004-3973, AIAA, July-2004.

PINNING PROPERTIES OF YBCO SAMPLES PINNED WITH VARIOUS METHODS OF ADDITION

FINAL REPORT

M.D. Sumption

Oct 15, 2006

1. Introduction/Abstract

YBCO samples of various types were measured using a magnetic and electrical measurements. For the sake of completeness, data taken here is compared to previous measurements. In general, J_cs, pinning energies, α, and B^* are under study. The J_c curves are parameterized for J_{sv}, B^*, and α, and compared to existing models. The dimensionality of the pinning is considered, and the differences in the pinning enhancements with various pinning precipitates and distributions are compared. The 3-D nature of the pinning is evident, and the pinning is seen to be effective.

2.0 Pinning Measurements

2.1 Measurement Methods

A vibrating sample magnetometer has been used to extract magnetic J_c values for various YBCO thin film samples with several types of doping. Measurements were performed in a face-on orientation at lower fields from 4.2 K to 77 K. Two basic series of measurements were performed. In the first, a series of loops with increasing amplitude were measured at a constant loop time at each temperature. Using these loops, high data density was achieved over the whole field range. From these measurements, magnetic J_c curves could be extracted. From an analysis of these measurements, we can parameterize these curves with a field below which magnetization-derived J_c is flat, B^*, a low field (maximal) J_c value at lowest fields, $J_{c,max}$, and the exponent for J_c decay with field, α. In theory, B^* should be the field that separates single vortex pinning regime from the collective pinning regime. However, in practice, critical state artifacts tend to mask this. Below some calculations to show this are given. Nevertheless, some apparent influence of pinning on B^* does appear, attempts to distinguish real effects from artifacts are given below. Above B^* the functional dependence will typically go as $J_c \propto B^{-\alpha}$, with $\alpha \cong 0.5$ for control samples, and significantly lower for some samples with additional pinning. All measurements were performed with a vibrating sample magnetometer in conjunction with a varitemp He-gas flow cryostat and a water-cooled electromagnet. The results are given in the sections below. Three groups of samples were measured. The first set is a series of 211 pinned samples, random and layer, with control and minute doping samples as well. These samples were previously measured but here are shown with more detailed measurements and analysis. The second set consisted of BaSn-oxide pinned samples. These samples are presented, analyzed, and

discussed parallel to the method used for the first series. The last set includes an additional layer 211 sample, and Ba-Zirconate pinned sample, and one additional control sample. These samples are again analyzed as the first set.

2.2. Samples

Sample specifications are listed in Table 2.2.1, in preparation for magnetic J_c comparisons. These numbers have been verified. Included also are magnetization values at 4.2 K and 77 K.

Table 2.2.1. Sample Specifications.

Sample	Δm, emu, 4.2K, 0T	Δm, emu, 77K, 0T	J_c factor (emu to MA/cm^2)	Type	t, μm	Vol., 10^{-6} cm^3	$\langle w \rangle$, mm
TJ127	1.051	{0.0326}	33.44	211 layer	0.269	2.76	3.25
TJ360	0.932	{0.0343}	34.23	Control	0.301	2.80	3.13
PV89	3.80	0.100	10.54	Random 211	0.884	8.95	3.18
PV45	1.524	0.0958	22.64	Random 211	0.417	4.063	3.26
TJ804A	1.853	0.0790	36.83	Control	0.2635	2.553	3.19
TJ834	2.195	0.0734	28.42	Layer 211	0.3448	3.309	3.19
JK06B	1.151	0.034	39.33	MD-A (.001 Ce)	0.267	2.376	3.21
JK08	1.309	0.0559	45.45	MD-B (.01 Tb)	0.229	2.129	3.10
TJ978B	2.195	0.0687	19.33	211	0.4873	4.834	3.21

2.3. Magnetic J_c Comparison, B and α*

The results of the magnetic measurements at 77 K and 4 K are displayed in Figures 2.3.1 and 2.3.2, respectively. What we can see is that generally, the layer pinned samples hold up better with field that the control samples, with the random pinned samples in-between control and random pinned samples. We note that there is some sample-to-sample variation in the absolute J_c, but that the field dependence properties seem more stable.

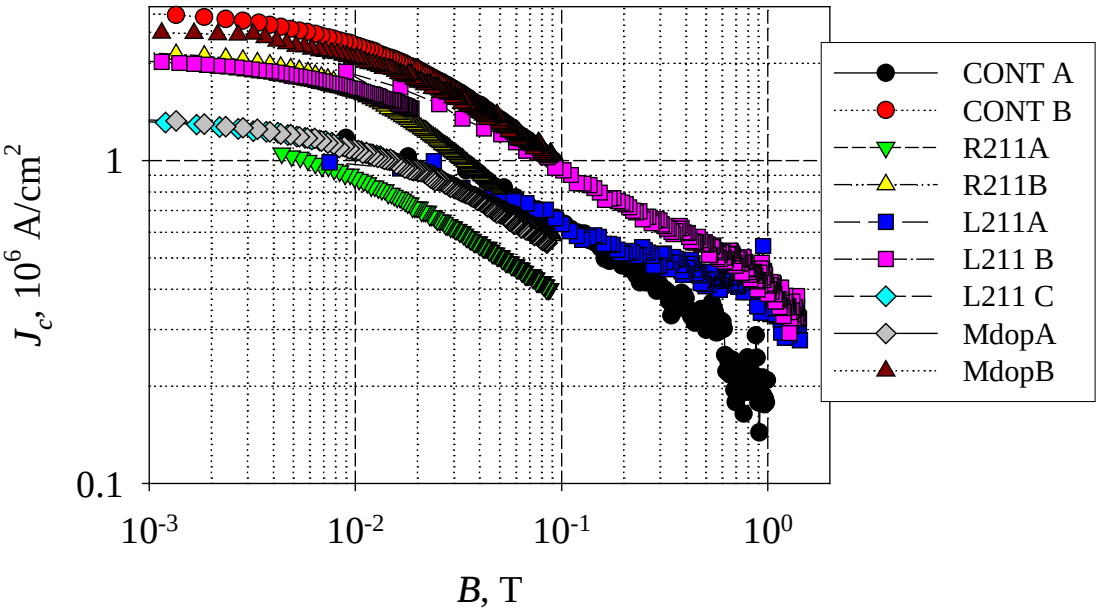

Figure 2.3.1. J_c/J_{c0} vs. B for various samples at 77 K.

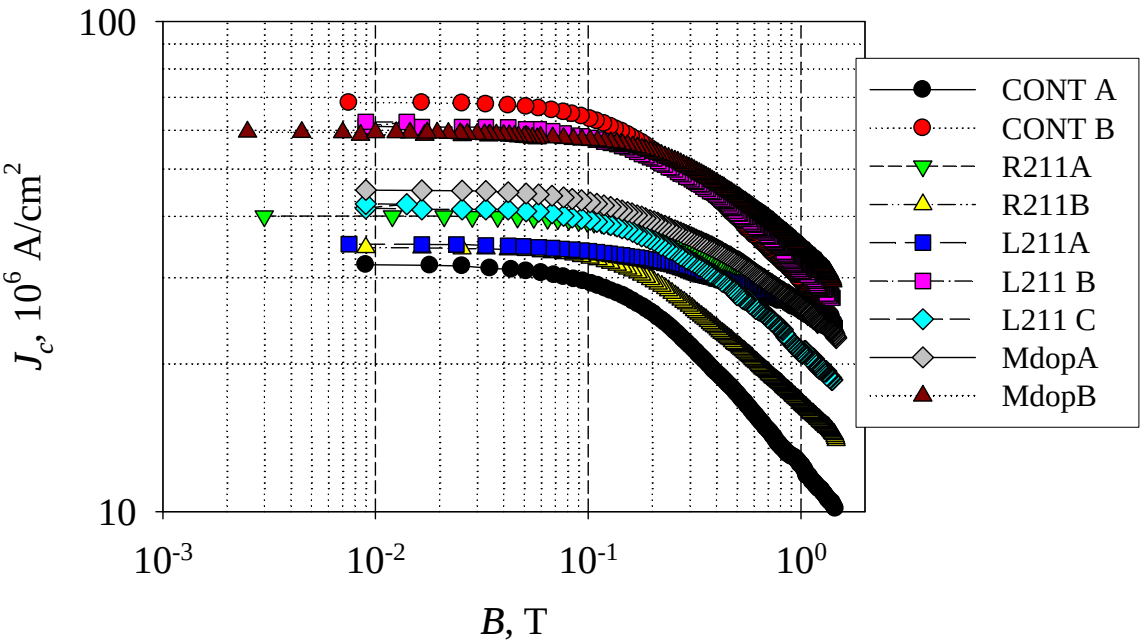

Figure 2.3.2. J_c/J_{c0} vs. B for various samples at 77 K.

Table 2.3.1. 77 K and 4.2 K values for J_{sv}, B^*, and α

Sample	J_{sv}, MA/cm^2 (4 K)	J_{sv}, MA/cm^2 (77 K)	B^*, mT (4 K)	B^*, mT (77 K)	α (4 K)	α (77 K)
Cont-A	31.90	1.56 est	60	--	0.49	0.43
Cont-B	68.24	2.911	78.5	1.85	0.44	0.47
R211-A	40.05	1.05	140	5.9	0.25	0.48
R211-B	34.50	2.17	110	2.8	0.39	0.53
L211-A	35.14	1.50	>135	7.5	0.16 (10K)	0.28
L211-B	62.38	2.08	98	2.2	0.39	0.38
L211-E	42.42	1.32	137	2.2	0.28	0.32
MD-A	45.27	1.34	102	2.35	0.30	0.38
MD-B	59.49	2.54	136	3.5	0.36	0.36

Table 2.3.1 gives J_{sv}, B^* , and α for all samples at 4 K and 77 K. Generally, we see a better (lower) α for various kinds of pinning. The random 211 samples do not show such an improved α, but the do show an improved B^*, which does indicate more pinning is being introduced. This apparent discrepancy may have to do with non-optimization of random 211 pinning methods.

$BaSnO_3$ Precipitate Samples

Two YBCO thin film PLD samples were made with $BaSnO_3$ nano-precipitates distributed randomly (made using a $BaSnO_3$ pie-wedge target). These samples were seen to have good pining, specially at high fields, with a double-hump structure in the Fp vs B curve. The two samples measured in this study were: (1) PV119D, a $BaSnO_3$ (30 degree pie) doped 317 nm YBCO layer deposited on LAO, and (2) PV104 C, a $BaSnO_3$ (30 degree pie) doped 273 nm YBCO layer on LAO. These samples were 0.33 mm square. Thus, V = 0.33*0.33*0.317/10000 = 3.45e-6 cm^3 for PV119D, and V = 0.33*0.33*0.273/10000 = 2.97e-6 cm^3 for PV104 C. Since w = 0.033 cm, and using $\Delta M = dJ_c/30$, with ΔM in emu/cm^3 and J_c in A/cm^2, we get

Table 2.3.2. Second Sample Set: $BaSnO_3$-doped sample specifications.

Sample	YBCO volume, cm^3	Conversion factor	ΔM, emu/cm^3	*4K J_c*, MA/cm^2	*77 K Jc, MA/cm^2*
PVD119D	3.45 x 10^{-6}	26.3 x 10^6	0.45	11.8	0.50
PV104C	2.97 x 10^{-6}	30.6 x 10^6		8.60	0.30

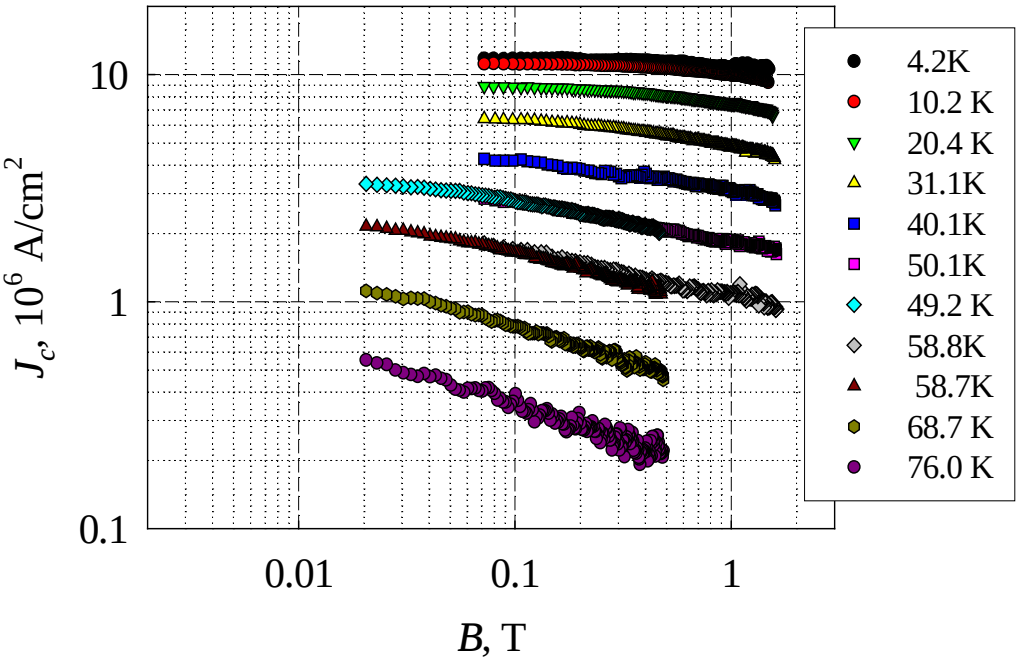

Figure 2.3.3. J_c vs. B for PVD119D at various T.

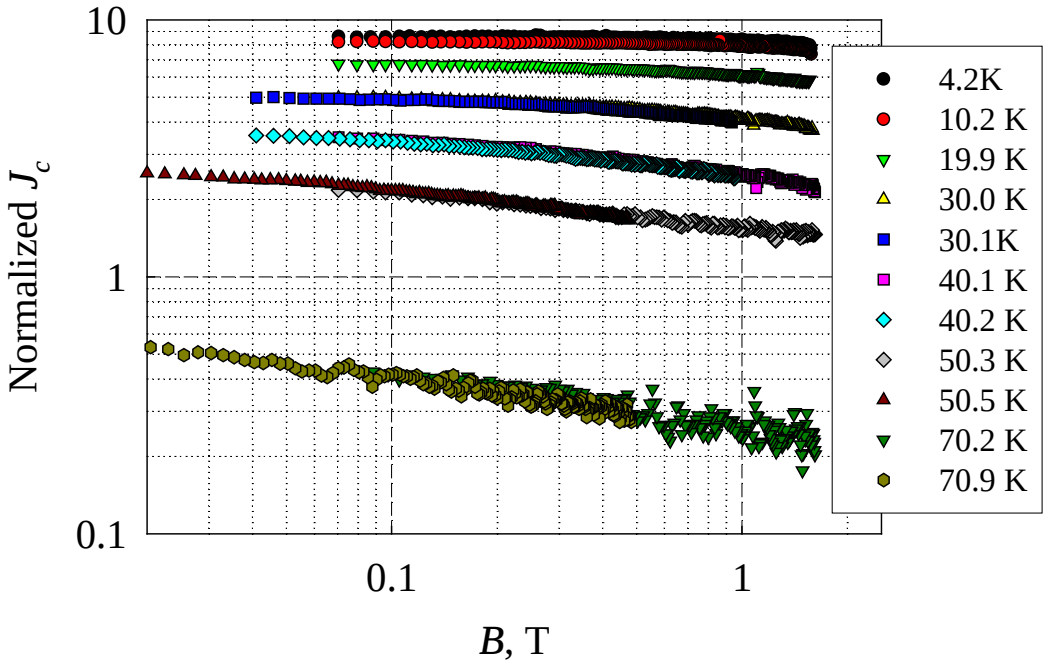

Figure 2.3.4. J_c vs. B for PVD104C at various T.

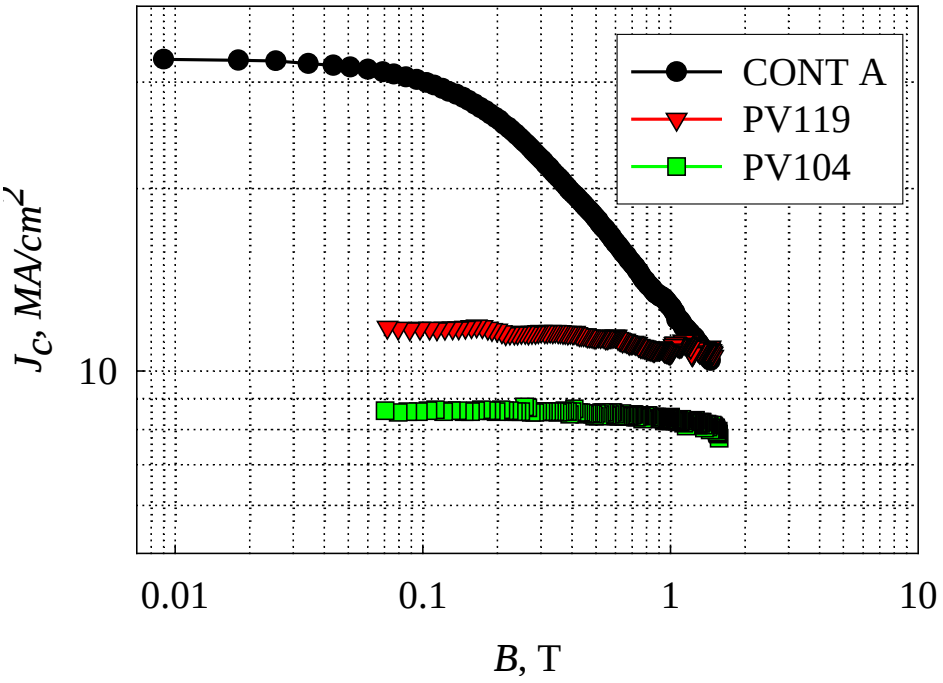

Figure 2.3.5. J_c vs. B for PVD119 and PVD104 at 4.2 K as compared to the control sample.

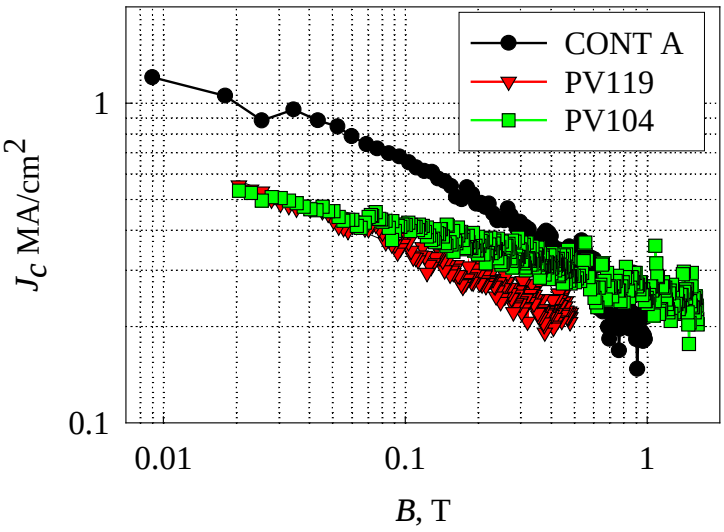

Figure 2.3.6. J_c vs. B for PVD119 and PVD104 at 77 K as compared to the control sample.

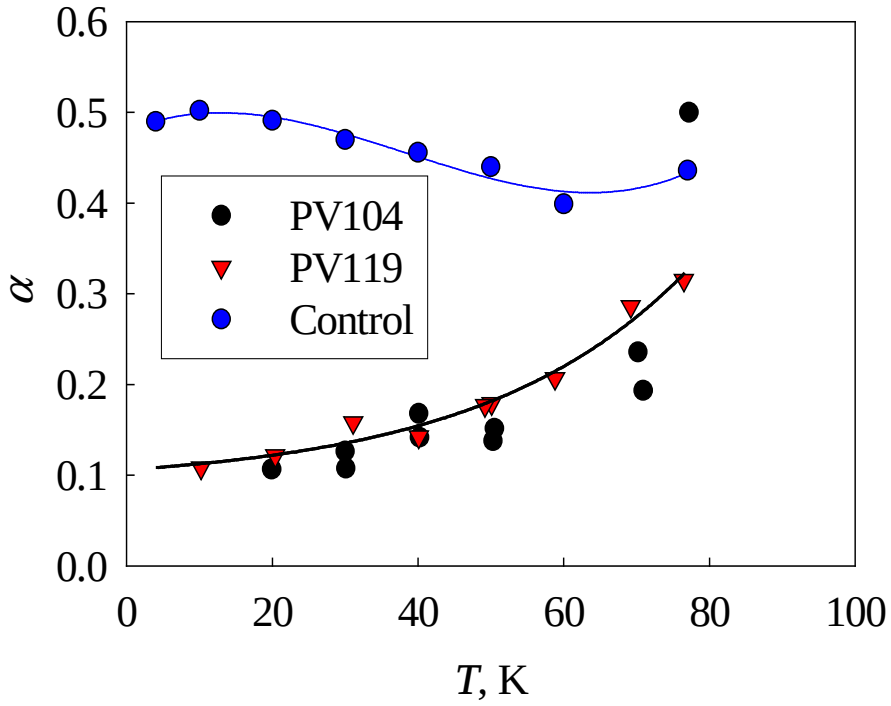

Figure 2.3.7. α for PVD119 and PVD 104 vs the control sample as a function of *T*.

2.4. Magnetization Decay

Magnetization decay was characterized using the ramp rate dependence of the *M-H* measurements of several samples. The samples chosen were the random 211 pinned samples R211A and R211B. These are compared below to previous measurements on a layer 211 pinned sample L211 A and a control sample Cont A. *M-H* loops were measured for samples using ramp rates ranging from 1 mT/s to 70 mT/s. Standard expressions were then used to convert from this ramp rate dependence to an apparent pinning energy, *U*. We then can use the collective creep-vortex glass interpolation expression to describe the results, where

$$U(J) = \frac{U_0}{\mu}\left[\left(\frac{(J_c)}{J}\right)^{\mu} - 1\right] \tag{2.4.1}$$

where μ is the glassy exponent. The U_0 in this case is the "true" pinning well depth, at least for inter-valley flux motion. For comparison to literature, we will convert into pinning potentials in Kelvin, by diving all *U* values by the Boltzmann constant. In that case, we can plot the data as shown in Figure 2.4.1. The activation potential *U* has been normalized by two factors, a temperature scaling factor

$$G = \left[1 - \left(\frac{T}{T_c}\right)^2\right]^{3/2} \tag{2.4.2}$$

and a field scaling factor of $(H/H_0)^{1/4}$. Here H_0 is the lowest field of measurement analysis, 1 kOe.

Figure 2.4.1 shows the R211 samples as compared to the L211 and the control sample. Clearly, the R211 samples have a similar curvature and response to that of the layer pinned sample, although the absolute values of the pinning energies are lower for the R211 samples. It should be pointed out that the R211 samples may not be as optimized as the L211 sample. However, what we generally see is that at lower fields and temperatures where J is high, the apparent pinning energies are higher for the pinned samples. At higher fields and temperatures, where J begins to drop off, the apparent pinning energies are not as high as for the control sample. It must be pointed out here that these are the intra-valley pinning energies, and thus not the sample as the inter-valley pinning energies. Thus, we note that the in-field J_c for the pinned samples is generally better at higher fields, this points to a difference in the intra-valley pinning and the intervalley pinning in the two field regimes.

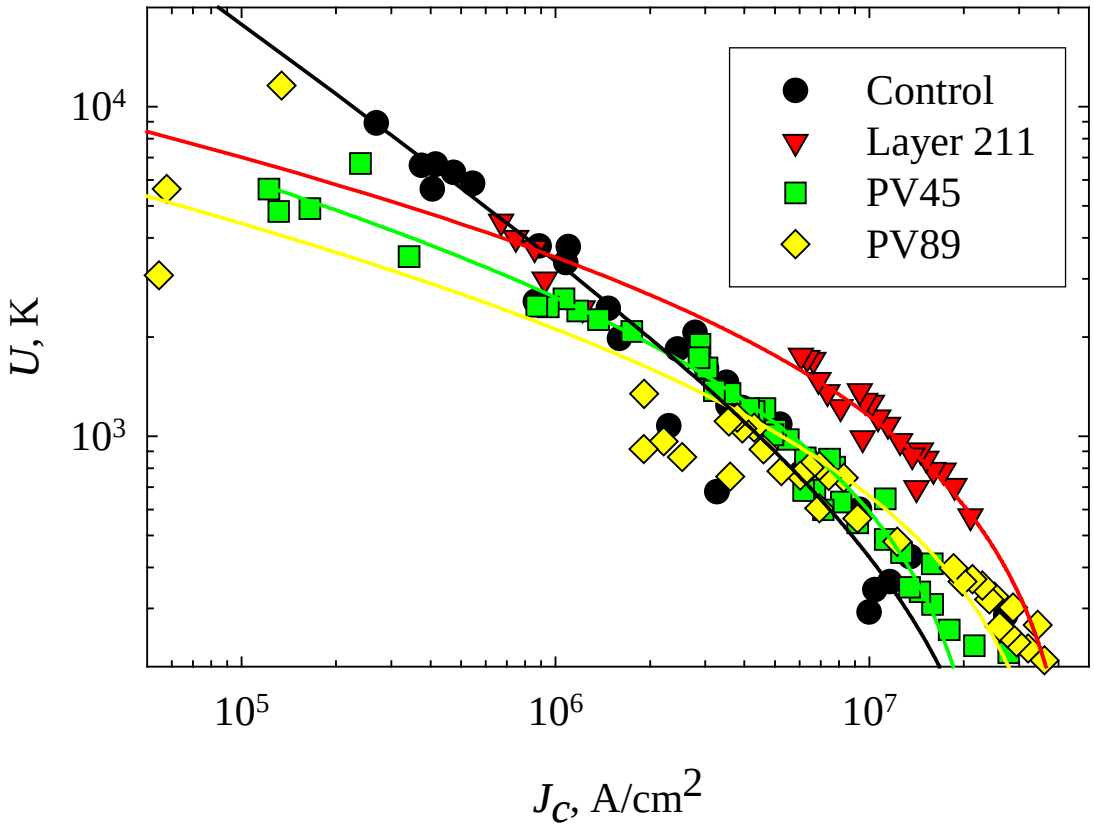

Figure 2.4.1. Apparent Pinning Energy (U) vs J for Control (TJ360), L211A (TJ127), R211A and R211B. Full Fit (using Interpolation Function). U/k_B normalized by the G-function and $B^{1/4}$.

Figures 2.4.2 and 2.4.3 show the R211 samples and the L211 and control sample sets, respectively. They are presented so that the field scaling can be clearly demonstrated. Finally, the parameters coming from the fits to the above interpolation expression are given in Table 2.4.1. There are two items to note from this table. The first is that the intrinsic pinning energy U0 is increased with both layer and random pinning. The second is that the glassy exponent is reduced from approximately 0.7 to near 0.2. This may indicate some kind of flux shear, and would be associated with the difference between inter and intra-valley pinning energies.

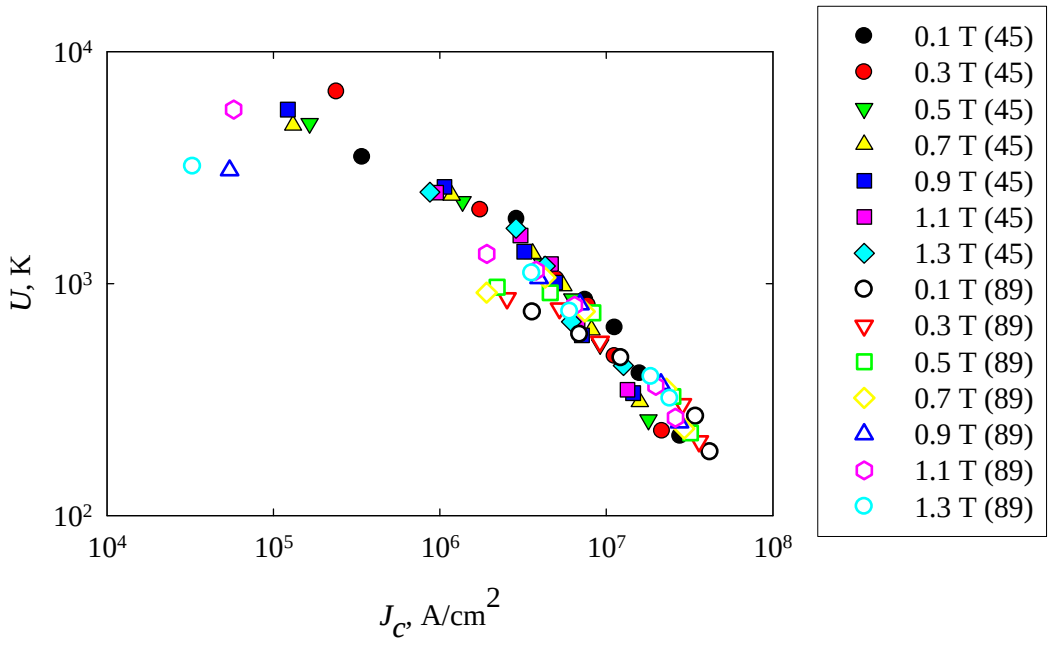

Figure 2.4.2. Apparent Pinning Energy (U) vs J for R211A and R211B. Full Fit (using Interpolation Function). U/k_B normalized by the G-function and $B^{1/4}$. Here different fields are differentiated.

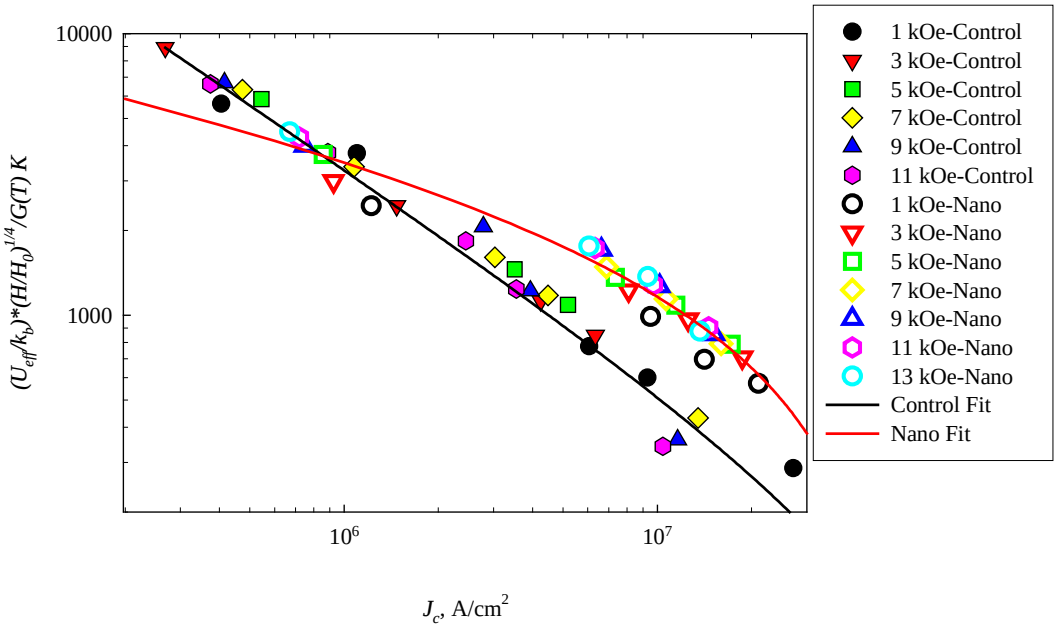

Figure 2.4.3. [Reprinted data for Comparison]. Apparent Pinning Energy (*U*) vs *J* for ContA and L211A. Full Fit (using Interpolation Function). U/k_B normalized by the *G*-function and $B^{1/4}$. Here different fields are differentiated.

Table 2.4.1. Ramp Rate Relaxation based Pinning Energies and Glassy Exponent Values.

Sample	TJ360	TJ127	PV45	PV89
Initial (linear) fit				
U_{c0}, *K*	235	323		
μ	0.75	0.78		
J_c, *MA/cm*^{2}	32.7	50		
Secondary /Interpolation				
U_{c0}, *K*	235 K	618 K	545	365
μ	0.685	0.178	0.22	0.2
J_c, *MA/cm*^{2}	32.7	50	26.3	46.6

3.0. Transport Measurements

Several samples were placed in the variable temperature rig for J_c measurements at field and temperature (see Table 6.0.1, below). Previous measurements on MgB_2 and Nb_3Sn samples have shown that the rig can achieve temperatures up to 77 K and fields out to 12 T; fields out to 15 T should be achievable. Several power supply options are available: (1) up to 200 mA, (2) up to 5 A, and (3) up to 220 A. These power supplies are well behaved. The measurement is lab-

view controlled, and is a DC measurement, taking from 30 sec to several minutes. However, good results have not yet been achieved. The difficulty seems to be the current contacts, attempts to solder have damaged the samples. To date, low power levels of soldering with a fine tip solder and woods metal have been used (being a low temperature solder). Indium solder is available, and it may be used next, although the melting temperature of this solder is higher than that of woods metal, which has been used successfully with coated conductor samples. However, it may be that the Ag layer is simply too thin on these samples to use a solder technique, and thus mechanical contact-based pogo-pins will be the best way to make the contacts. A rig with the capability has been constructed.

4.0. LN_2 –Based Studies

In the second period, a series of studies was performed to increase data precision at 77 K. Various samples were measured. For several samples, the volumes are still being determined, for the remaining quantitative analysis is possible. Figure 4.1 shows the *M-H* for sample TA36 at various ramp rates at 77 K.

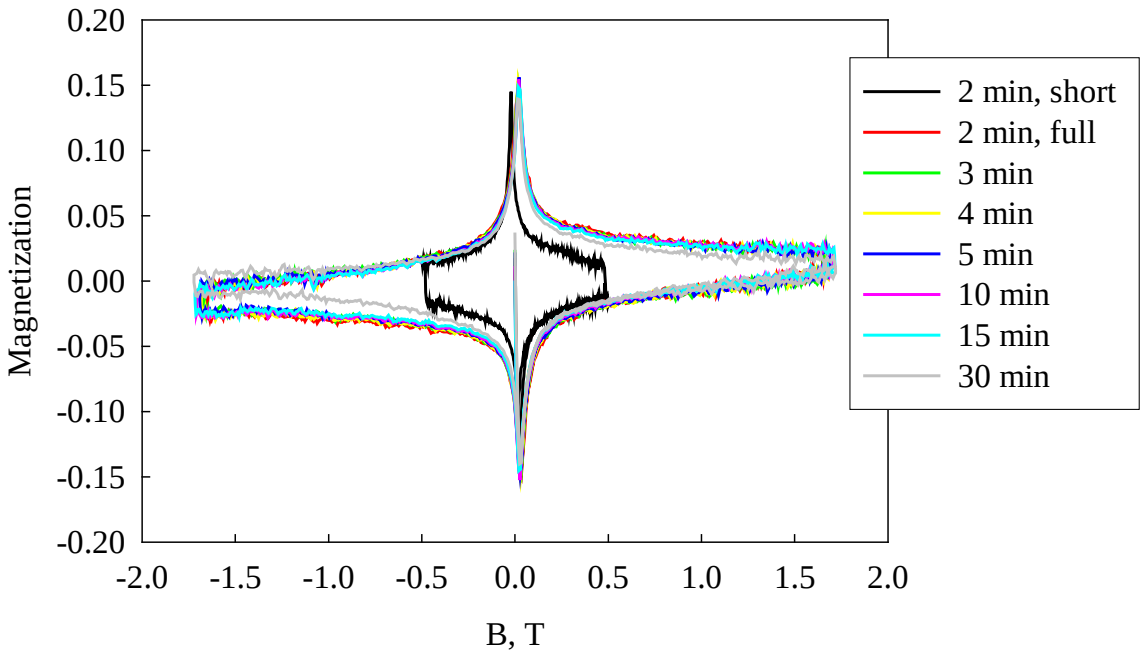

Figure 4.1. *M-H* for TA36 at 77 K in Liquid nitrogen.

These results are given as normalized J_c vs B for various ramp rates in Figure 4.2. Here we see some difference in the overall slope at the longest ramp rate, i.e., α is increased. This is converted into a ramp rate dependence of the magnetization for Figure 4.3 From this, relaxation rates and pinning energies can be extracted. In Figure 4.4, we see the J_c values compared for three different strands. The first is T1130 A; this is a BZO sample, and achieves the highest low

field J_c at about 2 MA/cm^2 77 K. The second is 885, which is a 211 layer sample, achieving about 1.5 MA/cm^2. Lastly, we have the control sample, at about 1 MA/cm^2.

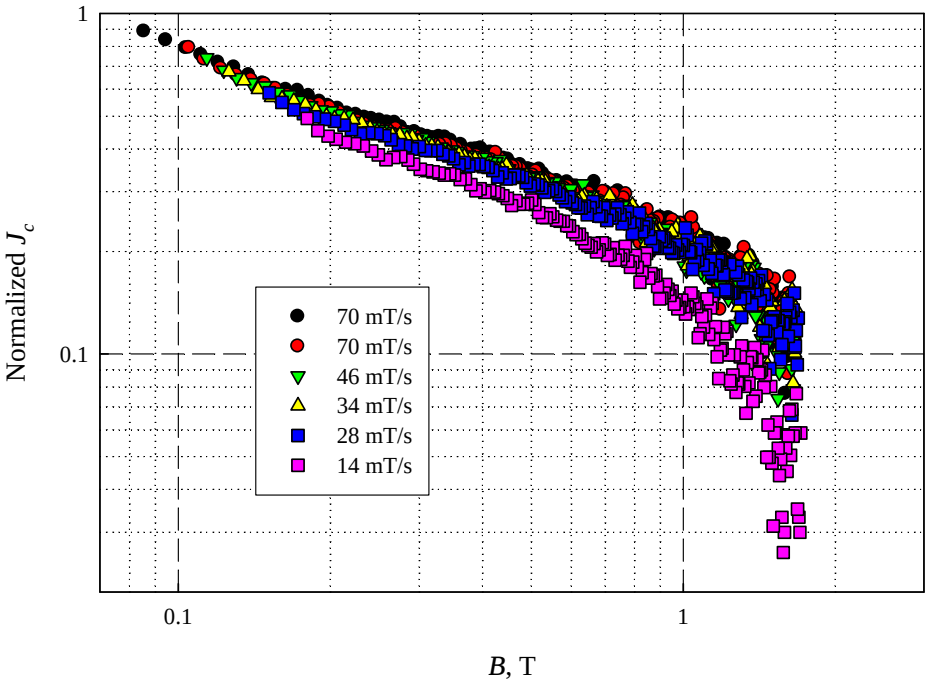

Figure 4.2. Normalized J_c for TA36 for various ramp rates at 77 K in Liquid nitrogen.

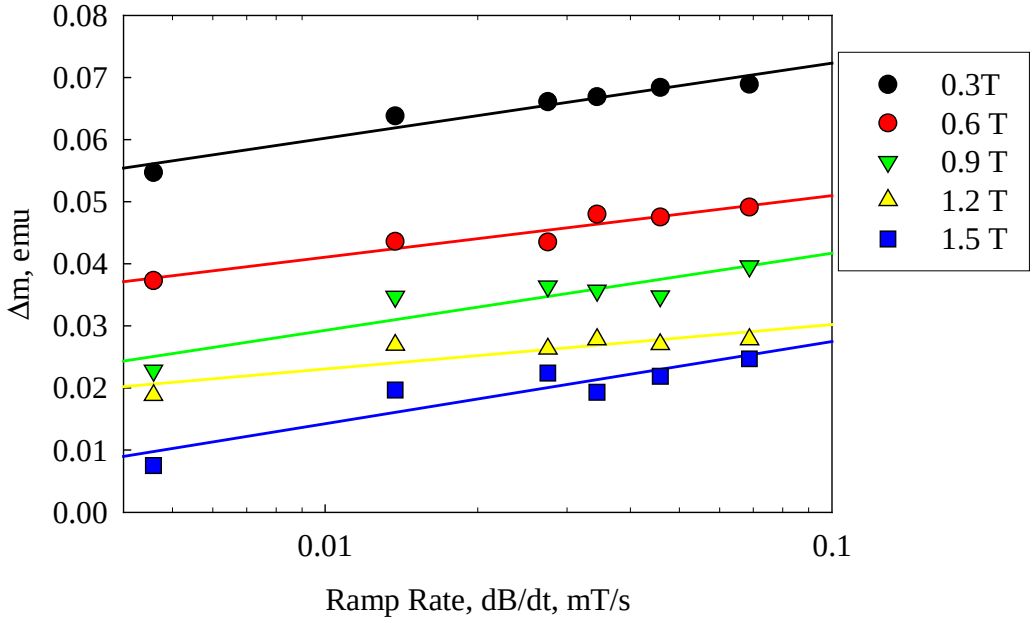

Figure 4.3. Ramp Rate Dependence of *M-H* TA36 at 77 K in Liquid nitrogen**.**

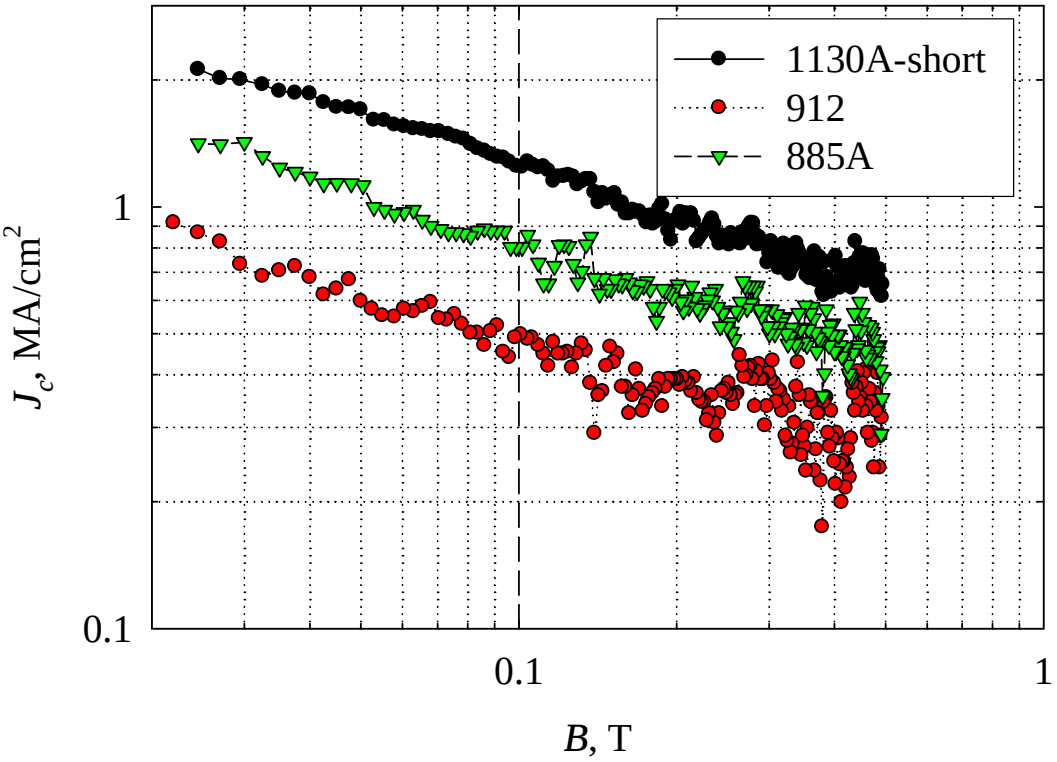

Figure 4.4. 77 K J_c vs B for several samples.

5.0 Third Sample Set Data (Ba-Zr, 211 and Control Samples)

The final set of samples measured was the third set, completing the series of J_c, α, and B^* for all samples available. The samples from the second set are listed again here for comparison purposes. In Table 5.1 the sample specifications are given, in Table 5.2 the results. Figures 5.1 and 5.2 give *M-H* loop results and the normalized J_c vs B for TJ912A, a control sample with 2 MA/cm2 at 77 K self field. Figures 5.3 and 5.4 give the results for TJ885A, a 211 layer sample. Figures 5.5 and 5.6 give the results for TJ1130, which is the Ba-Zr03 doped sample, which has 3 MA/cm2 at self field. Some of the B^* values are given in Table 5.2, along with the values of α at 4.2 K and 77 K. Values of α vs T are also given in Figure 5.7. Here we note that the Ba-ZrO3 sample does well with a-values well below the usual 0.5 for control samples. We also note, however, that TJ912A has an unusually low alpha value for control samples at all temperatures except 77 K.

Table 5.1 Third Sample Set Specifications.

Sample	Δm, emu, 4.2K, 0T	Δm, emu, 77K, 0T	J_c factor (emu to MA/cm^2)	Type	t, μm	Vol., 10^{-6} cm^3	$\langle w \rangle$, mm
PV119D	0.448	0.019	26.3	$BaSnO_3$	0.317	3.45	0.33
PV104C	0.281	0.098	30.6	$BaSnO_3$	0.273	2.97	0.33
TJ376A				Control YBCO			
TJ885A	1.632	?	39.1	$(Y211_{7p}/Y123_{630p})x7$	0.260	2.41	3.18
TJ912A	1.532	.0524	41.5	Control YBCO	0.265	2.26	3.20
J1130A	1.26	0.087	37.6	$Y123_{0.98}/BaZrO_{3\ 0.02}$	0.271	2.51	3.18

Table 5.2. Third Sample Set: 77 K and 4.2 K values for J_{sv}, B^*, and α

Sample	J_{sv}, MA/cm^2 (4 K)	J_{sv}, MA/cm^2 (77 K)	B^*, mT (4 K)	B^*, mT (77 K)	α (4 K)	α (77 K)
PV119D	11.8	0.50	0.4	?	VS	0.50
PV104C	8.60	0.30	0.3	?	VS	0.30
TJ376A						
TJ885A	63.8	?	?	?	0.344	?
TJ912A	63.5	2.17	0.06	?	0.334	0.546
J1130A	47.4	3.28	0.13	?	0.14	0.341

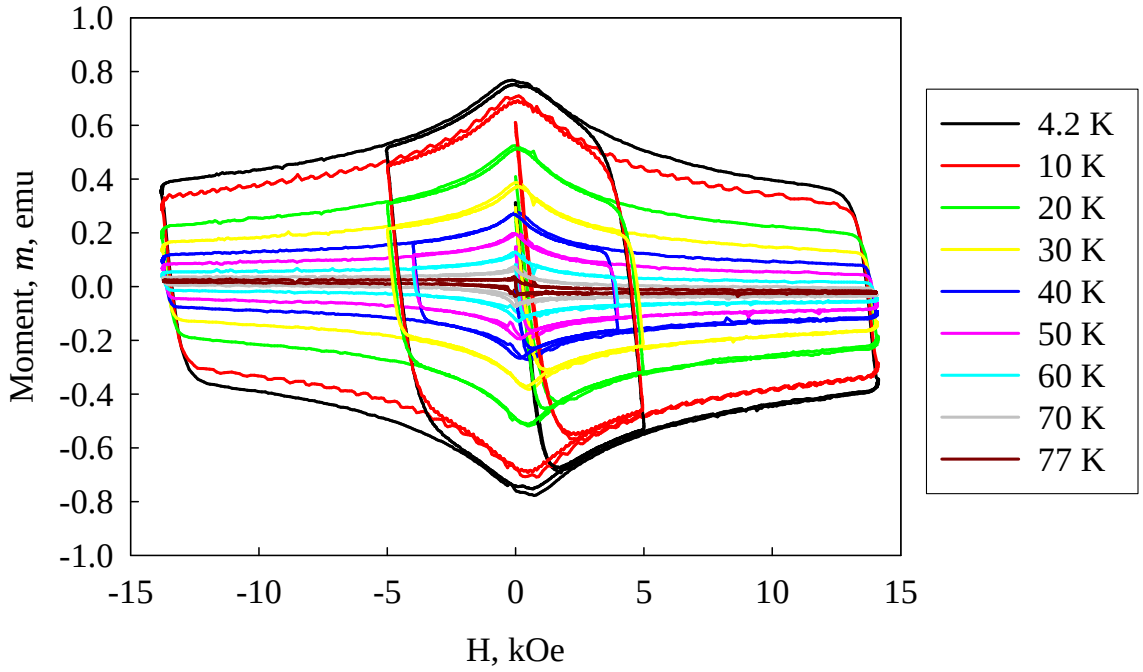

Figure 5.1. TJ912A *M-H* loop measurements.

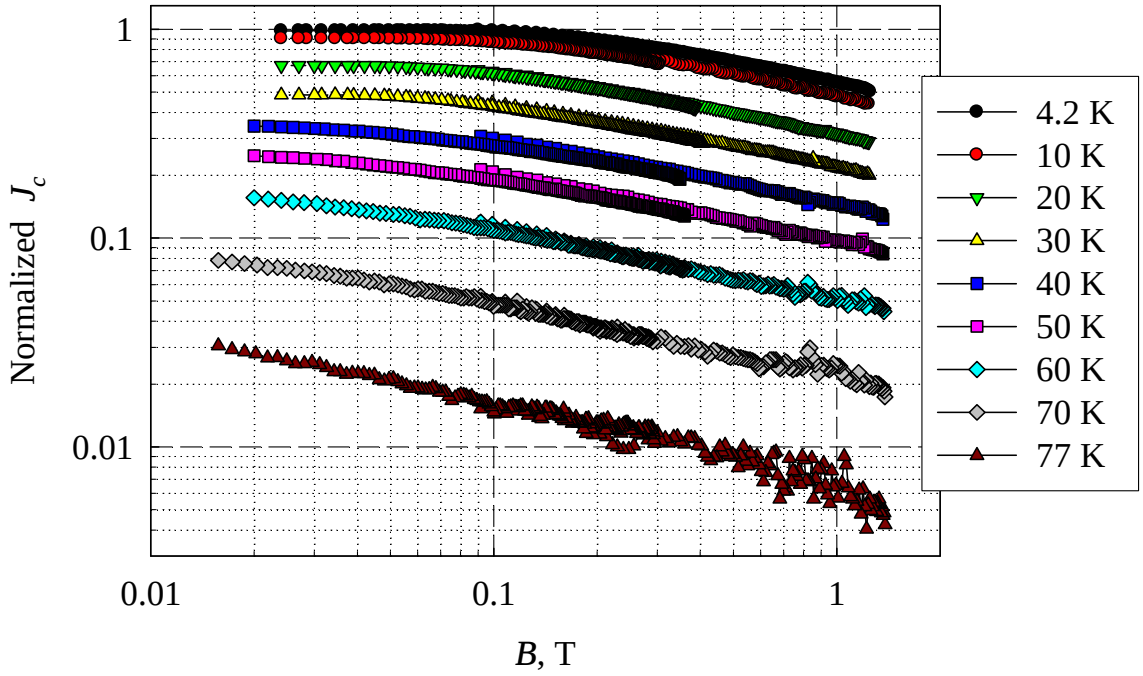

Figure 5.2. Normalized J_c vs B for TJ912A.

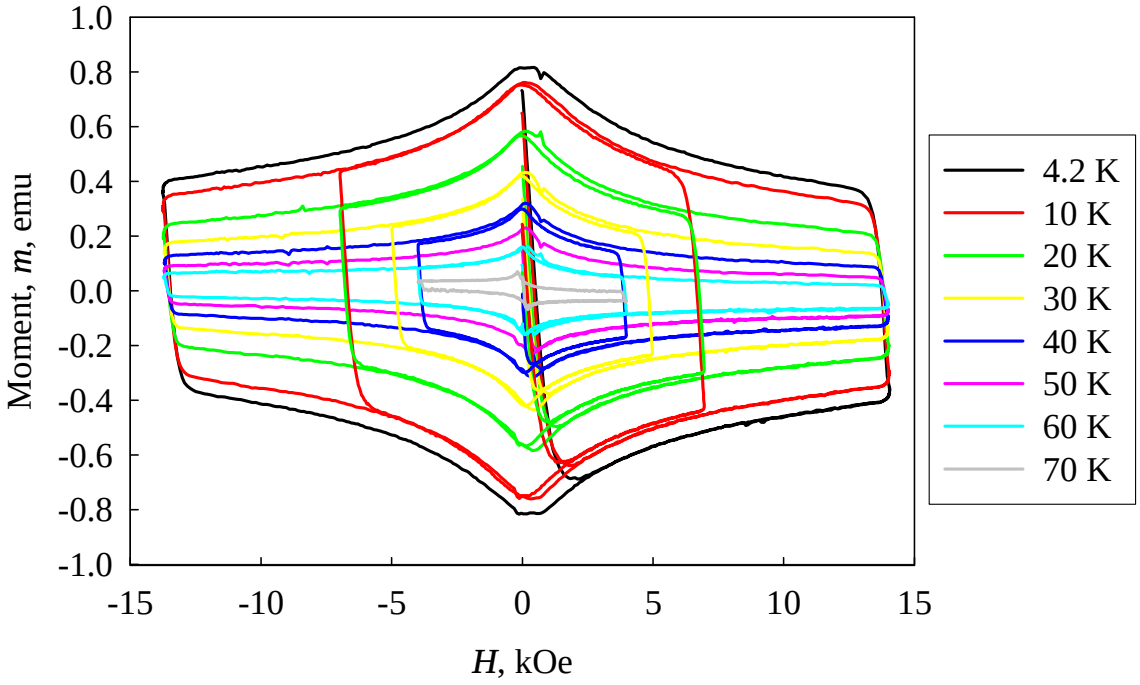

Figure 5.3. TJ885A *M-H* loop measurements.

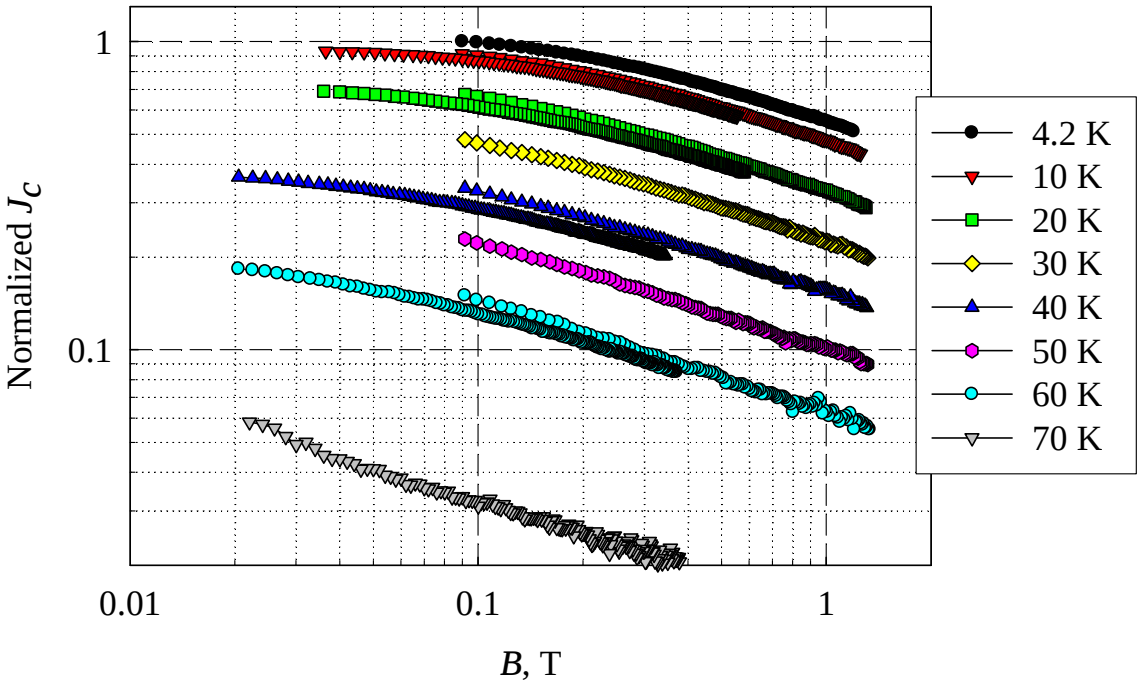

Figure 5.4. Normalized J_c vs B for TJ885A.

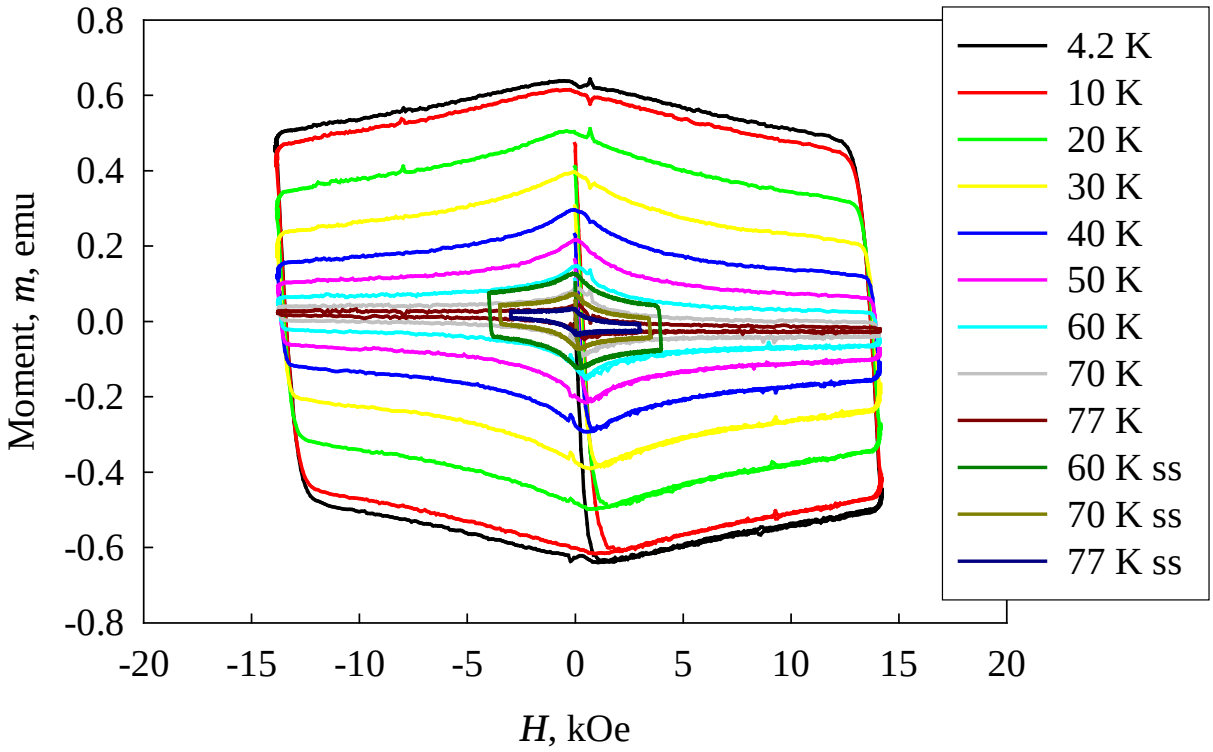

Figure 5.5. *M-H* for TJ885A.

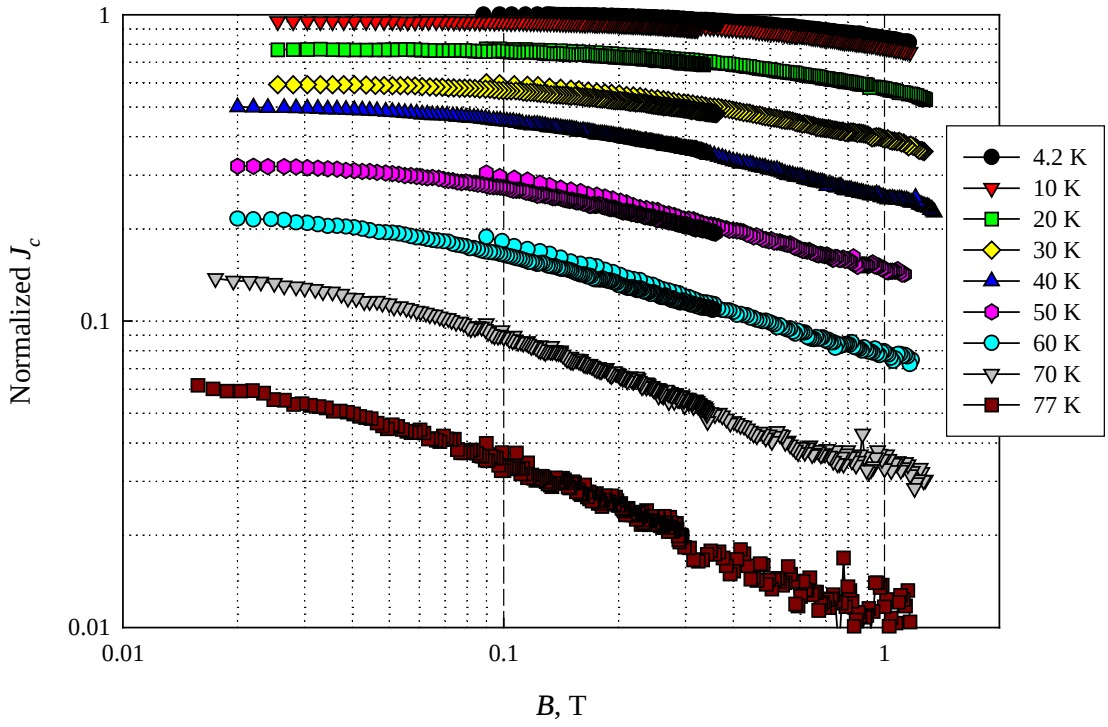

Figure 5.6. Normalized J_c vs B for TJ1130.

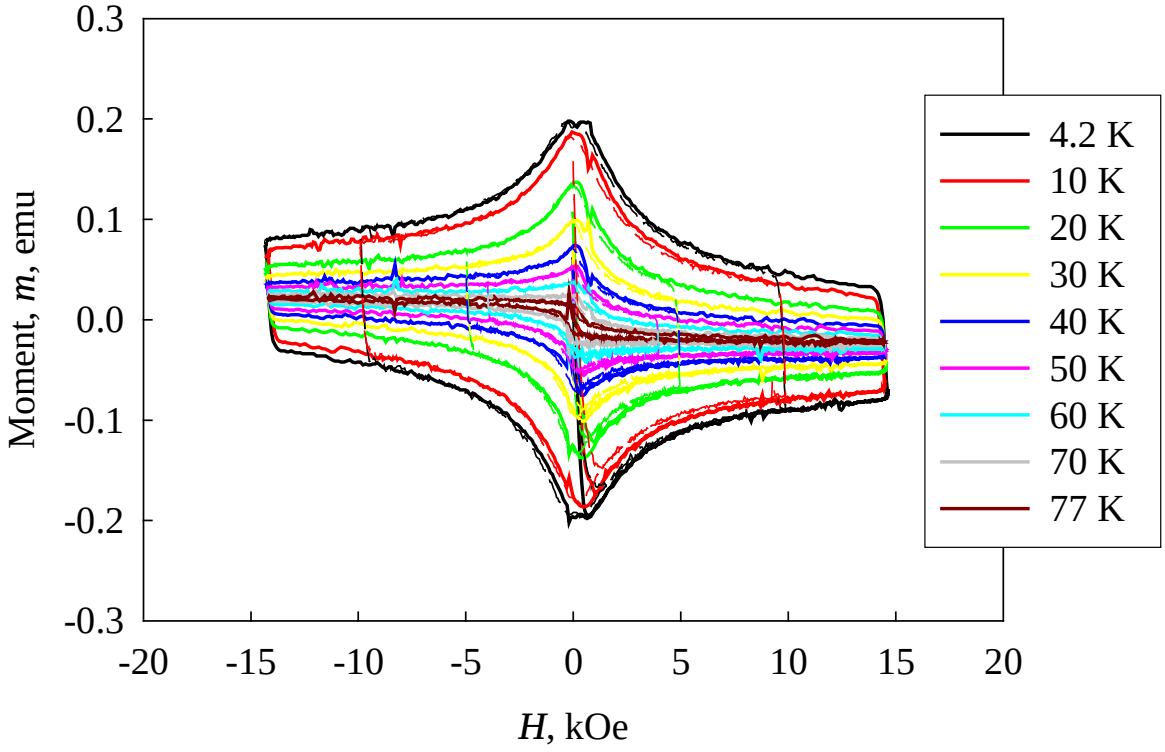

Figure 5.7. *M-H* for TJ376A

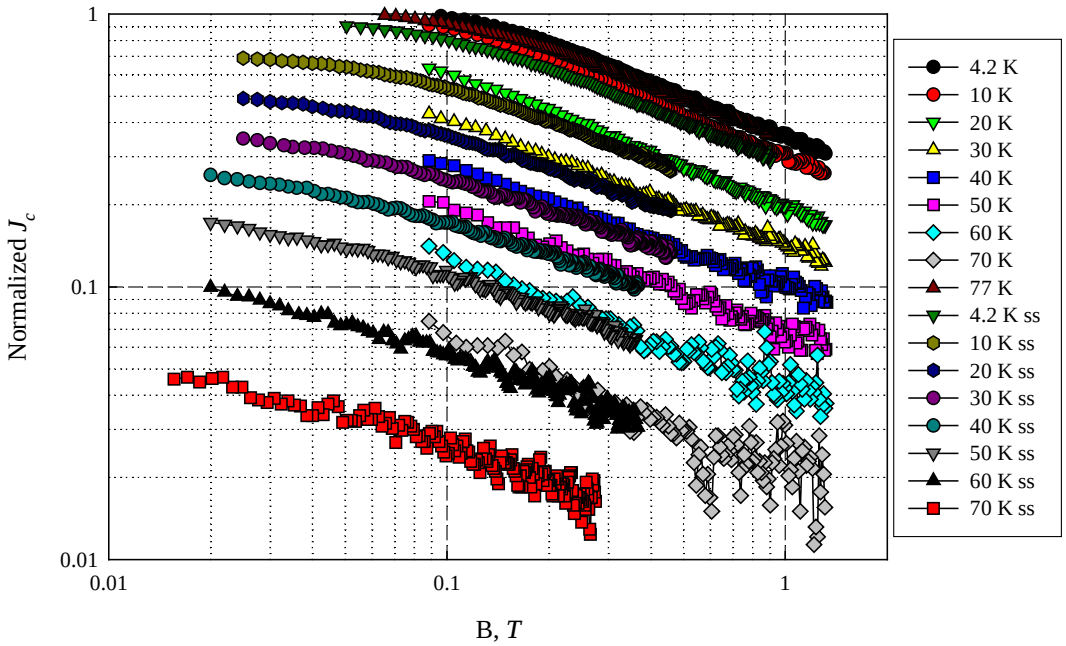

Figure 5.8. Normalized J_c vs B for TJ376A

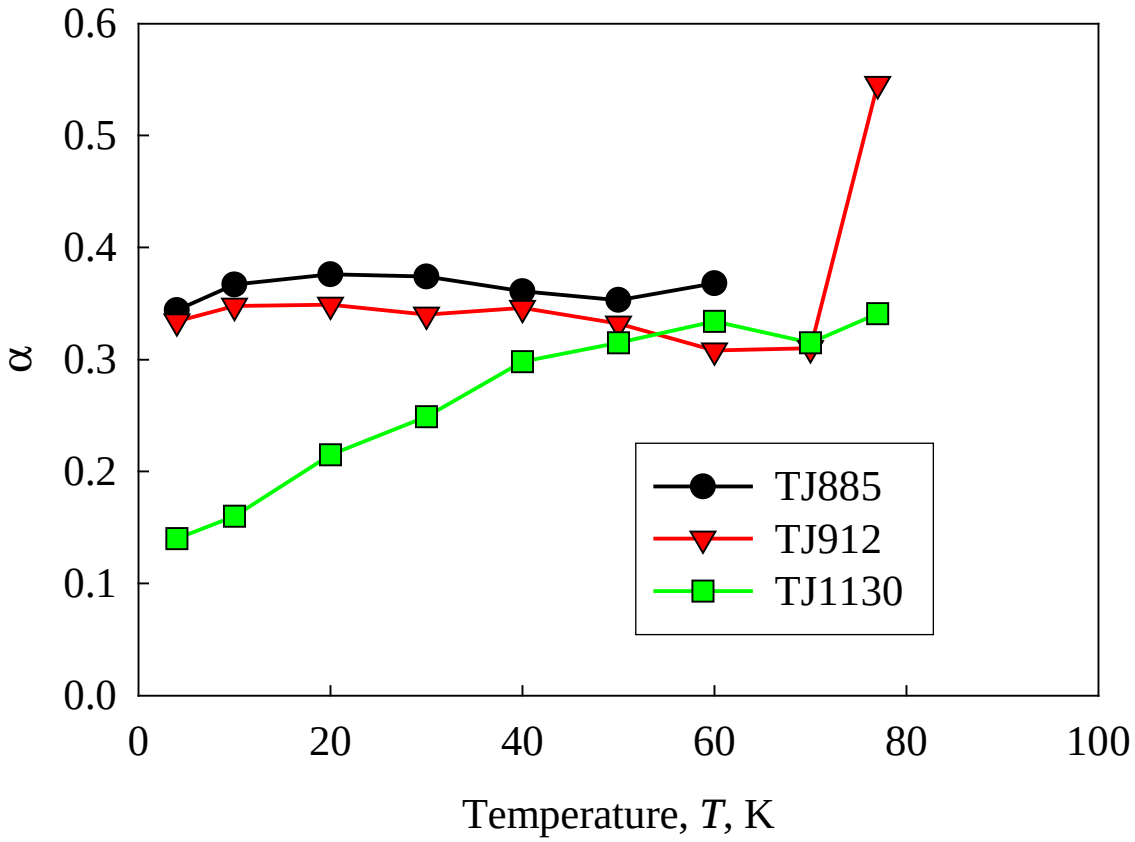

Figure 5.9. α for various samples.

7.0 *B**-Related Critical State Artifacts

While in principle there is a low field regime where the fields can be sufficiently low that each vortex is pinned by an individual pinning site (the single vortex regime), and in that regime, the field dependence should be zero, in practice this regime is difficult to access without the situation being complicated by artifact. This is because the critical state related to either transport or magnetic measurements (arguably worse for magnetic measurements) obscures the very-low-field response of the sample. Nevertheless, some differences are seen with doping in this regime, and it is worth considering whether we can find a way to extract the artifact from the data, and leave ourselves with a measurable single vortex field boundary. Here we denote crossover from the single vortex regime, the accommodation field, by B^*. and its associated apparent crossover, the apparent accommodation field, by B^*_{app}. Knowing, then, the theoretical expectation for J_c, which is that it is field independent below B*, and drops off as $B^{-\alpha}$ above this field, we will use

$$J_c = \mu_0 A(B_{loc}+B^*)^{-\alpha}$$

as the form for J_c. This has the proper form since as $B \rightarrow 0$, $J_c \rightarrow AB^{*-\alpha}$

8.0. Summary and Conclusions

The following points can be brought out as initial considerations.

1. Pinning is enhanced by artificial structures and doping, including in this case, layer 211 pinning, random 211 pinning, minute doping, Ba-Sn-O additions, and Ba-Zr-O additions.
2. Higher Field properties are frequently improved (α suppressed to 0.2)
3. Samples made at similar times show enhancement in *Jsv* with nano-additions – but recent control samples are just as high in *Jsv* – GB effects?
4. B^* enhanced with nano-pinning
5. These PLD films, intentionally nano-pinned or not, are 3-D, rather than 1-D or 2-D in nature (arguing against 3D-2D transition – for these samples – both pinned and control).

In particular, it is worthwhile to point out that some of the samples with the lowest alpha-values have suppressed self field J_c. In addition, there is noticeable variation and scatter, with some control samples having very good properties. Sample TJ912A is one such sample, and exhibits both high self field transport at 4.2 K and 77 K, but also, surprisingly, a suppressed α. The reasons for this are unknown. Nevertheless, it is apparent that nano-pinning is useful in increasing the average transport properties of YBCO thin film samples.

Appendix A. List of YBCO samples by group.

Sample List	Group (Objective)	Status					
		H_{irr}, B_{c2} vs T		LN_2 J_c		Variable T J_c	
TA39	Trans J_c	Now					
TA42	Trans J_c						
TA45	Trans J_c	Damage					
TJ388	Trans J_c	Damage					
TJ925	Trans J_c						
		VSM J_c	B^*, α, J_{sv}	Field Ramp U	Mag Decay U	LN_2 repeat	Other
TJ127C	VSM	X	X	X	X		X-radia
TJ360B	VSM	X	X	X			
TJ376A	VSM	X	X			**X**	
TJ531A	VSM	--	--	--	--	--	at AFRL
TJ804A	VSM	X	X				
TJ834A	VSM	X	X				
TJ885A	VSM	X	X			**X**	
TJ912A	VSM	X	X			**X**	
TJ978B	VSM	X	X				
TJ1130A	VSM	X	X			**X**	
PV45	VSM	X	X	X	--	--	at AFRL
PV89	VSM	X	X	X	--	--	at AFRL
PV119D	VSM	X	X			Now	
PV104C	VSM	X	X				
JK06B-C	VSM	X	X				
JK08B-T	VSM	X	X				
PV95E	VSM		--	--	--	--	--
PV95F	VSM		--	--	--	--	--
PV15A						**X**	
TA36						**X**	

Electrical Control of the Thermodiffusive Instability in Pre-Mixed Propane-Air Flames - DRAFT

S. D. Marcum and D. L. Wisman
Department of Physics, Miami University, Oxford, OH 45056

B. N. Ganguly
Air Force Research Laboratory, Wright-Patterson AFB, OH 45433

Abstract

This work focuses upon the effects of DC electric fields on the stability of downward propagating, atmospheric pressure pre-mixed propare-air flames under experimental conditions that provide close coupling of the field to the flame. With the appropriate electrode geometry, modest applied voltages are shown to drive a stable conical flame front (laminar flow) first into a wrinkled laminar flamelet (cellular) geometry, and further toward either a highly turbulent distributed flamelet regime or a collective oscillation of the flame front. Applied potentials up through 5 kV over a 40-mm gap encompassing the flame front have been used to force that transition sequence in flames with equivalence ratios between 0.8 – 1.3 and flow velocities up to 1.7 m/s. Experiments designed to characterize the field-induced changes in the geometry of the reaction zone and the stability of the resulting turbulized flame are reported. The former is quantified by combustion intensity enhancement estimates derived from high-speed two-dimensional direct and spectroscopic imaging, and Fourier transforms of current and flame-front optical signal waveforms are used to quantify observed field-induced oscillatory combustion modes. The flame fluid mechanical response to the applied field, brought about by forcing positive flame ions counter to the flow, drives the effective flame Lewis number below unity and on to levels below the critical value for the onset of the thermodiffusive instability, even near stoichiometric conditions. Possible field-driven flame ion recombination chemistry that would inject light reactants near the burner head and precipitate the onset of a thermodiffusive instability is proposed and discussed. Electrical measurements are also reported which establish that minimal electrical power input is required to produce the observed flame instabilities, and which allow estimates of the level of deficient light reactant necessary to turbulize the flame. This effect could serve as a potentially attractive means of controlling flame fluid mechanical characteristics and validating combustion instability models.

Introduction

Under the experimental conditions of interest here, a pre-mixed flame that exhibits a stable, laminar flame front deceptively masks the fact that the stability is due to the simultaneous action of competing instabilities. The temperature (density) difference across the thin flame front, and the concomitant thermal expansion, together with the significant differences between the thermal diffusivity of the mixture and mass diffusivities of various light reaction limiting species, give rise to the hydrodynamic[1,2] (1-Darrieus'38, 2-Landau'44) and thermodiffusive[3,4] (3-Zeldovich'49, 4-Markstein'49) instabilities, respectively. The former is a fluid mechanical effect, while the latter is driven by flame chemistry that, heretofore, has been associated with flames near flammability limits. This study shows that applied electric fields that are well coupled to near-stoichiometric hydrocarbon flames can force the flame chemistry modification necessary to cause the transition from laminar to highly turbulent flame fronts due to an *induced* hydrodynamic instability.

Spontaneous instability (or self turbulization) of a premixed flame front arises when combustion conditions cause either the competition between those instabilities to be sufficiently diminished, or the instabilities to act in concert to destabilize the flame. For example, beginning with a stable laminar flame with a near stoichiometric mixture, increasing the overall flow rate sufficiently (e.g., cold flow Reynolds numbers on the order of 2500 and above) will cause the flame front to take on an unsteady wrinkled geometry indicating that the hydrodynamic instability is increasingly dominating over the competing thermal diffusive instability. Increasing the flow rates still further will cause the common observation of the flame front spontaneously exhibiting increasing levels of turbulence. Increasing nozzle burner flow rates are generally accompanied by increasingly turbulent flame fronts due to the introduction of shorter wavelength disturbances that are closer to the optimum (critical) wavelength for amplification by the coupled hydrodynamic and thermodiffusive instabilities.

Theoretical analyses of the thermodiffusive instability were developed first by Sivashinsky[5] (Sivashinksy'77) for adiabatic flames, and then by Joulin and Clavin[6] (C&F'79) for non-adiabatic flames. Following the qualitative descriptions of that instability of Zeldovich[3] and Markstein[4], and the initial attempt at quantification of observed effects by Barenblatt, Zeldovich and Istratov[7] (BZI'62), they showed that a laminar flame would spontaneously exhibit a thermodiffusive instability and take on a cellular structure when the Lewis number (***Le***) of the combusting mixture becomes smaller than a critical value[5,6] which is slightly less than one. Such a condition will occur if the diffusivity of the species limiting the reaction exceeds the thermal conductivity of the combusting mixture, i.e. the Lewis number of the deficient light reactant will determine the effective global Lewis number of the flame.

Some of the more important combustion species and their associated Lewis numbers[8,9] (8-Smoke, 9-Chen) have been published. Collectively, such listings suggest a limited number of light reactants that would be capable of causing such a diminution of the effective Lewis number of a flame, specifically, atomic hydrogen and oxygen and the hydroxyl radical, which have species Lewis numbers of 0.18, 0.70 and 0.73, respectively. Thus, control of the concentration and distribution of those radical species within a combusting mixture would allow manipulation of the thermodiffusive instability.

Early observations of self turbulization[3] in hydrogen-air flames due to the thermodiffusive instability occurred in lean mixtures, and somewhat later in rich hydrocarbon-air[4] mixtures. To date, self turbulization of downward propagating flames of those fuels oxidized by air still requires equivalence ratios far from stoichiometric.

The results of the work reported here shows that electric-field-***induced*** turbulization of propane-air flames can be accomplished arranging the appropriate electrode geometry and applying modest applied potentials over the interesting range of equivalence ratios spanning stoichiometric. The effects are best described from a combustion dynamics viewpoint as a continuously variable electric-field-induced diminution[10] (10-Marcum, Ganguly) of the flame Lewis number from typical values (≥ 1), past the critical flame Lewis number[11,12] (0.7-0.9) (11-Sivashinky, 12-Law), to thermal-diffusive-instability dominated values below the critical Lewis number at the higher applied potentials. Possible field-driven flame-ion chemistry process that could produce the observed effects are presented and discussed.

Governing Theory

Sivashinksy's review[11](11-Sivashinsky, Phys. Fluids), and the references therein, describe the development of the understanding of flame pattern formation and turbulence due to coupled

hydrodynamic and thermodiffusive instabilities. Sivashinsky has written an expression for the net instability growth[11] rate due to the combined effects of the hydrodynamic and thermal-diffusive instabilities. That relation is shown in Equation 1 below, where S_L is the laminar flame speed, k is the wavenumber of the disturbance, D_{th} is the thermal diffusivity of the mixture, and the factors Ω_o and Ω_1 are given by Equations 2 and 3, respectively.

$$\sigma = \Omega_0 S_L k - \Omega_1 D_{th} k^2 \qquad [1]$$

$$\Omega_0 = \frac{\sqrt{\varepsilon + \varepsilon^2 - \varepsilon^3} - \varepsilon}{1+\varepsilon} \qquad [2]$$

$$\Omega_1 = \frac{\varepsilon(1-\varepsilon)^2 - \varepsilon \ln \varepsilon (2\Omega_0 + 1 + \varepsilon)}{2(1-\varepsilon)[\varepsilon + (1+\varepsilon)\Omega_0]} - \frac{\varepsilon(1+\Omega_0)(\varepsilon+\Omega_0)\beta(1-Le)}{2(1-\varepsilon)[\varepsilon+(1+\varepsilon)\Omega_0]} \int_0^{1/\varepsilon - 1} \frac{\ln(1+\xi)}{\xi} d\xi. \qquad [3]$$

In the latter two relations, ε is the ratio of the burned to the unburned gas densities, and β is the Zeldovich number,

$$\beta = \frac{E(T_b - T_u)}{RT_b^2},$$

where E is the activation energy of the for the fuel mixture of interest, T_b and T_u are the burned and unburned gas temperatures, respectively, R is the gas constant and Le is the global flame Lewis number.

The first term in Equation 1 represents the contribution to the net instability growth rate due to hydrodynamic instability present in the flame. Hydrodynamic instabilities tend to dominate most all flows at high flow velocities (or high Reynolds numbers), and it has been shown experimentally[13] that as the flame speed (S_L) increases, so does the hydrodynamic instability of a premixed combusting flow. Under standard conditions, the factor Ω_o depends only on the flame temperature since that determines the density of the burned gas. The second term in Equation 1 represents the effects of the thermal-diffusive instability. For growth rates that are small or negative, the flame is stable to any disturbing influence. Thus, a stable laminar flame is the result of a balance between the competing influences of the hydrodynamic and thermal-diffusive instabilities.

Normally, the thermal-diffusive instability is dominant only under conditions very non-optimal fuel/air ratios, which naturally result in lower combustion temperatures (e.g. fuel rich hydrocarbon flames, or fuel lean hydrogen flames). For fixed flow conditions over an interesting range of lean and rich equivalence ratios near optimal, we have previously demonstrated electrical control over the magnitude of thermal-diffusive instability[10] in light propane-air flames via a process we have called electrical pressure. The theory outlined above suggests that the electrical pressure effect acts to lower the Lewis number of the flame.

Mathematically, setting Ω_1 in equation 3 equal to 0 and solving for Le, yields the critical Lewis number (Le_c) of a flame. If the Lewis number drops below Le_c by any influence, it is clear that the overall sign of equation 3 would become negative. In turn, below Le_c the instability growth rate of

Equation 1 ceases to be moderated by the thermal diffusive instability and the flame becomes unstable to any disturbance. The electrical pressure effect allows continuous control of effective flame Lewis number over a wide range, and thus electrical control of stable laminar geometries allowing de-stabilization toward thermodiffusive cellular geometries and ultimately to highly turbulent states.

Flame-Field Interactions

The first detailed theories on the effect of electric fields on flames were introduced in the 1960's by Lawton and Weinberg[14]. They coined the term "ionic wind" to explain the effects of an applied field on a flame that they and others observed. This ionic wind was the drag that was experienced by the selective targeting of the field on the ions. Their theory predicts a maximum current density of 250 $\mu A/cm^2$ when using an applied voltage of approximately 30 kV.[14] The maximum electric-field-induced pressure change predicted by this theory is only 0.0004 atm[14,15], which suggests that the ionic wind is not responsible for the large changes in flame structure that we see in our work. We have shown[10] previously that current densities comparable to the maxima stated for the ionic wind can be achieved with much smaller applied voltages. Further, the associated observed effects on the flame[10] are much more pronounced that observed in the ionic wind experiments.

We propose the following alternate explantion: the electric field acts directly on the highly localized, chemiionization-derived H_3O^+, HCO^+ and other positive ions in the flame reaction zone, significantly increasing their mass diffusivities and thereby modifying the Lewis numbers of the ionic species. The observed result is a diffusive-thermal instability, typical of flames with global Lewis numbers less than one; it is most likely caused by the production of H atom and OH radicals by the dissociative recombination of $H_3O^+ + e \rightarrow H_2O + H$ or $H + H + OH$, and $HCO^+ + e \rightarrow H + CO$ near the burner head, which is the cathode surface for the polarity of the applied voltage. The increased differential diffusional velocity of the reaction zone positive ions strongly affects the bulk flame speed, and the instability results in the flame front collapsing toward the burner head and taking on a wrinkled laminar geometry.

Experimental Apparatus and Procedures

The principal experimental flame diagnostics used to gauge the efficacy of externally applied voltage-to-flame coupling and quantify the degree and time scale associated with the flame dynamic response to a DC bias voltage are shown in Figure 1. The burner used was a commercial atomic absorption type (Perkin-Elmer) with a modified cylindrical (44-mm diameter x 50 mm) stainless steel head. The premixed gas inlet orifices consisted of five concentric rings of close spaced 0.8-mm diameter holes, the largest ring having a 17-mm diameter. The hollow, 25-mm diameter portion of the burner head is filled with multiple layers of fine mesh wire screen in series with the standard burner body to ensure complete fuel/air mixing. The lower electrode was a patch of 100-mesh stainless steel wire cloth stretched across the inlet array. Both array/electrode arrangements produce axially symmetric flows, as evidenced by the highly symmetric conical laminar flame fronts produced at moderate flow speeds (< 2 m/s).

The dc current/voltage characteristics of the electrically stressed flames were recorded with the burner grounded and the upper electrode biased up to + 5 kV (Glassman, Model 6516A). Such measurements were used to quantify the voltage-to-flame coupling of the various electrode arrangements, and thus guide efforts to improve the coupling efficiency. The anode used for all work reported here was a perforated, stainless steel disk suspended 40-mm above the burner, and always

above the tip of the unperturbed inner come. This version of upper electrode geometry provides a simple parallel-plate-like electrode geometry at the cost of perturbing the burnt gas flow field downstream of the flame front

The apparatus used to record high-speed (100 μs exposures) two-dimensional images of the flame's response to as functions of applied voltage, fuel-to-air ratio and flow rate is shown schematically in Figure 1. DC fields were applied to the flames through a 500 kΩ ballast resistance connected between the bias supply and the anode, and a 100 kΩ current sense resistor was placed between the floating burner and ground. The images used to document the flame's dynamic response to the DC bias were made using an intensified, gateable CCD camera (Princeton Instruments Model ICCD-576). Direct (broadband) images, and images produced by the major flame emitting species (chemiiexcited CH, OH and C2) were recorded with the aid of interference filters (10 nm bandpass).

Flame front motions were monitored by imaging the reaction zone onto the end of an optical fiber (0.5-mm diameter) using the simple single lens system shown. Either broadband, or spectrally filtered signals entering the fiber were detected using a photomultiplier tube (RCA 9265). Variations in light signals, as well as any fluctuations in the bias circuit current were digitized and processed using an oscilloscope (LeCroy Waverunner).

The fuel and air flow rates were set and monitored by simple ball-float type flow meters (rotameters, Cole Parmer) capable of flow rates up to 2.7 standard liters per min (slm) for propane, and up to 66 slm for air. Typical flow rates used for results reported here were between 5 and 25 slm for air, with the corresponding flow rates for propane varied to provide the desired equivalence ratio. For most data reported here, the flow velocity was approximately 1.7 m/s, and the range of equivalence ratios used during this study was between 0.8 and 1.3. The propane used was a standard commercial grade, and the air was supplied by a small, portable compressor.

Results and Discussion

Electrical Measurements

To enhance an electrically driven process it is advantageous to provide effective coupling of the power source to the load. Here, bulk circuit current/voltage (I/V) characteristics are the most straightforward electrical measurements that can be made to assess the efficacy of external bias voltage-to-flame coupling. I/V characteristics for a flame with total pre-mixed fuel/air flow rate of 21 slm (flow velocity = 1.7 m/s, and an equivalence ratio of 1.2, is shown in the upper plot of Figure 2. The points marked A, B and C refer to bias potentials near which major modifications of the reaction zone geometry occurred. Point A locates the potential needed to cause the inner cone to be reduced in height and be made even more stable than the low velocity laminar flow inlet stream allows. For the conditions used to produce the IV curve of Figure 2, the cold flow Reynolds number was near 2000. Point B indicates the potential needed to cause the inner cone to distort noticeably from cone shape and begin large amplitude (audible) oscillation. Point C denotes the potential that must be applied to depress the reaction zone close to the burner head and induce more random motion of the reaction sheet typical of strong turbulence. Another significant feature of the IV characteristic is that there is no indication of reaching a saturation current up to the maximum applied potential of 5 kV. Also note that the maximum electrical power input is on the order of a few watts.

The effect of varying the fuel flow rate at a fixed air flow rate of 20 slm (essentially the same flow velocity of 1.7 m/s) and a fixed bias of 3 kV is shown in the bottom plot of Figure 2. The data shown essentially maps the combined variation in flame conductivity and coupling to the external circuit as a function of equivalence ratio. The peak power input occurs at an equivalence ratio slightly above 1.1. If the bias potential is reversed, the current drawn at a 3 kV bias is less than 10 μA indicating a diode like response of the flame to external bias. Points marked A, B and C here mark equivalence ratios for which the flame front is collapsed near the burner head, undergoing significant collective oscillation, and recovering from collapsed near the burner head, respectively.

Although the diode-like behavior has been noted previously[1,3,4], the magnitude of the current drawn with the disk anode is better than an order of magnitude higher than previously reported for electrically biased pre-mixed hydrocarbon flames. All results reported here are derived from experiments that use the grounded burner, disk anode (forward bias) arrangement. Another significant feature of the I/V curve of Figure 1 is that a only a small amount of electrical input power is required to produce the significant flame front modifications observed during this study. The largest current drawn under the conditions cited above is approximately 600 μA at 5 kV forward bias, or roughly 3 W of electrical input power applied to a burner that is generating heat at the rate in excess of 1 kW. Also of note is that although the general trend is towards some saturation current, saturation is not reached up to the maximum voltage (+5 kV).

High-Speed Two-Dimensional Imaging

The typical flame response to an applied electric field is shown in Figure 3. The total flow rate was once again 21 slm and the equivalence ratio used was 1.2. The effect of a bias potential of 5 kV is compared to the unperturbed laminar flame in each set of high-speed images shown in Figure 3. Figure 3a shows a direct image of the flame using an exposure time of 500 μs. That time exposure is sufficiently short to essentially freeze all motion of the turbulent flame front in the case of the field-perturbed flame. Adjacent to each photo is a set of intensity profiles that correspond to the emission intensity as a function of distance from the flame axis for the six horizontal bands marked in the corresponding image. The increase in combustion intensity is clearly indicated by comparison of the plots.

The following three sets of images and intensity plots, Figures 3b, 3c and 3d, correspond images taken through 10-nm bandpass filters that select for CH, C_2 and OH emissions respectively. The exposure times used for those images were 10 ms for each of the CH and C_2 image sets, and 20 ms for the OH images. Note that the flame front is sharply imaged in all cases (a-d) for the unbiased flame. However, the 10- and 20-ms exposure spectral images show increasing blurring due to the rapid turbulent motion of the cellular reaction sheet. The corresponding emission intensity profiles show that *all* major chemiluminescent flame emission have the same response to the applied field, i.e. they all indicate a strongly enhanced combustion intensity as the applied field induces a strong instability in the normally laminar flame front.

The imaging results suggest that the effective fluid mechanical response of the flame is altered by the applied field, resulting in an increased flame speed. To achieve the conservatively estimated doubling of the flame speed shown in Figure 3 by preheating[16] the gas mixture would require a temperature increase of 150 K. Assuming a volume flow rate of 16 slm, effecting such a temperature change would require approximately 65 W of electrical power – greatly in excess of the maximum electrical power input of roughly 3 W shown by the I/V curve of Figure 2. By comparison with the

preheating the gas mixture to increase flame speed, the electric-field-induced flame speed modifications observed here are better than a factor of 20 more energy efficient than preheating the gas.

Flame Oscillation Characterizations

The final data reported here are derived from measurements of the current and flame front optical signal oscillations. Figure 4 shows a series of fast Fourier transforms (FFTs) of broadband and spectrally filtered flame front emissions, as well as the FFT of the oscillating current drawn from the external bias supply. Again, the experimental conditions are the same as those used for the imaging data shown in Figure 3 (21 slm overall flow and equivalence ratio of 1.2) except that the bias used was only 4 kV (corresponding to point C in the IV curve of Figure 2).

The top left FFT of Figure 4 shows the very low amplitude, featureless power spectrum of the flame's broadband emissions under zero bias. It indicates stable laminar flow. With a 4 kV bias the flame front is driven into a large amplitude resonate-like oscillation with a fundamental frequency near 300 Hz and harmonics ranging up to 1.8 kHz. Essentially the same responses are seen again from broadband emissions and those corresponding to chemiexcited CH, C_2 and OH. Further, the current passing through the flame exhibits a power spectrum that is essentially identical to that of the flam front emissions. The details of the cause(s) of the observed oscillatory response of the flame to and externally applied *DC bias* are currently unknown.

Conclusions

Under the flow conditions studied here, with the upper electrode in place but no potential difference applied to the flames, stable laminar pre-mixed propane/air flames with highly symmetric right circular cone geometries result. Clearly under such conditions Fick's law applies, strong temperature gradients give rise to significant thermal diffusion[16], and stable conical flame fronts result. Such a stable laminar flame has small negative curvature everywhere on the flame front, with the largest curvature at the apex of the laminar inner cone. The primary results of this study shows that with effective voltage-to-flame coupling, normal bias of such flames at modest voltages rapidly converts (within ~ 5 ms) the stable flame to one that is quite unstable and unable to support a laminar combusting flow. The flame speed is substantially increased, and the resulting wrinkled laminar flame exhibits strong negative curvature. One way to interpret the destabilizing effect of the external electric field is that it gives rise to an additional *electric pressure* induced diffusion effect which significantly increases the flame speed. A possible mechanism by which such a minority flame constituent as the flame ions (1 part in roughly 10^7 in terms of overall density, or a peak density in the range[14,17] of 10^{10} – 10^{11} cm^{-3}) can effect such a dramatic change in flame geometry follows.

The electric field can act directly and effectively only on the highly localized, chemiionization-derived positive ions in the flame reaction zone. The resulting force on the flame ions significantly increases their mass diffusivities and thereby lowers the ionic species Lewis numbers. The observed result is a diffusive-thermal instability[18,19], typical of flames with global Lewis numbers less than one and negative curvatures[23-25]. The electric-field enhanced differential diffusional velocity of the reaction zone positive ions toward the burner head strongly affects the bulk flame speed[18,19,23-25], and the instability causes the burning speed of the negatively curved[23] reaction zone to increase and collapse toward the burner head taking on a wrinkled laminar geometry. Analogous to very similar flame front modifications produced by changes in ambient air pressure[22], the overall process is labeled an *electric*

pressure effect. In some cases pocket formation results with clear indications of turbulence, suggesting that electrically stressed hydrocarbon flames can be quite sensitive to *electric pressure*.

That such increases in flame speed can occur without concomitant increases in flame temperature can be understood from two points of view. Considering that the input electrical power to the flame in the experiments reported here is on the order of one-one thousandth of the rate at which chemical energy is converted to heat in the flame, conservation of total energy would certainly speak against the possibility of any global temperature increase for the flame. Essentially, since the flame ions are present in such minor concentrations in hydrocarbon flames, even though they could be forced to diffuse by the field into regions where reactant concentrations differ significantly from those of laminar flow, their total contribution to the enthalpy of the mixture may be insufficient to produce any modification in the flame temperature. From the point of view of observed flame structure changes, Echekki and Chen[24] noted that for similar flames the net enhancement in the volumetric heat release and fuel consumption rates is primarily due to the increase in flame surface area by wrinkling. They noted that the heat release and fuel consumption per unit flame area is reduced relative to the laminar flame.

Future work will focus on the scaling effects of the increased applied voltage to the flame to determine the extent to which the laminar flame speed could be increased by increasing the electric pressure to the propane/air flame.

References

1. G. Darrieus, “Propagation d’un front de flame: assai de theorie des vitesses anomales de deflagration par developpement spontane de la turbulence,” communication presented at La Technique Moderne, 1938.
2. L. D. Landau, “On the theory of slow combustion,” Acta Physicochim, URSS **19**, 77-85 (1944).
3. Y. B. Zeldovich, “Theory of combustion and detonation of gases,” U.S.A.F. Technical Report No. F-iTS1226-IA (GDAM A9-T-45), pp. 41-52, Wright-Patterson AFB, Dayton, Ohio, May 1949. (Translation from Russian, originally published in 1944).
4. G. H. Markstein, “Cell structure of propane flames burning in tubes,” J. Chem. Phys. **17**, 428-429 (1949).
5. G. I. Sivanshinky,”Diffusional-thermal theory of cellular flames,” Combust. Sci. Technol. **15**, 137-145 (1977).
6. G. Joulin and P. Clavin, “Linear stability analysis of non-adiabatic flames diffusional combustion model,” Combust. Flame **35**, 139-153 (1979).
7. G. I. Barenblatt, Y. B. Zeldovich and A. G. Istratov, “On heat and diffusion effects in stability of laminar flames,” J. Appl. Mech. Tech. Phys., **4,** 21-26 (1962). (In Russian. Translation needed.)
8. M. Smooke: *Reduced Kinetic Mechanisms and Asymptotic Approximations for Methane-Air Flames*, Lecture Notes in Physics, Springer-Verlag, Berlin 1991.
9. J. H. Chen, T. Echekki and W. Kollmann, “The mechanism of two-dimensional pocket formation in lean premixed methane-air flames with implications to turbulent combustion,“ Combust. Flame **116**, 15-47 (1999).
10. S. D. Marcum and B. N. Ganguly “Electric field induced flame speed modification,” Combust. Flame **143,** 27-36 (2005).
11. G.I. Sivashinsky “Instabilities, pattern formation and turbulence in flames,” Ann. Rev Fluid Mech.**15**, 179-199 (1983).

12. J. Yaun, Y. Ju, and C.K. Law, "Coupled hydrodynamic and diffusional-thermal instabilities in flame propagation at subunity Lewis numbers," Phy Fluids **17**, 1-10 (2005).
13. C. Clanet and G. Searby "First experimental study of the Darrieus-Landau Instability," Phys. Rev. Lett. **80,** 3867-3870 (1998).
14. J. Lawton, F. Weinberg "Maximum ion currents from flames and the maximum practical effects of applied electric flames" Proceedings of the Royal Society **227** (1964) pp 468-497.
15. Pedersen, R Brown "Simulation of electric field effects in premixed Methane flames" Combustion and Flame **94** (1993) pp 433-448.
16.

Figure Captions

Figure 1. Experiment configurations for high-speed two-dimensional imaging, current/voltage and flame oscillation measurements.

Figure 2. Typical current/voltage characteristic measured for field-modified flames (upper plot). Note that the total electrical power input is quite small (~ 3 W at the highest bias). The lower plot shows the variation of flame current with equivalence ratio for fixed air flow rate and external bias.

Figure 3. High-speed two-dimensional images of the flame response to a 5 kV bias taken using broadband and spectrally filtered flame front light emissions. The corresponding intensity profile plots show the degree of combustion intensity enhancement that is achieved.

Figure 4. Current and flame front optical signal oscillations quantified by computing the power spectrum of the time-varying signal.

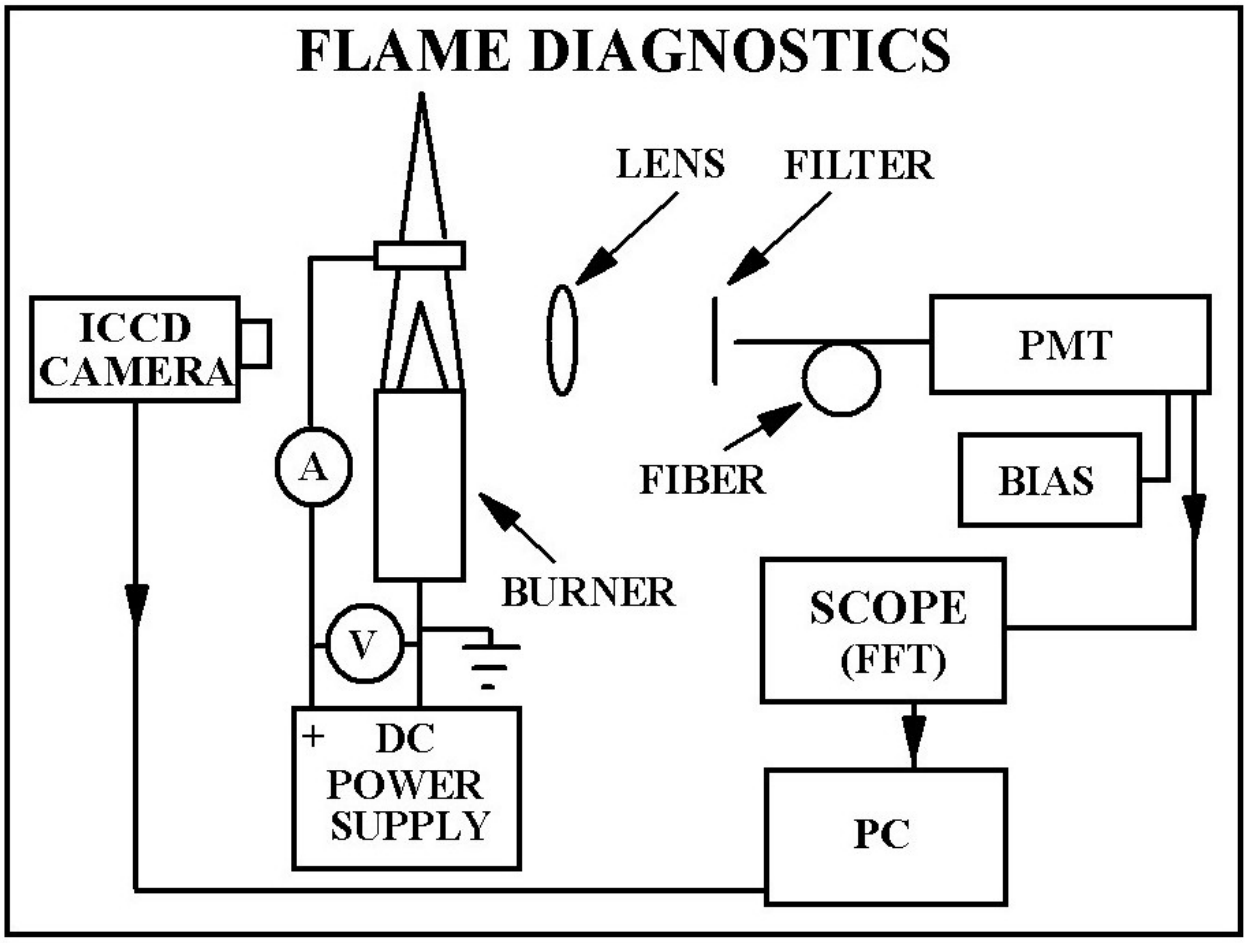
FLAME DIAGNOSTICS
LENS
FILTER
ICCD CAMERA
PMT
A
FIBER
BIAS
BURNER
SCOPE (FFT)
V
+ DC POWER SUPPLY
PC

Figure 1:

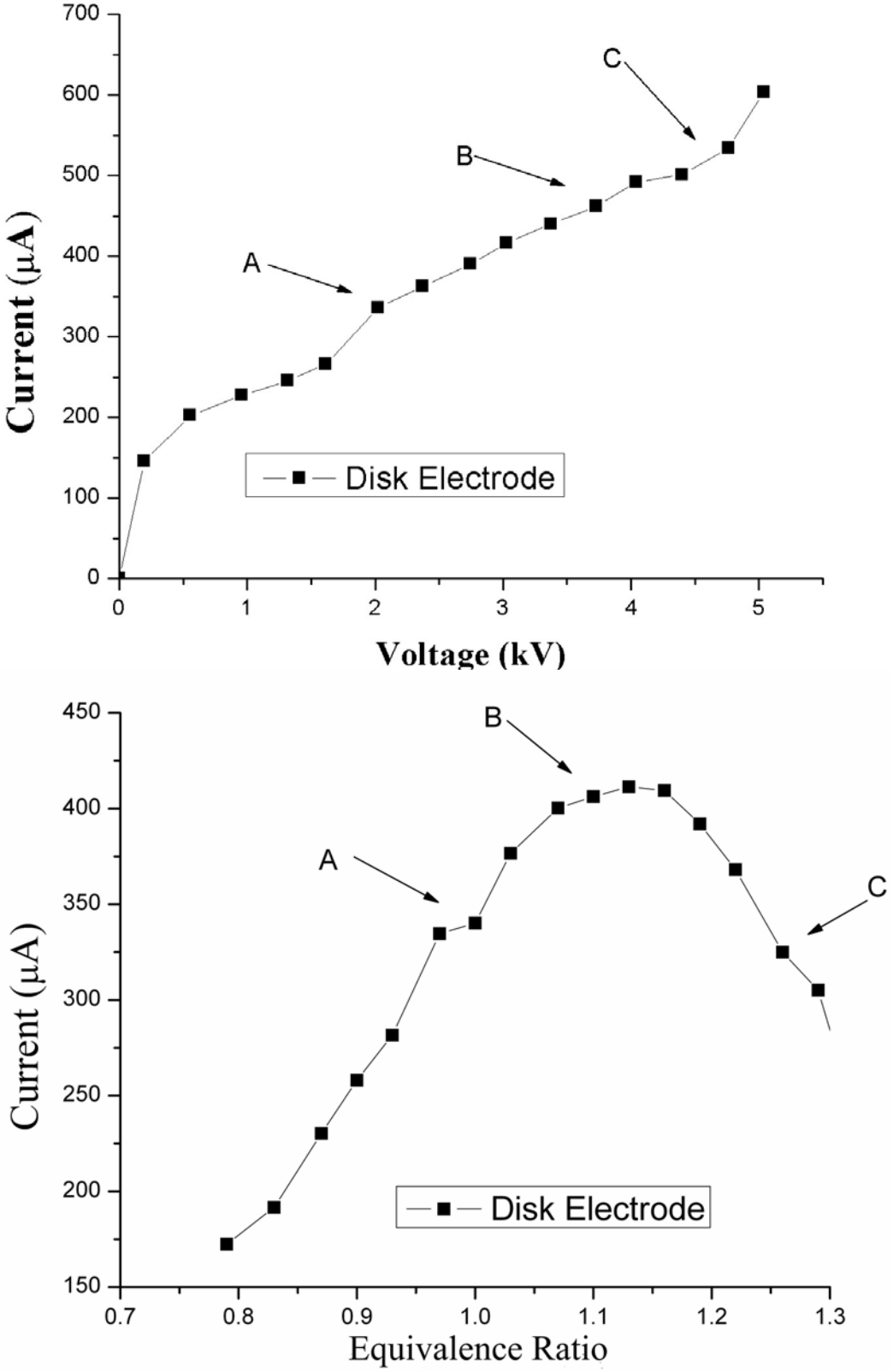
Current (μA)
Voltage (kV)
Disk Electrode
A
B
C
Current (μA)
Equivalence Ratio
Disk Electrode
A
B
C

Figure 2:

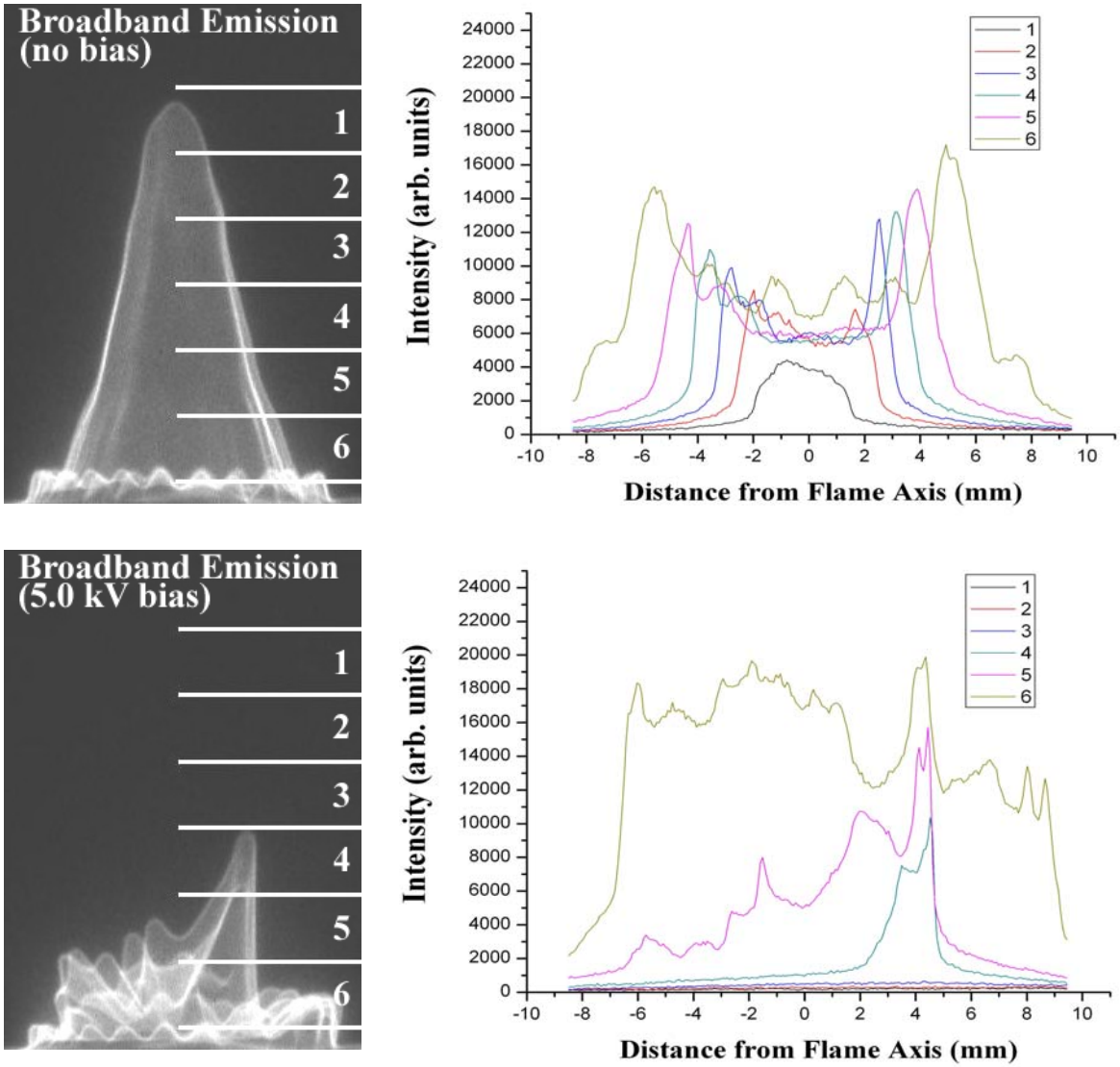
Broadband Emission
(no bias)
1
2
3
4
5
6
Intensity (arb. units)
Distance from Flame Axis (mm)
Broadband Emission
(5.0 kV bias)
1
2
3
4
5
6
Intensity (arb. units)
Distance from Flame Axis (mm)

Figure 3a:

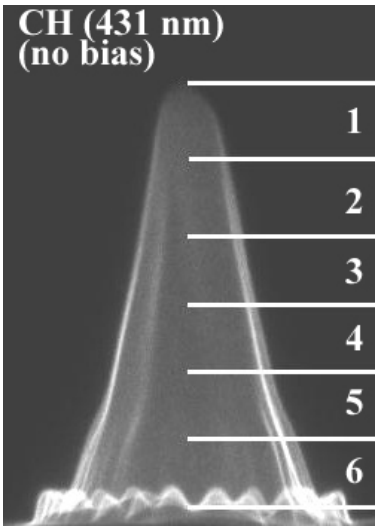
CH (431 nm)
(no bias)
1
2
3
4
5
6

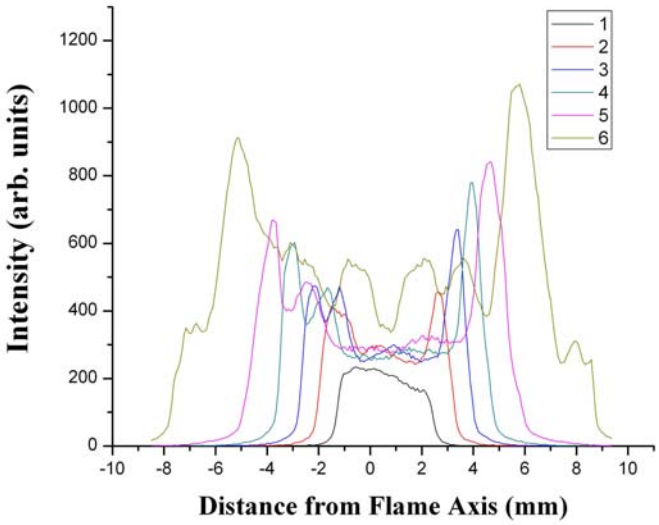
Intensity (arb. units)
Distance from Flame Axis (mm)
1
2
3
4
5
6

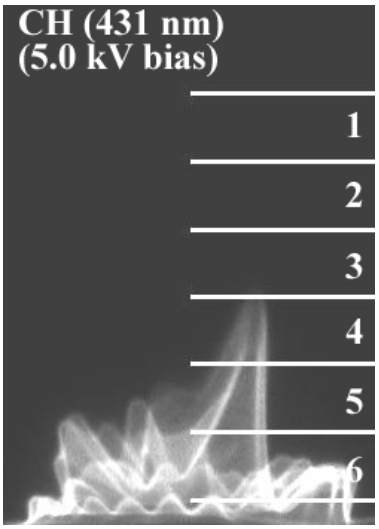
CH (431 nm)
(5.0 kV bias)
1
2
3
4
5
6

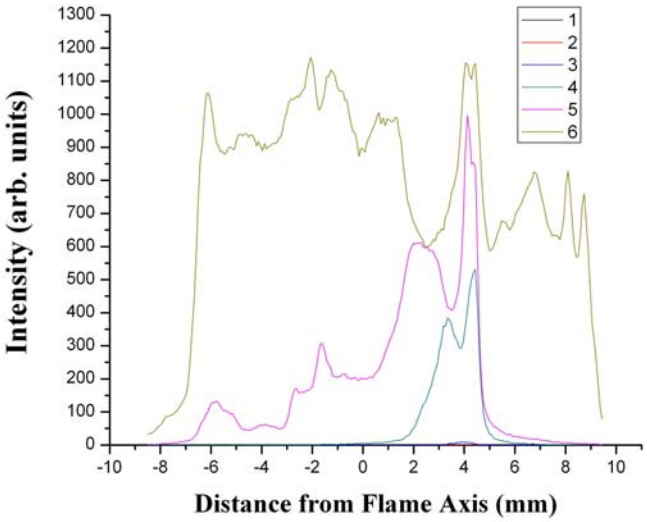
Intensity (arb. units)
Distance from Flame Axis (mm)
1
2
3
4
5
6

Figure 3b:

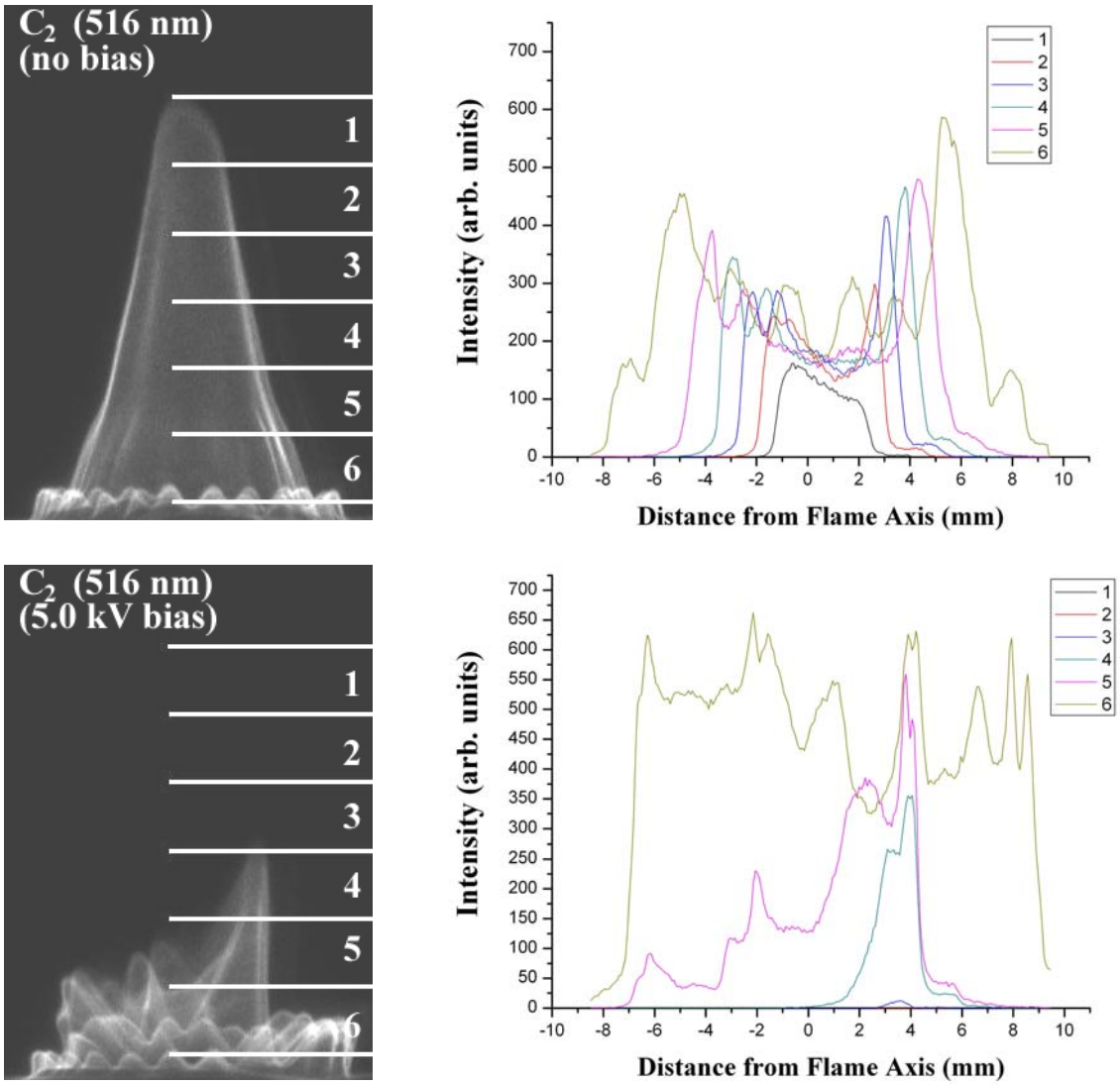
C2 (516 nm)
(no bias)
1
2
3
4
5
6
Intensity (arb. units)
Distance from Flame Axis (mm)
C2 (516 nm)
(5.0 kV bias)
1
2
3
4
5
6
Intensity (arb. units)
Distance from Flame Axis (mm)

Figure 3c:

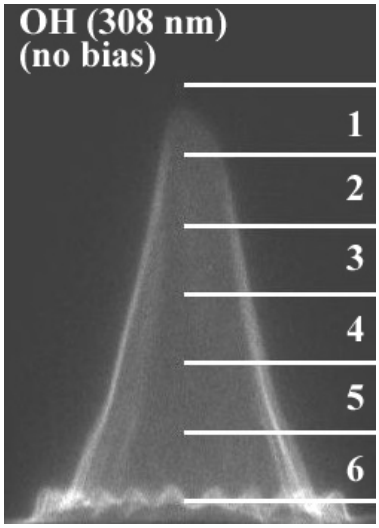
OH (308 nm)
(no bias)
1
2
3
4
5
6

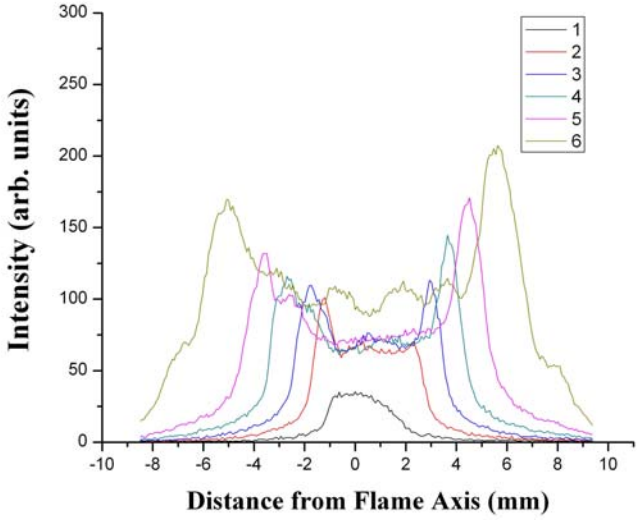
Intensity (arb. units)
Distance from Flame Axis (mm)
1
2
3
4
5
6

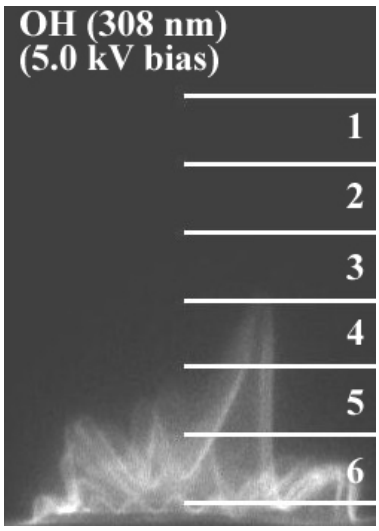
OH (308 nm)
(5.0 kV bias)
1
2
3
4
5
6

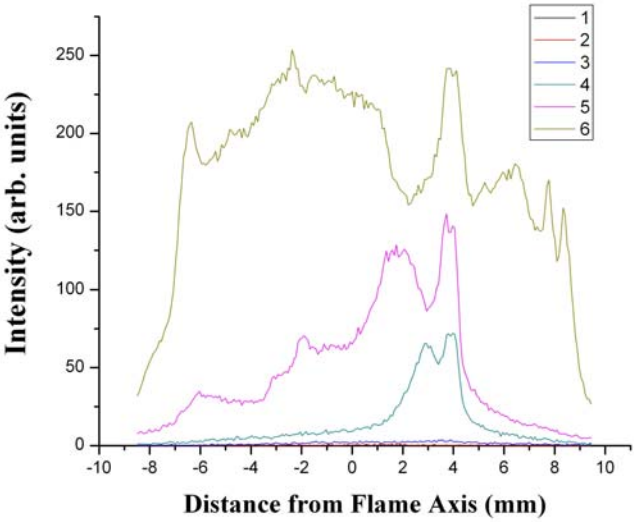
Intensity (arb. units)
Distance from Flame Axis (mm)
1
2
3
4
5
6

Figure 3d:

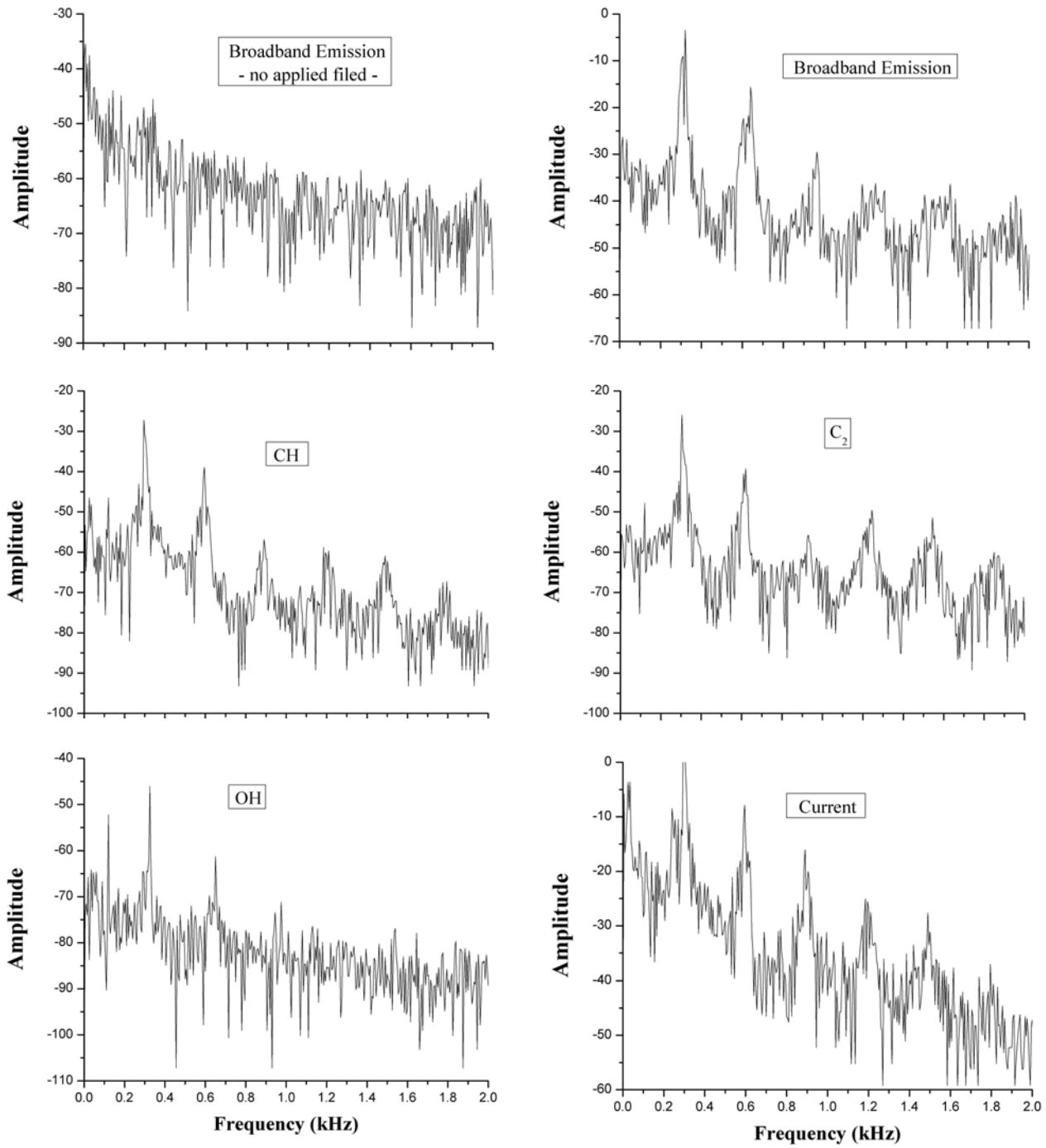
Broadband Emission
- no applied filed -
Broadband Emission
CH
C2
OH
Current
Amplitude
Frequency (kHz)

Figure 4:

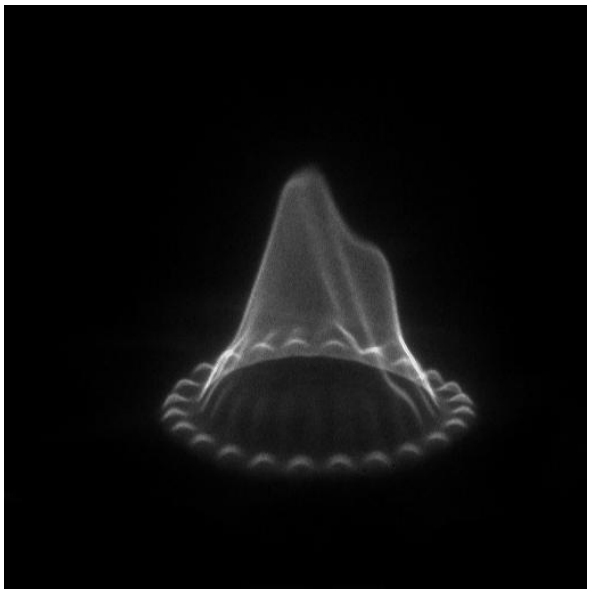

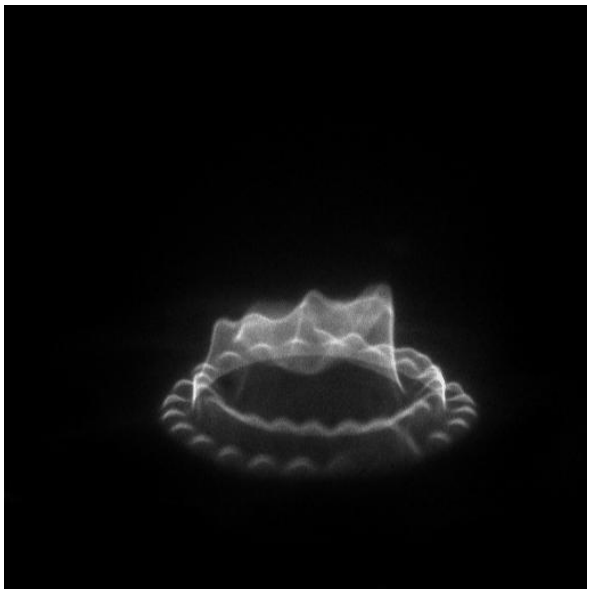

Figure 5: Images showing the wavelength of the disturbance.

Other References for later use

1. D. Bradley, in Advanced Combustion Methods, F.J. Weinberg, Ed., Academic Press, New York, 1986, p. 331.
2. A.P. Chattock, Phil. Mag **48** (1899) 401-403.
3. H.F. Calcote and R.N. Pease, Ind. Eng. Chem. **43** (1951) 2726-2731.
4. H.F. Calcote and C.H. Berman, in Fossil Fuels Combustion Symposium PD-Vol. 25, S.N. Singh, Ed., ASME Book No. H00453, 1989, p. 25.
5. D. Bradley and S.H. Nasser, Combust. Flame **55** (1984) 53-58.
6. D. Bradley and S.M.A. Ibrahim, Proc. Combust. Inst. **15** (1974) 1023-1029.
7. H.C. Jaggers and A.von Engel, Combust. Flame **16**, (1971) 275-285.
8. D.S. Maclatchy, R.M. Clements and P.R. Smy, Combust. Flame **45**, (1982) 161-169.
9. M. Kono, F.B. Carleton, A.R. Jones and F.J. Weinberg, Combust. Flame **78** (1989) 357-363.
10. G.A. Gulyaev, G.A. Popkov and Yu.N. Shebeko, Phys. Combust. Explosion **21** (1985) 23-25.
11. J. Lawton and F.J. Weinberg, Proc. Roy. Soc. **A227** (1964) 468-497.
12. J. Lawton, P.J. Mayo and F.J. Weinberg, Proc. Roy. Soc. **A303** (1968) 275-298
13. J. Lawton & F.J. Weinberg, Electrical Aspects of Combustion, Clarendon Press, Oxford, 1969, pp. 285-336.
14. T. Pedersen and R.C. Brown, Combust. Flame **94** (1993) 433-448.
15. B.A. Strayer, J.D. Posner, D. Dunn-Rankin and F.J. Weinberg, F.J., Proc. R. Soc. Lond. A, Math. Phys. Eng. Sci. **458** (2002) 1151-1166.
16. S.R. Turns, An Introduction to Combustion, 2nd Edition, McGraw-Hill, Singapore, 2000, p 86, pp 450-470.
17. J.M. Goodings, D.K. Bohme and Chun-Wai Ng, Combust. Flame **36** (1979) 45-62.
18. F.A. Williams, Combustion Theory: The Fundamental Theory of Chemically Reacting Flow Systems, 2nd Edition, The Benjamin/Cummings Publishing Company, Menlo Park, CA, 1985, pp 357-365, pp 429-440.
19. A. Linan and F.A. Williams, Fundamental Aspects of Combustion, Oxford University Press, New York, 1993, pp 32-37, 111-151.
20. L.P. Goss, V. Vilimpoc, B. Sarka and W.F. Lynn, Jour. Engr. Gas Turb. Pwr. **111** (1989) 46-52.
21. V. Vilimpoc, L.P. Goss and B. Sarka, Optics Lett. **13** (1988) 93-95.
22. A.G. Gaydon and H.G. Wolfhard, Flames: Their Structure, Radiation and Temperature, 4th Edition, Chapman and Hall, London, 1979, pp 182-194, plate 14, p 359.
23. J.H. Chen and H.G. Im, Proc. Combust. Inst. **27** (1998) 819-826.
24. T. Echekki and J.H. Chen, Combust. Flame **106** (1966) 184-202.
25. J.H. Chen, T. Echekki and W. Kollmann, Combust. Flame **116** (1999) 15-48.

Increasing the Performance and Reliability of Ceramic Fuel Cells

Summer Fellowship Progress Report: June - Aug 2008

Mary S. Ayyadurai

Independent Contractor agreement # 08-S530-0010-01-C35

In order to assess the viability of direct-write method to deposit functional electrode interlayers and electrolytes for SOFC application, ink-jet printing was explored. The advantages of direct-write fabrication method over conventional methods such as spray coating and screen printing lies in the ability to engineer film microstructures in multilayer structures in an efficient and highly reproducible manner. Single SOFC cells with multi-layers were fabricated. The multi-layers consisting of anode functional layer, electrolyte, cathode functional layer and cathode electrocatalyst layer were ink-jet printed using inks prepared from precursor materials. The cells were assessed by dc polarization and ac complex impedance methods. Hydrogen was used as fuel and air as oxidant. The cells were operated in the temperature range from 650-850 ^{o}C.

In the first phase of work, an anode interlayer, 60 wt %NiO-40 wt %YSZ (Yttria-stabilized zirconia) and electrolyte layer, YSZ were ink-jet printed on a tape cast anode support, 50 wt%NiO-50 wt 50 wt%YSZ. The tape cast anode support was supplied by a commercial vendor (ElectroSciences Inc.). The single cells were completed by hand pasting a slurry of the cathode functional layer, 50 wt %LSM ($La_{0.8}Sr_{0.2}MnO_3$) /YSZ and cathode electrocatalyst layer, LSM. The results of the work in Phase I are shown in Fig. 1. All cells showed good open circuit voltage between 1.1 and 1.2 V at 800 ^{o}C. It can be seen that cells 1, 2 and 3 show poor unstable performance on applying load (polarizing). Cell-4 shows stable performance with a maximum power density of 500 mW/cm^2 at 850 ^{o}C. The difference between cells 1,2 & 3 and cell-4 is the

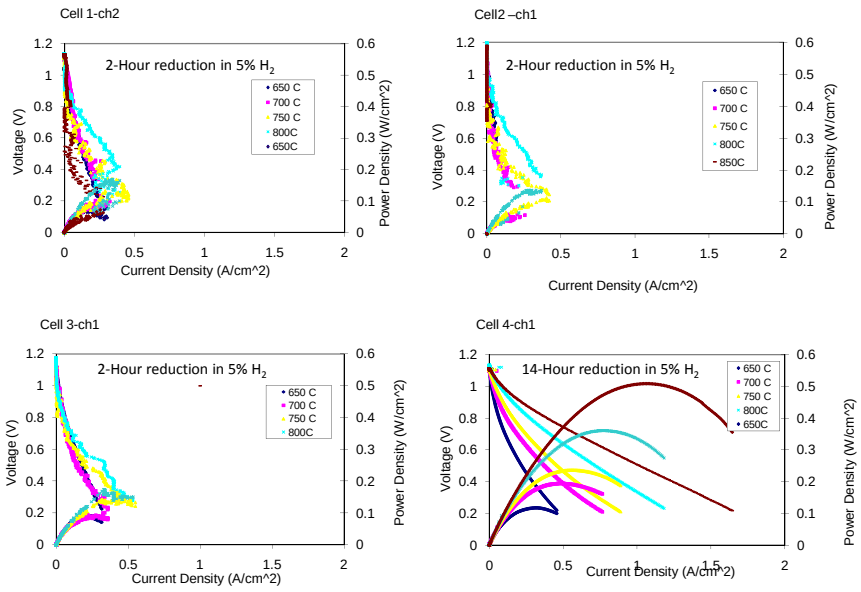

Fig. 1: Current-Voltage performance curves for different cells fabricated

method of processing. Reduction of anodes, NiO-YSZ for initial trials of cell testing (cells 1,2 and 3) was carried out in forming gas (5%H_2 in Ar) for 2 hours, whereas the reduction for cell-4 was carried out for 14 hours.

In the second phase of work, in addition to the electrolyte and anode functional layers, the cathode functional layer as well the cathode electrocatalyst layers were also ink-jet printed. These layers were previously (in Phase I of work) hand pasted from a slurry.

From Fig.2 it can be seen that the performance of the all printed cell (all layers, anode and cathode functional layer, electrolyte and cathode electrocatalyst layer) has decreased compared to the cells with pasted cathode. This could be due to several factors such as thickness of the printed cathode layers and porosity. Further optimization of the cathode ink used for printing is required. A systematic study of cell performance as a function of cathode functional layer and cathode electrocatalyst layer will help understand the present observation. Although the performance of the all-printed cells do not match that of cell-4 in fig.1, the two cells in fig.2 show almost identical performance curves. This reproducibility was one of the goals of printing.

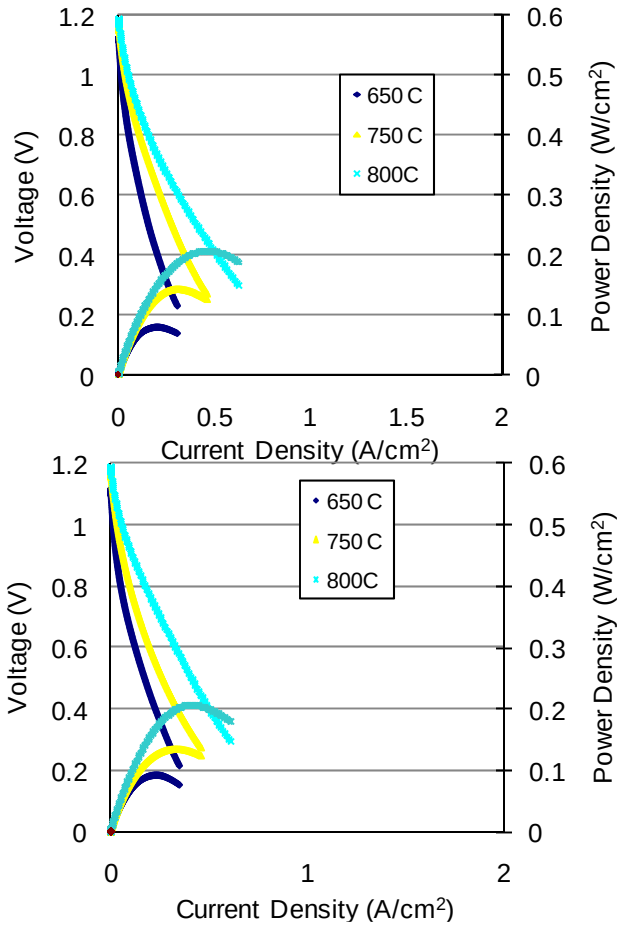

Fig. 2: Current-Voltage performance curves for two all-printed cell (all layers printed on thick anode support).

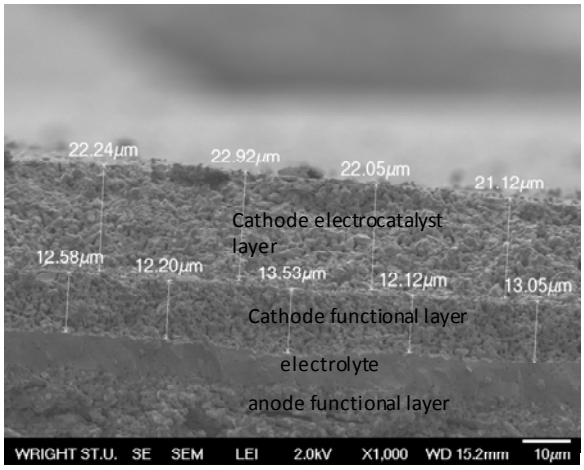

Fig. 3: Scanning electron micrograph of a typical all -printed cell (all layers printed on thick anode support).

Dynamic plastic modeling of fatigue failure in bearings

UTC Final Report

Nathan Branch

University of Florida graduate student

AFRL Summer Intern

Propulsion Directorate

Air Force Research Labs

Wright Patterson Air Force Base

Dayton, Ohio

Summer 2008

Background

Military jet aircraft engine bearings are designed to support large operating loads and high rotating speeds. Bearing manufacturers and military research labs have a strong desire to design and build the best bearings possible. Better bearings mean faster and more maneuverable aircraft. Fatigue failure is the dominant source of bearing failure due to the large number of loading cycles experienced by the bearings contacting surfaces.

Bearing fatigue failure is caused by the large subsurface shear stresses experienced just below the point of contact between rolling elements. Repeated cycling of this shear stress leads to the initiation of subsurface fatigue cracks. After perhaps many thousands or millions cycles these fatigue cracks tend to grow towards the surface forming pits or craters. These pits and craters are called “spalls.” Fatigue cracks can also be initiated by foreign particles that get pinched between the ball and raceway. These particles can leave an indention on the raceway which acts as a stress riser and a future site of fatigue damage.

unspalled raceway

one spall

grown spall

Spalls are a common surface failure mode in bearings. Spalls can cause excessive vibrations, excess heat generation, and higher loads on balls. Vibrations cause erratic and excessive loading conditions within the bearing. Excess heat leads to undesired higher operating temperatures in engine components. Higher temperatures also may cause material phase transformation within the material which may weaken certain stressed areas. All of these events lead to catastrophic failure of the bearing and loss of engine and aircraft. Spalls are a relatively unpredictable phenomenon with serious consequences.

Many different design issues are used to try to prevent spalls. The bearing geometry, applied loads, type of material, and time of operation are controlled to try to prevent the formation and propagation of spalls. Due to the ever increasing demands of aircraft technology, bearings are desired to endure very high thrust loads and function properly for an infinite amount of time. To achieve this, the designer is only left with direct control over the material selection and the geometry of the bearing.

This summer's research was focused on spalls that occur in the bearing raceway and not the ball. Different raceway materials cause different characteristics of spalls. The spall's depth, size, texture, and growth rate are heavily dependent on the raceway's material type. Designers have to optimize the material properties in order to reduce the severity of the spalls. This project will be devoted to how raceway material properties affect the propagation of spalls.

Experimental Research

Experimental research on fatigue failure is being done at the Air Force Research Labs located in the Wright Patterson Air Force base in Dayton, Ohio. Numerous test rigs have been designed and implemented to study the factors that control spall formation and propagation. These test rigs allow the engineer to control the applied thrust load and bearing raceway material. Various instrumentation alerts the engineer when a spall has formed and the rate of spall growth can be recorded.

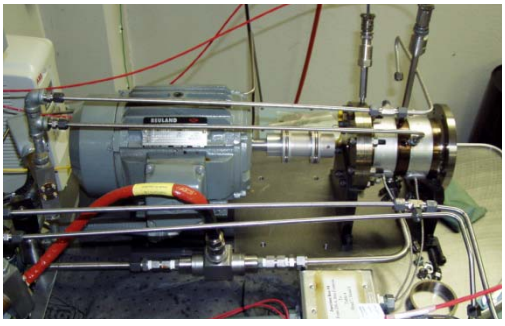

Experimental test rig

In order to reduce the amount of experimental time, spalls are artificially initiated. They are initiated by Rockwell C indentions purposefully placed on the raceway. These

indentions behave as stress risers and fatigue crack initiation sites. The balls used in these tests are ceramic, silicon nitride balls. These balls are much harder and have a higher elastic modulus than the steel raceways. The occurrence of spalls on the ceramic balls *in this test* is extremely rare.

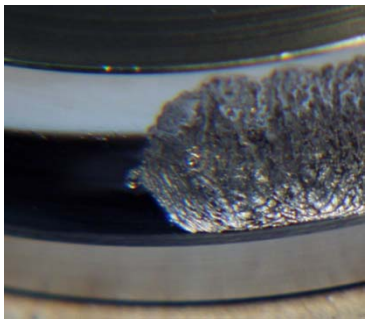

Spall initiated from Rockwell C indention

Goals

The purpose of the summer internship was to research ways to better understand the governing mechanisms that dictate spall growth using computer models. This summer, ABAQUS finite element analysis software was used as a tool to analyze this problem. Computer software allows the designer to vary different aspects of design, and examine how it affects the results of the analysis without having to implement time consuming experiments. The types of calculations desired by the Air Force cannot be easily done by hand. This is the motivation for using FEA software.

The goals of this summer's work were to build dynamic FEA models to better simulate the dynamics of ball on spall impact, calculate the residual stress profiles between ball impacts, and develop a plan for simulating crack growth

Computer software

ABAQUS is a finite element analysis software that transforms complex material displacement and deformation fields into engineering design parameters that are useful to the engineer, namely stress and strain. Stress and strain are fundamental parameters that are used to predict fatigue life of machine components as mentioned earlier. The

calculations ABAQUS performs will be used to better understand where and how fatigue spalls form and grow.

Calculations of important fracture criteria can also be done by ABAQUS. There are many theories on how to grow a crack and consequently, a spall. Crack growth direction can be determined by specified planer extension, the maximum stress criterion, or the maximum strain energy release rate criterion. Crack extension is calculated by da/dn vs ΔK data, Paris Law constants, or a user specified amount. Calculations to find stress intensity factors (SIF's) are done by a computer algorithm called the J-Integral.

Current models

The models built this summer were mainly designed to capture the dynamic effects of ball and spall interactions. The figures below give an idea of how the model is built and approximates the physics and geometry of the actual phenomenon as accurately as possible.

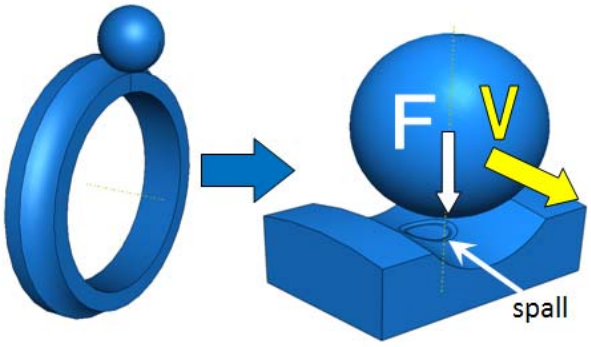

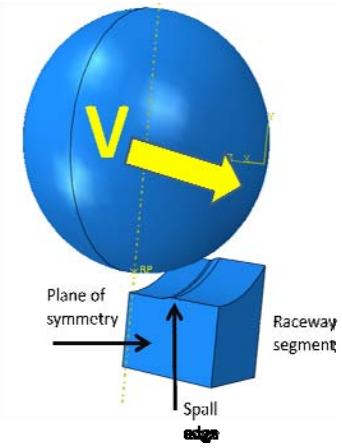

An analytical rigid ball was used for all analysis shown here. This is a valid assumption because the raceway will be feeling the brunt of the damage during impact. At this time there is no interest in the stress state within the ball during impact. The models this summer assumed the mass properties of a steel ball as a conservative estimate because the ceramic silicon nitride balls used in the experiments are much lighter and will not impart as much momentum compared to the steel balls during impact. Linear

hexahedral elements were used throughout the models. This is the best element choice for dynamic impacts that take into account plasticity.

The residual stress profiles in the region close to the spall's edge were of great interest to the air force. Residual stress profiles can give a good idea of how and where fatigue cracks initiate and consequently grow to liberate a chunk of spalled material. Past experience has shown that compressive residual stresses are beneficial to the fatigue life of machine components. Compressive residual stresses tend to retard crack formation and growth. Tensile residual stresses tend to have the reverse effect. History has shown that cracks can easily form and grow within tensile residual stress fields. The existence of tensile and compressive residual stress fields within the spall's edge would give the engineer a better idea of how and why spalls propagate.

Results

The figures below show a typical residual stress profile in the hoop or circumferential direction resulting after one impact. One will notice relatively large compressive residual stresses just beneath the spall's edge. These compressive stresses are believed to keep spall damage isolated to the surface during impact. High tensile residual stresses are seen at the initial location of ball and spall edge contact. This is a likely location of fatigue crack initiation. Residual stress profiles as a function of depth are shown in the next figure. The shape of these profiles are similar to what is calculated experimentally, however the values differ somewhat. This is due to the actual bearing experiencing millions of loading cycles whereas the FEA model only saw one hit.

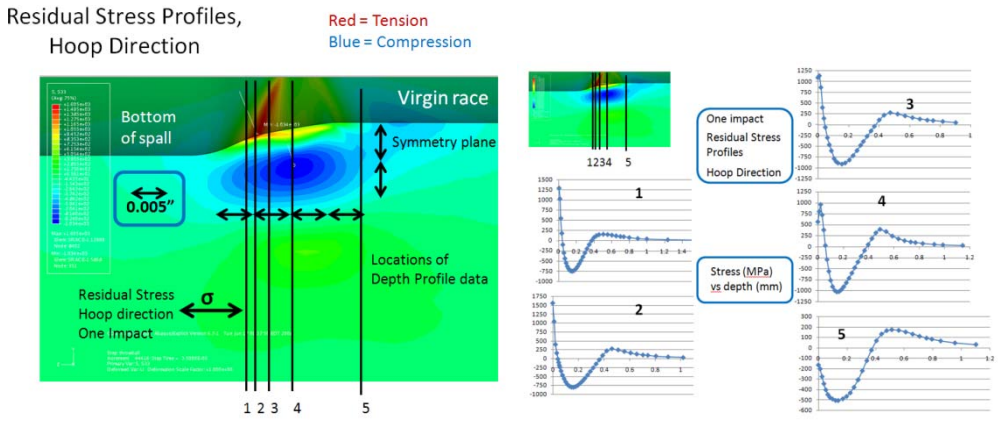

The residual stress profile in the radial direction is shown below. The high tensile stresses in red are likely locations for fatigue crack initiation. Once again we see a compressive region just beneath the edge of the spall. Tensile radial residual stresses are very important because this is the most critical direction in spall growth.

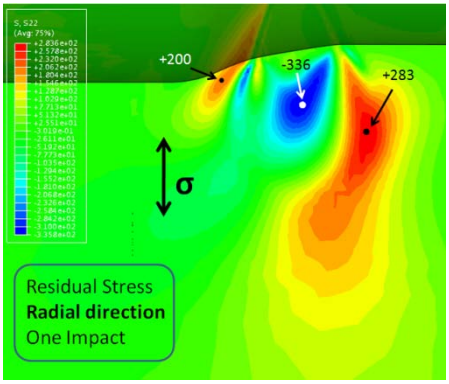

Fracture Modeling

Modeling crack growth in three dimensions is a challenging task undertaken by few people. This summer, various skills were learned and practiced in two dimensions to better understand the capabilities of the software. The abilities displayed here will be applied to three dimensional models at a future time.

The great challenge of this project is if one can grow a crack in a residual stress field without losing information. As a crack grows in a residual stress field, the stress state will change due to the increasing size in the material's discontinuity. Stresses around the crack faces will relax and essentially be stress free. In order to perform a proper analysis, one must keep track of the relaxation of residual stresses as the crack begins to grow.

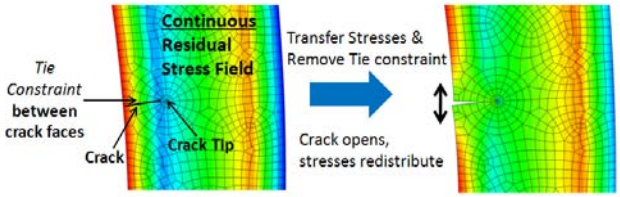

The above figure proposes the use of a few tools available in ABAQUS FEA software. ABAQUS has its own built in algorithms for calculating important fracture design criterion. In order to simulate crack growth, it is proposed that tie constraints be

used to constrain the crack faces together so the model essentially behaves like a material with no cracks. The engineer has full control over when to turn the tie constraint off and allow the crack to grow.

This is done through the following process. First the results shown above regarding the ball and spall impact models will be used to decide where and how large a crack should be inserted into the model. The crack faces of this model will be tie together and the original analysis will be run again. Upon getting the same stress states as the original uncracked model, the tie constraint will be turned off and the crack will open.

After the crack has opened, the stresses will redistribute and the ball will be allowed to impact the edge of the spall again. This process will repeat itself until the crack is long enough that the stress intensity factors become quite comparable to the fracture toughness of the material. When this occurs it can be said that severe fracture and liberation of material will commence and spallation will be achieved.

Future Work

Future work will involve including the influence of preexisting residual stresses caused by shakedown and material phase transformation. Those residual stress fields were determined experimentally using x-ray diffraction techniques and should be included in a final analysis. The models shown here did not use strain rate dependent material properties. These properties will give a better approximation to the actual physics of the spallation phenomenon. The dynamic material properties will be obtained by using a dynamic indenter in future research.

The contribution from friction effects will also be explored in future analyses. This may turn out to be a major contributing factor because it is believed that hydrodynamic lubrication breaks down at this sharp corner and during impact. Localized heating due to impact can also be modeled in ABAQUS granted the right material

properties are available and implemented. This heating of a small region may cause heat and stress induced material phase transformation to occur within the edge of the spall.

More research needs to be done in the area of calculating J integrals in a region of severe plasticity. Stress intensity factors are only valid for Linear Elastic Fracture Mechanics regimes and may not be used here. Proper cyclic hardening properties of bearing steels are also necessary due to the high and low cycle fatigue nature of this phenomenon.

Conclusion

A better understanding of the controlling mechanisms of spall growth is crucial to the design of high performance bearings. The approach to use FEA models to get an accurate representation of the active and residual stresses that occur during and after impact is a critical first step on a long road to spall modeling. The work this summer has been beneficial as seen in the ability to model dynamic impacts of ball and spall, achieve residual stresses between impacts, and develop new tools to model crack growth and consequently spall propagation.

Acknowledgements

The author would like to thank from the Air Force Research Labs: Dr. Nelson Forster, Vaughn Svendsen, Dr. Lewis Rosado, Hitesh Trivedi, and Kevin Thompson for their help, support, and guidance this summer in pursuit to solve and better understand this problem. Special thanks go out to Dr. Nagaraj Arakere for support of the author's graduate studies at the University of Florida. Gratitude is expressed to UTC managing the contract this summer, thanks to Roger Rucker, Kandi Granato, Andrew Detrick, and Michele Puterbaugh.

Air Force Summer Faculty Fellowship Program Final Report
Summer 2008

AN ENERGY-BASED FATIGUE LIFE PREDICTION METHOD FOR OBJECTS UNDER MULTI-AXIAL LOADING

by

Dr. M.-H. Herman Shen, Professor
Department of Aerospace Engineering
The Ohio State University
2036 Neil Ave, rm 328 Bolz Hall
Columbus, Ohio 43210
Tel: (614) 292-2280; Fax: (614) 292-8290
E-mail: shen.1@osu.edu

Host Adviser:
Dr. Charles Cross & Dr. Tommy George
Turbine Engine Division
Propulsion Directorate
Air Force Research Laboratory
1950 Fifth Street, Bldg. 18
Wright-Patterson AFB, OH 45433-7251

Tenure: Prof. MH Herman Shen [May 23, 08] to [August 22, 08]

Submitted [September 2, 2008] to:
Air Force Research Laboratory
SFFP Point of Contact (John Horner, AFRL/RZOP) and
Adviser (Dr. Charles Cross, AFRL/RZTS)

Final Report, AFRL/RZ Summer Research Fellowship Program 2008
Dr. Herman Shen

EXECUTIVE SUMMARY

This report summarizes the research and scholarly activities on the 12 weeks summer research assignment at Turbine Engine Fatigue Facility (TEFF), AFRL/RZ under the Summer Research Fellowship Program. In the summer research period, the faculty from OSU (Prof. Herman Shen) in collaborating with Dr. Charles Cross and Dr. Tommy George of AFRL/RZTS were conducting research at the Turbine Engine Fatigue Facility (TEFF) at Wright-Patterson AFB. The objective of the summer research is to extend the research activities of Prof. Shen's multiaxial high cycle fatigue research programs previously funded by AFRL and DAGSI (The Dayton Area Graduate Studies Institute). The overall concept of the research approach is to accumulate fatigue energy at high frequency resonant modes of base excited test specimens that are comparable, by mode shape and material, to real engine order fatigue of turbine blades. Base excitation testing is conducted by the vibration-based multiaxial fatigue testing methodology, which has been demonstrated by the experimental results from steel, 6061-T6 aluminum, and Ti-6Al-4V plate specimens subjected to fully reversed uniaxial and biaxial bending stress states. Results were compared with those produced using traditional fatigue test machines. Additionally, this vibration-based fatigue method has the advantage of being able to produce a fatigue crack in the test specimen while it is still in the initiation stage. Furthermore, a prestraining technique has been also developed to produce residual stress, enabling vibration-based fatigue testing at various stress ratios.

In order to extrapolate the results from the experience accumulated under the previous projects and foresee the needed directions of the fully realized implementation of this new technology, recently, our efforts has been focused on the development of An accelerated method for determining the material strength of Aluminum 6061-T6 has been developed for prediction of fully-reversed shear and biaxial fatigue life. The framework for this accelerated method is developed in accordance with a previously developed uniaxial energy-based prediction approach, which states: the total strain energy dissipated during a monotonic fracture and a cyclic process is the same material property, where each can be determined by measuring the area underneath the monotonic true stress-strain curve and the area within a hysteresis loop, respectively [1]. The developed framework consists of the following two elements: (1) The development of a life prediction and estimation implementation scheme for calculating effective shear fatigue life cycles, and (2) the development of a constitutive law for multi-axial fatigue life prediction based on analytical comparison with biaxial fatigue experimental data. A comparison between these two framework elements and experimental results for Al 6061-T6 has been conducted to show that there is good agreement, thus validating the prediction method and the developed procedures of the entire framework.

The scope of the approach is quite significant and complex and the completion of all the issues addressed in this research exceeded the 12 weeks time frame of the summer faculty research program scope, therefore, during this summer, we aimed to explore all the possibilities that this new methodology can achieve and lay down a solid theoretical and experimental foundation for the follow-up research. The accomplishments during this summer tenure are summarized as follows

ACKNOWLEDGMENTS

The summer faculty (Dr. Herman Shen) would like to thank the Air Force Research Labs, specifically the TEFF Lab of AFRL/RZTS, for their financial support, facility and equipment access, and encouragement of this summer research.

1. INTRODUCTION

Structural components in gas turbine engines are often designed to be failure free for significantly large cycle durations. Fatigue design tools such as a stress versus cycles plot, or S-N curve, have been used to visualize fatigue strength due to the respective cycle to failure. Other tools for assessing fatigue properties are the Goodman diagram and the modified Goodman diagram [2]; which are the popular choices for a failure-free aircraft engine design criterion. The Goodman diagram is a plot of alternating stress vs. mean stress and represents the fatigue properties of a material for a specified number of cycles. The Goodman diagram and the S-N curve are often constructed with uniaxial fatigue data, which is conventionally acquired via servo-hydraulic machinery that usually operates in tension/compression (axial) loading at a frequency of approximately 40 Hz. High cycle fatigue (HCF) of turbine engine blades, however, often occurs under high order bending or combined bending and twist modes [3]. Therefore, the uniaxial fatigue results from the Goodman diagram and the S-N curve are insufficient means for characterizing the fatigue that occurs in gas turbine engine blades. Adding to this insufficiency, conventional uniaxial fatigue testing (tension/compression) requires significant amounts of time to obtain HCF results. For example, at the fore mentioned operating frequency of 40 Hz, nearly 70 hours is required to accumulate ten million cycles (10^7). Therefore, extremely long time periods are necessary to characterize uniaxial fatigue properties of a material.

In order to generate experimental data that provided a more realistic turbine engine blade fatigue life comparison than conventional uniaxial data, a vibration-based testing methodology was developed to acquire uniaxial bending fatigue results [4,5]. The thought behind the methodology is that a dynamic base excitation from an electro dynamic shaker is supplied to a cantilever specimen at a specified high resonant frequency, roughly between 1200-1600 Hz, showing free-edge bending behavior [3]. This methodology, along with a pre-straining procedure [6], is also capable of acquire fatigue for various stress ratios; thus the capability exist to construct a uniaxial bending Goodman diagram [7,8]. Due to the operational frequency of the vibration-based testing device, which is significantly higher than conventional tension/compression devices, Goodman fatigue data can be constructed at more efficient time intervals: In other words, the use of the vibration-based method requires only 1.5 to 2.5 hours to accumulate 10^7 cycles as opposed to nearly 70 hours for the conventional method.

Along with representing the actual loading mechanisms (bending) that occurs in turbine engine components at high resonant frequencies, a common property was essential for comprehensible observation of fatigue behavior for combined loading situations. This led to the examination of the association between strain energy and failure. Scientific investigators have been intrigued by the relationship concerning energy conversion and the failure of materials since the earlier part of the 20^{th} century. Curiosity of the fatigue/energy relationship can be dated back as early as the 1920's [9]. In the 1940's and 50's, however, a number of well-publicized attempts to relate strain energy

per cycle to the number of cycles for failure were considered and resulted in minimal success [10]. Success in this area was achieved by introducing the hypothesis that implied; under cyclic loading there exists a critical energy value for which failure occurs [11]. This hypothesis was later justified by displaying agreement between the theoretical and the experimental results on an S-N curve. Further investigation of the assumption made in [11] led to the introduction of a more sufficient correlation between the fatigue life of a material and the strain energy dissipation during the fatigue process. It has been suggested that the strain energy required to fracture a material monotonically is the same as the strain energy accumulated during a cyclic fatigue procedure [10,12]. Thus, the critical energy value for each material is the monotonic strain energy. Based on this understanding, an improved energy-based criterion has been developed to allow one to systematically determine fatigue life based on the amount of strain energy loss per fatigue cycle [1]. This previously developed energy-based theory shows the capability of accurately predicting fatigue life of Al 6061-T6 in both uniaxial cases (bending and Tension/compression) at various stress ratios [13]. Although the results from this prediction are promising, progress towards a more realistic application was still needed. This led to experimental analysis for fatigue in the case of shear loading and biaxial loading, individually.

In this study, the development of a constitutive multi-axial law for predicting fatigue will be discussed. Prior to the construction of this constitutive law, however, a shear fatigue life prediction criterion is developed for completion of all possible loading mechanisms in a multi-axial case (tension/compression, bending, shear). The shear prediction criterion was executed and compared with Al 6061-T6 experimental results on an S-N curve for validation of the methodology. Proceeding from the shear analysis, the constitutive law behind multi-axial loading was compared with experimental fatigue results from the biaxial case [14], thus validating the encouraging accuracy of the prediction method.

2. PREVIOUS RESEARCH SCOPE

Improved energy-based prediction method for tension/compression (axial)

Though several energy-based methods for predicting tension/compression fatigue life have been developed [10,12], an improved energy-based criterion for tension/compression with the capability to easily incorporate the effects of stress gradient on fatigue life was essential for the future possibility of developing a general prediction criterion to address fatigue in different loading cases. This improved energy-based criterion was developed from the stress-strain representation of the monotonic (Equation 1 & 2) and cyclic (Equation 3) loading behavior shown in the following equations, where Equation 1 and 2 represent the stress-strain relation prior to and after the necking phenomenon, respectively [1,12].

$$\varepsilon = \frac{\sigma}{E} + \varepsilon_o \sinh\left(\frac{\sigma}{\sigma_o}\right) \quad (1)$$

$$\sigma = \beta_1 \varepsilon + \beta_o \quad (2)$$

$$\varepsilon_{cycle} = \frac{\sigma_{PP}}{E} + \frac{1}{C}\sinh\left(\frac{\sigma_{PP}}{\sigma_c}\right) \quad (3)$$

The parameters displayed are defined as follows: σ is the value for stress at the surface of the specimen (in the bending case, max stress), ε is the strain corresponding to the stress σ, β_1 & β_o are the respective slope and intercept of the stress-strain relationship in the necking region (From ultimate tensile to point of fracture), σ_{pp} is the generalized stress value corresponding to the

generalized cyclic strain ε_{cycle} (i.e. the minimum fully reversed point is observed as the origin), E is the modulus of elasticity, and the variables σ_c, σ_o, ε_o, and C are curve fit parameters [1]. These curve fit parameters for the cyclic and monotonic representations (Equation 1-3) are statistically acquired by comparison between low cycle experimental results and experimental monotonic results, respectively [1].

Fatigue life is systematically determined for the improved criterion by taking the total monotonic strain energy density and dividing it by the strain energy density for one cycle. The total strain energy dissipated during a monotonic process is determined as the area underneath the curve constructed by Equations 1 & 2. The strain energy density for one cycle, however, is more difficult to calculate. In order to calculate cyclic strain energy density, two assumptions were made. First, a generalized coordinate system is used; where the origin of the coordinate system is defined as the point of minimum stress and strain for one cycle (Example shown in Figure 1). Second, it is assumed that the tensile behavior of the Hysteresis loop on the generalized coordinate system is the same as the compressive behavior. Therefore, cyclic strain energy density is defined by Equation 4. With a strain energy density expression for the monotonic and the cyclic cases, the improved criterion for systematically determining fatigue life at a specified stress amplitude level (σ) is given as Equation 5 [1].

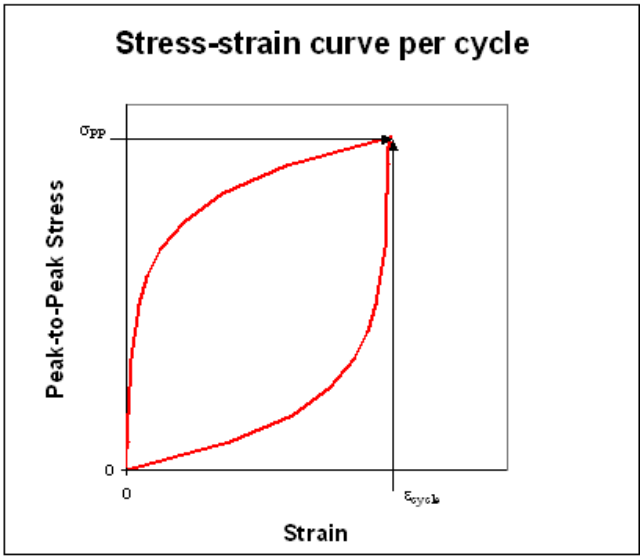

Figure 1. Generalized cyclic curve

$$W_{cycle} = \sigma_{PP}\varepsilon_{cycle} - 2\int_0^{\sigma_{PP}} \varepsilon_{cycle}\, d\sigma_{PP} \qquad (4)$$

$$N = C\frac{\sigma_n\left(\varepsilon_n - \frac{\sigma_n}{2E}\right) - \varepsilon_o\sigma_o\left[\cosh\left(\frac{\sigma_n}{\sigma_o}\right) - 1\right] + \frac{\beta_1}{2}\left(\varepsilon_f^2 - \varepsilon_n^2\right) + \beta_o\left(\varepsilon_f - \varepsilon_n\right)}{2\sigma_c\left\{\frac{\sigma}{\sigma_c}\sinh\left(\frac{2\sigma}{\sigma_c}\right) - \left[\cosh\left(\frac{2\sigma}{\sigma_c}\right) - 1\right]\right\}} \qquad (5)$$

Where σ_n is the necking stress, ε_f is the facture strain, and ε_n is the necking strain. The results from Equation 5 are compared to previously acquired fully-reversed tension/compression test results and the corresponding linear regression curve on the S-N plot of Figure 2. The comparison shows that the criterion provides good life estimations for tension/compression fatigue results. To further validate the accuracy of the comparison, strain energy density per cycle is calculated from low cycle results and matched with the experimental linear regression cycles to failure. These results are then compared with the energy-based predicted cyclic strain energy density and the related cycles to failure, which are all displayed in Figure 3. It has been previously presented that the logarithmic slop of this comparison is roughly -0.6 [15]. Though the experimental results of Figure 3 concur with this belief, further analysis of the cyclic strain energy density calculation method is conducted to provide reasoning for this agreement. Conclusion of this analysis shows that the variation between experimental and analytical results is more obvious in test data with a higher standard deviation of the hysteresis loop curve fit constructed by Equation 3. Due to a more sensitive stress-strain comparison, minor changes in the standard deviation (Standard deviation displayed on each point of Figure 3) of the curve fit causes major variation in strain energy density calculation. Based on this sensitivity issue, the cyclic curve fit parameters that provided minimal standard deviation where used in Equation 5 for prediction-experimental comparison. This comparison, as stated, validated the encouraging output of the criterion. Therefore, the chosen cyclic curve fit parameter provides an assuring comparison between the experimental results and the predicted curve.

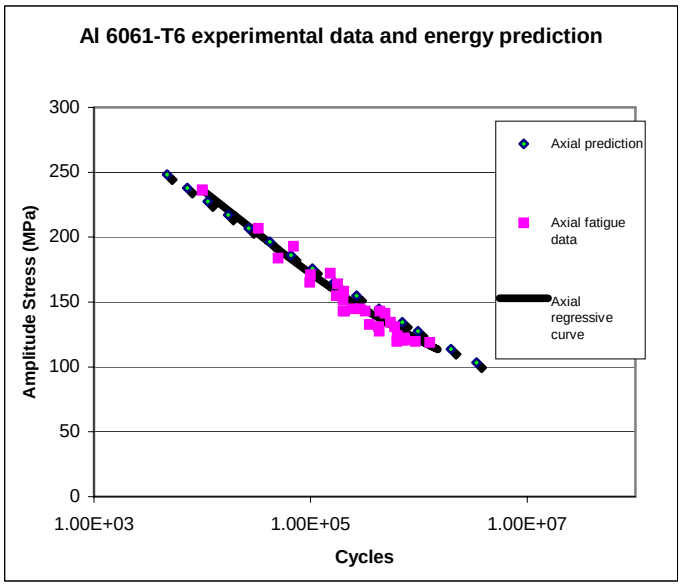

Figure 2. Comparison of prediction and experimental results [1]

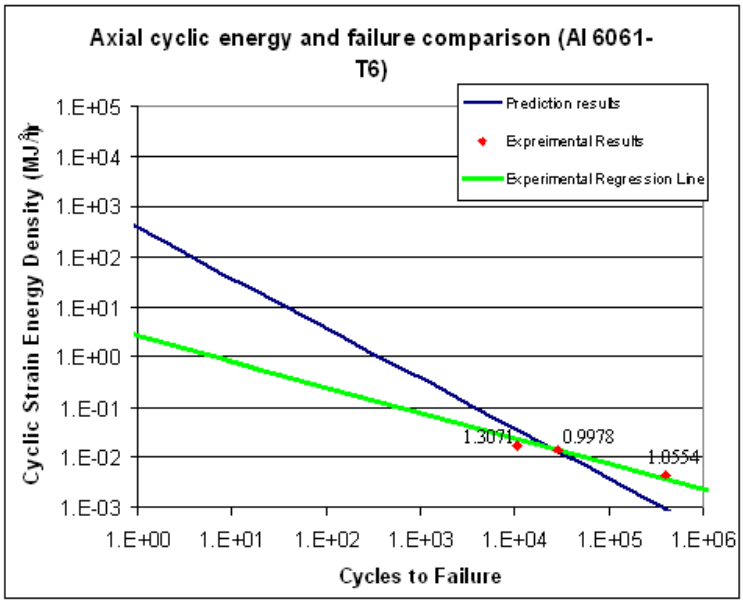

Figure 3. Cyclic strain energy versus cycles to failure plot

Improved energy-based prediction method with stress gradient effect (bending)

In order to extend the improved energy-based criterion to the bending case, the difference between stress gradient effect through the thickness of the bending and tension/compresion specimen was evaluated. This difference is illustrated in Figure 4. Since the distribution of the bending specimen shown in Figure 4 varies with respect to the distance from the neutral axis, the strain energy through the thickness of each bending fatigue specimen (effective strain energy) was evaluated. In order to determine the total effective-strain energy (strain energy per surface area), the alternating stress from the monotonic and cyclic strain equations was written as a function of the distance from the neutral axis. After determining the respective effective-strain energy from the monotonic and cyclic procedures, the previously mentioned fatigue life determination method was used to develop the improved criterion with stress gradient effect (Equation 6) [13]. Fatigue life prediction results were calculated from Equation 6 and an encouraging comparison is made on Figure 5 with the bending experimental data, tension/compression test data, and the improved energy-based prediction results for tension/compression (Equation 5).

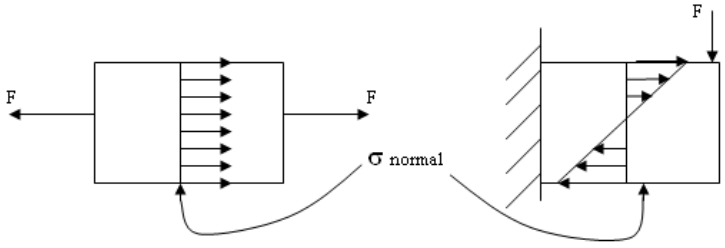

Figure 4. Stress distribution as a result of the respective uniaxial loading application [13]

$$N = C\frac{\sigma_n\left(\varepsilon_n - \frac{\sigma_n}{2E}\right) - \varepsilon_o\sigma_o\left[\cosh\left(\frac{\sigma_n}{\sigma_o}\right) - 1\right] + \frac{\beta_1}{2}\left(\varepsilon_f^2 - \varepsilon_n^2\right) + \beta_o\left(\varepsilon_f - \varepsilon_n\right)}{\sigma_c\left[\cosh\left(\frac{2\sigma}{\sigma_c}\right) - \frac{3\sigma_c}{2\sigma}\sinh\left(\frac{2\sigma}{\sigma_c}\right) + 2\right]} \quad (6)$$

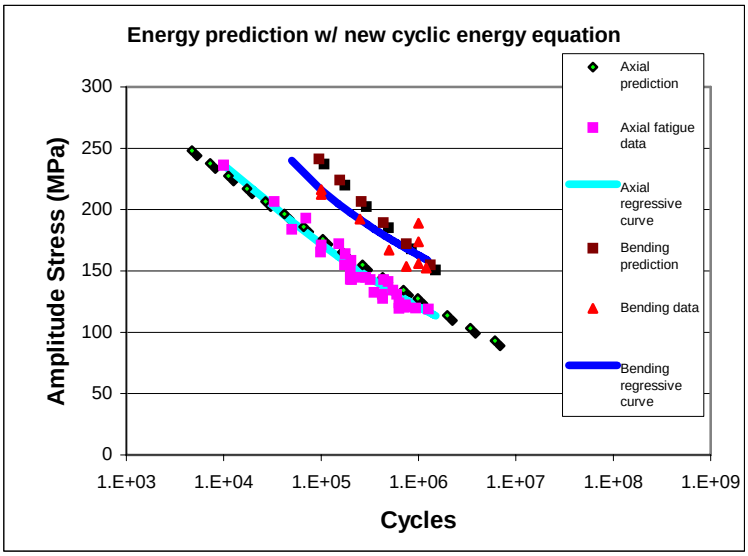

Figure 5. S-N test data and energy-based prediction results (bending and tension/compression) [13]

Improved energy-based method with mean stress effect

When positive mean stress is included in a fatigue procedure, it dissipates strain energy monotonically and increases the plastic strain per cycle; thus reducing the amount of cycles required to fatigue a specimen [13]. The residual strain energy occurrence caused by mean stress is described as follows: When conducting a cyclic test at stress ratios ($R=\sigma_{min}/\sigma_{max}$) > or = -1.0, a mean stress is monotonically applied. Therefore, some of the total strain energy required for monotonic fracture has already been dissipated by the applied mean stress; thus reducing the total strain energy required for fatigue. This reduced total strain energy is acquired by subtracting the monotonic mean strain energy from the total strain energy during monotonic fracture [13].

When evaluating the fully-reversed tension/compression cyclic behavior, two assumptions were set in place: the strain equation was determined from a generalized coordinate system, and the compressive portion of the cyclic stress-strain relation is identical to the tensile [13]. Both of these statements are also assumed for cyclic loading with mean stress effect, therefore Equation 3 and all the corresponding parameter values are still used to characterize the stress-strain behavior. However, unlike the fully-reversed stress-strain loop formed in [1], the loop formed with mean stress effect is much different. This assertion is proven by the experimental results in Figure 6, where the compressive curve does not connect to construct a complete loop. From this observation, it is assumed that the initial and final points per cycle are located on the mean stress line of the generalized coordinate system. Thus the required changes are applied to the tension/compression calculation method of Equation 5.

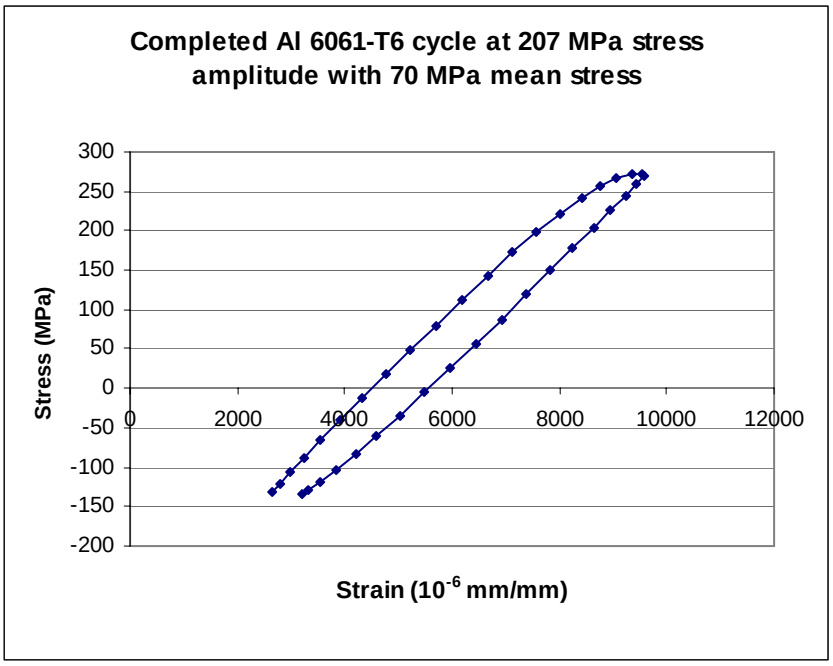

Figure 6. Hysteresis loop for loading with mean stress [13]

Based on the alteration to the total failure strain energy and the given assumption of the experimental stress-strain results for one cycle, the fully-reversed tension/compression prediction criterion can be extended to accurately determine fatigue life of specimens at various stress ratios. The experimental-analytical comparisons validating the criterion are plotted on Figures 7 & 8. The minimal variations at lower cycles may be associated with some control issues of the available MTS servohydraulic machine (Figure 9 of Section 3). Nonetheless, the strain energy density analysis of axially loaded specimens under mean stress effect provides a valid means for fatigue life prediction and estimation.

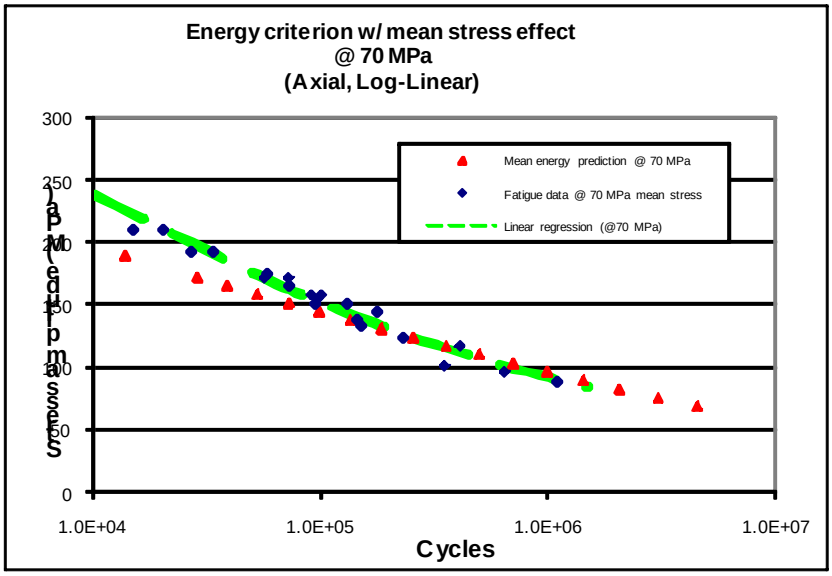

Figure 7. Fatigue prediction comparison with 70 MPa mean stress effect [13]

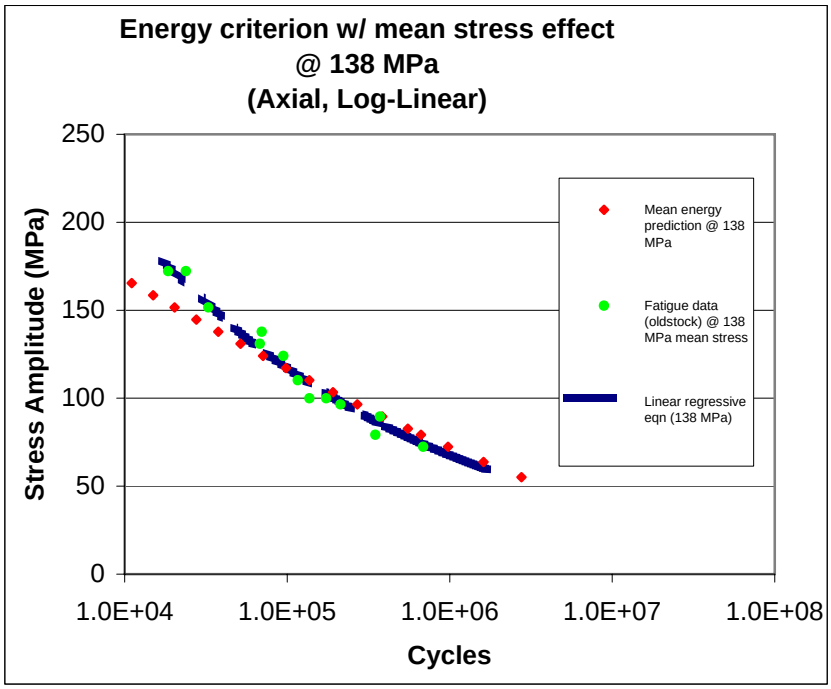

Figure 8. Fatigue prediction comparison with 138 MPa mean stress effect [13]

3. EXPERIMENTAL PROCEDURES

Shear testing procedures

Three types of experimental tests were conducted using the shear loading procedure: (1) fatigue (i.e. construction of an S-N curve), (2) monotonic, and (3) low cycle testing. Each of the three shear experiments were conducted using the ASTM D5379 standard for composites and polymers, which suggest the Iosipescu testing fixture shown in Figure 9 [16]. The recommended specimen under shear is a v-notched flat strip coupon that is referenced by the ASTM D5379 standard and shown in Figure 10 [16]; where the thickness is desired to be ¼ in to prevent a moment about the longitudal axis, based on an offset/eccentric load. The pure shear load is distributed to the v-notched specimen using the MTS machine shown in Figure 9. Therefore, the test specimen and the experimental set-up are the same for all shear tests.

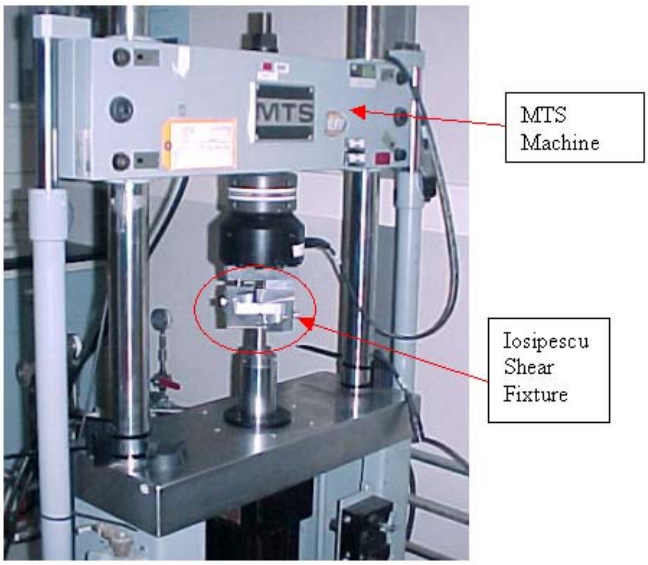

Figure 9. MTS with Iosipescu fixture and setup

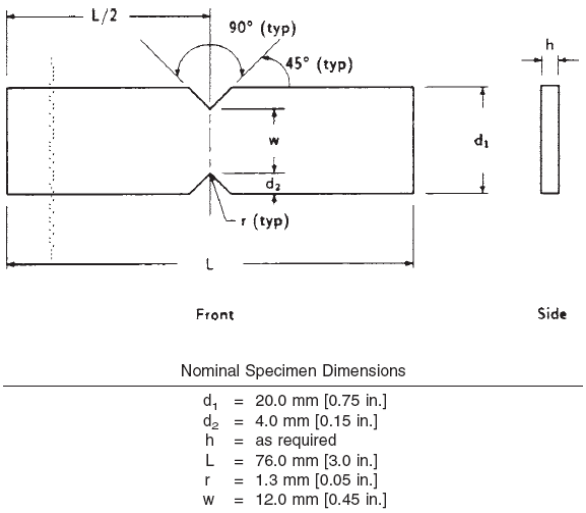

Nominal Specimen Dimensions

d_1	=	20.0 mm [0.75 in.]
d_2	=	4.0 mm [0.15 in.]
h	=	as required
L	=	76.0 mm [3.0 in.]
r	=	1.3 mm [0.05 in.]
w	=	12.0 mm [0.45 in.]

Figure 10. ASTM D5379 V-notched beam specimen [16]

Several strain gage configurations were used to acquire experimental strain results. The popular choices, however, were perpendicular stacked gages located at plus and minus 45 degrees from the specimen's horizontal axis (CEA-13-062WT-350), and two individual large elongation gages, also located at plus and minus 45 degrees from the horizontal axis (EP-08-125AC-350) [17]. Based on the conventional transformation of strain laws, it is possible to acquire shear strain by simply subtracting normal strain results of the minus 45 degree gage from the results of the plus 45 degree strain gage [16]. This form of measurement was only used for the low cycle and the monotonic testing procedures. Data desired for fatigue did not require strain gages because the only results observed were the load, cycles, and stroke (initial and final absolute displacement position); which where acquired with the MTS data acquisition system (TestStarIIs).

Similar to the fatigue study of the previously analyzed vibration-based uniaxial bending case [4,5], crack detection for shear fatigue is not a straightforward observation. This is due to a significantly

slower crack propagation rate than the, almost instantaneous, tension/compression case. Also like the bending case, a crack is detected by observing the inconsistency of cyclic experimental results. For the bending case, inconsistent experimental data is detected by observing the dramatic drop in cyclic velocity due to a shift in the natural frequency, which is caused by the stiffness of the specimen changing due to the presence of a crack [3,4,5]. As for the shear case, inconsistency can be observed in an analysis of relative displacement position versus number of cycles. The belief behind this particular observation goes as follows: when a crack is formed in the specimen, the material strength decreases. Since the shear fatigue testing is controlled by a load amplitude, a larger displacement is required as a crack propagates. Therefore, based on the reverse polarity of the MTS data acquisition system (TestStar IIs), the initial stroke displacement value begins to decrease in a non-linear manner when a crack is present in a shear fatigue specimen. This non-linear decrease can be seen in the initial stroke position versus cycle plot of Figure 11.

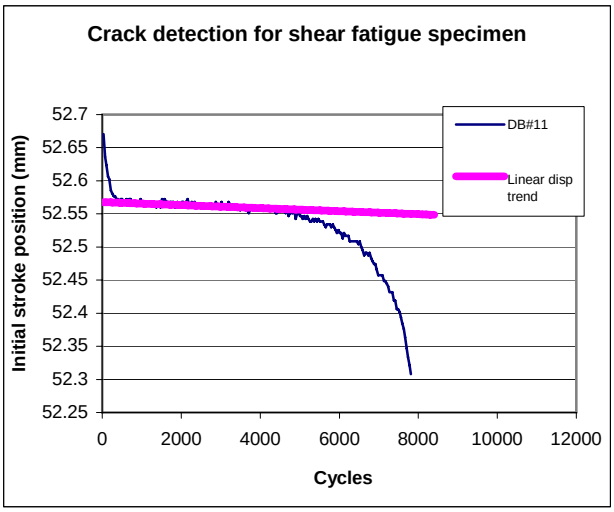

Figure 11. Relative specimen position at individual cycles

It is understood that crack initiation and complete fracture in conventional HCF cases (tension/compression) have a negligible difference in cycle count [18]. Therefore, in order to correlate the failure from the monotonic and cyclic procedures, monotonic axial failure is defined as the point of complete fracture. This application, however, is not valid for the monotonic shear case based on the slow crack propagation rate; In other words, crack initiation and complete fracture have individually distinct life durations. An example of this understanding can be seen on the previous plot of Figure 11; where the crack initiates at approximately 4500 cycles and at the last plotted test result of 7500 cycles the specimen has still not reached complete fracture. Based on this particular understanding, monotonic shear failure is observed at the point of crack initiation. The method for determining the point of crack initiation can be observed from the load versus displacement plot on Figure 12, where crack determination is due to a sudden decrease in applied loading. This determination is possible because each monotonic shear test is controlled by a specified displacement rate. Therefore, when a crack is present, in order for the MTS control system to keep the same displacement rate, the load on the specimen must be decreased drastically. This decrease in the applied load provides a clearly visible method for crack detection of monotonic shear failure.

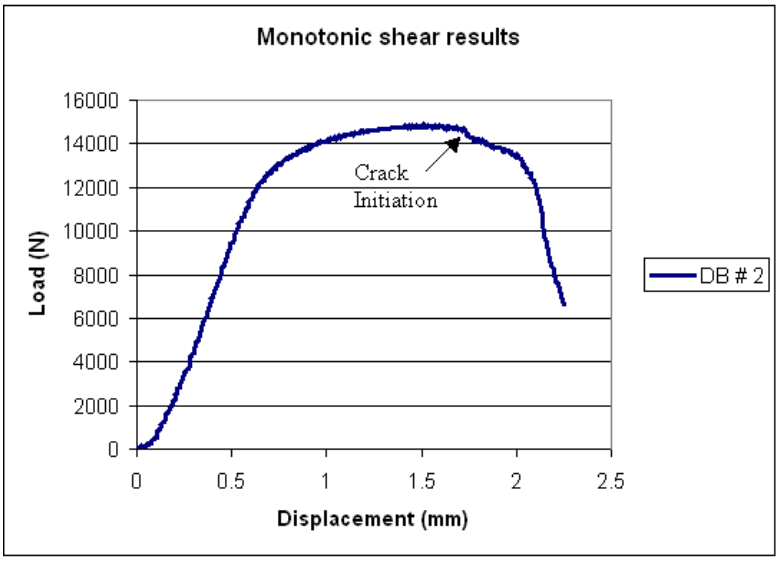

Figure 12. Load-displacement monotonic shear results

Biaxial fatigue testing procedure

Biaxial fatigue results are acquired with the same vibration-based testing methodology used for the uniaxial bending case [4,5]. Stated previously about the vibration-based testing procedure in the introduction, the thought behind the methodology is supplying a dynamic base excitation to a cantilever specimen at a specified high resonant frequency, which generates biaxial bending behavior. Base excitation is supplied to the specimen with the Unholtz Dickie 6000 lb electrodynamic shaker (Figure 13) located in the Turbine Engine Fatigue Facility (TEFF) of the Air Force Research Laboratory (AFRL) in the Propulsion Directorate at Wright-Patterson Air Force Base. This particular test has been successfully conducted in previous research [14].

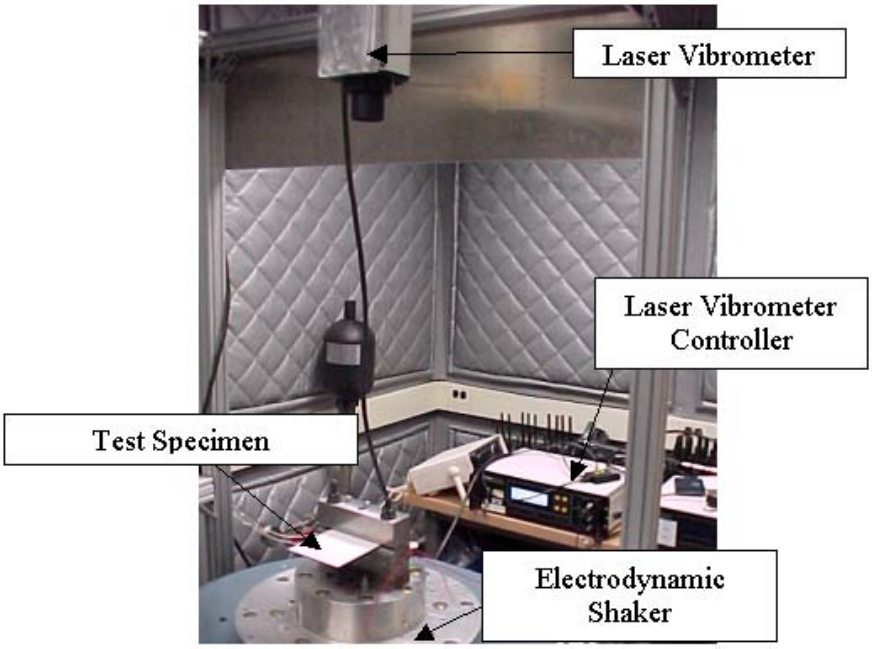

Figure 13. Vibration-based fatigue experimental setup

The biaxial specimen of choice is the so-called aluminum winger shown in the schematic of Figure 14. This specimen was developed via a geometrical design procedure discussed in [14] and was further optimized based on some constrained parameters from the original design [19]. The purpose of the geometrical design procedure is to provide an optimal specimen, which is capable of generating high excitation and an unique mode shape that produced a more significant von Mises stress level at a region other than the clamped boundary and the edges of the test specimen. It is also desired that the geometrical design procedure should provide the worst-case scenario for biaxial stress ratio (i.e. x-to-y stress ratio of 1.5).

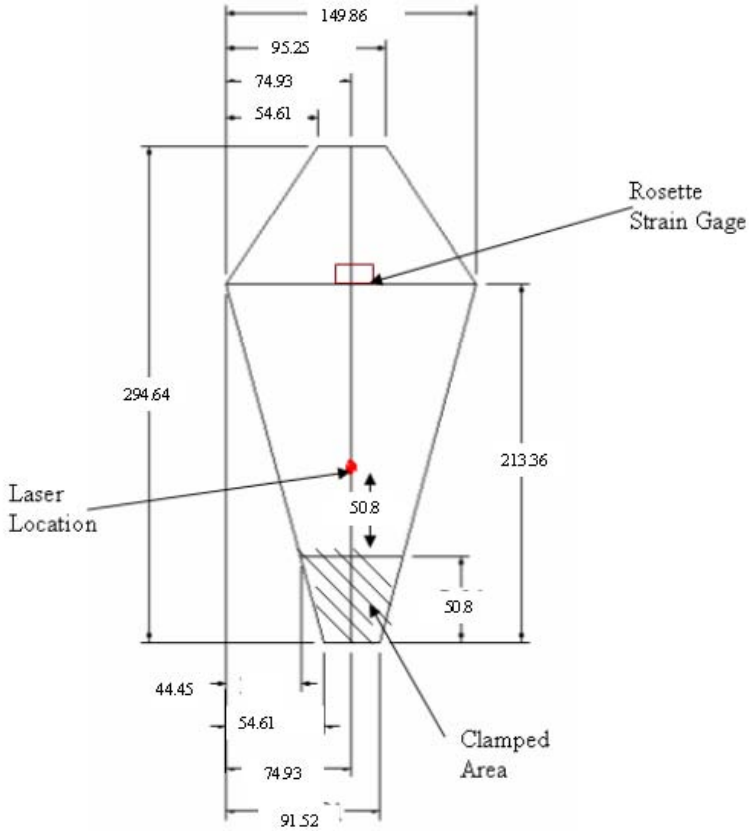

Figure 14. Biaxial winger specimen (modified geometry) [19]

Prior to conducting a biaxial fatigue test, a Finite Element Method (FEM) harmonic analysis is carried out for three main reasons: (1) to validate the geometrical optimization procedure, (2) establish the location of the measurement instrumentation on each specimen, and (3) determine the frequency at which biaxial bending occurs. This FEM analysis is generated using the following software: ABAQUS for processing only, and IDEAS for pre and post processing [14]. Results from a previous FEM analysis of an aluminum winger is shown in Figure 15. In this figure, the von Mises results (Figure 15b) shows the maximum stress level is, indeed, considerably larger in a region away from the clamp edge. Also shown, the corresponding normal stress ratio for x versus y (Figure 15c and 15d respectively) is approximately 1.5, thus implying that the biaxial fatigue crack will propagate along the y-axis.

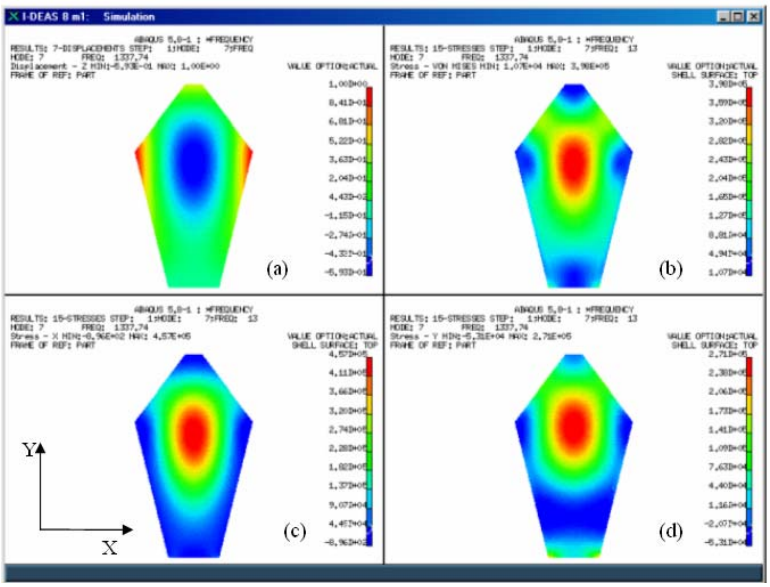

Figure 15. (a) Mode shape, (b) von Mises stress, (c) x-direction stress, (d) y-direction stress [14]

Measurement instrumentation for the biaxial case is also similar to the uniaxial bending, where a laser vibrometer and a strain gage are used to acquire velocity and strain results, respectively. The uniaxial bending case, however, uses a CEA-05-062UW-350 strain gage, which is capable of reading strain in only one direction. Therefore, in order to account for the two directional strains in the biaxial case, a 60° rosette strain gage (SK-05-060WY-350) is essential. Due to the limited fatigue rating of this particular gage, a linear correlation is made between each of the strain directions of the rosette and the velocity data from the non-intrusive laser vibrometer (Laser vibrometer shown in Figure 13). This correlation, displayed on Figure 16, shows good linear accuracy between the respective comparisons.

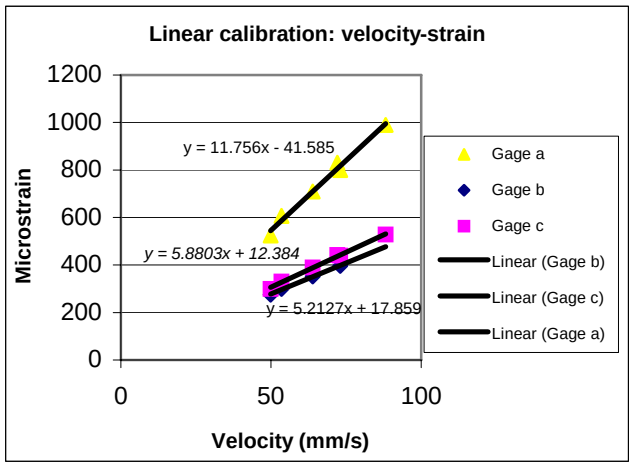

Figure 16. Linear calibration of the delta rosette strain gage and the laser vibrometer

In the case of biaxial loading, a valid assessment of fatigue strength requires the calculation of an equivalent stress. Since there doesn't exist a static stress during biaxial fatigue testing, the equivalent stress calculation method used for this experiment is the von Mises approach. To reduce

the tedious calculation steps required to obtain a von Mises stress value, the following equation is used to acquire the principal strains acting on the fatigue zone during cyclic loading [17].

$$\varepsilon_{1,2} = \frac{\varepsilon_a + \varepsilon_b + \varepsilon_c}{3} \pm \frac{\sqrt{2}}{3}\sqrt{(\varepsilon_a - \varepsilon_b)^2 + (\varepsilon_b - \varepsilon_c)^2 + (\varepsilon_c - \varepsilon_a)^2} \quad (7)$$

In Equation 7 the subscripts are defined as followed: a, b, and c represent strain in the three directions of the 60^o rosette, and the numbers 1 & 2 represent the two principal strains due to two dimensional strain transformation analysis [17]. After acquiring the principal strains, the values for the principal stress can be determined by applying Hooke's law of general stress state (Equation 8-10), where ν is poisson's ratio and E is the modulus of elasticity. Using the principle stress results, the von Mises stress calculation method of Equation 11 can be used to acquire the equivalent stress (σ_{equiv}) of specimens under fully-reversed biaxial loading.

$$\sigma_1 = \frac{E}{(1-\nu^2)}[\varepsilon_1 + \nu\varepsilon_3] \quad (8)$$

$$\sigma_2 = 0 \quad (9)$$

$$\sigma_3 = \frac{E}{(1-\nu^2)}[\varepsilon_3 + \nu\varepsilon_1] \quad (10)$$

$$\sigma_{equiv} = \sqrt{\frac{(\sigma_1 - \sigma_2)^2 + (\sigma_2 - \sigma_3)^2 + (\sigma_3 - \sigma_1)^2}{2}} \quad (11)$$

4. TEST RESULTS AND DISCUSSION

Monotonic shear

Stress-strain shear results from the monotonic test are shown on the plot of Figure 17. The figure only displays results for one method of strain measurement (strain gages) due to the fact that monotonic shear strain measurement can only be conducted with a rosette or a stacked strain gage configuration, and not displacement. This is the case based on the following; along with the measured vertical displacement from the MTS data acquisition device, there also exist a horizontal displacement simultaneously occurring due to the internal moment present with the fixture design. Though the horizontal displacement from this moment cannot be measured experimentally, it does not affect the result of the pure shear acting through the fracture zone; which is measured with the strain results.

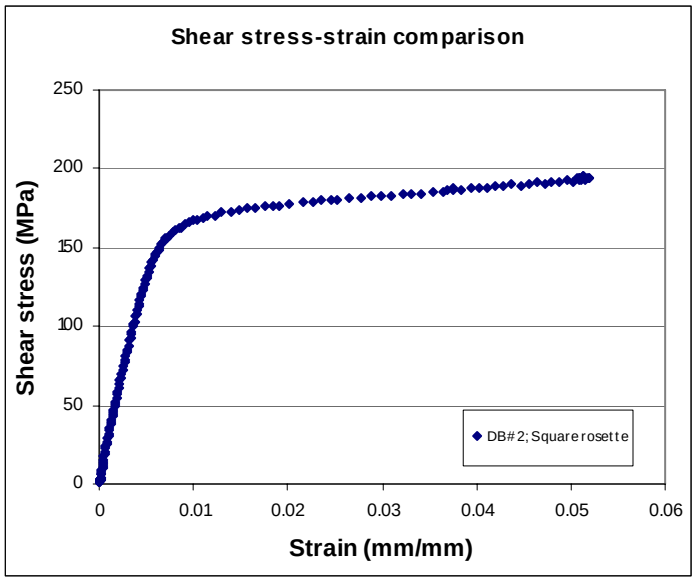

Figure 16. Monotonic shear stress-strain results

The unfortunate problem faced with having strain gages as the only method of measurement is that the available and easily applied gages are rated for strains lower than fracture strain (i.e. 3% strain). In order to acquire strains up to the point of fracture, the accuracy of the strain gage positioning was sacrificed due to the gage manufacturer's inability to provide a stacked gage configuration with large elongation capacity. However, a comparison is made between the large elongation (22% strain) and the conventional gages in order to validate an accurate measurement of shear strain versus average shear stress all the way to fracture. This comparison, shown in Figure 18, displays some variation, which could be a result of the inaccuracy of gage positioning. Nevertheless, the gage comparison shows good correlation.

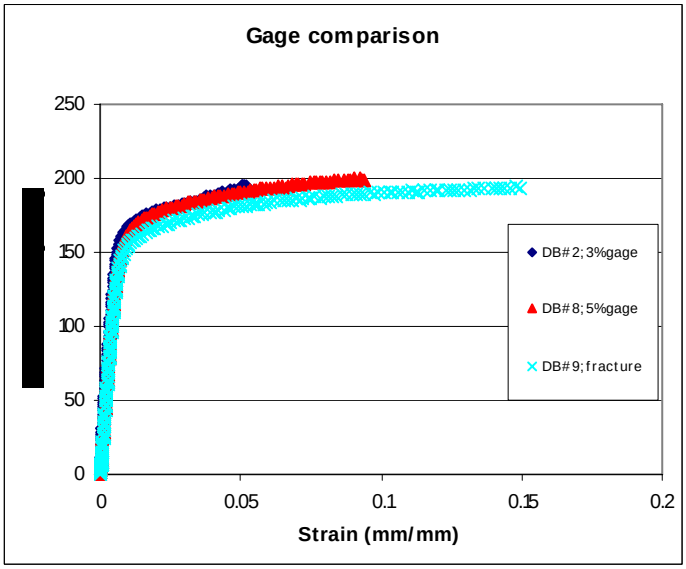

Figure 18. Comparison between 3 different gage results

Based on the accuracy of the gage positioning, curve fit evaluations were compared with experimental results from the 3% gage in Figure 18. Using the acquired experimental data from this conventional elongation strain gage (CEA-13-062WT-350), parameters for the shear strain approximation equation (Equation 12) are determined in the same manner as the monotonic axial strain equation from Section 2. The parameters for the equation are defined as follows: τ is the corresponding shear stress level, G is the Shear Modulus obtained from the elastic portion of the test results in Figure 17, and τ_o & γ_o are curve fit constants. The curve fit constant τ_o is acquired using an equation similar to the monotonic axial case analyzed in [1]. This constant (τ_o) is represented by Equation 13; where τ_u is the applied stress of gage failure, τ_y is the 0.2% yielding shear stress, and γ_u is the shear strain at the final reading of the gages. The parameter γ_o is acquired using a Matlab code [20]. This code is executed by matching Equation 12 with the test results from Figure 17 as the curve fit parameter (γ_o) is adjusted, as necessary, within the code until an optimal result is acquired (less than 1% average difference between equation and experimental results). The results for these parameters and other material properties are shown in Table 1.

$$\gamma = \frac{\tau}{G} + \gamma_o \sinh\left(\frac{\tau}{\tau_o}\right) \qquad (12)$$

$$\tau_o = \frac{\tau_u - \tau_y}{\ln(\gamma_u / 0.002)} \qquad (13)$$

τ_y (MPa)=	165.1
τ_u (MPa)=	195.0
γ_u ($^{mm}/_{mm}$)=	0.034205
τ_o (MPa)=	10.6
γ_o ($^{mm}/_{mm}$)=	6.20E-11

Table 1. Material properties for shear strain approximation

Low cycle testing

The purpose of low cycle experimental testing is to develop adequate cyclic stress-strain data for the generation of an expression that will calculate strain energy density per cycle. This expression represents the generalized stress-strain curve (i.e. minimum fully-reversed amplitude is viewed as the origin); where the tensile and compressive curves are formed by Equation 14. Parameters for this equation are defined as follows: C_s, & τ_c are the curve fit parameters and τ_{pp} is twice the alternating shear stress (2τ). However, based on the assembly of the Iosipescu fixture and its inability to handle large tensile loads, only low stress and extremely low cycle fully-reversed applications are manageable. For the cases here, fully-reversed low cycle applications were conducted up to an arbitrarily selected number of cycles (4 or lower) to ensure stability in the test fixture. Based on this limitation, three low cycle cases where conducted: two at fully-reversed loading and one incorporating mean stress effect. A noticeable observation can be made that the cycle count for the low cycle test is not at the magnitude where most materials experience stationary surface temperature. However, the material under analysis (Al 6061-T6) experiences minimal temperature change during cyclic loading [21]. Therefore, the low cycle application conducted for shear analysis is acceptable.

$$\gamma_{cycle} = \frac{\tau_{pp}}{G} + \frac{\sinh\left(\tau_{pp}/\tau_c\right)}{C_s} \qquad (14)$$

In the fashion similar to the axial analysis of [1], Equation 14 is curve fit with each individual low cycle case using a MATLAB optimization code. The core of this code is the calculation of the standard deviation in the percent difference between Equation 14 and the low cycle shear data (from τ=0:τ_{PP}) of the generalized coordinate; where as stated earlier, the minimum fully-reversed stress-strain point is defined as the origin. The results acquired, based on the optimization code, are shown in Table 2. Due to the limited fully-reversed loading cases, Table 2 shows that results were acquired at more than one cycle to increase the chances of attaining a more desirable fit. Based on the standard deviation results from Table 2, the fully reversed data at the 3rd cycle of the 82.7 MPa load shows the best fit.

τ (Mpa)	τ_{mean} (Mpa)	Cycle #	C_s	τ_c (Mpa)	**STD**
68.9	68.9	2	1.43E+07	20.3	**6.0859**
82.7	0	2	1.00E+05	64.8	**2.2969**
82.7	0	3	1.00E+05	93.4	**1.7009**
96.5	0	1	1.00E+05	50	**2.4535**
96.5	0	2	1.00E+05	47.9	**2.6532**

Table 2. Computational results for cyclic stress-strain curve fit

Shear fatigue results

It was stated previously in this section that based on the assembly of the Iosipescu fixture and its inability to handle large tensile loads, only low stress and extremely low cycle fully-reversed applications are manageable. Therefore, to negate the problem of tensile loading effects on the test fixture, all fatigue tests were conducted at R = –10; meaning, the test fixture stays in compression throughout the entire fatigue process. Since a shear load cannot be designated as compressive or tensile, however, the experimental fatigue loads were observed on a positive scale (i.e. R=0.1) to simplify the fatigue prediction manipulations. Shear fatigue results, based on this positive loading scale, are shown on Figure 19. Due to the lack of confirmed/specified fatigue limitations for the test fixture, the shear fatigue life results of Figure 19 extend from approximately 10^3 to only 10^5 cycles to assure no experimental inaccuracy. However, this fatigue life range should prove more than sufficient for the comparison with the shear life prediction calculations.

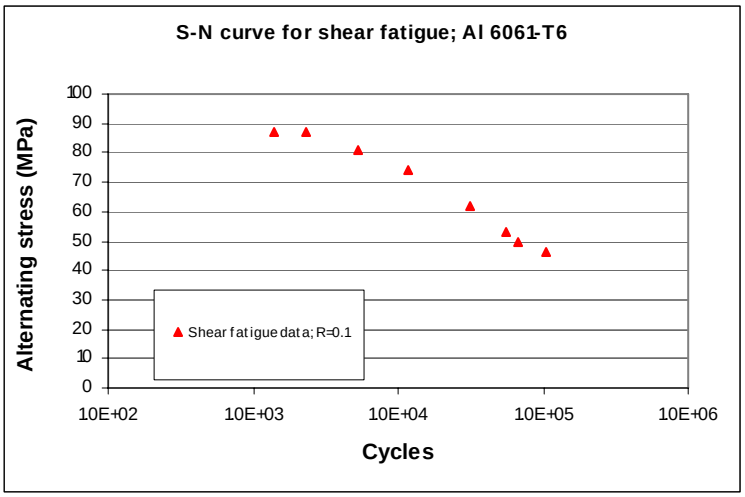

Figure 19. S-N data for shear loading

Biaxial fatigue results

Experimental fatigue results were acquired from two biaxial specimens at 10^6 cycles [14]. Alternating stress levels for each of the two biaxial tests were acquired using the step test method [22]. These experimental results can be seen on Figure 20. Observation of this figure shows minor variation in the fatigue stress level. The slight variability in the biaxial fatigue data could be a result of a few conditions such as follows: precision of gage placement, accuracy of the dimensions for the machined specimens, residual stresses resulting from surface finish, etc. Nevertheless, it can be assumed that the biaxial fatigue results of Figure 20 fall within an expectable scatter at a duration of 10^6 cycles.

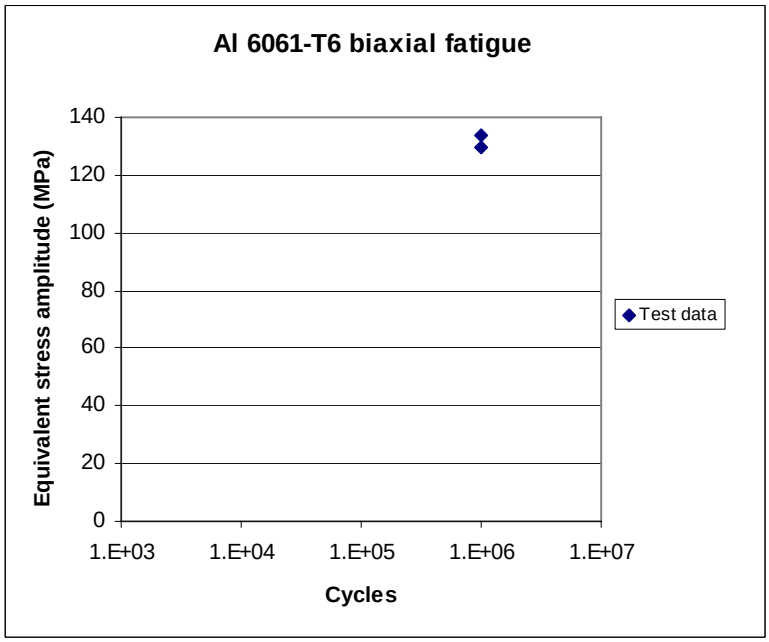

Figure 20. Experimental fatigue results for biaxial stress case [14]

5. SHEAR ENERGY-BASED FATIGUE ANALYSIS

Energy-based fatigue prediction analysis is developed based on the belief which states; the total strain energy required for monotonic fracture is equivalent to the strain energy accumulated from cyclic loading fracture (i.e. fatigue). According to this statement, it is essential to develop an analytical calculation method for strain energy from the monotonic case and from one cycle during a cyclic case. For the shear loading case, it is only necessary to calculate the strain energy density (strain energy per volume) as opposed to the entire strain energy. This is true because the experimental strain is analyzed at one point and is assumed to be uniform through the cross section of the specimen, with respect to the average shear stress.

Based on the previously stated belief that correlates energy and fatigue/fracture, each respective strain energy density representation is used to formulate the fully-reversed energy-based shear fatigue prediction criterion expressed by Equation 15.

$$N = C_s \frac{\tau_{fail}\left(\gamma_{fail} - \frac{\tau_{fail}}{2G}\right) - \gamma_o \tau_o \left[\cosh\left(\frac{\tau_{fail}}{\tau_o}\right) - 1\right]}{2\tau_c \left\{\frac{\tau}{\tau_c}\sinh\left(\frac{2\tau}{\tau_c}\right) - \left[\cosh\left(\frac{2\tau}{\tau_c}\right) - 1\right]\right\}} \qquad (15)$$

Due to the available experimental shear fatigue results from the previous section, the incorporation of mean stress effect was essential in this analysis. Mentioned in Section 2, the two observed effects of an applied mean stress on fatigue life are: (1) strain energy from the constant applied static load reduces the total energy required for fatigue, (2) plastic deformation in the cyclic stress-strain relationship is increased. The incorporation of these two occurrences into the expression of Equation 15, simultaneously, results in the reduction of the amount of cycles required to fatigue a specimen [13]. In other words, applying the mean shear stress (τ_{mean}) effect to the monotonic and cyclic shear strain energy density yields the expressions for the total required strain energy to failure (W_N) and the strain energy per cycle (W_{cycle}), which are represented by Equation 16 and Equations 17-20, respectively. By adhering to the understanding that the strain energy required to fracture a material monotonically is the same as the strain energy accumulated during a cyclic fatigue procedure, Equations 16 and 17 where used to construct an energy-based fatigue cycle calculation method with respect to the applied mean and alternating stress (Equation 21).

$$W_N = \tau_{fail}\left(\gamma_{fail} - \frac{\tau_{fail}}{2G}\right) + \gamma_o \tau_o \left[\cosh\left(\frac{\tau_{fail}}{\tau_o}\right) - 1\right] \qquad (16)$$
$$- \left\{\tau_{mean}\left[\frac{\tau_{mean}}{G} + \gamma_o \sinh\left(\frac{\tau_{mean}}{\tau_o}\right)\right] + \gamma_o \tau_o \left[\cosh\left(\frac{\tau_{mean}}{\tau_o}\right) - 1\right]\right\}$$

$$W_{cycle} = \tau_{pp}\left(\gamma_{pp} + \gamma_{mean}\right) - \int_{\tau_{mean}}^{\tau_{pp}+\tau_{mean}} \gamma_{cycle} d\tau_{pp} - \int_{0}^{\tau_{pp}} \gamma_{cycle} d\tau_{pp} \qquad (17)$$

$$\tau_{pp}\left(\gamma_{pp} + \gamma_{mean}\right) = 2\tau\left[\frac{2\tau + \tau_{mean}}{G} + \frac{\sinh\left(\frac{2\tau + \tau_{mean}}{\tau_c}\right)}{C_s}\right] \qquad (18)$$

$$\int_{\tau_{mean}}^{\tau_{pp}+\tau_{mean}} \gamma_{cycle} d\tau_{pp} = \frac{1}{2GC_s}\tau_{mean}^2 C_s + 2\tau_c \cosh\left(\frac{\tau_{mean}}{\tau_c}\right)G - \frac{1}{2GC_s}(2\tau+\tau_{mean})^2 C_s - 2\tau_c \cosh\left(\frac{2\tau+\tau_{mean}}{\tau_c}\right)G \quad (19)$$

$$\int_0^{\tau_{pp}} \gamma_{cycle} d\tau_{pp} = \frac{-\tau_c G + 2\tau^2 C_s + \tau_c \cosh\left(\frac{2\tau}{\tau_c}\right)G}{GC_s} \quad (20)$$

$$N = \frac{W_N}{W_{cycle}} \quad (21)$$

For the purpose of validating the prediction technique, the energy-based fatigue calculation method for the fully-reversed and the R=0.1 case were compared to the experimental results of Figure 19 on the S-N plot of Figure 21. The comparison between the prediction and the experimental results at lower cycles seem more inconsistent than higher cycle comparisons. This inconsistency may be due to uncertainties in the load distribution through the Iosipescu fixture for higher applied stresses and the larger magnitudes of possible internal moments caused by misalignment. However, the results of the comparison still show promise.

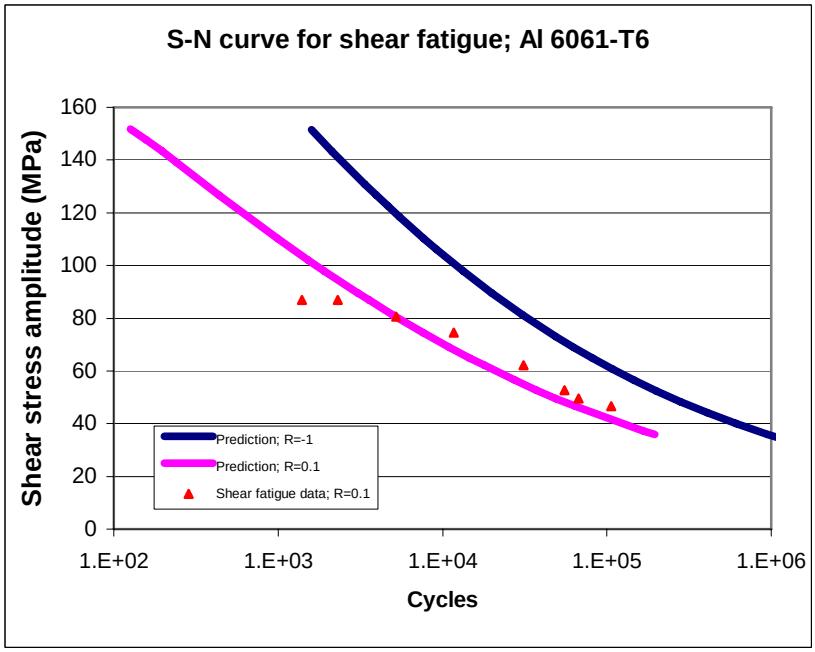

Figure 21. S-N comparison between predicted and experimental shear fatigue

6. MULTI-AXIAL ENERGY-BASED FATIGUE ANALYSIS

Fatigue prediction analysis for multi-axially loaded structures is a tumultuous task. In fact, there is no fatigue life calculation technique that can be directly applied to a multi-axial fatigue analysis without simplification of the total stresses acting on the multiple axes. The most popular simplified multi-axial fatigue life calculation method is the equivalent stress analysis [23]. This particular analysis is conducted by studying the 3-D stresses on an infinitesimal element from the fatigue zone

under observation, followed by the use of von Mises stress and the Goodman diagram relation to determine a single equivalent stress value [23]. This process, however, cannot be adopted by the constitutive stress-strain law of Equation 3; due to the unconventional incorporation of plastic effect. Therefore, the Distortion Energy Theory is observed in this literature with the assumption that the displacements are functions of nonlinear external loads.

The distortion energy theory is based on the understanding that the total strain energy is stored in two parts: (1) energy from the change in volume, and (2) energy from the change in shape [24]. Equation 22 displays the expression for this understanding.

$$U_T = U_v + U_D \tag{22}$$

The parameters for Equation 22 are defined as follows: U_T is the total strain energy, U_v is the strain energy of the change in volume, and U_D is the strain energy for the change in shape. Note that for this research, the aforementioned strain energy parameters in Equation 22 are observed as either strain energy density or strain energy per effective volume (i.e. strain energy per surface area).

To develop a constitutive law for multi-axial fatigue life prediction via strain energy-based analysis, the case of a structure in a general state of stress is observed. Since energy is a scalar, the critical (monotonic) total strain energy density value is constant. For the cyclic case, however, it is agreed that the strain energy density is acquired with the summation of strain energy density for the six stress components acting on a general structure, which is expressed by the following equation.

$$U_T = \sum \frac{2\sigma_c}{C}\left\{\frac{\sigma}{\sigma_c}\sinh\left(\frac{2\sigma}{\sigma_c}\right) - \left[\cosh\left(\frac{2\sigma}{\sigma_c}\right) - 1\right]\right\} + \sum \frac{2\tau_c}{C_s}\left\{\frac{\tau}{\tau_c}\sinh\left(\frac{2\tau}{\tau_c}\right) - \left[\cosh\left(\frac{2\tau}{\tau_c}\right) - 1\right]\right\} \tag{23}$$

Equation 23 is the basic form for the total strain energy calculation, where the first term is the strain energy summation based on the normal stresses (i.e. σ is equal to σ_x, σ_y, or σ_z) and the second term is the strain energy summation based on the shear stresses (i.e. τ is equal to τ_{xy}, τ_{yz}, or τ_{zx}). Observation of this total strain energy density calculation shows that the effect of Poisson's ratio is neglected. The effect of Poisson's ratio on strain is determined by the deformation of the cross-section area of an object that is subjected to an applied load. High cycle multi-axial fatigue, however, operates at stress levels well within the elastic region of most metallic alloys. Based on this, the cross-sectional deformation experienced during high cycle multi-axial fatigue is minimal. Therefore, to simplify multi-axial fatigue life prediction, the effect of Poisson's ratio was omitted.

The importance of this general form is based on the study conducted in Section 2, which observed the effect of stress gradient on uniaxial fatigue results. The study shows that the general form is important because the possibility of a case with simultaneous tension/compression and bending loads acting on a specimen exist. Therefore, a general total strain energy density calculation method is necessary for the evaluation. For case where the uniaxial loading mechanism is the same, however, principle direction stresses can be used. Therefore, if the principle axes are used as the coordinate axes, the expressions for shear loading become zero and the general expression is written as:

$$U_T = \sum_{p=1}^{3} \frac{2\sigma_c}{C}\left\{\frac{\sigma_p}{\sigma_c}\sinh\left(\frac{2\sigma_p}{\sigma_c}\right) - \left[\cosh\left(\frac{2\sigma_p}{\sigma_c}\right) - 1\right]\right\} \quad (24)$$

Where the subscript p denotes the principle direction strain energy expression being added in the summation.

Analytical biaxial bending fatigue life calculation procedure for comparison with experimental results was a straightforward task. Using Equation 24, the principle stresses related to the acquired experimental results of Figure 20 where used to determine the total effective strain energy per biaxial cyclic loading. By applying the belief behind the fracture-energy correlation to the biaxial case, multi-axial fatigue life can be determined by dividing the monotonic strain energy per effective volume with the total effective strain energy per cycle (Equation 25).

$$N = \frac{\sigma_n\left(\varepsilon_n - \frac{\sigma_n}{2E}\right) - \varepsilon_o\sigma_o\left[\cosh\left(\frac{\sigma_n}{\sigma_o}\right) - 1\right] + \frac{\beta_1}{2}\left(\varepsilon_f^2 - \varepsilon_n^2\right) + \beta_o\left(\varepsilon_f - \varepsilon_n\right)}{U_T} \quad (25)$$

Single point energy-based biaxial fatigue predictions have been generated using Equation 25, which is the criterion for multi-axial fatigue assessment. The results are compared with experimental step test data at 10^6 cycles on Table 3. A visual/graphical comparison, however, is not available with the use of conventional von Mises stress calculation. In order to develop a graphical comparison between experimental and prediction results, a new equivalent stress calculation scheme is required. To determine the calculation method for equivalent stress due to multi-axial cyclic loading, the total cyclic strain energy is observed in the energy distortion expression of Equation 26, where σ_E is the equivalent stress required. Furthermore, due to the unknown changes of the principle stresses with respect to each other, it is difficult to calculate the necessary integrations for strain energy density per cycle. This difficulty, along with the minimal Poisson effect on the overall fatigue life calculation, leads to the omission of the Poisson's ratio factor in the constitutive law and in the strain energy density calculation of Equation 26. The completion of these results will be further discussed in future documentation. Based on this incompletion of an equivalent stress expression, the fatigue life comparisons are made with experimental cycles versus prediction cycles on Table 3. Though the results from the table shows little variation, the absence of graphical validation and the lack of experimental results gives a skewed understanding of whether the prediction falls within an acceptable scatter. To provide a more clear validation, a comparison is made between the tension/compression fatigue life prediction result and a corresponding experimental point shown in Figure 1 of Section 2, which is displayed in Table 3 along with the biaxial comparisons. Observing the experimental-prediction comparison from Figure 1 implies that more biaxial experimental data and a graphical observation should provide a more sufficient visual validation of the comparison between the multi-axial energy-based prediction and experimental results.

$$\frac{2\sigma_c}{C}\left\{\frac{\sigma_E}{\sigma_c}\sinh\left(\frac{2\sigma_E}{\sigma_c}\right) - \left[\cosh\left(\frac{2\sigma_E}{\sigma_c}\right) - 1\right]\right\} = \sum_{p=1}^{3} \frac{2\sigma_c}{C}\left\{\frac{\sigma_p}{\sigma_c}\sinh\left(\frac{2\sigma_p}{\sigma_c}\right) - \left[\cosh\left(\frac{2\sigma_p}{\sigma_c}\right) - 1\right]\right\} \quad (26)$$

	Prediction cycles	Experimental cycles	Relative error
Biaxial 1	1292462	1000000	22.6

Biaxial 2	1100494	1000000	9.1
Axial 1	1000000	429862	57

Table 3. Numerical prediction and experimental comparison

7. CONCLUSION

The content of this document clearly provides two new and meaningful criteria for fatigue assessment: (1) Energy-based shear fatigue prediction, and (2) a constitutive law for showing the simultaneous effect of multi-axial cyclic loads on fatigue life. Each criterion has been validated through comparison with experimental shear and biaxial fatigue results. Variations do exist between the comparisons. However, these variations can be attributed to a multitude of inconsistent occurrences such as the following: MTS actuator inconsistency, specimen positioning, fixture alignment, strain gage placement, residual stresses from machining process, other surface finish problems during machining, etc. Nevertheless, the comparisons are consequential, and indicate that accurate life estimation is possible for fatigue under shear or biaxial loading via a strain energy-based approach.

Since the prediction method introduced in this manuscript is energy-based, it can also be easily incorporated into a minimal potential energy calculation. This is extremely influential, especially, to aircraft engine design via FEM software due to the fact that most FEM software don't have a fatigue life prediction mechanism. FEM software with a fatigue life prediction mechanism often uses the Goodman diagram; which was stated as insufficient for multi-axial fatigue in Section 1. Therefore, the development of the energy-based fatigue life prediction method for objects under shear and multi-axial loading is a stepping-stone for the advancement of future FEM software.

8. REFERENCE

[1] Scott-Emuakpor, O., Shen, M.-H. H., Cross, C., Calcaterra, J., and George, T., "Development of an Improved High Cycle Fatigue Criterion," Journal of Engineering for Gas Turbines and Power, 2007; Vol. 129, Issue 1, pp. 162-169.

[2] Goodman, J., 1899, *Mechanics Applied to Engineering*, Longmans, Green, and Co., London.

[3] George, T., Seidt, J., Shen, M.–H. H., Cross, C., and Nicholas, T, "Development of a Novel Vibration-Based Fatigue Testing Methodology", International Journal of Fatigue 2004; 26: 477-486.

[4] Shen, M.–H. H., Seidt, J., George, T., Cross, C., Whaley, P.W., and Nicholas, T., "Development of a Novel Method for Evaluating Material Behavior under Turbine Engine Operating Conditions, Part I: Design of Accelerated HCF Testing Procedures," 6th National Turbine Engine High Cycle Fatigue Conference, 2001.

[5] Shen, M.–H. H., Seidt, J., George, T., Cross, C., Whaley, P.W., and Nicholas, T., "Development of a Novel Method for Evaluating Material Behavior under Turbine Engine Operating Conditions, Part II: An Empirical Vibration-Based Fatigue Assessment Framework," 6th National Turbine Engine High Cycle Fatigue Conference, 2001.

[6] Lanning, D., Nicholas, T., and Haritos, G., "Effect of Plastic Prestrain on High Cycle Fatigue of Ti-6Al-4V," International Journal of Fatigue 2002; 34: 127-134.

[7] George, T., Shen, M.-H. H., Scott-Emuakpor, O., Nicholas, T., Cross, C., and Calcaterra, J., "Goodman Diagram via Vibration-Based Fatigue Testing," Journal of Engineering Materials and Technology, 2005; Vol. 127, Issue 1, pp. 58-64.
[8] Scott-Emuakpor, O., **"**Development of an Improved Energy-Based Criterion for Fatigue Life Assessment", Thesis (M.S.), The Ohio State University, 2004.
[9] Jasper TM, "The Value of the Energy Relation in the Testing of Ferrous Metals at Varying Ranges of Stress and at Intermediate and High Temperatures," Philosophical Magazine, Series. 6, Oct. 1923; 46: 609-627.
[10] Feltner, C. E., and Morrow, J. D., "Microplastic Strain Hysteresis Energy as a Criterion for Fatigue Facture," 1960; ASME Paper No. 60-MET-2.
[11] Enomoto, N., "On Fatigue Tests Under ProgressiveStress," ASTM, 1955; Vol. 55, pp. 903.
[12] Stowell, E., "A Study of the Energy Criterion for Fatigue," Nuclear Engineering and Design, 1966; pp. 32-40.
[13] O. Scott-Emuakpor, M.-H. H. Shen, T. George, and C. Cross, *A New Energy-Based Uniaxial Fatigue Life Prediction Method for Commonly Used Gas Turbine Engine Materials*, 2008, Journal of Engineering for Gas Turbines and Power, Accepted for Publication.
[14] George, T., Shen, M.-H. H., Cross, C., and Nicholas, T., "A New Multiaxial Fatigue Testing Method for Variable Amplitude Loading and Stress Ratio", Journal of Engineering for Gas Turbines and Power, 2006; Vol 128, pp. 857-864
[15] Garud, Y., S., "A New Approach to the Evaluation of Fatigue Under Multiaxial Loading," *Proceeding of Symposium on Methods for Predicting Material Life in Fatigue*, ASME, New York, 1979; 247-264.
[16] American Society for Testing and Materials, "D5379-05: Standard Test Method for Shear Properties of Composite Materials by the V-Notched Beam Method," *ASTM Book of Standards*, 2005; Vol:15.03, ASTM International, West Conshohocken, PA.
[17] Vishay measurement instrumentation website, http/www.vishay.com
[18] Nicholas, T., "Critical Issues in High Cycle Fatigue," International Journal of Fatigue, 1999; 21:S221-S231.
[19] Miyano, T., "High Cycle Fatigue Specimen Topology Design", Thesis (M.S.), The Ohio State University, 2003.
[20] Scott-Emuakpor, O., **"**Development of a Novel Energu-Based Method for Multi-Axial Fatigue Strength Assesment", Dissertation (Ph.D.), The Ohio State University, 2007.
[21] Sih, G., C., and Jeong, D., Y., "Hysteresis loops predicted by isoenergy density theory for polycrystals. Part II: cyclic heating and cooling effects predicted from non-equilibrium theory for 6061-T6 aluminum, SAE 4340 steel and Ti–8Al–1Mo–1V titanium cylindrical bars," Theoretical and Applied Fracture Mechanics, 2004; Vol 41, Issues 1-3, pp. 267-289
[22] Nicholas, T., and Maxwell, D., "Mean Stress Effects on the High Cycle Fatigue Limit Stress in Ti-6Al-4V," Fatigue and Fracture Mechanics: 33rd Volume, ASTM STP 1417, W.G. Reuter and R.S. Piascik, Eds., American Society for Testing and Materials, West Conshohocken, PA, 2003; pp. 476-492.
[23] Collins, J., *Mechanical Design of Machine Elements and Machines*, John Wiley & Sons, Inc, 2003.
[24] Boresi, A., Schmidt, R., 2003, *Advanced Mechanics of Materials*, John Wiley and Son Inc.

Interim Report I

INITIAL RESISTANCE MEASUREMENTS – SAMPLE TJ1959 – $SrRuO_3$ doped

M.D. Sumption
Aug 5, 2008

Introduction

In this report, a number of YBCO PLD samples were measured resistively and magnetically, in order to see if ferromagnetic pinning was present. Additionally, a high performance BZO based YBCO PLD sample was measured at high fields magnetically, in order to see its high field performance. Samples TJ1959 and TJ1971, configured for resistance measurements, were individually inserted into the ACMS option of the PPMS, and measured for resistance both in the normal state, and through the transition. The main objective was to look for an increase in magnetoresistance due to the $SrRuO_3$ (1959) or YIG (1971) doping, expected in the case of a ferromagnetic doping layer. This method was chosen because the magnetic signature of these samples was expected to be weak in the VSM measurements. Some initial measurements were performed by VSM without observing a ferromagnetic signal. This lack of observation may have either been due to the low level of $SrRuO_3$ present, or because it is not actually ferromagnetic in the present environment, perhaps because of interactions with the underlying YBCO. The objective was, then, to use normal state resistivity, checking for the presence of magnetoresistance, which should be a good probe of the presence of ferromagnetic material. These measurements were compared to a control sample. After this, a high quality BZO sample was also studied.

Resistive Measurements

Figure 1 shows the present set of measurements, plotted as R vs T for sample TJ1959. This data can be re-plotted as R vs $1/T$ as shown in Figure 2.

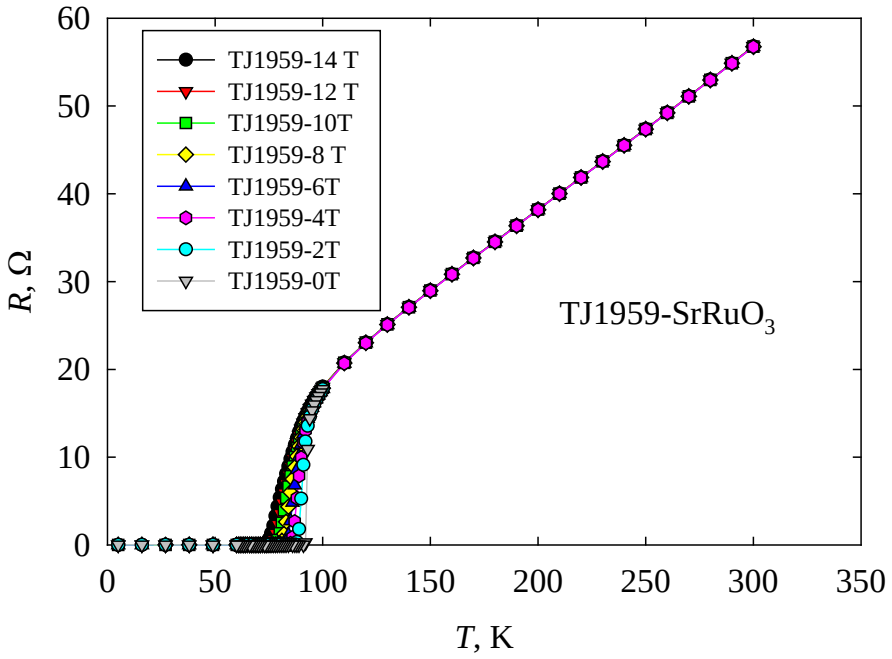

Figure 1. *R* vs *T* for TJ1959, a $SrRuO_3$ doped YBCO sample.

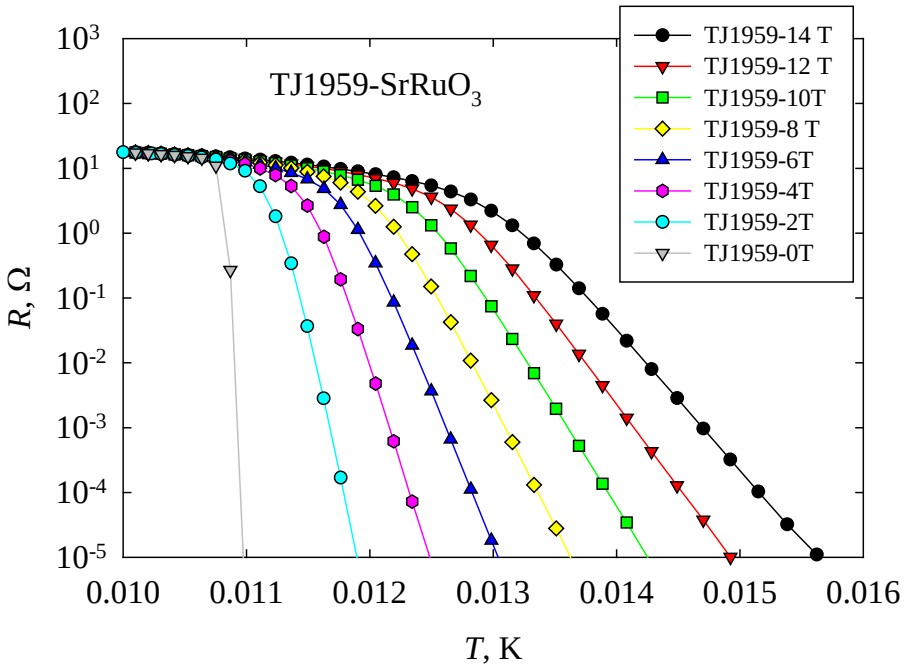

Figure 2. *R* vs 1/*T* for sample TJ1959.

Here we can extract the slopes and use the relation

$$\rho = \rho_0 \exp[-\frac{U}{k_b T}]$$

to extract the effective pinning potential, *U*. Such a *U* has been extracted for this sample and is shown in Figure 3 as a function of *B*. U was seen to have a power law dependence on *B*, in the form $U = U(0)B^{-\nu}$, where *U(0)* = 15,800 K, and $\nu = 0.726$. The power law dependence of *U* on *B* is expected. Such values for ν are common, and the *U*(0) value (the *U* in the limit of zero *B*) is generally consistent with previous magnetic measurements of *U* done by magnetization decay as well as ramp rate dependent measurements on other AFRL YBCO samples (where values in the limit of $J \rightarrow 0$ are in the 20,000 K range). It should be of interest to compare these results with other samples, both control YBCO samples, samples with non-magnetic pinners, and other magnetic pinner samples.

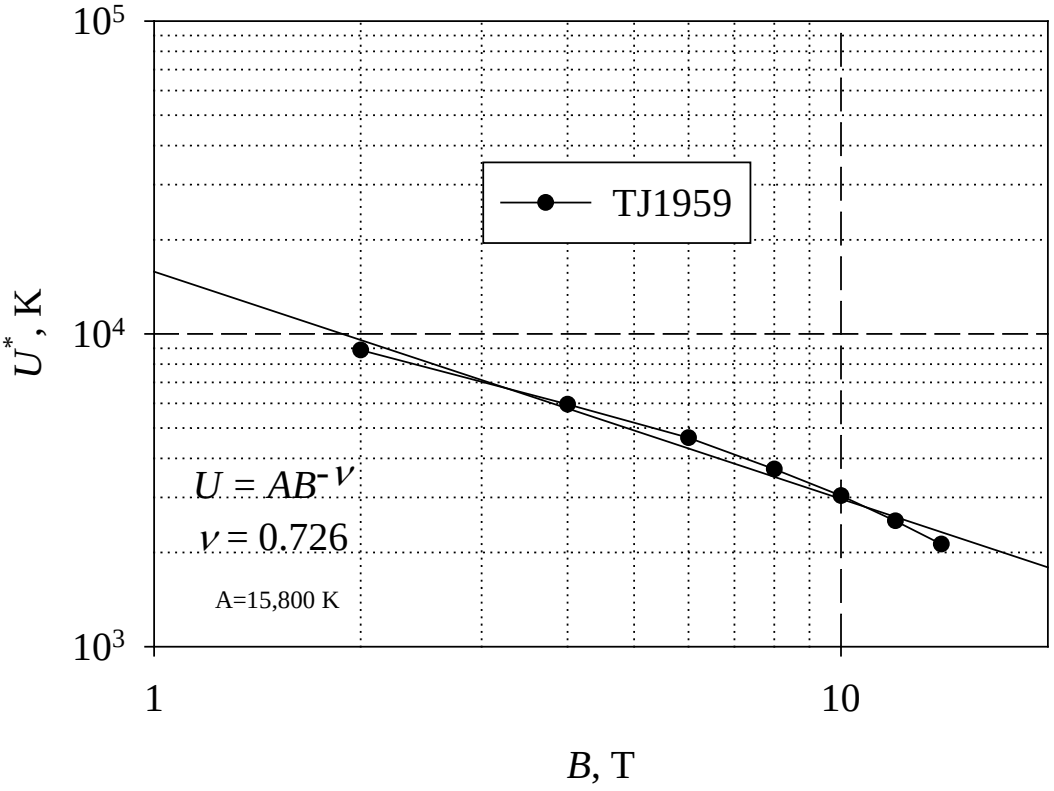

Figure 3. *U* vs *B* for TJ1959 from resistance measurements of the transition. *U* has a power law dependence on *B*, with a $\nu = 0.726$ and a zero *B* value of 15,800 K.

Figure 4 shows a close up of the transition region for TJ1959. Resistance measurements are then shown for sample TJ1971 (YIG doped) in Figure 5, and Figure 6 shows a close-up of the transition. .

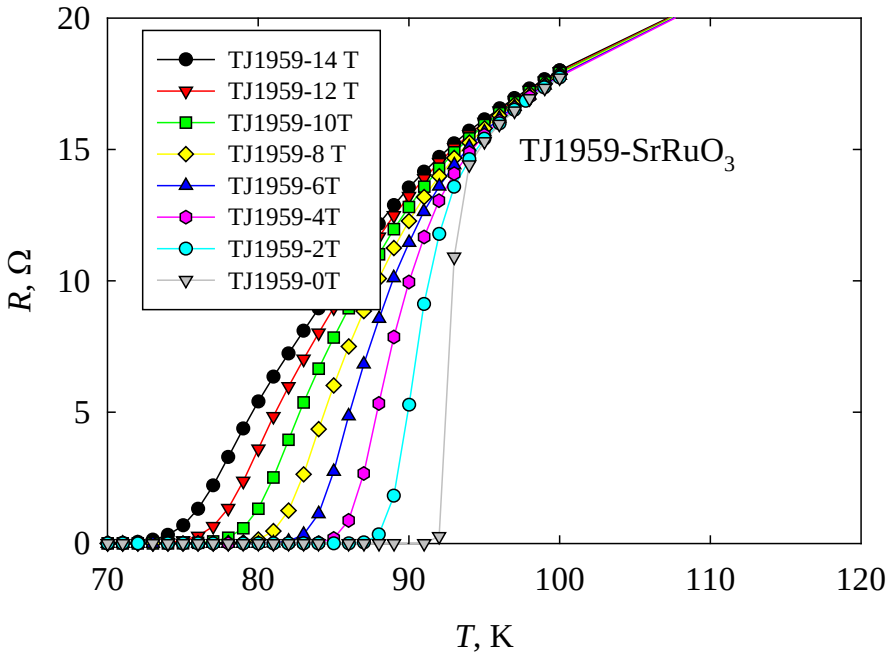

Figure 4. A close up of the transition region for TJ1959.

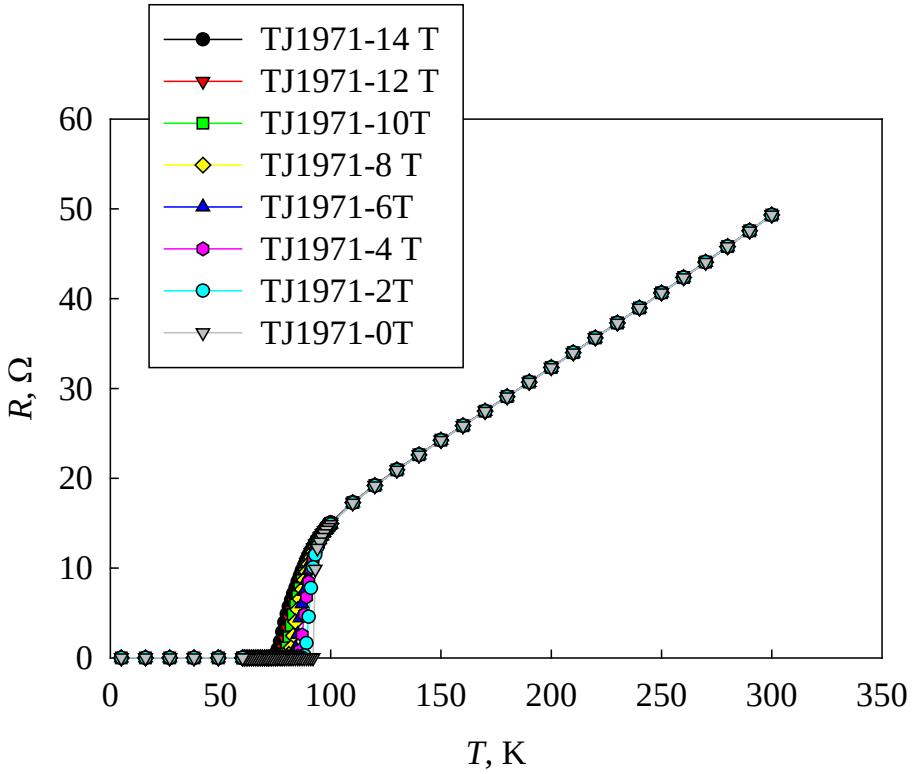

Figure 5. The resistive transitions for TJ1971.

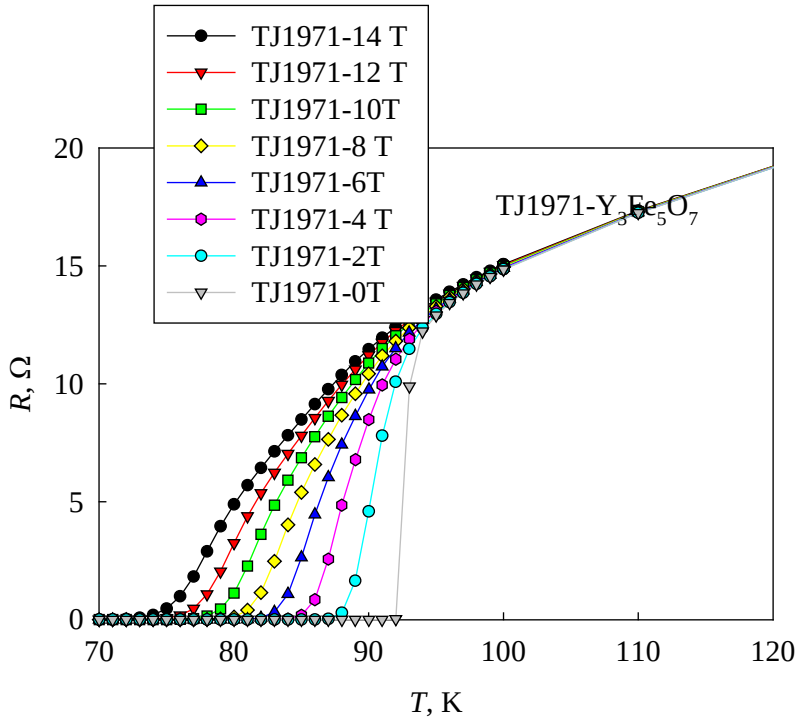

Figure 6. A close-up of the resistive transition for TJ1971.

Figure 7 shows the transition data as $1/T$ so that the pinning energies can be extracted.

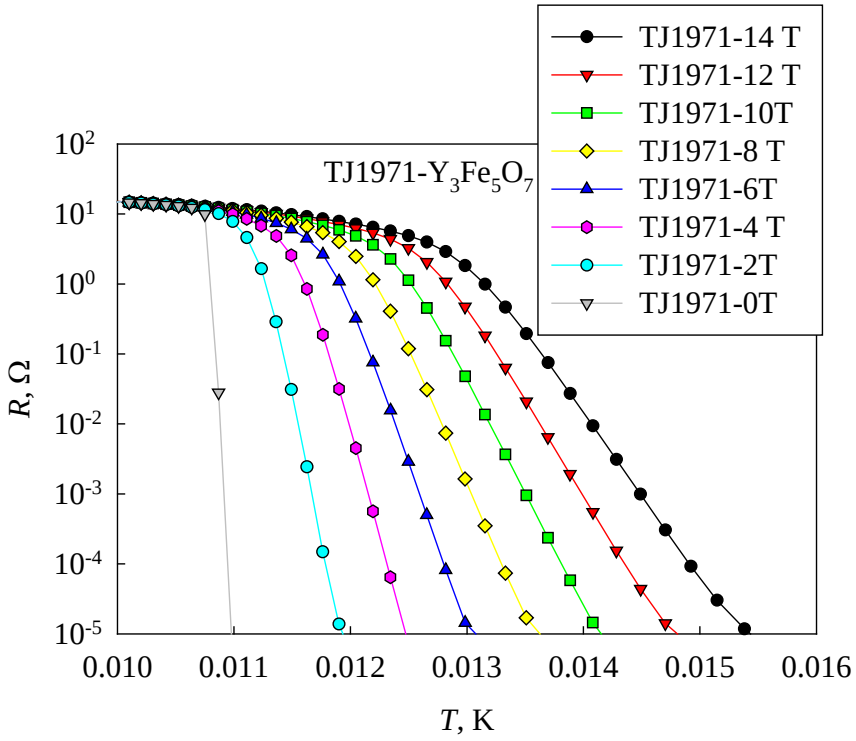

Figure 7. R vs $1/T$ for TJ1971.

Figure 8 shows the *R* vs *T* for sample TJ1805, a control sample, and Figure 9, the close up of the transition, and Figure 10, *R* vs 1/*T*.

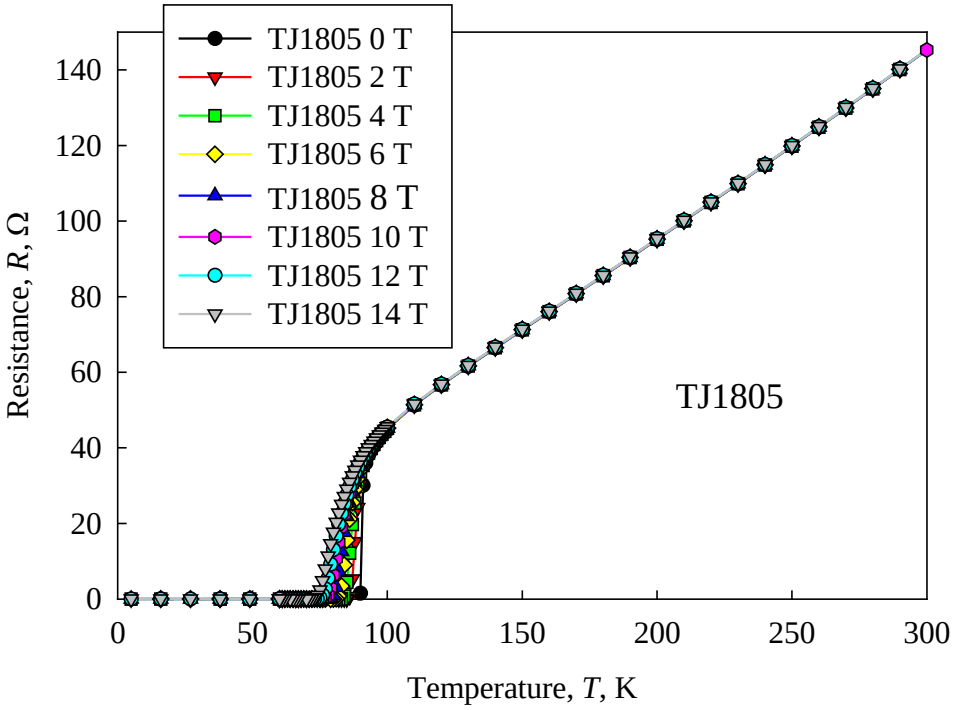

Figure 8. *R* vs *T* for TJ1805.

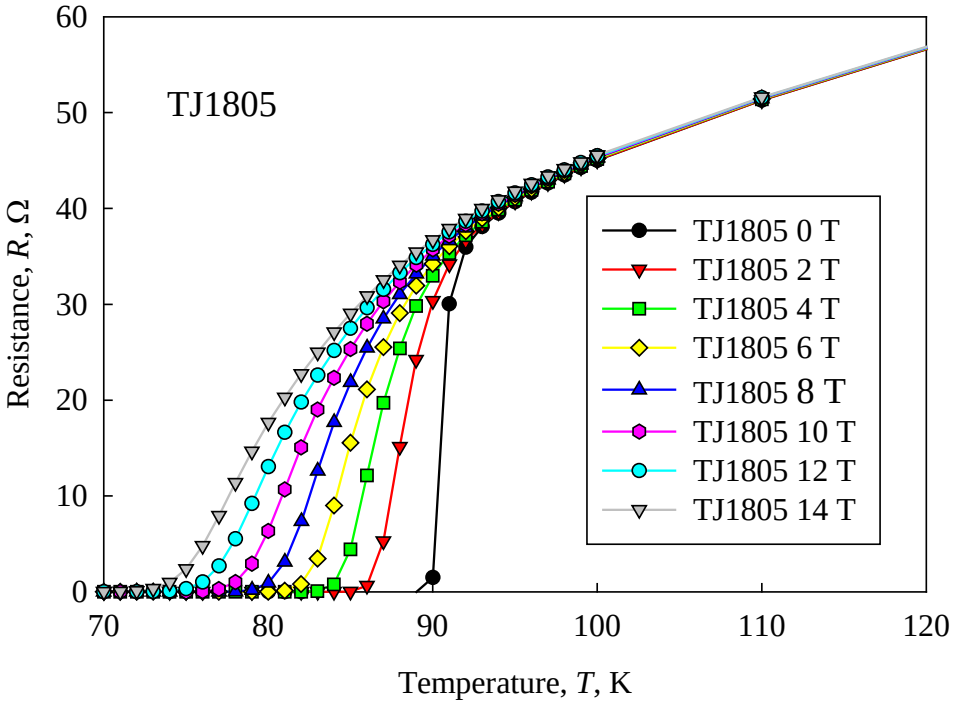

Figure 9. A close up of the resistive transition for TJ1805.

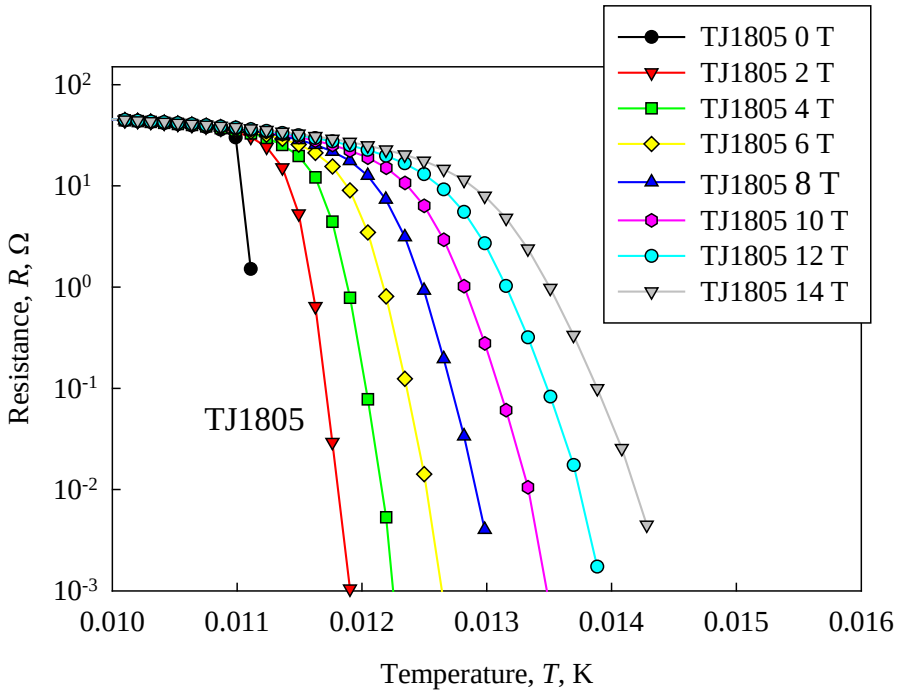

Figure 10. R vs 1/T for TJ1805.

Figure 11 shows the *U** summary.

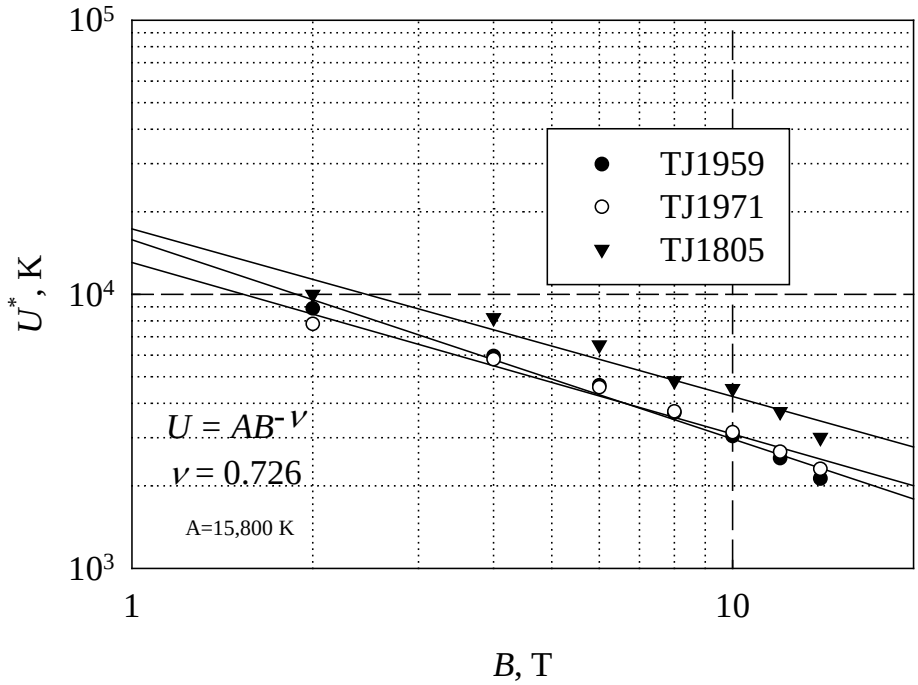

Figure 11. A summary of *U** for three samples, SRO (1959), YIG (1971) and a control (1805).
Figure 12 shows a comparison of the magnetoresistance for the samples TJ1959 and TJ1971.

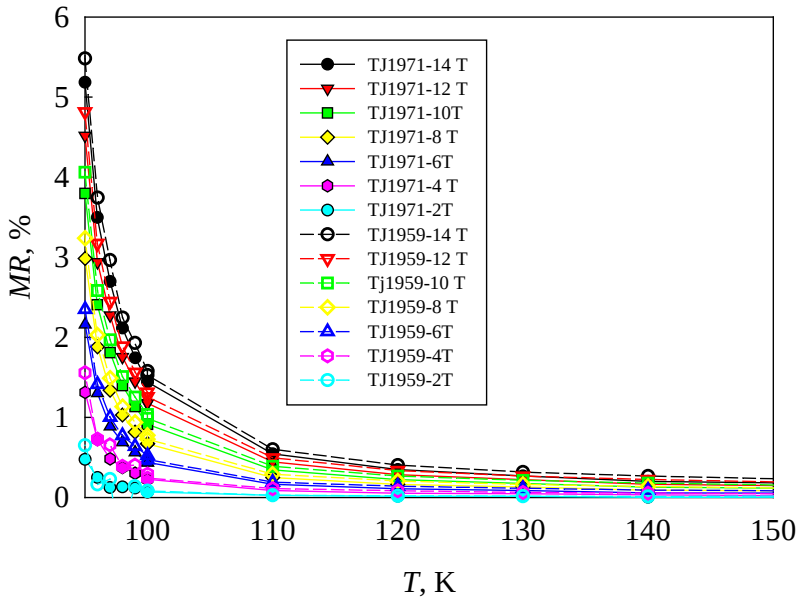

Figure 12. A comparison of the magnetoresistance for TJ1959 and TJ1971.

Figure 13 shows the magnetoresistance of the control sample.

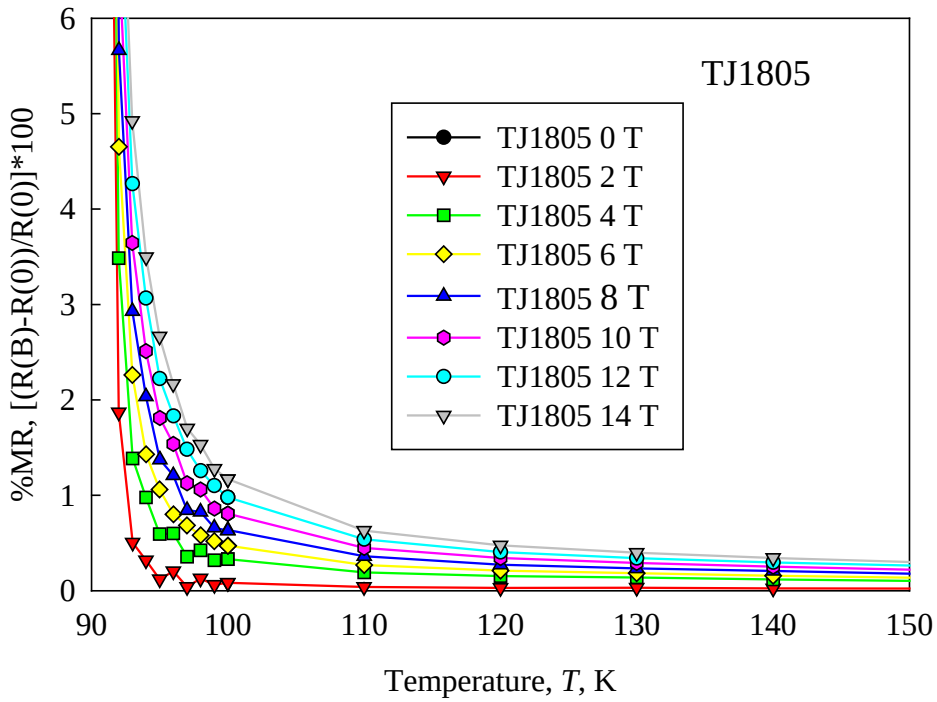

Figure 13. Magnetoresistance of the control sample TJ1805.

Figure 14 shows a comparison of magnetoresistance vs *B* at various temperatures for all three samples, with a focus on the higher temperatures. Figures 15 and 16 show lower temperature results as well.

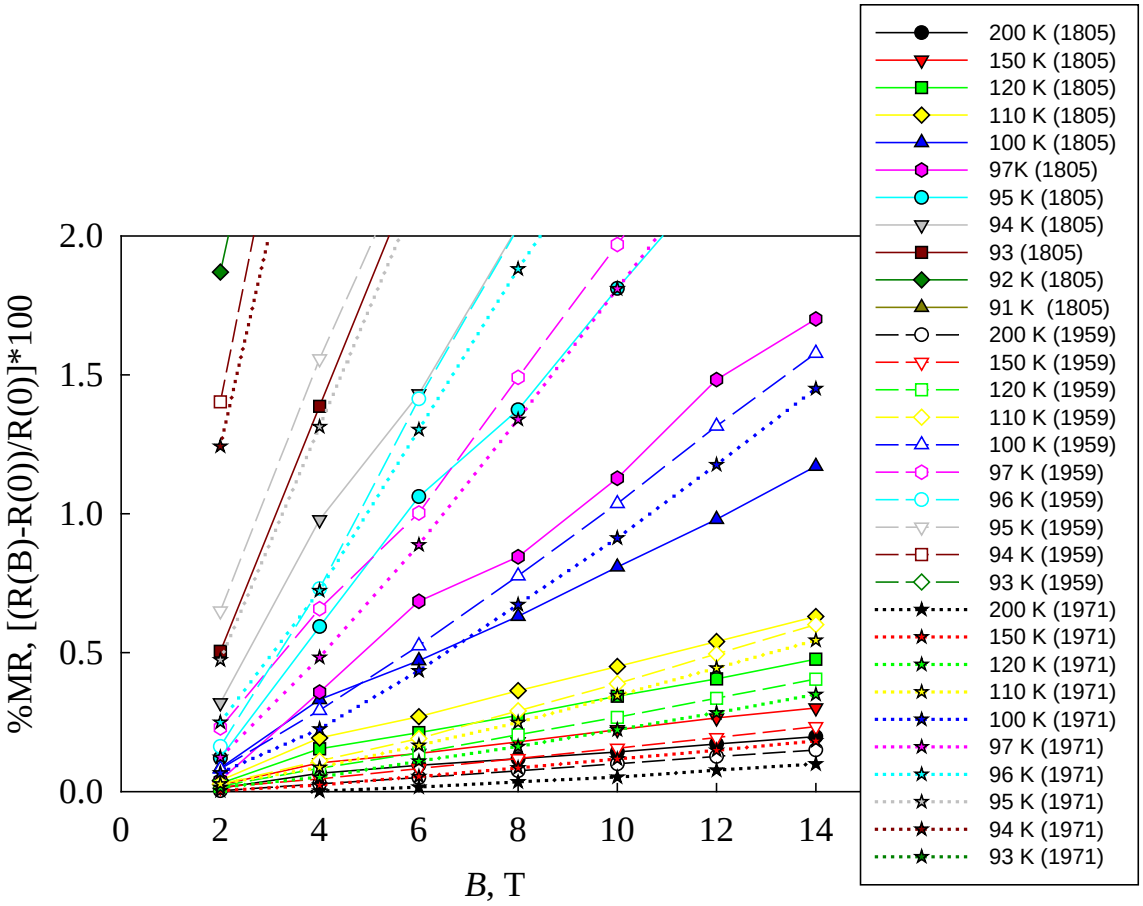

Figure 14. Magnetoresistance vs *B* for all three samples with high temperature region expanded.

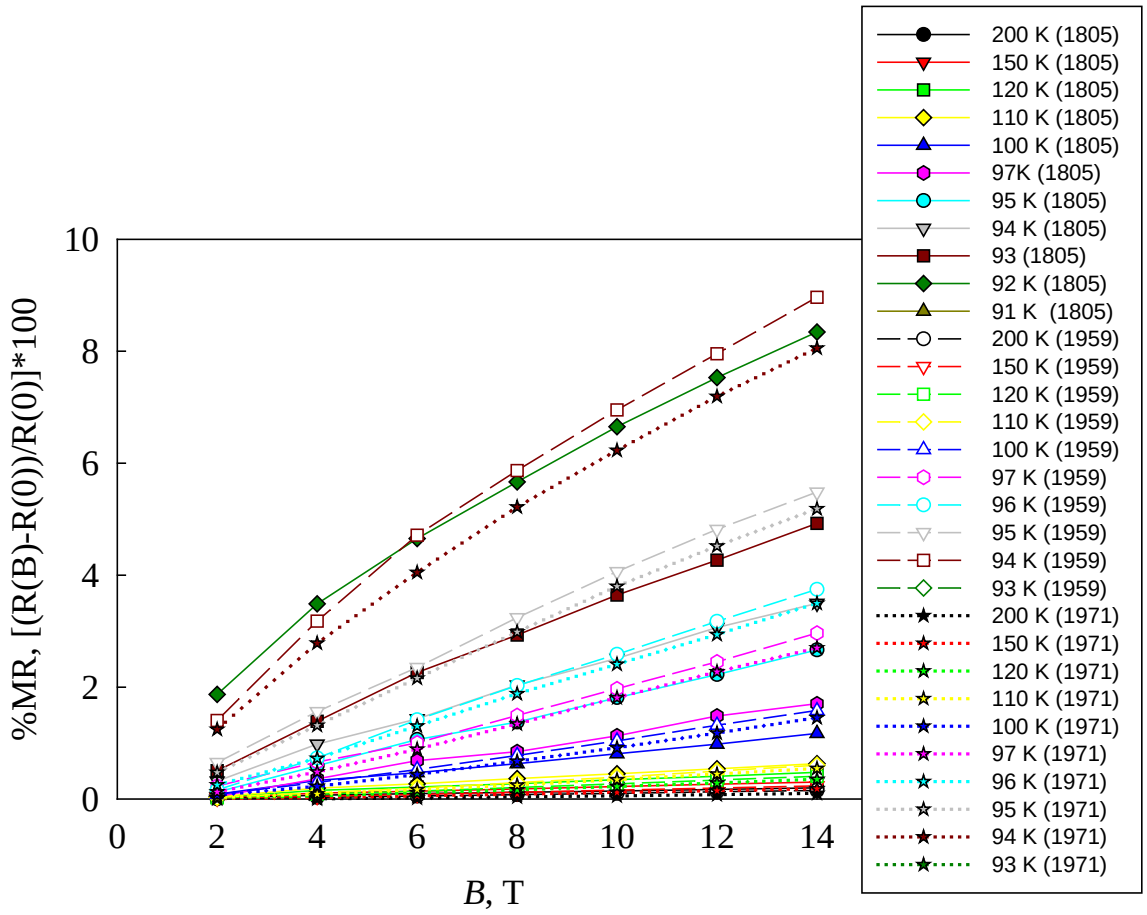

Figure 15. Magnetoresistance vs *B* for all three samples with middle temperature region expanded.

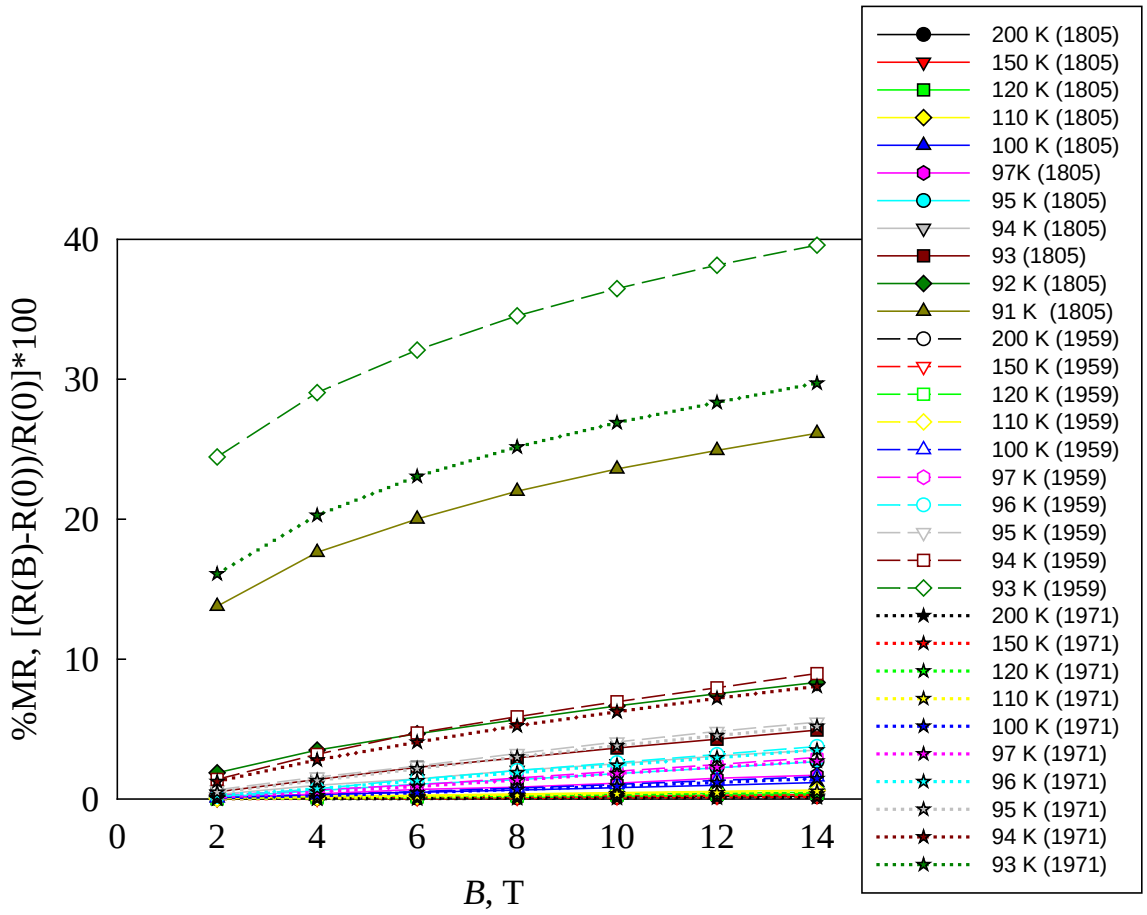

Figure 16. Magnetoresistance vs *B* for all three samples with lower temperature region expanded.

Figure 17 shows the T_c response of the samples.

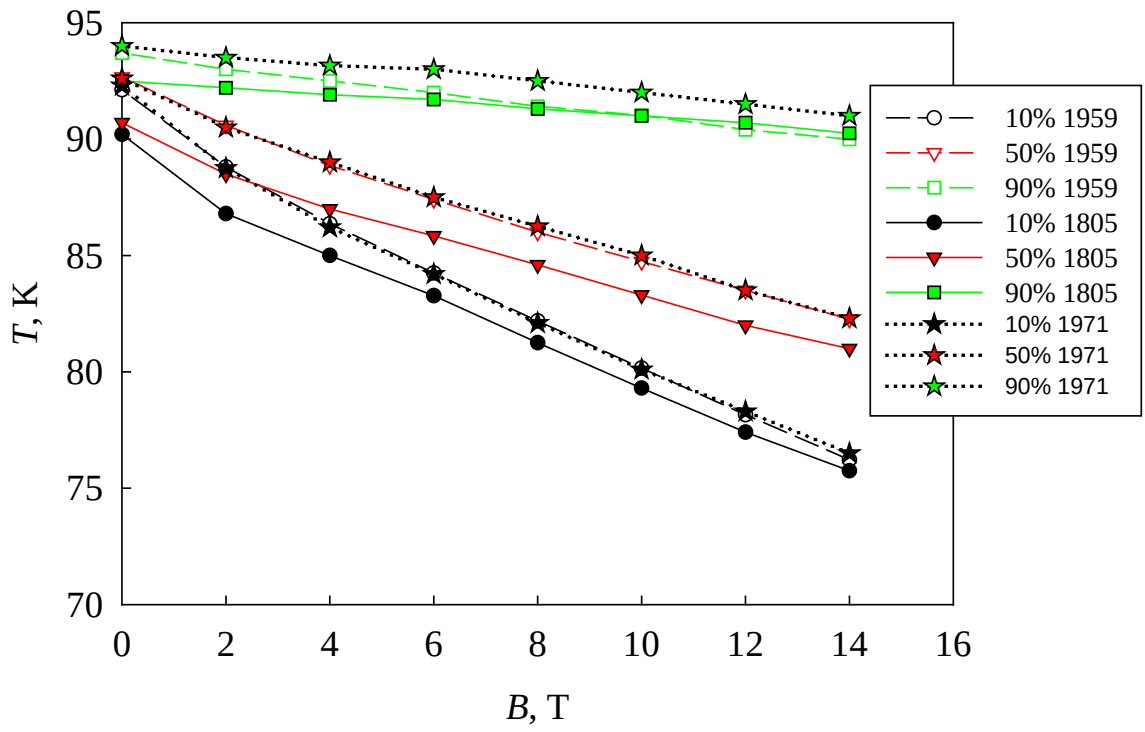

Figure 17. T_c response of samples, which can also be interpreted as B_{c2} and B_{irr}.

Magnetic Measurements

Table 1. M-H Sample Specifications .

Sample ID	Tracer ID	*Δm*, emu, 4.2K, 0T	*Δm*, emu, 77K, 0T	J_c factor (emu to MA/cm^2)	Vol., 10^{-6} cm^3	*t*, μm	<*w*>, mm
BZO-F YIG-A	TJ2019B TJ1970			41.1	2.28	0.223	3.20

[a] error is 4%
[b] Post etch volumes

For a square geometry, with field applied along the c-axis, (perpendicular to film) $\Delta M = dJ_c/30$, with ΔM in emu/cm^3 and J_c in A/cm^2, thus we get as a conversion factor from ΔM in emus to J_c in A/cm^2 the factor $30/(Vw)$, where w is the average width and V the total volume, each in cm and cm^3 units, respectively.

Figure 18 shows the M-H loops for TJ1970, a YIG doped sample.

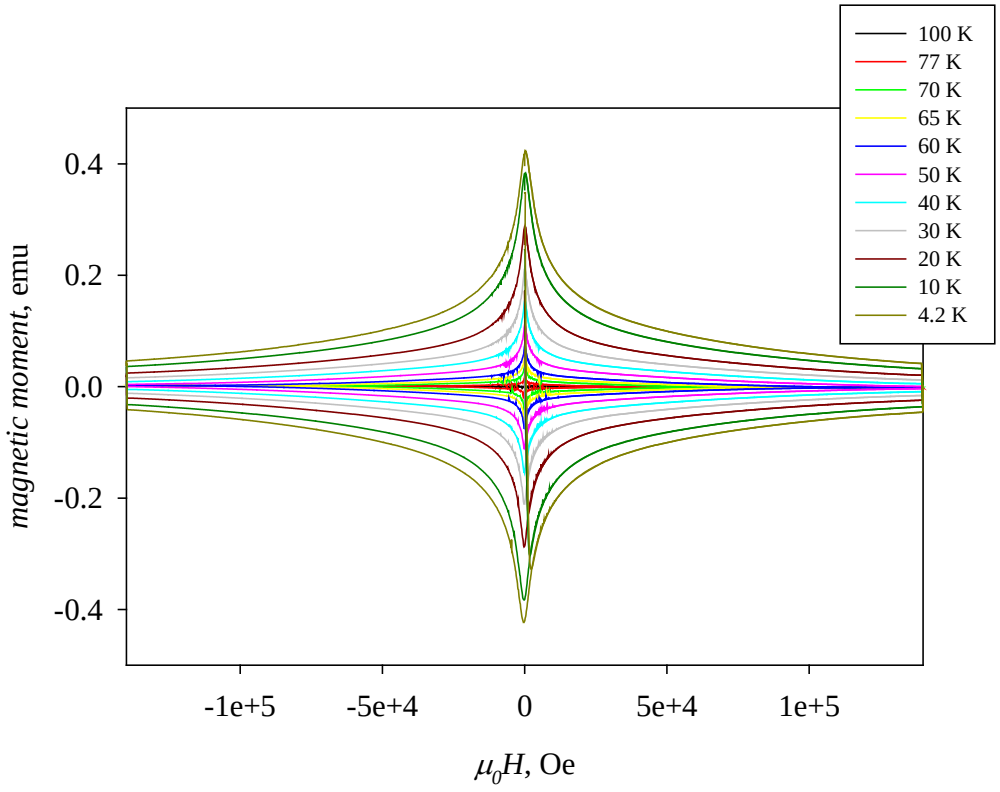

Figure 18. M-H loops for TJ1970.

Figure 19 shows the 100 K response of TJ1971. While it is quite noisy at low fields due to the Nb_3Sn magnet system, it will be re-measured in a NbTi magnet based system. In any case, the offset between the positive B branch and the negative B branch may suggest the existence of a ferromagnetic signal.

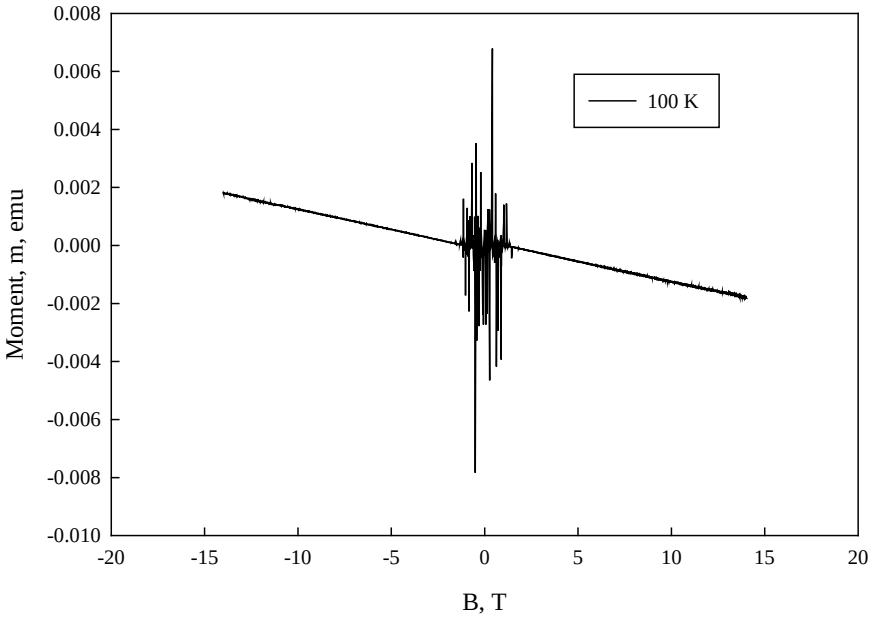

Figure 19. Possible ferromagnetism in TJ1971.

Figure 20 shows the M-H of the BZO sample TJ2019B.

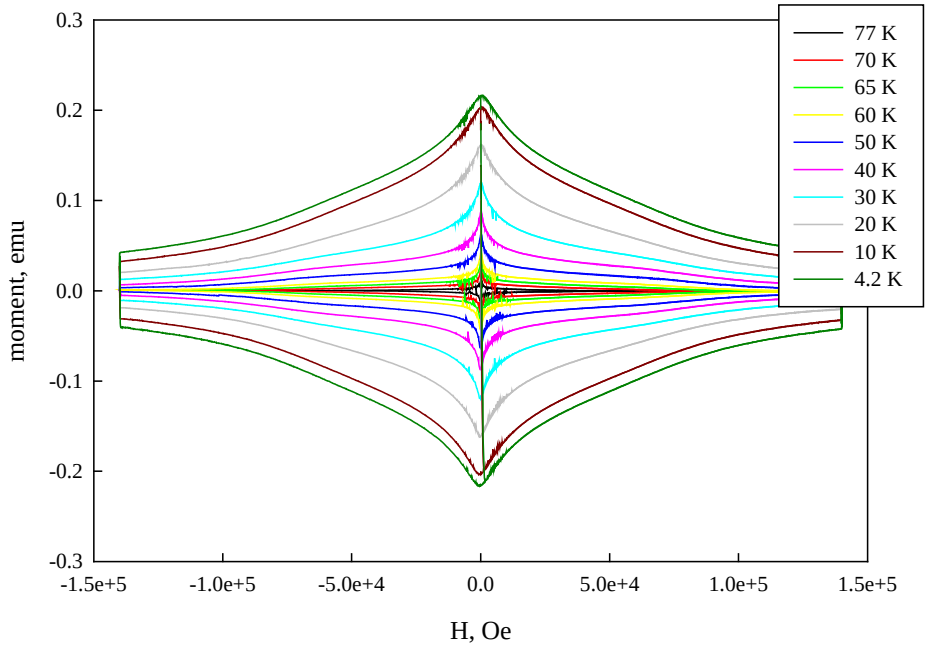

Figure 20. The M-H for BZO laced sample TJ2019B**.**

These *M-H* curves have not yet been reduced to magnetic J_c, but this is in progress.

Discussion and Next Steps

The magnetoresistance measurements at higher temperatures suggest little difference between the magnetically doped samples and the control sample. As the temperature nears T_c, however, there does seem to be a difference, with considerably more magnetoresistance being seen for the magnetically doped samples. This may be in the regime where fluctuation superconductivity is beginning to be seen, and so a comparison to that theory is suggested. In any case, it does suggest the magnetic inclusions may be somehow active.

Beyond this, the *M-H* for TJ1971 above T_c is interesting, and may show ferromagnetic signatures. This needs to be confirmed using better low field runs, and also background runs, so this is a at the moment tentative result.

Moving forward, while some comparison of this data to theory is in order, including the interesting functional dependence of the magnetoresistance and the difference with ferromagnetic inclusions, the main focus should shift to direct measurements of *M-H* above T_c to confirm the presence of ferromagnetic signatures, and the measurement of the B_{irr} and magnetic J_cs at high fields for the BSO and BZO samples. Also, the next period will include measurement of the grain boundary Ca doped samples.

APPENDIX Z

Microwave Enhanced Combustions

Emanuel Stockman
Olden Street
EQuad – MAE
Princeton, NJ 08544
estockma@princeton.edu
UTC Prime Contract #F33615-02-D-2299

Wright Patterson Air Force Base Summer 2008 Fellowship – UTC Report

Work conducted at Wright Patterson Air Force Base this summer generated several quality datasets for use in the microwave enhanced combustion research project. As a part of the propulsion directorate, and working with Dr. Michael Ryan and Dr. Campbell Carter, my work mainly focused on improving the repeatability of the experiment and also quantifying the microwave coupling to the flame. The research project was motivated by the need to improve certain aspects of hydrocarbon combustion towards the development of hypersonic scramjet technology. Microwave enhanced combustion research falls under the larger field of plasma assisted combustion and aims to mitigate issues of flame stability and blowoff at supersonic speeds. The experimental work focused on the application of laser induced fluorescence (LIF) and filtered Rayleigh scattering (FRS) to a laminar, hydrocarbon, flat flame that has been shown to have increased flame speed when radiated with microwave energy. Almost 20 gigabytes of data were collected and the processing of the raw information has yet to be completed. Qualitative results will be shown in this report to point out several successful aspects of the summer work. Additionally, preliminary development of a computer model of the interaction was started using the software package, CHEMKIN. Productive conversations with other researchers in the propulsion branch yielded helpful insight into how best to approach problems encountered throughout the summer.

Experiments previously performed at the Air Force Base in December of 2007 motivated the long term summer visit after compelling results were observed when 1.3 kW of 2.45 GHz, continuous-wave (CW) microwave energy was applied to a hydrocarbon flame. In work at Princeton University, this effect was quantified as a 20% increase in the laminar flame speed with particle image velocimetry diagnostics. The LIF measurements at Wright-Patterson in 2007 quantified changes in the OH-radical concentration as seen in Figure 1. This work was performed with an energy-costly CW magnetron. The practical next step was a move towards more efficient microwave coupling. With a high peak-power microwave source, it was expected that a similar flame speed enhancement could be generated in the same laminar hydrocarbon flame system. Evidence of a flame-speed enhancement using the 30 Watt average power, 0.1% duty-cycle pulsed magnetron was observed in experiments at Princeton prior to bringing the

testbed to Wright-Patterson. The qualitative images of the pulsed microwave enhanced flame seen in Figure 2 show the effect that was quantified with laser diagnostics during the summer fellowship.

The microwave cavity used in this experiment is not well suited for laser diagnostic access due to the nature of resonant microwave propagation. All holes in the cavity must be less than the microwave cutoff quarter-wavelength (~1.5") to prevent radiation leakage. This guideline limits the microwave cavity to narrow laser slots and meshed, vignetting windows which contribute to increased laser background scattering and a reduction in the overall collection efficiency of imaging diagnostics like FRS and LIF. The equipment and expertise available at Wright-Patterson made it possible to perform these laser diagnostics to high accuracy despite these factors.

The first two weeks of work were devoted to bringing the microwave enhanced combustion system to an operating point that would prove interesting to probe with laser diagnostics. The desired enhancement proved difficult to achieve and the flame speed increase was only around 50% as large as what had been seen in the work leading up to the summer research. Nonetheless, the slight shifting of the flame with the application of pulsed microwave radiation still represented a flame speed enhancement worth studying at the facilities. The subsequent LIF and FRS laser diagnostics were both performed to investigate this condition and the details of the experiments are presented in this report.

To measure OH number density changes in the pulsed microwave enhanced flame, planar LIF measurements were performed by exciting the $Q_1(8)$ $A^2\Sigma^+ - X^2\Pi$ (1,0) transition of the OH radical with laser radiation near 283.553 nm. The purpose of the experiment was to observe any changes in the characteristic OH profile of a CH_4/air flat flame when microwave energy was applied. As seen in Figure 3, the preliminary analysis of the raw data shows a slight change in the peak concentration of OH and a definitive change in the characteristic decay of OH from superequilibrium. It appears that the data will provide important information regarding a potential coupling of the microwave radiation to flame chemistry. Although I had some familiarity with the LIF experimental procedures, the work this summer provided training well beyond my previous level of knowledge.

Because the energy of the pulsed microwave system is much less than that used in the preceding CW magnetron experiments, it was expected that the pulsed interaction would generate similar flame speed increases without significant heating of the bulk combustion gases. To investigate this hypothesis, a FRS

thermometry diagnostic was configured to resolve temperature changes in the flame when the microwave energy was applied. In previous attempts to perform the planar FRS diagnostic at Princeton, issues with laser power and laser seed stability all prevented accurate two-dimensional measurements of the flame's temperature field. The limited optical access to the microwave cavity still hindered measurements at Wright-Patterson, but with their more powerful laser system, larger diameter Iodine vapor cell, and lower f# camera lenses, full planar FRS images of the microwave enhanced flame were obtained. Datasets were collected at the same experimental settings used during the LIF trials. It is expected that the temperature information derived from the FRS data will yield a better understanding of the previously discussed change in OH radical concentration.

The accuracy and precision of the FRS data collected at Wright-Patterson will be near 10% once certain issues in the conversion from raw data to actual temperature are resolved [1]. Preliminary FRS thermometry images are presented in Figure 4 that show both the enhanced propagation rate of the microwave enhanced flame front and the slight increases in temperature in the post flame gases. The absolute accuracy of the conversion to temperature is calculated from the convolution of the Rayleigh scattering profile and the Iodine vapor cell transmission profile. Typically, both of these profiles are derived from theoretical models that give their shape and magnitude at different gas temperatures and laser frequencies [2]. As shown in Figure 5, the theoretical transmission profile of the Iodine vapor cell does not match the set of experimental values measured this summer. Slight changes like the ones seen in the figure can account for a bias in the temperature by almost ±50 K. Future work will evaluate this issue discovered at Wright-Patterson and decide whether a theoretical, experimental, or possibly a spliced transmission profile should be used in the FRS temperature measurements.

The original research proposal for the summer fellowship at Wright-Patterson also anticipated the development of a computer simulation to model the microwave flame speed enhancement with the CHEMKIN software package. The experimental work performed over the summer consumed the majority of my time, and the progress I made towards a theoretical model was limited to gaining familiarity with the complicated CHEMKIN package and informative discussions with Dr. Skip Williams. Along the lines of past attempts at a model, the approach this summer was to focus on adding important chemiionization and charged species reactions to the CHEMKIN kinetic database [3]. In discussions with Dr. Williams, it became apparent that electron recombination kinetics should also be included in addition to an experimental prediction of the actual amount of energy transferred to the

charged species in the flame zone. With reference to a maximum energy transfer, more insight can be brought into the selection of the electron recombination reactions by disregarding those that require electron energies above the threshold of what can possibly be enhanced by the microwave radiation. These concepts will be brought into my future work to develop the model with the resources available at Princeton.

The Wright-Patterson Summer Research Fellowship provided an opportunity to greatly accelerate the experimental work for the pulsed microwave enhanced combustion research project. The results are worthy of publication in a scholarly journal and should generate interest throughout the field of plasma enhanced combustion. Future collaborations with the propulsion directorate are definitely possible if the experiment can make progress towards showing similar enhancements in turbulent flames that are more applicable to the branch's practical hypersonic combustion technologies.

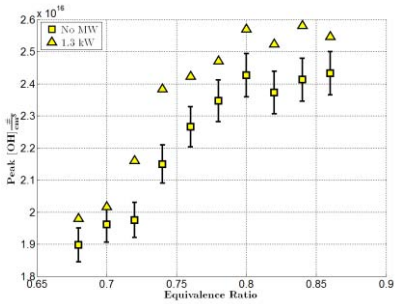

Figure 1: Summary of work performed at WPAFB in December 2007 with CW microwave system. The peak concentration of the OH radical in the flame was measured to significantly increase with the addition of microwave energy.

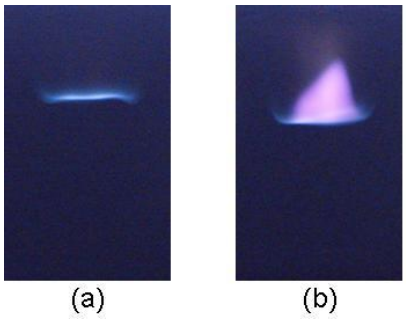

Figure 2: Long exposure luminosity images of a laminar CH_4/air flat flame (a) and an observation of the enhancement with pulsed microwave radiation (b). The gas flow direction is from the bottom of the images to the top.

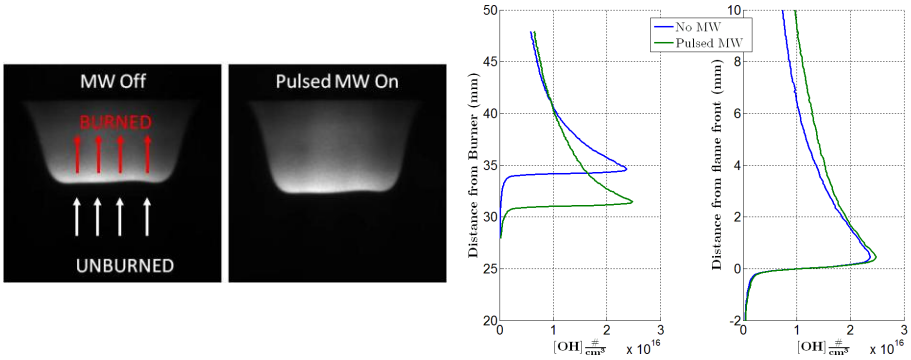

(a) **(b)**

Figure 3: (a) Raw PLIF images of flame will give full 2D approximation of OH number density. (b) Preliminary processing of the raw images give number density along the centerline of the flame with (blue) and without (green) radiation from a 30 W pulsed microwave magnetron. The profile plot in the flame shifted coordinate system (right) indicates an alteration of OH chemistry.

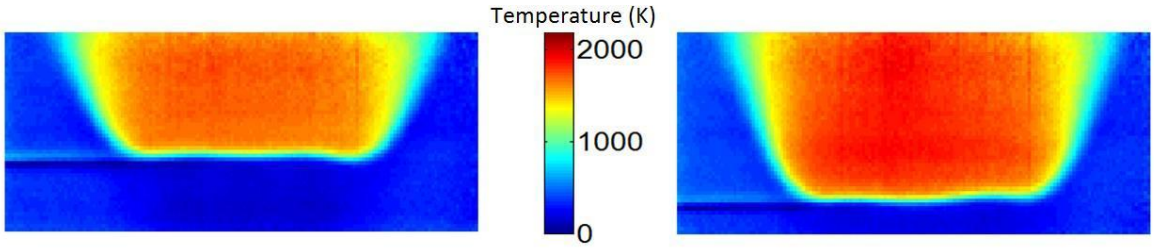

(a) **(b)**

Figure 4: Processed FRS thermometry images of the flame with (a) and without (b) pulsed microwave radiation.

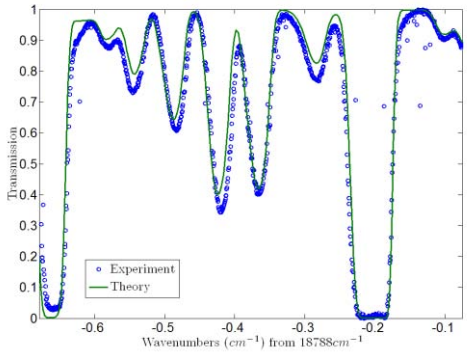

Figure 5: Transmission scan of Iodine vapor cell demonstrating inconsistencies between experimental and theoretical results.

[1] S.P. Kearney, S.J. Beresh, T.W. Grasser, R.W. Schefer, P.E. Schrader, R.L. Farrow, "A Filtered Rayleigh Scattering Apparatus for Gas-Phase and Combustion Temperature Imaging," *41st Aerospace Sciences Meeting and Exhibit*, Reno, NV, 2003, 2003-584.
[2] G.S. Elliott, N. Glumac, C.D. Carter, A.S. Nejad, Combustion science and technology, 125 (1-6) (1997) 351-369.
[3] Y. Ju, S.O. Macheret, M.N. Shneider, R.B. Miles, D.J. Sullivan, "Numerical Study of the effect of microwave discharge on the premixed methane-air flame," *40th AIAA/ASME/SAE/ASEE Joint Propulsion Conference and Exhibit*, Fort Lauderdale, FL, 2004, 2004-3707.

Three-Dimensional Quench Simulation and Protection in HTS Devices

YEAR 1 REPORT

2007

Team Members:
Prof. Cesar Luongo, Principal Investigator
Dr. Philippe Masson, Research Associate
Ms. Makita Phillips, Graduate Student

I. Motivations and scope of work

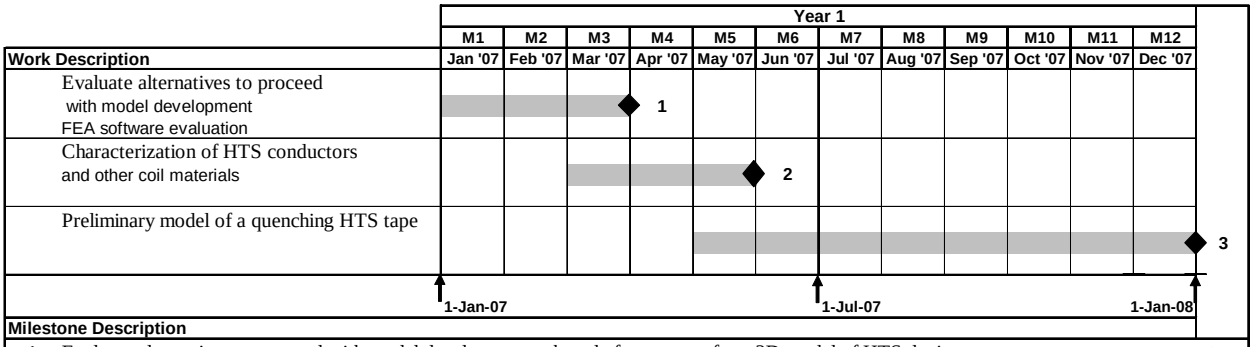

Milestone Description		
1	Evaluate alternatives to proceed with model development, what platform to use for a 3D model of HTS devices	1-Mar-07
2	Electrical, thermal and mechanical characterization of HTS conductors and other coil materials	1-Jun-07
3	Combined thermal/electrodynamic 3D model of a quenching HTS tape	1-Jan-08

Figure 1. Year 1 task plan

II. Programmatic

The project kick-off teleconference meeting took place on Monday February 12th at 10AM and was attended by Prof Luongo and Dr. Masson from Florida A&M University, Mr. Rodriguez, Mr. Gordon and Dr. Oberly from the Air Force Research Laboratory.
The following items have been discussed during the meeting:

- The project starting date of January 1st has been confirmed.
- Dr. Masson was asked to apply for permanent residency within the first year of the project to allow for different sources of funding if needed.
- Monthly teleconferences will follow the monthly updates.
- FAMU team is actively looking for a graduate student to join the project.
- The research approach was discussed and is described in next section.
- A technical discussion about numerical methods and physical phenomena took place as comments to the research approach flowchart.

An account for the ongoing project has been opened at FAMU and we are allowed to start spending. FAMU is in the middle of a major payroll department slow down, and there is a moratorium in the creation or modification of any appointment. Additionally, there will be a new president/administration at FAMU starting in June further slowing down all administrative functions.

Two international students have joined the project for 5 months and will be working on the implementation of global simulation models using ANSOFT and COMSOL:

- Guillaume Hoffmann will work on a model of racetrack coil using COMSOL.
- Vincent Rouault will work on a model of solenoid coil using Maxwell 3D and ePhysics.

Dr Masson's appointment transfer to this project has been delayed due to a significant FAMU administration slow down. This delay has generated unused funds in the range of

$20k. It has been decided during last teleconference that any excess of funds would not be spent on items not included in the original budget.
A license for COMSOL Multi-physics needed for this project will be purchased using other sources of funding.

Two students have been appointed for the summer 2007: Kristin Carroll and Dionne Jones, they are currently working part time on lumped parameter models of multilayer tapes using Matlab and on the development of a website for our research team.

Ms. Makita Phillips joined the team as a graduate student. She will start working on the effect of thermally induced stress on quench propagation. First step will be to include the dependence of current density to stress in the global model already developed in COMSOL.
An invoice of $95,397 has been send to UCT on October 5th including the expenses charged to the account through Sept. 30th.

The computer needed to perform a simulation of quench propagation in a tape including an actual representation of the layers has not yet been purchased. We are still working with UTC and AFRL to obtain authorization to use available funds from this project to purchase a powerful workstation.
The current limited computing power is significantly slowing down progress on the project and some simulations cannot be currently performed. However, it is to be noted that year 1 milestones have been accomplished on schedule.
We are now focusing on different aspects of the research that do not require large computing power.
A no-cost extension for year 1 has been granted; year 1 end date is now extended until the end of April 2008. This extension will be used to give time to UTC and FAMU to finalize the collaborative agreement for year 2 and 3.

III. Research approach

The proposed research approach to develop a 3D quench simulation tool is based on two different tasks as represented in the flow chart of figure 1. The two tasks are needed to reach our objectives and will be performed simultaneously: first, we need to understand the physics of the quench in YBCO tapes. Indeed, the tape is composed of multiple layers that could cause physical phenomena that are usually neglected. However, current and temperature diffusion alone cannot explain the experimental data available in the literature and a new theory needs to be developed taking into account effects such as accumulation of charges, tunneling, Hall effect, etc that could very well drive the quench. This work is described in the right hand side of the chart of figure 1. Once the physics is understood and a first set of equations formulated, a solver needs to be used to perform the simulation. This represents the second aspect of the work which consists in identifying a Finite Element Code, or numerical method for in-house coding, to solve the found equations at the tape level. Once the quench mechanism is understood and successfully simulated for a tape, a global current sharing law, which would most likely

depend on more than the temperature, can be developed and implemented into FEA software to perform simulations at the device level.

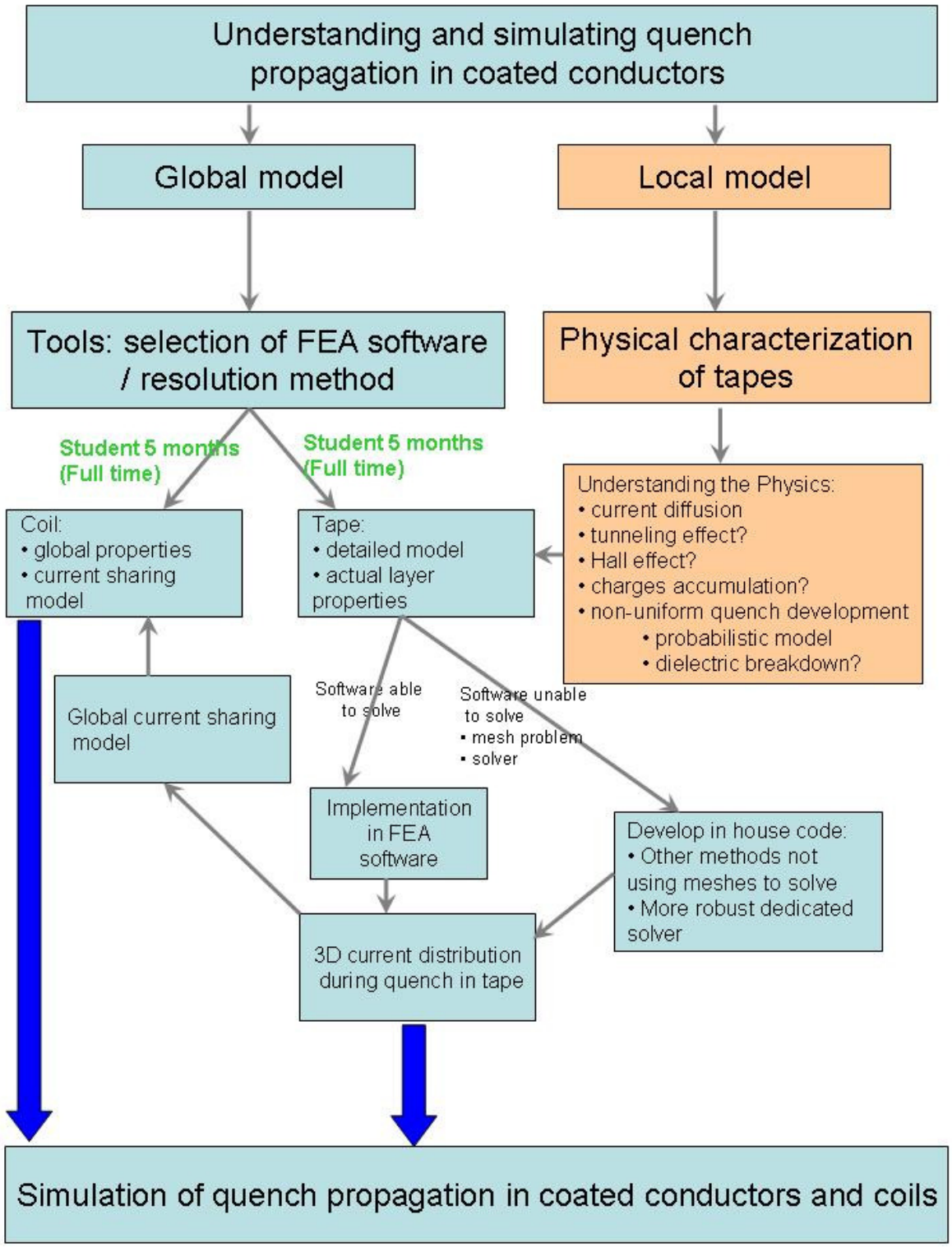

Figure 2: Research approach (flow chart)

IV. Key accomplishments

A. Global model

1. Choice of simulation method and software

In January, two FEA codes have been considered as good candidates to solve the quench simulation problem. ANSOFT Maxwell-ePhysics-Optimetrics is a very complete package mostly dedicated to electro-mechanical systems simulation. The software is user friendly and has a very robust solver. It is capable of transient coupled simulations. However, ANSOFT software has very little flexibility and may not be able to solve equations that are not already coded in its core. Script can be used and we will evaluate if it allows for "out of the box" simulations. The second code we have identified is COMSOL Multiphysics; it is very flexible and allows the users to solve their own set of equations.

The objective was to determine if a quench simulation was possible with the impressive new features advertised by ANSOFT. The results have been disappointing as many of the announced features did not operate as they should have: we were unable to implement
• temperature dependent electrical conductivity
• temperature dependent thermal conductivity
• anisotropic thermal conductivity
• multiple thermal sources
Those features are paramount to quench simulation and therefore, we have decided to stop using ANSOFT software and focus on the model development using COMSOL Multiphysics.

2. Model of an HTS magnets using YBCO coated conductors

a) Model of an example coil

The model chosen for a quench simulation is a racetrack coil that generates a 2T magnetic flux density on its axis.

The superconducting tape used is YBCO coated conductor. It is a second generation of HTS that is composed a follows:

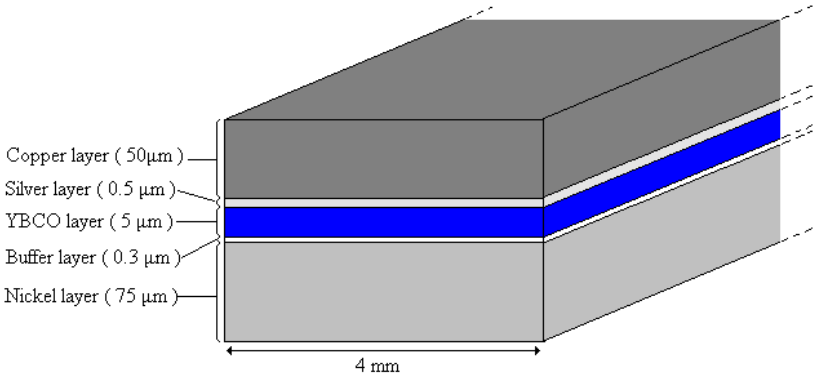

Figure3: Coated conductor model

Je is the engineering current density representing the total amount of current carried over the total conductor cross section. Je versus magnetic flux density is presented on figure 4**.** Its analytical expression is:

$$\left\|\vec{J}_e\right\| = \frac{\left\|\vec{J}_c\right\| \cdot S_{YBCO}}{S_{conduc}} \cdot \frac{V_{conduc}}{V_{coil}}$$

This curve is helpful to determine the conductor operating point. The load line of the magnet can be plotted, translating the coil operation domain.

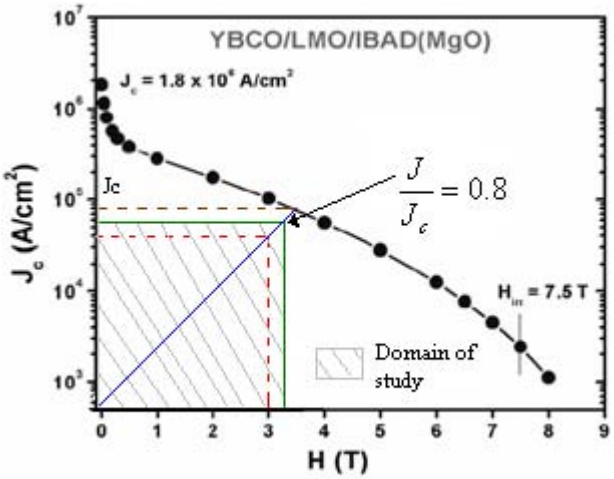

Figure 4: YBCO wire Je(B) curve

The coil of interest will be operating at 0.6*Je, that safety margin will influence the quench dynamics. The simulated system is shown in figure 5.

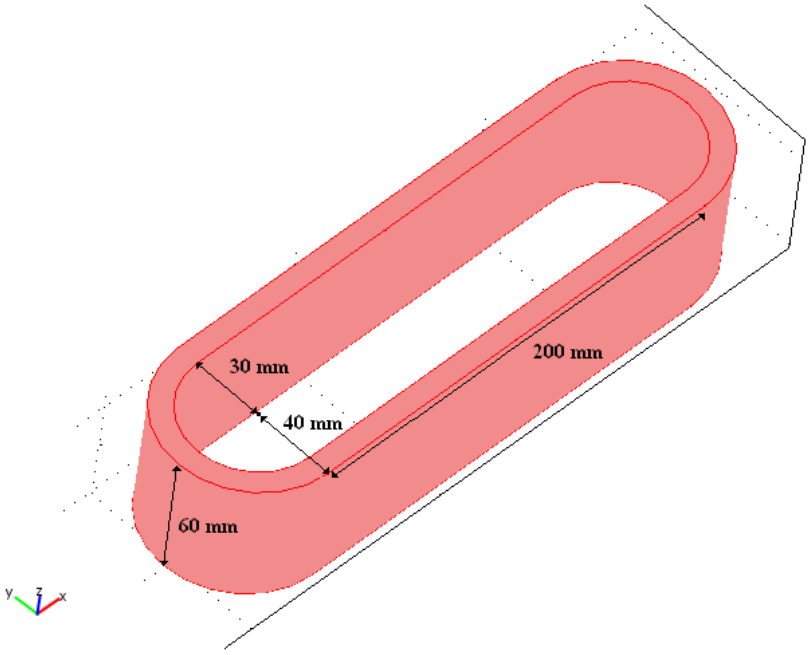

Figure 5: Modeled coil

As the model is built, its boundaries conditions have to be decided. This coil will be immersed in a 77K liquid nitrogen bath. The cooling is considered to be acting only on the interior wall.

b) Electro-thermal parameters

A quench is characterized by a significant increase of temperature. This phenomenon acts on the superconducting wire electro-thermal parameters. Indeed, electrical conductivity, thermal conductivity and specific heat are functions of temperature and therefore, the Joules losses and thermal diffusivity are also function of the temperature.

In order to complete the quench simulation, all electro-thermal parameters will be studied in the view to be implemented in the numerical program. This section will be divided in three sub-sections:

- Coil equivalent electrical characteristics
- Coil equivalent thermal conductivity
- Coil equivalent specific heat

The buffer being very thin, it electro-thermal characteristics will be considered negligible.

(1) Coil equivalent electrical characteristics

During the superconducting state, the current is only carried by the superconducting layer. During the normal state, the superconducting layer resistivity being much higher than the others, the current is carried by the stabilization layers only. We have built an equivalent electro-thermal model of the coil by calculating the anisotropic parameters along the three axis.

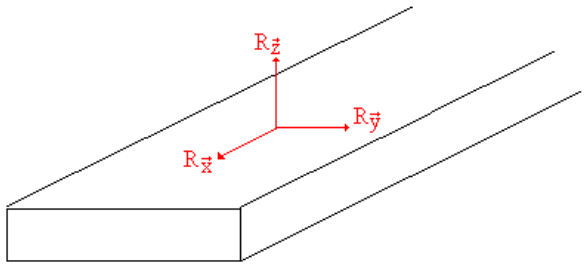

Figure 6: Wire model representing the electrical resistance anisotropy

Equivalent resistance following $\vec{z}$, R_z:

The equivalent electrical lumped circuit following $\vec{z}$ is:

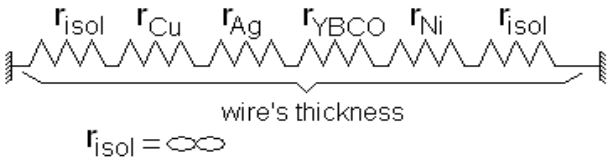

Figure 7: wire equivalent electrical lumped circuit following $\vec{z}$

As $r_{isol} = \infty$, we can conclude that $R_z = \infty$.

Equivalent resistance following $\vec{y}$, R_y:

Following $\vec{y}$ two domain of study can be considered:

- if the wire is in its superconducting domain

$R_{YBCO} << R_{Cu}$ and R_{Ni}

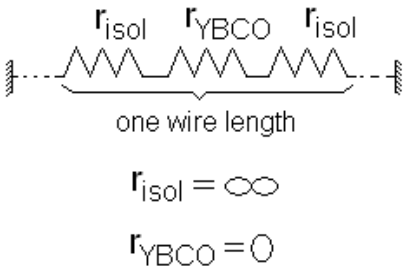

Figure 8: coil equivalent electrical lumped circuit following $\vec{y}$ (superconducting state)

- if the wire is not in its superconducting state:

$R_{YBCO} >> R_{Cu}$ and R_{Ni}

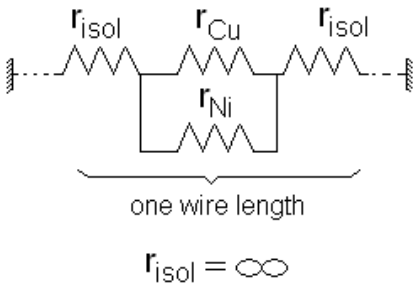

Figure 9: coil equivalent electrical lumped circuit following $\vec{y}$ (normal state)

In the two cases introduce above, the resistance following $\vec{z}$ can be considered infinity.

Equivalent resistance following $\vec{x}$, R_x:

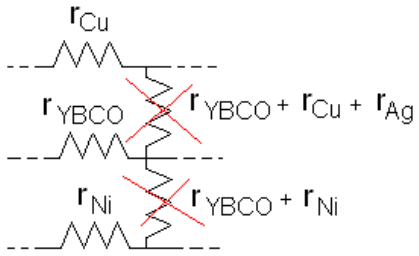

Figure 10: coil equivalent electrical lumped circuit following $\vec{x}$

$$\boldsymbol{R} = \frac{\prod_{i=1}^{N} \boldsymbol{R_i}}{\sum_{j=1}^{N}\left(\prod_{k\neq j} \boldsymbol{R_k}\right)}$$

The inter-layer contact resistances are neglected at this point.

This study allows finding the wire equivalent electrical resistivity versus temperature. To complete the calculation, the electrical resistivity versus temperature of Silver, Copper and Nickel is shown in appendix**.** YBCO electrical resistivity can be calculated as follows:

$$\begin{cases} \boldsymbol{Jco}(\boldsymbol{T}) = 1{,}05.10^{11}.\left(1 - \dfrac{\boldsymbol{T}}{\boldsymbol{Tco}}\right)^{1.08} \\ \qquad = \dfrac{10^{-4}}{\boldsymbol{Jco}(\boldsymbol{T})} \cdot \left(\dfrac{\boldsymbol{J}}{\boldsymbol{Jco}(\boldsymbol{T})}\right)^{20} \end{cases}$$

The resistivity is a function of current density and temperature. An example plot is shown below:

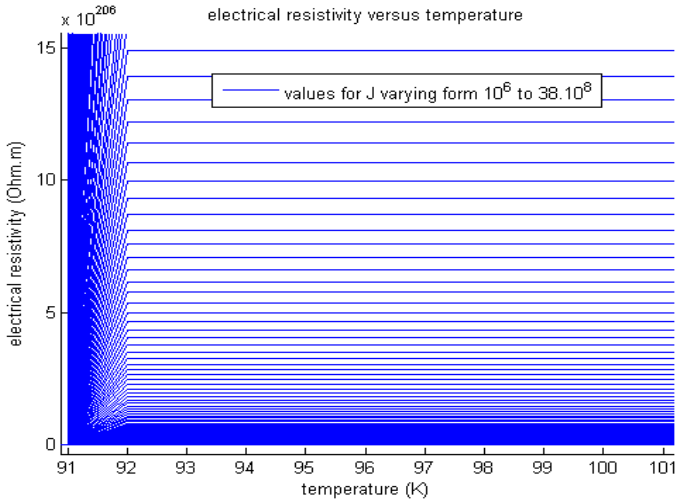

Figure 11: YBCO electrical resistivity versus temperature and current density;

Temperature=77K, 0,0028.Jc < J < 10.Jc

The wire equivalent electrical resistivity is then a function of temperature and current density.

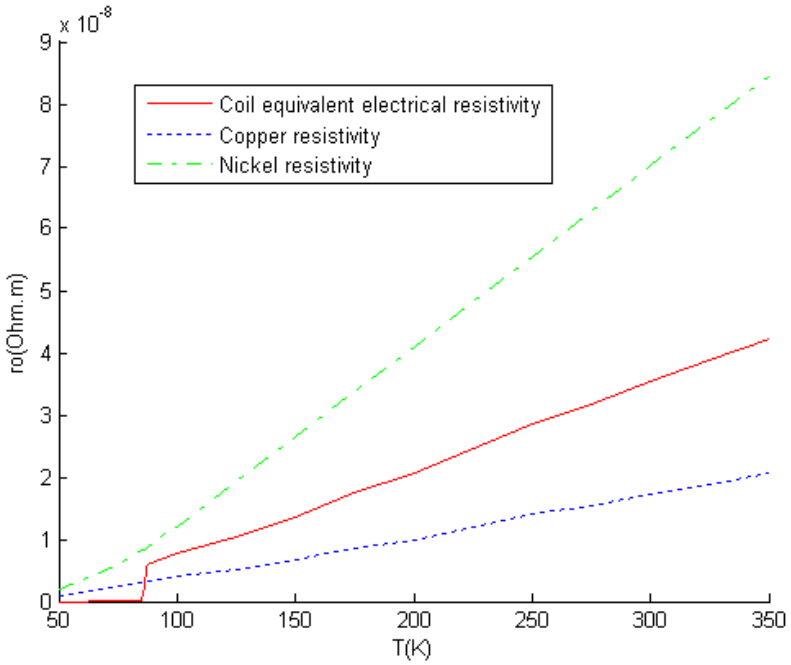

Figure 12: Wire equivalent electrical resitivity

(2) Coil equivalent thermal conductivity

By using the same way method, the thermal conductivity of the coil can be modeled.

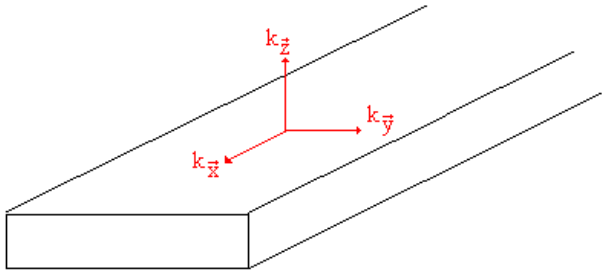

Figure13: Wire model representing the thermal conductivity anisotropy

- Thermal conductivity following $\vec{z}$

As the YBCO layer has an anisotropic thermal conductivity that is much smaller than the others following $\vec{z}$ and that each layers are in chain, the YBCO thermal conductivity was considered for the z direction.

- Thermal conductivity following $\vec{y}$

As all the layers are thermally in parallel, except for the Kapton, and because the insulator thermal conductivity is smaller than the equivalent wire conductivity, the Kapton thermal conductivity was considered.

- Thermal conductivity following $\vec{x}$

Following $\vec{x}$, the equivalent lumped thermal parameter circuit is:

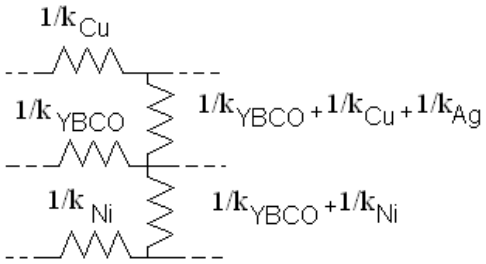

Figure 14: coil equivalent thermal lumped circuit following $\vec{x}$

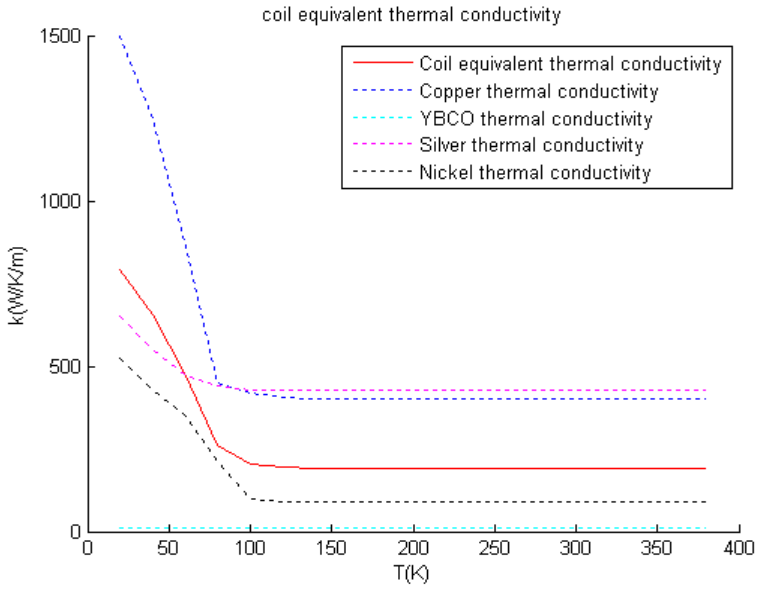

Figure 15: Coil equivalent thermal conductivity following $\vec{x}$

There is a really large decrease of the coil equivalent thermal conductivity between 20K and 100K.

(3) Coil equivalent mass specific heat

As I introduced above, the coil is made of a wire composed of different materials. The specific heat is the derivative of energy versus temperature. As a volumetric energy can be introduced, the specific heat increases linearly with the volume. All in all, as each layer has got the same length and width, the equivalent mass specific heat will be found using this expression:

$$C_{coil} = \frac{\sum_{layers} C_{layer} . h_{layer}}{\sum_{layer} h_{layer}}$$

with:

C_{layer} = layer mass specific heat
h_{layer} = layer thickness

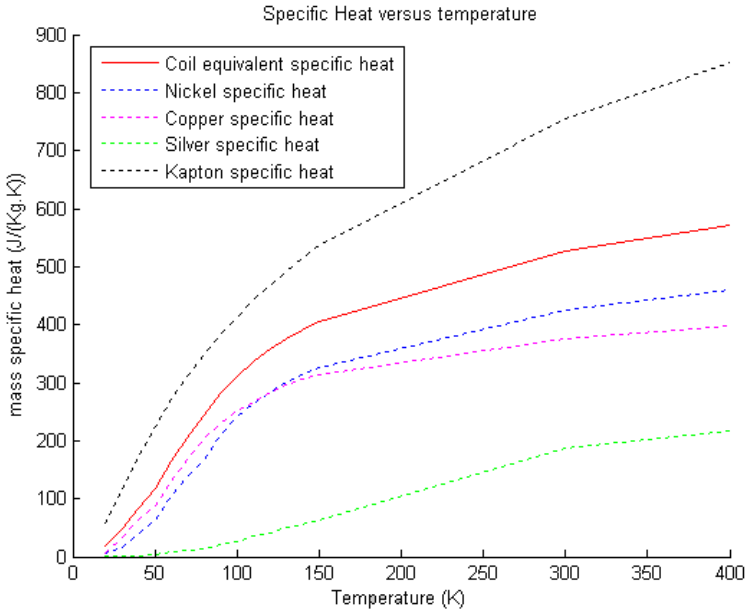

Figure 16: Superconducting wire equivalent specific heat

The coil equivalent thermal diffusivity is represented by the following equation.

$$a = \frac{k}{.C_P}$$

where:

- "a" is the thermal diffusivity

- "k" is the thermal conductivity
- "ρ" is the mass density
- "C_P" is the mass specific heat

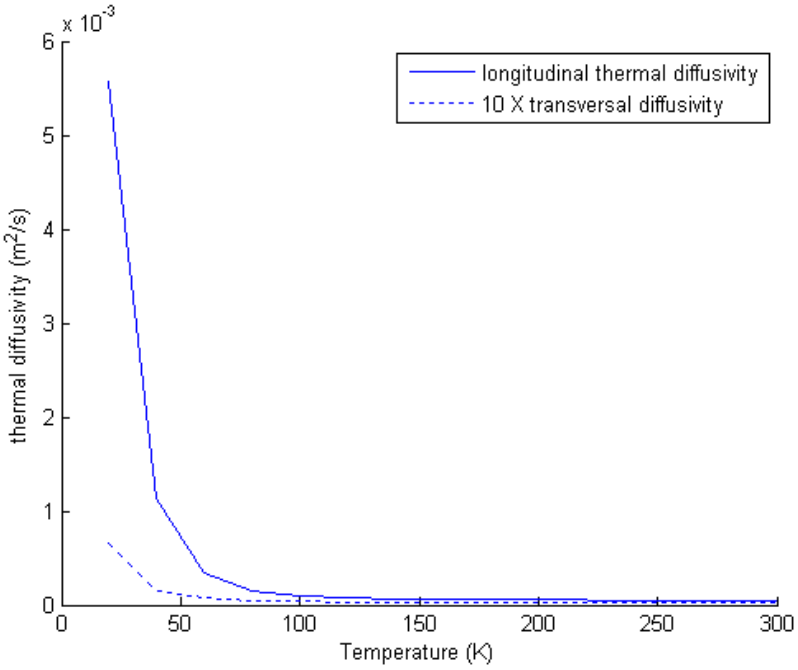

Figure 17: Superconducting wire equivalent specific heat

Figure 17 shown the very low normal zone propagation velocities are to be expected.

c) Electro-thermal parameters implementation

The study above allowed finding wire equivalent electro-thermal parameters. In order to avoid very thin mesh, the coil needs to be represented by a solid domain instead of wire layers. To do that, electro-thermal parameters will be implemented in cylindrical coordinates. In fact, as a coil is wire wound around an axis, the ($\vec{x}, \vec{y}, \vec{z}$) coordinate becomes ($\vec{\ }, \vec{z}, \vec{r}$). The figure below illustrates the parameters component, introduced above, in a cylindrical coordinate.

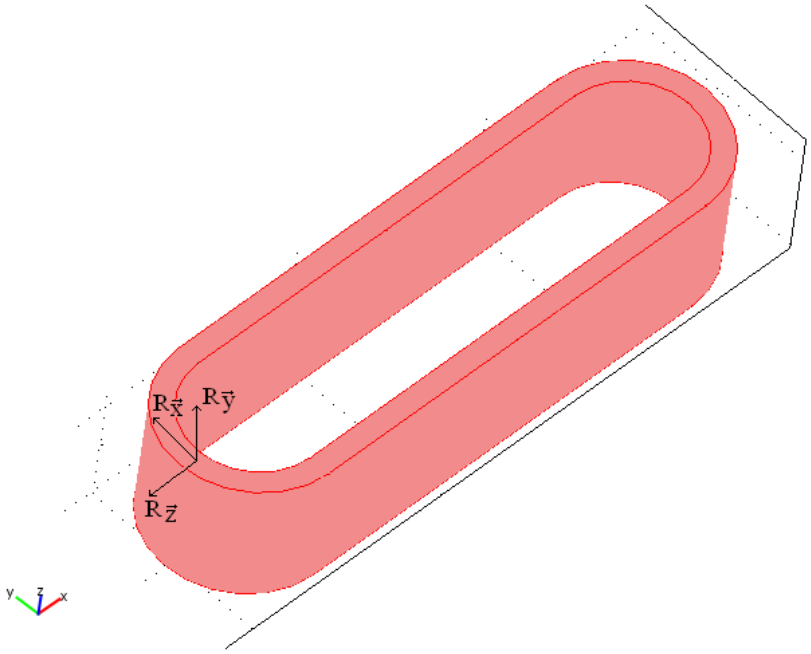

Figure 18: Coil model showing the wire electro-thermal parameters anisotropy

Comsol allows to implement anisotropic parameters. All electro-thermal will be implemented in order to represent an n-turns coil.

d) Graphic interface

Simulations done and presented above can be controlled by a graphic interface designed with the help of Comsol script, a Comsol extension. This program allows to run simulations through a graphic interface giving rights to modify simulations parameters.

For quench simulation, an example of graphical interface is shown below.

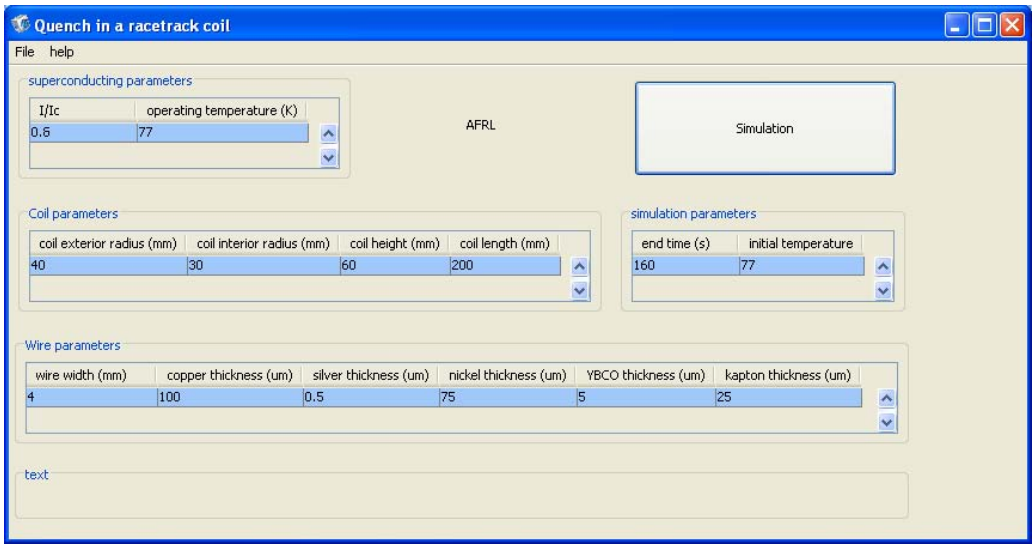

Figure 19: Graphic interface

By choosing different parameters, simulations can be done without drawing the geometry.

3. Simulation results and comparison with experimental data

a) Normal Zone Propagation

Figure 20 shows the temperature front propagation after a quench was induced through the use of a heater.

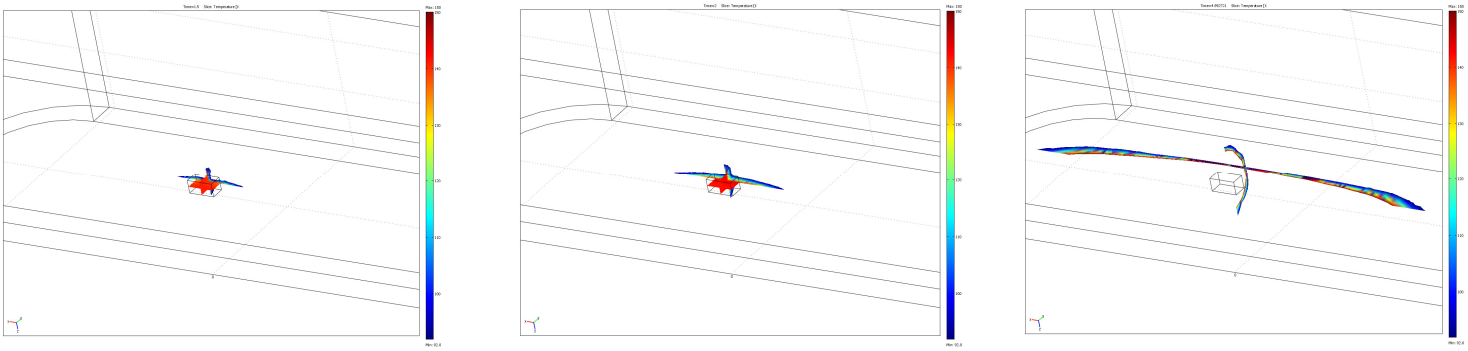

t = 1.5s t = 2s t = 5s

Figure 20: Illustration of the way used to calculate the NZP

From the time evolution of the temperature, the normal zone propagation velocity can be calculated.

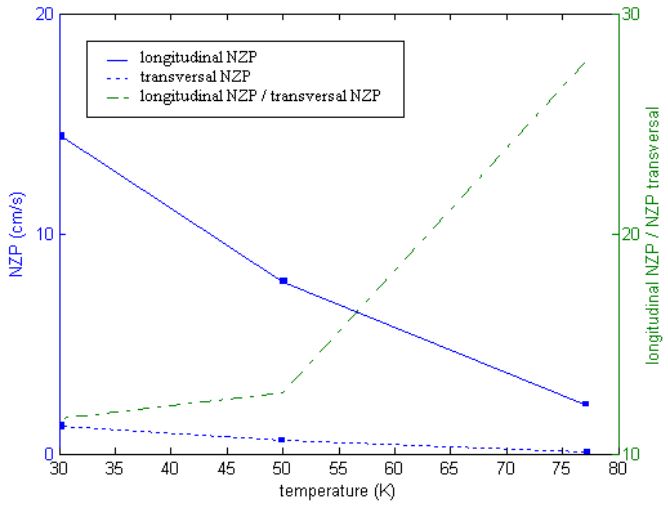

Figure 21: Longitudinal and transversal NZPV

Figure 21 shows the differences between longitudinal and transversal NZP. The most part of the energy will be dissipated along the wire.

b) Voltage and hot spot temperature evolution

In LTS wires, a quench is detected by a voltage drop measurement. In fact, as a quench is characterized by a local electrical resistivity growth, the voltage across de coil increases too. This phenomenon is directly link to the thermal evolution. Indeed, the quicker the quench will be propagated, the quicker the coil equivalent resistance will increase then the voltage evolution will be faster.

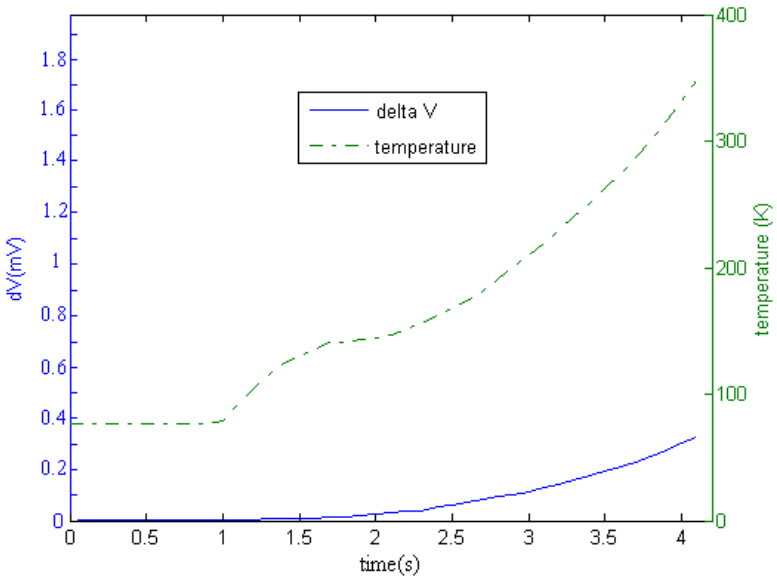

Figure 22: Temperature evolution and dV versus time

In HTS second generation wires, the thermal diffusivity being very low, the normal zone is propagating very slowly. The voltage evolution is therefore much slower than the hot spots thermal evolution. That means that the quench may not be detected on time and the wire can be destroyed.

c) Temperature field

Comsol allows to plot temperature field at different times. The figure below illustrates the thermal evolution in the three directions:

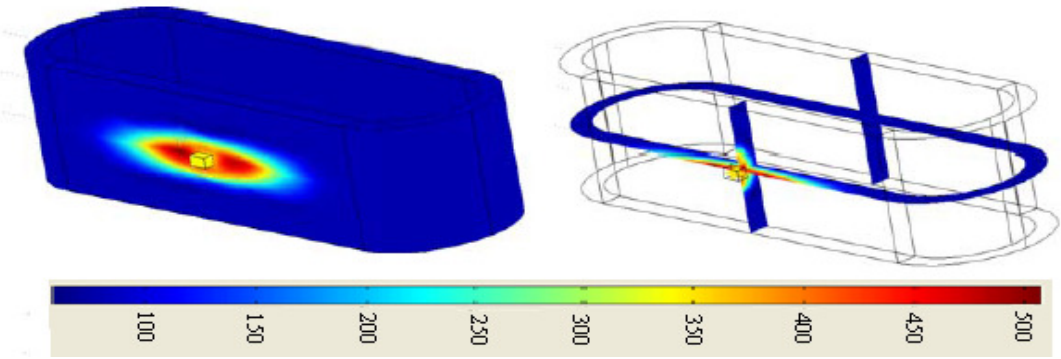

Figure 23:Temperature field

Figure 23 shows the hot spot temperature going over 500 K. In addition the different propagations following the three directions can be observed.

B. Tape level models

1. Model and simulation Challenges

2D simulations were performed with the objective of comparing a global model for a tape to a multi-layer model for the tape represented only by three layers: 50 m of copper, 1 m of YBCO and 75 m of Nickel.
The mesh needed for convergence is very small and the solver needs to be adjusted (pre-conditioner). The problem becomes ill-defined when the aspect ratio length/thickness becomes too large. The tape configuration is shown in figure 24.

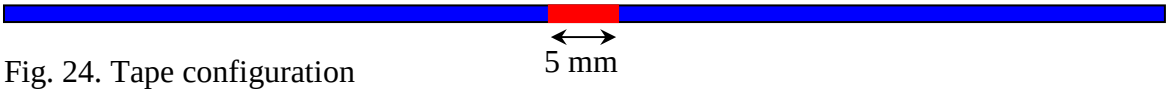

Fig. 24. Tape configuration

The red part in figure 1 represents the length of conductor simulated. Only 5 mm could be represented to keep the mesh size to a reasonable number of elements. The objective of the simulation is to compare the normal zone propagation velocity between the 3D coil simulation developed previously and that of a single conductor.Current is assumed to be uniform and constant at 0.8*Jc.

The implementation in Comsol is show in figure 25.

C.

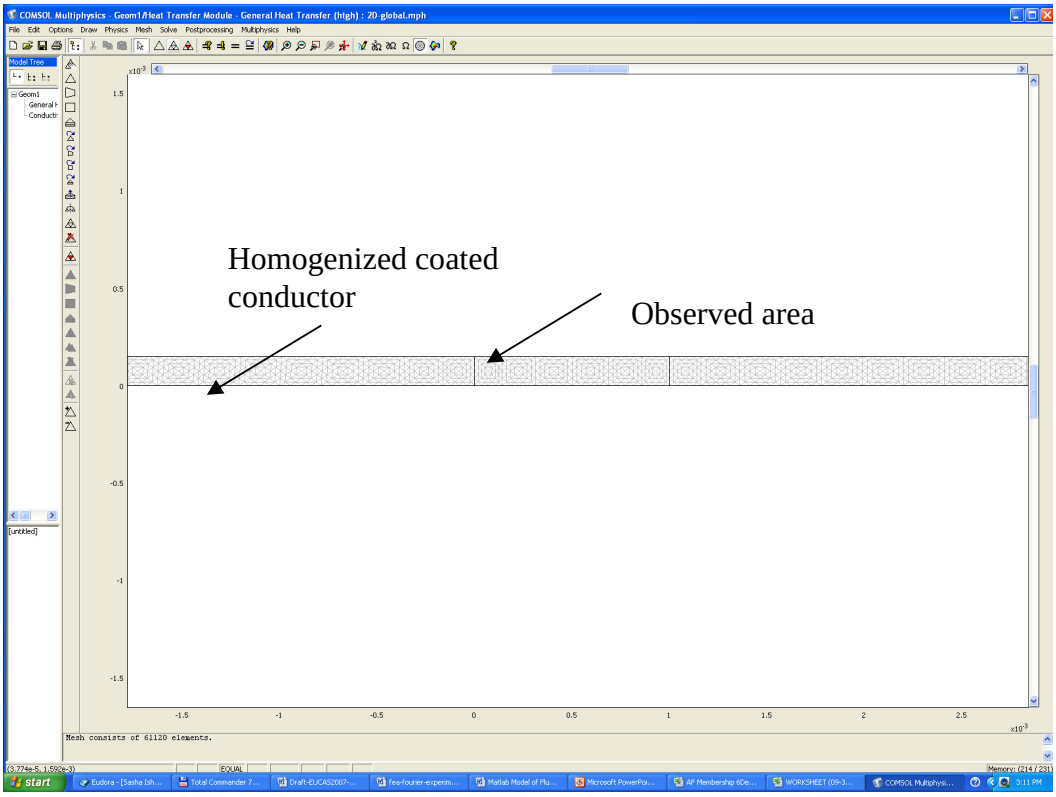

Fig. 25. Tape with a homogeneous model (no layers)

The mesh of figure 25 is composed of about 60,000 elements, the following temperature plots are shown in the area labeled “observed area” in figure 25.
The quench is induced by a heater thermally bonded to the tape. A pulse of 1 s is applied to induce a normal zone. In this particular example, the quench onset time is about 1 second. The time evolution of the electrical conductivity is represented in figures 26 to 29.

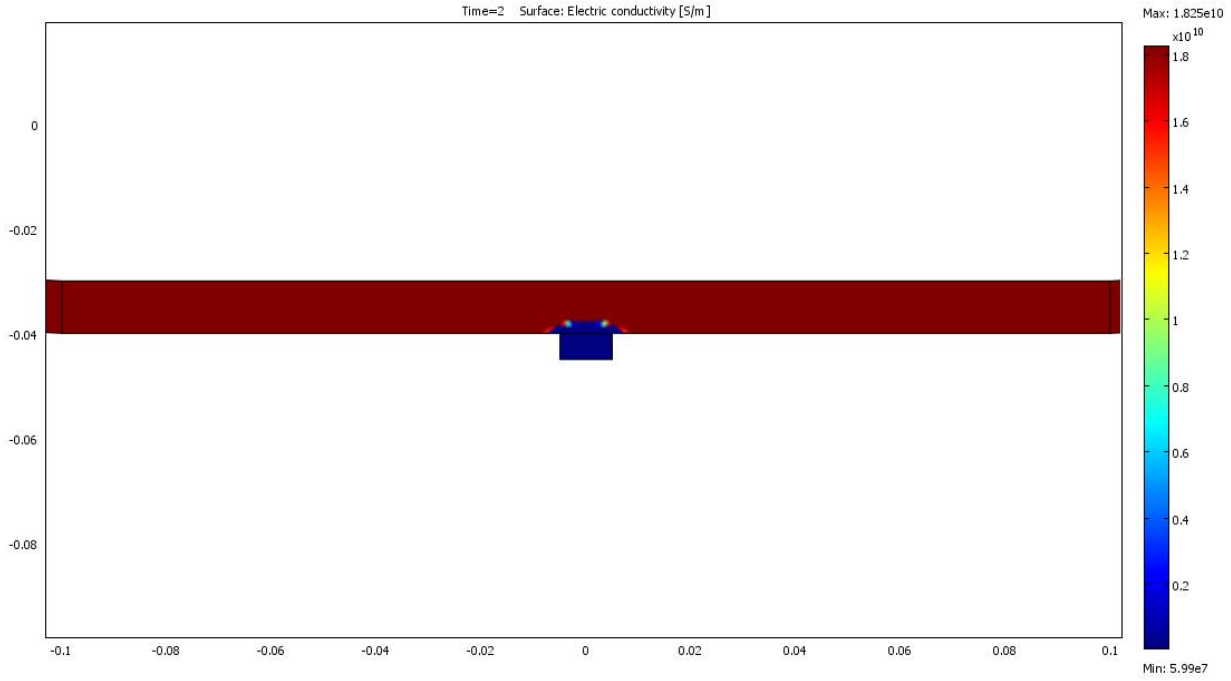

Figure 26. electrical conductivity distribution at t=2 s

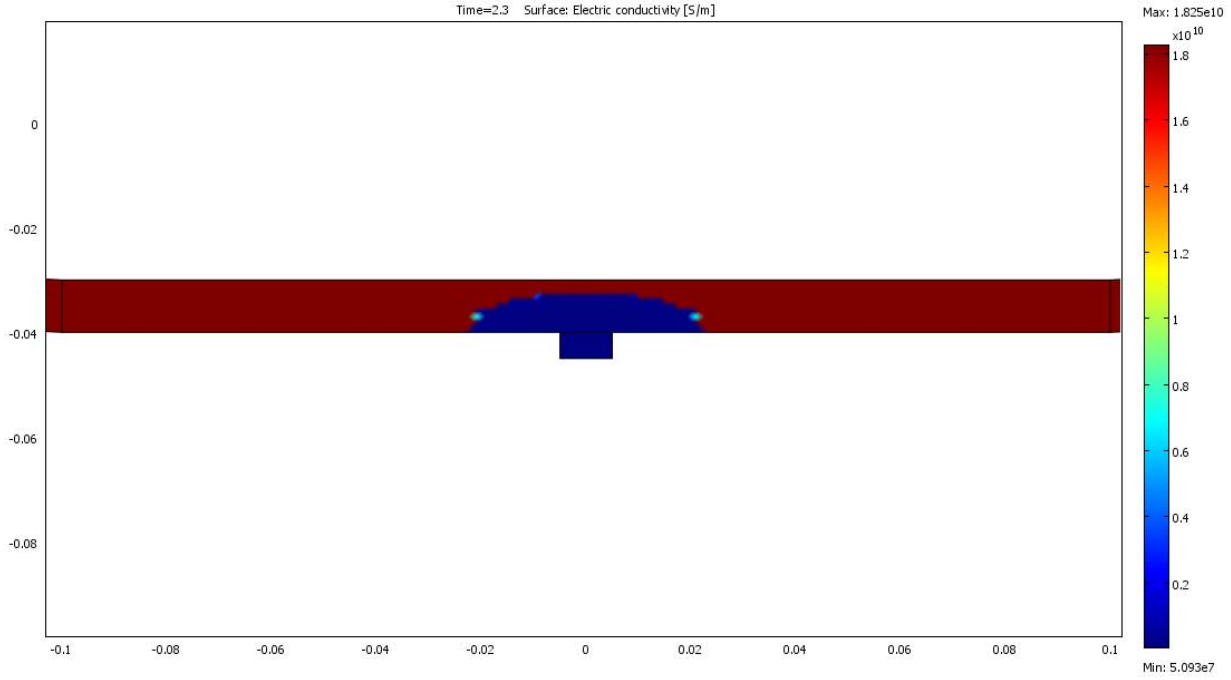

Figure 27. electrical conductivity distribution at t=2.3 s

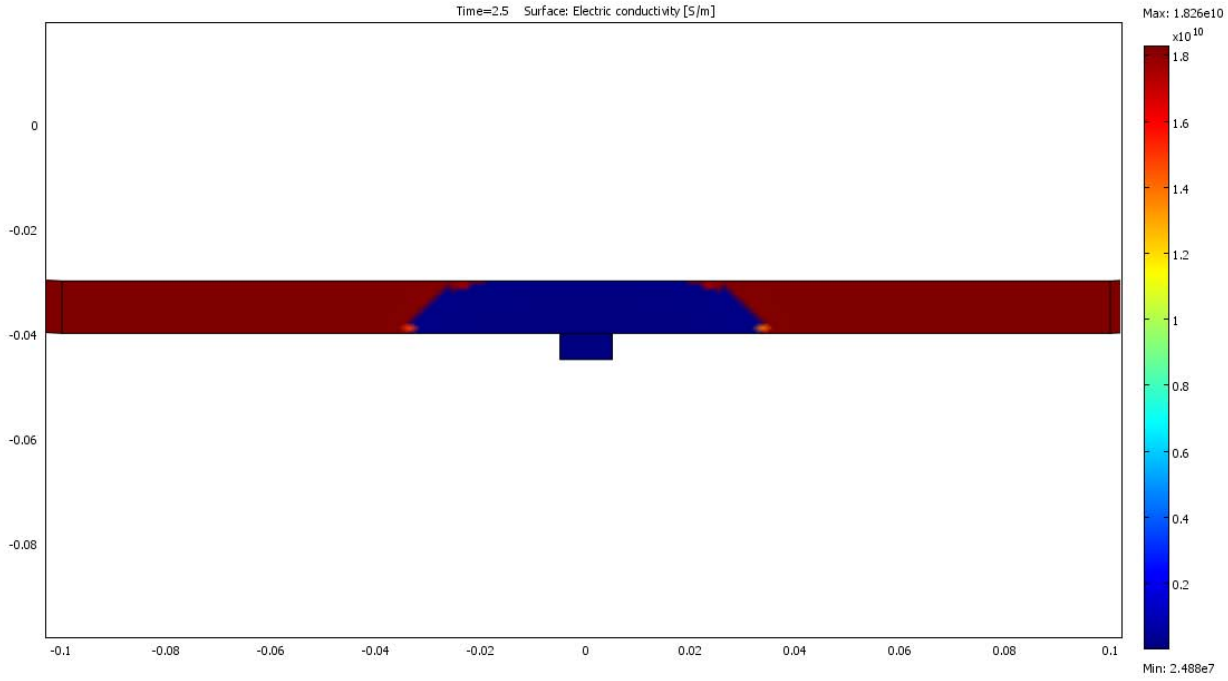

Figure 28. electrical conductivity distribution at t=2.5 s

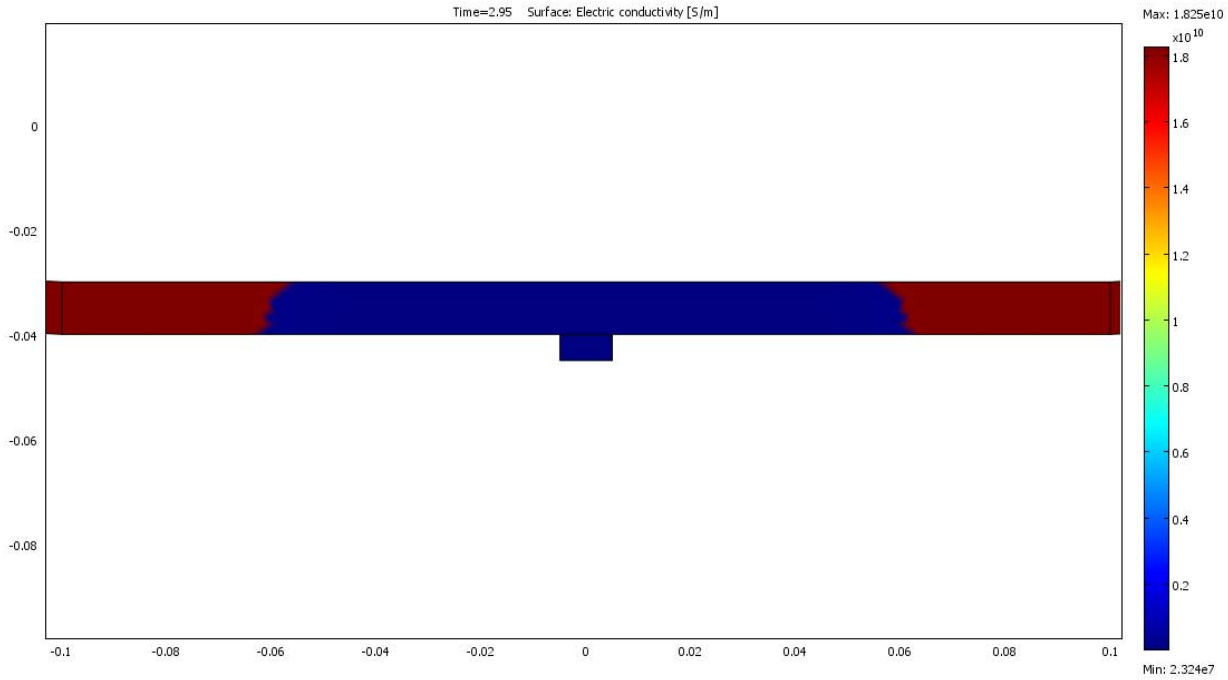

Figure 29. electrical conductivity distribution at t=3 s

As expected, the normal zone propagation velocity is higher for a single tape than for a coil. Simulation results suggest a 15 % difference.

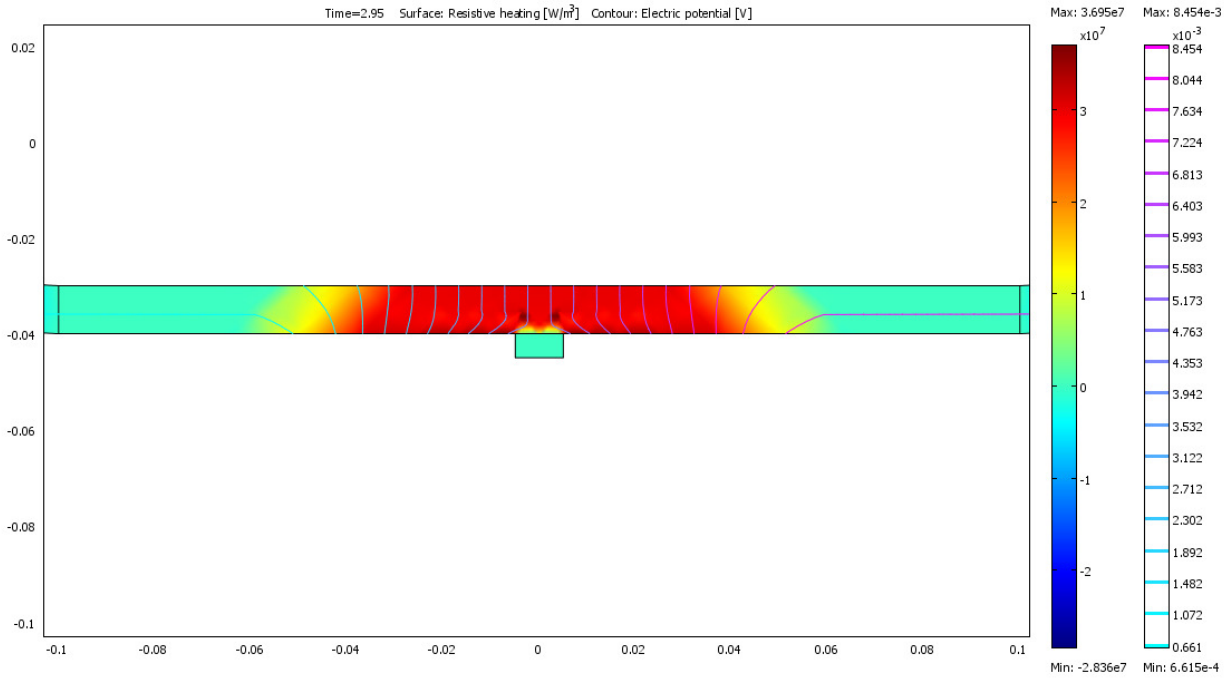

Figure 30. Joule heating and iso-V distribution during quench.

Figure 30 shows the Resistive losses of the tape, at this point in time, the tape is very likely to be destroyed. The 2D model is able to represent the quench propagation but misses the actual current distribution.

2. Comparison with experimental data

We were able to leverage experimental results from Prof. Justin Schwartz' team, allowing us to validate our simulations. Even though the experiment was using a coil with a different topology: pancake coil, our simulations of a racetrack coil wound with the same material gave very close results in terms of normal zone propagation velocity as shown in figure 31 and 32.

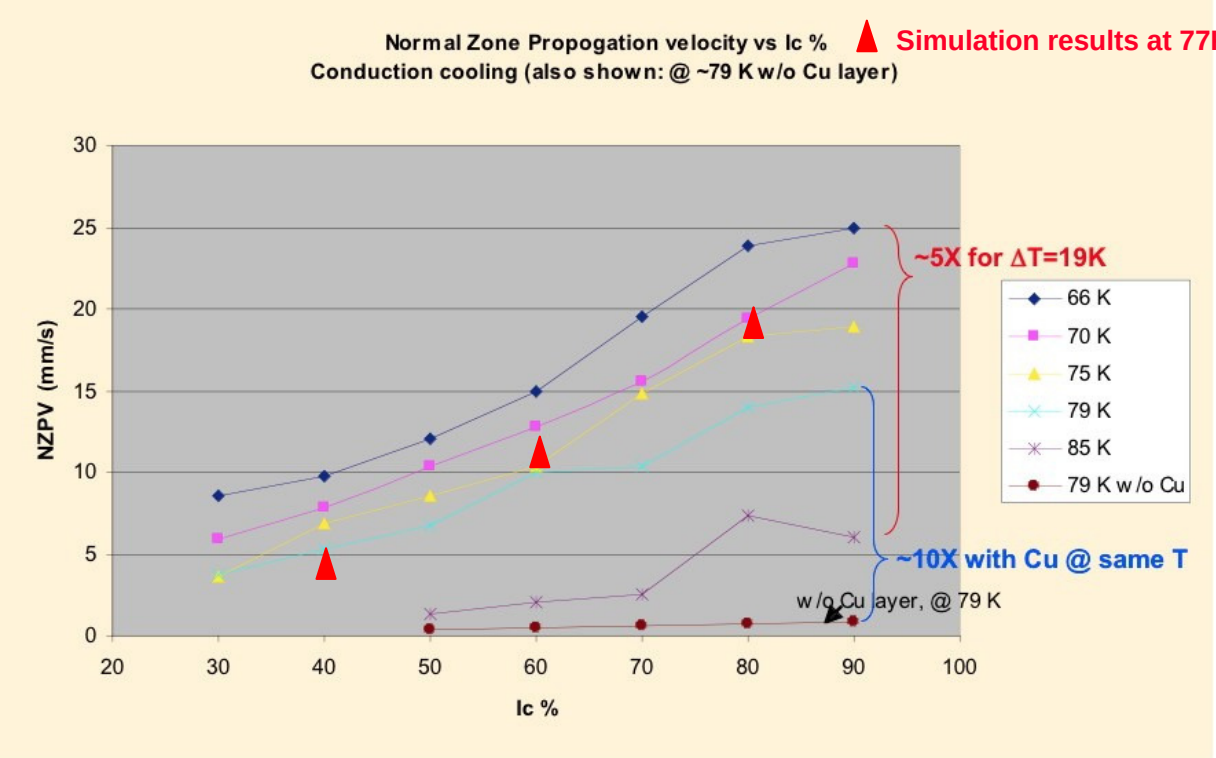

Figure 31. Longitudinal NZPV: comparison simulation/experiment

In figure 32, red triangles show simulation points. Simulations were done for 40%, 60% and 80% of Ic at 77 K and generated results comparable to experimental data. The correct order of magnitude was obtained; between 1 and 2 cm/s.

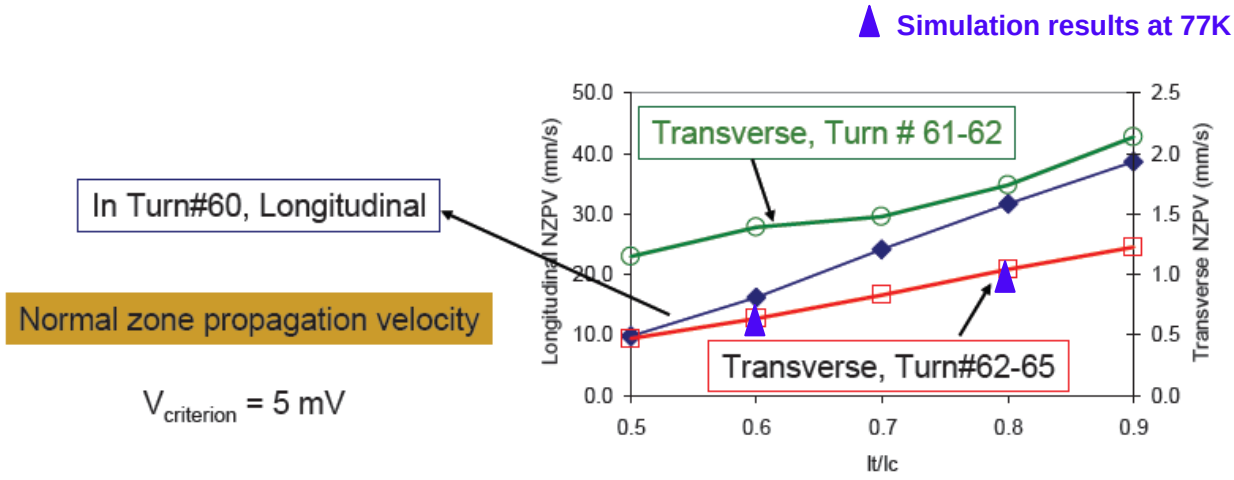

Figure 32. Transverse NZPV: comparison simulation/experiment

Experiments performed at the NHMFL by Prof. Schwartz' team on a YBCO coil provided by American Superconductor generated results in terms of transverse normal zone propagation velocity for different current levels. Once again, simulation results and experiments show very good agreement. Transverse velocities are in the range of 0.5-1.5 mm/s.

In order to get a more accurate comparison, the exact experimental configuration will be modeled including sensors using COMSOL and simulation results will be compared to experimental data. The comparison may give ideas regarding how to make the global model evolve towards higher fidelity.

3. *Computer* needs

The scope of the effort funded by AFRL through UTC is the development of a simulation of quench propagation in a coated conductor. At the beginning of the project, we decided to use an existing finite element analysis (FEA) tool to solve the problem and identified a commercial FEA code able to handle the highly non-linear model as well as the multi-physics aspect of the problem.

The geometry of a coated conductor is represented below.

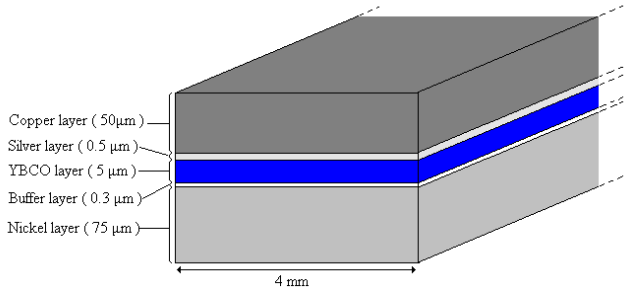

Fig. 33. Coated conductor topology

Fig 1 does not show the conductor up to scale because nothing would be visible; indeed, the actual size of a tape is about 130 um thick, 4 mm wide and 20 cm long. An actual 2D representation of the tape is shown in fig. 34.

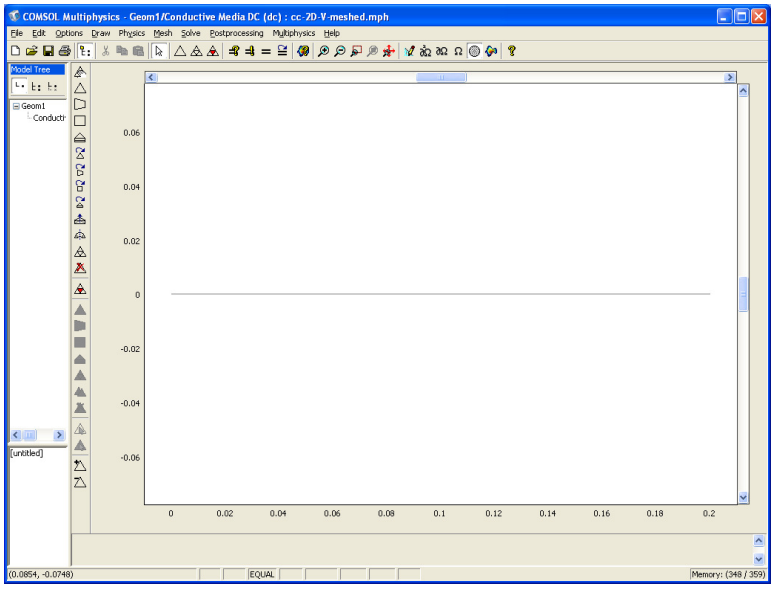

Fig. 34. 2D tape modeled in Comsol.

A zoom on the edge reveals the mesh along with the layered structure. In the presented case, the mesh size in the YBCO layer is about 1 um, which is close to a 1D representation of the layer.

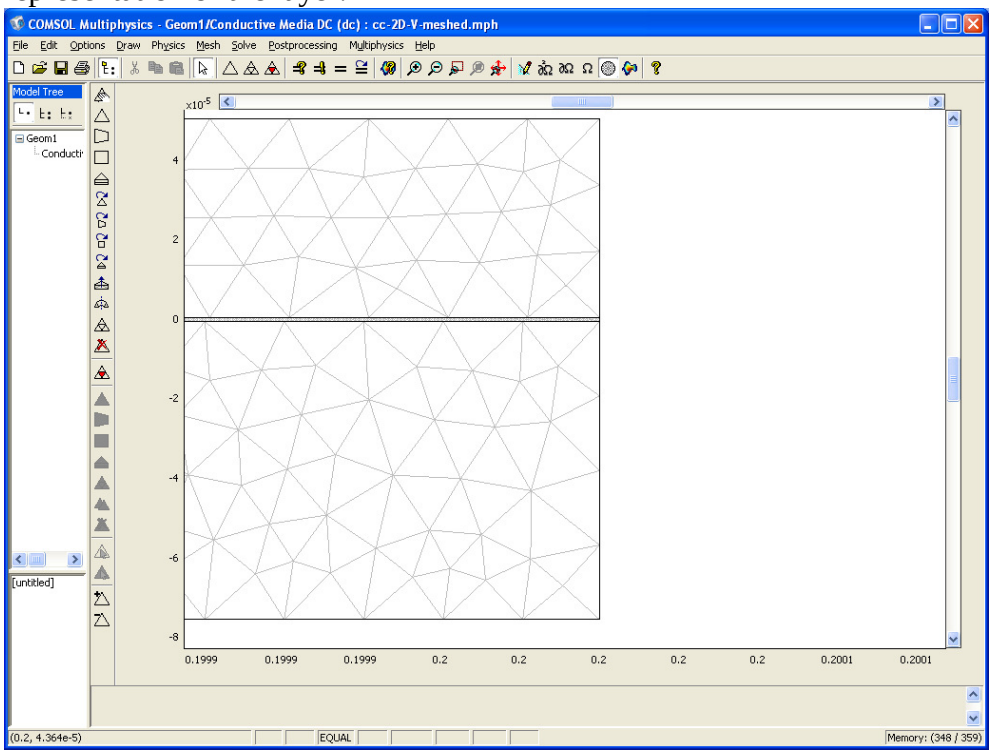

Fig. 35. Meshed 2D model

The mesh presented can be qualified of “coarse” for this specific geometry, it is composed of about 850,000 elements which represents a problem with more than 2 millions degrees of freedom. This 2D geometry can be meshed on a computer with 2 Gb of memory but not solved.

The presented model is too large to be simulated on the 4 Gb memory dual-core machine available at CAPS for this project.

Due to the very high aspect ratio of the geometry, we need a very powerful workstation able to handle a much larger number of elements even for 2D simulations.
Moreover, we think that 3D effects play a very important role in quench propagation that only a powerful workstation will be able to simulate.

V. Presentations and publications

A. Publications and conferences

– Philippe J. Masson, Guillaume Hoffmann, Vincent Rouault, Cesar A. Luongo, "***Development of Quench Propagation Models for Coated Conductors***", ", I.E.E.E. Transactions on Applied Superconductivity, Vol. 18, No 2, June 2008, pp1321-1324

– Philippe J. Masson, Guillaume Hoffmann, Vincent Rouault, Cesar A. Luongo, "***Development of Quench Propagation Models for Coated Conductors***", oral presentation at MT20

– Workshop on Collaborative University Research for More Electric Aircraft Technologies and Thermal Energy Management, "***Quench Propagation Models for Coated Conductors***", Tallahassee, FL, March 5th, 2008

B. Research Reviews

– AFOSR Superconductivity Program Review, "***Progress on Quench Simulation in Coated Conductors***", San Francisco. CA, March 28th, 2008

– AFRL HBCU Review and Research Seminar, "***3D simulation of quench propagation in coated conductors***", Dayton, OH, Oct. 2-3, 2007

– AFOSR Superconductivity Program Review, "***Progress on Quench Simulation in Coated Conductors***", San Francisco. CA, April 13-14, 2007

C. Students Involved

- Makita Phillips, ME graduate student, FAMU
- Guillaume Hoffmann, ME graduate student, INPL, France (graduated in 2007)
- Vincent Rouault, ME graduate student, INPL, France (graduated in 2007)
- Kristin Carroll, EE undergraduate student, FAMU (graduated in 2007)
- Dionne Jones, graduate student, FAMU (graduated in 2007)

VI.APPENDIX – MATERIAL PROPERTIES

YBCO Jc(B) curve:

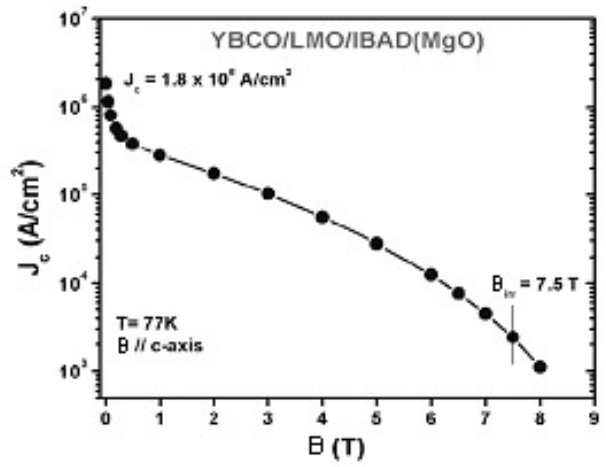

Appendix1: YBCO wire Jc(B) curve

Silver resistivity:

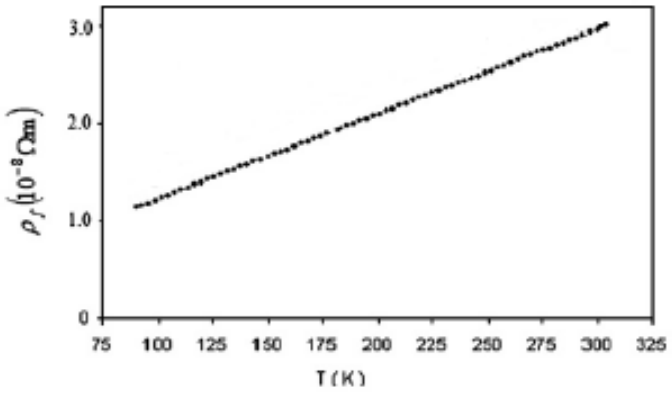

Appendix2: Silver's resistivity (empirical curve with a pure element)

Copper resistivity:

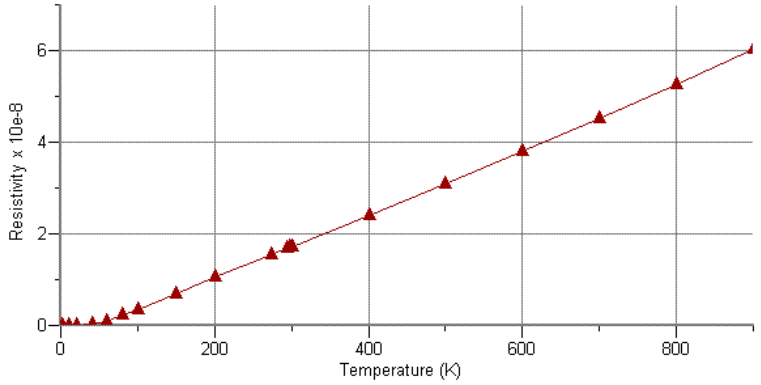

Appendix3: Copper's resistivity (empirical curve with a pure element)

Nickel resistivity

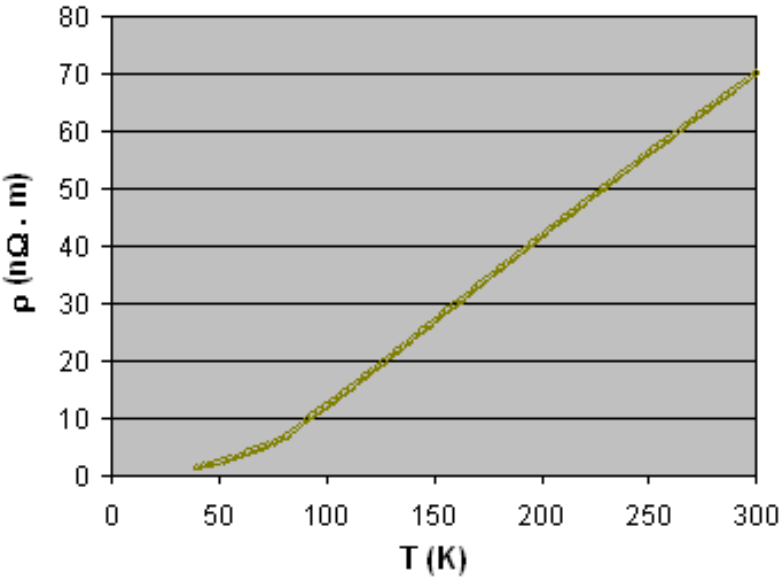

Appendix4: Nickel's resistivity (empirical curve with a pure element)

Materials thermal conductivity:

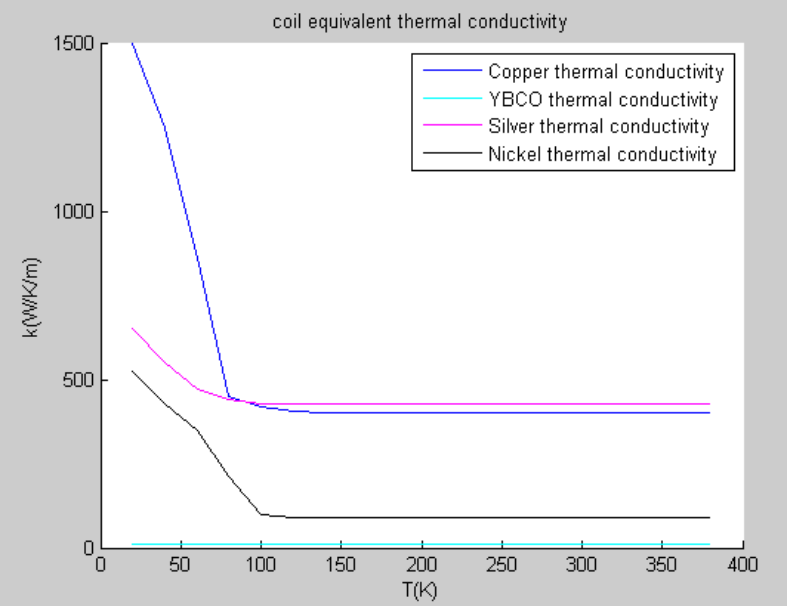

Appendix5: Tape element thermal conductivity

YBCO transversal thermal conductivity:

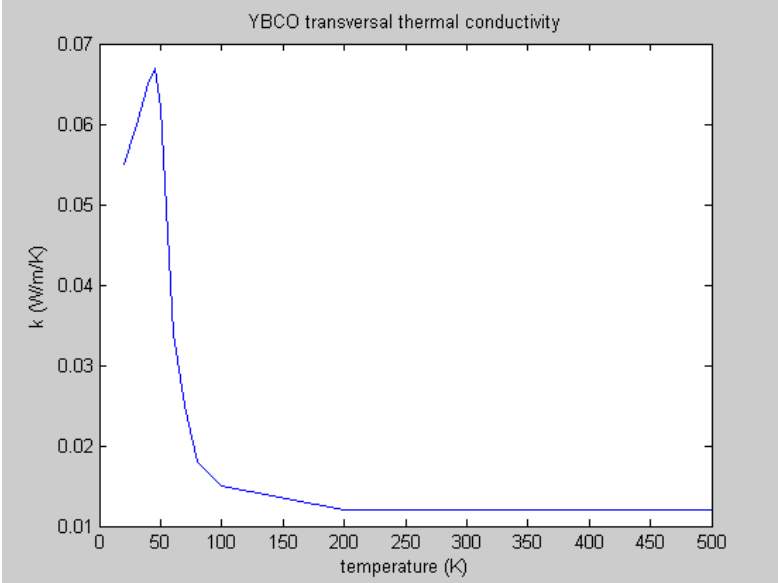

Appendix6: YBCO transversal thermal conductivity

Kapton thermal conductivity:

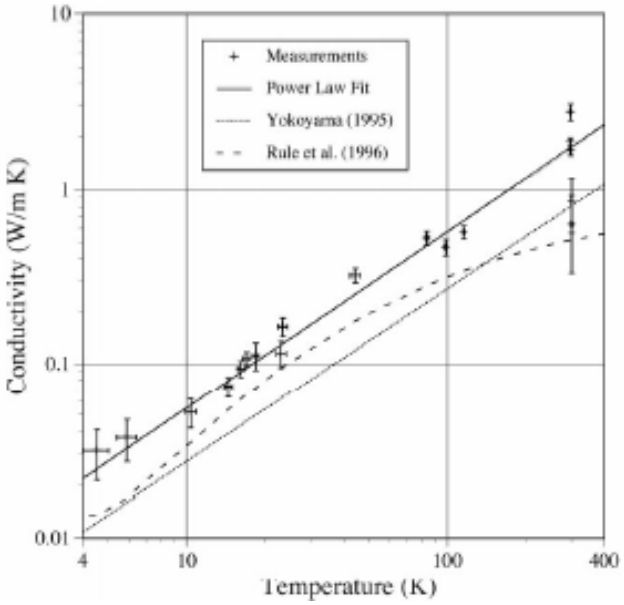

$$\kappa_{Kapton} = 5.24e-3\times T^{1.02}$$

Appendix7: Kapton thermal conductivity

Materials specific heat:

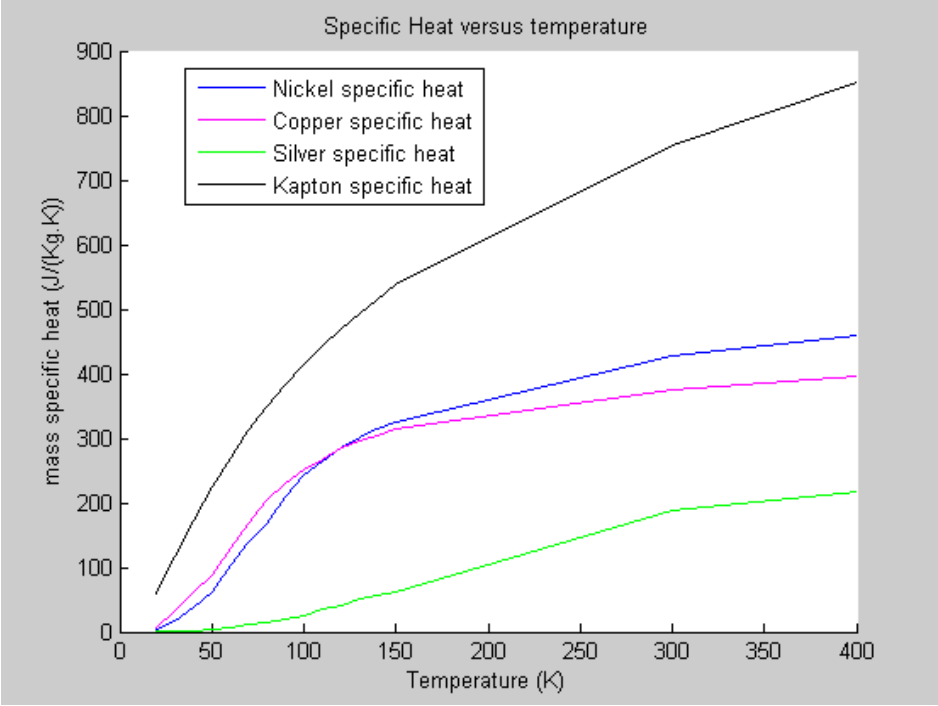

Appendix8: Each wire component specific heat

Development of Quench Propagation Models for Coated Conductors

Philippe J. Masson, *Member, IEEE,* Vincent R. Rouault, Guillaume Hoffmann, and Cesar A. Luongo, *Senior Member, IEEE*

***Abstract*—Due to their intrinsic thermal properties that lead to very slow heat diffusion, coated conductors are very difficult to protect against thermal instabilities and quench. This is particularly critical as the device increases in size and stored energy. Many experiments showing low quench propagation speeds and surface voltage distributions have identified the problem but, as of today, no models are available to perform high fidelity simulation of the quench process in a single tape, or in a full device. YBCO tapes are very promising conductors that would allow the development of high power density power devices such as generators and motors operating at liquid nitrogen temperature. The Department of Defense through the Air Force Research Laboratory launched a new project aiming at simulating quench propagation in YBCO tapes. The first step of the project deals with the understanding of the current diffusion in the different layers forming the tape. Experimental data on normal propagation zone (NZP) velocities and fault current limiters using this material show that the quench is most likely a 3-D phenomenon involving many non trivial physical phenomena. Experimental data will help to understand the physics of the quench and develop a local electromagnetic/thermal model of YBCO tapes. This paper presents the preliminary results of this work including a discussion of the physics of current sharing between layers. We will evaluate different commercial codes and present a simplified 3-D homogenized model applicable to a racetrack coil.**

***Index Terms*—Coated conductors, HTS, minimum quench energy, quench simulation.**

I. Introduction

SECOND generation high temperature superconductors (HTS) are now very close to be commercially available and large magnets will be tested very soon, as part of the Air Force research effort. Coated conductors exhibit very good performances in terms of current density magnitude and dependence to magnetic field even when operating at fairly high temperatures between 65 and 77 K. This temperature range is of high interest as the required cooling system can be reduced to a very small fraction of the device weight. Unfortunately, in this temperature range of interest, thermal properties of coated conductors are so that if a hot spot is generated, it will propagate very slowly, if at all, and therefore generate a very high local temperature while no significant voltage increase is measurable across the coil. Hence, a destructive hot spot can occur undetected. As an attempt to address this problem, the Air Force Research Laboratory (AFRL) is funding a new project at Florida A&M University aiming at investigating the physics of quench propagation in coated conductors and at developing a simulation tools that would help design magnets and develop quench detection and protection schemes.

The project is carried out following two parallel thrusts, one being the simulation of quench propagation in a tape including investigation of multiple physical phenomena of importance. Indeed, in addition to the influence of contact resistances between layers, Hall Effect, capacitor effects, and short time scale phenomena will be investigated to generate a local model of current distribution during a quench. The second task deals with the development of a global simulation tool able to simulate a quench at the device level and based on the identified local physics. This paper deals with the results generated by the first version of the global model. The physics taken into account consist of electro-thermal interactions in non-linear, temperature-dependent materials. A HTS racetrack coils has been modeled in different FEA software, only COMSOL Multiphysics was found to be flexible enough to simply implement the model and to show promising results.

II. Conductor Configuration and Physical Properties

A. Conductor Topology

The superconducting tape considered for the simulation is a generic multi-layer configuration as shown in Fig. 1. The substrate is composed of nickel alloy on which is deposited a very thin buffer layer. The YBCO layer is only a few microns thick and is connected to a stabilizer copper layer through silver.

B. Equivalent Electrical Characteristics

Based on the multilayer configuration of Fig. 1, an equivalent electrical resistance for the tape can be calculated. In the case of the presented study, current sharing is assumed to take place as soon as the YBCO layer, carrying all the current, becomes more resistive than the other layers. The transversal electrical resistances noted for example "$\mathrm{r_{YBCO}} + \mathrm{r_{Ni}}$" in Fig. 2, play an important role at short timescales that are not relevant to the proposed homogenized simulation. Therefore, the global simulation assumes the current to share based on the longitudinal values of the resistances of each layer and will not capture small time constant phenomena. Moreover, each turn of the coil is assumed to be perfectly electrically insulated using kapton film and no current can go directly from one layer to another. The

Manuscript received August 28, 2007. This work was supported by the Department of Defense through the Air Force Research Laboratory and Universal Technology Corporation. When the presented work was done, V. R. Rouault and G. Hoffmann were visiting from the ENSEM-INPL, Nancy, France.

The authors are with the FAMU-FSU College of Engineering and the Center for Advanced Power Systems, Tallahassee, FL 32310 USA (e-mail: masson@caps.fsu.edu).

Color versions of one or more of the figures in this paper are available online at http://ieeexplore.ieee.org.

Digital Object Identifier 10.1109/TASC.2008.921260

1051-8223/$25.00 © 2008 IEEE

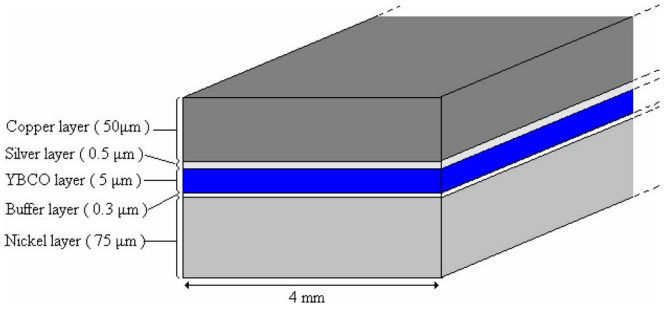

Fig. 1. Coated conductor topology (not to scale).

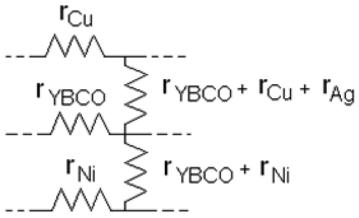

Fig. 2. Equivalent lumped parameter electrical circuit.

equivalent resistance along the tape can be calculated using a lumped-parameter equivalent circuit as shown in Fig. 2.

The homogenized electrical resistance can then be calculated as follows.

$$R_N = \frac{\prod_{i=1}^{N} R_i}{\sum_{j=1}^{N}\left(\prod_{k\neq j} R_k\right)} \tag{1}$$

The resistivity of YBCO is calculated using the following equations [1].

$$R_{YBCO} = \frac{E_c}{J_{c0}(\sigma,T)\frac{B_0}{|B|+B_0}}\left(\frac{J}{J_{c0}(\sigma,T)\frac{B_0}{|B|+B_0}}\right)^{n(T,B)}$$
$$J_{c0}(T) = \alpha\left(1-\frac{T}{T_{c0}}\right)^{\beta} \tag{2}$$

Where $\mathrm{T_{c0}}$ is the critical temperature at zero field, $\mathrm{E_c}$ is the critical electric field defining the critical current density, σ represents mechanical stress, α, β and $\mathrm{B_0}$ are constants determined experimentally. The resistivity of each material is temperature dependent. The equivalent electric resistance of the coils as a function of temperature at $\mathrm{I/I_c} = 0.6$ and 2 T is shown in Fig. 3.

C. Equivalent Thermal Characteristics

The proposed simulation tool is based on a global homogenized model in which the winding is represented by anisotropic conductivities and heat capacity is averaged.

1) Thermal Conductivity: Due to their multi-layer configuration, coated conductors present a very anisotropic thermal conductivity. It can be calculated using the same approach as

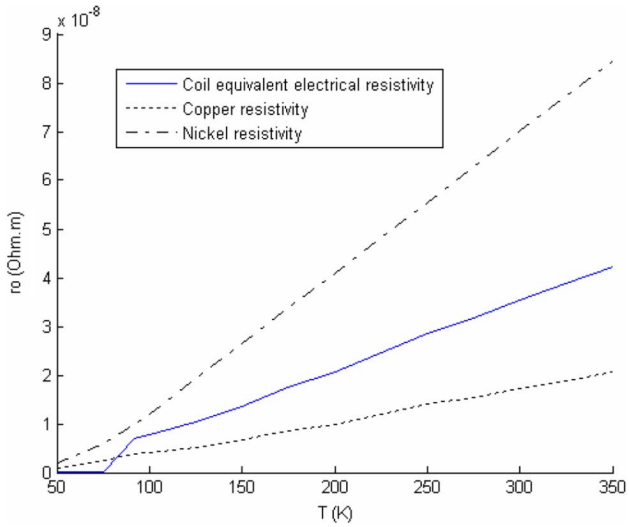

Fig. 3. Coil equivalent electrical resistivity vs. temperature for operation at $0.6 * \mathrm{Ic}$.

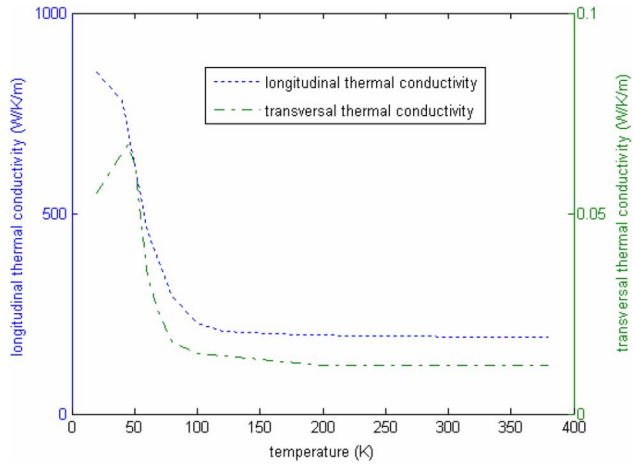

Fig. 4. Coil equivalent thermal conductivity.

used for the electrical conductivity applied to the configuration of Fig. 1, leading to the plots of following figure (Fig. 4).

2) Specific Heat and Thermal Diffusivity: Equivalent specific heat can be determined as a function of temperature taking into account the material configuration of Fig. 1. As shown in Fig. 5, specific heat drops very fast at low temperature thus leading to very slow heat propagation in the material. This can be better seen through the thermal diffusivity $a = k/\rho.Cp$ (where k is the thermal conductivity, ρ is the mass volume and Cp is the mass specific heat), as shown in Fig. 6. Thermal diffusivity becomes orders of magnitude smaller above 77 K than at room temperature thus confirming that a hot spot cannot propagate and would see its temperature dangerously rise.

III. FEA Model Implementation

As a first step of this research projects, we had to find a piece of software able to handle the highly non-linear equations as well as multi-physics coupling. Two options were investigated; ANSOFT Maxwell-ePhysics and COMSOL Multiphysics. Only COMSOL FEA software was able to successfully couple the different physics involved in transient simulation and also to handle

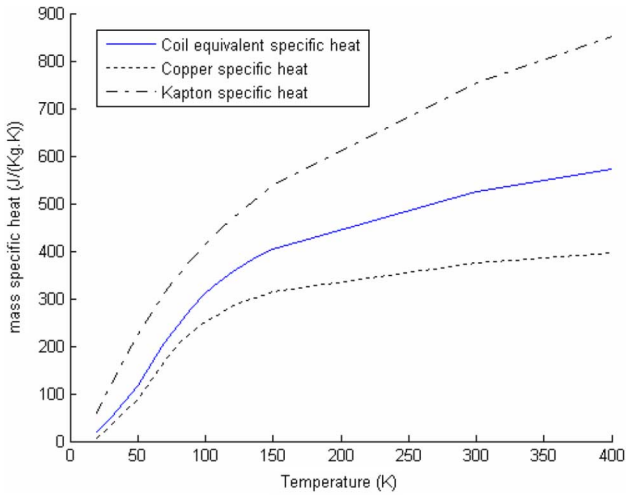

Fig. 5. Coil equivalent mass specific heat versus temperature.

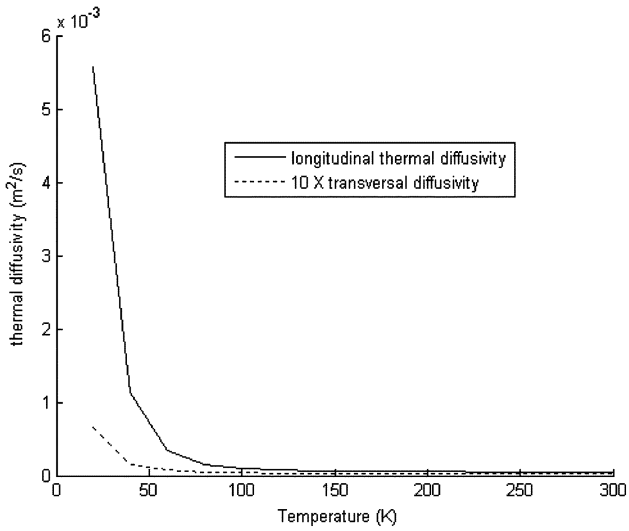

Fig. 6. Thermal diffusivity (estimated) vs. temperature.

the non-linear electrical characteristic. Therefore, all the simulation results presented in the next sections have been generated using COMSOL software.

A. Geometry and Cooling

As a test study for quench propagation, we have modeled a racetrack coil that is conduction cooled from the inside wall. This type of coil could be used, for example, in the rotor of a superconducting synchronous machine. A diagram of the coil is shown in Fig. 7.

B. Boundary Conditions and Sources

The coil has been designed for operation at 77 K and 60% of the critical current density. The conductor used for the design is a conventional stabilized commercial conductor exhibiting a current density of $1.5 * 108$ A/m^2 (at $0.6.J_c$, 2 T and 77 K). Cooling is done from the inside surface by conduction where the temperature is assumed constant at 77 K.

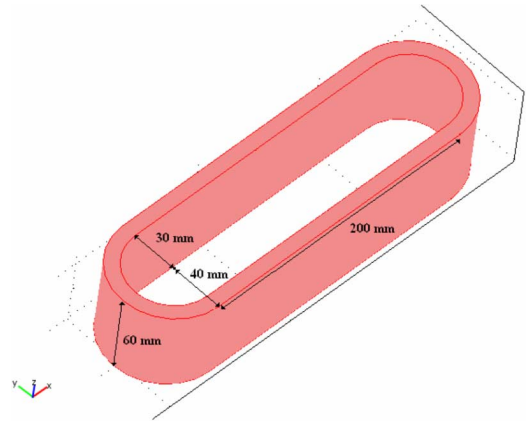

Fig. 7. Conduction cooled racetrack coil.

IV. Model Description

The problem has been approached as a coupling between heat transfer, non-linear electrical conductivity and magnetic flux density. The thermal equation leading to the quench propagation is the following.

$$C_p(T).\frac{\partial T}{\partial t} = div\left(\overline{\overline{\Lambda}}(T).\vec{\nabla}(T)\right) + P(T,B) \qquad (3)$$

With $\overline{\overline{\Lambda}} =$ thermal conductivity tensor;

$$\overline{\overline{\Lambda}} = \begin{pmatrix} \lambda_x(T) & 0 & 0 \\ 0 & \lambda_y(T) & 0 \\ 0 & 0 & \lambda_z(T) \end{pmatrix} \qquad (4)$$

λ_z is the longitudinal thermal conductivity and λ_x and λ_y the transversal thermal conductivities.

P represents the heat source coming form the product of the electrical field and the current density squared, it can therefore be considered as resistive losses that strongly depend on temperature and applied magnetic field.

V. Result and Discussion

The model described earlier allows for simulation of quench propagation in a coated conductor wound coil. The model is fully integrated and can be solved using the COMSOL Multiphysics coupling capability. Fig. 8 shows the state of propagation of a quench after 4 seconds. We can notice two hot spots located on each side of the heater in which temperature rose up to above 450 K. the quench is initiated from the surface of the coil through a heater able to input controllable energy levels.

A. Normal Zone Propagation Velocity

3D simulations allow for the determination of normal zone propagation (NZP) velocity for different temperatures. Fig. 9 shows propagation velocities in the range of a few centimeters per second, which is in good agreement with experimental results [1], [2]. The plots of Fig. 9 also show that a quench propagates much slower in the radial direction than along the conductors which lead to higher temperatures. Studies are ongoing

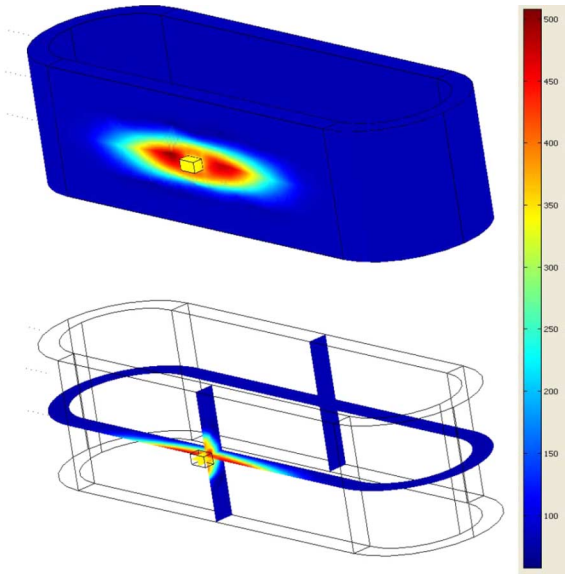

Fig. 8. Quench propagation in racetrack coil.

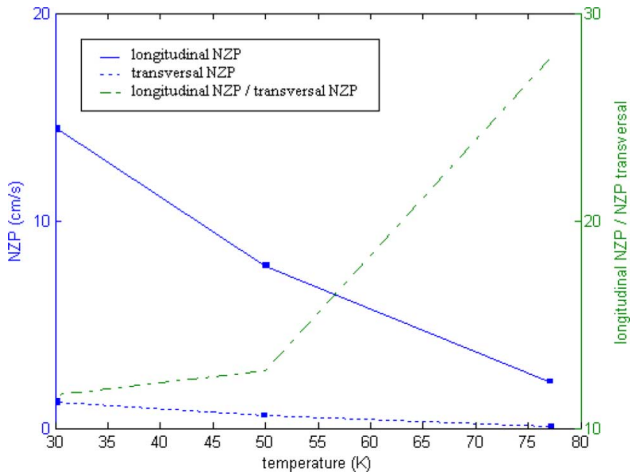

Fig. 9. NZP versus cooling temperature.

on the possibility of using good thermal conductors as electrical insulation between layers in order to make heat propagate faster between layers and then limit the hot spot temperature [3].

B. Quench Protection

As seen in experiments, the voltage increase due to a quench is not measurable before the quench has already spread and the temperature reached destructive values. Fig. 10 shows the simulated evolution of the voltage across the coil and that of the hot spot temperature versus time. A quench is initiated through a heater energized at 1 second. The curves of Fig. 10 clearly show the contribution of the heater up to 2 seconds when a runaway occurs. When the temperature reached 350 K, voltage has increased of only 0.3 mV which is not easily measurable in a noisy environment. In the simulated case (Fig. 8), the hot spots are very local and have spread to only a few centimeters when temperature has risen to a level at which YBCO can be damaged.

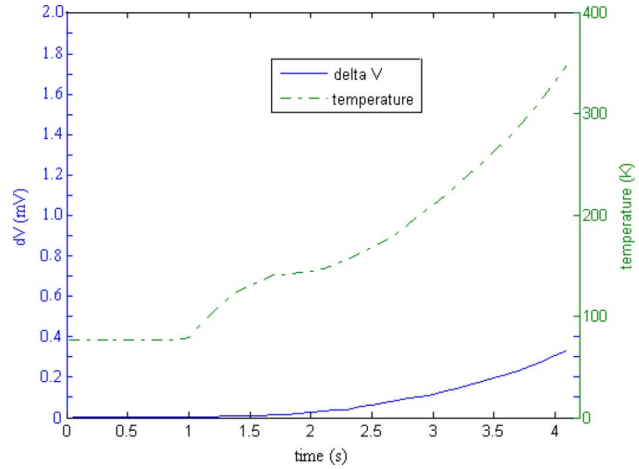

Fig. 10. Voltage across the coil and temperature evolution during a quench at 77 K and $0.6 * \mathrm{Ic}$.

VI. Conclusions and Future Work

The use of HTS magnets using second generation conductors is very promising but also very problematic as quench becomes undetectable when the operating temperature is in the 65–77 K range. The integrated model implemented in COMSOL Multiphysics allows for the simulation of quench in large coils. Results in terms of normal zone propagation velocity and hot spot temperature are in good agreement with experimental results reported in [1]. Previous comparable modeling efforts have been performed for low temperature superconductors [4] in which a 1-D current sharing model could effectively represent the quench. The presented work is the first task of a research program aiming at understanding the physics of quench propagation in which thermal stress, delamination, charge accumulations and other phenomena are expected to play an important role. Future work includes the study of current redistribution at the tape level and will try and capture the small time scale events occurring during a quench. Contact resistances between layers will modify the current sharing length. Thermal stress is very likely to affect J_c locally at the edges of the quench thus contributing to modifying the propagation velocity. In large magnets, current sharing can also be affected by non uniform charge distribution stemming from Hall Effect or capacitor effect. Due to the high aspect ratio of the geometry, considerable computing power is needed to perform a 3-D quench simulation in a tape, however, new features of COMSOL Multiphysics allows for generation of assembly meshes thus making the resolution feasible. Once a high fidelity simulation tool is available, detection and protection schemes will be investigated.

References

[1] X. Wang *et al.*, "Normal zone initiation and propagation in Y-Ba-Cu-O coated conductors with Cu stabilizer," *IEEE Trans. Appl. Supercond.*, vol. 15, no. 2, pp. 2586–2589, 2005.
[2] A. Ishiyama *et al.*, "Normal transition and propagation characteristics of YBCO tape," *IEEE Trans. Appl. Supercond.*, vol. 15, no. 2, pp. 1659–1662, 2005.
[3] C. E. Oberly, "Improved dielectric material for passive quench protection of superconductor operating near 77 k," in *CHATS 06*, Berkeley, CA, Sep. 5–7, 2006.
[4] S. Caspi *et al.*, "Calculating quench propagation with ANSYS," *IEEE Trans. Appl. Supercond.*, vol. 13, no. 2, pp. 1714–1717, Jun. 2003.

SPONSORED BY THE AIR FORCE RESEARCH LABORATORY / UTC

Development of Quench Propagation Models for Coated Conductors

Dr. Philippe Masson, Dr. Wan Kan Chan
Ms. Makita Phillips
Prof. Cesar Luongo, Prof. Justin Schwartz

Year 1 Project Review

October 3rd, 2008

Motivation

- New Air Force applications require high power density systems

- HTS materials can provide desired power density, but size of cooling system has to decrease
- Operation at temperatures near 77K would lead to manageable cooling systems
- In the temperature range of interest, quench detection and protection becomes problematic
- Understanding the physics of quench propagation and developing simulation tool is paramount to the future of 2nd generation wound HTS magnets

Project Objectives

- 3 year project sponsored by AFRL

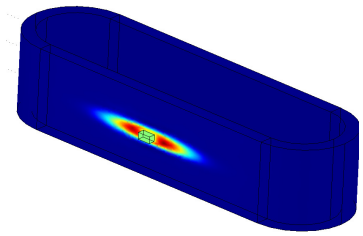

- Objectives:
  - Understand current re-distribution during quench in coated conductors
  - **Develop tool to simulate quench propagation in coated conductors**
  - Simulate quench propagation in coils
  - Investigate passive and active quench protection schemes

Develop next generation of "QUENCH" for HTS coils

The Problem: Quench and Stored Energy

- The magnetic energy stored in the field:

$$E_m = \int_V \frac{B^2}{2\ 0} dv = \frac{1}{2} LI^2$$

is converted to heat through Joule heating RI^2. ***If this process happened uniformly*** in the winding pack:

  - Cu melting temperature 1356 K
  - corresponding E_m=5.2 10^9 J/m^3

limit would be $B_{max} \leq 115$ T: NO PROBLEM !

BUT

The process does not happen uniformly

- As little as 1 % of the coil mass can absorb all the energy → Destruction if unprotected

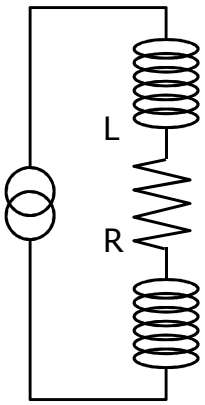

From Luca Bottura, 2002

Quench in Superconductors

Quench is an irreversible transition from superconducting to normal state.

Observed as a temperature increase that propagates along the conductor.

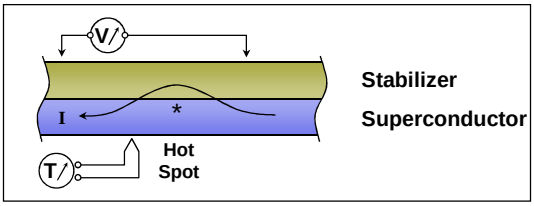

	Operating Temperature (K)	ΔT (K)	Normal Zone Propagation Velocity	Quench Modeling & Simulation	Quench Detection	Quench Experience Base
LTS						
$NbTc/Nb_3Sn$	4 - 8	< 1	High	1D/2D/3D OK	Easy	Huge
HTS						
BSCCO	20 - 35+	Several	Low	1D/2D OK?	Difficult	Small
YBCO	40 - 77+	Several	Very Low	3D Required?	Very Difficult	None

Courtesy Dr. Oberly, AFRL

Year 1
Summary and Accomplishments

Year 1 Task Plan

Work Description	M1 Jan '07	M2 Feb '07	M3 Mar '07	M4 Apr '07	M5 May '07	M6 Jun '07	M7 Jul '07	M8 Aug '07	M9 Sep '07	M10 Oct '07	M11 Nov '07	M12 Dec '07
Evaluate alternatives to proceed with model development FEA software evaluation				1								
Characterization of HTS conductors and other coil materials						2						
Preliminary model of a quenching HTS tape												4

Year 1

1-Jan-07 1-Jul-07 1-Jan-08

Milestone Description		
1	Evaluate alternatives to proceed with model development, what platform to use for a 3D model of HTS devices	1-Mar-07
2	Electrical, thermal and mechanical characterization of HTS conductors and other coil materials	1-Jun-07
4	Combined thermal/electrodynamic 3D model of a quenching HTS coil	1-Jan-08

- Milestone 3 was replaced by milestone 4:
  - Combined thermal/electrodynamic 3D model of a quenching coil
- All milestone were completed on schedule

Research Approach

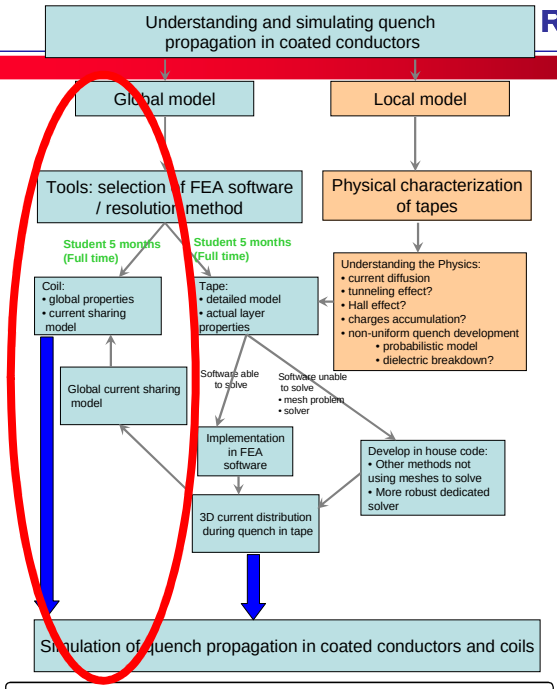

- Year 1 results deal with global simulation
- Conventional current sharing model
- Integrated electro-thermal model
- Physical characteristics depend on temperature

FEA Software selection

3 Options:

- Develop in-house code
  - Time consuming, not trivial problem to solve, would delay results
- Use existing codes
  - ANSOFT Maxwell – ePhysics
    - Allows for transient coupled electro-thermal-structural simulations
  - COMSOL Multiphysics
    - Very flexible tools, allows for coupling of any physics represented by PDEs.
- Other potential tools such as Flux3D (Cedrat) or ANSYS have been considered for cost reason

Superconductor model

- Magnetic model: $\vec{B} = {}_o \vec{H}$
- Electric model: $\vec{E} = (E,B)\,\vec{J}$

$$(E,B) = \frac{E_c}{J_c(B)}\left|E\right|^{\frac{n(B)-1}{n(B)}} + {}_o$$

Convergence reasons

$$\frac{1}{1000}\frac{E_c}{J_c} < {}_o < \frac{1}{100}\frac{E_c}{J_c}$$

Standart: $J_c(B) = J_{co}$; $n(B) = n_o$

$$J_c(B) = \frac{J_{co}}{1+\frac{|B|}{B_o}} \quad ; \quad n(B) = \frac{n_o}{1+\frac{|B|}{B_1}}$$

+ user subroutines

10

Evaluation of ANSOFT Package for Quench Simulation

- Maxwell and ePhysics are two separate pieces of software
  - Data exchanges through linked
- Simple anisotropic thermal problems could not be solved properly
- Non linear electrical conductivities cannot be implemented.

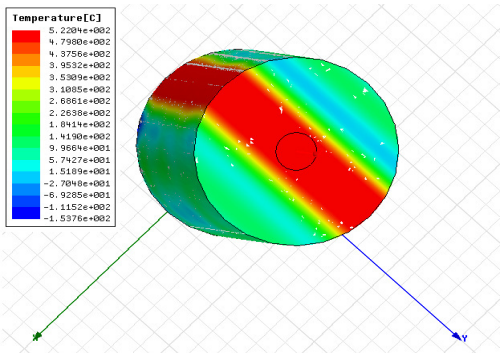

Simulation of Quench Propagation in Coated Conductors

FAMU Florida A&M University

Evaluation of Comsol Package for Quench Simulation

- Transient multiphysics problem is solved at once
- Thermal module enables simulating cooling system coupled with fluid dynamics
- The non-linear electrical conductivity representing the superconductor can be implemented as a function of temperature, B and stress
- Comsol is chosen to simulate quench propagation for this project

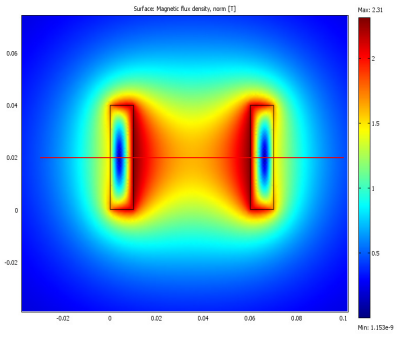

Simulation of Quench Propagation in Coated Conductors

FAMU Florida A&M University

Tape Configuration of Electrical Resistivity

$$R_{YBCO} = \frac{E_c}{J_{c0}(\ ,T)\frac{B_0}{|B|+B_0}}\left(\frac{J}{J_{c0}(\ ,T)\frac{B_0}{|B|+B_0}}\right)^{n(T,B)}$$

$$J_{c0}(T) = \left(1-\frac{T}{T_{c0}}\right)$$

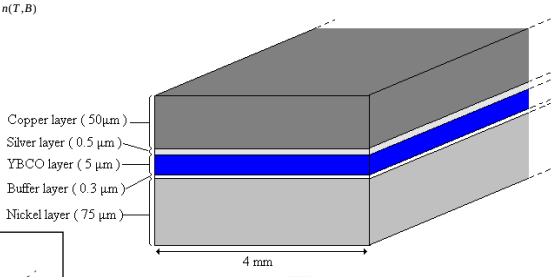

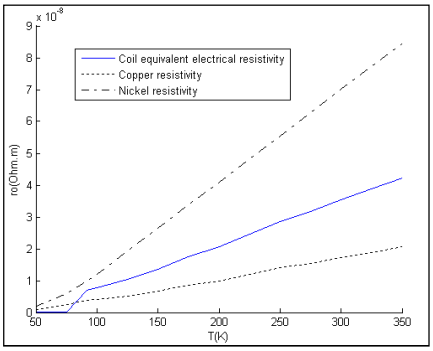

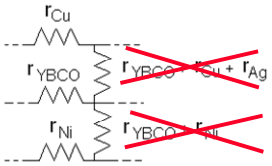

Simulation of Quench Propagation in Coated Conductors

Equivalent Thermal conductivity following theta

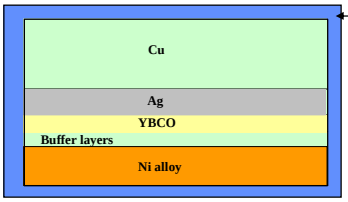

AFOSR Superconductivity Review

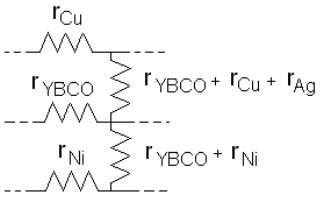

Equivalent lumped parameter circuit

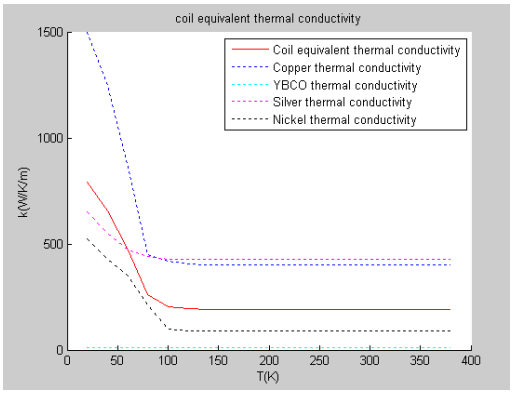

Simulation of Quench Propagation in Coated Conductors

Equivalent Thermal conductivity following r and z

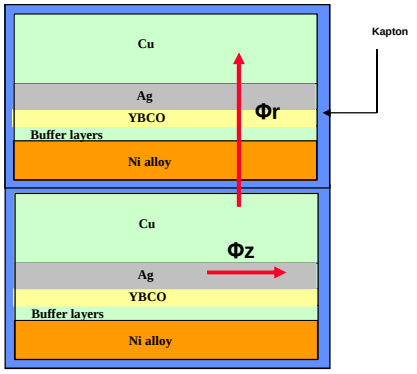

AFOSR Superconductivity Review

Following z

$$\Lambda_{YBCO} \ll \Lambda_{Kapton} \ll \Lambda_{equivalent_wire} \ll \Lambda_{other_Materials}$$

Thermal conductivity following r

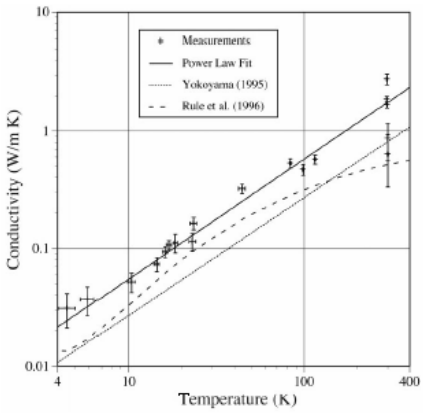

Source: Thermal conductivity of Kapton tape, Cryogenic 39 (1999), 93-95

Equivalent Specific heat

$$C_{coil} = \frac{\sum_{layers} C_{layer} . h_{layer}}{\sum_{layer} h_{layer}}$$

h= layer thickness

C_{layer}=layer specific heat

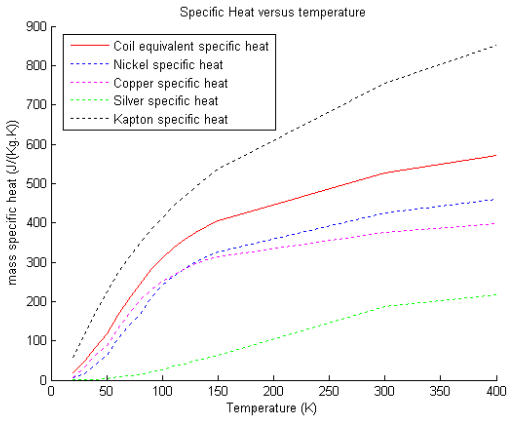

Thermal Properties of Winding

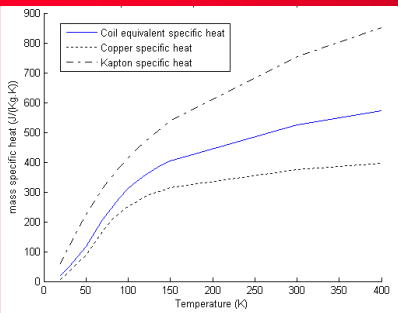

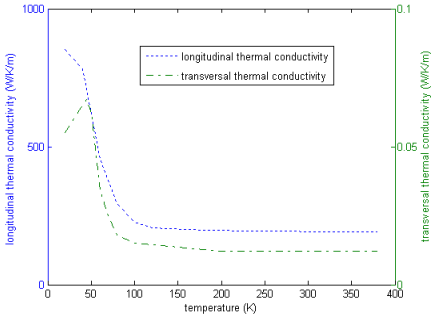

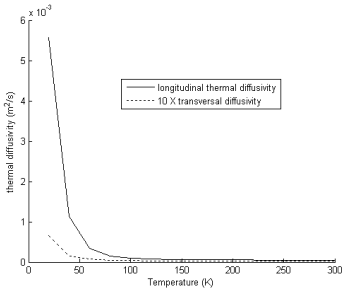

Very small thermal diffusivity at high temperature (>60 K)

Very slow heat propagation

Very high hot spot temperature

Coil Configuration and Boundary Conditions

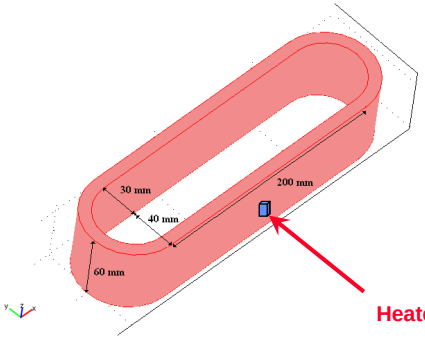

- **Conduction cooling at 77 K through inner surface**
- **J=0.6*Jc (2T, 77K)= 1.8*10^8 A/m^2**
- **Rest of the boundaries are considered adiabatic**

$$C_p(T).\frac{\partial T}{\partial t} = div(\overline{\overline{\Lambda}}(T).\vec{\nabla}(T)) + P(T,B)$$

$$\overline{\overline{\Lambda}} = \begin{pmatrix} k_x(T) & 0 & 0 \\ 0 & k_y(T) & 0 \\ 0 & 0 & k_z(T) \end{pmatrix}$$

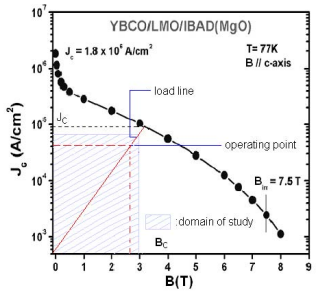

Graphical User Interface

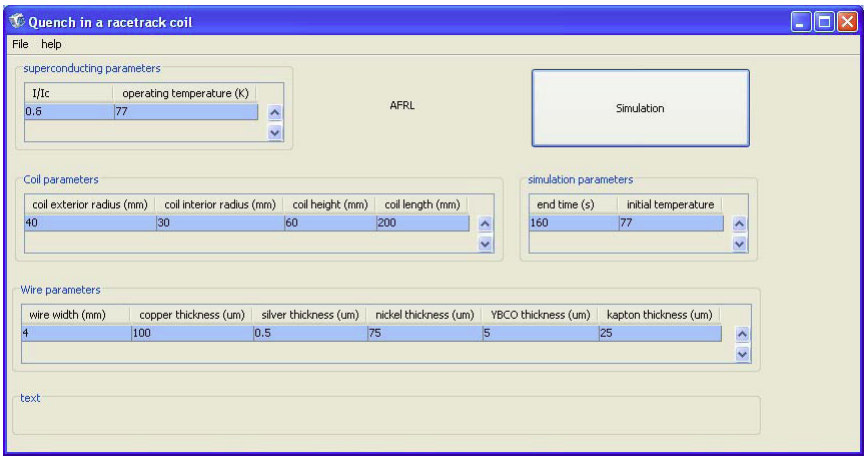

- Simple user interface
- Will be modified according to AFRL needs

Quench Propagation

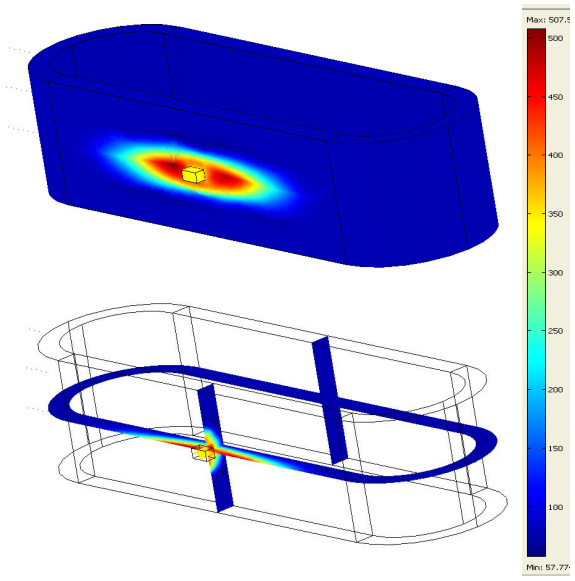

Normal Zone Propagation Velocity

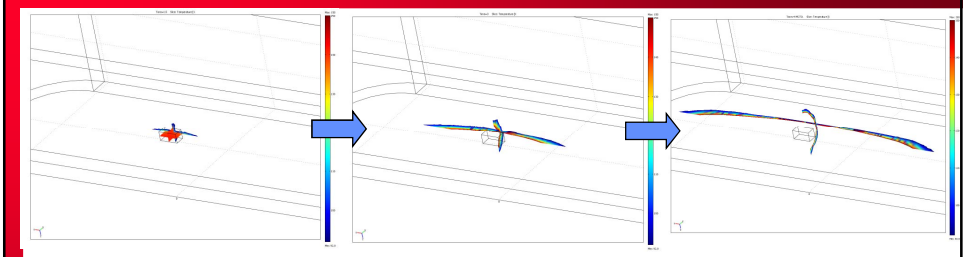

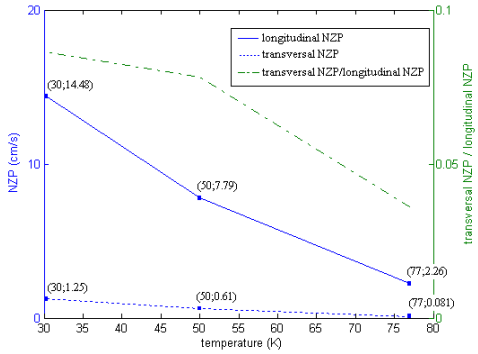

- NZP velocity is only a few cm/s
- NZP velocity decreases as temperature increases
- Simulated values in agreement with experimental data

Simulation of Quench Propagation in Coated Conductors

Global model validation longitudinal NZPV

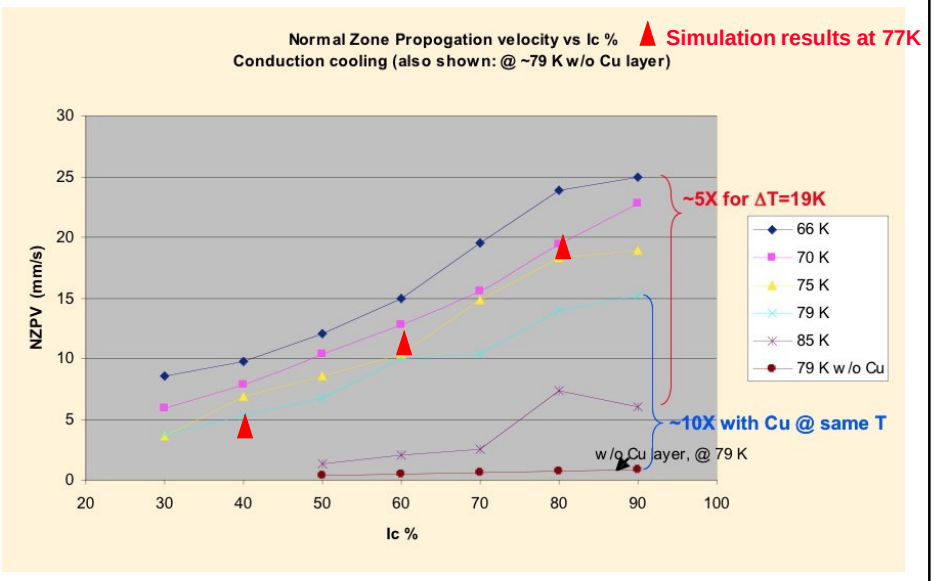

Simulation of Quench Propagation in Coated Conductors

Global model validation transverse NZPV

- Data from Prof. Justin Schwartz- FSU/NHMFL

Simulation results at 77K

In Turn#60, Longitudinal

Normal zone propagation velocity

$V_{criterion}$ = 5 mV

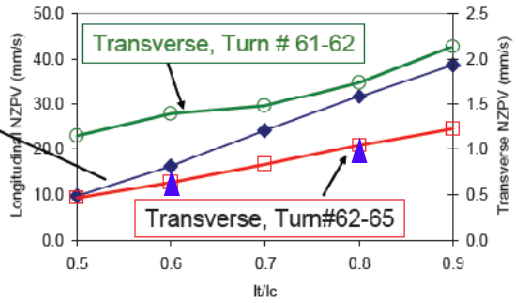

- Experimental coil is being modeled
- More simulation points are being generated
- Global model also validated for Bi2223 winding

Quench Detection and Protection

- @ 77 K, quench may be difficult to detect through voltage increase across the magnet

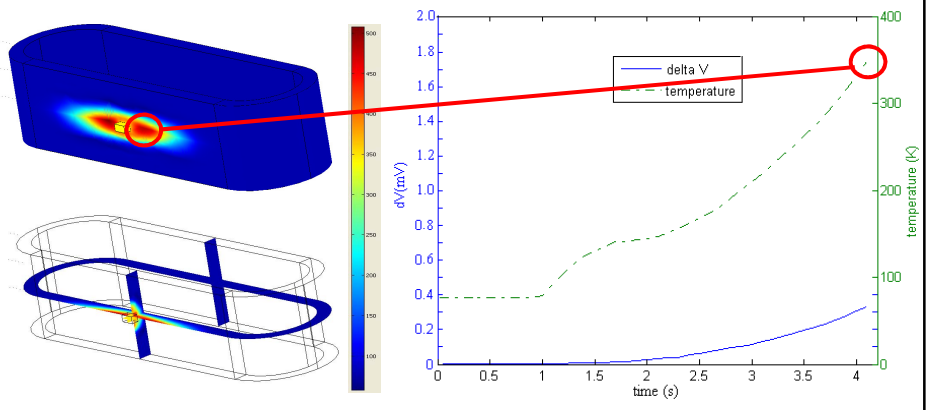

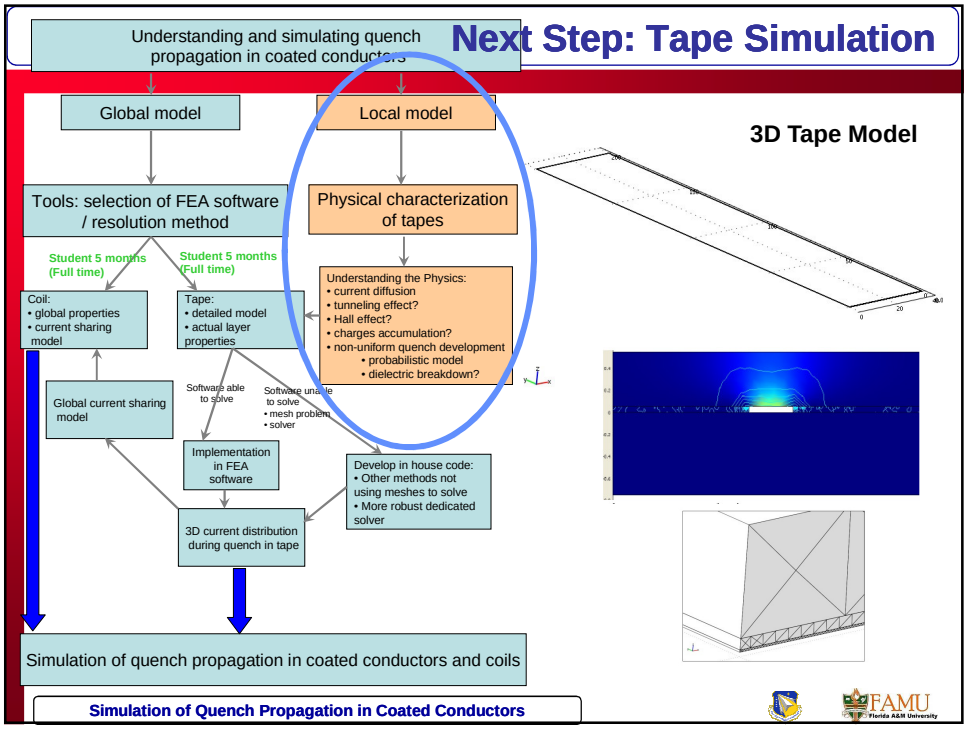
Next Step: Tape Simulation
Understanding and simulating quench propagation in coated conductors
Global model
Local model
3D Tape Model
Tools: selection of FEA software / resolution method
Physical characterization of tapes
Student 5 months (Full time)
Student 5 months (Full time)
Coil:
• global properties
• current sharing model
Tape:
• detailed model
• actual layer properties
Understanding the Physics:
• current diffusion
• tunneling effect?
• Hall effect?
• charges accumulation?
• non-uniform quench development
• probabilistic model
• dielectric breakdown?
Global current sharing model
Software able to solve
Software unable to solve
• mesh problem
• solver
Implementation in FEA software
Develop in house code:
• Other methods not using meshes to solve
• More robust dedicated solver
3D current distribution during quench in tape
Simulation of quench propagation in coated conductors and coils
Simulation of Quench Propagation in Coated Conductors
FAMU

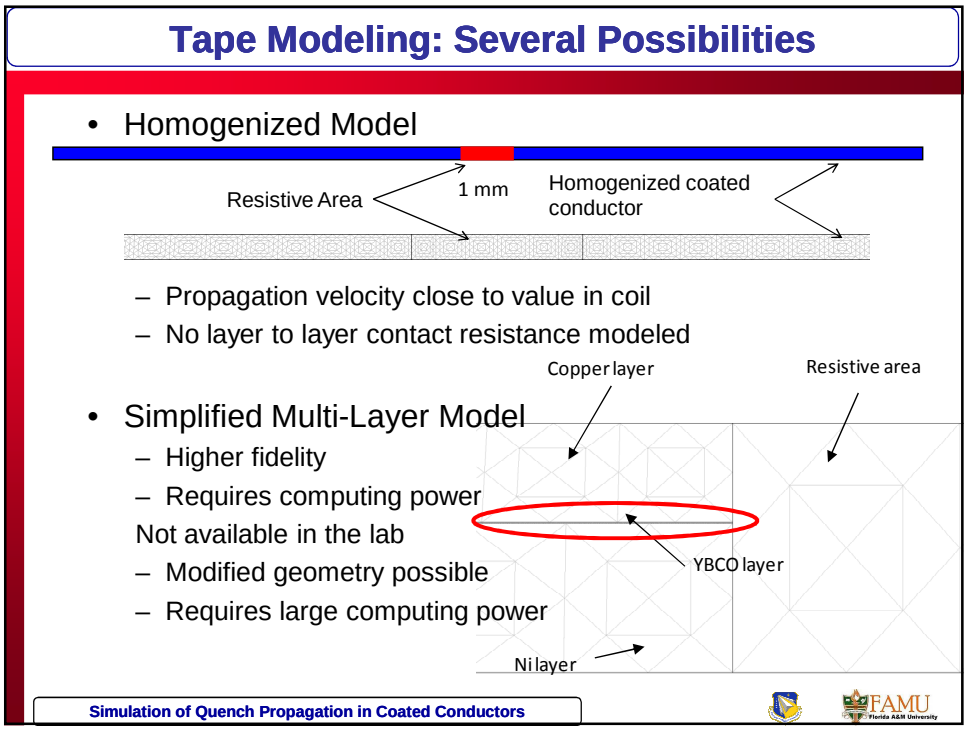
Tape Modeling: Several Possibilities
• Homogenized Model
Resistive Area
1 mm
Homogenized coated conductor
– Propagation velocity close to value in coil
– No layer to layer contact resistance modeled
• Simplified Multi-Layer Model
– Higher fidelity
– Requires computing power
Not available in the lab
– Modified geometry possible
– Requires large computing power
Copper layer
Resistive area
YBCO layer
Ni layer
Simulation of Quench Propagation in Coated Conductors
FAMU

Tape homogenized Model

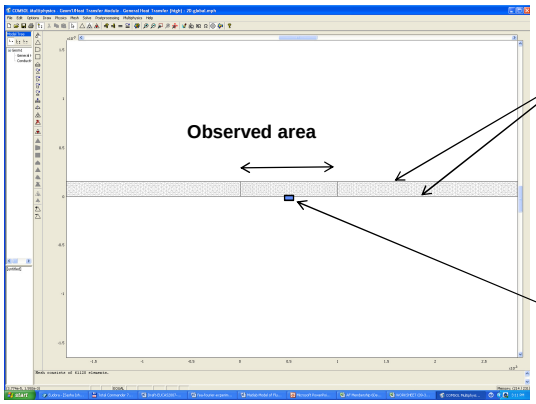

- Tape modeled with homogeneous equivalent properties
- No dependence on B was considered

Tape Simulation Results

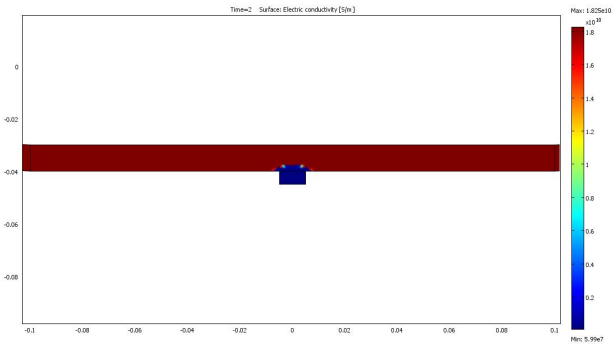

- Electrical conductivity shows quench propagation in tape

Tape Simulation Results

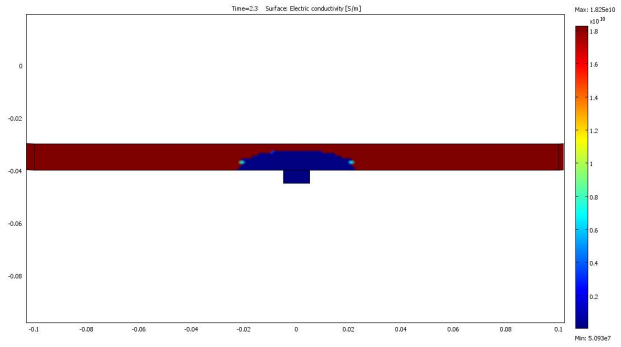

- Electrical conductivity shows quench propagation in tape

Tape Simulation Results

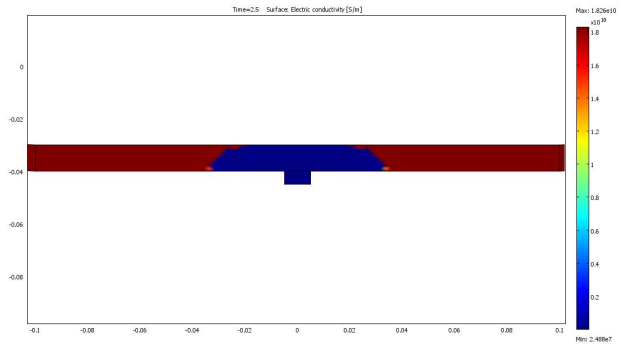

- Electrical conductivity shows quench propagation in tape

Tape Simulation Results

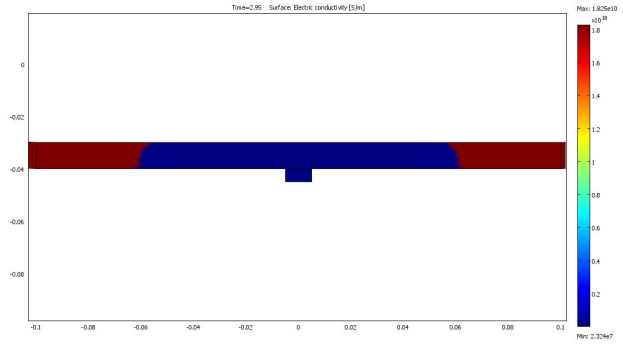

- Electrical conductivity shows quench propagation in tape

Normal Zone Propagation Velocity and Thermal Gradient

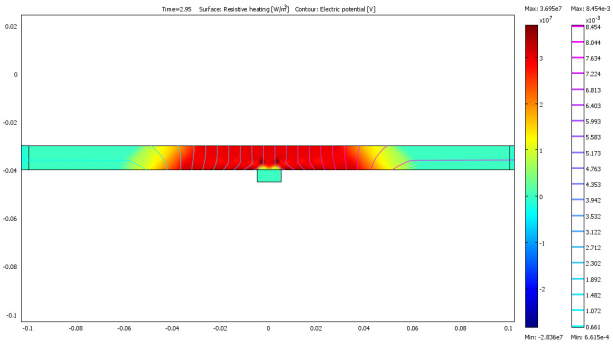

- Simulation shows a thermal gradient along the thickness of the tape
- Normal zone propagation velocity is 15 % larger than in coil simulation (as expected)

Magnetic Coupling and Current Distribution

- So far, all simulations included simplified model for the superconductor
- A detailed model was implemented to validate that Comsol can handle the non-linearity
- Magnetic shielding with and without thermal coupling were performed

Example: Geometry

- YBCO cylinder
- Cut perpendicular to c-axis

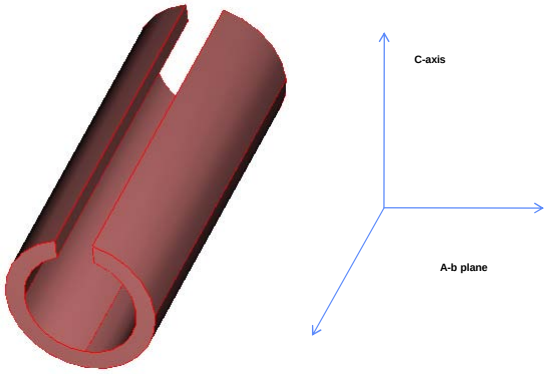

Example: FEA Model

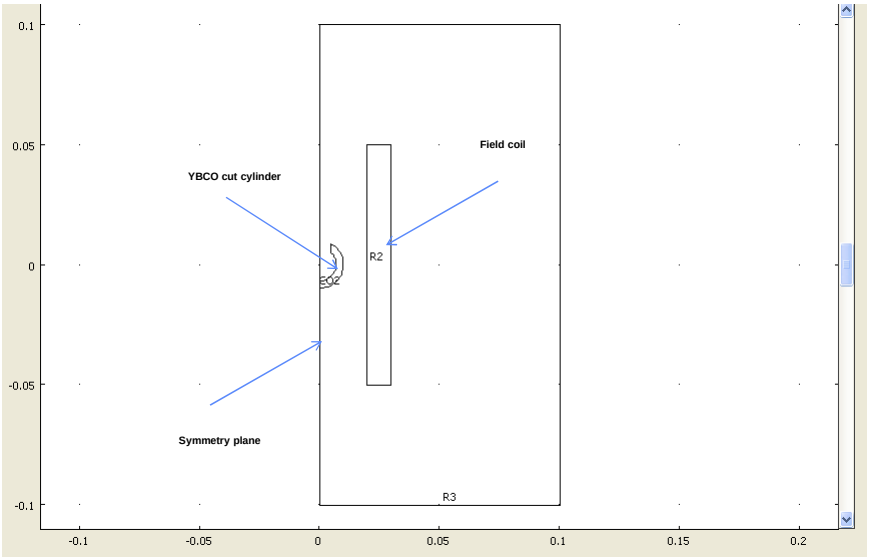

Superconductor Model

- E(J) n-power law

  (S/m)

$$= \frac{J_{c0}}{E_c}\left(1-\left(\frac{T}{T_c}\right)^2\right)^{\frac{3}{2}}\left(\frac{1}{1+\frac{B}{B_0}}\right)\left(\frac{E}{E_c}\right)^{\frac{1}{n}-1}$$

  - J_{c0}=1.89e9 A/m^2
  - T=77 K
  - Ec= 1e-4 V/m
  - B_0=1.3 T
  - Tc=92 K
- Model parameters from literature, can be modified

Current Distribution and Flux Density

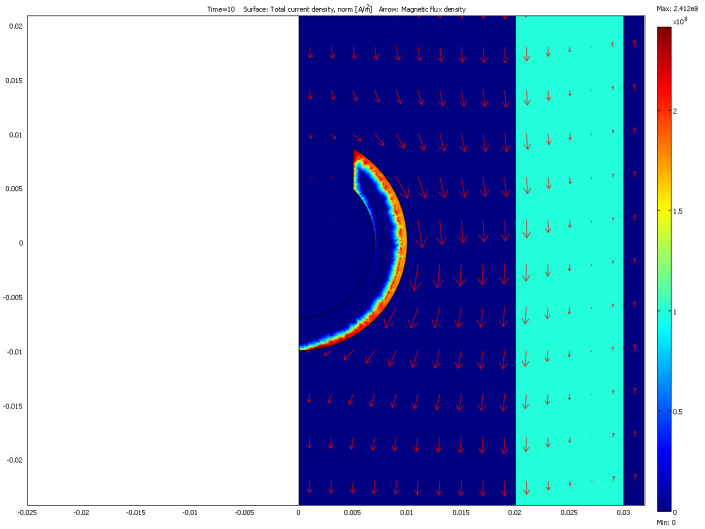

Simulation of Quench Propagation in Coated Conductors

Flux Density and Current Density

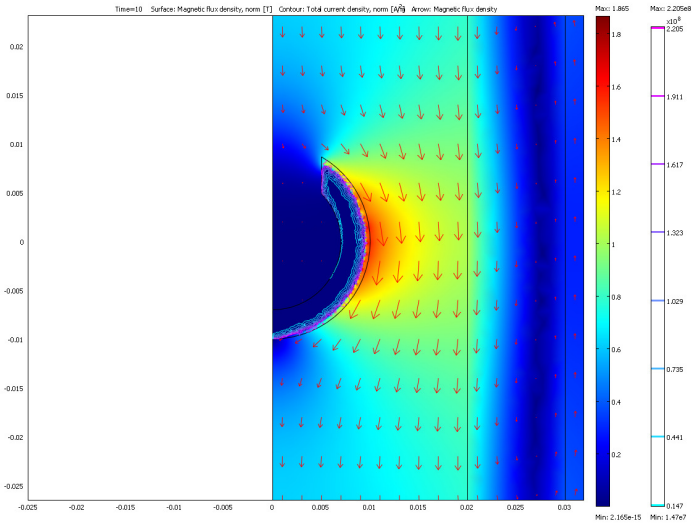

Simulation of Quench Propagation in Coated Conductors

Example 2: Trapped Flux Magnet

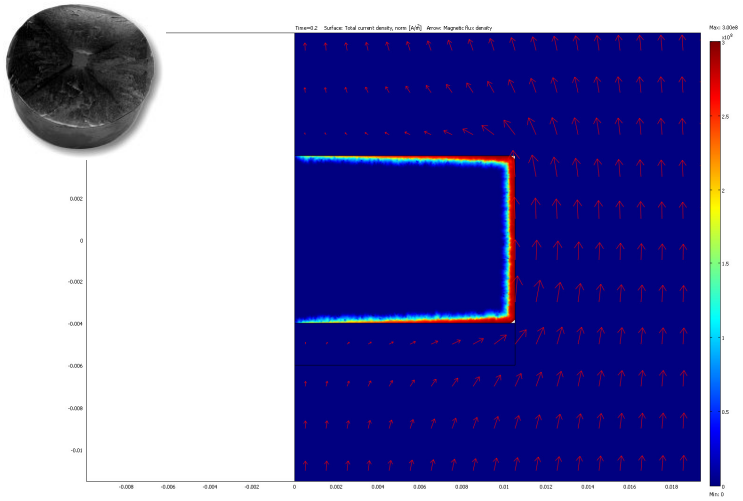

Simulation of Quench Propagation in Coated Conductors

Example 2: Trapped Flux Magnet

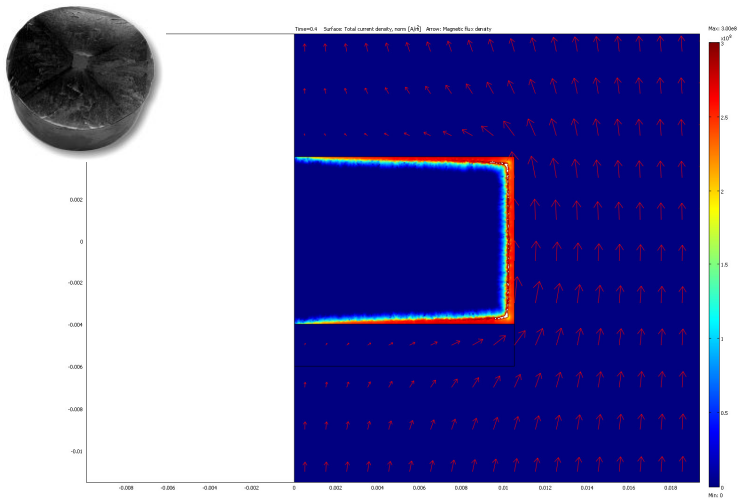

Simulation of Quench Propagation in Coated Conductors

Example 2: Trapped Flux Magnet

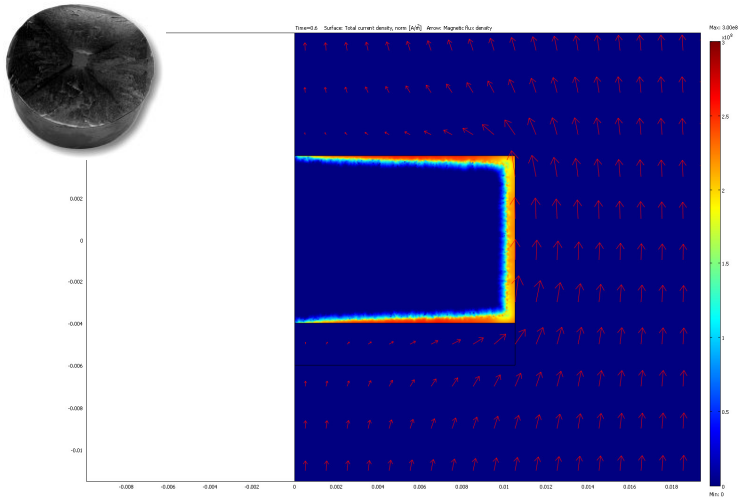

Simulation of Quench Propagation in Coated Conductors

Example 2: Trapped Flux Magnet

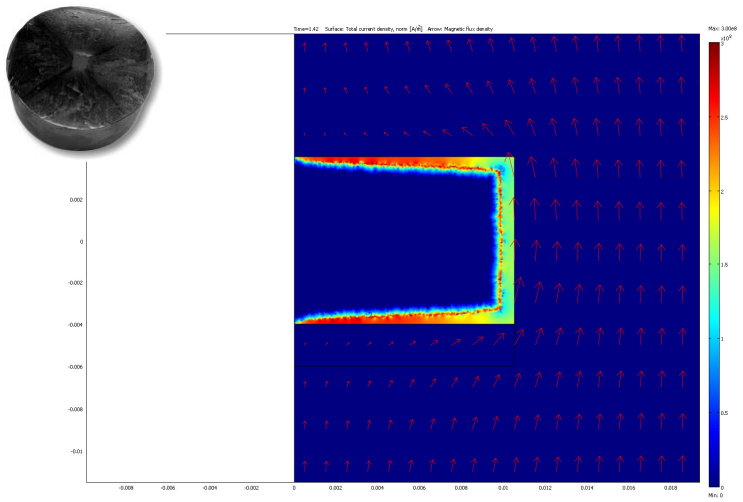

Simulation of Quench Propagation in Coated Conductors

Summary and Future Work

- Objectives of the research project
  - Develop simulation code for quench propagation in HTS conductors
  - Develop an engineering design tool to help design and protect HTS magnets
- First phase of the project completed
  - Coupled 3D simulations using global model
  - Good agreement with experimental data
  - Comsol is the right tool
- Future work
  - Get access to large computing power (FSU, AFRL?)
  - Increase fidelity by adding other physics to the model
  - Compare to experimental results performed on tapes
  - Explore possibility of using real time models as a detection/protection scheme
- Education
  - Training one minority graduate student (MS, ME expected 2009)

Presentations and Publications

- Publications
  - Philippe J. Masson, Guillaume Hoffmann, Vincent Rouault, Cesar A. Luongo, "***Development of Quench Propagation Models for Coated Conductors***", '', I.E.E.E. Transactions on Applied Superconductivity, Vol. 18, No 2, June 2008, pp1321-1324
- Presentations
  - AFOSR Superconductivity Program Review, "***Progress on Quench Simulation in Coated Conductors***", San Francisco. CA, March 28th, 2008
  - Workshop on Collaborative University Research for More Electric Aircraft Technologies and Thermal Energy Management, "***Quench Propagation Models for Coated Conductors***", Tallahassee, FL, March 5th, 2008
  - AFRL HBCU Review and Research Seminar, "***3D simulation of quench propagation in coated conductors***", Dayton, OH, Oct. 2-3, 2007
  - AFOSR Superconductivity Program Review, "***Progress on Quench Simulation in Coated Conductors***", San Francisco. CA, April 13-14, 2007

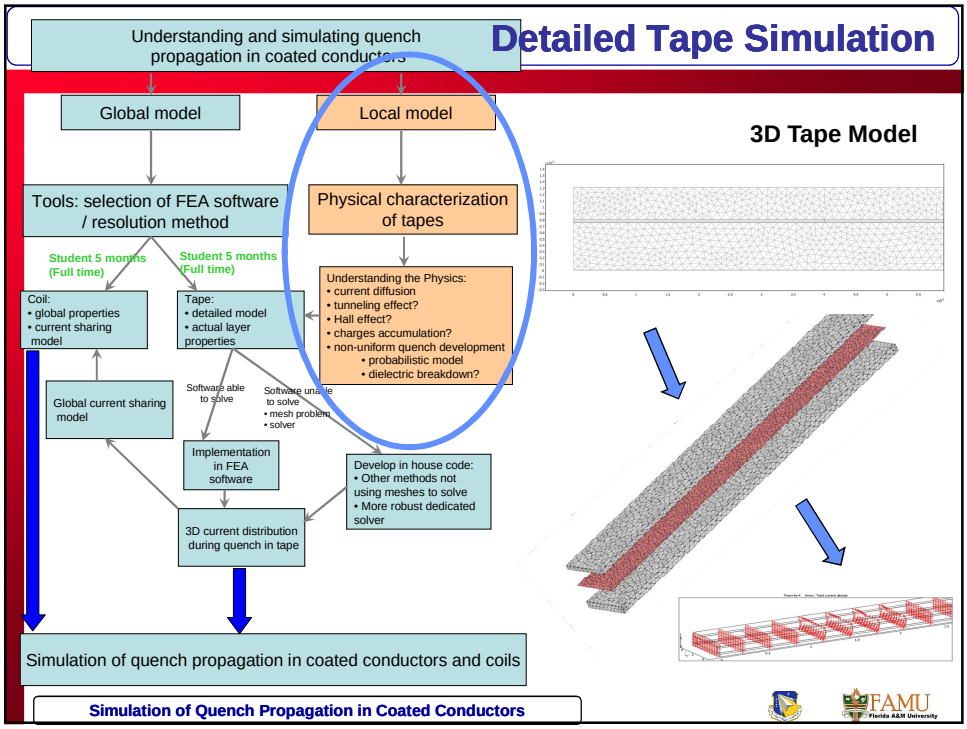
Detailed Tape Simulation
Understanding and simulating quench propagation in coated conductors
Global model
Local model
Tools: selection of FEA software / resolution method
Physical characterization of tapes
Student 5 months (Full time)
Student 5 months (Full time)
Coil:
• global properties
• current sharing model
Tape:
• detailed model
• actual layer properties
Understanding the Physics:
• current diffusion
• tunneling effect?
• Hall effect?
• charges accumulation?
• non-uniform quench development
• probabilistic model
• dielectric breakdown?
Global current sharing model
Software able to solve
Software unable to solve
• mesh problem
• solver
Implementation in FEA software
Develop in house code:
• Other methods not using meshes to solve
• More robust dedicated solver
3D current distribution during quench in tape
Simulation of quench propagation in coated conductors and coils
3D Tape Model
Simulation of Quench Propagation in Coated Conductors
FAMU
Florida A&M University